Etude 'in-situ' et en laboratoire sur le comportement dynamique des matériaux constitutifs des plateformes ferroviaires classiques dans le contexte d'augmentation du trafic

Francisco Lamas-Lopez

HAL Id: tel-01425466

https://pastel.hal.science/tel-01425466

Submitted on 3 Jan 2017

Thèse présentée pour obtenir le grade de

Docteur de l'Université Paris-Est

Spécialité : Géotechnique

par

Francisco LAMAS-LOPEZ

Ecole Doctorale : Sciences, Ingénierie et Environnement

Etude 'in-situ' et en laboratoire sur le comportement dynamique des matériaux constitutifs des plateformes ferroviaires classiques dans le contexte d'augmentation du trafic

Thèse soutenue publiquement à Champs-sur-Marne le 15 Avril 2016

JURY

Antonio Gomes Correia	Président	Universidade do Minho
Geert Degrande	Rapporteur	KU Leuven
Pierre Breul	Rapporteur	Université Blaise Pascal
Pedro Alves Costa	Examinateur	Universidade do Porto
Jean-François Semblat	Examinateur	IFSTTAR
Jean-Claude Dupla	Examinateur	Ecole des Ponts ParisTech
Nicolas Calon	Examinateur	SNCF
Yu-Jun Cui	Directeur de Thèse	Ecole des Ponts ParisTech

Invités :

Sofia Costa D'Aguiar (SNCF), Jean Canou (ENPC), Anh-Minh Tang (ENPC),
Alain Robinet (SNCF), Gilles Saussine (SNCF)

Dissertation presented for the degree of

Doctor of Philosophy from Université Paris-Est
Field: Geotechnical Engineering

by

Francisco LAMAS-LOPEZ

Doctoral School: Science, Engineering and Environment

Field and laboratory investigation on the dynamic behaviour of conventional railway track-bed materials in the context of traffic upgrade

PhD Viva: April 15th 2016

JURY

Antonio Gomes Correia	President	Universidade do Minho
Geert Degrande	Referee	KU Leuven
Pierre Breul	Referee	Université Blaise Pascal
Pedro Alves Costa	Examiner	Universidade do Porto
Jean-François Semblat	Examiner	IFSTTAR
Jean-Claude Dupla	Examiner	Ecole des Ponts ParisTech
Nicolas Calon	Examiner	SNCF
Yu-Jun Cui	PhD Supervisor	Ecole des Ponts ParisTech

Guests of honour:

Sofia Costa D'Aguiar (SNCF), Jean Canou (ENPC), Anh-Minh Tang (ENPC), Alain Robinet (SNCF), Gilles Saussine (SNCF)

« Les rodomontades espagnoles certes elles surpassent toutes les autres, de quelque nation que ce soit; d'autant qu'il faut confesser la nation espagnole brave, bravache et valeureuse, et fort prompte d'esprit, et de belles paroles proférées à l'improviste »

Pierre de Bourdeille, Seigneur de Brantôme (1537-1614)
Rodomontades et jurements des Espagnols

« La verdad de ninguna cosa tiene vergüenza sino de estar escondida »

Félix Lope de Vega y Carpio (1562-1635)

A mi abuelo Francisco López Gómez
Un granadino ejemplar con un enorme corazón

ACKNOWLEDGEMENTS

PUBLICATIONS

Journal papers

1. Cui, Y-J., **Lamas-Lopez, F.**, Trinh, V. N., Calon, N., D'Aguiar, S. C., Dupla, J.-C., Tang, A. M., Canou, J., and Robinet, A., 2014. Investigation of interlayer soil behaviour by field monitoring. Transportation Geotechnics, Elsevier Ltd, 1(3), 91–105.

2. **Lamas-Lopez, F.**, Cui, Y-J., Calon, N., Costa D'Aguiar, S., 2016. Geotechnical auscultation of a French conventional railway track-bed for maintenance purposes. Soils and Foundations. Vol. 56-2. April 2016.

3. **Lamas-Lopez, F.**, Cui, Y-J., Calon, N., Costa D'Aguiar, S., Peixoto de Oliveira, M., Zhang, T., 2016.Track-bed mechanical behaviour under the impact of train at different speeds. Soils and Foundations. Vol. 56-4. August 2016.

4. **Lamas-Lopez, F.**, Cui, Y.J., Calon, N., Robinet, A., Dupla, J.C., Costa D'Aguiar, S., Tang, A-M., Canou, J., 2016. Field monitoring of the mechanical behavior of a French conventional railway track. Submitted to 'Soils and Foundations'

5. **Lamas-Lopez, F.**, Cui, Y-J., Calon, N., Costa D'Aguiar, S., 2016. Assessment of integration method for displacement determination using field accelerometer and geophone data. Submitted to 'Journal of Zhejiang University-SCIENCE A'

6. **Lamas-Lopez, F.**, Cui, Y-J., Calon, N., Costa D'Aguiar, S., Zhang, T., 2016. Assessment of train speed impact on the mechanical behaviour of track-bed materials. Submitted to 'Journal of Zhejiang University-SCIENCE A'

7. Zhang, T., **Lamas-Lopez, F.**, Cui, Y-J., Costa D'Aguiar, S., Calon, N., 2016. Development of a simple 2D model for railway track-bed mechanical behaviour based on field data. Submitted to 'Soil dynamics and earthquake engineering'

8. Zhang, T., Cui, Y-J., **Lamas-Lopez, F.**, Calon, N., Costa D'Aguiar, S., 2016. Modelling stress distribution in substructure of French conventional railway tracks. Submitted to 'Construction and Building Materials'. *Accepted for publication*

9. Zhang, T.W., Cui, Y-J., **Lamas-Lopez, F.**, Dou, Y-C., Calon, N., Costa D'Aguiar, S., 2016. Changes of density, suction, and stiffness of soils with remoulded water content. Submitted to 'Géotechnique'

Conference papers

1. **Lamas-Lopez, F.**, Cui, Y-J., Dupla, J-C., Canou, J., Tang, A-M., Costa D'Aguiar, S., Calon, N., and Robinet, A., 2014. Increasing loading frequency: effects on railways platforms materials. Proceedings of the Second International Conference on Railway Technology: Research, Development and Maintenance. 8-11 April 2014. Ajaccio, Corsica (France). Paper 48.

2. **Lamas-Lopez, F.**, Alves-Fernandes, V., Cui, Y-J., Calon, N., Robinet, A., Dupla, J-C., Costa D'Aguiar, S., Tang, A-M., Canou, J., 2014. Assessment of the double integration method using accelerometers data for conventional railway platforms. Proceedings of the Second International Conference on Railway Technology: Research, Development and Maintenance. 8-11 April 2014. Ajaccio, Corsica (France). Paper 58.

3. Escobar, E., Benz, M.A., Haddani, Y., **Lamas-Lopez, F.**, Calon, N., Costa D'Aguiar, S., 2014. Reconnaissance dynamique des sites ferroviaires à l'aide du pénétromètre PANDA-3, in: Journées Nationales de Géotechnique et de Géologie de l'Ingénieur JNGG2014. 8-10 July 2014. Beauvais (France)

4. **Lamas-Lopez, F.**, Cui, Y-J., Calon, N., Robinet, A., Dupla, J-C., Costa D'Aguiar, S., Tang, A-M., Canou, J., 2014. Field instrumentation to study the behaviour of a conventional railway platform. Proceedings of the second international conference on railway geotechnical engineering GEORAIL 2014. 6-7 November 2014. Marne-la-Vallée (France)

5. **Lamas-Lopez F.**, Cui, Y-J., Calon, N., Costa D'Aguiar, S., 2015. In-situ investigation of the behaviour of a French conventional railway track. 94rd Annual Meeting of the Transportation Research Board, Washington, DC (USA). Paper 15-1076.

6. **Lamas-Lopez, F.**, Cui, Y-J., Calon, N., Robinet, A., Dupla, J-C., Costa D'Aguiar, S., Tang, A-M., Canou, J., 2015. Influence of moisture content on the dynamic properties of an interlayer soil under cyclic loading. Proceedings of Railway Engineering 2015. 29 June - 1 July 2015. Edinburgh (United Kingdom).

7. **Lamas-Lopez, F.**, Cui, Y-J., Dupla, J-C., Tang, A-M., Canou, J., Calon, N., Costa D'Aguiar, S. 2015. Effect of water content on long-term cyclic behaviour of railways platforms materials. Proceedings of the Asia-Pacific Unsaturated Soils conference: Research & Applications. 23-26 October 2015. Guilin (China). Pages 1415-1421.

8. **Lamas-Lopez, F.**, Cui, Y-J., Zhang, T., Dupla, J-C., Calon, N., Costa D'Aguiar, S., Canou, J., Tang, A-M. 2016. Cyclic strain amplitude impact on soil dynamic parameters of conventional railways' track-bed materials. The Third International Conference on Railway Technology: Research, Development and Maintenance.5-8 April 2016. Cagliari, Sardinia (Italy)

9. Costa D'Aguiar, S., Lopez-Caballero, F., Bonilla, F., **Lamas-Lopez, F**., 2016. Estimation of mechanical properties of railway soil foundations from field buried instrumentation. The 3rd International Conference on Transportation Geotechnics, ICTG. September 4-7, 2016. Minho, (Portugal)

ABSTRACT

As in other European countries, in France the conventional lines constitute the main part of the whole railway network (94%) and they are generally over a century old. Nowadays, facing the demand of upgrading both the traffic load and speed, it is of paramount importance to acquire good knowledge on the corresponding impact on the mechanical behaviour of tracks, at both short and long terms. In this context, this PhD work aims at investigating the influence of train speed and axle load on the dynamic behaviour of materials constituting the conventional track-beds, through both '*in-situ*' monitoring and laboratory testing.

For the field monitoring, a representative track was selected from the French conventional network following well-defined criteria. The selected site underwent a geophysical and geotechnical prospection, allowing the site critical speed and the geotechnical properties of different soils constituting the track-bed to be determined. The first data allowed assessing the influence of the track state conditions and the traffic loading on the measurements of each sensor. The train speed and axle load impacts on the vertical stress, deflection/strain, in particular their amplifications with speed increase were evaluated based on the data with an Intercity test train running at different speeds from 60 km/h to 200 km/h and the different axle loads applied by Coaches (105 kN/axle) and Locomotive (225 kN/axle). A statistical analysis was made to assess the variability of track response and their dynamic amplification with speed based on the data with passages of commercial trains. The dynamic amplification of track response due to train speed was found to be directly related to the ratio of train speed to the surface wave velocity.

The laboratory test conditions were defined based on the field measurements. A material representative of an interlayer soil was prepared and tested in a large-scale cyclic triaxial cell to investigate its mechanical behaviour. Both Sine-shaped and M-shaped loads were applied and in addition, two water contents were considered. The variations of dynamic parameters such as resilient modulus and damping ratio with number of cycles were assessed, and the effects of loading parameters such as consolidation pressure, load shape, load amplitude and load frequency were investigated. The effect of water content was studied as well. It was observed that the response of energy developed during cyclic loading is an important parameter controlling the soil mechanical behaviour at both small and large numbers of

cycles. Also, the Sine-shaped loading was found more aggressive than M-shaped loading since the former results in higher energy and therefore larger soil deformation. This is particularly the case when the soil is saturated.

Based on the results obtained in the field and laboratory, two 2-D analytical models were developed allowing the description of vertical stress and vertical deflection transmissions in track-beds. Some mechanical parameters such as the moduli of track-bed layers, their damping ratios, thicknesses as well as the average track surface wave velocity were found to be the key parameters governing the track dynamic behaviour.

A comparison between field and laboratory results was also made. The track response to the loading by different train types, considering equivalent loads but different spatial loading configurations from TER and TGV train axles is presented. It was found that for each monitored position in the track, the response energy was higher for TGV than for TER. This larger developed energy suggests a higher aggressiveness to the track structure. Thus, the energy response is a key indicator to be taken into account when performing a track mechanical behaviour monitoring.

RESUME

Comme dans d'autres pays européens, en France, les lignes classiques constituent la plupart du réseau ferroviaire (94%) et elles sont généralement âgées de plus d'un siècle. Aujourd'hui, il est demandé d'améliorer les réseaux pour faire face à une augmentation de la charge du trafic et de la vitesse de service. Pour ce faire, il est indispensable d'acquérir une bonne connaissance sur l'impact de la vitesse et de la charge sur le comportement mécanique, à court et long termes. Dans ce contexte, ce travail de thèse vise à étudier expérimentalement l'influence de la vitesse et de la charge sur le comportement dynamique des matériaux constituant les voies classiques, à travers à la fois le suivi «*in-situ*» et des essais en laboratoire.

Pour les études «*in-situ*», une section de ligne représentative du réseau classique a été sélectionnée dans le réseau français en suivant les critères bien définis. Le site choisi a fait l'objet d'une prospection géophysique et géotechnique, ce qui a permis de définir la vitesse critique du site et les propriétés géotechniques des différents sols constituant la plateforme. Les premières données ont permis d'évaluer l'influence de l'état de la voie et de la charge engendrée par le trafic sur les mesures de chaque capteur. L'impact de la vitesse du train et la charge à l'essieu sur la contrainte verticale, déflection/déformation, et en particulier leurs amplifications ont été évalués avec l'augmentation de la vitesse d'un train d'essai Intercités roulant à des vitesses différentes de 60 km/h à 200 km/h et les différentes charges à l'essieu appliquées par des voitures de passagers (105 kN/essieu) et la locomotive (225 kN/essieu). Une analyse statistique est aussi réalisée afin d'évaluer la variabilité de la réponse de la voie et leur amplification dynamique avec la vitesse, en se basant sur les données enregistrées lors des passages de trains commerciaux. On observe que l''amplification dynamique de la réponse de la voie due à la vitesse des trains est directement liée au rapport entre la vitesse des trains et la vitesse des ondes de surface du site.

Les conditions des essais en laboratoire ont été définies à partir des mesures effectuées «*in-situ*». Un matériau représentatif du sol intermédiaire des voies classiques a été préparé et testé dans une cellule triaxiale cyclique de grandes dimensions pour étudier son comportement mécanique. Deux types de charges, de forme sinusoïdale et de forme M, ont été appliqués et, en outre, deux teneurs en eau ont été examinées. Des variations des paramètres dynamiques des sols tels que le module élastique et le rapport d'amortissement avec le nombre de cycles

ont été évalués, et les effets des paramètres de chargement tels que la pression de consolidation, la forme de la charge, l'amplitude de la charge et la fréquence de la charge ont été étudiés. L'effet de la teneur en eau a été étudié également. Il a été observé que la réponse de l'énergie développée pendant le chargement cyclique est un paramètre qui gouverne le comportement mécanique des sols à petit et grand nombre de cycles. En outre, la charge en forme sinusoïdale a été trouvée plus agressive que celle en forme de M parce que ce chargement sinusoïdal développe plus d'énergie, engendrant ainsi plus de déformations permanentes du sol à grand nombre de cycles. Ceci est particulièrement le cas lorsque le sol est saturé.

A partir des résultats obtenus sur le terrain et en laboratoire, deux modèles analytiques en 2-D ont été développés permettant de décrire la distribution de contrainte verticale et la propagation des déflections verticales. Certains paramètres mécaniques tels que les modules élastiques des couches de la voie, leurs rapport d'amortissement, leurs épaisseurs, ainsi que la vitesse moyenne des ondes de surface dans la section de voie considérée se sont révélés être les principaux paramètres contrôlant le comportement dynamique de la voie.

Une comparaison entre les mesures effectuées sur le terrain et les résultats des essais en laboratoire a été également réalisée. La réponse de la voie sous différents types de trains, TER et TGV avec des charges équivalentes mais avec différentes configurations spatiales des essieux, est présentée. On observe que pour chaque position de la voie, la réponse en énergie est plus élevée pour un TGV que pour un TER. Cette plus grande énergie développée suggère une plus grande agressivité vis-à-vis de la structure de la voie. Ainsi, la réponse en énergie est un indicateur important à prendre en compte lors d'un suivi du comportement mécanique d'une voie.

Mots-clés : Voie classique; couche intermédiaire; suivi in-situ; essais en laboratoire; impact de la vitesse du train; amplification dynamique; comportement dynamique de la voie; modélisation analytique

RESUMEN

Al igual que en otros países europeos, en Francia las líneas ferroviarias convencionales constituyen la parte principal de la red en su conjunto (94%) y tienen por lo general más de un siglo de antigüedad. Hoy en día, frente a la creciente demanda de los administradores de infraestructuras ferroviarias de mejorar el servicio ofertado, aumentando tanto la carga de tráfico como la velocidad del material rodante, es de vital importancia tener un buen conocimiento del impacto del aumento de la velocidad y de la carga en el comportamiento mecánico de la plataforma ferroviaria, tanto a corto como a largo plazo. En este contexto, la presente tesis doctoral tiene como objetivo investigar la influencia de la velocidad del tren y la carga por eje sobre el comportamiento dinámico de los materiales que constituyen las líneas férreas convencionales, a través de estudios experimentales '*in-situ*' y en laboratorio.

Para el estudio '*in-situ*', una línea representativa de la red convencional francesa fue seleccionada siguiendo criterios bien definidos. El sitio seleccionado se sometió a una prospección geofísica y geotécnica, permitiendo que la velocidad crítica de la vía y las propiedades geotécnicas de los diferentes suelos que constituyen la plataforma fueran determinadas. Los primeros datos recolectados sobre el sitio permitieron determinar la influencia de las condiciones de estado de la plataforma y la carga de tráfico en las mediciones de cada sensor instalado. El impacto de la velocidad del tren y de la carga por eje sobre la tensión vertical, la deflexión / deformación vertical y en particular sus amplificaciones con el aumento de velocidad, se evaluaron sobre los datos recolectados utilizando un tren de pruebas Intercity que circuló a diferentes velocidades de 60 km/h a 200 km/h, con diferentes cargas por eje aplicadas por los vagones (105 kN/eje) y la locomotora (225 kN/eje). Se realizó también un análisis estadístico para evaluar la variabilidad de la respuesta de la vía y su amplificación dinámica con velocidad en base a datos provenientes de trenes comerciales. La amplificación de la respuesta dinámica de la plataforma debido a la velocidad del tren está directamente relacionada con la proporción de velocidad del tren respecto a la velocidad de las ondas de superficie en el sitio considerado.

Las condiciones de los ensayos en laboratorio se definieron a partir de las mediciones en el terreno. Un material representativo de un suelo de intermediario se preparó y ensayó en un triaxial cíclico de gran escala para analizar su comportamiento mecánico. Dos tipos diferentes de carga cíclica, en forma de seno y en forma de M, se aplicaron sobre las muestras y además

dos estados hídricos diferentes fueron considerados. Se analizó la evolución con el número de ciclos de los parámetros dinámicos del suelo como el módulo de elasticidad y coeficiente de amortiguamiento frente a parámetros de carga tales como la presión de consolidación, forma de la carga, la amplitud de carga y la frecuencia de carga. Del mismo modo, el efecto del coeficiente de saturación del suelo se estudió también. Se observó que la respuesta de la energía desarrollada durante la carga cíclica es un parámetro que controla el comportamiento mecánico del suelo a reducido y elevado número de ciclos. Además, se observó que la carga aplicada en forma de seno es más agresiva que la carga en forma de M, ya que la primera desarrolla un mayor contenido energético y por lo tanto induce mayores deformaciones plásticas en el suelo. Esto es particularmente cierto en el caso de suelos saturados.

Basándose en los resultados obtenidos '*in-situ*' en laboratorio, dos modelos analíticos en 2-D se desarrollaron, permitiendo la descripción de la distribución de tensión vertical bajo carga de tráfico y la propagación de deflexiones verticales a lo largo de la vía. Se encontraron algunos parámetros mecánicos fundamentales que rigen el comportamiento dinámico de la vía tales como los módulos elásticos de las distintas capas de la plataforma, sus coeficientes de amortiguación, sus espesores, así como la velocidad media de las ondas de superficie en la sección de vía considerada.

También se realizó una comparación entre los resultados de laboratorio y del terreno. La respuesta de la vía a la carga efectuada por diferentes tipos de trenes fue estudiada utilizando trenes tipo TER y TGV, teniendo en cuenta cargas equivalentes pero diferentes configuraciones espaciales de los ejes. Por lo tanto, para cada una de las posiciones monitorizadas de la plataforma, la energía de respuesta fue mayor para la configuración de ejes de los trenes TGV en comparación con la de los trenes TER. Esta mayor energía desarrollada está relacionada con la agresividad de un tren sobre una estructura de vía concreta. En consecuencia, se observó que la respuesta energética de la vía es un indicador clave que debe de tenerse en cuenta al realizar un control del comportamiento mecánico de la plataforma.

Palabras clave: línea convencional; capa intermedia; monitorización mecánica de vía férrea; experimentación en laboratorio; impacto de la velocidad del tren; amplificación dinámica; comportamiento dinámico de la plataforma; modelización analítica

NOTATIONS

Latin alphabet

a_{wheel}	circular wheel loading surface
a_{mass}	ratio between masses
A	amplitude deflection
A_{rail}	rail section surface
A_s	contact surface between sleeper and ballast
B	width of sleeper
c'	apparent cohesion
c_{dis}	confining pressure actuator displacement
c_{plate}	LWD plate rigidity coefficient
C	cementation
C_u	uniformity coefficient
d	grain diameter
d_{act}	axial actuator displacement
d_{axles}	distance between two axles in a bogie
d_{max}	maximum grain diameter
d_R	displacement of the PANDA rod into the soil
D	load diffusion coefficient
D_{50}	medium grain size
D_r	soil damping ratio
D_{radial}	initial distance between the boundaries for radial sensors
e	void ratio
E	elastic modulus
E_D	equivalent elastic energy transferred to the system
E_K	kinetic energy
E_{loop}	dissipated energy by the system
E_S	deformation energy
E_{sg}	modulus of subgrade layer
E_{up}	modulus of upper layer
E_{v2}	static modulus
E_{vd}	dynamic deformation modulus
f	frequency
f_{axles}	excited frequency by inter-axle wavelength
f_{AC}	function of attenuation coefficient in depth
f_{bogies}	excited frequency by inter-bogies wavelength
f_c	cut-off frequency
f_s	sampling frequency
f_v	volumetric fraction
f_{vanes}	excited frequency by inter-vane wavelength
F	axial force
F_2	safety factor
F_I	fouling index
g	gravity acceleration
G	shear modulus
G_{max}	maximum shear modulus
H	sample height
H_{mass}	mass falling height

I	inertia moment
k	stiffness of Winkler foundation
K_0	earth pressure coefficient
L	effective length of sleeper
L_{axial}	initial distance between the boundaries for axial sensors
L_b	length of benders
L_{spec}	length of the specimen
L_{tt}	tip-to-tip distance
L_{vec}	number of recorded positions of a vector
m	soil mass
m_{layer}	soil layer mass
M	dimensionless load speed; Mach number
M_0	principal mode of ground waves dispersion
M_H	hammer mass
M_i	percentage of material i
M_r	resilient modulus
$MD50_i$	passing percentage at intersection between D_{50} of material i and its GSD
n	vector position
n_{cyclic}	cyclic stress level
N	number of loading cycles
p	triaxial mean stress
p_{max}	maximum mean stress ratio
pos_{axles}	number of signal positions between two axle peaks
P	dynamic axle load
P_4	percentage of material passing through the 4.75 mm sieve
P_{200}	percentage of material passing through the 0.075 mm sieve
P_s	static axle pressure
PI	plasticity index
q	triaxial deviator stress
q_D	rod-tip dynamic resistance
q_{max}	maximum deviator stress level
q_r	maximum rail seat load
Q	wheel load
r	radius, sample radius
r_c	axial jack radius
r_d	confining pressure jack radius
S_r	saturation rate
t	time
t_g	geological age
T	temperature
u, u_z	vertical displacement/deflection
u^*	normalized displacement
v_{cr}	critical train speed of a track
v_R	Rayleigh wave velocity
v_p	compression wave velocity
v_s	shear wave velocity
v_T	train speed
V	sensor response voltage
V_{spec}	specimen volume
w	moisture content
w_L	liquid limit

w_{opm}	optimum moisture content
x	longitudinal distance, spatial coordinate
y	spatial coordinate
z	depth, spatial coordinate
z_{inst}	sensor installation depth

Greek alphabet and other symbols

Δa_x	longitudinal acceleration amplitude
Δa_y	lateral acceleration amplitude
Δa_z	vertical acceleration amplitude
$\Delta axial_i$	displacement amplitude of axial local sensor i
Δd	displacement amplitude
Δd_z	vertical displacement amplitude
$\Delta d_z^{\ i}$	low-pass cyclic vertical displacement amplitude filtered at i Hz
Δd_i	vertical displacement amplitude at train speed i
Δq	cyclic deviator stress amplitude
Δq^i	low-pass cyclic deviator stress amplitude filtered at i Hz
Δq_{cycle}	cyclic deviator stress amplitude for one cycle
Δq_{yield}	failure cyclic deviator stress amplitude
$\Delta radial_i$	displacement amplitude of radial local sensor i
Δu	interstitial pressure amplitude
Δv_z	vertical acceleration amplitude
$\Delta \varepsilon$	cyclic strain amplitude
$\Delta \varepsilon_1$	axial cyclic strain amplitude
$\Delta \varepsilon_1^{\ i}$	low-pass axial cyclic strain amplitude filtered at i Hz
$\Delta \varepsilon_z$	vertical cyclic strain amplitude
$\Delta \delta_x$	cyclic displacement amplitude in X axis direction (Chapter I)
$\Delta \delta_y$	cyclic displacement amplitude in Y axis direction (Chapter I)
$\Delta \delta_z$	cyclic displacement amplitude in Z axis direction (Chapter I)
$\Delta \sigma$	stress amplitude
$\Delta \sigma_{xx}$	cyclic stress amplitude in X axis direction (Chapter I)
$\Delta \sigma_{yy}$	cyclic stress amplitude in Y axis direction (Chapter I)
$\Delta \sigma_z$	vertical stress amplitude
$\Delta \sigma_{zz}$	cyclic stress amplitude in Z axis direction (Chapter I)
β	frequency ratio
γ	strain rate
δ	Dirac delta function
$\delta \varepsilon_1^{\ p}$	relative permanent axial deformation
$\varepsilon_a^{\ p}, \varepsilon_1^{\ p}$	axial permanent deformation
ε_1	axial strain
ε_{1max}	maximum axial strain
ε_3	perpendicular strain to axial axis
ε_v	volumetric strain
$\dot{\varepsilon}_1$	axial strain rate
ξ	damping ratio
θ_i	load spread angle trough layer i
κ	wave number

λ	wave length
ρ	total density
ρ_d	soil dry density
ρ_s	soil specific density
σ'_0	mean effective stress
σ_3	triaxial confining pressure
σ_{3max}	maximum confining pressure
σ'_c	effective consolidation pressure
σ_z	vertical stress
$\overline{\sigma_z}$	expected vertical stress
φ'	internal friction angle
ϕ	diameter
ϕ_{sp}	stress amplification factor expressed as function of train speed
ϕ_c	confining pressure actuator diameter
ϕ_d	axial actuator diameter
υ	Poisson's ratio
υ_{dif}	diffusivity coefficient
ψ	normal cumulative Gaussian distribution function
ω	angular frequency

ABBREVIATIONS

ADIF   Administrador de Infrastructuras Ferroviarias (Spain)
AVE   Alta Velocidad Española (Spanish HST)
BRGM   Bureau de Recherches Géologiques et Minières (France)
CBR   California Bearing Ratio
cdf   cumulative density distribution
CN   Canada National Railways
CV   Coefficient of Variation
CWR   Continuous Welded Rail
DAF   Dynamic Amplification Factor
DB   Deutsche Bahn (Germany)
DCP   Dynamic Cone Penetrometer
FB   Fresh Ballast
FEM   Finite Element Method
FFT   Fast Fourier Transform
FoB   Fouled Ballast
GIS   Geographical Information System
GPR   Ground Penetrating Radar
GSD   grain size distribution
GTR   Guide des Terrassements Routiers (France)
HSL   High Speed Line
HST   High Speed Train
ITL   Interlayer soil
IP   IP code, International Protection Marking
KP   Kilometric Point
LVDT   Linear Variable Differential Transformer
LWD   Light Weight Deflectometer
MASW   Multichannel Analysis of Surface Waves
MBTA-CS   Massachusetts Bay Transportation Authority – Commuter Services (USA)
MDD   Multi-Depth Deflectometer
NIR   North-Ireland Railways
OCR   over-consolidation ratio
OPM   Optimum Proctor Modified
PANDA   Pénétromètre dynamique léger à énergie variable
PSD   Power Spectrum Density
PSR   principal stresses rotation
PVC   polyvinyl chloride
SASW   Spectral Analysis of Surface Waves
SBG   Subgrade soil
SM   Stress Mobilization Factor
SNCF   Société Nationale des Chemins de Fer Français (France)
SPT   Standard Penetration Test
TGV   Train à Grande Vitesse (French HST)
TL   transition layer
UIC   Union Internationale des Chemins de Fer
USP   Under-Sleeper Pads

TABLE OF CONTENTS

INTRODUCTION

BACKGROUND AND MOTIVATIONS

Nowadays, there are about 1.3 M km of railway lines under operation all over the world. Almost 50% of them are located in USA and Europe. Moreover, in the last two decades, some countries such as China, Spain, Japan and France have prompted the set-up of high-speed lines (HSL). Note that the first HSL was constructed in Japan (1964). Now the total length of HSL built or under construction all over the world is 20.000 km, representing 1.6% of the worldwide railway network. This percentage can reach 10% in some of the four previously mentioned countries. It is thus deduced that the HSL tracks are almost negligible in the whole railway network, even though they represent a high ratio of utilisation. On the other hand, the low percentage of HSLs is also due to their high construction costs. In this content, facing the high demand of upgrading the train speed and load, the innovation of the conventional lines becomes a priority. According to Lopez-Pita, (2010), a reduction of 5 min in railway journey time allows gaining 2% in the 'railway-airplane' market share, especially for distances up to 1000 km.

Recently, the French national railway company (SNCF) have also planned to upgrade their conventional lines by increasing the train speed and axle weight, in order to provide a better service to the client, especially in the highly used passenger corridors where the renewing and improvement works should be accomplished in short periods of time. The maximum service speed on the conventional network is 220 km/h, while for the last inaugurated lines (HSL-East Line) it ranges from 250 km/h to 320 km/h. Some studies propose to increase these speeds to 360 km/h in some lines (international European lines) (Couvert 2007). This traffic upgrade will greatly affect the mechanical behaviour of tracks. However, in the practice of SNCF, the impact of train speed on track-bed behaviour has been taken into account only in an empirical way. In this context, the SNCF launched the 'INVICSA' project (*INfluence de la VItesse sur le Comportement des Structures d'Assise*, train speed impact on the mechanical behaviour of conventional track-beds), aiming to investigate the influence of train speed and axle weight on the behaviour of conventional track-bed and to further optimize the track service speed upgrades and maintenance operations.

OBJECTIVES

This thesis consists of field monitoring and laboratory testing. The main scientific objectives are:

- To investigate the train speed and axle load effect at short and long terms on track-bed materials by performing field monitoring with a representative conventional track section.
- To assess the evolution of elastic and dynamic parameters such as resilient modulus M_r and Damping ratio D_r, of materials constituting the track-bed and track subgrade.
- To estimate the effect of cyclic loading frequency and loading shape on track-bed materials behaviour.
- To define the mechanical potential of a conventional track-bed soil to accept a train service speed upgrade.
- To define appropriate parameters for quantifying the effect of railway load on the mechanical behaviour of track-bed materials.

The industrial objectives are:

- To define how to integrate the effect of train speed in the maintenance or renewal operations for the conventional track-beds by considering the constitution of the track-bed materials and their positions in the track. Once completed, this could be integrated in further new SNCF standards.
- To establish an experimental protocol for the preliminary studies before a track renewal, to assess the train speed influence on the mechanical behaviour of the track or to define a monitoring system able to detect the track sections sensitive to changes in train load, speed and configuration.

OUTLINE

This thesis is organized in four chapters and a general conclusion.

Chapter 1 is devoted to a literature review on different aspects of mechanical behaviour of railway tracks. Firstly, a global description is given on the railway structure and the mechanical specifications of track-bed materials as well as railway loading characteristics. Secondly, the main geophysical and geotechnical track prospections methods generally used in French railway network are presented. Thirdly, different factors influencing the track-bed soil behaviour are discussed, starting by the dynamic track behaviour and finishing by the soil hydro-mechanical parameters including the elastic parameters under cyclic loading and those describing the development of permanent deformations. Finally, an overview of different '*in-situ*' experimentations is provided, at the scales of real tracks and of physical models.

Chapter 2 is dedicated to the '*in-situ*' experimentation. Firstly, the selection of the experimentation site, representative of the French conventional network is conducted. Secondly, the geotechnical and geophysical prospection survey performed on the selected track is presented. Thirdly, the installation of sensors, the verification and the analysis methods used to assess the mechanical behaviour of track-bed layers are described. The main instrumented soils are the Interlayer (ITL) and the subgrade (SBG). Different variables such as cyclic stress, acceleration, displacement or strain under train passages are analysed. Fourthly, a test campaign using a real *Intercity* test train that is composed of a locomotive and 7 coaches and runs at 6 different speeds over the experimentation track is presented. The data recorded by the sensors are analysed. Lastly, a statistical analysis using the measurements from all the Intercity trains that run on the experimentation site during five months is performed, and the results obtained are compared with the recorded data.

Chapter 3 describes the laboratory tests on an ITL material. As it is difficult to obtain intact ITL soils from conventional tracks, the tested ITL material is reconstituted in the laboratory using 13 different standard materials based on previous studies (Trinh 2011). As the ITL soil is a coarse-grained soil, and its mechanical behaviour depends on the volumetric fraction and plasticity of fine matrix soils (Duong et al. 2013), three fine matrix soils with different plasticity indexes (*PI*) are also reconstituted and tested using bender elements. The variations of the maximum shear modulus of the fine matrix soils with different hydric conditions are

investigated. A comparison of the ITL behaviour with other ITL soils presented in literature is also made. The ITL soil is tested in a large scale cyclic triaxial cell following four different procedures to assess the cyclic behaviour at short and long terms under different ITL hydric conditions, loading amplitudes, frequencies and shapes. Special emphasis is put on the evolution of dynamic parameters and the development of permanent deformations at large number of cycles.

Chapter 4 is devoted to the industrial applications of the results obtained. Two simple analytical models of track-bed behaviour (stress and deflection propagation respectively) are proposed, and a comparison between the '*in-situ*' and laboratory experimentations is made. The first analytical model describes the vertical stress transmission through the track-bed taking into account the amplification by the train speed increase. This train speed amplification effect is also taken into account in the second analytical model that deals with the deflection propagation from a loading point to the rest of the track-bed in 2D (longitudinal direction and track depth). Finally, the results obtained in the laboratory are used to develop new analysis technique for '*in-situ*' measurements to evaluate the energetic track response under equivalent loadings from different trains. A qualitative correlation is performed between the track energetic response and the track degradation.

I. LITERATURE REVIEW

I.1 INTRODUCTION

In this chapter the different components of the track system are firstly presented, as well as a description of the loads exerted by trains. Then, an 'In-situ' tests section exposes some geophysical and geotechnical tests used in ballasted track prospections. Afterwards, different factors including the train speed influencing the behaviour of track-bed materials are presented. The soil's dynamic parameters and long-term cyclic behaviour are also described focusing on the different parameters related to the dynamic behaviour of coarse-grained soils. Finally, some results from on real tracks and physical models experimentations are presented.

I.2 TRACK SYSTEM

Most of the European railway lines were built during the second half of XIX century, between 1860 and 1910 (Figure I.1). The maximum railway length in Europe was reached between the 1940's and 1950's (Martí-Henneberg 2013) (Figure I.2). Many countries nationalized and centralized the administration of their railways at this time (Spain, France, Italy, etc.), contributing to a first homogenization of their railway networks. Several lines were closed to the traffic in Europe between 1965 and 1985 just when the first high speed lines (HSL) were planned in France. Since then, no significant changes have been applied to the conventional network. The European railway network has a continental scale, and the technical questions such as the track gauge, electrical voltage and cross-border connections between different railway systems should be considered to compare different systems (Merger and Polino 2004; Roth and Dinhobl 2008). The most important barrier in the network interconnections is the track gauge (Knowles 2006; Puffert 2009). However, the track structure is similar for the entire European network; it consists of the superstructure (rail + fastening system + sleepers + ballast) and the track-bed (sub-ballast + capping layer + subgrade) (Selig and Waters 1994).
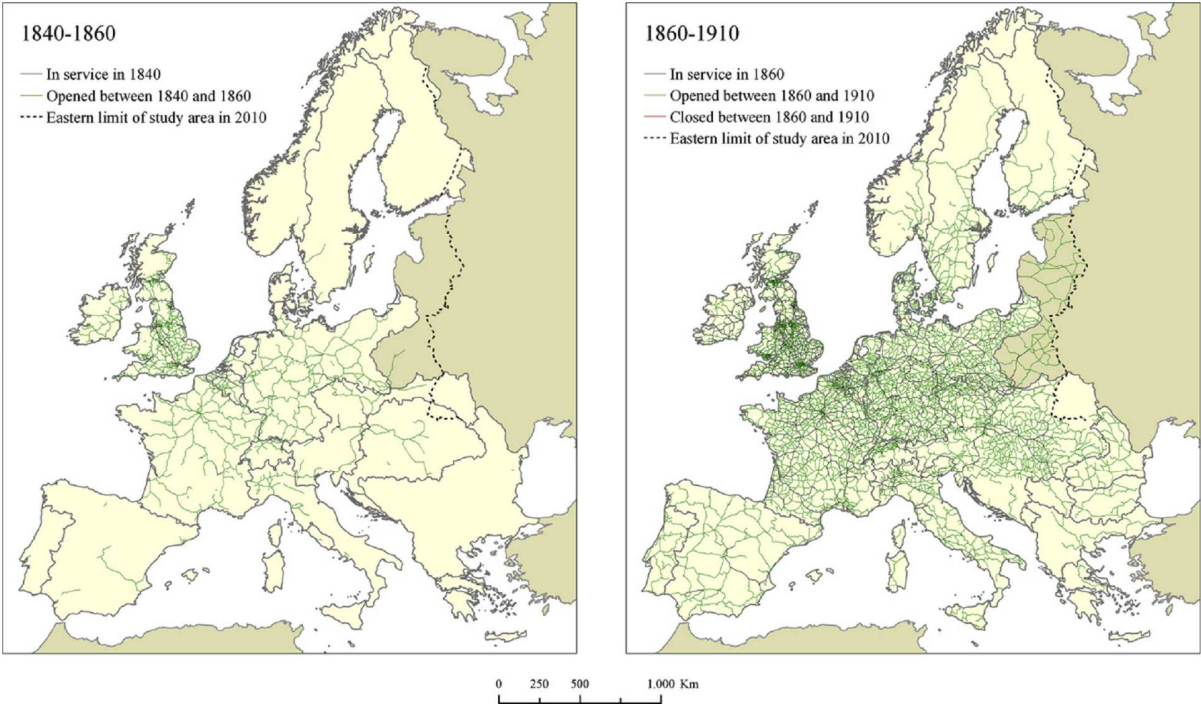
Figure I.1. Evolution of the railway network in Europe (1840–1910) (Martí-Henneberg 2013)
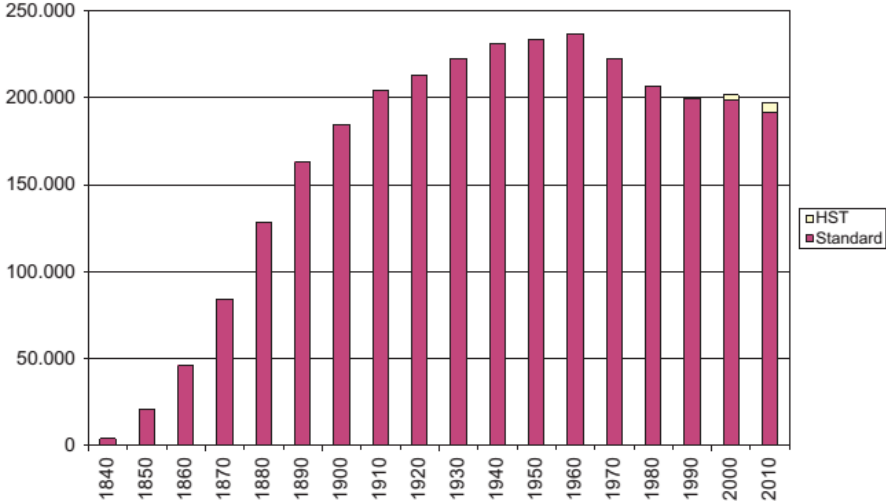
Figure I.2. Total length of railways in Europe, in km (Martí-Henneberg 2013)

Two types of tracks are used in the world nowadays: ballasted and slab tracks (Figure I.3). There are two main advantages of the slab track: the significantly reduced maintenance need in combination with its higher serviceability life and its higher structural track stability (Bastin 2005; Esveld 2001; Franz and Nigel 2001; Lichtberger 2005). Usually a lower maintenance effort is needed for slab tracks during its life-cycle because there is no need for tamping. Then, the absence of ballast cleaning and track levelling operations results in a

reduced cost of approximately 20-30% for repairs compared to a conventional ballasted track. However, the initial construction costs are 30% higher compared to ballasted tracks. In addition, a higher life cycle is obtained using these lines, around 50-60 years compared to ballasted conventional tracks (30-40 years) with the possibility of almost full replacement at the end of the service life. Nevertheless, sometimes deterioration of the track geometry is observed when the operational strength of the concrete slab track is reached. Moreover, a low adaptability to large displacements in the embankment, as well as the limited options in adjustments after construction and the higher air-borne vibration emissions are few of the main reasons that slab track is not the dominant track type used (Franz and Nigel 2001). In some countries like China, Germany and Japan, slab tracks are mostly used for the high speed trains (Esveld 2001).

The European conventional railways are almost entirely composed of ballasted tracks, with some exceptions in tunnels, metro systems and some high speed line sections in Germany and UK. Note however that in the Netherlands and Spain, slab tracks have been adopted. Note also that at least 90% of the European railway networks are composed of ballasted conventional tracks. Ballasted tracks have high elasticity and high maintainability at relatively low cost. Another important advantage of ballasted track is the high noise absorption (Esveld 2001). The 150 years of experience using ballasted tracks makes engineers more confident to deal with ballasted track problems and also to avoid the higher risk of dealing with problems concerning the new ballastless tracks (Bezin et al., 2010).
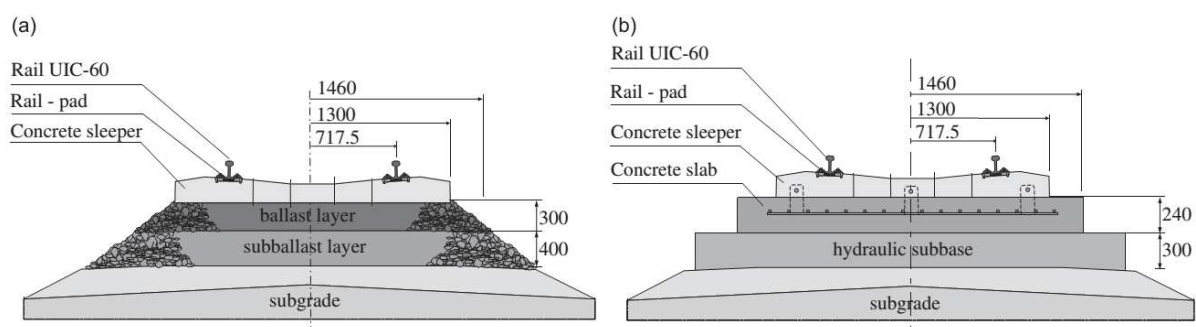
Figure I.3. (a) Ballasted track system and (b) slab track system. Units in mm (Galvín et al. 2010)

This study involves the case of France where about 32,000 km ballasted tracks are under operation nowadays, with about 94% conventional lines and only 6% High Speed Lines (HSL) (Figure I.4). In addition, this thesis will focus on the conventional network for the

7

reason of service speed upgrading of this network. Most of the conventional French lines were designed and built during the second half of XIXth century, reaching the maximum at late 30s of the XXth century (42700 km of lines). The main characteristics of the French conventional ballasted tracks are presented in the following sub-sections.
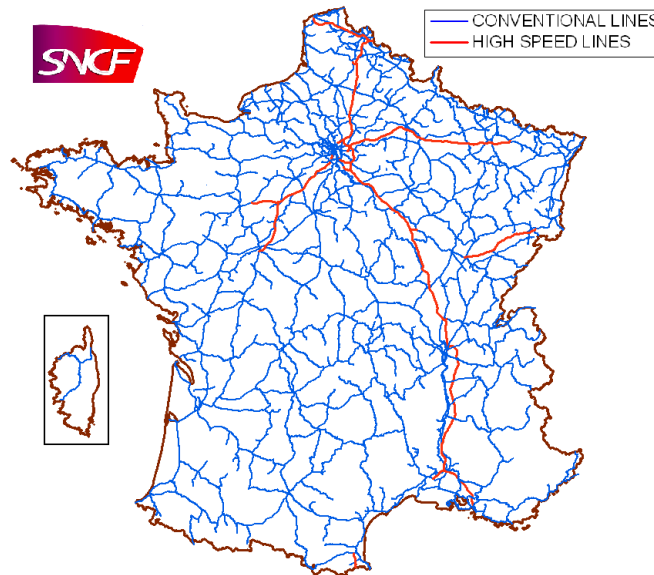
Figure I.4. Conventional and HSL under operation in France (Lamas-Lopez et al. 2014)

I.2.1   Railway track design

The main functions of railway system are to distribute the loads caused by traffic from rail to subgrade, maintain the track gauge and geometry by reducing the track materials' deformations (Selig and Waters 1994). The highly concentrated loadings at rail level are reduced in depth through the subgrade foundation (Araujo 2010). A railway track combines materials in a structural system designed to resist the combined effects of traffic and weather conditions, to provide a protection to the natural subgrade, to minimize the operational costs and to increase the safety and comfort for passengers. Brandl (2004) pointed out that the reversible deflections of track-bed materials is an essential characteristic of the conventional railway structures. The deformability facilitates the load distribution from the rail to the adjacent sleepers. Stiffer track-bed layers can present abrasion of grains due to friction or constitute local stiffness and thus lead to differential longitudinal rail deformations. This spatially variability of stiffness can accelerate the degradation process of a track: by worsen the rail geometry and accelerating the wheel/rail and rail/sleeper wear (Araujo 2010; Fröhling 1997).

The specifications of each element of a ballasted track system depend on the characteristics of the line involved (i.e. if the track is in tunnel or over a bridge where maintenance operations are more frequent, the characteristics of elements may significantly differ from a regular track). Even the track composition could be different (ballasted or slab) when passing through different elements as tunnels or bridges (Miura et al. 1998). The main goal is to optimize costs for both construction and maintenance of track.

Each railway network has their own standards defining the technical specifications for different working conditions (Calon 2011; SNCF 2007). The deformation limits under different loadings or the maintenance parameters such as the longitudinal levelling (Duong 2013) are defined for each line. In addition, the international union of railways publishes recommendations for design and maintenance operations in railways for all the associated operators around the world (UIC 2009).

I.2.2 Ballasted track components

This section will focus on the different track-bed materials for ballasted tracks. Details about their respective role in the railway system and their behaviour under different loads and train speed will be presented. Firstly, a sub-section describing the elements of the super-structure is shown (rail, rail-pad, fastening system, sleeper and under-sleeper pads). Secondly, the main roles of track-bed and their impact on track's performance are described. Thirdly, a comparison between conventional and high speed lines is made to highlight the differences and similitudes between both, focusing on sub-structure materials like sub-ballast and interlayer. Lastly, traffic load on each track-bed material is presented regarding their amplitudes and excitation frequencies.

I.2.2.1 Track superstructure

A general scheme of super-structure elements is presented in Figure I.5. The first element at the top is the rail. This element consists of a longitudinal steel beam that supports and guides the train wheels. Nowadays, the most used is the profile introduced by Charles Vignole in 1830, the Vignole rail (Al-Shaer 2006).
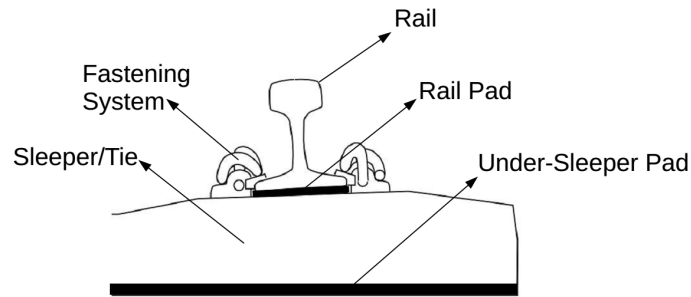
Figure I.5. Scheme of track's superstructure elements (Dahlberg 2003)

The contact surface of rail is adapted to support the stress caused by the rail flexion under the train wheel loading, in other words, this profile leads to higher rail inertia and allows train loads to be transferred to sleeper more easily (Dahlberg 2003). Just under the rail, an elastic pad is installed to ensure the contact between the lower surface of the rail and the sleeper. The pad is made of rubber, high density polyethylene, thermoplastic polyester elastomer and ethylene vinyl acetate (Kaewunruen and Remennikov 2006). Depending on their stiffness, different applications can be aimed to in terms of track deflections, track noise, vibrations or reducing maintenance operations (Sol-Sánchez et al. 2015). The sleepers (or ties in USA) are rectangular supports for the other elements of the super-structure to maintain track-gage and track's layout. The two most common are made of wood (conventional or lowly used lines) or pre-stressed/reinforced concrete (Araujo 2010; Selig and Waters 1994). Concrete sleepers are heavier, give more inertia to the system and present a more secure fastening and have longer life cycles compared to wood sleepers (Miura et al. 1998). Moreover, significant dynamic amplification of loadings appears when there are unsupported sleepers. This phenomenon appears due to the degradation of ballast under sleepers. For low train speeds the effect of unsupported sleepers is like a quasi-static superposition with the adjacent sleepers. The dynamic contribution with speed becomes significant (Nielsen and Igeland 1995). In addition, under sleeper pads (USP) are used in some of the networks from central Europe (Austria and Germany). These pads attached under the sleepers provide resiliency between sleepers and ballast (Kaewunruen et al. 2015). The performance of USP over the track system depends mainly on its stiffness (Sol-Sánchez et al. 2015).

I.2.2.2 Track-bed

The super-structure is supported by the ballast layer. Therefore, ballast has many functions and plays a very important role in the system (Alias 1984; Selig and Waters 1994). Some of the ballast layer functions are listed below (Quezada 2012):

- Allow a proper longitudinal and lateral anchorage of the super-structure
- Absorb a part of mechanical and acoustic vibrations propagated by trains
- Spread through the subgrade the concentrated loads applied by the sleepers with acceptable level of stress for the subgrade, limiting the settlement of the track
- Facilitate the maintenance operations and installation of the track
- Drain storm waters from the track

The good performance of ballast depends on the size distribution, the shape, the hardness, and surface state (Saussine 2004). This material follows the European standard (AFNOR 2003). The grain size varies from 25 to 61.5 mm (Figure I.6). Moreover, ballast is usually considered as a uniformly graded material (Freitas da Cunha 2013). The hardness is tested with the Deval test (AFNOR 2011) to assess the grain abrasion loss and Los Angeles test to analyse the fragility to shocks (AFNOR 2010). The shape criteria limit the 'needle' shape flat elements larger than 92 mm length to 12% of the total mass (Quezada 2012). No sand particles or other finer soil particles may surround ballast grains. These finer soils could influence the roughness, and consequently, the shear strength.
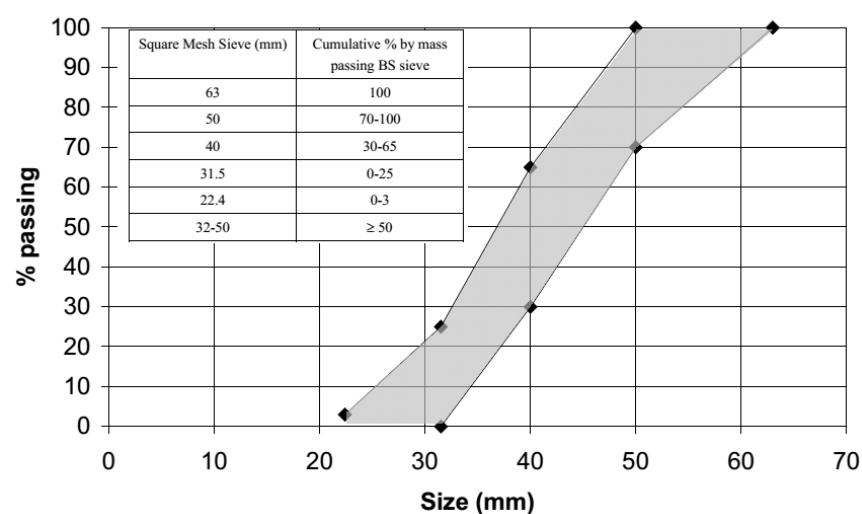
Figure I.6. Specification for ballast particle size distribution (Aursudkij 2007)

The angularity or surface roughness has a significant effect on the stress-strain behaviour of granular materials like ballast (Araujo 2010). The angularity of ballast leads also to stress concentration and heterogeneous stress distributions (Lu and McDowell 2007). The corner breakage and changes in angularity is the first reason of ballast degradation (Brandl 2004). Raymond (2000) demonstrated that small percentages of rounded materials added to the crushed one could cause a drop of bearing capacity (Figure I.7). This corner breakage could be the consequence of railway traffic loading (Lim 2004).

The thickness of ballast layer is defined to be large enough to spread the stress and dissipate its amplitude over depth. The goal is to make the stress arriving to the rest of track-bed layers sufficiently low in order to be supported by softer subgrade materials (Li and Selig 1998).
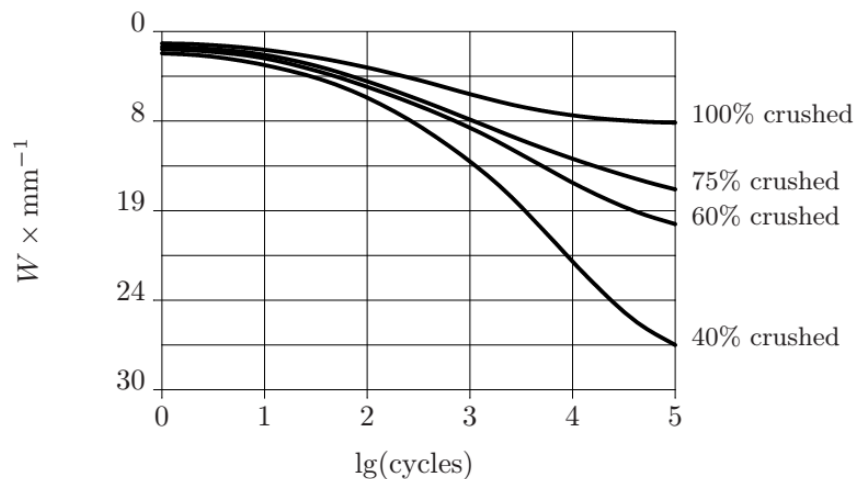
Figure I.7. Effect of crushed particles on the static bearing capacity of ballast (Raymond 2000)

The degradation of the track geometry is mainly caused by the settlement of track-bed layers (ballast, sub-ballast and subgrade). If the track is founded on a good subgrade, most of the settlement will be caused by the ballast layer (Varandas 2013). While the subgrade contribution to the total settlement is significant during the early life of the track (Shenton 1985), the settlement of ballast depends on the loading amplitude and history (Stewart 1986). Nevertheless, the accumulation of permanent settlement is related to the deviator stress (Lekarp et al. 2000).
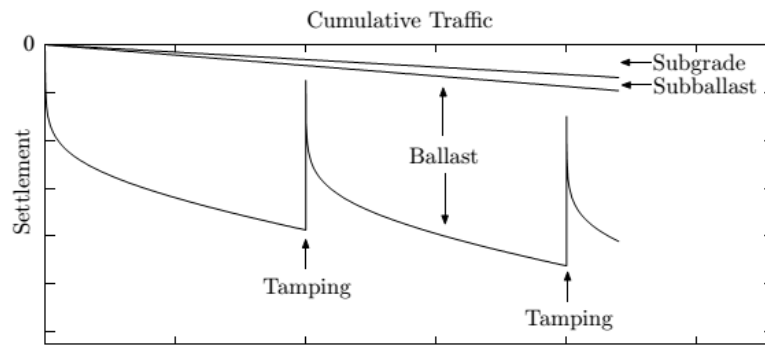
Figure I.8. Relative contributions of substructure to the settlement of track (Selig and Waters 1994)

Tamping operations are needed to bring the track to its former position after the settlement of the ballast layer (Figure I.8). Tamping produces particle rearrangement inserting the tamping pikes at both sides of each sleeper and vibrating the ballast (Selig and Waters 1994) (Figure I.9). This action may cause ballast breakage, though small. Moreover, frequent tamping operations on track can add a significant amount of particles breakdown. The cumulative vertical strain in a layer depends on the loading history. Moreover, ballast layer accelerates its degradation if more tamping operations are held on it. Over time, tamping cycles are shorter and more recurrent (Selig and Waters 1994). The ballast fouling index increases with loading cycles and some of the ballast functions like maintaining drainage are degraded. The strength weakening of the material may cause large strains.
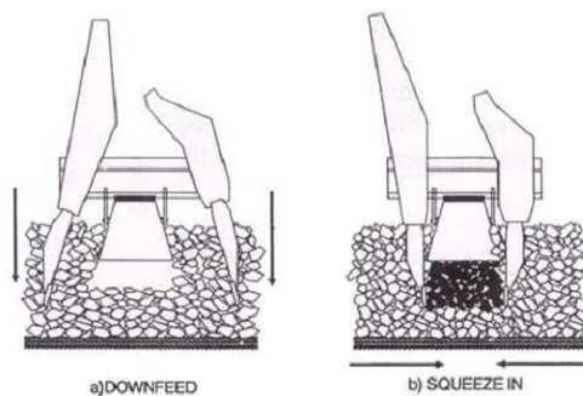
Figure I.9. Ballast tamping (Selig and Waters 1994)

13

I.2.2.3 New track versus conventional track

Below the ballast layer, other materials can be placed. There are some differences between the newly constructed lines and conventional lines. The main difference between both is the existence of an Interlayer (ITL) between ballast and subgrade in the case of conventional lines (Cui et al. 2014). On the other hand, for new lines (including high-speed lines) a transition 'sub-ballast' layer and a capping layer are placed between ballast and subgrade (Figure I.10). There are some similarities and differences between the materials for both kinds of lines, in terms of fabrication process for each material. Specifications of the different materials are described as follow:
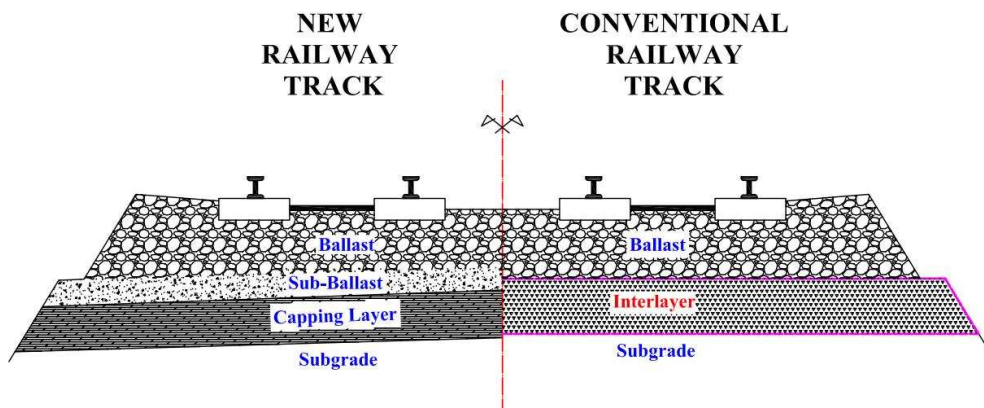
Figure I.10. Comparison between new and conventional railway tracks (Cui et al. 2014)

Most of the conventional French lines were built, in late XIXth century and early XXth, with ballast layer set directly over subgrade. The ITL layer is formed of ballast grains mixed with fines originated mainly from ballast wearing, subgrade fines interpenetration and track environment (sleepers, rails, freight trains, etc.) (SNCF 1996a; Trinh 2011). Visually, this layer is heterogeneous and contains more fines from the subgrade and other smaller materials than ballast compared to a fouled ballast layer. The thickness of the ITL layer and its nature depends on the ballast used at the site, the subgrade soil and the traffic loading. Unlike the fouled ballast layer, the ITL presents usually a high density ($\rho_d > 2.3$ Mg/m^3) and a very low permeability (Trinh 2011). The grain size distribution ranges from 60 mm (ballast) to the clay size (subgrade). Over its thickness the composition is not the same, resulting in larger grains at the beginning (just below ballast) and more fines near the subgrade (Trinh 2011). Grains from ballast layer account for at least 50% in mass of the ITL material. For regular

conventional railways where an ITL appears in its composition, the thickness of this layer ranges from 30 to 50 cm.

The sub-ballast layer, set during construction in new lines, has the same role as the originated ITL in conventional lines. This granular layer is well graded with grain size of 31.5/0 mm (SNCF 1996b) compacted at 100% OPM. The thickness of this layer is about 20 cm. The main functions of the sub-ballast are:

- to transmit loads from ballast to the subgrade;
- to ensure the grain size transition between ballast and subgrade;
- to protect the subgrade from rainwater seeping and to protect the track from frost attack.

The grain size distribution of studied ITL soils in France is similar to the specifications imposed on sub-ballast layer (Cui et al. 2014) (Figure I.11). More differences are found comparing different fouled ballast soils in the fine soils amount rather than in the coarse grains soils part (larger grains) (Fortunato et al. 2010).
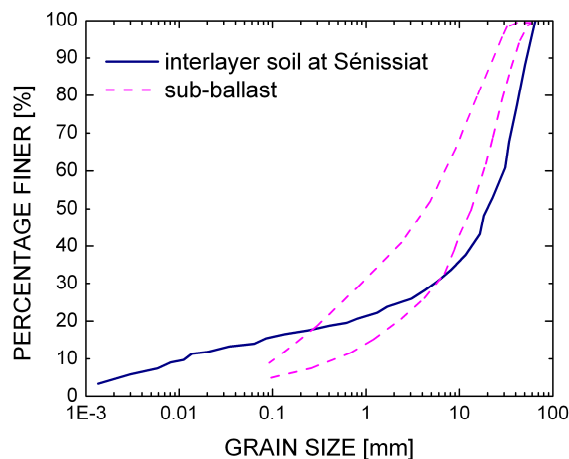
Figure I.11. Comparison of grain size distribution between sub-ballast and interlayer soil (Cui et al. 2014)

The mechanical behaviour of a representative French ITL soil was studied by (Trinh 2011) showing the influence of confining pressure and moisture content (Figure I.12). There is a strong influence of moisture content on the mechanical behaviour and the shear strength increases notoriously with increasing confining pressure (Indraratna et al. 2013). As fine particles are normally sensitive to moisture content, it can be deduced that the fines in ITL play a determinant role in the behaviour of ITL (Duong 2013; Trinh 2011).

Due to the heterogeneity of ITL soils, mainly in their fines amount and nature, several authors (Duong 2013; Fortunato et al. 2010; Indraratna et al. 2013; Rujikiatkamjorn et al. 2012) studied the impact of fine content on the mechanical behaviour of the ITL/fouled soils (Figure I.13). The different amounts of fines can be expressed with the fouling index described by (Selig and Waters 1994):

$$F_I = P_4 + P_{200}$$

(I.1)

where P_4 and P_{200} are the percentages of the materials passing through the 4.75 mm and the 0.075 mm sieves, respectively.
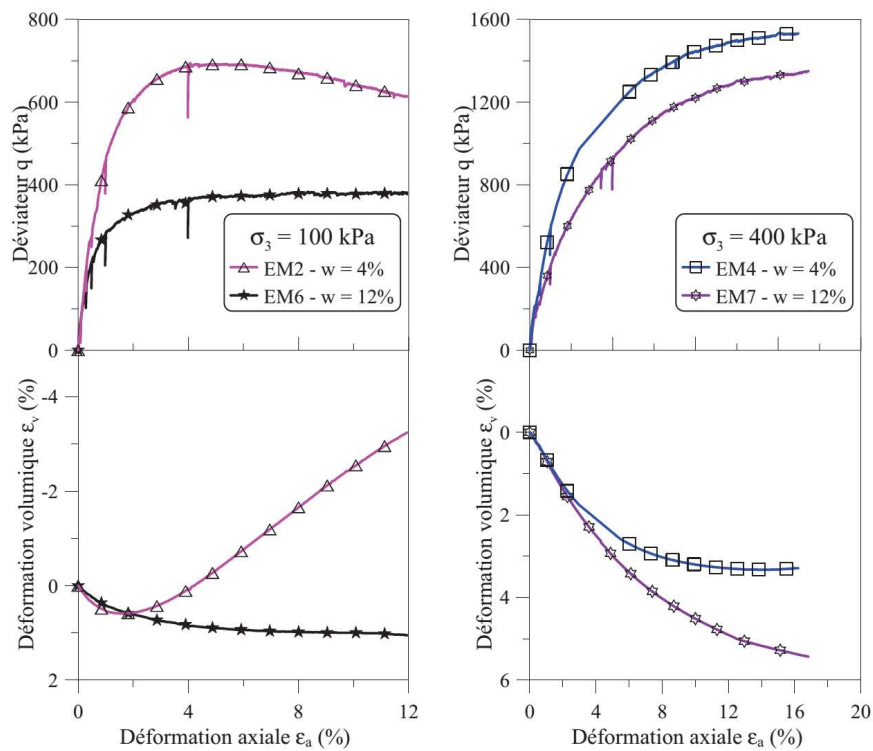
Figure I.12. Triaxial test results for Interlayer soil at different moisture contents (4% and 12%) and different confining pressures (100 kPa and 400 kPa) (Trinh 2011)

The mechanical behaviour of blanket layer or ITL with different percentage of fines was studied by (Rujikiatkamjorn et al. 2012), showing similar results to those of French ITL soils (Duong 2013; Trinh 2011). Increasing confining pressure increases the shear strength. However, increasing the confining pressure while there is a bigger amount of fines leads the soil to lightly decrease its deviator resistance if all the other parameters are kept stable.

Moreover, the compressibility of soil increases also with the increase of amount of fines (Figure I.14).
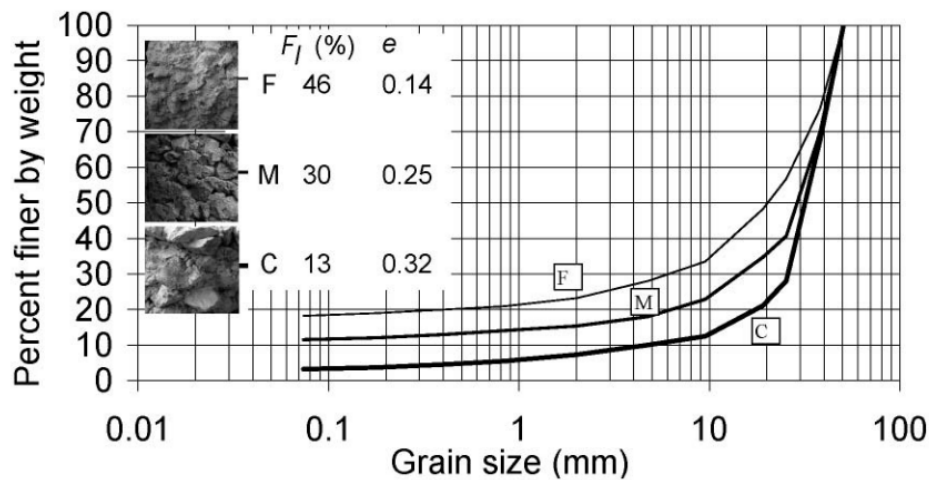
Figure I.13. Grain size distribution of fouled ballast soils with different fouling indexes (Fortunato et al. 2010)
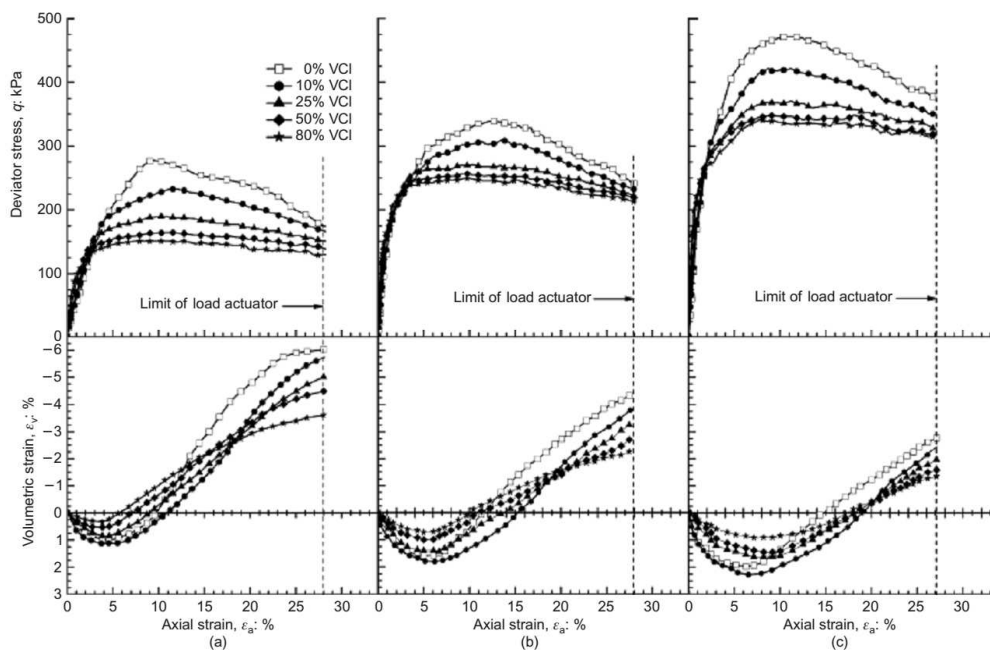
Figure I.14. Stress–strain behaviour in isotropically consolidated drained tests for different fouling degrees at confining pressures: (a) 10 kPa; (b) 30 kPa; (c) 60 kPa (Rujikiatkamjorn et al. 2012)

The capping layer below the sub-ballast layer in new lines is the layer on which the track-bed and super-structure are built. This layer provides a stable foundation for sub-ballast and ballast layers. The stiffness of capping layer can influence the super-structure performance

(Araujo 2010). Moreover, the capping layer is composed of sandy gravel of 0/31.5 mm (SNCF 1995). This layer is also compacted at 100% OPM and must be insensitive to moisture content changes (Selig and Waters 1994). In addition, this layer allows the traffic of machinery for the implementation of the sub-ballast layer without risk of damage to the subgrade (Trinh 2011). The implementation of a capping layer is only mandatory when poor subgrade soils are found (with low bearing capacity). The thickness of this layer is always larger than 15 cm (Trinh 2011) for all the types of railway lines loadings (UIC 2009).

The subgrade can be natural ground or placed soil. If the natural mechanical properties of the soil to be used as subgrade are not satisfactory, stabilizations could be applied using lime or cement (Selig and Waters 1994). The poor quality of subgrade constitutes one of the most important causes of failures due to the impossibility of maintenance operations after construction (Araujo 2010; Duong et al. 2014).

I.2.3   *Railway loading*

The railway track supports the vertical, lateral and longitudinal forces caused by train loads. However, transverse and longitudinal loads from trains have less influence on the track behaviour than the vertical loads (Trinh 2011). The elements of the super-structure and their geometrical design (track lateral banking and inclination of rails with respect to the direction of wheel's load) are configured to transmit the train loads vertically from the train wheels through the rest of structure (Calvo-Poyo 2005). Other longitudinal and lateral stresses are inferred to the track structure elements such as rails, sleepers and ballast through the strains caused by temperature changes in CWR sections (Continuous Welded Rail), especially in curve tracks. In this section, loads caused by train traffic are analysed: the amplitudes of stress to each part of the track and the excited frequencies due to train loading.

The load from one wheel located just over one sleeper is supposed to be distributed along the rail through the adjacent sleepers (Figure I.15) (Selig and Waters 1994). The load is transferred from the wheel/rail contact to the sleepers that transmit the load down to the structure by their contact surface with under-sleeper ballast grains. Compression stresses may appear in the two sleepers adjacent to the loaded one and smaller tractions at the third consecutive sleeper (remote from load). About 39 % of the load is received by the sleeper under the load while 48% is distributed between the two sleepers adjacent to the loaded one,

and the rest of the load (14%) is supposed to be shared between the sleepers at third position from the loaded one (Profillidis, 1983).
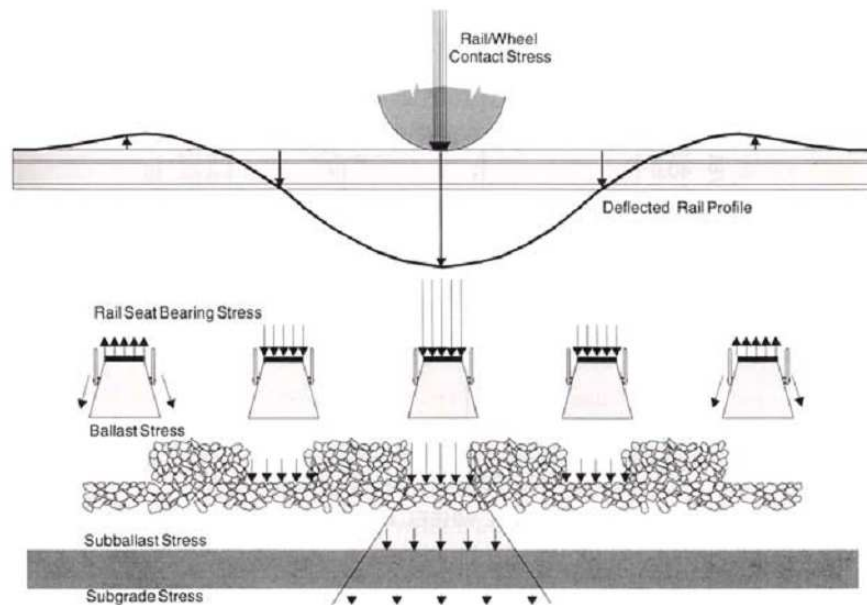
Figure I.15. Load distribution along 5 adjacent sleepers to the wheel contact (Selig and Waters 1994)

I.2.3.1 Loading amplitude

The load amplitude is reduced from the wheel/rail contact point at the rolling surface through the subgrade soil. The materials can spread the load amplitude in different manners. The empirical method of load diffusion is presented in Figure I.16.

The UIC classifies railway lines into several categories, depending on the type of traffic which is allowed to run on it (UIC 2009), taking into account the vertical forces in a track and other characteristics. Hence, the requirements for vertical load limits in terms of axle distance, maximum load per axle and per unit length, are established in four categories (A,B,C and D for 160, 180, 200 and 225 kN/axle respectively) (Ferreira 2010). In most of European networks the static load is limited to 225 kN/axle while in the north-American railways this load could go up to 400 kN/axle for freight trains.

The total vertical train loads can be classified into two groups: quasi-static and dynamic loads (Esveld 2001). In Europe, the part of static axle load refers to the train gravity load and is

limited to 225 kN. Axle loads are normally lower than 150 kN for passenger coaches (i.e. HST or regional passenger trains) and between 200 kN to 225 kN for full-loaded freight wagons and locomotives. The locomotives used in conventional lines at 200 km/h also apply 225 kN per axle, being 900 kN their total weight on 4 axles (Ferreira 2010). The dynamic component of traffic load is related to the amplification due to a moving mass that will be discussed later in this study.
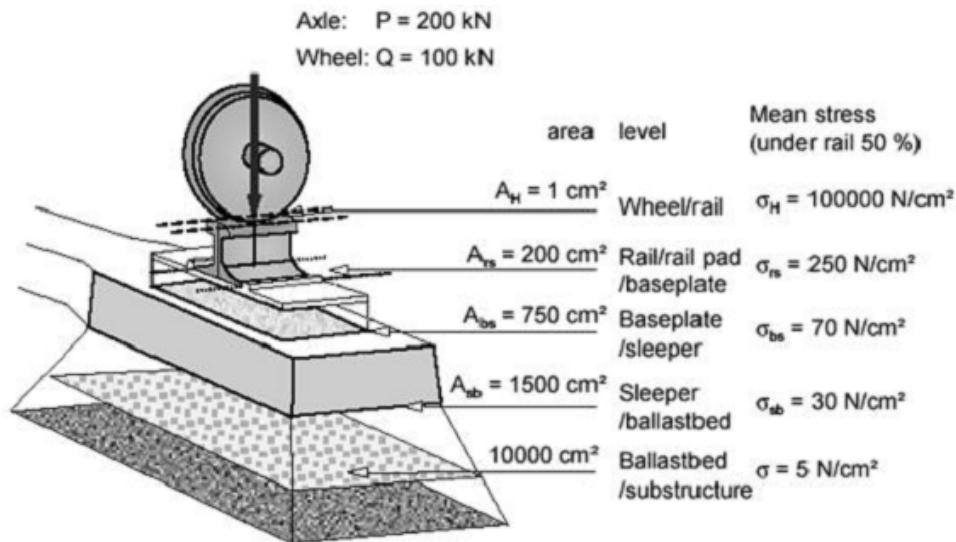
Figure I.16. Example of transmission of loads through railway components from wheel to ballast layer, in (Esveld 2001) cited by(Paderno 2010)

To assess the load amplitude cause by traffic loading transmitted through the subgrade, the elasticity Boussinesq solutions can be used (Doyle 1980). A comparison between a theoretical, a semi-empirical and an empirical method are presented in Figure I.17.

Considering the loading surface as a rectangle (the contact surface A_S between sleeper and ballast), the circular wheel loading surface a_{wheel} could be approximately calculated with Equation (I.2) (Kurzweil 1972):

$$a_{wheel} = \left[\frac{A_S}{\pi} \right]^{0.5} = \left[\frac{B \cdot L}{\pi} \right]^{0.5}$$

(I.2)

where B is the width of sleeper (in meters); L is the effective length of sleeper in contact with the ballast (also in meters). Between the methods presented in Figure I.17, the load diffusion

empirical method is the most used in practice. This method supposes that the load is vertically distributed with a 1:1 or 1:2 slope for all the sub-structure materials. The 1:2 slope of load diffusion seems closer to the theoretical method. The load amplitude decreases over depth in an exponential way; the amplitude decrease is higher in the first meters for larger diffusion slopes (1:1).
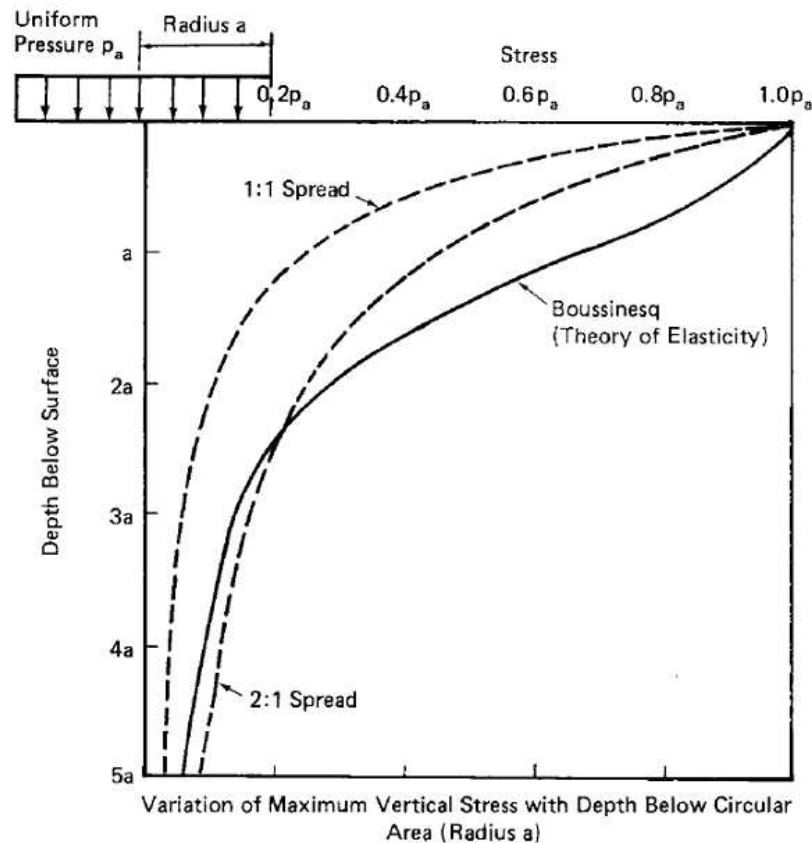
Figure I.17. Comparison between Boussinesq and load diffusion methods (Doyle 1980)

Zuada Coelho (2011) studied the load amplitudes generated in a transition zone under traffic loading (160 kN/axle). In the middle of the ballast layer (30 cm under sleeper contact surface), before a transition zone, vertical stresses of about 30 kPa and deflections of 0.8 mm were found (Figure I.18). The displacements were slightly larger just under the rail (even larger under the right rail due to the embankment slope). Higher differences in the calculated stresses were found just under the rail or in the middle of a sleeper. The longitudinal and lateral stresses have less than half the amplitude of the vertical stress amplitude developed by the soil just under the axle load. The longitudinal and lateral displacements are almost negligible.

21
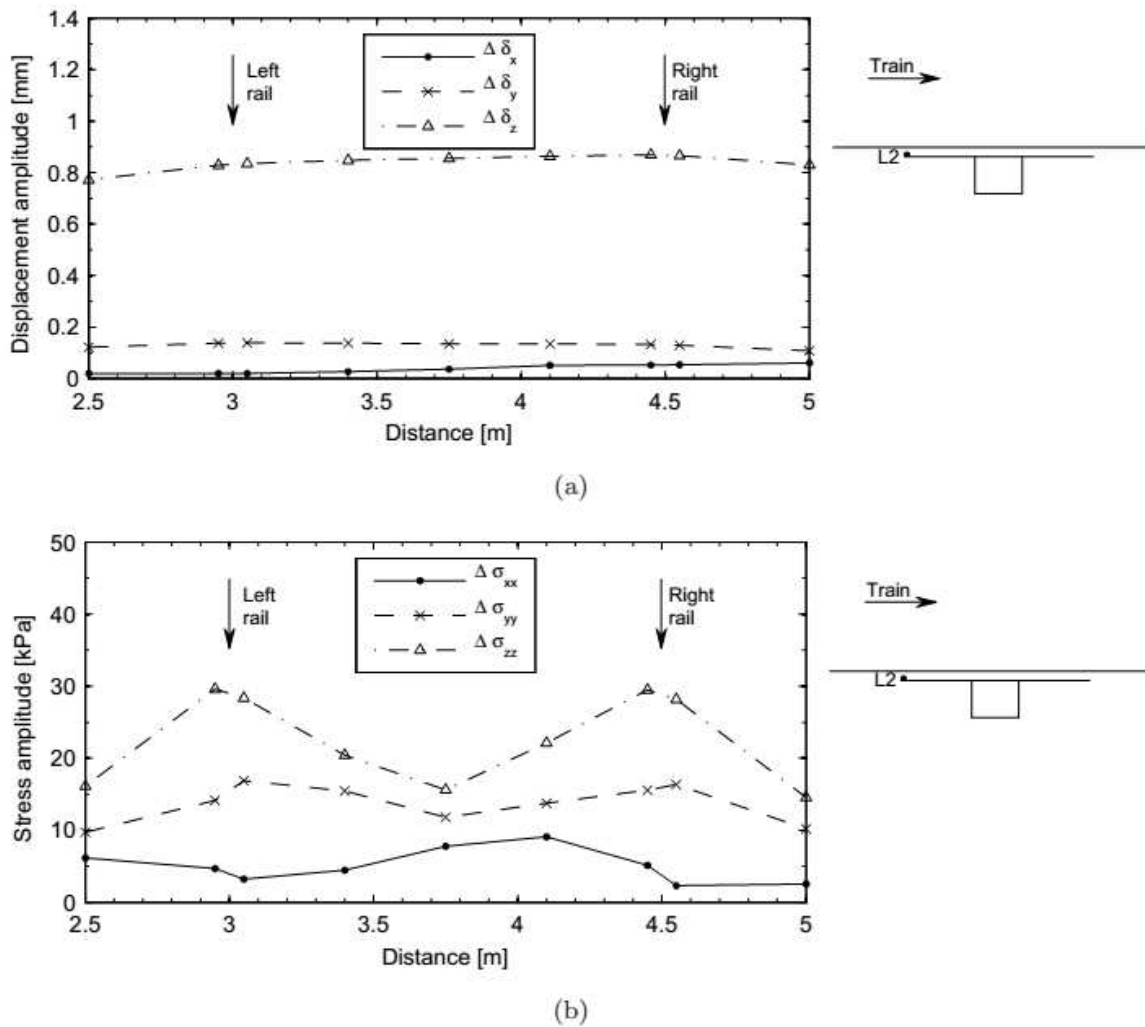
Figure I.18. Values under the sleeper for: (a) average displacements ($\Delta\delta_x$, $\Delta\delta_y$ and $\Delta\delta_z$) and (b) average stresses ($\Delta\sigma_{xx}$, $\Delta\sigma_{yy}$ and $\Delta\sigma_{zz}$), for an alignment located on an embankment(position L2) (Zuada-Coelho 2011)

Similar results of vertical stress amplitudes were found by Kempfert and Hu (1999), at z=-0.46 m and at z=-1 m depth under the sleeper/ballast contact. A similar stress distribution over depth, as that proposed by the diffusion method (Paderno 2010), and analogous transversal distribution through a sleeper as for Zuada-Coelho (2011), were also presented in literature. Results are presented in Figure I.19. Considering the stress amplitudes caused by a locomotive at 280 km/h, the stress amplitudes measured at 0.86 m under the rail running surface were higher (about 50 kPa) just under the rail position for ballasted tracks than the value in the middle of sleeper (21 kPa). At 1.46 m below the running surface, the difference between rail and middle sleeper was reduced compared with upper positions. Lower stress amplitudes and lower differences in transversal distribution of loads were measured for concrete and asphaltic slab-track compared to a ballasted track.
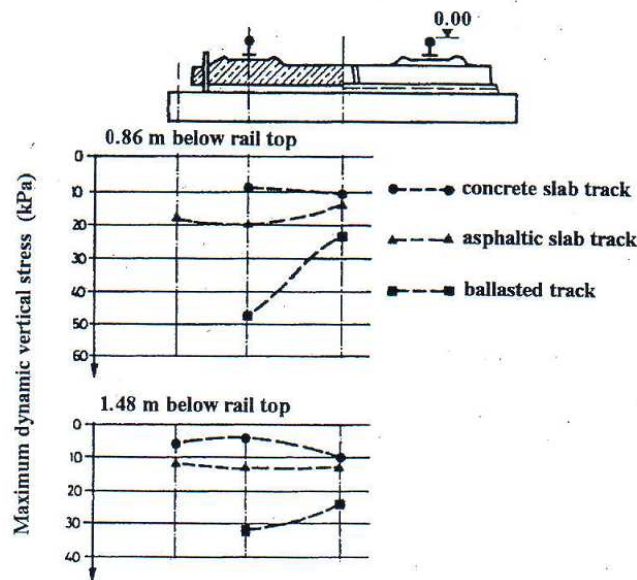
Figure I.19. Dependency of maximum dynamic stress in substructure and subsoil on superstructure (Kempfert and Hu 1999)

I.2.3.2 Loading frequency

When a train loads a track, several frequencies are excited. Each wavelength in track system or rolling-stock geometry will excite a different frequency during a train passage. A frequency excitation f corresponds to a wavelength λ of the railway system at a given train speed v_T (Auersch 1994), see Equation (I.3):

$$f = \frac{v_T}{\lambda} \tag{I.3}$$

For instance, if the axles-distance wavelength in a locomotive is $\lambda = 2.8$ m, and the locomotive is running at $v_T = 200$ km/h, the excited frequency is $f = 19.8$ Hz. The excited frequencies considering the wavelengths of a TGV train over a French track are presented in Figure I.20 (adapted from Müller-Boruttau and Breitsamer, 2004). Five speeds from 20 km/h to 200 km/h are considered in the figure, being 220 km/h the maximum service speed in European conventional tracks.
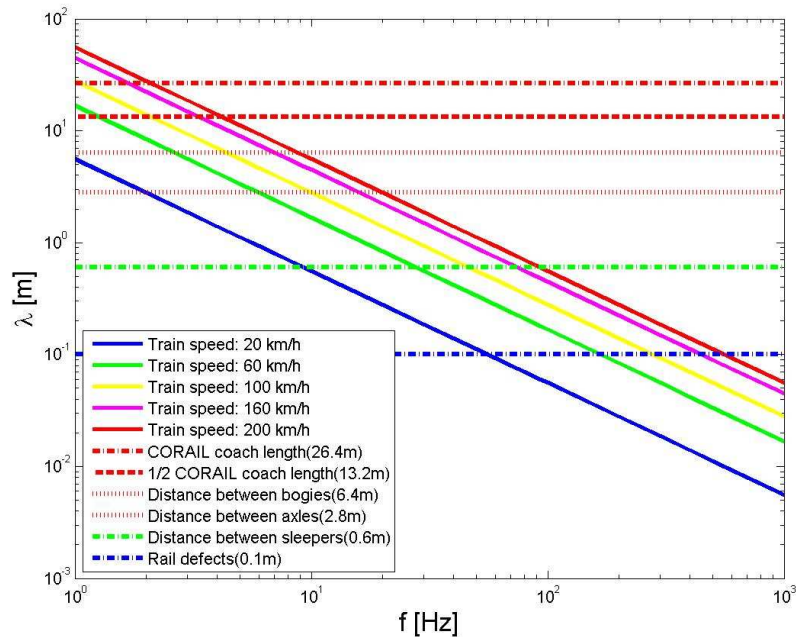
Figure I.20. Relationship between train speed, wavelength and frequency in the train/track system (Adapted from Müller-Boruttau and Breitsamer, 2004)

The energy provided by each frequency depends on the types of loading of track (Galvín et al. 2010). Low frequencies (f< 50 Hz) are the most energetic frequencies in ballasted tracks (Galvín and Domínguez 2009) and responsible for the movements and strains of track elements (Vega et al. 2012). Moreover, frequencies corresponding to long wavelengths such as coach distance, half-coach distance, bogies-distance and axle distance are the most energetic in ballasted tracks (Cui et al. 2014; Ferreira 2010; Galvín and Domínguez 2009). For a given type of loading (same train) running at different speeds, each wavelength increases the excited frequency and the amount of energy provided to the system (Figure I.21).
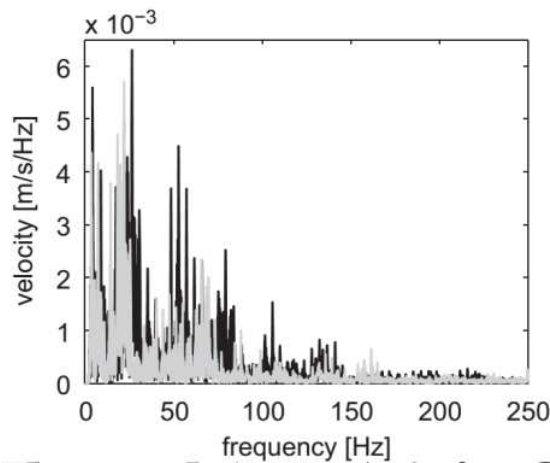
Figure I.21. Power spectrum density content from vertical velocity measurements at the sleeper during a AVE-Alstom train passage: v_T= 298 km/h (black line) and v_T= 250 km/h (grey line) (Galvín and Domínguez 2007)

I.3   TRACK AUSCULTATION METHODS

This section mainly presents the in-situ prospection methods used in this study to analyse the different constitutive materials of a track-bed. Different in-situ methods can be used to assess the performance of track-bed materials. The soil behaviour depends on the amplitude of loadings (Nasreddine 2004; Studer and Koller 1997). Each test permits to prospect a different amplitude range of soil; consequently different type of responses can be obtained (Sawangsuriya 2012; Sawangsuriya et al. 2005). Different methods are used in railway auscultations. They can be classified as geophysical, geotechnical and classical methods.

The common geotechnical prospection methods used by SNCF are the core sampling train and the excavator surveys. The core sampler train is a special train which is able to extract core samples from track-bed (SNCF-INFRA 2011), allowing the nature and thickness of every layer to be analysed (Duong et al. 2014). A camera takes photographs of each sample. The layers thicknesses are analysed from the images. Samples till 1.50 m depth could be obtained, enough for identifying the most important layers in conventional track-beds. This investigation method was also reported in literature (Brough et al. 2003, 2006). On the other hand, surveys made by a digger (Trinh 2011) could take samples till 1.5 m in conventional tracks. This sampling method uses an excavator and is more intrusive to track materials compared to penetrometers or core sampling methods. This method could also define the thicknesses and natures of the soils constituting the track-bed, by analysing the profile of soil

after the extraction of the materials. This kind of test could be performed in the space between sleepers (about 40 cm) to check the ballast fouling or layers' thicknesses. Nevertheless, these tests are also commonly conducted before installing a new super-structure during track renewals.

The geophysical and geotechnical methods used in this study are described in the following sub-sections.

I.3.1 Geophysical methods

Wave propagation methods become popular techniques in evaluating the stiffness of geomaterials and in field monitoring (Sawangsuriya 2012). Cross-hole, Up and Down hole, GPR and MASW/SASW tests are used in railway prospection for research purposes but not for periodic maintenance operations (Hall 2003; Sussmann et al. 2003). These tests are characterized by the low strain amplitudes. For example, the cross-hole test measures the p-wave and s-wave velocities between two boreholes (Karl 2005). By testing at various depths, a velocity profile can be obtained. Mok et al., (1988) described the application of the attenuation coefficient method for the determination of damping ratio based on a cross-hole test. However, the up-hole and down-hole tests could also be used to determine the wave velocities profile (Karl 2005), with a different set-up of source and vibration receivers. Additionally, GPR is based on the transmission of short electromagnetic waves into the subsurface and the display of the reflection and propagation energy at each interface of subsurface materials (Sussmann et al. 2003). The data obtained from a GPR test represent the electromagnetic energy transmitted from the antenna and reflected from the subsurface boundaries back to the antenna (Ulaby 1997). Moreover, the relative difference in dielectric constant at an interface defines the magnitude of the reflection. The dielectric constant is affected mostly by soil moisture content, soil type, density, and structure. As water and soil type variations are the major contributors to the deterioration of tracks, GPR could provide an indication of track performance because it could detect water and soil changes (Vorster and Gräbe 2013). The thicknesses of different materials of track-bed, marked changes in water content or ballast fouling could be also determined using GPR (Su, Indraratna, and Rujikiatkamjorn 2011; Su, Indraratna, Rujikiatkamjorn, et al. 2011).

The method of Multi-channel Analysis of Surface Wave (MASW) is a geophysical (seismic refraction) method that is widely used for sub-surface characterisation (Anbazhagan et al. 2010). These methods use the surface wave generated by an impulsive source and recorded by, at least, a pair of receivers (Ganji et al. 1997; Stokoe II et al. 1994; Tokimatsu 1995). MASW could be used to analyse the propagation wave velocities in soil and the thicknesses of different layers of soil (Araujo 2010; Degrande and Schillemans 2001). However, MASW method is not easily applied on ballasted track surface due to contact failures between geophone pins and the large ballast grains (Jacqueline 2014). In the laboratory, measurements on track physic models were performed by Anbazhagan et al. (2010) to determine the shear modulus of ballasted tracks under different fouling conditions. MASW also identifies the sub-surface material boundaries and spatial variations of shear wave velocity (Lam and Wong 2011; Sitharam and Anbazhagan 2006; Zeng et al. 2012). MASW can also be used for the geotechnical characterisation of near surface materials (Anbazhagan et al. 2010).

There are three steps to perform this test: geophones are nailed into the soil and an excitation is produced with a hammer (scheme in Figure I.22), the dispersion curve is obtained from the analysis of the surface waves and then an inversion of the dispersion curves is performed to obtain a 1D shear wave velocity curve. Using several 1D curves (one per hammer excitation) a 2D figure could be obtained from interpolation. The distance between the first and the last geophones will define the maximum prospection depth (half the geophone line distance). The distance between geophones in the MASW line defines the minimum prospection depth in the track. The shorter the distance between geophones the better the resolution of the first centimetres of the prospected soil.
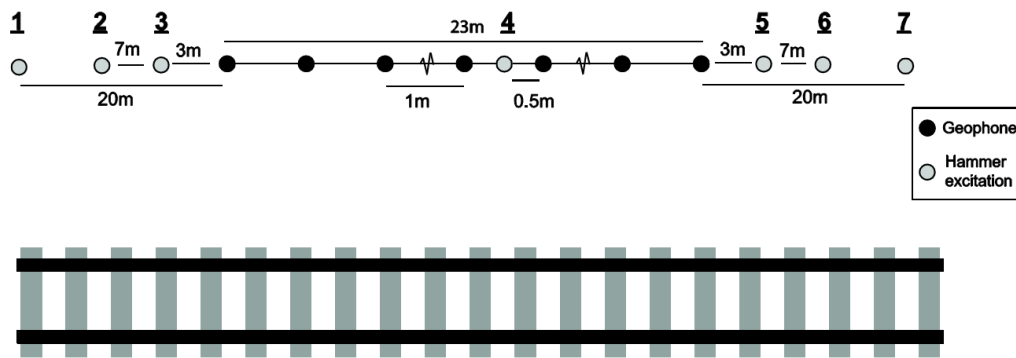
Figure I.22. MASW geophone configuration (Connolly, Giannopoulos, Fan, et al. 2013; D. Connolly et al. 2014)

From each hammer blow, all modes will be displayed in the dispersion figure. The main mode dispersion points (M_0 mode) must be defined and picked (corresponding to surface waves) (Figure I.23).
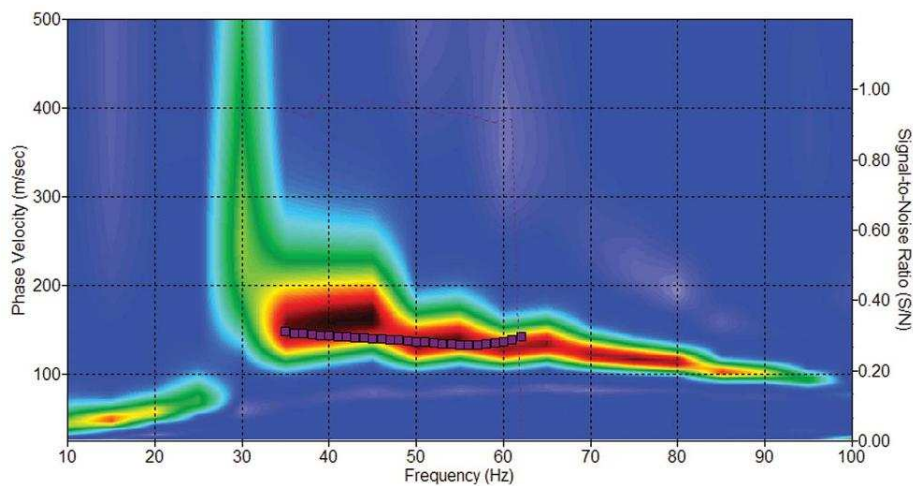
Figure I.23. Main mode dispersion curve of ballast bed (Anbazhagan et al. 2010)

Using the data obtained from MASW it is also possible to perform a refraction analysis and calculate p-waves (Connolly et al., 2014). The results can be presented by a shear wave velocity profile and a compression wave velocity profile for the prospected depth (Figure I.24). The wave velocity profile is estimated from the inversion of the surface wave data. This is because the type of data used for inversion was the fundamental-mode (M_0) dispersion curve, whose shape is determined mostly by the v_s structure of the earth (Bodet 2005). The shear wave velocity (v_s) is one of the main soil parameters used in geotechnical engineering because it is related to the soil shear modulus, which is associated with material stiffness and the ground bearing capacity.
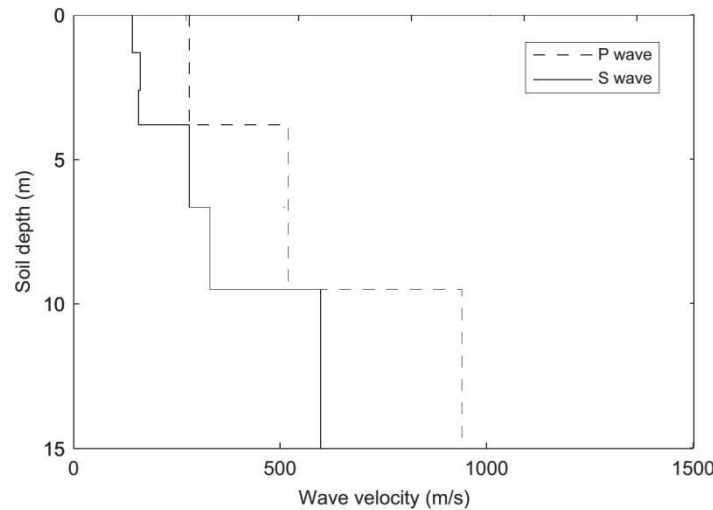
Figure I.24. Wave velocity profile of a track (embankment) determined by MASW (Connolly et al., 2014)

I.3.2   *Geotechnical methods*

Among the geotechnical prospection methods, there are some that are frequently used in railways like PANDA tests or other common tests as those mentioned before (core samples and excavated soil surveys). Other tests are less frequently used, such as deflectometers (in all their variety of sizes) that are used for different purposes during works planning, renewal or maintenance operations. These geotechnical methods are presented in this sub-section.

I.3.2.1 Panda & Geo-endoscopic tests

As other dynamic cone penetrometers (DCP), the PANDA test is to drive into the soil a cone (of 2, 4 or 10 cm²) fixed at the end of a set of rods using a hammer. Its originality relies in the use of variable energy after each hammer hit, which is measured in an indirect way by the sensors of PANDA (Benz 2009). For each hammer hit, the depth of rod insertion and the rod-tip dynamic resistance q_d are recorded automatically. This dynamic tip resistance, in the case of a constant energy penetrometer, is obtained from Equation (I.4):

$$q_d = \frac{M_H \cdot g \cdot H_{mass}}{(1 + a_{mass})} \cdot \frac{1}{d_R} \tag{I.4}$$

where M_H the hammer mass, H_{mass} its falling height, a_{mass} the ratio between masses ($a_{mass} = P/M$, being P the rod-system penetrated mass and M_H the hammer mass), g the gravity ($g = 9.8$ m/s²), and d_R the penetration of the rod after impact. The propagation of a mechanic wave through an elastic material as the rod, is done through energy transfer. The total energy transported by a wave is divided into two parts (Fairhurst 1961): kinetic energy $E_K(x,t)$ and potential energy of deformation $E_S(x,t)$. The total energy transferred by the rods is determined through the deformation of the rod and the speed of wave that is estimated from the responses of strain gages and an accelerometer installed at the top of the rod. This method is named E_{FV} and was introduced by Sy (1991) to estimate the amount of energy transferred to the rods in the SPT test after each blow. As a variable energy impact is applied, the hammer mass may not influence the measurements (Zhou 1997). The sensors installed allow the kinetic energy transferred under each blow to be estimated (Figure I.25a). Other displacement sensor, a LVDT installed at the data logger and connected to the rod, measures the penetration of the rod after each impact. The data logger receives this data after each hit and estimates q_d for each depth.

This is an easy and fast test to be performed on a track. The advantages of PANDA penetrometer are its weight and size but also its power of penetration, enough to prospect a large range of different soils: it is able to prospect up to 6 m depth depending on the soil resistance ($q_d < 50$ MPa) and the rod-soil friction. Normally, the feasibility of this test depends on the maximum size of particles (50 mm max); but some tests related to the control of the layer of ballast (up to 60 mm diameter) using PANDA showed valid results (Elaskar 2006; Révol 2005). Note that to ensure the validity of Equation 4, the energy impact should be adapted each time in order to obtain a penetration between 2 and 20 mm per impact (Chaigneau 2001). This makes PANDA test measurements almost continuous (in track-bed scale) and efficient to identify layer thickness or soil compaction defects through the q_d values (Figure I.25b).

Several authors developed formulas to relate soil elastic modulus to q_d determined from DCP tests (Amini 2003; Cassan 1988; Chai and Roslie 1998; Chua 1988; Lunne et al. 1997).
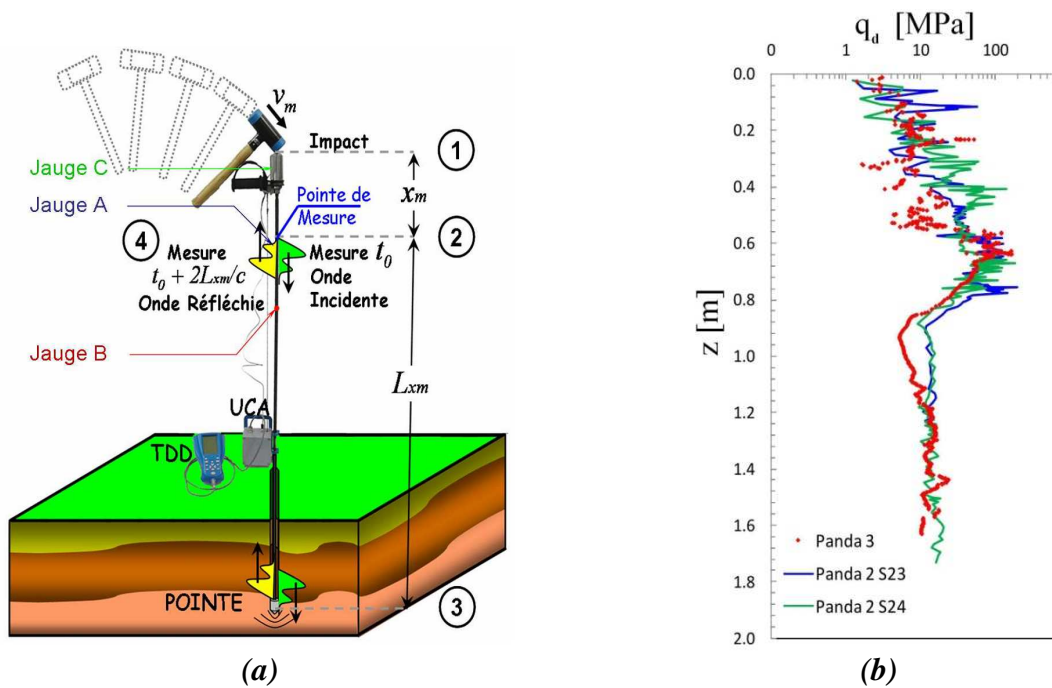
Figure I.25. (a) Measuring principle of PANDA test (Benz 2009); (b) example of results from PANDA tests performed on the same soil (Escobar et al. 2014)

The geo-endoscopic test uses a little video camera (wired to a data logger by a soft and flexible cable) to observe the soil. The camera is introduced into the hole of a previously performed PANDA test (15 mm of diameter). The results allow a qualitative characterization of soil, and even the estimation of the soil grain size distribution (Breul 1995; Haddani 2005; Haddani et al. 2011).

To perform a geo-endoscopic test, the following materials are required: hollow metric rods (inner diameter of 10 mm), a wired and waterproof little video-camera (with light) and a data logger able to record the camera images and the auscultation depth. Firstly, a 15 mm diameter hole (from PANDA tests) is used to perform the test. A wire connected to the camera (IP 65, 8.6 mm of diameter) is descended through the rod from the surface. The hollow rod has a lateral opened window of 5 mm width for taking soil images. To reach deeper auscultation points, additional rods can be added by screwing. A maximum auscultation depth of 6 m can be reached. While the wire is descended at a speed of 5 mm/s, images are recorded by the data logger. The intensity of the light coupled with the camera and the camera focus are controlled from the ground surface. An image is taken every 10 mm of depth and a continuous video is recorded for each test. The images and video obtained from this test allow the determination of different materials constituting the investigated soil layers: the thickness, the soil nature and even its hydric state. This information can help better analyse the PANDA

test results (Figure I.26). Consequently, PANDA and geo-endoscopic tests are often coupled for a same auscultation point.
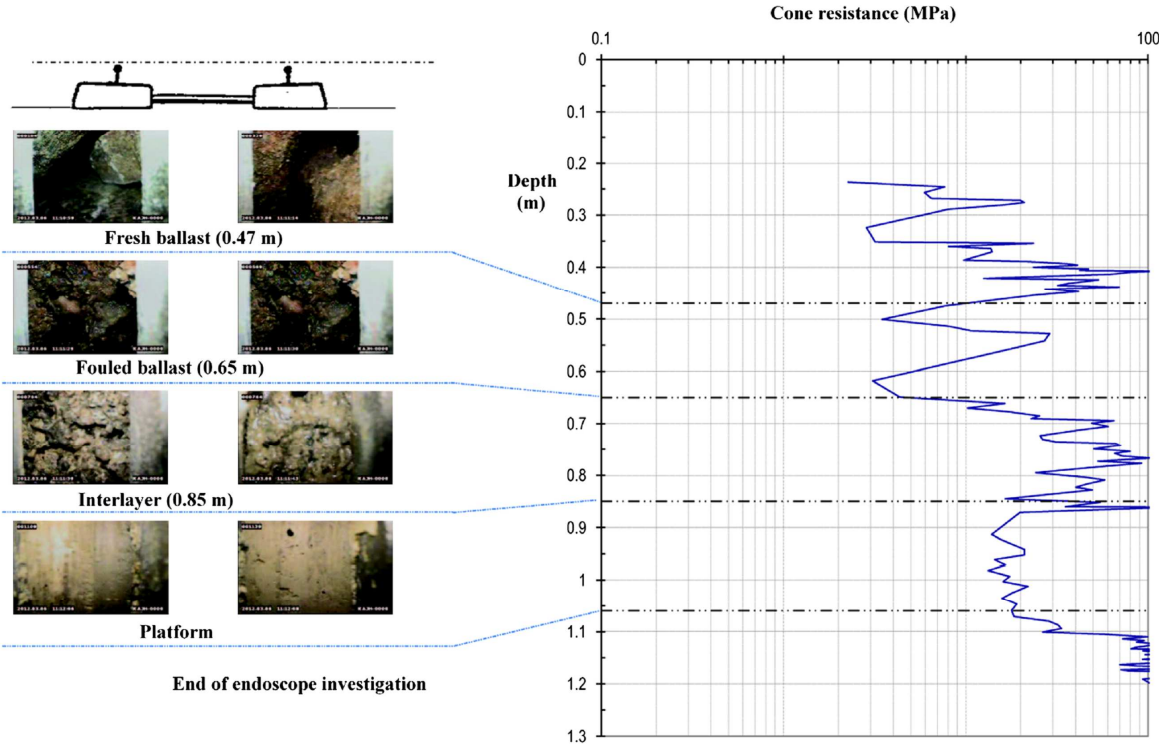
Figure I.26. Comparison between Panda and Geondoscope results obtained for the same railway track (Duong et al. 2014)

I.3.2.2 LWD (Light-Weight Deflectometer)

The dynamic plate loading test using LWD was developed as a technique to determine the dynamic deformation modulus E_{vd} (Bayerischen Staatsministerium 2012) and the static modulus E_{v2} of soil. This test can be used for soil compaction control and for the determination of the track bearing capacity. The LWD tests are faster and easier to operate than the PANDA test. This test applies a pulse load on soil via a disk-shaped steel plate that is assumed to be rigid (Figure I.27).
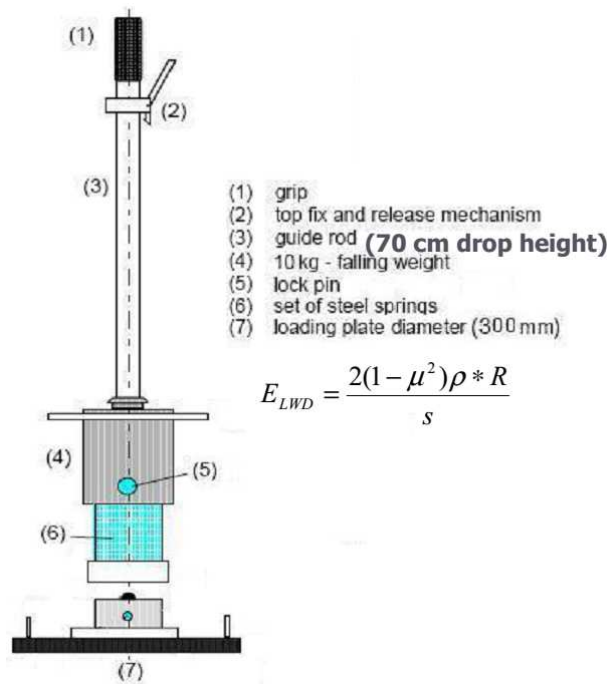
Figure I.27. Scheme of LWD test (Bayerischen Staatsministerium 2012)

The loading system consists of a 10 kg drop weight that, once released, falls along a rod from 72 cm height until the base disk. The force applied is 7.07 kN on a 30 cm diameter disk. The influenced soil thickness (testing depth) is considered to be equal to the disk diameter. The loading device is positioned on a sphere in the middle of the disk so that only compressive force can be transmitted to the loading plate. An accelerometer is installed in the middle of the plate, recording the maximum vertical displacement of the plate during the impact (Figure I.28). The applied stress is assumed to be constant. This test can be conducted on coarse-grained soils and mixed-grains soils as well as fine-grained soils. The percentage of grains in the soil larger than 63 mm must be limited. To obtain a valid measurement on a point, three impacts need to be applied as previous compaction. Then, three new impacts are applied and the mean displacement value by the three impacts is considered. The Boussinesq formula is used to estimate E_{vd} (Bayerischen Staatsministerium 2012):

$$E_{vd} = \frac{c_{plate} \cdot (1-v)^2 \cdot \Delta\sigma \cdot r}{\Delta d} \tag{I.5}$$

where r is the radium of the plate (radius equal to 15 cm), c_{plate} is the plate coefficient ($c_{plate} = \pi/2$ if rigid and $c_{plate} = 2$ if soft), $\Delta\sigma$ is the maximum stress applied (considered as constant, 0.1

MPa), υ is the Poisson coefficient (0.3) and Δd is the maximum displacement obtained during the test. With the values considered, Equation (I.5) can be rewritten as Equation (I.6):

$$E_{vd} = \frac{22.5}{\Delta d}$$ (I.6)

The relationship between the static (E_{v2}) and the dynamic modulus (E_{vd}) is given by Equation (I.7) (Bayerischen Staatsministerium 2012):

$$E_{v2} = 600 \cdot \ln\left(\frac{300}{300 - E_{vd}}\right)$$ (I.7)

From the obtained dynamic modulus it is also possible to estimate the California Bearing Ratio (CBR), commonly used to estimate the mechanical resistance and bearing capacity of soils (ASTM 2007). Note that the LWD test presents some limitations as the auscultation depth of 30 to 40 cm, a range of static modulus between 20 and 180 MPa and a maximum displacement of plate between 0.1 and 2 mm.
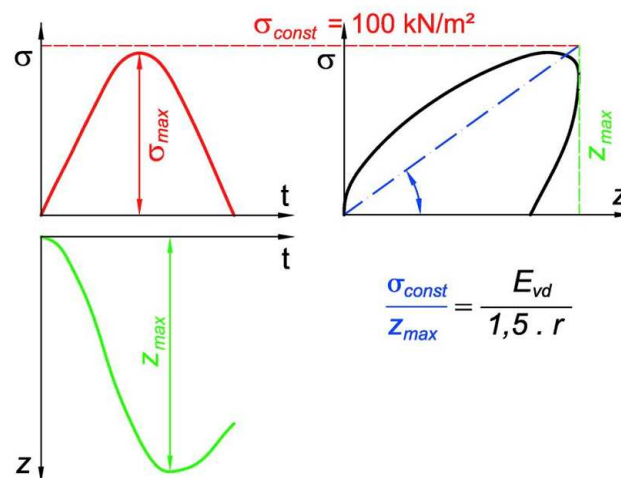

Figure I.28. Load acting on the soil and displacement and working diagram of the LWD plate (Adam et al. 2003)

I.4 INFLUENCING FACTORS ON TRACK-BED SOIL BEHAVIOUR

Some loading characteristics or soil state parameters have important effects on track-bed soil behaviour under train cyclic loading, at short and long terms.

In the following, critical speed, load amplification and vibration propagation are discussed first, followed by the main soil dynamic parameters (elastic modulus and damping ratio) as well as the permanent deformation and weather effect on track-bed soil behaviour.

I.4.1   Dynamic railway loading

The vibrations generated by trains cause two distinct effects: noise, and track vibration (Knothe and Grassie 1993; Krylov et al. 2000). Noise vibration occurs at high frequencies ($f > 100$ Hz) while displacements due to vibrations are caused mainly by low frequencies ($f < 50$ Hz). These vibrations are mainly generated from the wheel/rail contact, determined by the rail and the wheel states and the superstructure/track-bed interaction (Figure I.29).
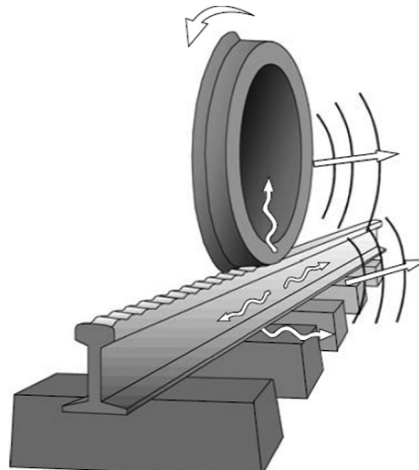
Figure I.29. Scheme of rolling noise generated by rough contact between rail and wheels (Thompson and Jones 2006)

Part of this vibration is transmitted through the track-bed and the soil (Figure I.30), and other part is reflected at the interfaces or transmitted through the soil (surface waves as Rayleigh or Love waves). While compression or shear waves are transmitted from the loading point through the interior of the track's platform, the surface waves being transmitted in surface. The surface waves, as Rayleigh waves, contains and transports more energy as compared to the compression and shear waves even though they are slower than the two others (Kouroussis 2009).
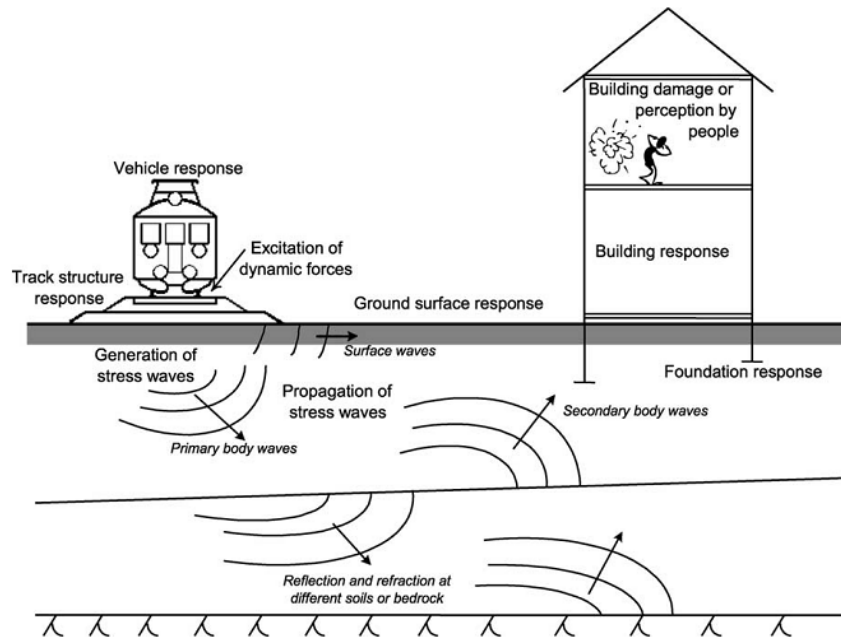
Figure I.30. The transmission process of train-induced ground vibrations (Hall 2003)

The particle movement associated with the Rayleigh wave passing through the surface of an infinite, elastic and isotropic half-space is elliptic and retrograde (Figure I.31). This movement results from the interference of P and SV (Shear-Vertical) waves. This movement in particular decrease exponentially in depth, such that the environment which is affected by this wave propagation is a function of its wavelength (Bodet 2005).
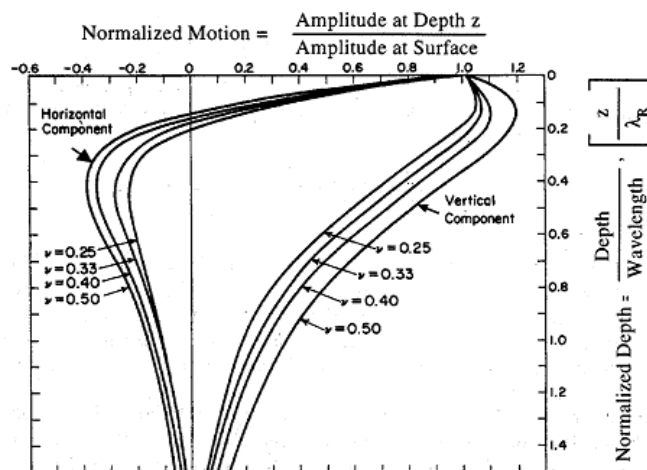
Figure I.31. Particle movement associated with the Rayleigh wave travelling at the surface of an infinite half-space, elastic, homogeneous and isotropic space (Richart et al. 1970)

I.4.1.1 Critical train speed

Increasing the service speed is one of the main priorities of the railway infrastructure administrators. There is a rapid evolution of this speed record since the 80's, getting up to 575 km/h and expecting to reach new records in the coming years (Ferreira 2010). The gap between the record speed and the operation speed is about 250 km/h and has been stable during the evolution of the reached records. The maximum commercial speeds could be found in high speed lines while in conventional lines the maximum train speed is limited to 220 km/h (UIC 2009). The evolution of maximum commercial speeds in the railway networks in Europe and Japan is similar. The maximum commercial speed of 350 km/h is expected to be reached in a near future. The increase of the commercial speed on the infrastructure requires advances in several scientific domains involving different elements of the network (catenary, rail, maintenance optimization, etc.). Madshus and Kaynia (2000) studied the effect of an increase of speed on the behaviour a conventional track. In Figure I.32 is presented the evolution of the negative and positive maximum vertical displacements under train axle loading. These displacements are supposed to be amplified since the train speed reached a 'cut-off' speed of a track until the critical speed of the track.
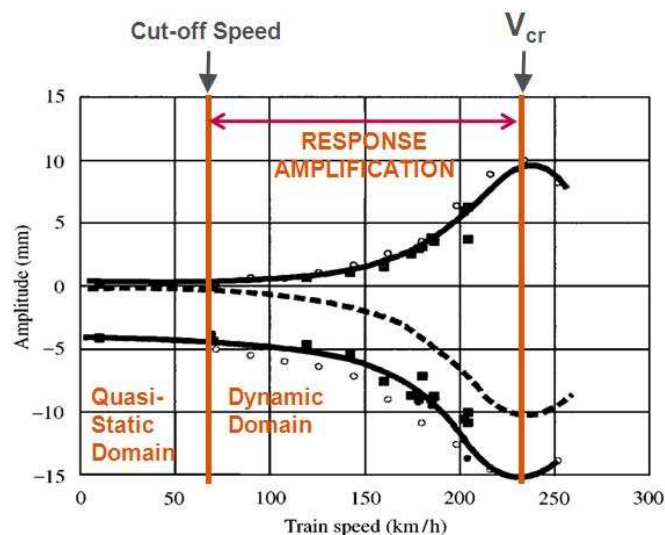
Figure I.32. Displacement amplitude versus train speed: measured and simulated: ■, Measured by Displacement transducer; ●, Measured by Accelerometer; ○, Simulated; ▬, Best fit line, total displacement, ---, Best fit line, isolated dynamic amplification (adapted from Madshus and Kaynia, 2000)

After Krylov (1995), the critical speed of a track is reached when a train runs at the Rayleigh wave velocity of the ground. The estimation of this Rayleigh wave velocity of a site is

complicated to be performed from conventional site investigations (Connolly et al., 2014). Calculations could be performed using previous works on soils characterizations (Jamiolkowski et al. 1979) obtaining correlations of the Rayleigh waves velocity with the soil plasticity index (Connolly et al., 2014). The increase of track's vertical displacement due to the increase of train speed is caused by the track inertia becoming a strong driving force. This inertia-driven displacement is not only in the downward direction but also upwards (Hendry 2007). This 'resonance-like' effect appears when a moving line point-load reaches the speed of the surface waves. This effect was previously demonstrated theoretically (De Barros and Luco 1995). Sheng et al. (2004) stated that critical speed of a track is then fully dominated by the properties of wave propagation in the embankment ground system and of the bending wave propagation in the track, that is controlled by the shear wave velocity of the track-bed materials (Alves Costa et al. 2015). The shear wave velocity (v_s) depends on the material properties:

$$v_s = \sqrt{\frac{G}{\rho}} \tag{I.8}$$

where G is the shear modulus and ρ is the material density. The Rayleigh wave speed v_R (controlling the displacement amplification in homogenous tracks) is related to the shear wave, and can be approximated with Equation (I.9) (Bergman 1948):

$$v_R = \frac{0.87 + 1.12 \cdot \upsilon}{1 + \upsilon} \cdot v_s \tag{I.9}$$

being ν the Poisson ratio (in the range 0 - 0.5). The track behaviour could be estimated using a Winkler foundation approach. The critical speed, considering the track as a beam-foundation system, in which large increases in beam displacements are expected with train speed, could be estimated using Equation (I.10) (Alias 1986):

$$c_{cr} = \sqrt[4]{\frac{4 \cdot kEI}{m^2}} \tag{I.10}$$

where k is the stiffness of Winkler foundation, E is the modulus of elasticity of the beam, I is the inertia moment of the beam and m is the mass per unit of length of beam (including ballast

and soil layers). In order to estimate the displacement amplification, semi-analytical models were developed and reported in literature (Alves Costa et al. 2015; Hendry 2007; Hendry et al. 2010; Sheng et al. 2004), with the track modelled by a range of beams, masses and spring-dashpots in order to take into account the dynamic behaviour of distinct components of track, namely rails, railpads, sleepers and ballast layer. However, when the geometry of the system is not compatible with the restrictions imposed by a semi-analytical approach (for instance when the embankment height is not negligible) it is necessary to apply 3D methods (Connolly, Giannopoulos, and Forde 2013; Hall 2003; Kouroussis 2009).

If a homogenous track-bed is considered, when the load speed is much lower than the Rayleigh wave velocity in the ground, the pattern of deformation on the ground surface is similar to the quasi-static deformation (Figure I.33 left). However, when the load speed reaches this limit the waves propagate in the ground give rise to the Mach cone (Figure I.33 right). If the embankment is homogeneous (Figure I.34a), only one P-SV mode occurs in correspondence with the Rayleigh wave velocity (Andersen and Nielsen 2003; Andersen 2002). However, when the ground is layered (Figure I.34b and Figure I.34c) the critical speed should be somewhere between Rayleigh wave velocity on track and the shear wave velocity of subgrade soil. Even though the critical speed is dominated by the properties of wave propagation in subgrade soil, the dispersive characteristics of the waves determine several differences in the dynamic behaviour pattern, as opposed to what happens in the homogeneous case. This effect is justified by the excitation of higher order modes, represented by the intersection of loading lines with the P-SV curves (Figure I.35). Then, for these cases, the critical speed becomes function of the frequency (Zuada-Coelho 2011). The estimation of the critical speed is performed by solving the 'eigenvalue' problem of the wave dispersion system due to the interaction between track and subgrade soil (Auersch 1994; Connolly et al. 2015; Wolf 1985).
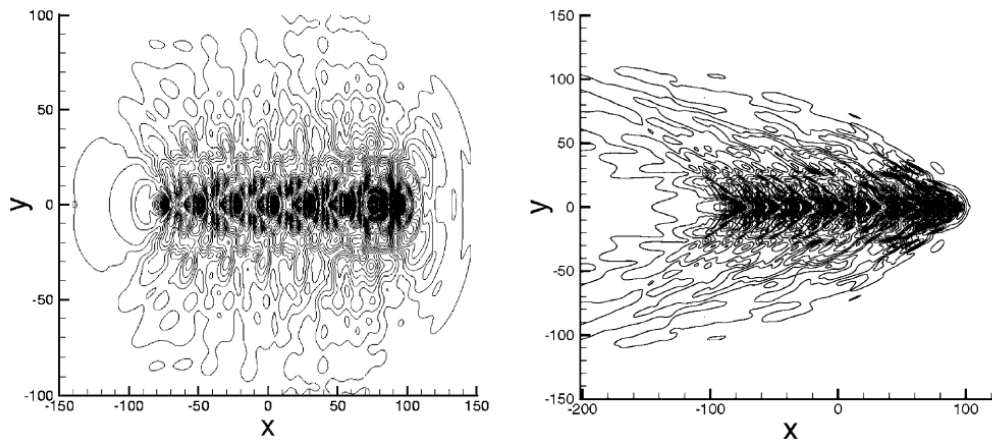
Figure I.33. Displacement field on soil surface for Corail train in sub- (left) and super-Rayleigh (right) regimes. Units of longitudinal and lateral distances in m (Picoux and Le Houédec 2005)
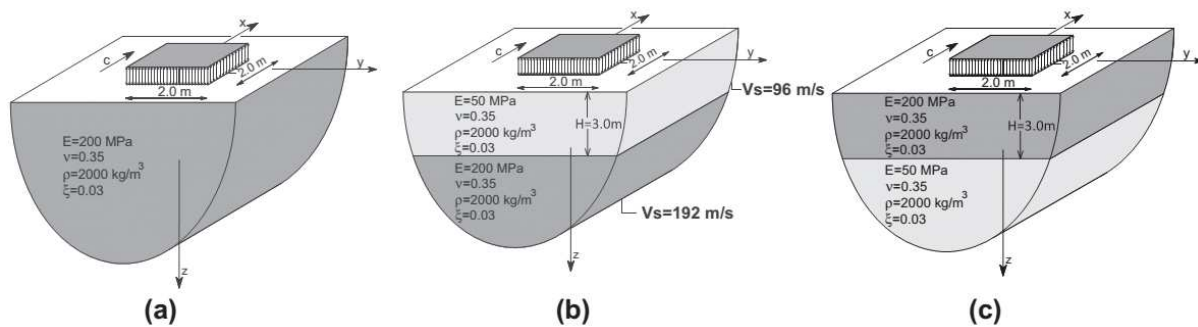
Figure I.34. General characteristics of the ground considered in parametric study of critical speed: (a) Ground 1; (b) Ground 2; (c) Ground 3 (Alves Costa et al. 2015)

In the case of half-space, the amplification of the rail vertical displacement as function of a dimensionless load speed ($M=v_T/v_s$) for different track types (slab and ballasted track, which require different boundary conditions for the semi-analytical model) shows higher values when the track flexibility is higher (Figure I.36a). However, the critical speed of the system does not vary with track properties and is dominated by the ground properties. Nevertheless, when a layered ground is taken into account (Figure I.36b and Figure I.36c), the critical speed depends on the properties of the propagating waves over the track and can be evaluated by analysing the dispersion characteristics of the track-bed (Alves Costa et al. 2015). The change in stiffness profile (with a lower stiffness layer between track and subgrade soil, Figure I.36b) modifies the behaviour pattern of the system because of the dispersive properties of the P-SV waves along the track. However, when the soil stiffness decreases over depth, the P-SV waves have inversely dispersive properties (propagating wave speed increases with the excitation loading frequency) and the thickness of layers become determinant in the critical speed

determination. For example, in case 3 (Figure I.34), the critical speed is mainly controlled by the ground properties and not by the track type.
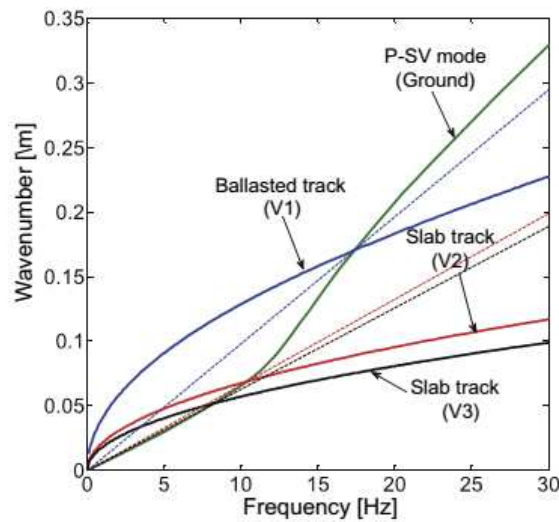
Figure I.35. Dispersion relationship for half-space and for different tracks (Alves Costa et al. 2015)

(a)   **(b)**   **(c)**
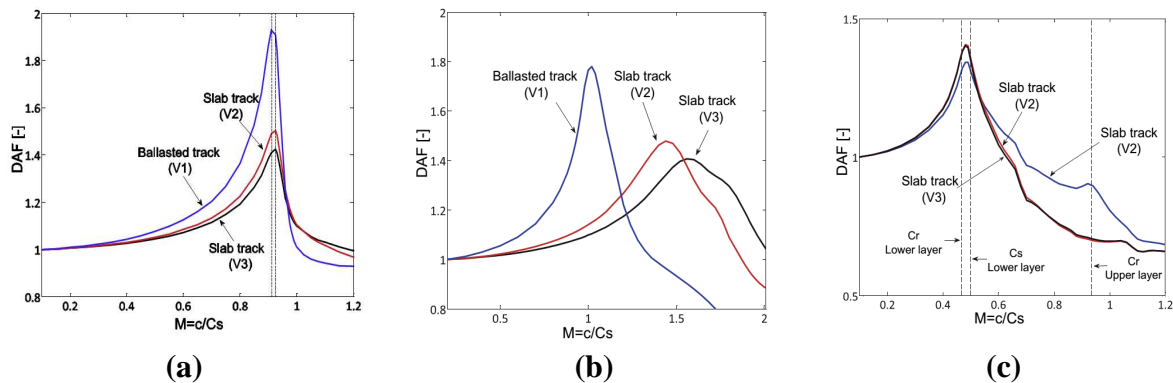
Figure I.36. Evolution of dynamic amplification with train speed of rail deflection (a) Ground 1 (b) Ground 2 and (c) Ground 3 (Alves Costa et al. 2015)

When train speed increases and approaches the critical train speed, the displacements under loading become larger and consequently the strains inferred to track-bed materials. This strain increase could lead to a track-bed material degradation. The degradation of the track-bed shear modulus with train speed increase was modelled by Alves-Costa et al. (2010) using FEM and obtaining degradations of up to 40% of the modulus (from shallower track materials) when the train approached the critical speed (Figure I.37).
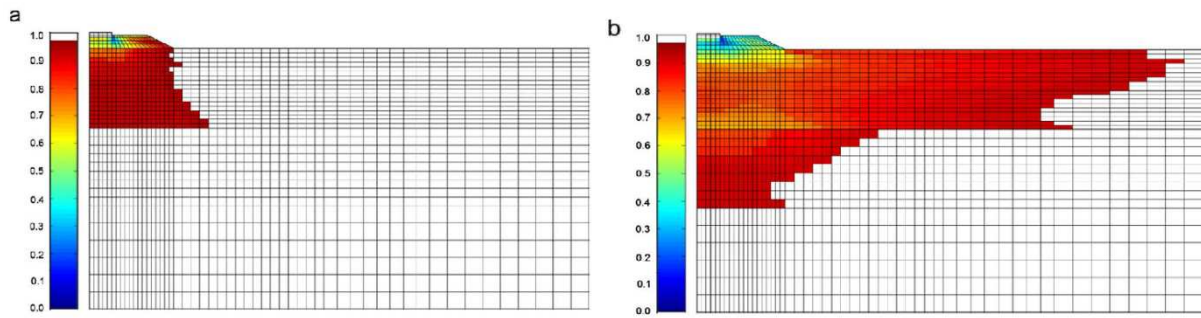
Figure I.37. Contours of shear modulus degradation (G_{sec}/G_{max}): (a) v_T=70 km/h; (b) v_T=204 km/h (adapted from Alves Costa et al., 2010)

I.4.1.2 Load amplification

The forces exerted to track-bed materials are generated by train axles. These loads are transmitted to different track elements and track-bed soils as presented in I.2.3.1. The loads may be distinguished following three main directions (Ferreira 2010; Lim 2004; Trinh 2011): vertical, transversal and longitudinal. The higher and more important loads to be considered are the vertical loads. These loads are due to the static loading (weight) and dynamic overloading (wheel/track interaction). Each one of these 3 force components has a specific incidence on track design and behaviour (Giannakos 2004, 2010).

The static loads might be amplified (dynamic overload) when the train speed increases depending on track-bed mechanical properties (Bian et al. 2014). Moreover, the dynamic overloading depends also highly on track condition such as rail defects and corrugation and track irregularity. Figure I.38 presents the static and dynamic wheel loads as cumulative frequency distribution (cdf) for a test track (Figure I.38a) and a real line between New York and Washington DC (Figure I.38b) (Lim 2004; Selig and Waters 1994). It can be noted that dynamic amplifications are more frequent for higher axle loads as compared to the smaller loading masses. Comparison of sub-figures (a) and (b) also shows that track conditions (better for the test track) could strongly influence the dynamic overloadings, being bigger for an operational track, with more track irregularities due to operation loadings (Lim 2004). In addition, in most of European networks when circulating at speeds over 250km/h, the maximum axle loads are significantly reduced to nearly 170 kN/axle in order to limit track damage (Ferreira 2010).
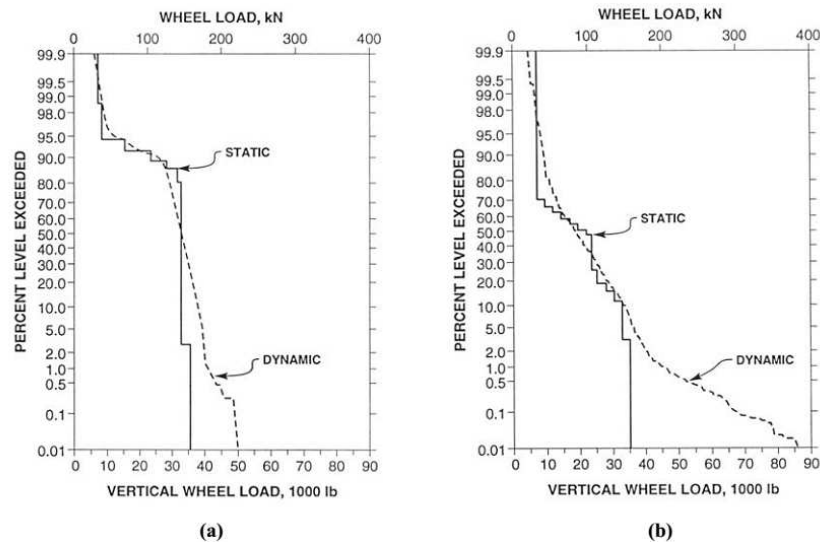
Figure I.38. Static and dynamic wheel loads for (a) Colorado test track and (b) mainline track between New York and Washington (Selig and Waters 1994) cited by (Lim 2004)

Amplifications are developed for vertical displacement and stress amplitudes generated at different track-bed layers under train loading (axles' loadings) when the train speed increases (Alves Fernandes 2014) (Figure I.39). These vertical stress amplifications (of about 10% considering a E=70 MPa subgrade) depend mainly on the critical speed of track (Bian et al., 2014; Chen et al., 2013; Chen et al., 2013).
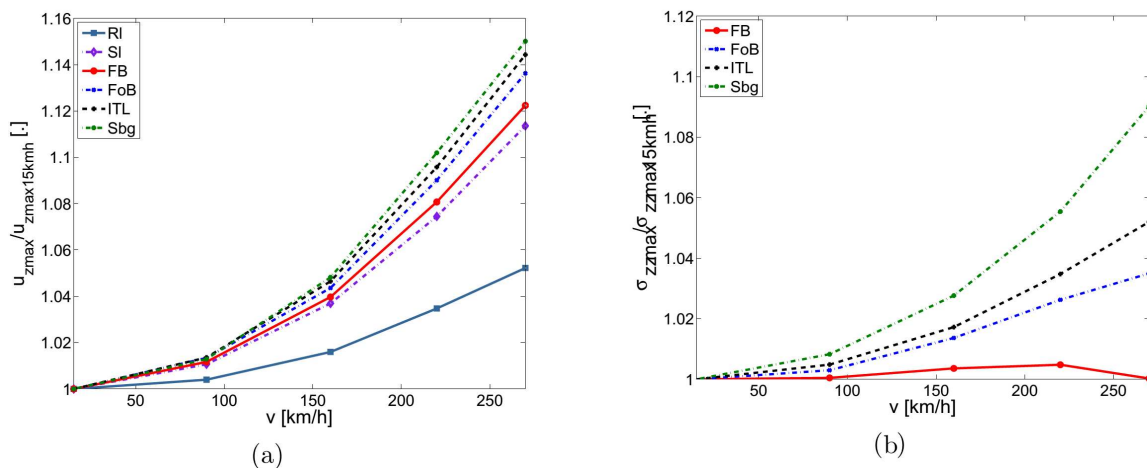
Figure I.39. Normalized kinematic response of track materials with increasing moving load speed. a) Vertical displacement (u_z); b) Vertical stress (σ_{zz}). Rl: Rail, Sl: Sleeper, FB: Fresh ballast, FoB: Fouled ballast, ITL: Interlayer, Sbg: Subgrade (Alves Fernandes 2014)

Stress amplifications appear in all the track-bed materials (from surface to subgrade) when the train speed is increased (Figure I.40). Absolute stress values are higher in shallower layers

43

and lower for deeper subgrade. The stress attenuation shape in depth is similar (exponential decay shape) for different speeds (Bian et al. 2014).
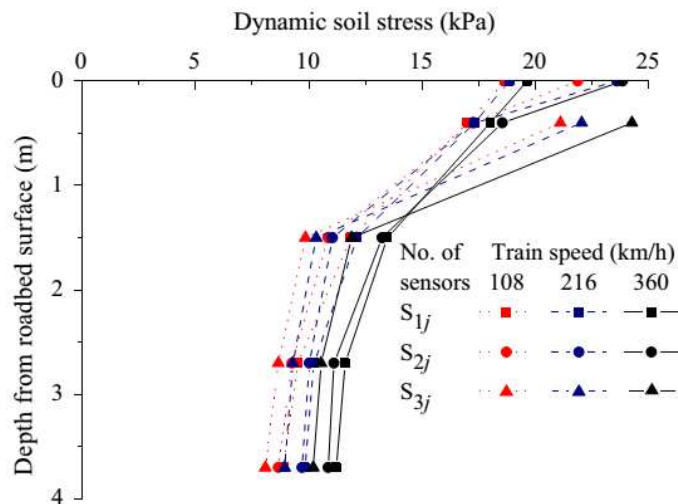
Figure I.40. Distributions of dynamic soil stresses over depth (which denote five measuring layers from roadbed surface; S1j, S2j, and S3j correspond to soil pressure sensors located under the track center, under the rails, and under the edge of the concrete base, respectively) (Bian et al. 2014)

Amplifications will be larger (compared to their quasi-static reaction under loading) for deeper layers in track-bed structure (Alves Fernandes 2014; Bian et al. 2014). Stress amplification with train speed at subgrade could be 5 times larger than that at interlayer depth. But for the absolute quasi-static loads, they are higher for interlayer than for subgrade (Figure I.40).

I.4.1.3 Vibration propagation and attenuation

The train-induced vibrations have been largely studied, especially during the past 15 years (Connolly et al. 2015; Degrande and Schillemans 2001; Kouroussis and Verlinden 2015; Kouroussis et al. 2011, 2015). These measurements were firstly motivated to study the effect of vibration increase in the nearby buildings if the train speed was upgraded (Degrande and Schillemans 2001; Kouroussis 2009). The train-induced vibrations in distance were studied on sites all over Europe (Sweden, Belgium, Spain, Portugal) (Connolly et al. 2015). The vibration amplitudes are strongly attenuated in distance from their origin at the track. This propagation in distance follows an exponential decrease of the amplitude (Figure I.41) (Auersch 1994; Connolly et al. 2015). More than 60% of the amplitude at the vibration source

is absorbed within the first 10 meters from the track. Similar results were found for similar train loadings (Connolly et al. 2015; Degrande and Schillemans 2001; Galvín and Domínguez 2009).. The train speed seems to increase the amplitudes at their source, and consequently the amplitudes will increase during its propagation (Connolly et al. 2015). Moreover, the vibration amplitude levels were higher in cutting sites than in embankments and at-grade tracks (Connolly et al., 2014). Nevertheless, embankment sites generated more vibration amplitudes in high-frequency values, but these vibrations are rapidly attenuated with distance compared to quasi-static or low frequencies loadings (Connolly et al., 2014). The influence of vibrations on structures near the track, in terms of train-induced vibrations, was studied by measuring and modelling their effects (Kouroussis et al. 2014; Lombaert 2014). It was proved that an embedded concrete wall could absorb part of the arriving vibration amplitudes from the track and consequently filter part of the vibrations between the source and the rest of the environment.
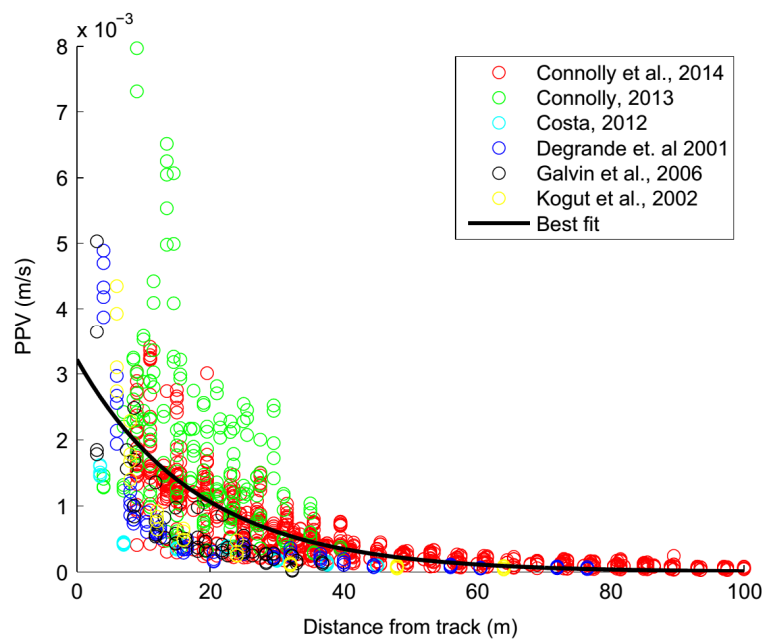
Figure I.41. Peak Particle Velocity variation in vibration levels with track offset (Connolly et al. 2015)

Some track elements like rail pads, under-sleeper pads or ballast mats could modify the track-soil interaction and the train-induced vibrations through the track-bed and the environment (Ferreira and López-Pita 2015; Sol-Sánchez et al. 2015). Softer pads reduce the vibration amplitudes (low-frequency vibrations) transmitted to the rest of the track-bed and environment while noise levels (high-frequency vibrations) increase near the source.

However, stiffer pads amplify low frequency vibrations and reduce noise levels near the source.

I.4.2 Hydro-mechanical properties

The hydric and mechanical state of track-bed materials could affect their behaviour under different railway loadings (in amplitude and frequency).

I.4.2.1 Dynamic soil response

The dynamic properties of materials are often expressed in terms of stiffness and material damping (Menq 2003). These properties are used to determine the velocities and amplitude decay of stress as they propagate through different materials. Stiffness can be expressed in terms of shear (G) or Young's (E) moduli. These moduli are related to the shear v_s and compression v_p waves velocities respectively. Material damping, expressed in terms of damping ratio, D_r, is also associated with each type of stress wave (Menq 2003). The damping ratio is a dimensionless parameter that represents the amount of energy dissipated by a material during a loading cycle compared to the equivalent elastic energy applied on it. In soil dynamics and geotechnical earthquake engineering, the response of materials to shearing motions is generally of most concern. Therefore, the elastic modulus and damping ratio are the required dynamic properties and they are described in the following sub-sections.

I.4.2.1.1 Soil elastic modulus

A harmonic cyclic loading to a soil element (as the railway traffic loading one) leads to a stress-strain diagram as shown in Figure I.42. A hysteresis loop occurs for each loading (a train axle for instance). The modulus is defined as the slope of the line that connects the point of origin and the inversion point between loading and unloading in the stress-strain diagram. This modulus is also called secant modulus or equivalent modulus. It decreases with the increase of load and strain amplitudes. Therefore, the stress-strain relationship is mainly non-linear (Coronado Garcia 2005; Karl 2005). A schematic sketch of the modulus evolution (shear modulus in this case) as a function of shear strain is given in Figure I.43. Three different regions could be differentiated, a linear range domain for very low strains, a

nonlinear elastic range (where low plastic deformations occurs) from 10^{-5} to 10^{-4} and a nonlinear range (where soil is strongly permanently deformed) for strains larger than 10^{-4}.
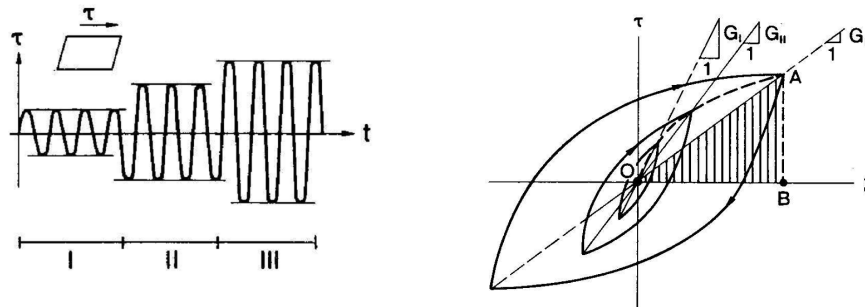
Figure I.42. Cyclic loading: load history and hysteresis loops (Karl 2005)

Laboratory tests have shown that the soil stiffness is strongly influenced by cyclic strain amplitude $\Delta\varepsilon$, void ratio e (or soil density ρ), mean effective consolidation stress σ_c', plasticity index *PI*, over-consolidation ratio (OCR) and number of loading cycles. The modulus decreases first with increasing strain amplitude, then becoming strain independent (Karl 2005). This modulus increases while the number of cycles increases (same cyclic strain amplitude). This occurs mostly if small strain amplitudes are considered in the case of non-cohesive soils. The parameters that influence the modulus are summarized (*G* case) in Table I.1.
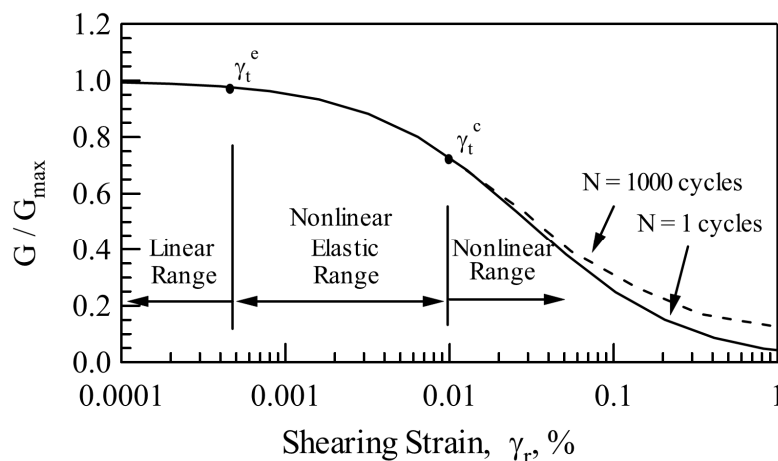
Figure I.43. Typical nonlinear G/G$_{max}$ – log γ curve (Menq 2003)

Table I.1. Influence of different parameters on G_{max} for normally to moderately over consolidated soils (Dobry and Vucetic 1987)

Increasing Parameter	G_{max}
Mean effective stress, σ'_0	Increases with σ'_0
Void ratio, e_0	Decreases with e_0
Geological age, t_g	Increases with t_g
Cementation, C	Increases with c
Over-consolidation ratio, OCR	Increases with OCR
Plasticity index, *PI*	Increases with I_p if OCR>1; stays approximately constant if OCR = 1
Strain rate, γ	No effect for non-plastic soils; increases with strain rate for plastic materials
Number of loading cycles, N	Decreases after N cycles of large cyclic strain amplitudes, but recovers with time in clays; increases with N for sand

The soil stiffness is also strongly affected by the moisture content (Duong, Tang, et al. 2013; Fortunato et al. 2010; Lamas-Lopez et al. 2015; Trinh et al. 2012) as shown in Figure I.44. When effective stress decrease and the saturation level increase, this produces a decrease of soil modulus (Duong, Tang, et al. 2013; Trinh et al. 2012). The loading frequency does not significantly affect the soil modulus (Menq 2003).

Moreover, the isotropic confining pressure makes the soil modulus increase, as shear wave velocity, for small deformations (Menq 2003). An increase of initial density (or decrease of void ratio) induces an increase of soil modulus (Menq 2003). Furthermore, soils constituted by larger grains (with larger D_{50}) increase their maximum soil modulus (Figure I.45). Therefore, if considering a fine matrix soil with large grains inclusions into it (defined by the volumetric fraction of these inclusions compared to the total soil volume, f_v,), the higher this volumetric fraction rate of inclusions grains, the larger the soil's modulus (Pedro 2004; Pedro et al. 2005; Seif-el-Dine 2007).

In addition, an increase of the uniformity coefficient C_u (more heterogeneous soil) (Trinh 2011) may decrease also the soil modulus, mostly for larger strains (Figure I.46).

$$EV_2 = 129.98e^{-0.0345w}$$
$$R^2 = 0.54$$
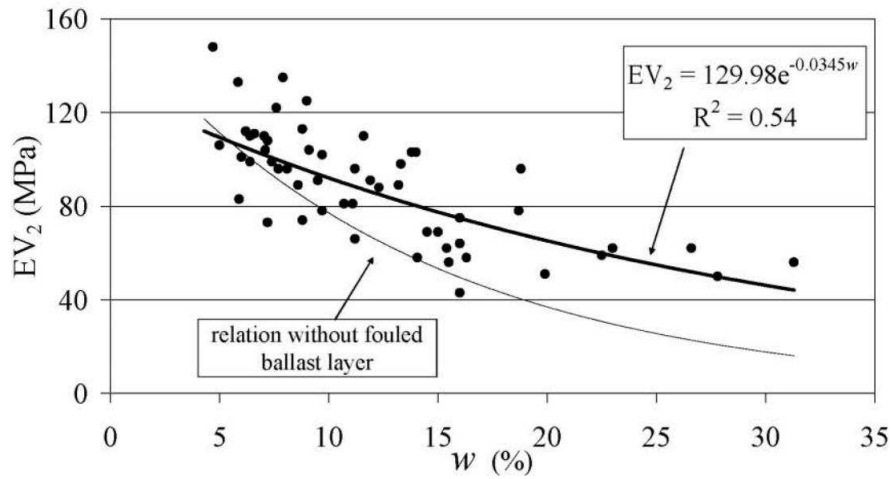
Figure I.44. Deformation modulus determined on fouled ballast soil versus the water content in subgrade soil (Fortunato et al. 2010)

Several authors studied the evolution of dynamic properties for different soils (Ishibashi and Zhang 1993; Ishihara 1996). It was observed that for similar strain amplitudes, more plastic soils present a higher modulus than low plastic soils as shown in Figure I.47. Moreover, the same trend was found for different confining pressures (Alves Costa et al. 2010; Ishihara et al. 1990).
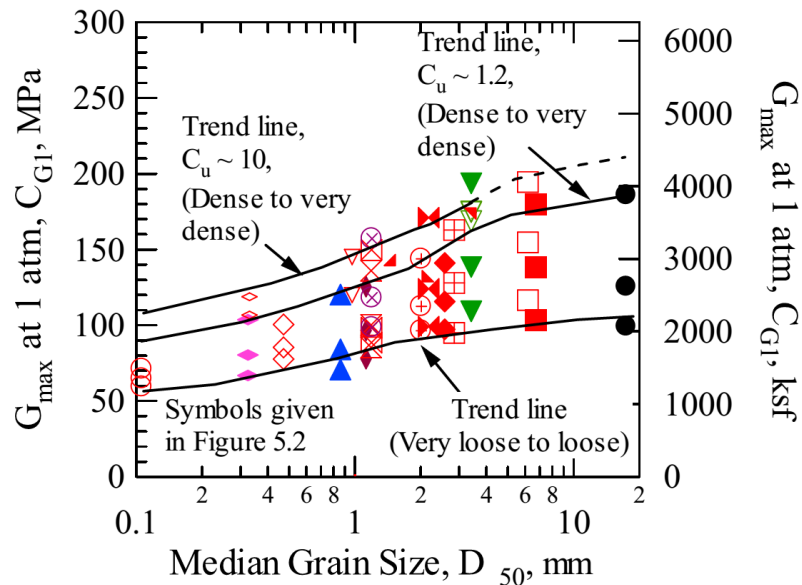
Figure I.45. Trends in the variation of Small-Strain shear modulus at 1 Atm with median grain size of sandy and gravelly soils (Menq 2003)

49
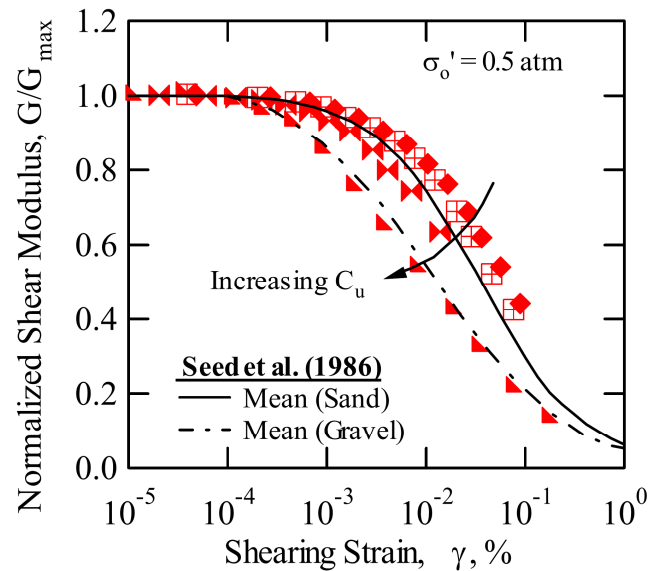
Figure I.46. Effect of Uniformity Coefficient, Cu, on Nonlinear Shear Modulus of Dense to Very Dense Specimens (Menq 2003)

Several studies examined the effect of frequency on the dynamic properties of soils (Bolton and Wilson 1990; d'Onofrio et al. 1999; Iwasaki et al. 1978; Kim and Drabkin 1995; Li et al. 1998; Wilson and Bolton 1989). In general, the dynamic properties of non-cohesive soils do not exhibit frequency dependency (Bolton and Wilson 1990; Hardin and Black 1966; Iwasaki et al. 1978; Menq 2003; Wilson and Bolton 1989). However, other authors showed more recently that loading frequency could strongly impact the modulus trend for cohesive soils as clays (Khan et al. 2009, 2011; Moayerian 2012; Rix and Meng 2005). Therefore, for cohesive soils, the modulus exhibit a moderate increase at frequencies up to 1 Hz and a larger increase at frequencies greater than 10 Hz (Khan et al. 2009, 2011) (Figure I.48).
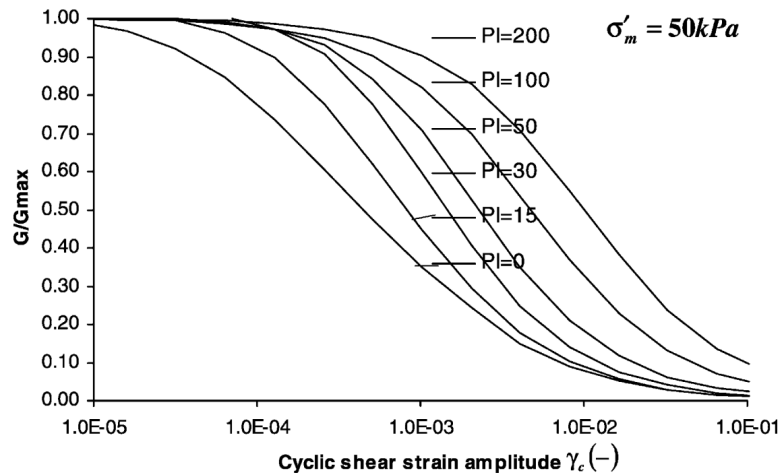
Figure I.47. Typical modulus reduction curves for soils of different plasticity index (Ishibashi and Zhang 1993)
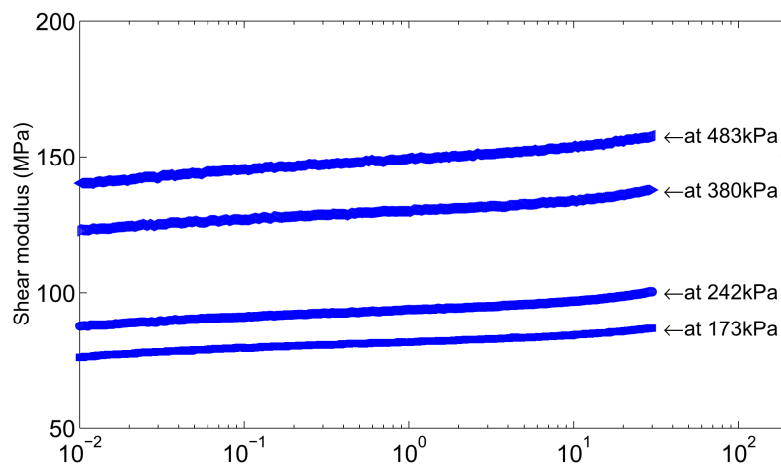
Figure I.48. Loading frequency impact on the modulus of a clay for different effective consolidation pressures (Meng 2003)

I.4.2.1.2   Damping ratio

The damping ratio is a dimensionless measure describing how a system can reduce the energy added by a loading. Energy is dissipated in soils and structures by several mechanisms, including friction, heat generation and plastic yielding. For soils and structures the dominating mechanisms are the effects of various loss mechanisms, usually lumped together and represented by some convenient damping mechanism. Therefore, the parameter that better represents this energy loss mechanism in soils is the damping ratio (Figure I.49) that symbolizes the dissipated energy by the system against the energy stored during its

51

deformation (Karl 2005). These energies are directly correlated to different surfaces developed by a material under a cyclic loading (Figure I.49).
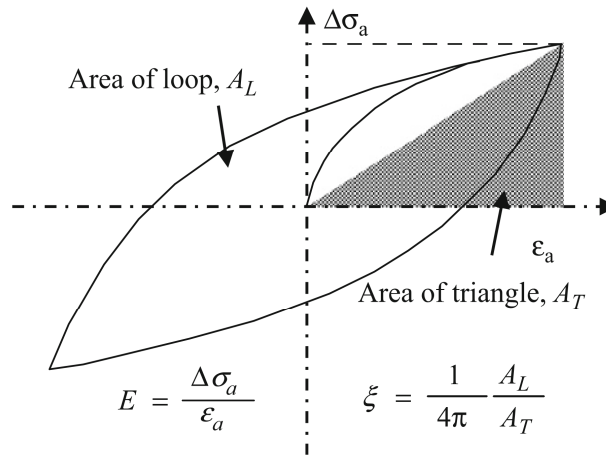
Figure I.49. Hysteretic loop in cyclic triaxial test and expression of the damping ratio (Khan et al. 2011)

The expression of damping ratio related to the system energy is:

$$\xi = \frac{E_{D,vis}}{4\pi \cdot E_S} \tag{I.11}$$

being E_D the dissipated energy by the system and E_S the strain energy stored in the system due to loading.

For very low cyclic strains, the damping ratio remains stable but when the cyclic strain amplitudes increase (from 10^{-5}), the damping ratio starts to increase from its lower value (Figure I.50) because the soils is entering a nonlinear range (Ishihara 1996; Meng 2003). In addition, the number of cycles at the same cyclic strain makes the damping ratio to decrease (Menq 2003), mainly for higher cyclic strain amplitudes.
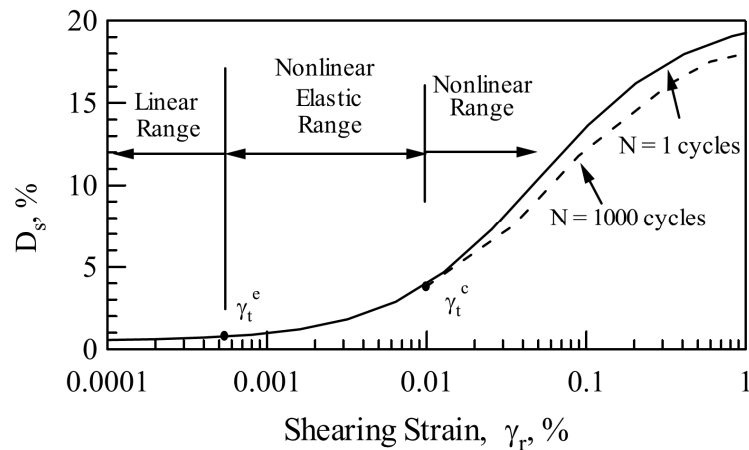
Figure I.50. Typical nonlinear Damping ratio – log γ curve (Menq 2003)

Several state parameters as initial void ratio, moisture content, effective confining pressure or plasticity index may influence the damping ratio (Dobry and Vucetic 1987) as presented in Table I.2. For example, a more heterogeneous soil (with higher uniformity coefficient, C_u) develops higher dissipation rates than homogenous soils (Figure I.51).

Table I.2. Influence of different parameters on ξ for normally to moderately overconsolidated soils (Dobry and Vucetic 1987)

Increasing Parameter	Damping ratio, ξ
Mean effective stress, σ'_0	Decreases with σ'_0; effect decreases with increasing I_p
Void ratio, e_0	Decreases with e_0
Geological age, t_g	Decreases with t_g
Cementation, C	May decrease with C
Overconsolidation ratio, OCR	Not affected
Plasticity index, *PI*	Decreases with *PI*
Strain rate, γ	Stays constant or may increase with strain rate
Number of loading cycles, *N*	Not significant for moderate γ and *N*
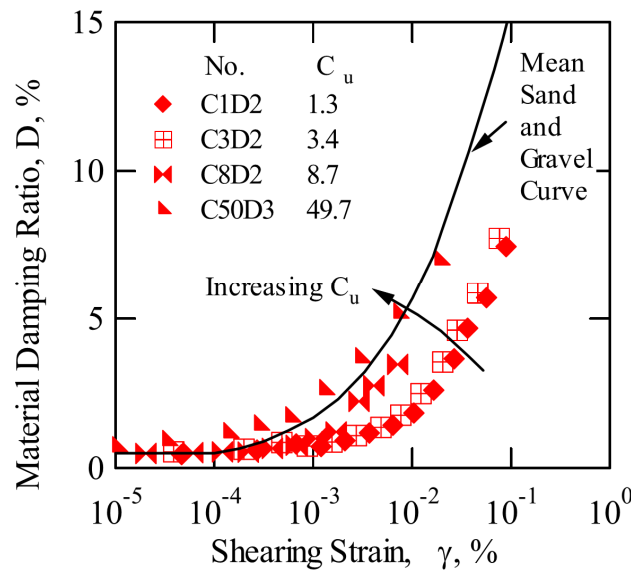
Figure I.51. Effect of Uniformity Coefficient, C_u, on material damping ratio of Dense to Very Dense Specimens (Menq 2003)

As for soil modulus, the validity of a frequency independent damping in soils was argued by different authors (Khan et al. 2011; Meng 2003; Menq 2003). Most soils are neither purely elastic nor viscous but viscoelastic; therefore, the evaluation of frequency effects on the dynamic properties is desirable. Some authors indicated a decrease of damping ratio with frequency mainly for clayey soils (Khan et al. 2009; Meng 2003). However, other studies showed that damping ratio increased with frequency at frequencies greater than 1 Hz and decrease for frequencies lower than 10^{-1}Hz (Meng 2003; Moayerian 2012) as shown in Figure I.52.
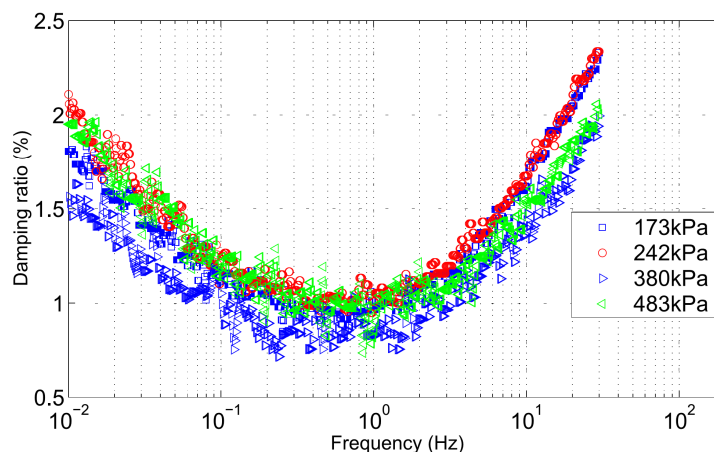
Figure I.52. Loading frequency impact on damping ratio of a clay for different confining pressures (Meng 2003)

I.4.2.2 Permanent deformation

The permanent deformations are determined by cyclic triaxial tests after a large number of cycles. Every single loading cycle could be used to calculate the elastic modulus or damping ratio as presented in the previous sub-sections. The triaxial samples may be adapted to the largest diameter of grains in the soil, being the diameter at least 6 times larger than the grain diameter (Indraratna et al. 2013). A European standard describes the test procedure to determine the permanent deformation evolution of a soil (AFNOR 2004). The cyclic loadings are repeated at least 20000 times for each loading amplitude level following the same loading path (in q-p) during every test. The loading cycles for these tests are performed under constant stress amplitudes in order to measure the development of permanent strains. Therefore, for every loading cycle there are two generated strains, a resilient elastic strain and a permanent plastic strain (Figure I.53).
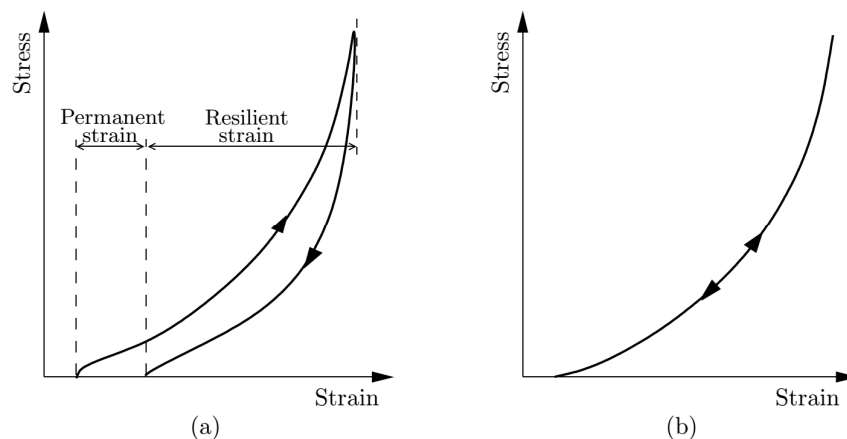
Figure I.53. Strains during one cycle of compression load application (a) Separation between permanent and resilient strains; (b) Non-linear elastic model (Varandas 2013)

The permanent strain developed per cycle is not constant over a repeated cyclic loading. The permanent deformation tends to stabilize. Thus, most of the plastic strains are accumulated during the first cycles of test (Allaart 1992; Duong 2013; Duong, Tang, et al. 2013; Indraratna et al. 2013; Lamas-Lopez et al. 2014; Trinh et al. 2012). Consequently, the permanent strain rate for each cycle is quasi zero after a high number of cycles even though the elastic strain remains stable for every loading cycle (Figure I.54). Therefore, when the permanent deformation evolution for a given cyclic loading are studied, only the permanent strains are taken into consideration (Figure I.55).
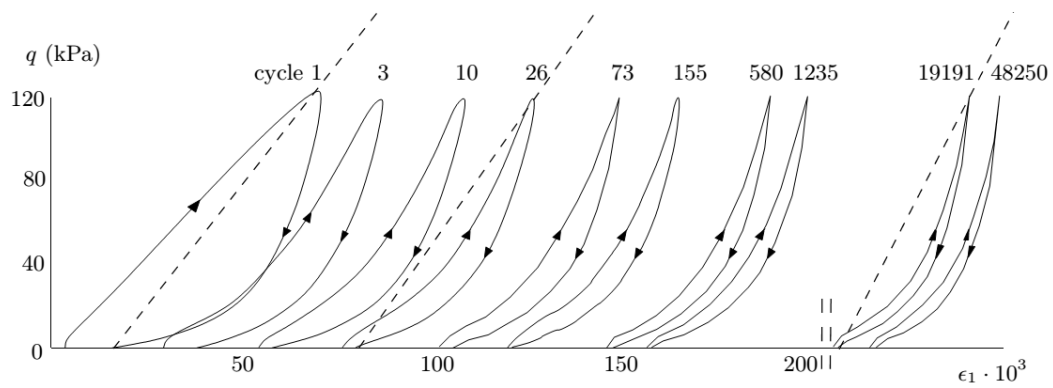
Figure I.54. Stress-strain diagram of a granular material under repeated loading (Allaart 1992)
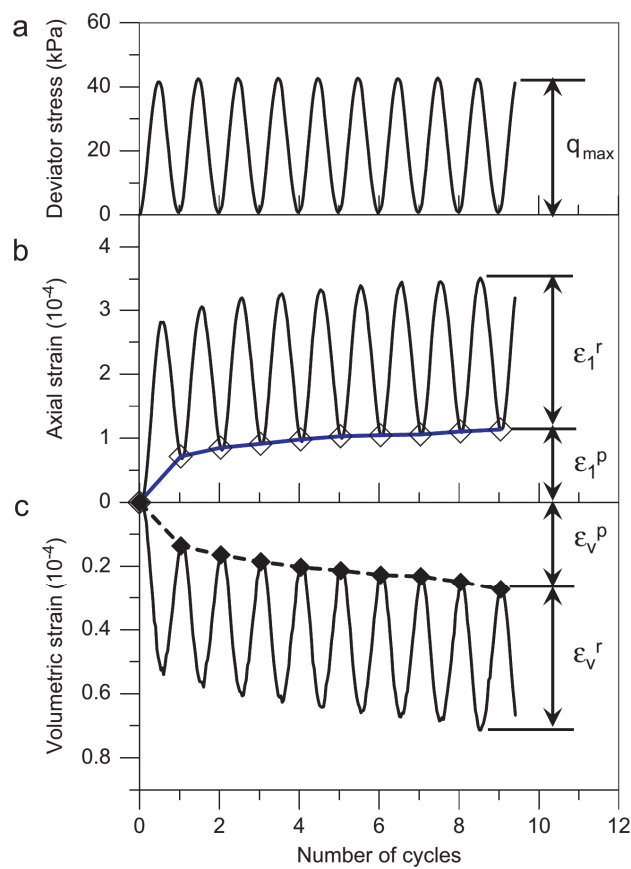
Figure I.55. Evolution of resilient (ε_r^1 and ε_r^v) and permanent (ε_p^1 and ε_p^v) strains with loading cycles (Trinh et al. 2012)

This permanent deformation evolution is affected by different soil state parameters and loading conditions (Coronado Garcia 2005; Gidel 2001a; b; Suiker 2005).

For instance, the level of permanent deformations reached at high number of cycles depends on the cyclic deviator stress level n_{cyclic} calculated as follows:

$$n_{cyclic} = \frac{\Delta q_{cycle}}{q_{max}}$$

(I.12)

being Δq_{cycle} the deviator stress amplitude for every loading cycle and q_{max} the maximum deviator level reached for the soil during a monotonic loading under similar state conditions. Thus, for a higher n_{cyclic} level, higher permanent deformations are expected at the same number of cycles N (Figure I.56). Nevertheless, the permanent deformations do not follow a linear trend with stress level n_{cyclic}. Moreover, the initial mean pressure during the test (Suiker 2005) and the loading-path in p-q plane (Coronado Garcia 2005; Gidel 2001b) impact also the evolution of permanent deformations. Higher initial mean pressures induce higher permanent deformations (Trinh 2011).
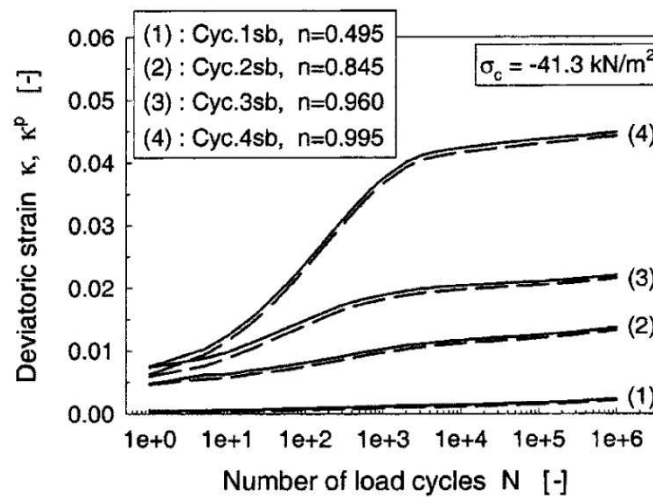
Figure I.56. Cyclic response of ballast material for various stress levels n_{cyclic}. Increase of total deviator strain and permanent deviator strain with load cycles N (Suiker 2005)

Furthermore, the influence of fines percentage and moisture content on permanent deformation from conventional railways track-bed soils materials were studied by Duong, (2013); Rujikiatkamjorn et al., (2013) and Trinh, (2011). For similar state conditions (including moisture content), a higher percentage of fines induces a larger permanent deformation, mainly when the soil is close to saturation (Figure I.57). Moreover, the permanent deformations increase exponentially with moisture content (Figure I.58). The saturation rate seems to be one of the main parameters controlling the evolution of permanent deformations.
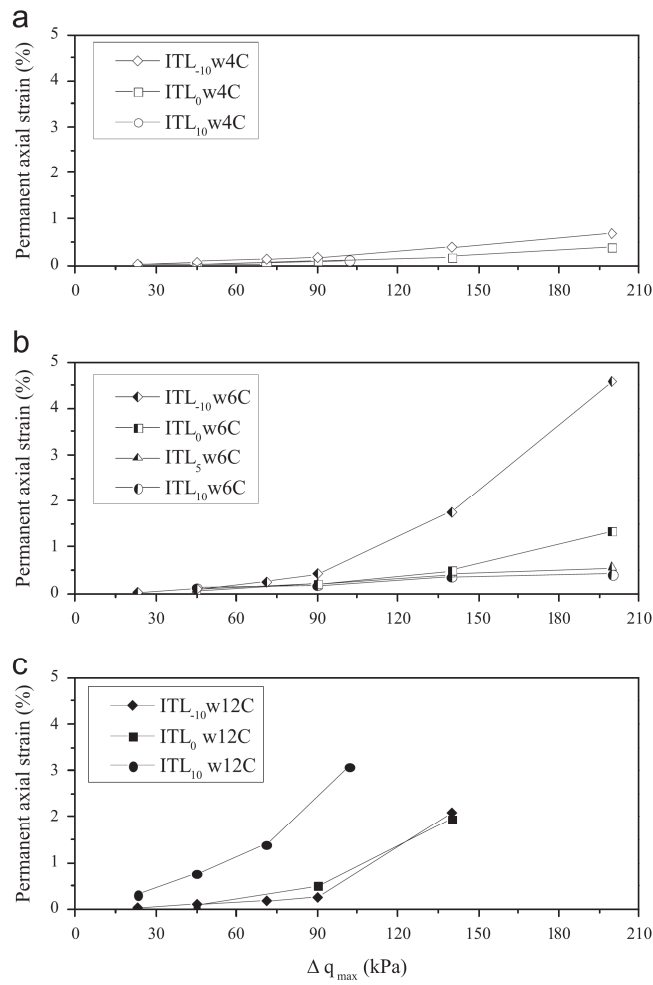
Figure I.57. Effect of fines content on the end-stage permanent axial strain at various water contents. ITL_x is an interlayer soil with $x\%$ of added fines (Duong, Trinh, et al. 2013)
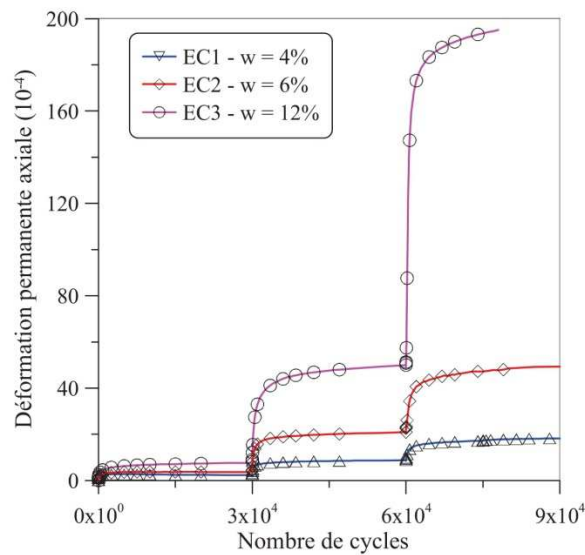
Figure I.58. Permanent deformation results of cyclic triaxial tests on Interlayer soils with different moisture contents (Trinh 2011)

Nevertheless, the loading frequency could also influence the permanent deformations of track-bed materials. Figure I.59 shows how after a higher loading frequency *f* the settlement, related to the permanent axial strain, increases too (Karrech 2007).
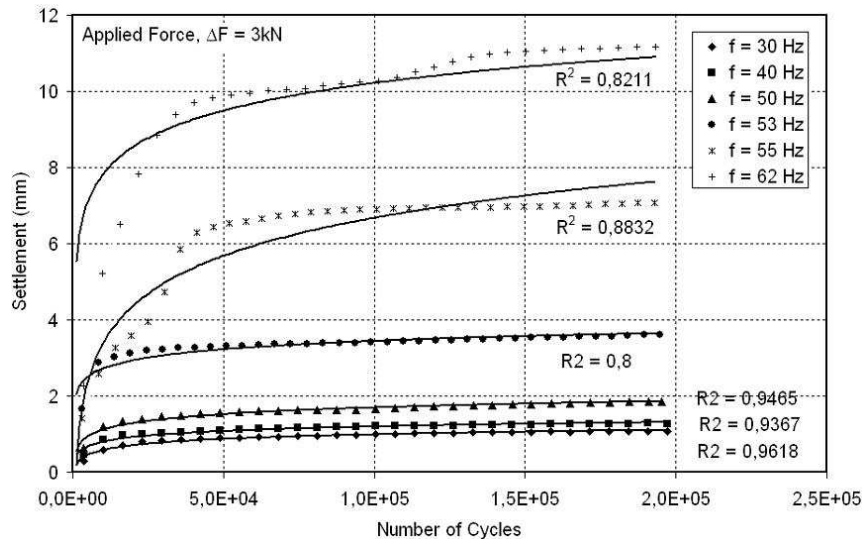
Figure I.59. Loading frequency impact on a granular material settlement versus number of cycles (Karrech 2007)

I.4.2.2.1 *Loading history impact*

The loading history of a soil affects the permanent deformation reached after each loading stage. The initial state of the soil controls how the permanent deformations are developed against cyclic loadings. For instance, an over-consolidated soil will develop lower permanent deformations than a normally consolidated soil at similar conditions. Gidel, (2001b) proposed a method with successive cyclic loading stages at different loading amplitudes (but the same *p-q* loading path). This method permits to obtain the permanent deformation accumulated on a soil for different loading amplitudes using the same sample (Figure I.58). Moreover, the order in which different cyclic loading amplitudes are applied on the sample matters.

If a new larger cyclic loading amplitude level is reached, new permanent deformations are developed (Figure I.60). However, if smaller cyclic loading amplitudes than the previous one are applied after, almost no new permanent deformations are developed.
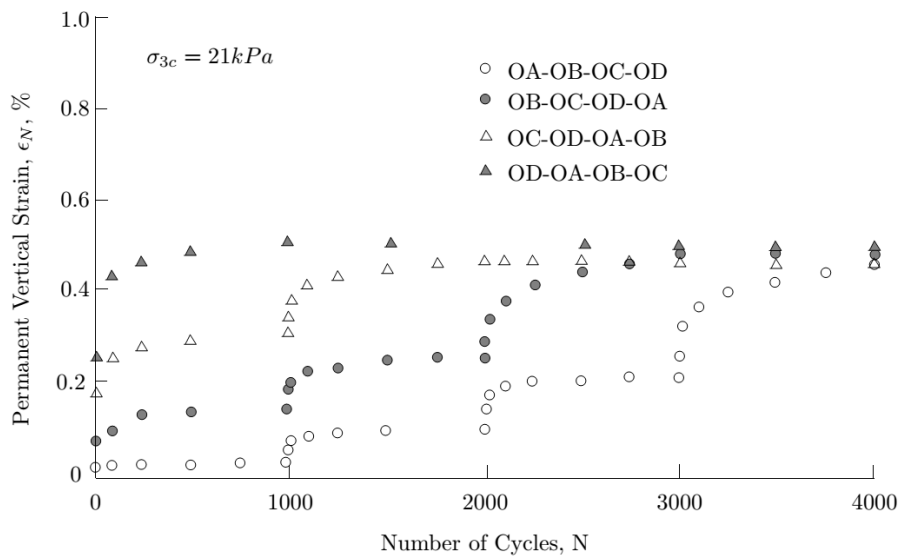
Figure I.60. Permanent strains of ballast from four triaxial tests with variable cyclic amplitude sequences of loading σ₁ - (variable) vertical stress; σ₃c - (constant) confining stress, being OD the highest cyclic loading amplitude and OA the lowest one (Stewart 1986)

Nevertheless, if the cyclic loading stages are applied to the sample from the smallest amplitude to the highest one, the total permanent deformation developed by a given cyclic loading amplitude (reference curve) could be estimated by adding the developed strain during the loading at the desired amplitude level to the strains developed by the previous loading stages (Figure I.61).
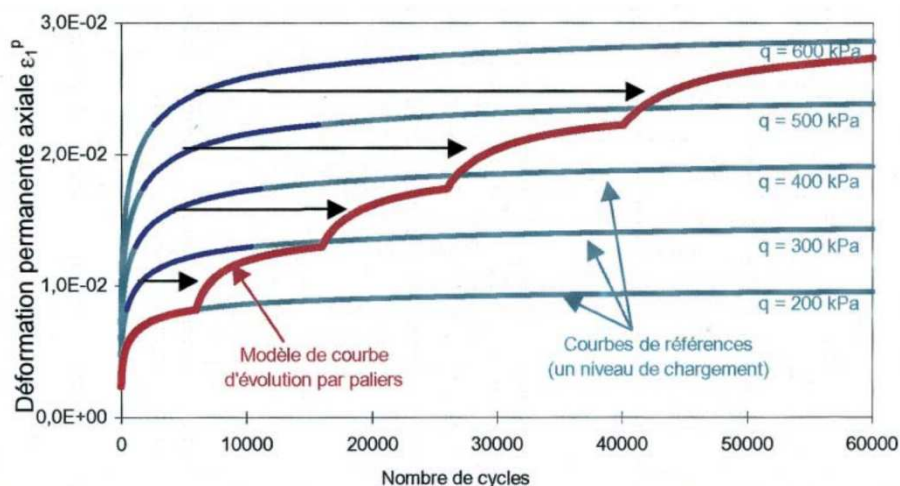
Figure I.61. Estimation of reference curves (one loading level) using several loading stages on one sample (Gidel 2001b)

I.4.2.2.2   Principal stresses rotation (PSR)

When a train runs over a railway, changes in principal stresses appear in track-bed layers (Figure I.62). Even though the axial stress is major compared to other stress components, the principal stresses change their directions while axles advance (Brown 1996; Powrie et al. 2007). In reality, shear and axial stresses are applied in sinusoidal waveforms to track-bed soils, and the shear stresses change their direction (before and after axle passage) while axial stresses are always compressive (Figure I.63). The Principal Stresses Rotation (PSR) can influence the cyclic behaviour of soil (Powrie et al. 2007). Cumulative axial strains (plastic strains) could be under-estimated if only the major stress (axial) is considered (Grabe and Clayton 2009).
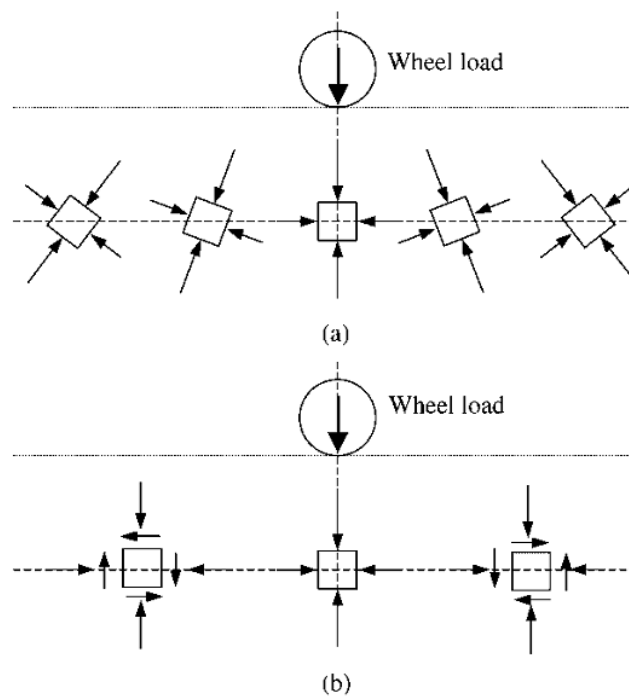
Figure I.62. Stresses on pavement elements: (a) principal stresses and planes; (b) shear and normal stresses on horizontal and vertical planes (Brown 1996)
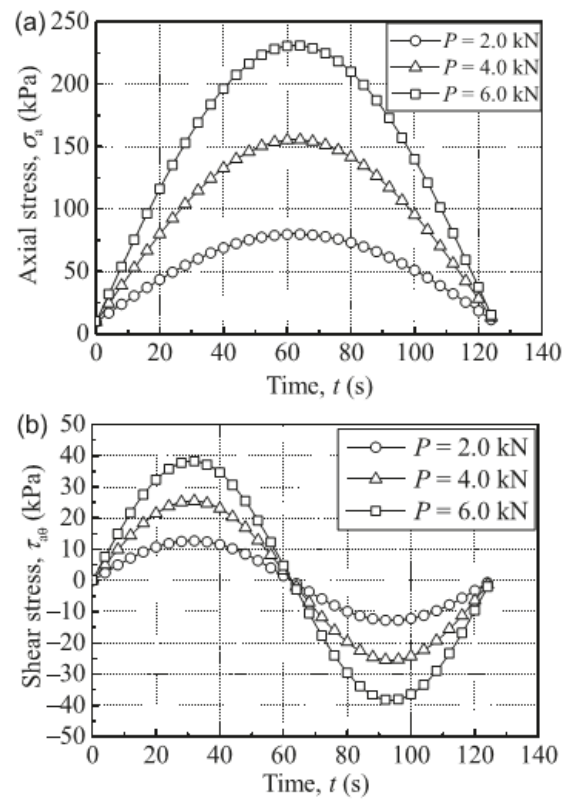
***Figure I.63. Loading conditions of multi-ring shear test using moving wheel loading mode:
(a) axial stress; (b) shear stress (Ishikawa et al. 2011)***

To study the effect of PSR on the mechanical behaviour of soils, different works were conducted such as the development of computational models (Powrie et al. 2007), hollow cylinder testing on small soil samples (Grabe and Clayton 2009) and physical modelling of a railway track (Ishikawa et al. 2011), showing similar results about cumulative strain evolution when comparing PSR loading with no-PSR loading. Under PSR loading a higher cumulative axial strain was found. This trend is valid for soils with different clay contents (Figure I.64). Nevertheless, the cumulative strains of plastic soils are larger than low plastic soils for similar number of cycles (Figure I.64).
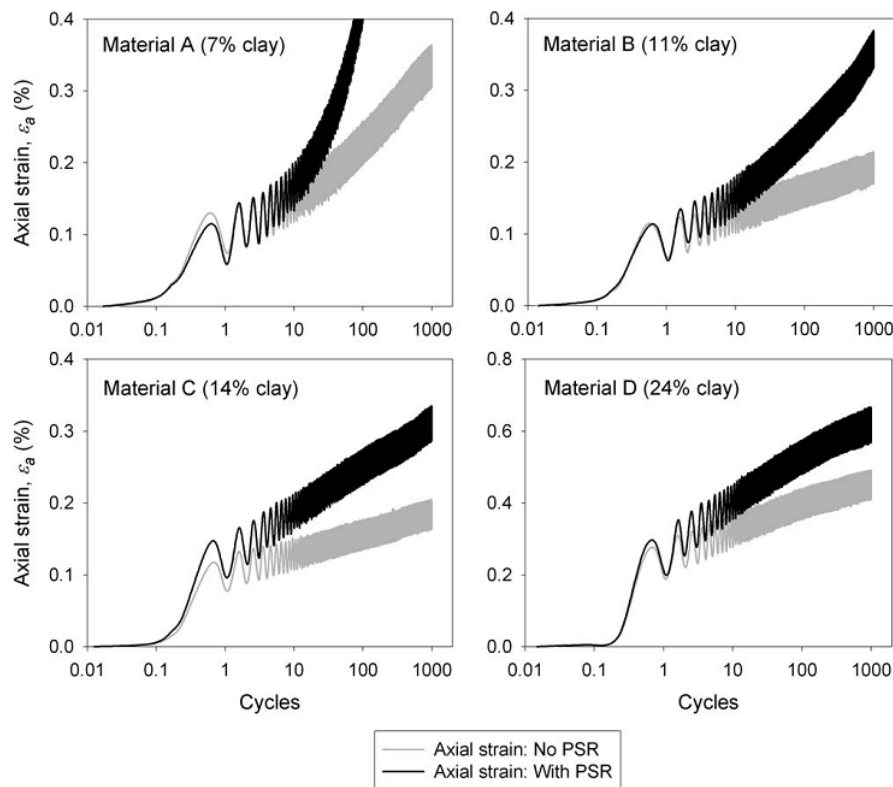
Figure I.64. Permanent deformation of Materials with different clay contents as a result of cyclic loading with and without principal stress rotation (Grabe and Clayton 2009)

I.4.2.2.3   Fatigue models

Several empirical models were reported in literature, allowing the assessment of the total deformation development. Some of them are mainly focused on the effect of the number of loading cycles (Barksdale 1972; Hornych et al. 1993; Sweere 1990; Wolff and Visser 1994) with empirical parameters. Some others are only focused on the effect of initial stress state (mean pressure) (Barksdale 1972; Lashine et al. 1971; Lekarp and Dawson 1998; Pappin 1979). Models considering both the number of cycles (n) and the maximal cyclic stress levels (deviator and mean stresses) were also developed (Gidel 2001b). However, some state parameters as saturation rate (related to soil's moisture content) were not taken into account. Recently, Trinh (2011) developed a model for interlayer materials taking into account the saturation effect. These empirical models are presented in Table I.3. The prediction results show that permanent strain at different soil state of moisture content and cyclic stress levels are well correlated with measurements after a large number of cycles (Figure I.65).

Table I.3. Some empirical models developed for assessing the soil's permanent deformation

Model based on	Author (year)	Axial permanent deformations model
Number of Cycles	Barksdale (1972)	$\varepsilon_a^p(N) = a + b \cdot \log(N)$
	Sweere (1990)	$\varepsilon_a^p(N) = a \cdot N^b$
	Wolff & Visser (1994)	$\varepsilon_a^p(N) = (c \cdot N + a)\left(1 - e^{-b \cdot N}\right)$
	Hornych et al. (1993)	$\varepsilon_a^p(N_{>100}) = a \cdot \left[1 - \left(\dfrac{N}{100}\right)^b\right]$
Cyclic Stress Level	Lashine et al. (1971)	$\varepsilon_a^p(q_{max}, \sigma_{3max}) = a \cdot \dfrac{q_{max}}{\sigma_{3max}}$
	Lekarp & Dawson (1998)	$\varepsilon_a^p(N_{ref}) = a \cdot \left(\dfrac{q}{p}\right)^b \cdot \left(\dfrac{L}{p_0}\right)$
Number of Cycles + Cyclic Stress Level	Gidel et al. (2001)	$\varepsilon_a^p(N, \Delta p_{max}, \Delta q_{max}) = g(\Delta p_{max}, \Delta q_{max}) \cdot f(N)$
Number of Cycles + Cyclic Stress Level + Soil Saturation	Trinh et al (2011)	$\varepsilon_a^p(N, S_r, \Delta q_{max}) = t(S_r, \Delta q_{max}) \cdot f(N)$
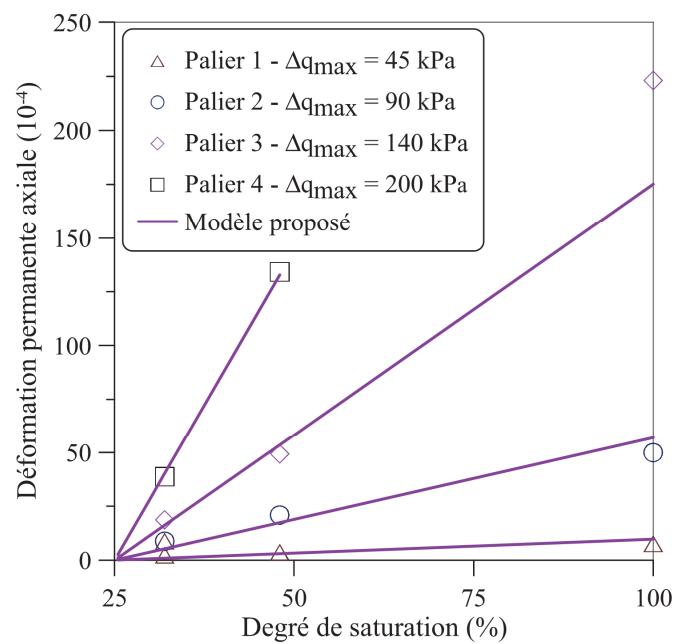
Figure I.65. Comparison between model and measurements (Trinh 2011)

I.4.2.3 Water impact

Moisture content is one of the main parameters influencing track-bed soils' behaviour: its increase reduces the effective stress in soils and thereby increasing soil deformation under loadings (Figure I.66). A failure or a lack of drainage system can develop higher deformations on materials because the moisture content becomes higher. These deformations may lead to degradation of the geometry and longitudinal levelling of the track (Selig and Waters 1994). For instance, shear failures due to poor subgrade drainage could appear if the cohesive subgrade soils are close to saturation (Selig and Waters 1994).

This higher deformation due to higher moisture content is even more evident in the transition zones (bridges or track typology transitions) where the track stiffness changes in a short space (Zuada-Coelho 2011). In addition, sudden changes in moisture content of track-bed materials (or a high saturation rate linked to the existence of low stiffness cohesive soils) could make an 'accelerated degradation zone' where a larger number of track maintenance operations could be needed.

Maintaining good drainage conditions is essential to limit the track's plastic deformations and to reduce maintenance operations (Alves Fernandes 2014; Lekarp et al. 2000).
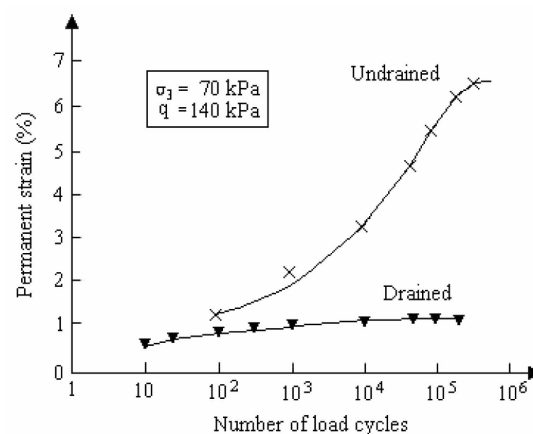
Figure I.66. Influence of drainage on permanent deformation development (cited by Lekarp et al., 2000)

The weather impact on track's mechanical behaviour was studied by Cui et al., (2014) and Trinh, (2011). Using suction measurements and meteorological data as the temperature, solar radiation, wind speed and humidity measurements, evapotranspiration variations could be

estimated at every track position (Cui et al. 2014). Measurements on a conventional line were performed (Trinh 2011). Three zones are separated in Figure I.67. Zones A and B correspond to interlayer and subgrade positions under a 50 cm ballast layer, while the two positions in zone C correspond to a lateral path soil beside the track without ballast layer. After rain events, suction decreased given that soil's moisture content increased (Trinh 2011). There is more variations of suction in zone C, where no ballast layer exists. However, there are limited variations of suction for zones A and B, where ballast is a protecting layer for deeper materials.
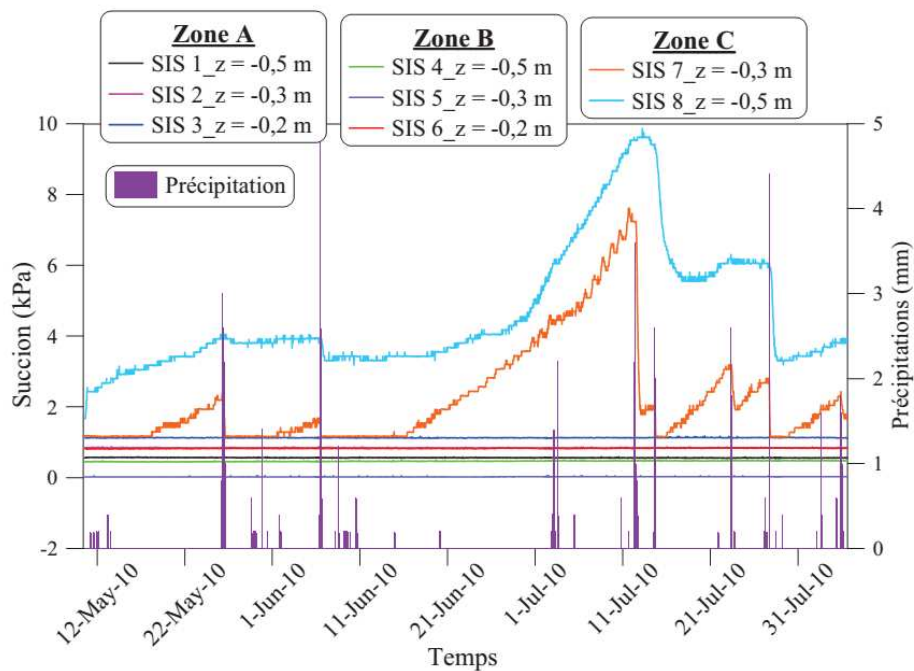
Figure I.67. Effect of rainfalls on soil suction at three different subgrad zones. Zones A & B under track and C under lateral track-path (w/o ballast layer) (Trinh 2011)

I.5 'IN-SITU' INVESTIGATION

Different investigations performed on real tracks and through physical models were reported in literature. Some of the most significant studies are presented in this subsection.

Several types of sensors are used in different investigations:
- Accelerometers: measurement of acceleration (depending on orientation and installation position); capacitive and piezo-electric accelerometers are used, depending on the monitored zone or position, loadings or element to be attached on.

- Geophones: measurement of particle velocity (depending on orientation and installation position); most of them are piezo-electric.

- LVDTs: measurement of deflections on surface if it is in contact with a track element (sleeper) or deflections during train passage in an embedded point of the track-bed if the LVDT is installed in other apparatus like a multi-depth deflectometer (MDD); video camera or laser sensors could be also used to measure displacements on surface.

- Stress sensors: measurement of the stress exerted to an embedded plate in a track-bed; the sensor diameter is adapted to the maximum grain size of soil.

- Pore-water pressure sensor: measurement of transient pore-water pressure variations generated under loading.

I.5.1   Real track instrumentation

Real tracks were instrumented for different purposes. The mechanical behaviour of track elements was monitored under train loading in several countries. For instance, the dynamic displacement under train loading of track-bed materials was measured using accelerometers and geophones in British lines (Bowness et al. 2007; Le Pen et al. 2014; Priest et al. 2010). In addition, experimentations on real track for investigating vibration propagation were performed in Belgium using vertical vibration signals at surface, showing the decay of peak particle's velocity in distance (Connolly et al. 2015; Degrande and Lombaert 2000). Other monitoring zones measured accelerations and deflections under train loadings at different track-bed positions in SUPERTRACK European project (France and Spain) (ADIF 2005; Ferreira 2010; SNCF 2005). These studies showed the increase of peak accelerations or deflections when trains run faster and the attenuation of loadings in depth, mainly for high speed lines (Ferreira and López-Pita 2015). The influence of track stiffness spatial variations on the maintenance cost was also investigated by field monitoring using deflectometers and accelerometers in conventional lines (Fröhling 1997). Results showed that there is a good correlation between the spatially varying track stiffness and the increase of maintenance operations.

In this section, four cases (Sweden, Northern Ireland, Canada and USA) are presented in more detail considering their relatively rich monitoring and interesting results.

I.5.1.1 Case I: Deflection amplification with train speed

The Swedish railway administration (Benkervet) found excessive vibrations of the railway embankment and the surrounding soil on the West Coast Line between Göteborg and Malmö. Moreover, these vibrations appeared when the train speed was close to 200 km/h. The subgrade was composed of clay of shear wave velocity as low as 30 m/s. As the subgrade soil was determinant on surface waves speed definition, Rayleigh waves in the site were estimated, around 235 km/h (Hall 2000; Madshus and Kaynia 2000). When trains run at this speed, a maximum displacement response of track is expected. Indeed, dynamic amplifications were expected at the critical speed (235 km/h) using numerical simulation. Madshus and Kaynia, (2000) studied this site using accelerometers, video-cameras and geophones installed at different positions. The results showed that quasi-static track responses were recorded only for speeds under 70 km/h. Symmetrical upward and downward dynamic deflections were measured for speeds lower than 200 km/h (Figure I.32).

In order to define the areas where dynamic amplifications appear regarding the effect of frequency (related to train speed) and wave number (related to geometrical characteristics of the train), Figure I.68 is established. Two main areas can be identified: quasi-static and dynamic amplification response domains. Each train speed, defined by a straight line, passes over different iso-amplification lines. The relationship between speed (frequency) and wave number (wavelength) is linear. The train speed relating frequencies and wavelengths at which maximum amplifications are reached corresponds to the line linking the origin point and the maximum displacement point in Figure I.68. Larger wavelengths give rise to higher amplifications for bigger frequencies.
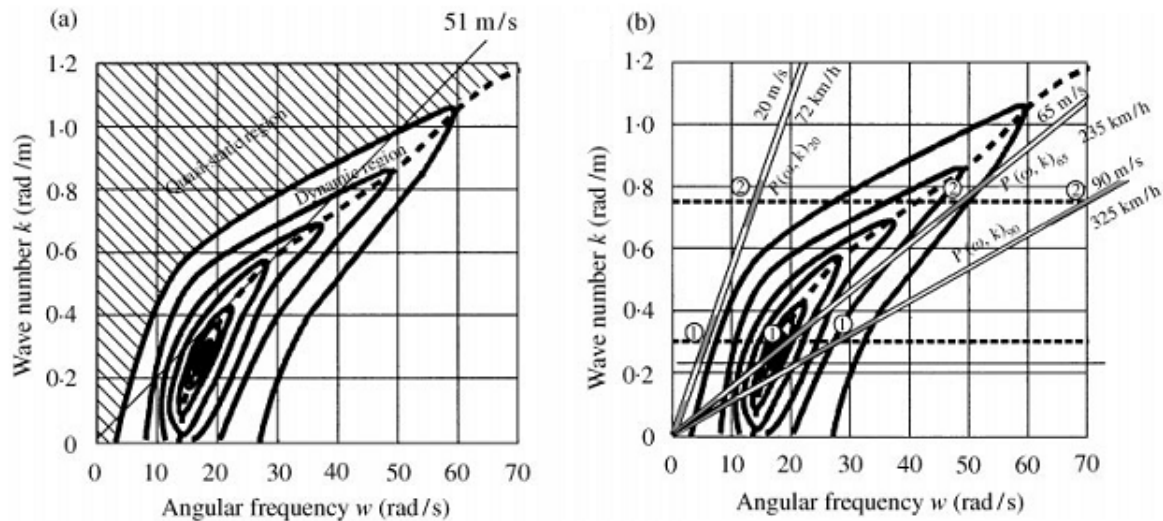
Figure I.68. Response calculation in the frequency wave number domain (Madshus and Kaynia 2000)

Hall, (2003) found that simulations could be performed using soil's dynamic parameters to obtain amplification results similar to measurements. From analysis of particle movement (motion orbit from 3D analyses), he found that Rayleigh waves are the dominating wave type in the embankment, causing the response amplification when train approaches this speed. Using accelerometers and geophones distanced up to 22 meters from track, an exponential decay of vibration amplitudes that increase with speed was found (Hall 2000).

I.5.1.2 Case II: Track response amplification with peaty subgrade soil

As for the Ledsgard's site in Sweden, train speed was limited in several sites from Northern Ireland Railways network (NIR) due to the accelerated degradation of track's geometry during the last 10 years. This degradation was caused mainly by the poor resistance of peaty subgrade soils under ballast (Hendry 2007; Hendry et al. 2010). Site prospection by dynamic penetrometers showed a stiffness decrease below the ballast layer due to the presence of peaty soils. Then, a monitoring system was installed to analyse the motion amplification at different levels of the track-bed (from sleeper to subgrade) with accelerometers, deflectometer-laser and Multi-Depth deflectometers. Different quasi-static deflections were recorded for different axle types (locomotive and passenger coaches) which were slightly increased by about 15% when train speed v_T was upgraded from 10 to 110 km/h (Figure I.69). Deflections caused by heavier axles seemed to be larger with train speed. FE numerical analyses were performed to evaluate deflections with different dynamic characteristics of subgrade, resulting in larger

deflections in case of smaller damping ratios (Figure I.69). In addition, stiffer subgrade soils bring the track to decrease its power loss if the train speed is increased (Hendry et al. 2010).
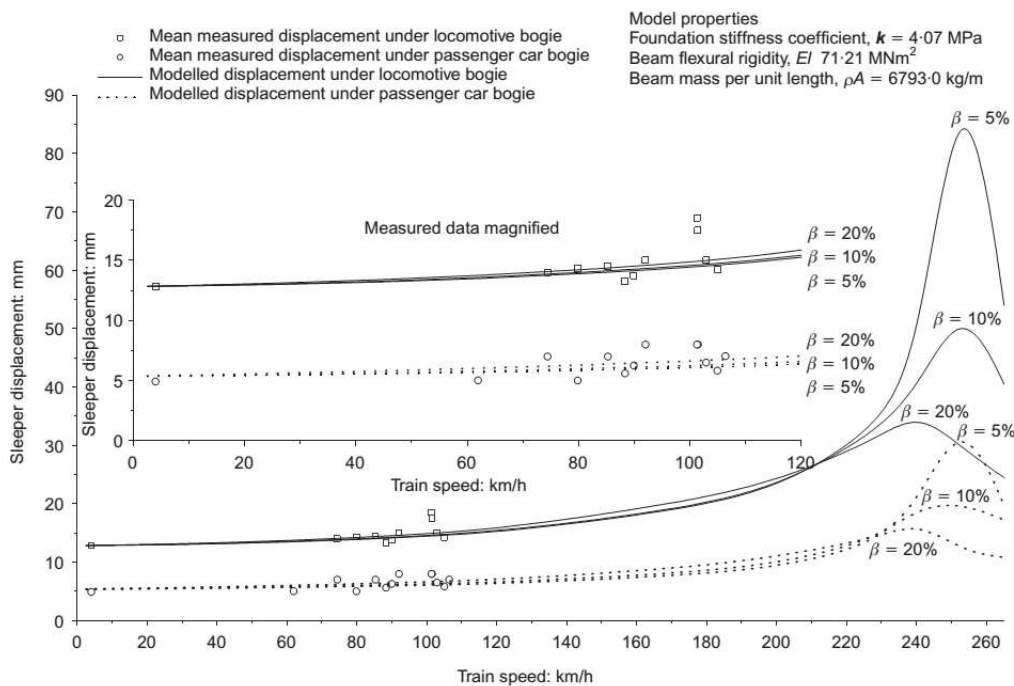
Figure I.69. Locomotive and coach deflection amplifications with train speed (Hendry et al. 2010)

I.5.1.3 Case III: Pore-water pressure increase under traffic loading

Some sites from Canadian National (CN) railway network presented high deformations and accelerated degradation when repeated traffic loads were applied to the infrastructure. This track degradation was mainly caused by the existence of poor resistance peats in its subgrade soil. Sites were instrumented in order to reveal the potential capacity of these soils to allow higher axle loads running on the infrastructure. The increase of train speed was found to have little effect on the magnitude of soils' deformations (Hendry 2011; Hendry et al. 2013; Konrad et al. 2007). Nevertheless, an increase of train speed could lead to an increase of pore water pressure, and the cyclically loaded peat foundations behave in an undrained manner (Wong et al. 2006). In order to study this phenomenon, three different peat foundation sites were instrumented in Canada (Hendry et al. 2013). Peat samples were taken from different depths and tested in laboratory under undrained conditions. Permanent monitoring instruments were installed at the sites such as extensometers (to measure average deformations in each layer), pore water pressures (to measure transient pore water variations

70

during the passage of a train) and accelerometers at different depths (Hendry et al. 2013). Analysing the pore-water pressure amplitudes under axle loading (about 5 kPa in average), the total stress amplitudes under axle loading and the undrained path slope from initial state conditions of peat soil in laboratory, the Stress Mobilization factor (SM) could be calculated using Equation (I.13) (Figure I.70):

$$SM = \frac{\Delta q}{\Delta q_{yield}}$$

(I.13)
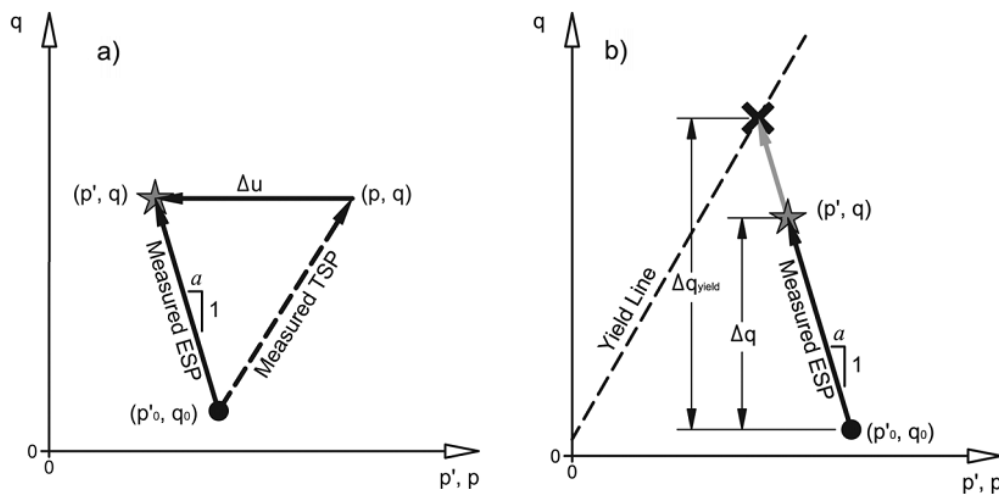
Figure I.70. (a) Plot of calculation of effective stress path from the measured in situ response and undrained laboratory response (b) Graphical depiction of parameters used in calculations for stress mobilization factor (Hendry et al. 2013)

The SM varies over depth (larger SM are found in shallower layers where higher stress amplitudes are transmitted from railway traffic) and with the drainage capacity of each material in dissipating pores pressure (Hendry et al. 2013) (Figure I.71).

71
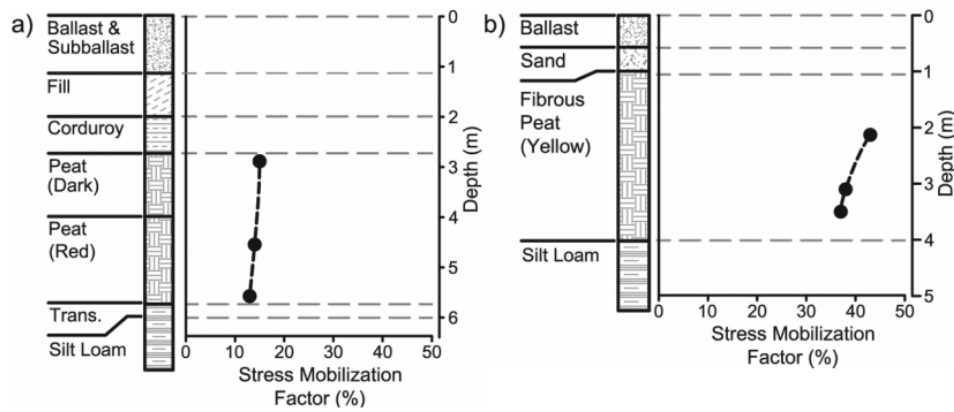
Figure I.71. Stress mobilization factor (SM) under heavy axle loads for (a) Edson site and (b) Anzac site (Hendry et al. 2013)

I.5.1.4 Case IV: Mud pumping zone and track settlement

In Boston (MBTA-CS network), problematic zones where the number of maintenance operations increased because of mud pumping issues were identified (Aw 2007). These mud pumping episodes were caused by saturated and low density cohesive soils in track subgrade. Moreover, the degradation was accelerated when lighter trains at higher speeds (as ACELA train) ran over the track. Some instrumentation was then installed (settlement sensors, piezometers and accelerometers) at different depths in both the problematic zone and a regular zone. Changes in matric suction were measured in deeper subgrade, negative in summer and close to zero in winter. More problems were detected in spring when frozen tracks start thawing. Moreover, the maintenance cycles influenced mainly the acceleration peaks after a train passage, being reduced after each operation (Figure I.72). However, the dissipated energy (Arias Intensity) (Arias 1970) decreased after each maintenance operation, starting to increase again until the next operation. Arias Intensity measures the intensity of the track response system and is defined as the energy dissipated per unit mass, effectively removing the effects of the mass in the system (Aw 2007). High-speed trains generate more energy than lower speed trains (commuter services). In addition, peak acceleration increased linearly with train speed (Aw 2007) as in European tracks (Ferreira 2010). The Arias intensity could be estimated using Equation (I.14) (Arias 1970):

$$I = \frac{\pi}{2g}\int_{0}^{\infty}\left|X(\omega)\right|^{2}\partial\omega \quad \text{where} \quad X(\omega) = \int_{-\infty}^{\infty}x(t)e^{-j\omega t}\partial t \qquad (I.14)$$

Apart from mud pumping problems, sudden track changes in transition zones lead to amplification of dynamic loadings and consequently reduce the levelling quality. Because of that, maintenance operations due to transitions zones are very expensive taking into account all the USA networks (Mishra et al. 2014), reaching 200M$ the annual expenditure. A transition zone in Pennsylvania was chosen to install a MDD anchored at 6 different levels in a borehole (Figure I.*73*). This kind of instrumentation could give information about displacement changes during train loading and also cumulative settlement of each level. From the results it could be explained that more than 90% of total settlement in the monitored transition zone corresponds to ballast and track elements such as sleepers (Figure I.*73*).
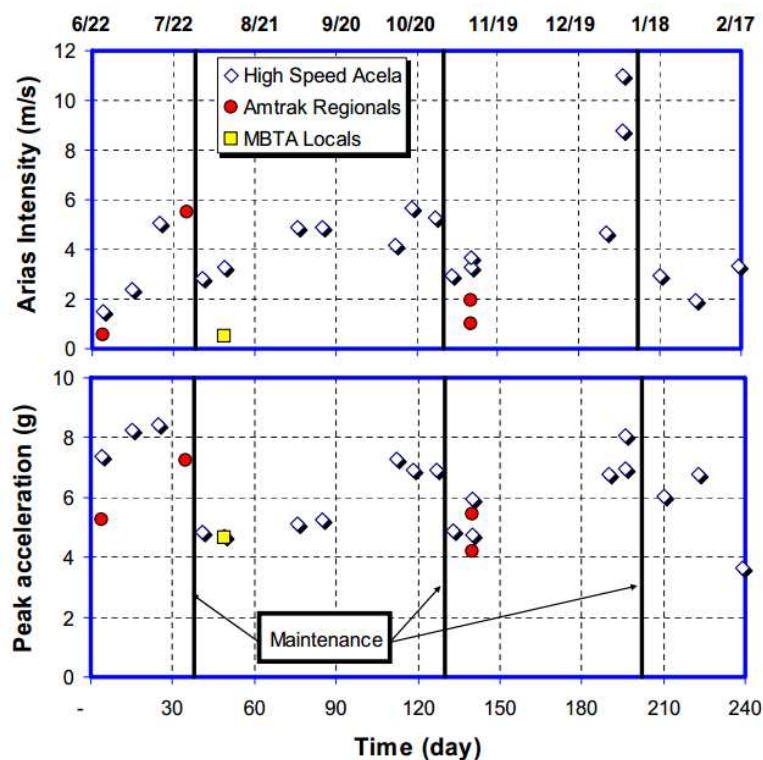
Figure I.72. Comparison between ACELA trains with regional and MBTA trains using Arias Intensity and peak acceleration methods (Aw 2007)
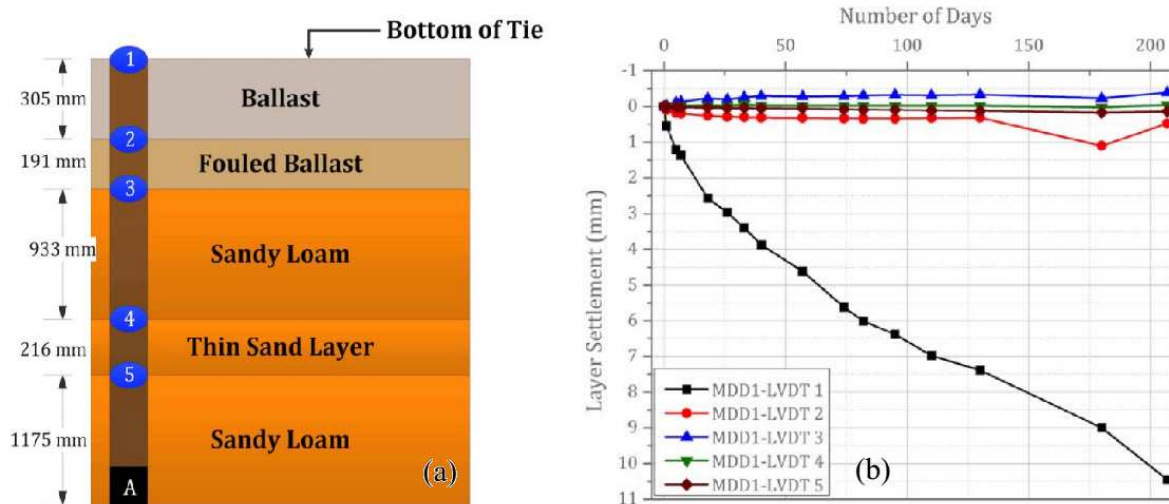
Figure I.*73. (a) Substructure Layer Profiles and MDD installation positions and (b) Track Settlement with Time for each LVDT position in MDD (Mishra et al. 2014)*

I.5.2   *Physical modelling*

There are several track physical models facilities allowing simulating and reproducing the behaviour of track's elements under well-defined conditions. Three of the most notorious railway track physical models are described in this section.

I.5.2.1 Case I: CEDEX track-box

The CEDEX track box is an experimental facility for testing railway tracks. It was developed by ADIF and CEDEX on the CEDEX´s premises. The testing station incorporates a 21 m long, 5 m wide and 4 m deep track-box where actual track structures can be tested at 1:1 scale. The track box was constructed with 9 steel frames where the reaction beams and load hydraulic actuators of 250 kN loading capacity take supports. Trains running at different speeds could be simulated using different actuators. In order to simulate materials' conditions, the construction could be adapted to testing needs such as moisture content or compaction. Furthermore, the sensors installed in the box depend on the test goal. Consequently, sensors such as accelerometers, geophones, LVDT transducers or axial pressure cells could be installed into the physical model to measure different variables. Fatigue curves, hysteresis behaviour and material deterioration curves could be obtained using the sensors installed in the facility.

I.5.2.2 Case II: China track-model facility

One facility was also built in China, composed of 8 hydraulic actuators that are able to simulate train speeds up to 400 km/h (Figure I.74). Apart from the loading specifications, the material's state can be modified using for example a water supply network in order to assess subgrade's moisture content variations in the global track behaviour under simulated train loadings. Several studies about dynamic behaviour and speed influence were performed using this facility (Bian et al. 2014; Cheng et al. 2014; Xu et al. 2013). The analysis was focused on dynamic load amplifications at different simulated train speeds, longitudinal propagation of vibrations and cumulative settlements of different track-bed materials. Moreover, as most of maintenance problems on Chinese tracks are related to differential settlements in ballast-less tracks (Chen et al., 2013), most of the projects on this physical model involved slab-tracks.
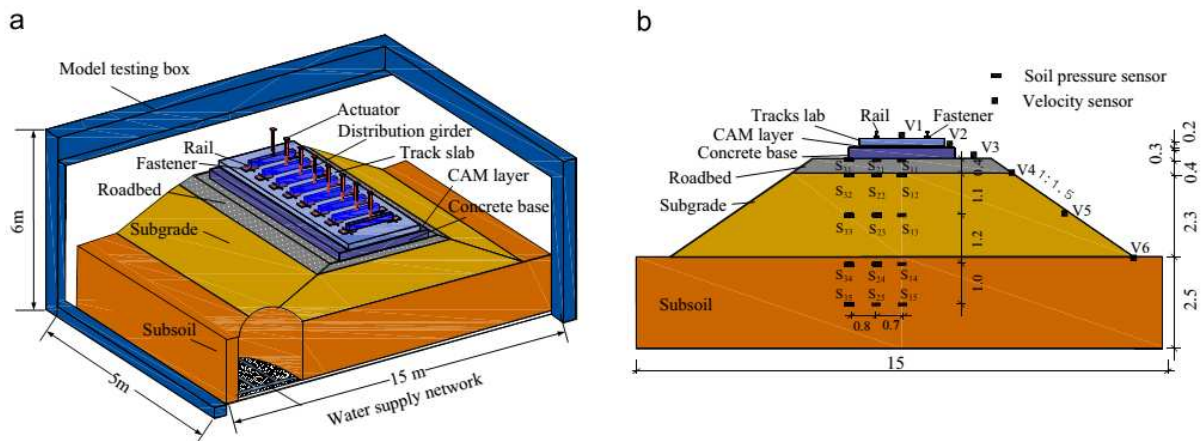
Figure I.74. Full-scale model testing of ballastless slab track. (a) Three-dimensional schematic view and (b) Cross-section view (unit: m) (Bian et al. 2014)

Good correlations between field measurements and physical models were found under similar loadings in longitudinal propagation of vibrations (Figure I.75a) and vibration amplitude amplification with train speed (Figure I.75b).

Linear axial stress amplifications were also found when the simulated train speed was increased (Figure I.76). Different depths and track-bed materials show different amplification rates for a similar train speed (Figure I.76). Larger stress amplifications with speed were found in deeper layers.
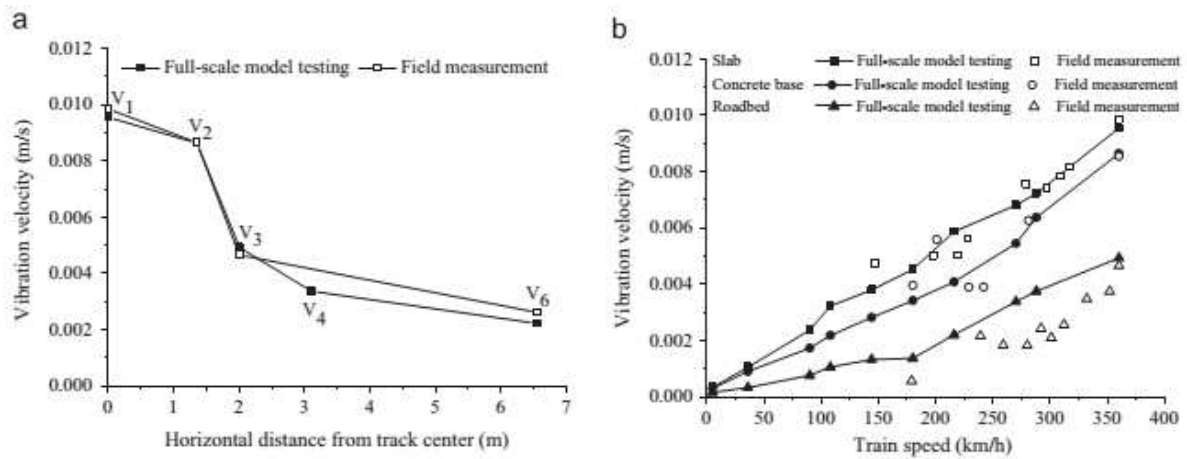
Figure I.75. Comparisons of vibration velocities between model testing and field measurements (axle load=140 kN). (a) Distribution in horizontal direction from the track center (v_T=360 km/h) and (b) Relation between vibration velocity and train speed (Bian et al. 2014)
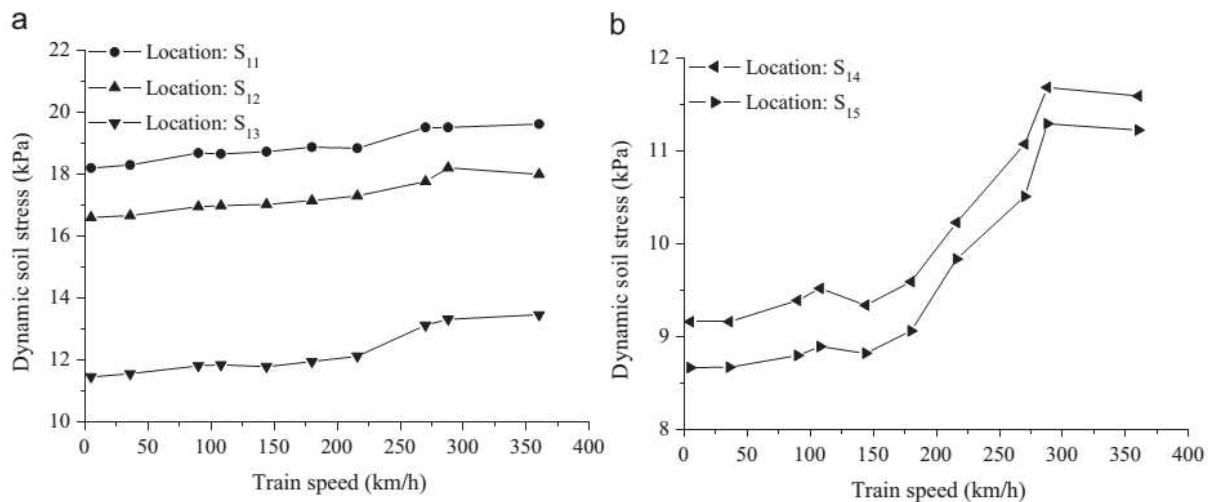
Figure I.76. Relationship between dynamic soil stress and train speeds. (a) track-bed and subgrade and (b) Subsoil (Bian et al. 2014)

I.5.2.3 Case III: 1/3 scale track model

Navier laboratory also developed a track physical model (Figure I.77), smaller than the two previous ones. This track allows 1/3 scale track components and reduced ballast grains (Al-Shaer 2006; Al-Shaer et al. 2008) and has 3 hydraulic jacks. The sensors used in this model are similar to those used for the real scale facilities. The studies conducted with this model are similar to the Chinese and Spanish track-boxes: dynamic behaviour of different track-bed layers, vibration assessment at different depths and cumulative settlement under different loadings (Al-Shaer et al. 2008). In addition, similar reduced models as this one were

developed by other institutions in order to test track behaviour, such as the Scottish Heriott-Watt University (Banimahd et al. 2012; Woodward et al. 2014).

The cumulative settlement seems to be different if the principal stress rotation is applied with a simultaneous three jack loading (Figure I.78). The loading frequency (simulated speed) has also a slight influence on the cumulative settlement - the higher the loading frequency the larger the cumulative settlement. And eventually, one of the main outcomes from these studies is the good repeatability of test results (Al-Shaer 2006), as for example the mechanical parameters such as the resilient modulus of each layer under different loading conditions.
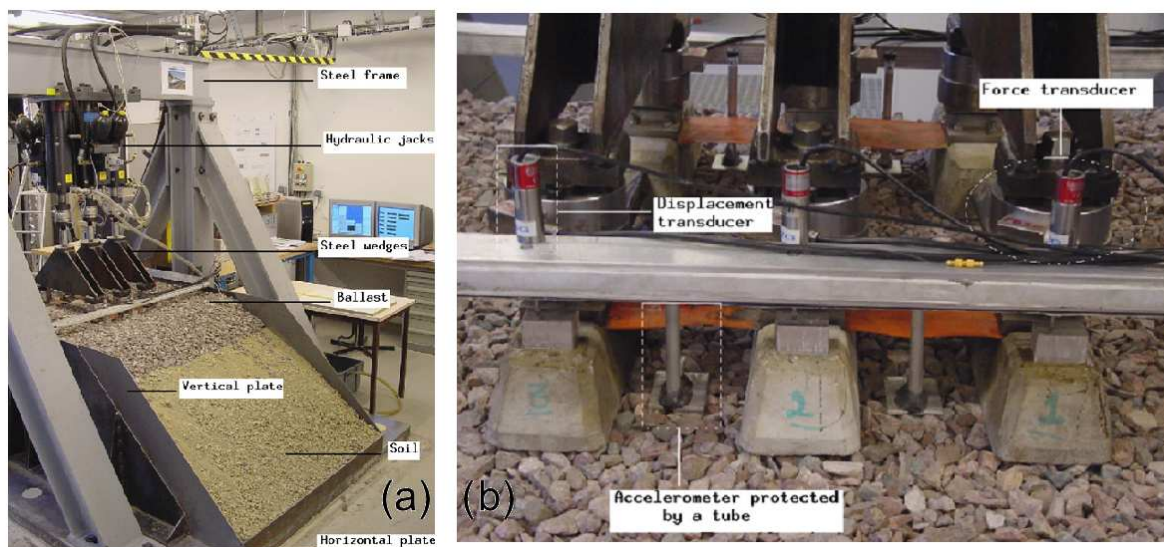
Figure I.77. (a) Physical modelling and (b) Transducers (Al-Shaer et al. 2008)
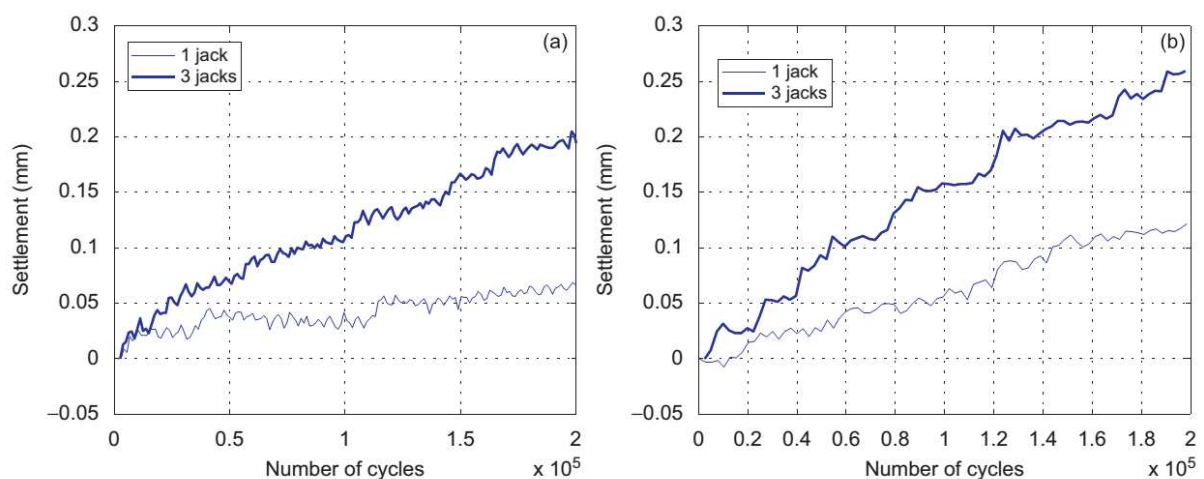
Figure I.78. Settlement of the left sleeper versus the number of cycles for (a) 160km/h and (b) 320km/h (Al-Shaer et al. 2008)

I.6   SUMMARY

More than 30000 km of tracks constitute the French railway network and about 96% among them are conventional ones. While for the new lines a transition layer (sub-ballast) is placed between ballast and subgrade in order to ensure the traffic and maintenance related requirements (resistance, quality of track geometry, maintenance optimisation, etc.), in conventional lines (mainly built during XIXth century) no transition material was placed between ballast and subgrade. Therefore, an Interlayer (ITL) was created over time by the interpenetration of subgrade's fines and the ballast grains attrition. Moreover, the nature and thickness of this layer is heterogeneous and its mechanical performance depends on each site material and traffic conditions (maximum axle-load, train speed, loading history, trains per day, etc.).

Due to the heterogeneity of ITL, track prospections may give important information related to the track's mechanical state. Different geophysical and geotechnical methods could be applied to track prospection. On the one hand the geophysical methods, that excite the soils at very low strains, are focused on wave velocities in soils related to their maximum elastic modulus (MASW, Cross-hole, down-hole…) or structure interfaces like moisture content variations (GPR). On the other hand, the geotechnical methods are able to investigate soil mechanical parameters like elastic modulus or damping ratio by exciting the materials at larger strain levels (dynamic penetrometers, LWD, etc.).

There are several factors impacting the short and long term behaviour of each ITL material under railway traffic loading. For instance, the shear wave velocity in track-bed materials will influence the surface wave velocity (Rayleigh wave), which marks the critical velocity of a track. While train speed approaches this critical speed, track load and response increases (a resonance-like phenomenon). This load amplification could cause decrease of the elastic modulus (increasing track deflections for a similar load). In addition, this load amplification is more notable on distant points from the traffic loading source where lower stress amplitudes are reached at lower train speeds. However, the loading effects decrease rapidly in the first meters from the loading source, especially for short wavelength waves. Regarding the dynamic behaviour of coarse-grained soils as ITL, two parameters need to be assessed: the elastic modulus and damping ratio. These two parameters are affected by loading conditions (maximum deviator stress amplitude, initial mean stress, loading path, loading frequency,

etc.) and initial state parameters (void ratio, initial dry density, grain size, plasticity, etc.). In addition, the loading and soil state parameters will also influence the cumulative deformations. A change in loading conditions (due to a change of traffic or an upgrade of service speed) could generate larger cumulative deformations, increasing maintenance costs and reducing track' life cycle.

Different experiences conducted on real experimentation tracks and through physical models showed the effects of increasing train speed for a given track and loading conditions. Nevertheless, some questions still remain in terms of the effects of each one of the loading parameters influencing the behaviour of the materials constituting the conventional track. These loading parameters to be studied in the following chapters will deepen the knowledge on soil's short and long term behaviour under the effects of axle-load, loading frequency, cyclic loading shape, material position in track (depth and distance), soil nature and moisture content.

II. '*IN-SITU*' EXPERIMENTATION

II.1 INTRODUCTION

In this chapter, the installation procedure and analysis of a field monitoring system installed at a site of conventional track is presented. The main objective of this field monitoring is to assess the dynamic behaviour of track-bed materials under different train loads. Firstly, the selection of the experimentation site is discussed. Secondly, the geophysical and geotechnical prospections are depicted. Thirdly, the sensors' selection, the installation process and the verification of sensors' response as well as the analysis methods are presented. Then, the results from a test campaign performed are presented to analyse the behaviour of track-bed materials under a given train load. Finally, a statistical analysis is performed based on the Intercity trains' passages data recorded for 5 months.

II.2 SITE SELECTION

The site selection is an important stage of the experimentation process, because the site must be representative of the conventional lines in France, and allows the dynamic behaviour of track-bed to be investigated.

II.2.1 Selection criteria

Specific criteria were adopted for the selection of the monitoring site (Figure II.1). Firstly, as the main objective is to analyse the train speed impact on the mechanical behaviour of track, a site with the maximum limit speed is required (220 km/h for the French conventional lines) to cover a large range of potential train speeds. Secondly, a maximum load of 225 kN/axle, the highest admissible load in France, is also required to analyse the effect of different axle loads (from different rolling stock) on track-bed behaviour. Thirdly, different types of train with different compositions should be involved (Intercity, Regional, TGV and Freight trains). These criteria were applied using a Geographical Information System (GIS) software and the French railway network data to obtain all the potential valid sites in the French network. The fourth criterion was to limit the site selection to the ones that verify the first criteria for at

least 10 km, because the limit speed could change in the same railway section. The fifth criterion was to limit the tracks to groups 3 to 5 in the International Union of Railways (UIC) classification (UIC 2009). The lines of group 2 are excluded because they bear significant traffics and they are part of the main structure of a network, thus very difficult to anticipate a time with no circulations for the installation of sensors. The lines of group 1 UIC are also excluded because they are not operated by SNCF. For the lines of groups 7 to 9, they are not exploited as much as the lines of other groups and their maintenance are thereby not at the same level as for other lines. Moreover, the service speeds for these lines are also not as high as for groups 1 to 6.

Based on this first group of 5 criteria, 540 km were identified within 17 lines in the entire French conventional network.
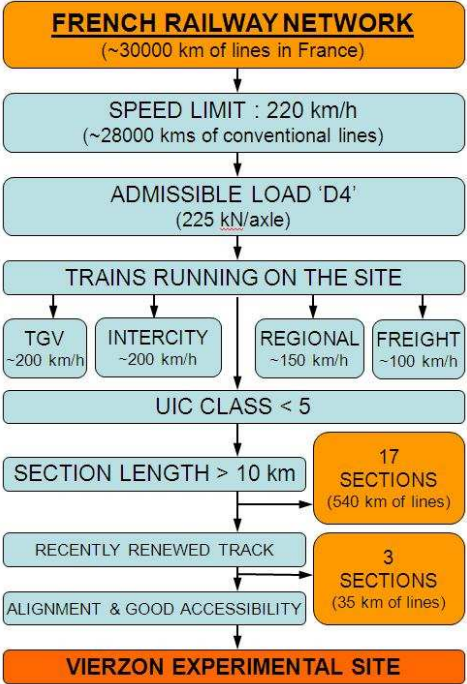
Figure II.1 Decision chart of 'Vierzon experimentation site'

To refine the selection, other criteria about the state of track were considered. A recently renewed track was required in order to minimize the influence of track geometry irregularities (Chen et al., 2013; Dahlberg, 2010). As the average life of track elements is around 30 years, it was decided to consider a third-life age of track components (ballast, sleepers and rail). A maximum age of 10 years was considered for sleepers or rail at the experimentation site. Special maintenance operations should not be carried out since the last track renewal - the

maintenance operations could be the result of the deterioration of track levelling and it is preferable to avoid it at the experimentation site. A rail of 60 kg/m was required at the experimentation site because it is the most common rail with the previously cited characteristics of traffic and service speed.

II.2.2 Pre-selected sites

With this second group of criteria, 3 sites of a total length of 35 km were pre-selected: the first one is in Vierzon (Centre Region), the second one near Strasbourg (Alsace Region) and the third one near Angouleme (Aquitaine Region). As Vierzon site involves UIC class 4, lower than the other two sites (of UIC class 3), it is more available for the instrumentation. In addition, the Vierzon site is closer to the laboratory, therefore more practical. Thus, it was decided to select Vierzon site for this study (Figure II.2).

II.2.3 Vierzon site

A specific area was chosen among the 12 km from Vierzon site satisfying the imposed criteria. Three different sections close to the kilometric point KP 187 were visited. The differences between the three considered sites were mainly the drainage system (present or not), the sleeper type (mono-block or bi-block) and the construction typology (cutting or embankment). Bi-block sleepers were preferred as the stress transmitted to the substructure is expected to be higher (because of the smaller contact surface with ballast layer). In addition, it was preferable to choose a cutting zone in order to only involve naturally formed subgrade. According to BRGM (Bureau de Recherches Géologiques et Minières), the predominating soil in the zone is silty sand. Nonetheless, from the borehole investigation, the soil at this site corresponds mostly to clayey sand, blue clay, grey clay and sandy clay through the first 3 m of depth (prospections available on BRGM website: infoterre.brgm.fr; boreholes performed close to the coordinates: 47°20'56.1"N 2°02'49.2"E). As a small river runs by the sites, the water table level is close to the ground surface and the zone is considered as a floodable area by BRGM. Moreover, a cutting zone is also interesting when evaluating the water effect (soil saturation) during different seasons. The main characteristics of the three different sites are presented in Table II.1.

Finally, site 2 (KP 187+200) of 30 m long, with bi-block (B450PI) sleepers and placed in a cutting of 2.5 m high was selected (Figure II.3).
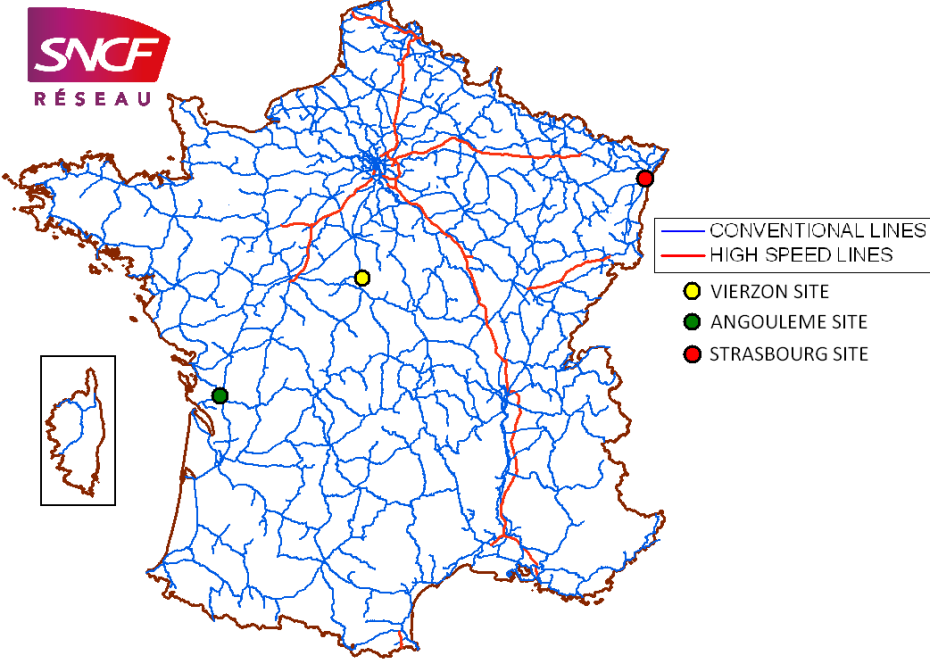
Figure II.2 French railway network and Vierzon site

Figure II.3. Selected site at Vierzon

Table II.1. Description of 3 visited sites in Vierzon

	Site 1		Site 2		Site 3	
	Track 1	Track 2	Track 1	Track 2	Track 1	Track 2
K.P.	187+800		187+200		185+200	
Rail	60-E1	60-E1	60-E1	60-E1	60-E1	UIC60
Year Rail	2006	2006	2006	2006	2006	1973
Sleeper	M450PI	M450PI	B450PI	B450PI	B450PI	B450PI
Year Sleeper	2006	2006	2006	2006	2006	2006
Cutting Embankment	Emb.	Emb.	Cut. (2 m)	Cut. (2 m)	Cut. (1 m)	Emb.
Drainage	No	No	Yes	Yes	Yes	Yes
Straight section	Yes		Yes		Yes	
Accessibility	Very good		Very good		Good	

II.3   SITE PROSPECTION

Different prospection tests were performed on tracks and lateral service paths from each track. For each prospection position, geophysical and then geotechnical prospection methods (MASW, Geo-endoscopic tests, PANDA tests and LWD) were applied on tracks 1 and 2 (see Chapter I). For the geotechnical tests, firstly a PANDA test was performed, reaching a depth of around 1.5 m from the surface (ballast surface level). In total, 10 PANDA tests were performed on each track and 5 PANDA tests were carried out on the service paths as described in Figure II.3. In addition, for some positions (12 in total) a Geo-endoscopic test was performed using the same hole created by PANDA rods. Geo-endoscopic tests were performed mainly on the track, and the tests on lateral paths are not as useful as on track because the soil on paths is supposed to be the same as the track's subgrade. Finally, LWD tests were performed on both tracks and lateral paths at every prospection point marked in Figure II.4 where all the test locations are presented.
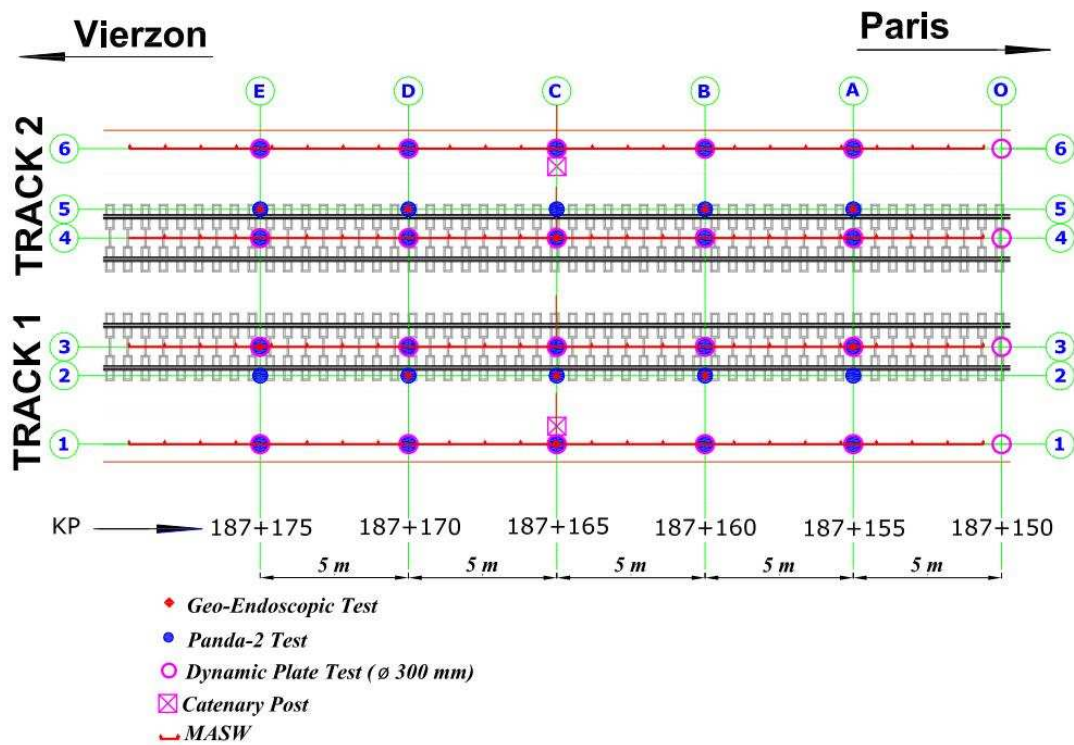
Figure II.4. Performed tests on both tracks from 'Vierzon experimentation site'

II.3.1 Geophysical survey

The main goal of geophysical prospection was to determine the mechanical properties of subgrade soil through the mean shear wave velocity. The average shear wave velocity of track-bed materials helps us to define the critical speed on the site, because the subgrade mechanical properties are associated with the surface wave velocity of a site (Kouroussis 2009). The selected geophysical test to prospect the railway platform was the MASW, commonly used in many other works (Anbazhagan et al. 2010; Connolly et al. 2014; Degrande and Lombaert 2000; Jacqueline 2014). In addition, a total of six *PANDA-3* tests (dynamic penetration tests with variable energy impacts) with measurement of wave velocity (compression and shear waves) were also performed. Only one test carried out on track 2 provided acceptable results for subgrade soil (a stabilized value of v_s=200 m/s and v_p=1000 m/s was obtained for the first meter of subgrade soil), the other five tests performed being problematic due to the influence of electromagnetical field.

II.3.1.1 MASW tests

MASW tests were carried out on track ballast and lateral paths (Figure II.4). Two MASW tests were performed along the middle of each track. Two other tests were performed on lateral paths (one line per path). A total of 4 lines were performed on the site. For each prospection line 24 geophones were installed with an inter-geophone distance of dx=1.2 m. Each line had 27.6 m of length (Figure II.5). Time spent by waves to arrive at each geophone for every impact was determined based on signals.

MASW tests performed on ballast could not be analysed because arriving waves were not identifiable in geophone signals. Moreover, trigger signal amplitude was not reached and no signal was registered in most cases. This problem could be originated by the lack of shear contact between geophones and ballast grains. Indeed, the grains are too large to allow a proper transmission of shear excitation. These kind of problems were previously reported in literature (Jacqueline 2014).
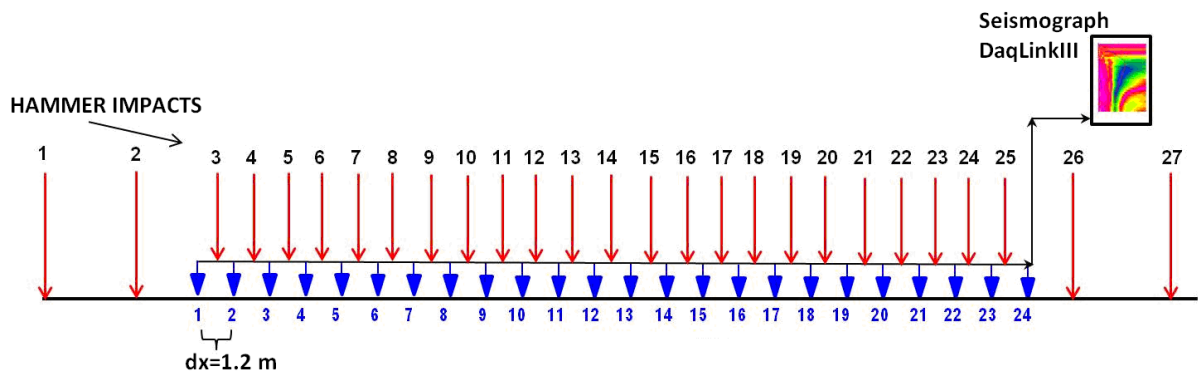
Figure II.5 Scheme of installed geophones (in blue) for each MASW test and hammer impacts

Both MASW tests performed along the lateral paths were analysed, obtaining similar results for each hammer impact. After every impact, a domochrone was obtained using the installed sensors and the arriving shear wave was identified for every geophone position (Figure II.6). From the arriving times, the dispersion curves (Mode 0, M_0) were pointed (Figure II.7) using SeisImager software. After obtaining the dispersion curves, a model of shear wave velocity in depth for every layer under the impact point can be generated. A similar result of shear wave velocity was obtained for the subgrade, v_s=200 m/s, for every impact along the geophones' line. The results for one impact at d=-15 m (impact number 1) at both lateral paths are

presented in Figure II.8. This result corresponds to an average Rayleigh wave velocity of v_R=0.934×v_s = 185 m/s (v_{cr}~v_R= 650 km/h). This velocity agrees with the critical speed on a site (v_{cr}) (Alves Costa et al. 2015; Hendry et al. 2010; Madshus and Kaynia 2000), the first resonant-like frequency, as it has been highlighted in chapter 1. However, no results were available for the first 2.4 m due to the distance considered between each two geophones.
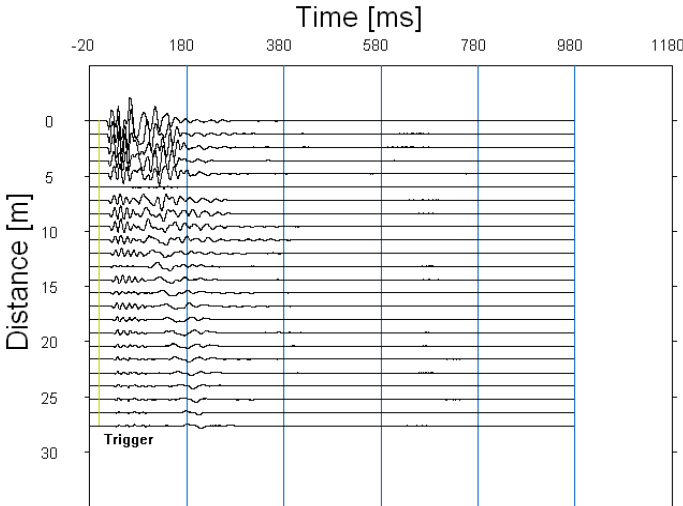
Figure II.6. Domochrone of a MASW hammer impact signals using 24 geophones
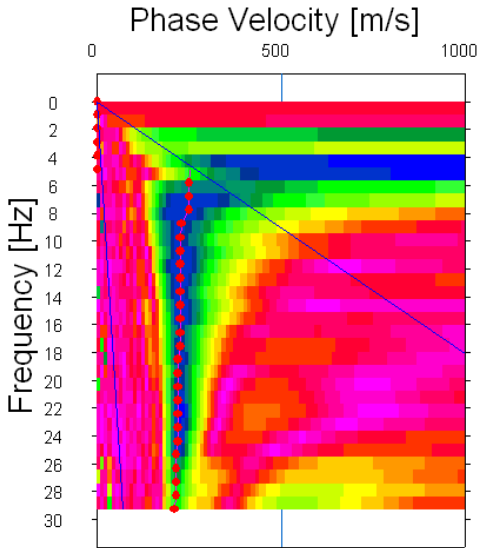
Figure II.7. Dispersion curve (Mode 0, M₀) pointed for one hammer impact

It is observed from Figure II.8 that the shear wave velocity slightly increases over depth for all the tested points. This result is coherent for silty or clayey sand as indicated by BRGM prospections for the first meters of subgrade soil (prospections available on BRGM website: *infoterre.brgm.fr*).
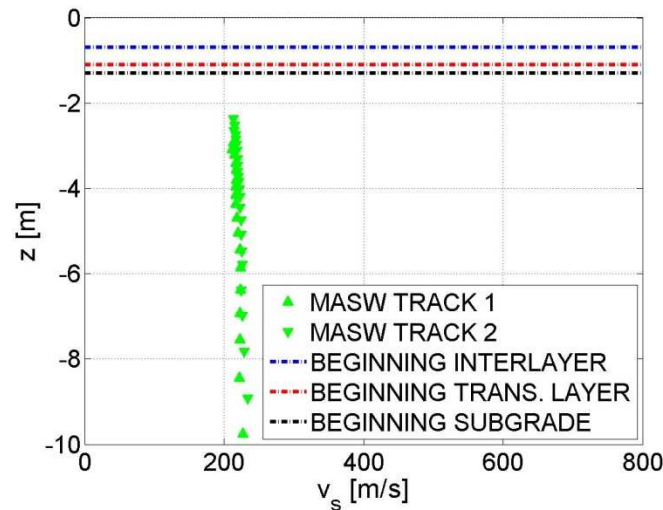
Figure II.8. Profiles of shear wave velocity in track 1 and track 2 determined with impact at 15.0 m on the lateral paths

II.3.2 Geotechnical survey

After the geophysical prospection, three different methods of geotechnical prospection were carried out in Vierzon site: Geo-endoscopic tests, PANDA-2 tests and Light Weight Deflectometer tests (LWD). For each auscultation position a PANDA test was performed firstly. In total 10 PANDA tests were performed on each track and 5 PANDA tests were executed on each lateral path. Then, for some positions (12 in total), a geo-endoscopic test was performed. Finally, 24 LWD tests were performed on the track centre and lateral paths at every spot marked in Figure II.4.

II.3.2.1 Geo-endoscopic tests

Geo-endoscopic tests (see Chapter 1) were analysed first to differentiate the materials and layers in the track, helping define the sensors' positions and facilitate the later analysis of PANDA test results. Figure II.9 shows some geo-endoscopic images from four different boreholes, two from each track ('zero' level corresponds to the rail surface in this case). A qualitative analysis of the grain size, the voids and soil's colour is performed to define the different materials and their layers thicknesses. It can be noted that the shallowest part of the track is composed of a fresh ballast layer (ballast grains without fine particles covering them). This layer is 45 cm thick in average (Table II.2). In a deeper level, a thin fouled ballast layer

is found. The ballast grains are fouled by small grains of about 2 mm around them. Nonetheless, there are still enough voids to allow water to percolate through, thus preserving one of the most important functions for ballast. The thickness of the fouled ballast layer is 9 cm in average for both tracks. A coarse-grained soil with no visible voids follows the fouled ballast layer, the interlayer (ITL). This soil layer is gradually changing with depth with less and less coarse grains. In the registered images, grains larger than 5 mm of diameter are always present in the ITL soil. One key characteristic of this ITL is that all coarse grains are totally covered by a fine matrix soil originated from Subgrade (SBG) and attrition of ballast grains. The existence of different fine soils (less dark, with yellow colour) and the gradual disappearance of coarse-grained soil mark the beginning of a Transition Layer (TL). In this first analysis of geo-endoscopic tests the beginning of a transition layer through the SBG is considered when most of the soil is composed of fine soil coming from SBG and when the amount of coarse grains starts to decrease.

An average layer of 35 cm thickness of ITL was found in each track-bed. Moreover, the standard deviation was higher for track 1 (6 cm) than for track 2 (3 cm). Below ITL, the coarse grain content decrease rapidly in depth. From ITL to SBG, the fine soil matrix changes its colour, defining a layer of TL, which can be considered as a transition soil between the ITL and the SBG. The thickness of TL is 21 cm in average for track 1 and 23 cm for track 2. Finally, SBG soil is found below the transition soil. It is easy to distinguish SBG soil from the other track-bed soils as ITL or TL soils. Almost the whole SBG soil is composed of fine soil (d < 1 mm) of the same appearance with a small quantity of coarse grains. Summarising, the track-bed is composed by 50 cm ballast (fresh and fouled), 40 cm ITL, about 20 cm TL overlying SBG that starts from z=-1.3 m starting at the rail surface.
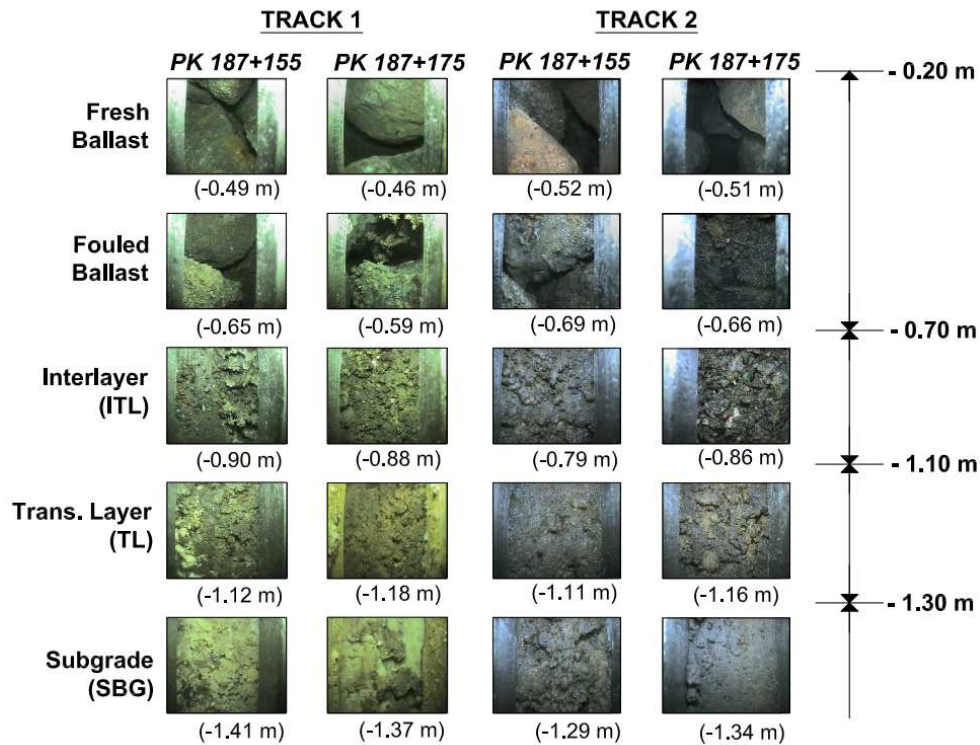
Figure II.9 Different materials identified by Geo-endoscopic tests

Table II.2. Thicknesses of track layers from geo-endoscopic tests performed on track 1 and track 2

	Track 1		Track 2	
	(μ) Average	(σ) Std. Deviation	(μ) Average	(σ) Std. Deviation
Fresh Ballast	0.45 m	0.03 m	0.44 m	0.02 m
Fouled Ballast	0.09 m	0.03 m	0.09 m	0.03 m
Interlayer	0.37 m	0.06 m	0.35 m	0.03 m
Transition Layer	0.21 m	0.04 m	0.23 m	0.02 m

II.3.2.2 PANDA-2

After the geo-endoscopic data analysis, PANDA results are analysed. For each penetrometer hit, both auscultation depth and tip resistance values were recorded. The tests were stopped when the SBG layer was reached and the tip resistance stabilized at 1.5 m depth under the rail surface (tests on track) and at 1 m depth if the test was performed on lateral service paths. The

tip resistance had different values depending on the traversed material. A PANDA tip resistance profile for one on-track test is shown in Figure II.10. Four different parts are easily distinguishable: the shallow part corresponding to the ballast with low tip resistance values but increasing moving average value while going down and with a great dispersion of values around the average. The low resistance values in the near surface zone are a result of reorganization of ballast grains. This grain arrangement allowed the tip (small compared to ballast grain size) to penetrate easily the first centimetres of ballast layer. While the tip went deeper into the track-bed, the grain arrangement becomes more difficult due to confining, as a result, the average resistance value increased. The second material below the ballast, ITL, shows a stabilized average value, of about 90 MPa, but with a still significant tip resistance dispersion around the mean value. The dispersion is also caused by the existence of coarse ballast grains in the soil. This is an indicator of the heterogeneity of this soil. Under ITL, the third material found is the TL. This material is characterized by a decreasing average resistance, from 80 MPa to 20 MPa in 20 cm of depth, along with a decreasing dispersion. The TL corresponds to a transition from ITL to SBG. The fourth material, the SBG, presents a lower tip resistance of about 15 MPa in average, compared to other materials. The resistance value dispersion is very low in SBG, the soil can then be considered as homogeneous. In general, these results show a good correlation between the quantitative mechanical responses of the different materials and the qualitative image analysis from geo-endoscopic tests (Figure II.10).
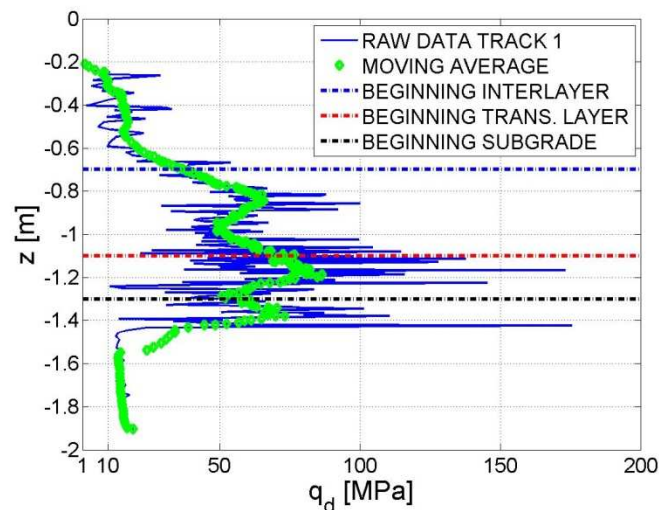
Figure II.10. PANDA test result on track 1 and moving average (Window Length = 8 signal positions)

If the PANDA test results from all the 30 tests (Figure II.4) are classified depending on previous found materials taking into account the thicknesses from geo-endoscopic tests, a histogram of tip resistance for different materials from track 1 and track 2 can be obtained (Figure II.11). The relative frequencies of tip resistance values are presented for (a) ballast, (b) ITL, (c) TL and (d) SBG. The most frequent resistance of ballast and SBG is lower than for ITL and TL. The lower resistance average obtained in ballast using PANDA does not mean that the ballast layer is less resistant than ITL or TL. However, given that there is no cohesion between grains, there is re-arrangement while introducing the rod, leading to lower average resistance. There is more dispersion of relative frequencies for ITL and TL materials, caused by the high cohesion contributed by the fines from SBG. The SBG frequency dispersion and its resistance are lower. The resistance values are in the range from 0 to 30 MPa.
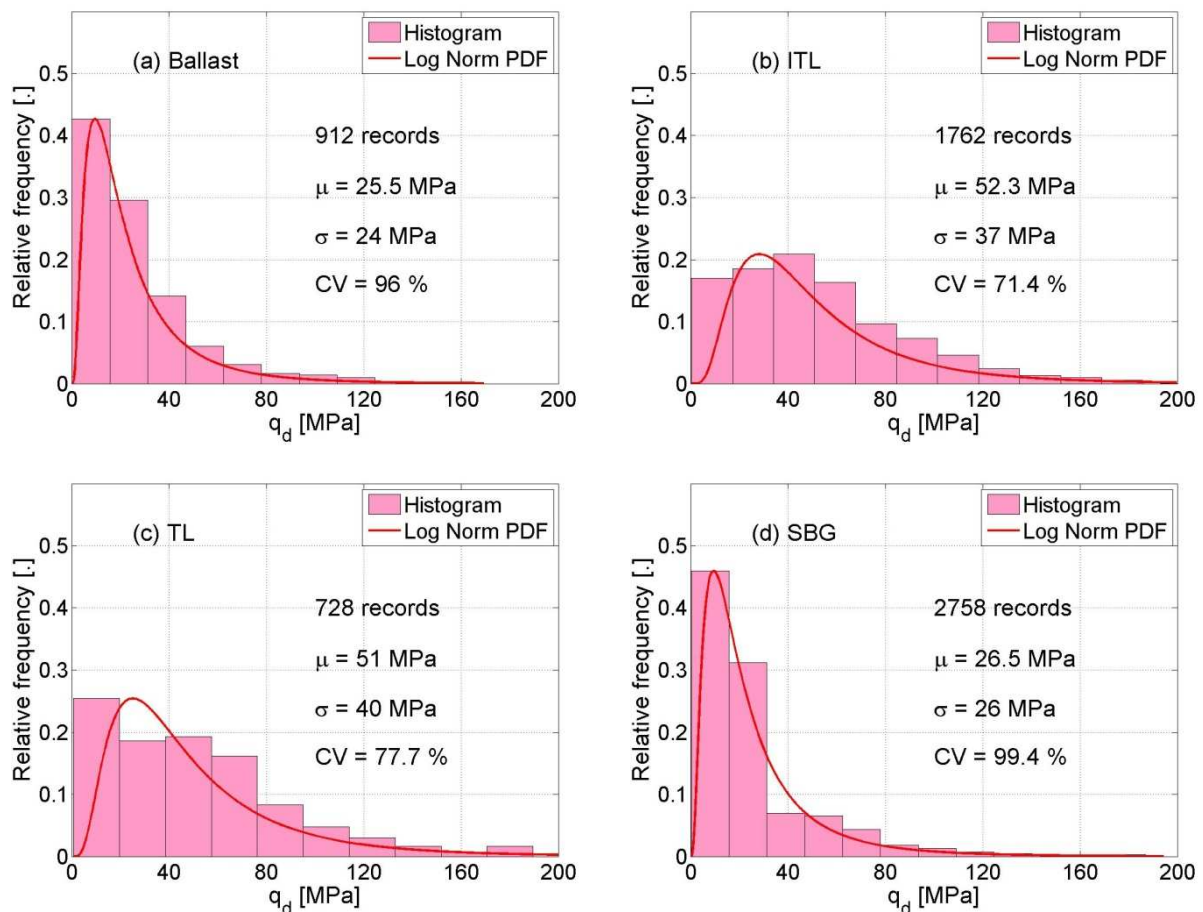
Figure II.11. Histograms of q_d for (a) Ballast, (b) ITL, (c) TL and (d) SBG in track 1 and track 2

Assuming a log-normal distribution of the PANDA resistance values for materials from conventional railways (Alves Fernandes 2014), the cumulative distribution frequency (cdf) of each material can be compared for both tracks (Figure II.12). It is observed that the resistance distributions show identical results in both tracks for ballast, ITL and SBG. However, for TL there are more differences than for ITL and SBG.
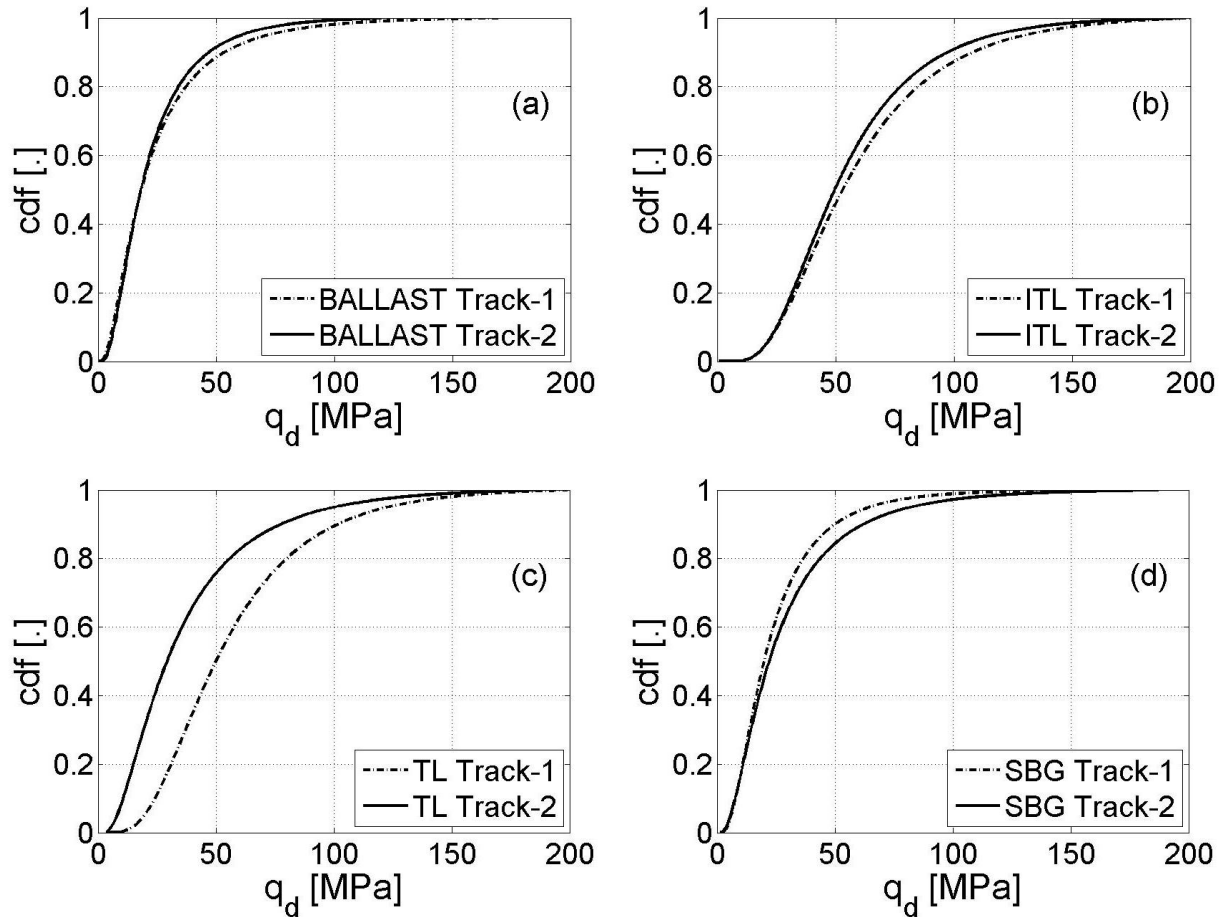
Figure II.12. Log-Normal distribution cdf (cumulative distribution function) of PANDA values for (a) Ballast, (b) ITL, (c) TL and (d) SBG on track 1 and track 2

Several authors developed formulas to relate soil's elastic modulus (E) to q_d measured in Dynamic Cone Penetrometer (DCP) tests (Amini 2003; Cassan 1988; Chai and Roslie 1998; Chua 1988; Lunne et al. 1997). In this study, the following equations were used to estimate the elastic modulus based on the results from PANDA tests. Equation (II.1) (Chai and Roslie 1998) was developed for using DCP results obtained in coarse grain-grained soils. It is also suitable for coarse soils mixed with sand. This equation is used in this study to estimate the moduli of fresh and fouled ballast.

$$E = 17.6 \cdot q_d{}^{0.64} \tag{II.1}$$

Equation (II.2), proposed by Chua (1988) is adapted to estimate the elastic moduli of granular soils like sand containing finer soils like clay and silt. It is used to calculate the moduli of ITL and TL soils.

$$E = 23.2 \cdot \log(q_d) + 12.5 \tag{II.2}$$

Equations (II.3) and (II.4) (Lunne et al. 1997) are used for sand natural soils:

$$E = 2 \cdot q_d + 20 \quad \text{if} \quad \forall\, 10 < q_d < 50 \tag{II.3}$$

$$E = 4 \cdot q_d \quad \text{if} \quad \forall\, q_d \leq 10 \tag{II.4}$$

As the similarity between materials from both tracks is verified with their statistical distributions, the estimations of elastic modulus are performed taking into account the tip resistance values for both tracks. The log-normal distribution parameters of the estimated modulus (*E*) are presented for each material. The average modulus values vary from 133 MPa for ballast to 77.1 MPa for SBG soil. The mean values of the estimated moduli of ITL and TL are halfway from the ballast and SBG results, being 103 MPa for ITL and 95 MPa for TL. It seems coherent as the nature of ITL and TL depend on the surrounding materials, ballast and SBG, of a site (and their values are in the middle of both ballast and SBG). Even though the mechanical characteristics of ITL soil are stable over its thickness, both ITL and TL constitute a transition from ballast to SBG. In addition, as ITL presents coarser grains than TL, its elastic modulus is higher, as shown in Table II.3.

Table II.3. Log-Normal distribution parameters of elastic modulus (E) for Ballast, ITL, TL and SBG, determined based on PANDA tests performed on tracks 1 & 2

| | Estimated modulus 'E' Tracks 1 & 2 | |
	(μ) Average	(σ) Std. Deviation
Ballast	127 MPa	78 MPa
ITL	103 MPa	17 MPa
TL	95 MPa	22 MPa
SBG	77.1 MPa	53 MPa

II.3.2.3 Light Weight Deflectometer

LWD tests were carried out every 5 m at the track centre and on the service paths as shown in Figure II.1. Following the German standard (Bayerischen Staatsministerium 2012), for each auscultation point 3 impacts were applied for compaction prior to 3 new impacts to determine the deflection average under the applied load. The general Boussinesq formula for estimating E_{vd} is given through Equation (II.5):

$$E_{vd} = \frac{c_{plate} \cdot (1-v)^2 \cdot \Delta\sigma \cdot r}{\Delta d} \qquad (\text{II.5})$$

being r the radium of the plate (r=0.15 m), c the plate coefficient ($c_{plate}=\pi/2$ if rigid and c_{plate} =2 if soft), $\Delta\sigma$ the maximum stress applied (considered constant, equal to 0.1 MN/m²), v the Poisson's coefficient (0.3) and Δd the maximum displacement obtained during the test. Considering these values, Equation (II.6) is obtained:

$$E_{vd} = \frac{22.5}{\Delta d} \qquad (\text{II.6})$$

The relationship between the static (E_{v2}) and the dynamic moduli (E_{vd}) is given by Equation (II.7):

$$E_{v2} = 600 \cdot \ln\left(\frac{300}{300 - E_{vd}}\right) \qquad (\text{II.7})$$

A total of 24 tests were analysed. Figure II.13 shows the results of dynamic and static moduli from the tests carried out on track and service path. The results are found more or less stable comparing both tracks along the 30 m site. Moreover, a statistical analysis was performed and the results were fitted with normal distributions, both tracks presenting similar modulus distributions (Table II.4). To compare these results with the modulus estimated from the PANDA results, it may be considered that for the 'on-track' LWD tests the only excited material is ballast (30 cm depth) while for the 'on-path' LWD tests the material considered is SBG. The estimated modulus differences from LWD between service path and track seem coherent. Comparing the mean values of ballast static modulus (E_{v2} from on-track tests) with the modulus values from PANDA tests (Table II.4), it can be also noted that the modulus values are of the same magnitude with less than 25% difference between tracks. The mean static modulus of lateral paths (about 30 MPa) is lower than the modulus for SBG below the track estimated from PANDA tests (77.5 MPa). This can be also a result of the densification process under railway traffic loading for the SBG soil below the track.

From the dynamic modulus value, it is also possible to estimate the California Bearing Ratio (CBR), commonly used to estimate the mechanical resistance and bearing capacity of soils, Equation (II.8), (ASTM 2007):

$$CBR = 0.85\sqrt{\left(-100 \cdot \ln\left(1 - \frac{E_{vd}}{300}\right)\right)} \tag{II.8}$$

Table II.4. Mean and standard deviation values for dynamic (E_{vd}), elastic moduli (E_{v2}) and CBR obtained from LWD tests for both tracks and track lateral paths

	E_{vd} [MPa]		E_{v2} [MPa]		CBR [.]	
	μ	σ	μ	σ	μ	σ
Track 1	46	6.1	99.6	14	11	1.2
Track 2	47.3	8.5	103.5	2	11.1	1.9
Path 1	10.6	3.9	21.1	8	3	0.8
Path 2	15.8	4	32.6	8.4	4.5	0.8

Regarding the CBR estimations obtained using Equation (II.8), the on-track tests give a mean CBR of 11, defining a gravel soil (ballast). The on-path tests give an average value of CBR of about 4, defining a silty sand in the CBR correlation table.
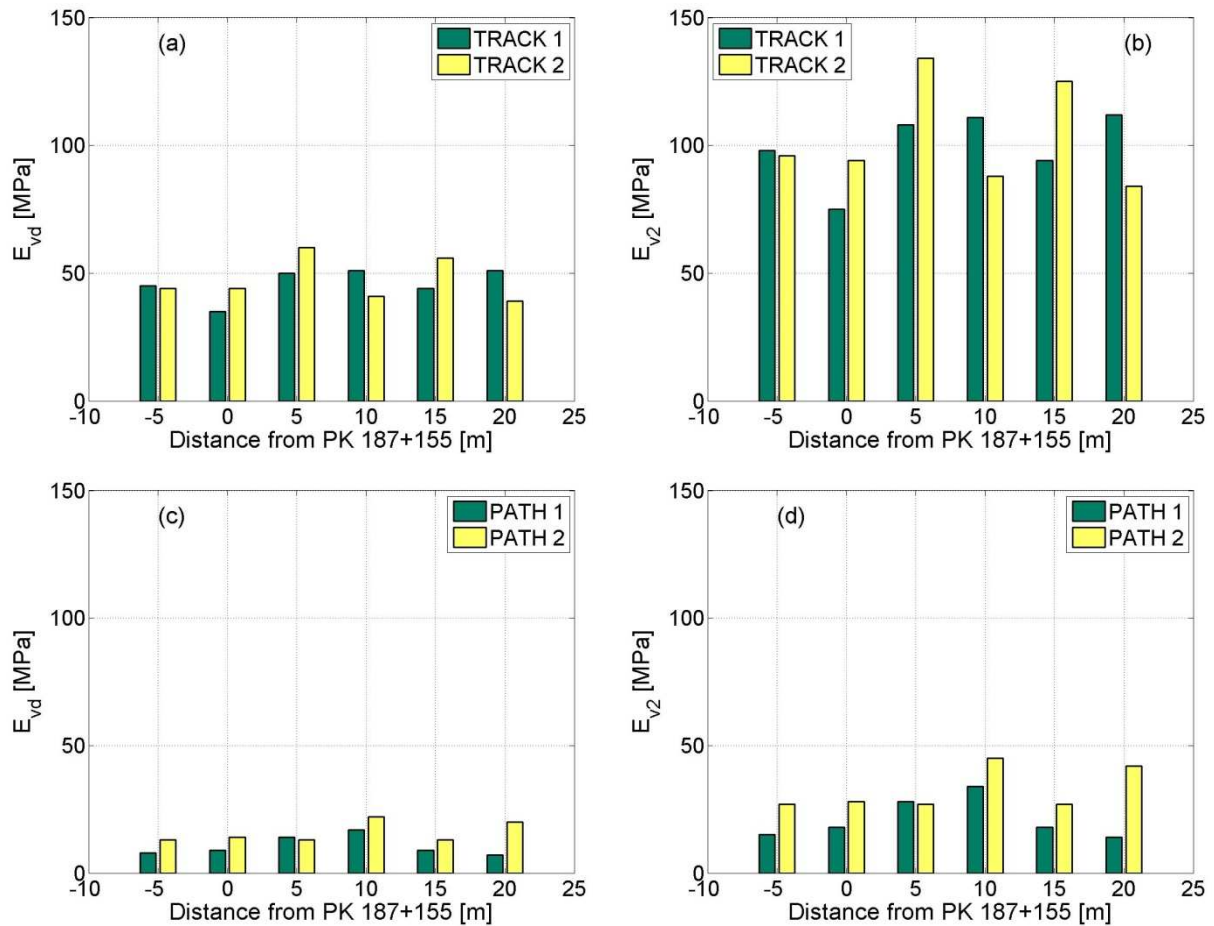
Figure II.13. Results of dynamic (E_{vd}) and elastic moduli (E_{v2}) from LWD tests performed on both tracks (a,b) and service paths (c,d)

II.3.3 Conclusions

For the prospected site, 4 materials are identified in track-bed: Ballast, Interlayer, Transition Layer and subgrade soil. A good correlation between thicknesses is found between qualitative analysis (geo-endoscopic tests) and quantitative results (PANDA). The statistical analysis of tip resistance values (PANDA) for different materials and tracks shows a good repeatability of results for both tracks and similar resistance distributions for ballast ITL and SBG. However, there is more variability on TL soils from both tracks.

Using empirical formulation, elastic modulus for different materials was estimated. The identified decreasing modulus in depth seems coherent taking into account the constitution of the track-bed and the nature of each material.

In order to verify the ballast modulus, LWD tests were carried out on the site. On-track and on-path tests were performed. The estimated static modulus on-track was compared to the ballast modulus estimated from PANDA tests. The static modulus of ballast obtained by the two considered methods (LWD and PANDA) was found similar. The SBG modulus could be inferred from LWD tests performed on the service paths, taking into account the lack of densification by railway traffic loadings that could result in a lower modulus than the SBG modulus below the track. The nature of the ITL depends on the mechanical response of surrounding layers: ballast and SBG. Consequently, surface deflectometer tests like LWD could be a good indicator to infer the mechanical properties of ITL by interpolating the measurements of the static modulus on-track (ballast) and on service path (SBG).

Based on the prospection performed, the structure of Vierzon track-bed was identified, as presented in Figure II.14.
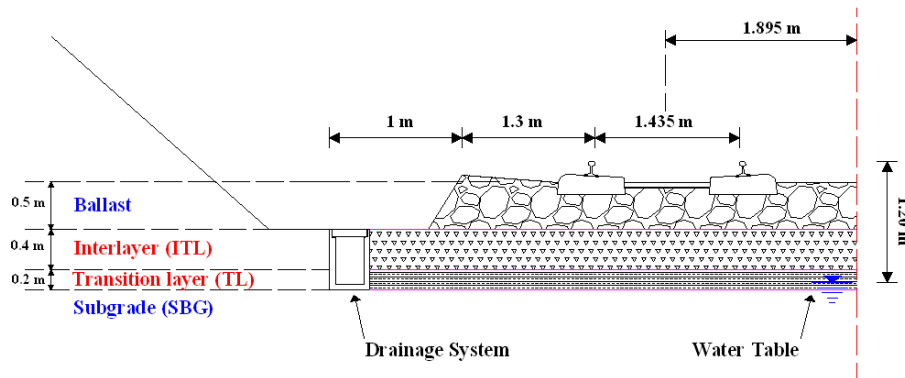
Figure II.14. Cross section of 'Vierzon experimentation site' defined after analysis of prospection tests

II.4   INSTALLATION AND ANALYSIS METHODS

Different sensors were installed at the site: accelerometers, geophones, pore-water pressure gauge and strain gauge. Each sensor was selected according to the emplacement, loading and working conditions (water, confining pressure, weather, etc.).

II.4.1 Sensor Selection & Installation

II.4.1.1 Sensor selection

Induced vibrations by train passages were measured by accelerometers and geophones. In the monitored track, there were more accelerometers than geophones because the former is mechanically more resistant during the installation process and it has been also used in other SNCF studies. The measured vibration amplitudes on substructure materials are expected to increase while the train speed increases (Alves Costa et al. 2010; Cai et al. 2008; Sheng 1999). Consequently, the expected acceleration amplitudes will depend mainly on the depth of sensor installation. If the track is loaded by a 170 kN/axle (TGV locomotive) at 250 km/h, an acceleration of about +/- 15g can be expected, and an average value of +/- 30 m/s² can be measured at sleepers (Aw 2007; SNCF-INFRA 2009).

Accelerations are attenuated in depth and distance by loading damping and radiation (Kempfert and Hu 1999; Kim and Lee 2000; Takemiya and Bian 2005). From the measurements performed in other conventional tracks (Cui et al., 2014), the maximum acceleration amplitude of 10 m/s² was recorded at -1.0 m depth. The maximum particle velocity expected at the level of sleeper is estimated at 0.2 m/s based on the analysis of Takemiya (2003). At z=-1.0 m depth the maximum velocity is estimated at 0.02 m/s, 10 times lower than that at sleeper.

Two different models of accelerometer were selected for this study (Table II.5). The first one (accelerometer type #1) was installed at the sleeper surface to properly measure the amplitudes till +/-50 g for the frequencies in the range from 0.47 to 10000 Hz. Note that in this location, the accelerometers were exposed to climatic conditions, and also higher loading amplitudes were expected. The second one (accelerometer type #2) is a capacitive accelerometer and it was embedded in boreholes. As mentioned before, accelerometer type #2 is more suitable for low amplitudes up to 10 m/s² and low frequencies (as low as about 0.5 Hz). Both accelerometer models were protected by a case and epoxy glue to avoid water problems in case of the phreatic level reaching the sensor. In addition to accelerometers, geophones were selected to be embedded in boreholes, allowing measurements of loading frequencies from 0.3 Hz and velocities up to 15 m/s.

Table II.5. Sensors installed in Vierzon site

	Brand and model	Units	Range	Dimensions	Other specifications
Accelerometer type #1	ICP PCB-601D01	m/s²	±50g	22 x 22 x 49.3 mm	Spectral noise at 10 Hz : 31.0 (µm/sec2)/√Hz Frequency range : 0.47 to 10000 Hz
Accelerometer type #2	TML ARH-10A	m/s²	±1g	16 x 16 x 28 mm	Rated Output Approx. 0.5 mV/V (1000×10^{-6} strain). Frequency response : 50 Hz Natural Frequency : 100 Hz
Soil pressure gauge	TML KDD-200 kPa	kPa	200 kPa	ϕ=100 mm H=20.5 mm	Rated Output Approx. 1 mV/V (2000×10^{-6} strain). Non-linearity : 2% RO. Resistance : 350 Ω
Porewater pressure gauge	TML KPD-200 kPa	kPa	200 kPa	ϕ=30 mm L=100 mm	Rated Output Approx. 0.8 mV/V (1600×10^{-6} strain). Non-linearity : 1% RO. Resistance : 350 Ω
Geophone	ION LF-24/0.3Hz	m/s	15 V/m/s	ϕ=32.5 mm L=78.6 mm	Operational Temperature : -20 – 60 °C. Natural frequency : 0.3 Hz. IP 65.
Strain gauge bridge	TML WFCA-3-1L	µm/m	(30000×10^{-6} strain)	Gauge=3 mm x 1.7 mm Backing=19 mm x 16 mm Thickness=1.5 mm	Operational Temperature : 0-80 °C. Applicable on : Metal. Element : Cu-Ni. Gauge Factor : 2.1 Resistance: 120 Ω
LVDT	OMEGA LD661-10	mm	10 mm	ϕ=19 mm L=169 mm	Operational temperature 0-65 °C. Vibration (sinudoidal), 10 to 50 Hz : 1 to 10 g rms linear IP 68

As far as the total stress measurements are concerned, stress gauges were installed at different depths to evaluate the vertical stress in the soil while trains were running over. It was preferred to install uni-axial sensors only, oriented in vertical direction, in order to facilitate the installation in the substructure (till 2.5 m depth). Note that the influence of speed on the vertical stress represents a major issue of the study. The sensors should be sensitive enough to capture the stress variation in the ITL and SBG at the considered speeds from 60 to 200 km/h. In the experiments carried out by Bian et al. (2014); Chen et al. (2013); Kempfert and Hu (1999); Xu et al. (2013) and Zhan and Jiang (2010), the vertical stress at 1 m depth reached 15 kPa, and the stress amplification ratio can vary from 1.05 to 1.7, depending on the type of soils, the depth, the train speed and the axle weight. In addition, the vertical stress decreases over depth, becoming lower than 7 kPa in SBG (Cui et al., 2014). The stress sensors were installed close to the rail zone to capture the higher stresses. Zuada-Coelho (2011) showed a maximum measured stress of about 30 kPa in ballast just below the rail and of 15 kPa in ballast in the middle of two rails, generated by a train running at 200 km/h. The sensors are able to measure a stress up to 200 kPa with an accuracy of 0.1 kPa. The diameter of the sensors is 100 mm, large enough to measure stresses in coarse soils as in ITL. Note that the largest grains in ITL can reach 61.5 mm (Trinh et al. 2012). In addition, the size of the sensors was also adapted to the size of boreholes performed between two sleepers.

Since the selected site does not need special maintenance operations, its total vertical settlement of the entire track-bed (including ballast) is estimated at 5 mm for 100 000 cycles based on the analysis of Kennedy et al. (2013) for a stabilized track-bed. A LVDT was then selected for measuring the settlement. It has a capacity of 10 mm and can work properly in a loading frequency range from 0 to 50 Hz.

The exerted load of each axle was measured by groups of 4 strain gauge in bridge configuration (Aw 2007). These bridges were glued to the rail (2 at each side of the rail profile), permitting to capture the elastic strain of the rail, and further determine the axle load. In addition, this sensor was used as trigger for every train running on the site.

The pore water pressure sensors were installed to measure the variations of water-pressure while a train is running over. In this study, the pore-water pressure sensor has a working range from 0 to 200 kPa. Its size is 30 mm diameter and 100 mm long, which is adapted to the borehole size of 100 mm diameter.

II.4.1.2 Sensor Installation

The experimentation zone was included in a track section containing 35 sleepers (21 m). The instrumentation mainly involved track 1 with a total of 24 sensors installed in 16 positions (Figure II.15), track 2 having been instrumented slightly with a total of 9 sensors installed in 6 positions (Figure II.16). Trains from Orléans to Montauban run on track 1. In track 1 the sensors were installed at 5 different depths. These installation position depths are listed in Table II.6.

Table II.6. Installation position depths

Installation positions depths	
On-Surface / Sleeper	$z=0.00$ m
ITL	$z=-0.9$ m
TL	$z=-1.2$ m
SBG #1	$z=-1.8$ m
SBG #2	$z=-2.3$ m

In two positions in track 1, there were 3 accelerometers of type #2 oriented in vertical, lateral and longitudinal directions respectively (accelerometers 3D, positions 3 & 5 in Figure II.15).
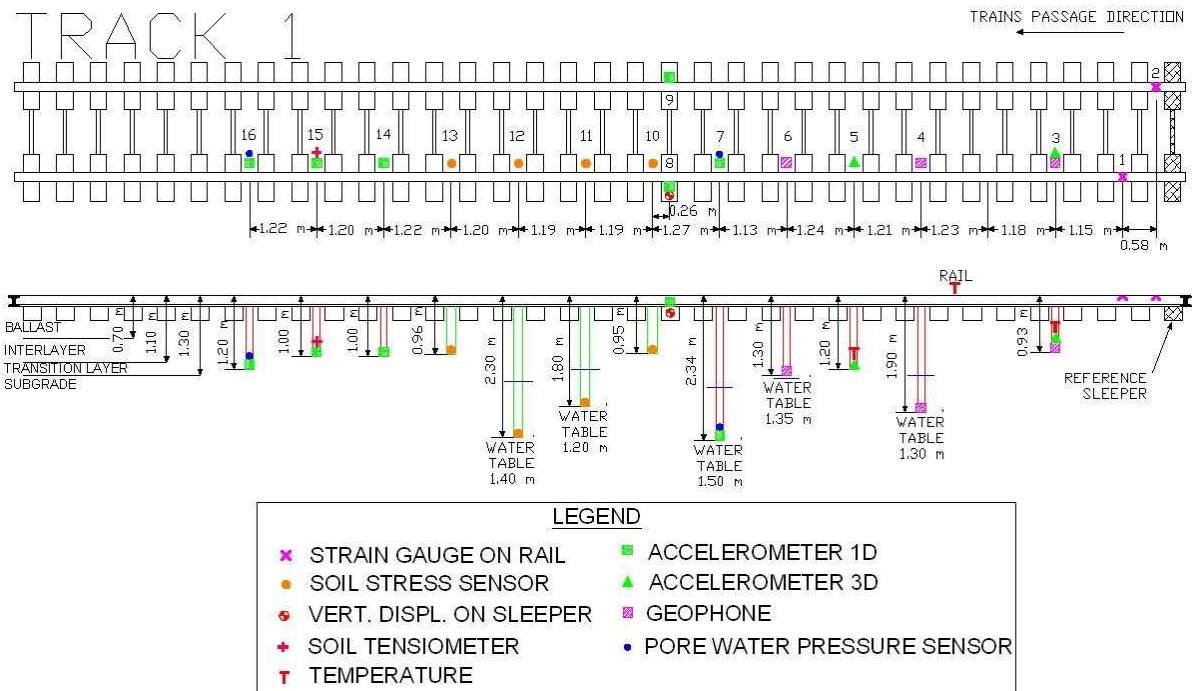
Figure II.15. Plan of the installed sensors and their positions in track 1

103

The installation process for each embedded sensor in the 15 boreholes was the same. This process consisted of 5 stages (Figure II.17). Firstly, a borehole was performed until reaching the target installation depth. A PVC tube was used mainly to retain the first 60 cm of track-bed to avoid the collapse of cohesionless ballast grains, the ITL and SBG being compact enough to resist any collapse. After verifying the borehole depth, a 5 cm layer of dry Fontainebleau sand was placed to ensure a good contact between the sensor and the soil. Secondly, the sensor was introduced carefully until the bottom of the borehole. Thirdly, the borehole was filled with an ITL material prepared in the laboratory by mixing 12 different materials (Lamas-Lopez, Cui, et al. 2014). The grain size distribution and plasticity index of the filling material are compared to the 'in-situ' materials in Figure II.18. For the first 10 cm refill in each borehole, in order to ensure a good positioning of the sensor, the prepared material was sieved through 2 mm and the finer soil was used to cover the sensor. Then the rest of the borehole until the bottom of ballast was filled with the prepared ITL material by compaction using a rod equipped with a plate of 80 mm diameter in its extremity. To facilitate the compaction process, the material was slightly humidified prior to use (water content was not specifically controlled). In order to ensure the homogeneity of the compacted ITL material, the compaction was carried out in layers of 10 cm each. Afterwards, the PVC tube was extracted from the ballast. The ballast was rearranged by hand-vibrating a "ballast-fork" commonly used in track maintenance. Finally, all cables are arranged and connected to the data logger model HBM/CX22.
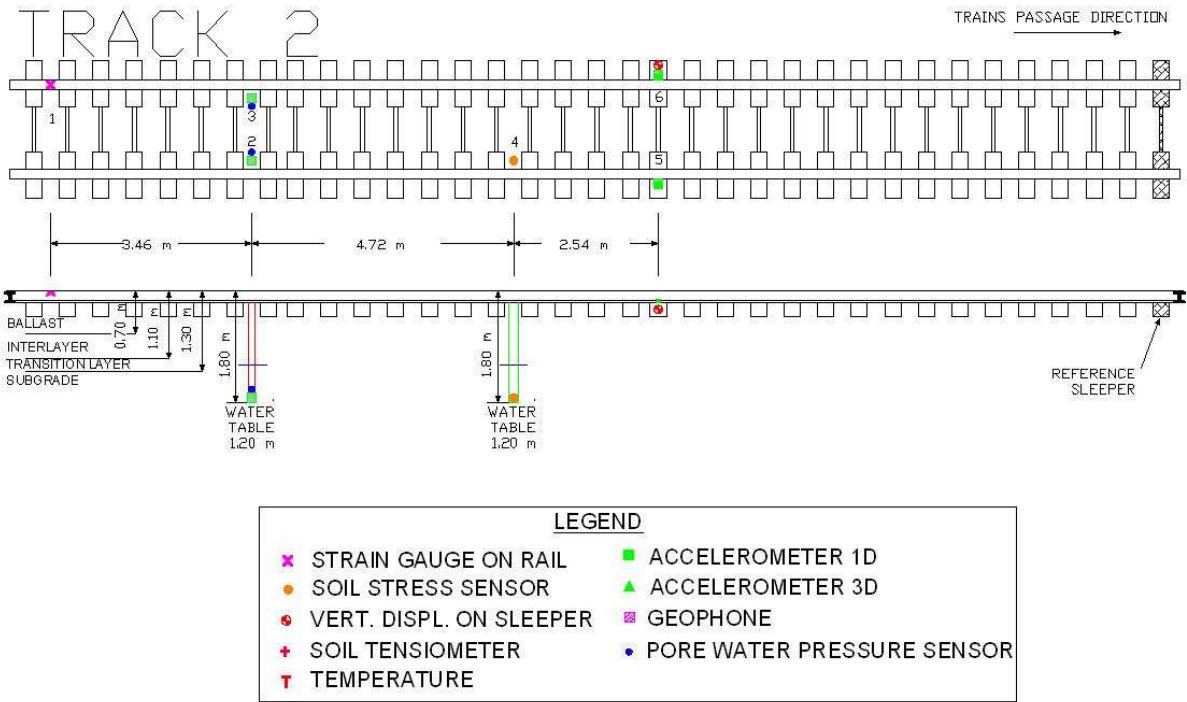
Figure II.16. Plan of the installed sensors and their positions on track 2

The surface sensors (LVDT, accelerometers and strain gauges) were installed after the embedded sensors (Figure II.19). Firstly, two aluminium structures were prepared with aluminium bars. These structures were fixed to the catenary posts situated in the middle of the experimentation zone (the vertical displacements of the posts were considered negligible compared to the sleepers). The LVDTs were installed touching a PVC plate glued to the surface of the sleeper at the exterior rail of each track. At the same sleepers where the LVDT's were installed, the accelerometers of type #1 were glued to the sleeper surface with a two-component fibre epoxy glue in order to compare sleeper's response using two different sensors. Finally, the 3 strain gauges bridges (two on track 1 and one on track 2) were installed after cleaning the installation zone of the rail.

(a) Execution of the boreholes and insertion of PVC tubes

(b) Installation of the buried sensors

(c) Refilling the boreholes and material compaction

(d) Extraction of the PVC tubes

(e) Arrangement and collection of the cables
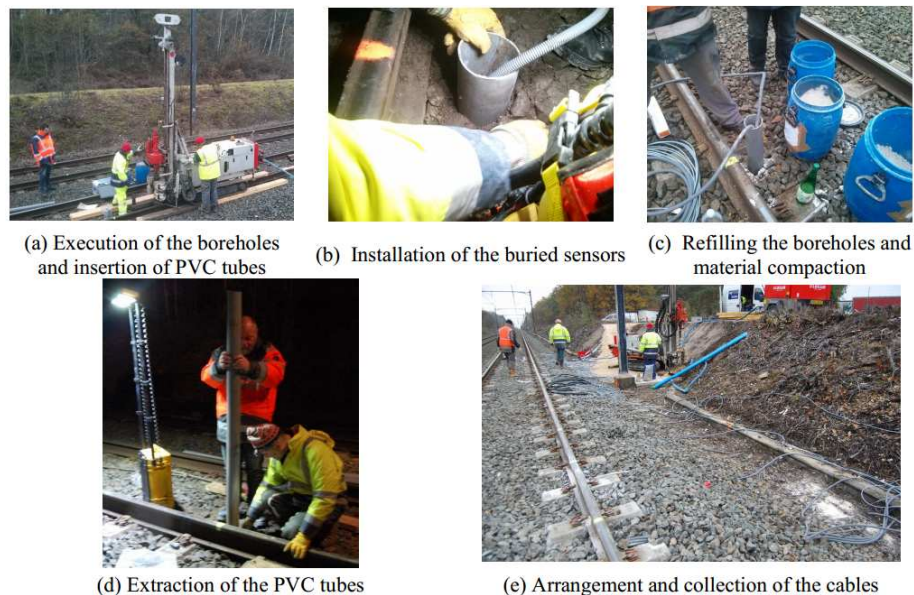
Figure II.17. Installation process for embedded sensors
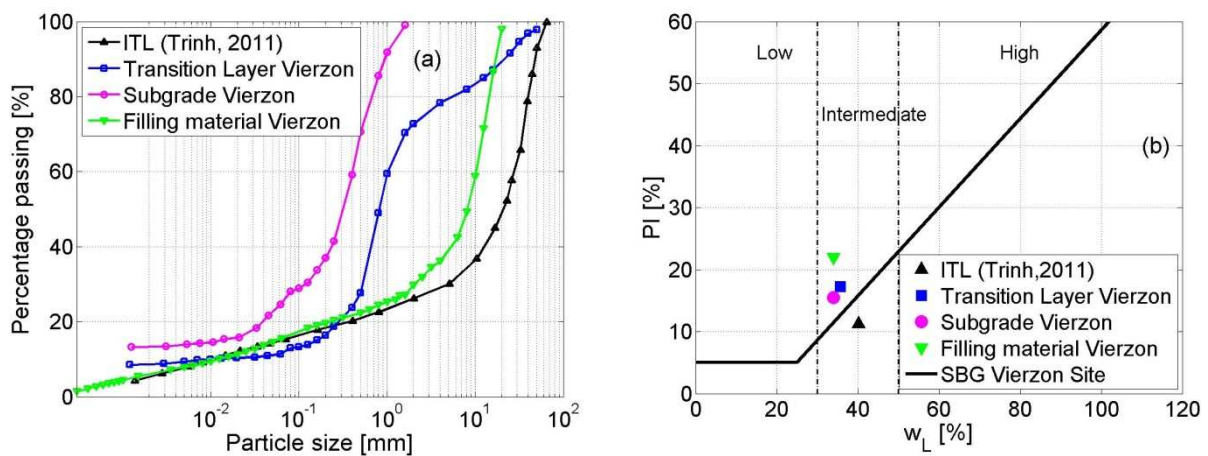
Figure II.18. Vierzon experimentation site soils: (a) Grain size distributions; (b) Casagrande plasticity chart

(a) LVDT on sleeper   (b) Accelerometers on sleeper   (c) Strain gauges on rail
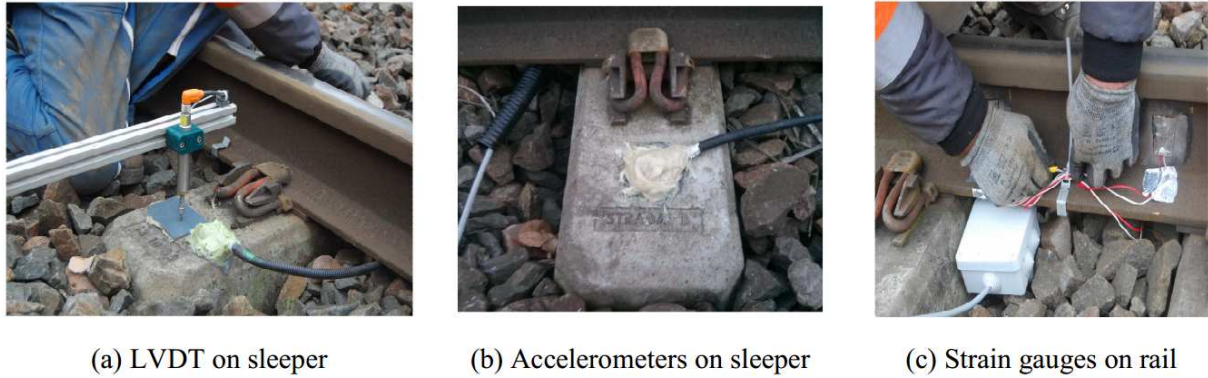
Figure II.19. Installation of the on-surface sensors

II.4.1.3 Measuring system verification

As the bogie ($\lambda = 6.3$ m) and axle ($\lambda = 2.8$ m) excitation frequencies correspond mainly to the range from 0 to 50 Hz considering the train speeds up to 200 km/h, it was chosen to apply a sampling frequency of 1200 Hz in order to obtain adequate responses for all these wavelengths. The 3 strain gauges bridges installed in both tracks are used as triggers to activate the measurements for the arriving train. For each passage, the signal of every sensor installed on the track was registered during 45 s, adding 5 s from the data logger buffer waiting for the trigger activation.

In this section, raw signals from different sensors are presented with the exception of the tensiometer data installed at the TL (position 15, see Figure II.15) because no valid measurements were registered.

All sensor responses presented in this section correspond to the passage of an Intercity train running at 200 km/h just after the installation. The train was composed of one locomotive of 17.48 m long (2 bogies of 2 axles each with an axle load of 225 kN) and seven 'CORAIL' coaches of 26.40 m long each (2 bogies per coach and 2 axles per bogie with 105 kN/axle load). The responses of the sensors of track 1 were excited by a train at 200 km/h in 'Montauban' direction while the responses of sensors of track 2 were excited by the same train running at 200 km/h in 'Orléans' direction.

For each train running over the experimentation site, it is possible to determine the load of each axle through the train 'signature', obtained from the strain gauges glued to the rail of both tracks (Figure II.20). The locomotive bogies can be detected in the first part of the signal

(about 225 kN/axle), and the seven CORAIL coaches are located behind the locomotive (about 105 kN/axle measured). In track 1 there is no great difference between the left rail signal and the right one, indicating that the load was evenly distributed between both sides of the track. The measurements do not present a large variability for the different loads (locomotives and coaches).
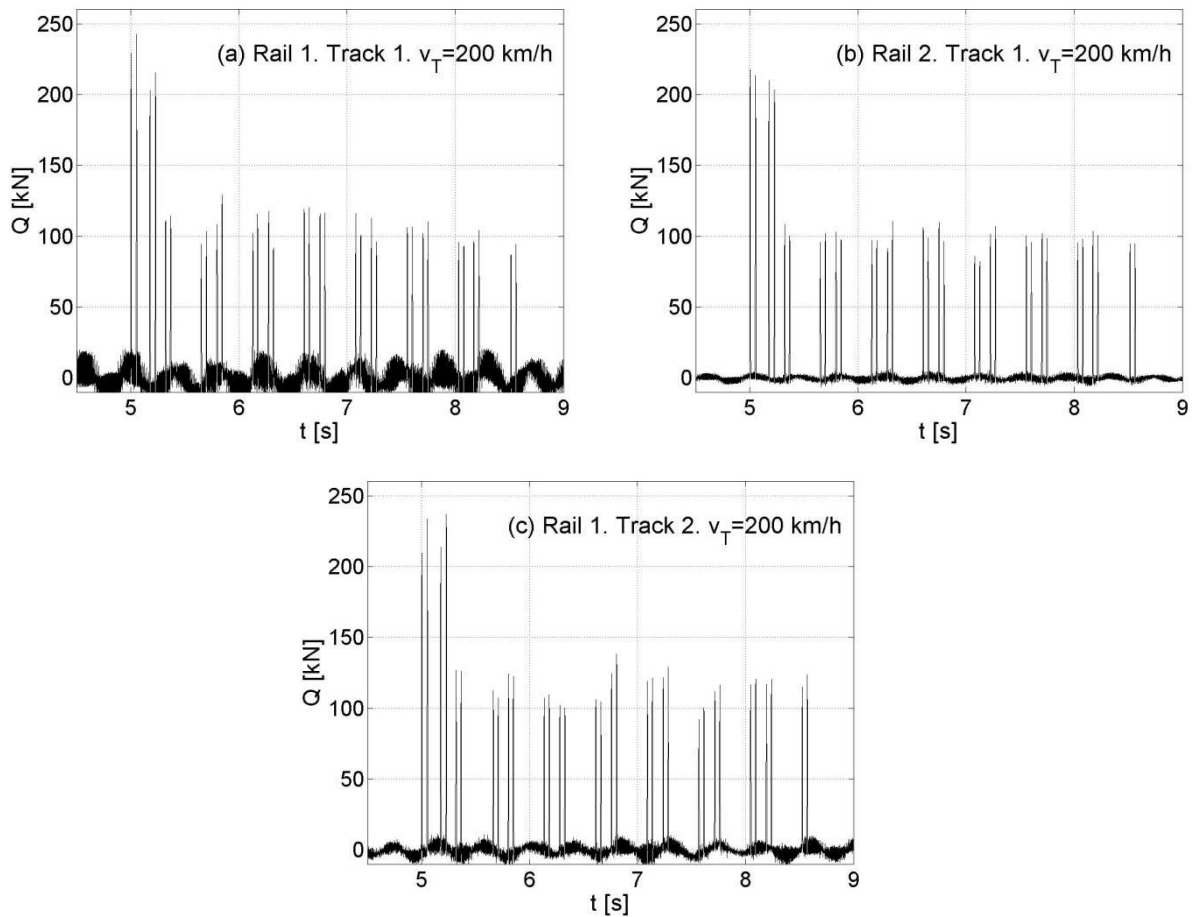
Figure II.20. Axle load determined from the response of strain gauges glued to the rails on Tracks 1 & 2 during the passage of an Intercity train at 200 km/h

The raw vertical acceleration signal from accelerometers type 1 at both sides of the sleepers (positions 8 & 9, see Figure II.15) of track 1 (Figure II.21) and on both sides of a sleeper (positions 5 & 6, see Figure II.16) of track 2 (Figure II.22) are presented. These raw acceleration amplitudes are very influenced by the small wavelengths related to rail defects ($\lambda < 0.01$ m) (Ferreira 2010; Müller-Boruttau and Breitsamer 2004). In the raw signal, it is not possible to differentiate the two axles from the same bogie, the only differentiable elements being the beginning and the end of each coach. Raw average amplitudes of about 25 m/s² are found. Some more pronounced peaks are produced by a punctual defect on rail or

wheel presented in the loading in the high-frequency range. It can also be observed that these maximum acceleration amplitude levels are, in average, similar for both rails and tracks, in spite of the large data scatter caused by tracks' irregularities (defects of rails and wheels) that are reflected in the raw signal.
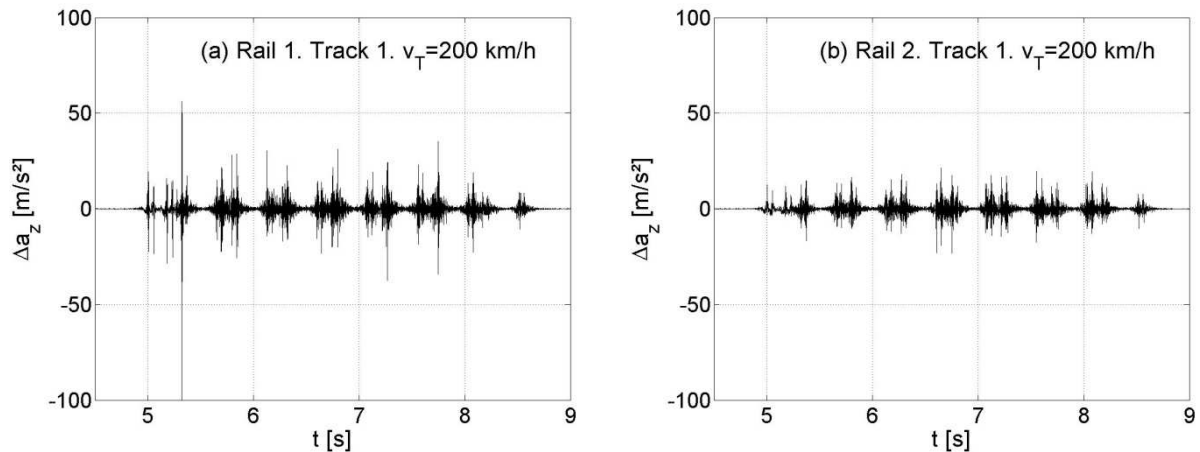
Figure II.21. Raw vertical accelerations at both sides of a sleeper on track 1, positions 8 (a) & 9 (b) (Figure II.15), during the passage of an Intercity train at 200 km/h.
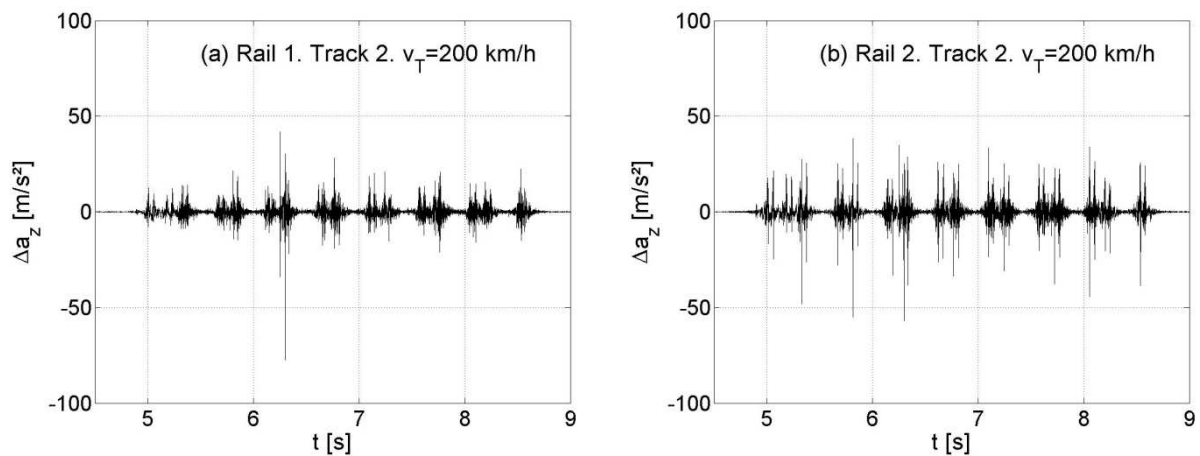
Figure II.22. Raw vertical accelerations at both sides of a sleeper on track 2, positions 5 (a) & 6 (b) (Figure II.16), during the passage of an Intercity train at 200 km/h.

Figure II.23 presents the vertical acceleration signals by the accelerometers of type #2 installed at three different depths of track #1 (ITL -0.9 m, TL -1.2 m, SBG -2.3 m). The amplitudes of raw vertical acceleration in ITL are not larger than 5 m/s², and decrease over depth. For the embedded sensors, it is possible to see the effect of different loads (locomotive and coach) on raw signals. The acceleration from the embedded sensors is less affected by high-frequencies (small wavelengths) compared to on-surface sensors; their amplitudes are caused mainly by the low-frequency (long wavelength) loadings.
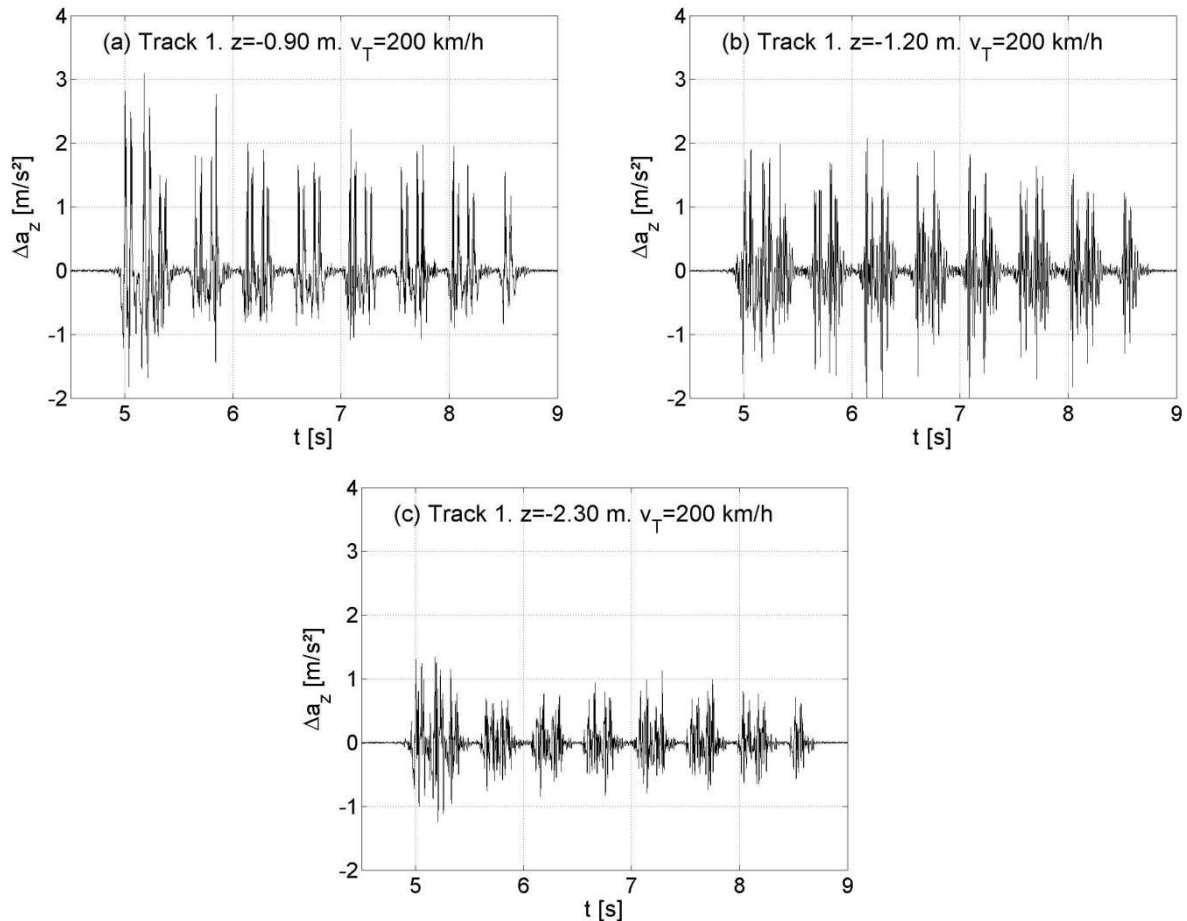
Figure II.23. Raw vertical accelerations at 3 different installation depths (ITL, TL and SBG) of track 1, positions 3 (a), 5 (b) & 7 (c) (Figure II.15), during the passage of an Intercity train at 200 km/h.

Three accelerometers of type #2 were installed at the same depth in ITL (-0.90 m) in order to verify the repeatability of measurements in track 1 (positions 14, 15 & 16, see Figure II.15). The responses of the three accelerometers under the same train excitation are shown in Figure II.24. Similar amplitude levels are obtained even for the raw data. The differences in loads due to locomotive and coaches are noticeable on these signals.
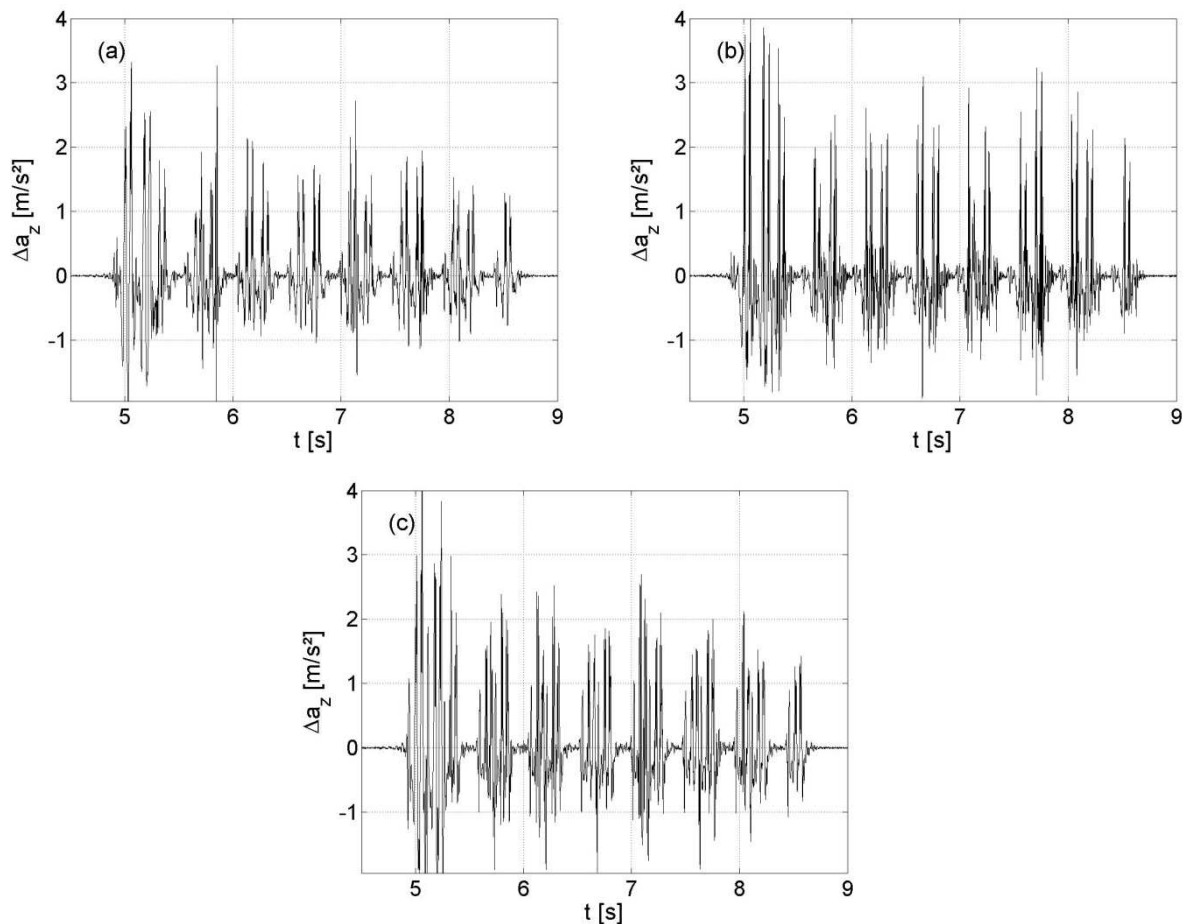
Figure II.24. Vertical accelerations of 3 different accelerometers installed in the ITL at -0.90 m depth of track 1, positions 14 (a), 15 (b) & 16 (c) (see Figure II.15), during the passage of an Intercity train at 200 km/h.

The responses of a triaxial accelerometer in the ITL (-0.90 m) of track 1 (position 3, Figure II.15) is shown in Figure II.25. The raw signal amplitudes are different for the three orientations. The vertical acceleration amplitude is dominant compared to the lateral and longitudinal ones, the lateral acceleration amplitude being the lowest. This is coherent because the experimentation site is a straight section.

The signals of the two geophone sensors in track 1 are presented in Figure II.26. It may be noted that amid the two geophones installed at z=-0.90 m depth in ITL (positions 3 and 6, see Figure II.15), only the one in position 3 worked properly, and the one in position 6 had a technical problem possibly due to lack of a good contact of the sensor with soil, a loss of verticality during the compaction or any damage suffered by the wires connecting the sensor to the data logger. Results show clearly that the signal amplitudes decrease over depth from

ITL to TL. For a given depth, the raw signal variations allow the distinction of the different applied loads by the locomotive and coaches.
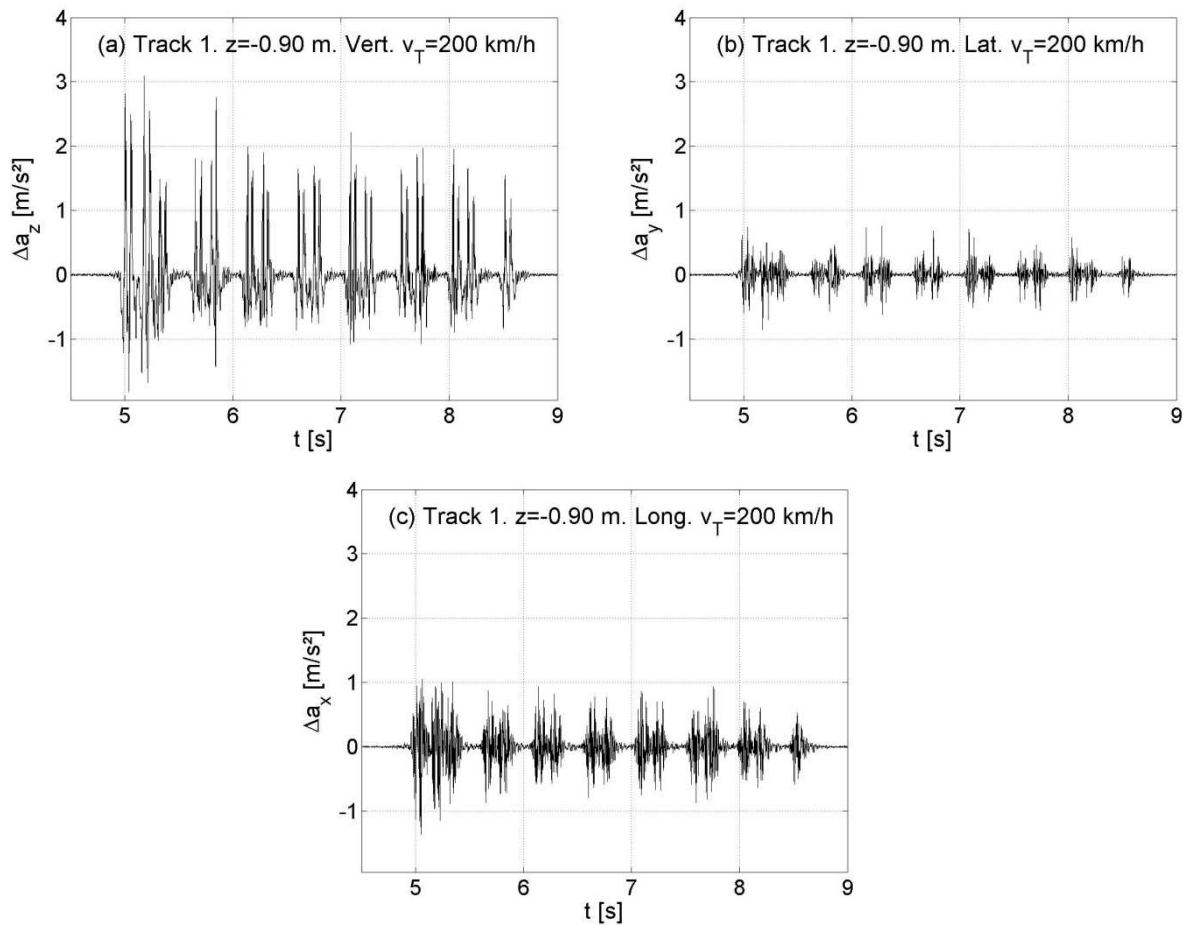
Figure II.25. Raw response of triaxial accelerometer, (a) vertical, (b) lateral & (c), longitudinal, position 3 (see Figure II.15), installed in the ITL at -0.90 m depth of track 1, during the passage of an Intercity train at 200 km/h.

The vertical displacements at sleeper, measured by the LVDT sensors (position 8 for track 1 see Figure II.15, and position 6 for track 2 see Figure II.16), at a train speed of 200 km/h are shown in Figure II.27. From this figure it is noted that there is more variation when heavier loads (locomotives) are passing than with lighter loads (coaches); these results are equivalent for both tracks. The displacements measured by LVDTs are consistent with the common values for a stable conventional ballasted track. The locomotive and coaches can be differentiated through the measurement signals, heaviest axles resulting in larger deflections of the track.
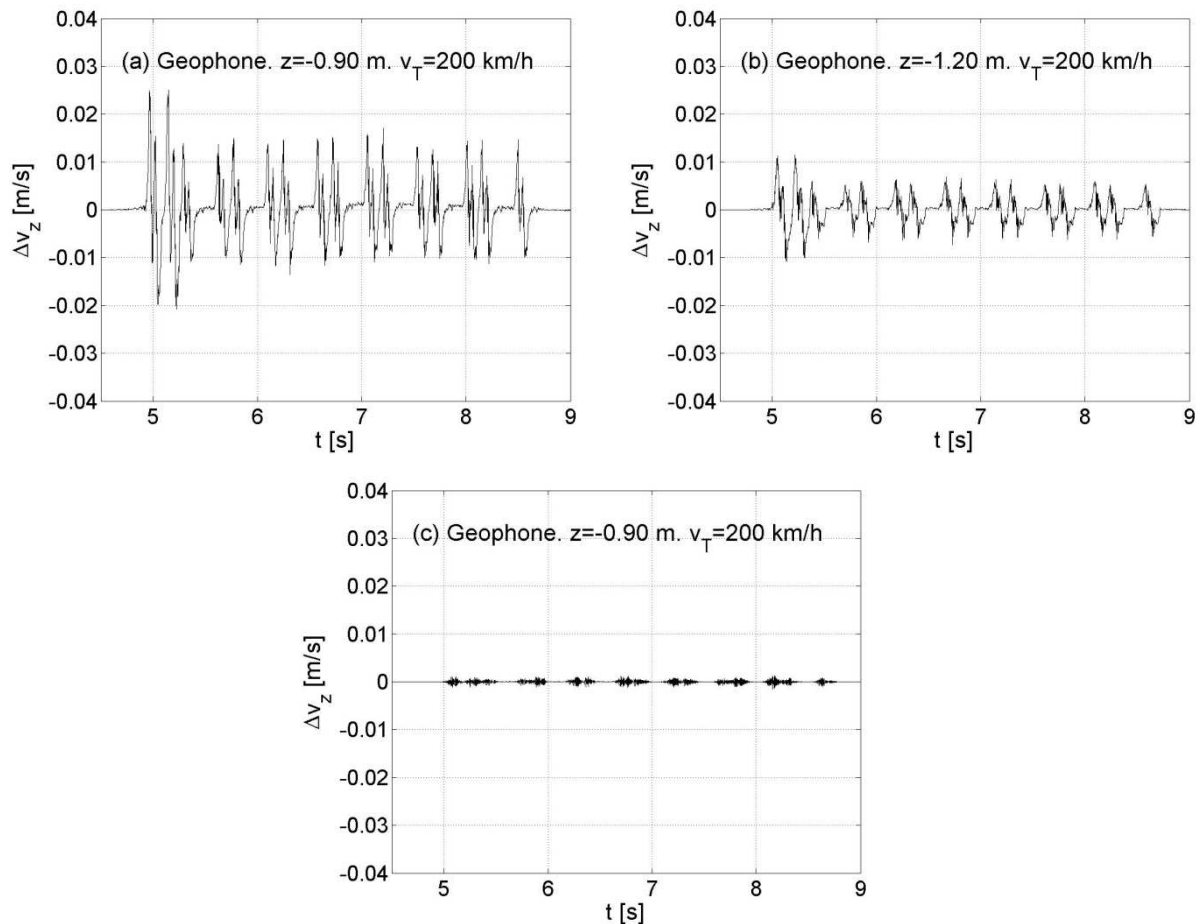
Figure II.26. Raw particle velocity signal from the geophones installed in positions 3 (a), 4 (b) & 6 (c) of track 1 (see Figure II.15) during the passage of an Intercity train at 200 km/h

The variations of vertical stress $\Delta\sigma_z$ measured by the soil stress sensors installed in ITL (z=-0.9 m) and SBG #2 (z=-2.30 m) of track 1 are shown in Figure II.28. For the soil pressure in the ITL of track 1 (Figure II.28a and Figure II.28b), some differences in amplitude are found comparing the measurements at the same depth of z=-0.9 m. As expected, the 'M' shape of each bogie passage is attenuated over depth. As it can be seen in Figure II.28, for a given depth, the 'M' shape between the adjacent axles is the same. The differences of $\Delta\sigma_z$ during train passage are well captured by the pressure gauges. The pressure gauge in position 13 (Figure II.28b), compared to the pressure gauge in position 10 (Figure II.28a) (see the installation locations in Figure II.15), seems to have a bad contact with the rest of soil structure. Even though the 'M' proportion between two axles of a bogie seems consistent for the considered depth (about 50% of the total $\Delta\sigma_z$), the total pressure amplitude in Figure II.28b is lower than that in Figure II.28a. Normally, a vertical pressure value of about $\Delta\sigma_z$= 15 kPa is expected (Bian et al., 2014; Chen et al., 2013; Xu et al., 2013; Zhan and Jiang, 2010). According to the vertical stress attenuation in a slab track (Bian et al. 2014), the

measurements by the pressure gauge in position 12 (see Figure II.15), SBG #2 depth (z=-2.3 m), seem to be consistent according to the load and the installation depth.
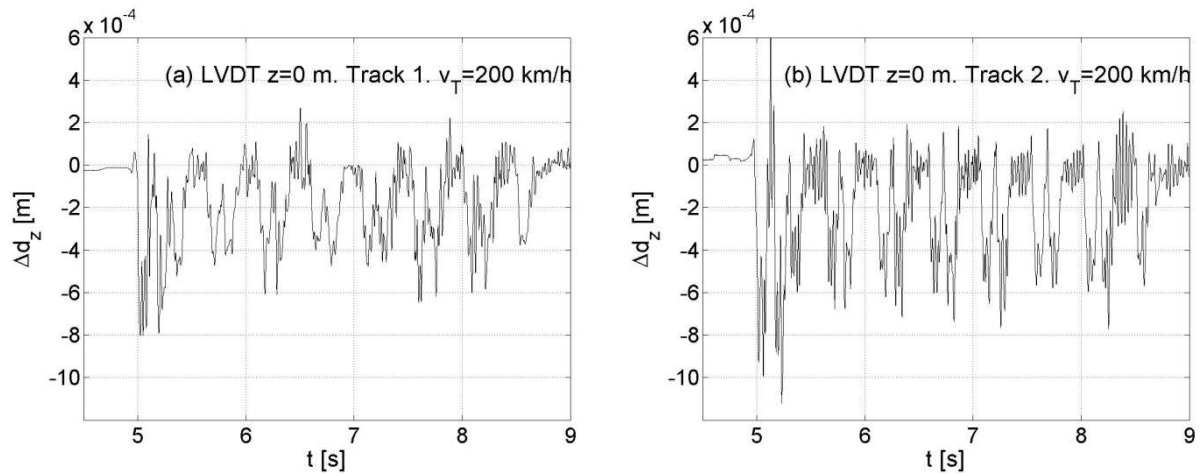
Figure II.27. Raw vertical displacement of sleepers measured with LVDT, sensors installed in (a) position 8 of track 1 (see Figure II.15) & (b) position 6 of track 2 (see Figure II.16), during the passage of an Intercity train at 200 km/h

The soil stress responses by sensors in SBG #1 depth (z=-1.80 m) of track 1 and track 2 under the same type of loading are presented in Figure II.29. The gauge installed in position 11 (see Figure II.15) shows a lower stress amplitude but a bigger 'M' shape (Figure II.29a) than the sensor in SBG #2 (Figure II.28c). As mentioned previously, for the pressure gauge in position 10 of track 1 (see Figure II.15), the soil pressure gauge in SBG #1 level, z=-1.8 m, of track 1 (Figure II.29a) may probably not have a good contact with the soil surrounding it. Figure II.29b shows the vertical stress amplitudes $\Delta\sigma_z$ at z=-1.8 m in SBG #1, track 2. The 'M' shape evolution is consistent with the depth, more pronounced in a position closer to the surface.

Consequently, it should be defined how stress amplitudes are calculated for further analysis in the study. When a train passes over the instrumented site, the stress sensors register the vertical stress ($\Delta\sigma_z$) from their average value at rest position (without train loading). Compression and extension stresses appear on signals for loadings from different axle loads. Compression amplitudes are measured from the positive stress peak originated by an axle to the mean rest position ($\Delta\sigma_z$=0 kPa), while extension stresses are originated in the middle of each coach (or locomotive) between two bogies. These extension amplitudes are measured from the peak originated in the middle of two bogies to the mean rest position. A scheme of how amplitudes in stress signals are defined is shown in Figure II.30. If several axle types are

present in a train (for example, locomotive and coaches), one value is registered for each axle load, and then the average of all the axles of a similar type. Normally, the standard deviation around the mean value of each axle load is lower than 5 %. Thus, the number of axles of each type will not be determinant on the average value.
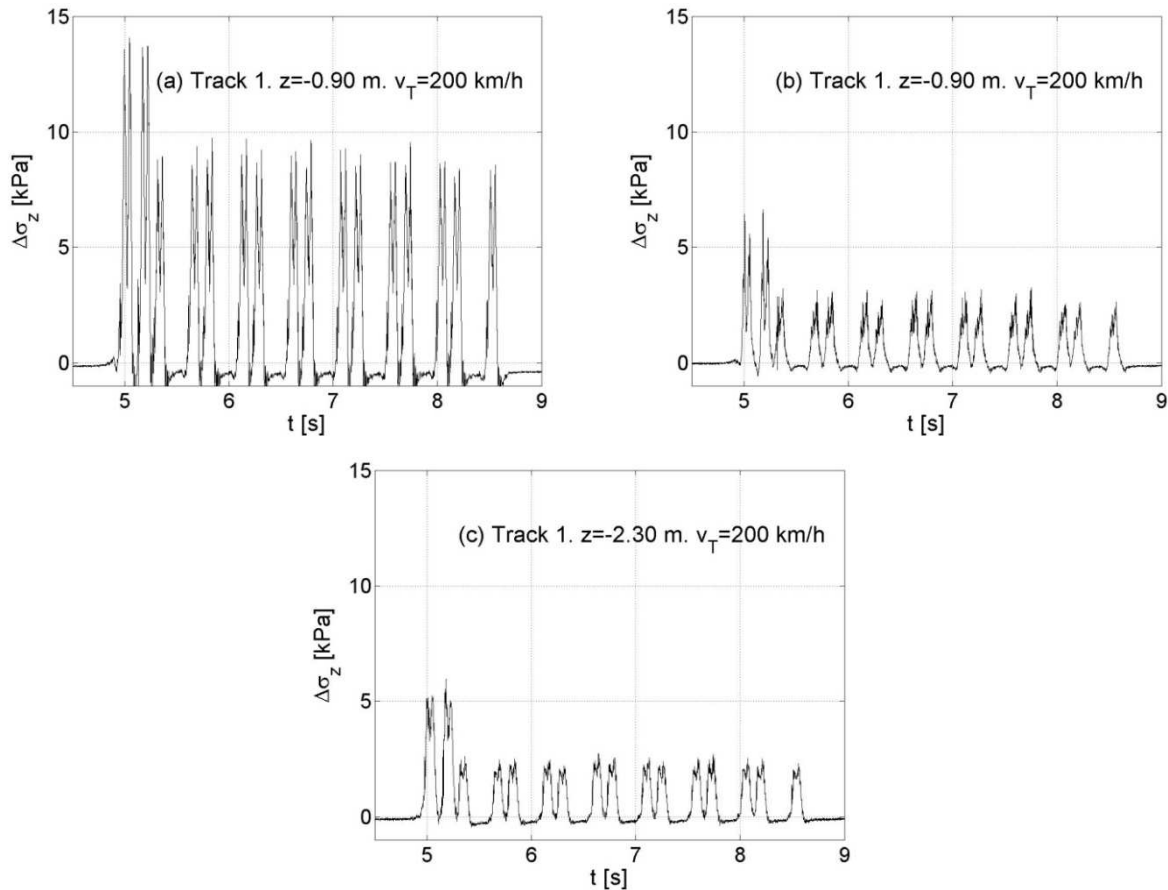
Figure II.28. Δσ_z measured by two different sensors installed in ITL at -0.90 m depth (a) & (b) and one sensor installed in SBG at z=-2.30 m depth (c) of track 1, positions 10 (a), 13 (b) & 12 (c) (see Figure II.15), during the passage of an Intercity train at 200 km/h
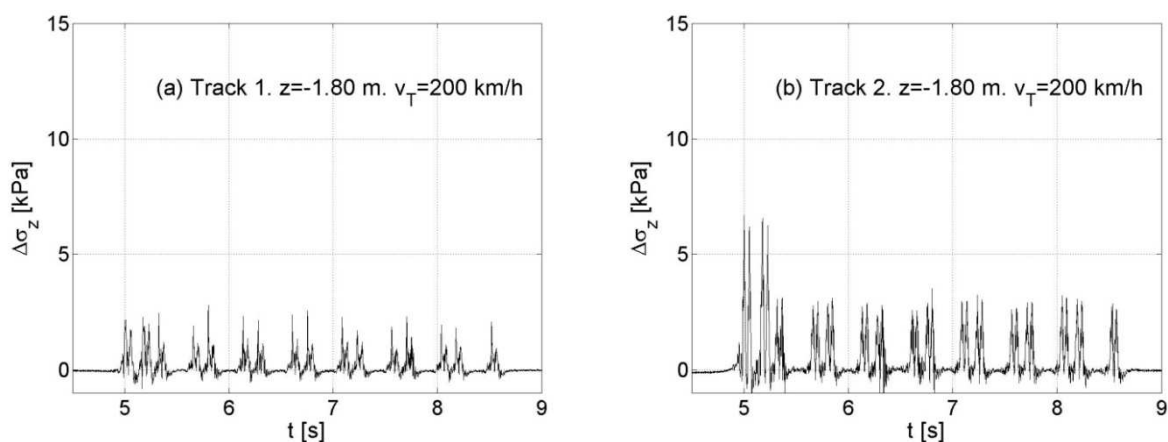
Figure II.29. Δσ_z in the SBG (-1.80 m) of track 1 (a), position 11 (see Figure II.15) and track 2 (b), position 4 (see Figure II.16), during the passage of an Intercity train at 200 km/h
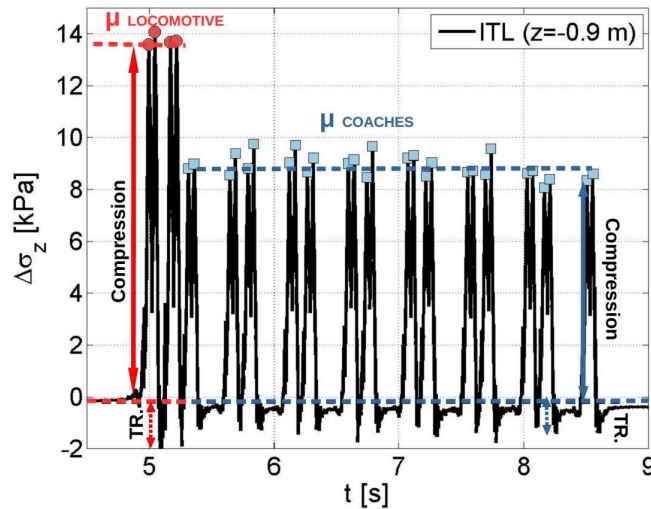
Figure II.30. Stress amplitude determination (compression and extension) from one vertical stress gauge during Intercity train passage at 200 km/h

From the measurements by the pore-water pressure gauges below the water table level (z=-1.20 m), it appears that no changes in pore pressure occurred during the train passages, for both tracks. In case of soft clays or peats, significant pore water pressure changes can be expected (Hendry et al. 2013).
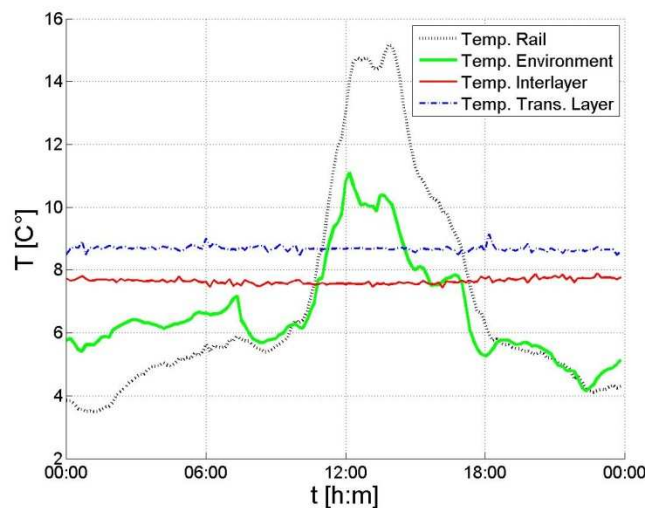
Figure II.31. Temperature evolution in four different track positions during a day

Finally, observing the records of temperature at the experimentation site (Figure II.31), it can be noted that there is no influence of the ambient or rail temperature on the track-bed temperature as presented also by (Cui et al., 2014) at another experimentation site. The ballast layer can be considered as an isolation layer for the substructure (Trinh et al. 2012).

115

Summarising, each sensor was selected depending on the working condition in the monitored zone: excitation frequencies, loading amplitudes, contact requirements between the sensor and the measured structure, installation process, size of the sensor and connection to the data logger. The effects of different axle loads (locomotive and coaches) were noticeable in the response of most installed sensors. Attenuation with depth was also visible with the records of the accelerometers, geophones and soil-pressure gauges. The dynamic amplification with speed was observed in the records of accelerometers, geophones, LVDT and soil pressure gauges, at the maximum speed on the line (200 km/h).

II.4.2 Analysis methods

II.4.2.1 Train speed estimation

The train speed is calculated using one strain gauge bridge signal glued to rail. This kind of signal is used because axles are very pronounced when the wheel is located just over the sensor. These peaks are easy to be defined in this type of signals, with an accuracy of 3 recorded positions at maximum (supposing a sampling frequency of $f_s=1200\ Hz$) in registered signals, for trains at 200 km/h. For the determination of train speed, the peak positions from the first two locomotive axles are identified (Figure II.32). As the sampling frequency is 1200 Hz and the distance between these two axles is 2.8 m, the train speed can be calculated using Equation (II.9).

$$v_T = \frac{(d_{axles} \cdot f_s)}{pos_{axles}}$$
(II.9)

where v_T is the train speed, d_{axles} is the axle distance (2.8 m), f_s is the sampling frequency ($f_s=1200\ Hz$ for all the measurements at 'Vierzon experimentation site') and pos_{axles} is the number of signal positions between the two considered axle peaks.

With the adopted method to determine the axle peaks, the train speed can be estimated with an accuracy of ±0.01 km/h.

116

$$v_T = \frac{(dist_{axles} \cdot f_s)}{(pos_{axle1} - pos_{axle2})}$$
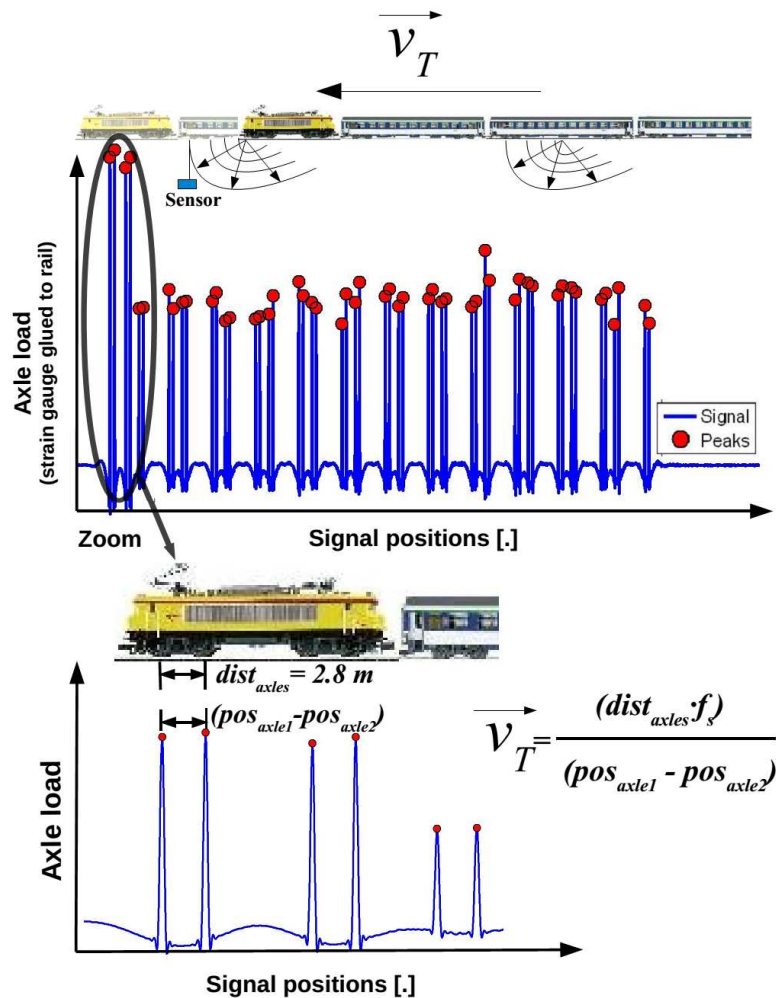
Figure II.32. Scheme of train speed calculation from strain gauge signals

II.4.2.2 Frequency range selection

Since low-frequency loadings are responsible for substructure material displacements (Lamas-Lopez, Alves Fernandes, et al. 2014) and concentrates most of the energy transmitted to the track (Figure II.33), a Butterworth low-pass filter with a cut-on frequency of 25 Hz can be used (for trains up to 200 km/h) in order to compare the amplitudes of different accelerometers at the same depth with similar energy content.
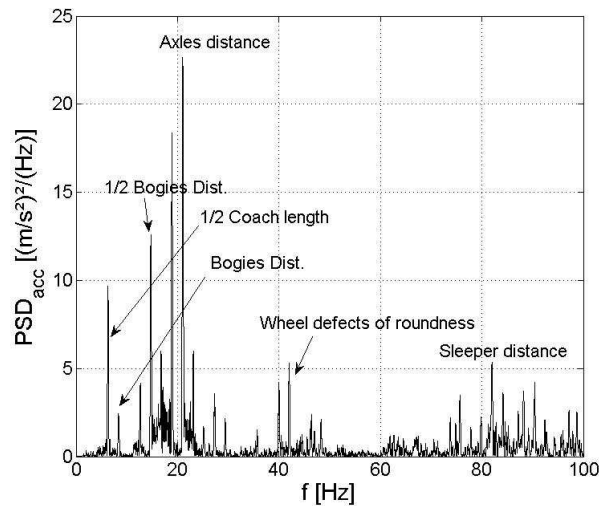
Figure II.33. Analysis of Power Spectrum Density (PSD) of an accelerometer at sleeper during a passage of an Intercity train at 200 km/h.

The filtered vertical acceleration signal, from accelerometers of type #1, at both sides of sleepers (positions 8 & 9, see Figure II.15) from track 1 are presented in Figure II.34. In the filtered signal, it is possible to note the difference between the axles from each bogie of the selected Intercity train (4 axles of locomotive and 28 axles of wagons). The signal amplitudes for both rails are quite similar, because the energetic content considered in the low range frequencies (1.5-25 Hz) is identical for the same train passage. However the small wavelengths that cause high frequency excitations induce more random energetic content in its range leading to amplitudes differences in previous raw signals. The differences between loads (locomotive and coach) are now identifiable. The acceleration amplitudes are equivalent for this frequency range in both signals. This put in evidence that a non-negligible part of acceleration signal amplitude was caused by short wavelengths. The high frequencies excited by the short wavelengths do not have necessarily the same energy content for both rails. But for the low frequencies, the energy content is similar for both rails. To compare the amplitude of accelerometer signals caused by identical loadings (same train), the amplitudes caused by short wavelengths related to rail defects and wheel roundness should be filtered. After this operation, the train axles become identifiable and the differences in loads (locomotive and coach) are noticed for these accelerometers.
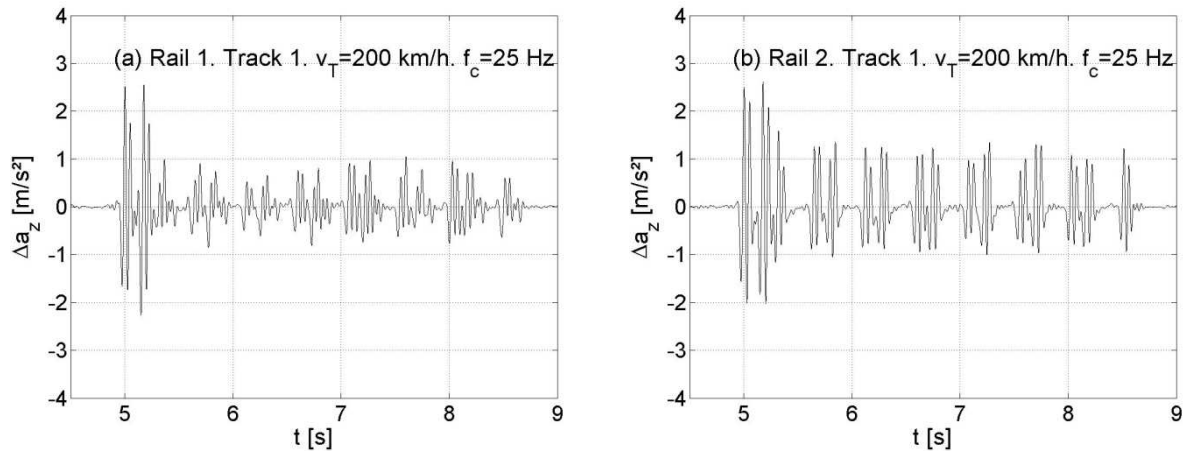
Figure II.34. Vertical accelerations at both sides of a sleeper of track 1, positions 8 (a),& 9 (b) (see Figure II.15), during the passage of an Intercity train at 200 km/h. Signals are filtered with a low-pass Butterworth filter with a cut-on frequency of 25 Hz.

Figure II.35 presents the vertical acceleration signals, for the accelerometers of type #2 installed at three different depths (positions 3, 5 & 7, see Figure II.15) of track 1 (ITL -0.9 m, TL -1.2 m, SBG -2.3 m) filtered with a low-pass Butterworth filter of 25 Hz. It appears that the differences of load per axle (locomotive and coach) are better noticeable on the filtered signal. Compared these filtered signals with the raw signal, the filtered signal show more clearly different acceleration amplitudes for different axle loads (regarding only the first 25 Hz). The decreasing amplitude also appears more evident in the filtered signal than in the raw signal.

For the Intercity train, most of the energy transmitted to the different accelerometers (installed at different depths) is included in the first 25 Hz. These low frequencies cover the loadings from wavelengths from coach length (λ=26 m), to axle distance (λ=3 m). The Power Spectrum Density (PSD) analysis of accelerometers at different depths is shown in Figure II.36. It can be appreciated that for an Intercity train, the excited frequencies are the same over depth but the energy amount decreases, especially after passing the ITL and TL. Therefore, this is also due to the energy absorption effect of the ITL soil. Figure II.37 shows the cumulated energy in a raw accelerometer signal if the cut-on frequency of the lower-pass filter is increased. Some low range frequencies as those excited by bogies or axles distance generate more energy to the track-system than others. More PSD energy is transmitted to the system by the long-wavelengths (inducing low frequencies).

119
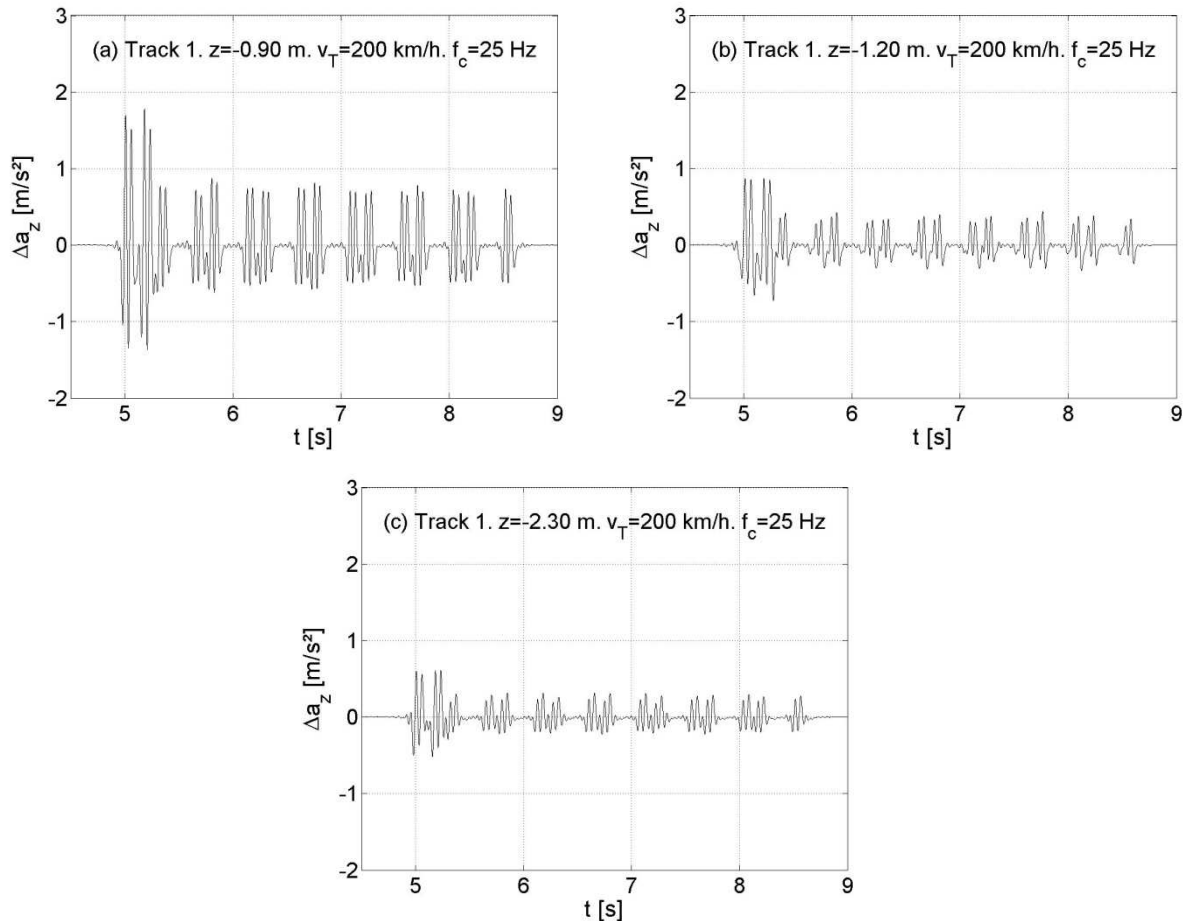
Figure II.35. Vertical accelerations at 3 different installation depths of track 1, positions 3 (a), 5 (b) & 7 (c) (see Figure II.15), during the passage of an Intercity train at 200 km/h. Signals are filtered with a low-pass Butterworth filter of 25 Hz.

The frequencies generating more energy to the system, for an Intercity train at 200 km/h, are those around 7 Hz which correspond to the bogie distance wavelengths (λ=6.3 m or λ=8 m), and those between 15 and 25 Hz corresponding to the wavelengths longer than the axle-distance (λ=2.8 m). The energy generated seems to be stabilized up to 50 Hz, where only other shorter wavelengths (corresponding to the wheel roundness defects or inter-sleeper distance) are involved.

As the energetic content is stabilized for the wavelengths shorter than the axle-distance (λ=2.8 m) (Figure II.37) accelerations in the range 0-25 Hz can be taken into account to be compared to other similar train passages. It is not possible to compare the amplitudes considering all the measured frequency range because the excitation caused by short wavelengths (as wheel or rail defects) is more random and depends on the wheel/rail interaction forces at each contact point for each train axle passage.
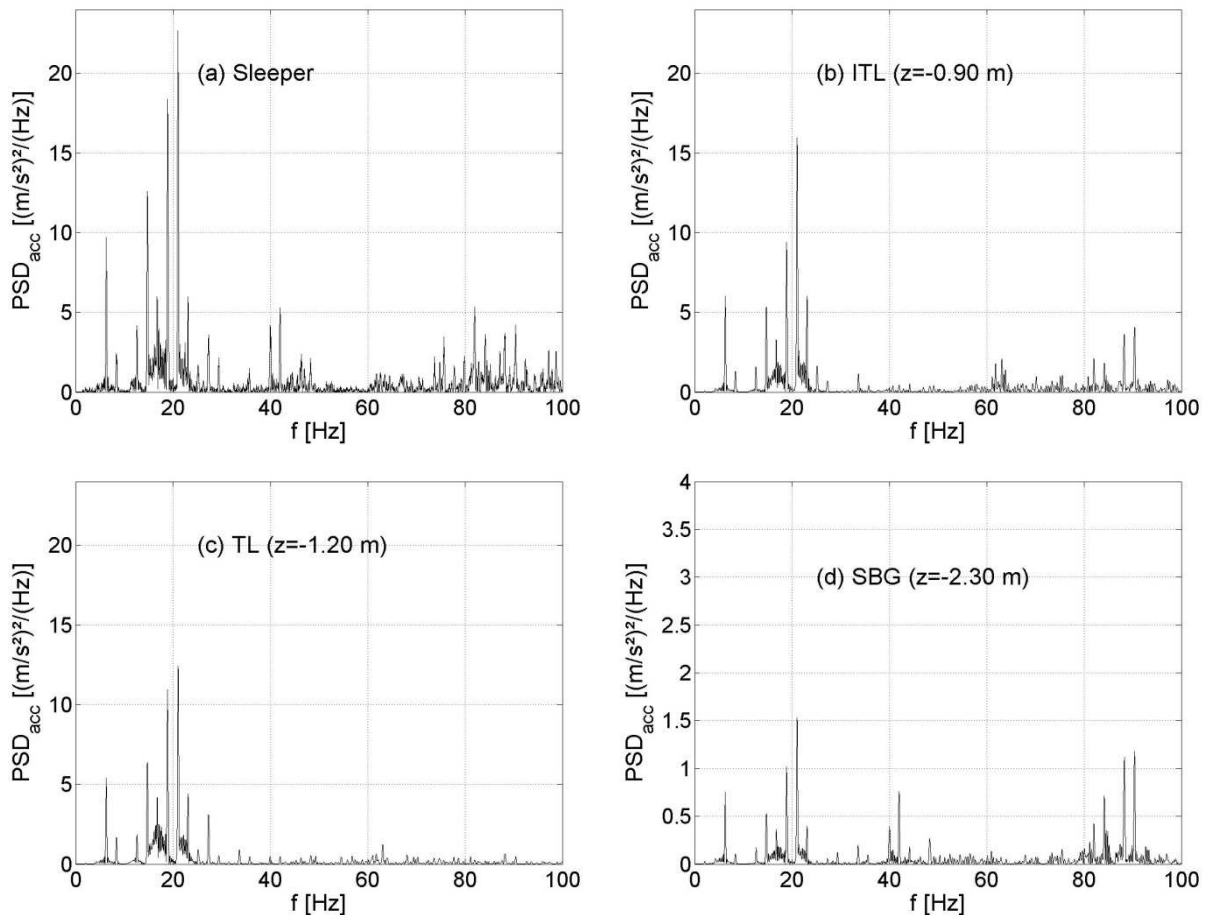
Figure II.36. Power Spectrum Density function for accelerometers at four different depths during Intercity train passage at 200 km/h
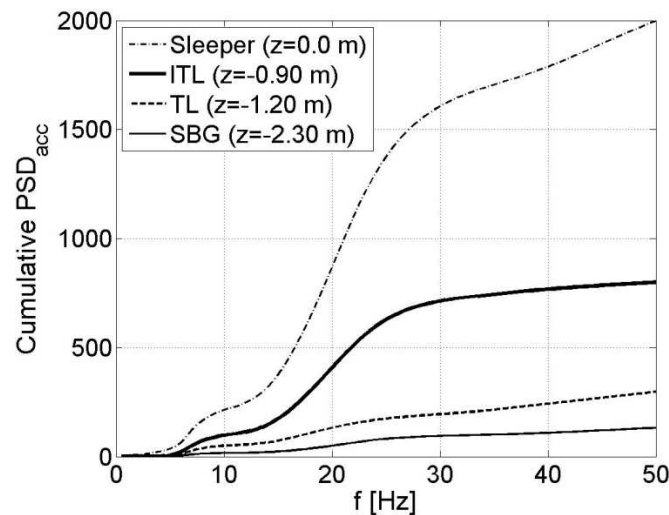
Figure II.37. Cumulative energy in PSD versus loading frequency (vertical acceleration). Measurements taken from accelerometers installed at different depths during the passage of an Intercity train running at 200 km/h

Therefore, to compare the axle's acceleration or velocity amplitudes, the signal amplitudes after filtered by a low-pass Butterworth filter of fifth order with a cut-on frequency of

f_c=25 Hz. Thereby, the measured amplitudes for all equivalent axles (same load) are energetically equivalent and comparable (and the only frequencies in the range of the tested speeds that cause displacements). In the analysis, the acceleration signal amplitudes are considered as the difference between each axle peak (positive acceleration if accelerometer is vertically oriented upwards) and the main rest position (Δa_z= 0 m/s²). As for the stress signals, one value is registered per axle type for each train passage which is the average of the measured amplitudes of the same axle type. Moreover, in velocity signals the amplitudes were measured following the same method as for accelerations. In addition, for velocity signals there is a lower impact of the applied filter because most of the excitation is due to low frequency range (not affected by small wavelength excitations).
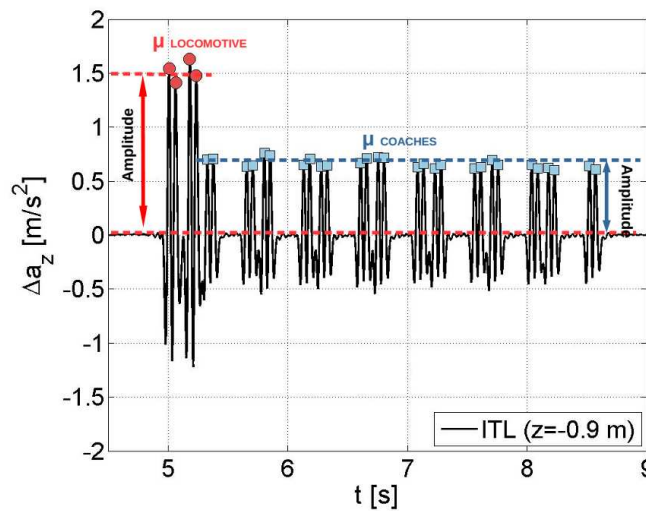
Figure II.38. Acceleration amplitude determination from one vertical stress signal during Intercity train passage at 200 km/h

II.4.2.3 Signal integration

II.4.2.3.1 Integration method

The integration of signals from accelerometer and geophones is made in order to obtain the mean displacement amplitudes caused by each train axle type. Therefore, it is possible to estimate the vertical displacements or strains of different track-bed layers based using the signals registered at different depths of track. A comparison between the displacement amplitudes obtained from the records of accelerometers, geophones and measured directly by LVDT on sleepers is developed in this section. Thus, this study enables the assessment of the

integration method for displacement determination using records of accelerometers and geophones under railway load excitation.

The scheme of the integration method is presented in Figure II.39. According to Figure II.39, to obtain displacements, raw accelerometers signals are filtered and integrated twice, while geophone signals are filtered and integrated only once.
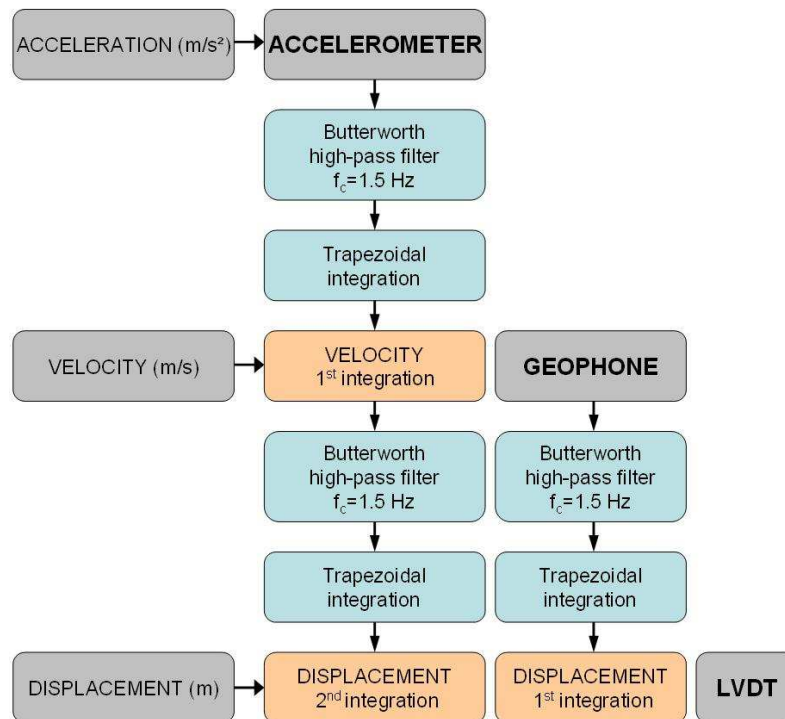
Figure II.39. Scheme of the integration procedure of the signals from accelerometers and geophones to estimate displacements

One high-pass filter is applied prior to each integration, in order to avoid the baseline effect on the integration result (Boore and Bommer 2005; Boore 2001, 2003; Boore et al. 2002; Yang et al. 2006). Then, a low cut-on frequency of 1.5 Hz is performed, allowing eliminating the very low frequencies that are not measured with accuracy by accelerometers and geophones. If these frequencies, lower than 1 Hz, are integrated, a baseline effect appears due to the sensors themselves. This high-pass cut-on frequency was chosen for two reasons. The first one is that almost all the Intercity trains run on the site at a speed faster than 80 km/h. The half coach wavelength is the lowest frequency of the four most energetic peaks caused by train loadings (Figure II.33). In order to obtain a valid displacement amplitude this frequency may not be filtered, for this train speed (f= 1.68 Hz). The second reason is that using cut-on frequencies lower than 1.5 Hz (high-pass Butterworth filter of fifth order,

Figure II.40), the integrated signals from accelerometers started to present a baseline defect and displacement signal shapes are no longer consistent with the axles & bogies loadings. All the signal amplitudes originated from frequencies lower than 1 Hz (close to the natural frequency of sensors) might be totally filtered (filter magnitude close to 0 at 1 Hz) in order to avoid the baseline defects after integration (Figure II.40).

A Butterworth filter was used in this study, because it is easier to be defined compared to the elliptical or Chebyshev one. Only two parameters are needed to define a Butterworth filter: cut-on frequency and filter order. By contrast, 5 parameters are needed with the elliptical filter. Moreover, unlike the elliptical filter that eliminates some amplitude variations, the Butterworth filter takes 100% of the amplitude of the original signal after the cut-on frequency (Cui et al., 2014). The Butterworth filter also allows a gradual transition of the amplitude of signal at frequencies around the cut-on frequency (for high-pass filter, Figure II.40) without modifying the signal amplitudes. On the contrary, the elliptical filter sharply eliminates the signal at nearly the cut-on frequency. The order in Butterworth filter determines the filter 'slope' after the cut-on frequency. The bigger the order, the higher the filter 'slope' at the cut-on frequency. The filters used in this study have an order 5, which is high enough to avoid very low frequencies (lower than 1 Hz) with a cut-on frequency of 1.5 Hz.

Once the filter parameters were obtained, the filter was applied in both directions from the beginning to the end of the signal and backwards to remove the phase distortion (Kornylo and Jain 1974). After filtering, a trapezoidal integration was performed. The boundary conditions for the signal integrations were velocity and displacement that were set to zero at the beginning and at the end of the signal. The integration of a discrete signal can be addressed by considering the trapezoidal rule as shown in Equation (II.10) and Equation (II.11) (Zuada-Coelho 2011).

$$v(n) = v(n-1) + \frac{\Delta t}{2} \cdot [a(n) + a(n-1)]$$

(II.10)

$$d(n) = d(n-1) + \frac{\Delta t}{2} \cdot [v(n) + v(n-1)]$$

(II.11)

where $v(n)$ and $d(n)$ are the first integration (velocity) and second integration (displacement) of the discrete acceleration signal $a(n)$, respectively.

124
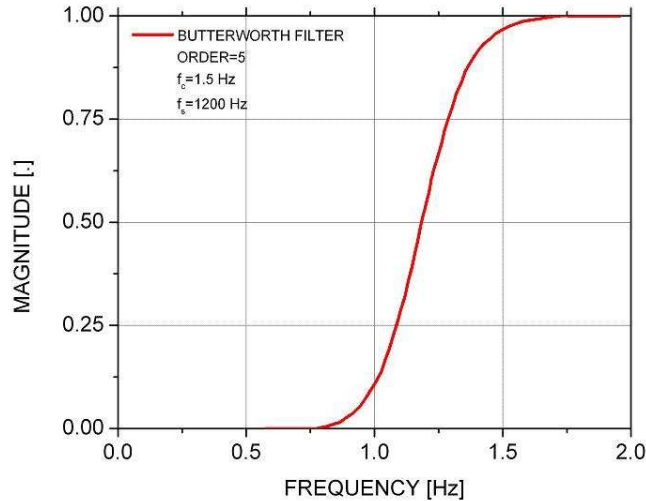
Figure II.40. High-Pass Butterworth filter of fifth order (f_c=1.5 Hz, f_s=1200 Hz)

As previously performed with accelerations, Figure II.41 shows the amount of cumulative PSD energy developed by each frequency following the presented method in Figure II.39. Figure II.41 presents that most of the displacement energy is developed in the low-frequency range (0-25 Hz). For frequencies exciting smaller wavelengths than the distance between axles (about f=21 Hz considering λ=2.8 m for trains at v_T=200 km/h) the estimated displacement signal is stabilized.
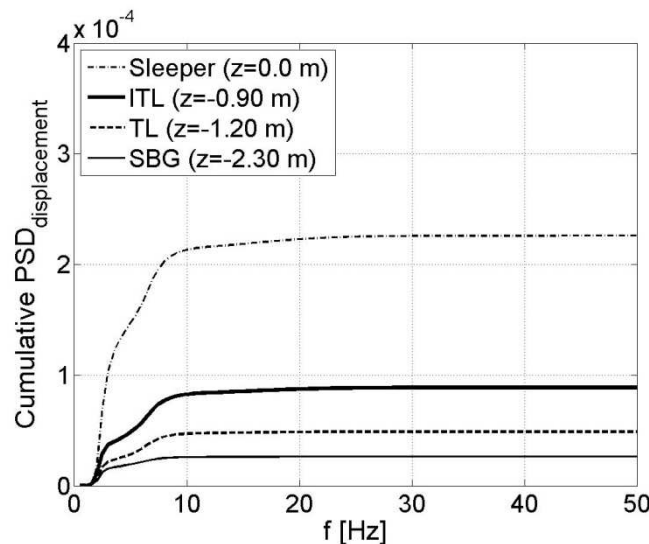
Figure II.41. Cumulative energy in PSD versus loading frequency (vertical displacements). Measures taken from accelerometers installed at different depths during the passage of an Intercity train running at 200 km/h

The accelerometer, geophone and LVDT signals were recorded during the passage of an Intercity train, as described in section 2 (locomotive + 7 coaches), running at 200 km/h.

Comparison of the obtained displacements in time-domain signals at the three considered positions (Sleeper, ITL & TL) in Figure II.42 shows that on surface and in ITL and TL the displacement amplitudes are the same for LVDT and the embedded geophones and accelerometers. Therefore, reliable data could be obtained using these three different sensors at every track position. On sleeper (Figure II.42a), the amplitudes are double (0.8 mm for locomotives and 0.5 mm for coaches) compared to the amplitudes at the ITL (0.4 mm for locomotives and 0.3 mm for coaches) or four times larger compared to the TL (0.2 mm for locomotives and 0.1 mm for coaches). The LVDT signals follow the same trend as the displacement signal obtained by double-integrating the accelerometer signals.
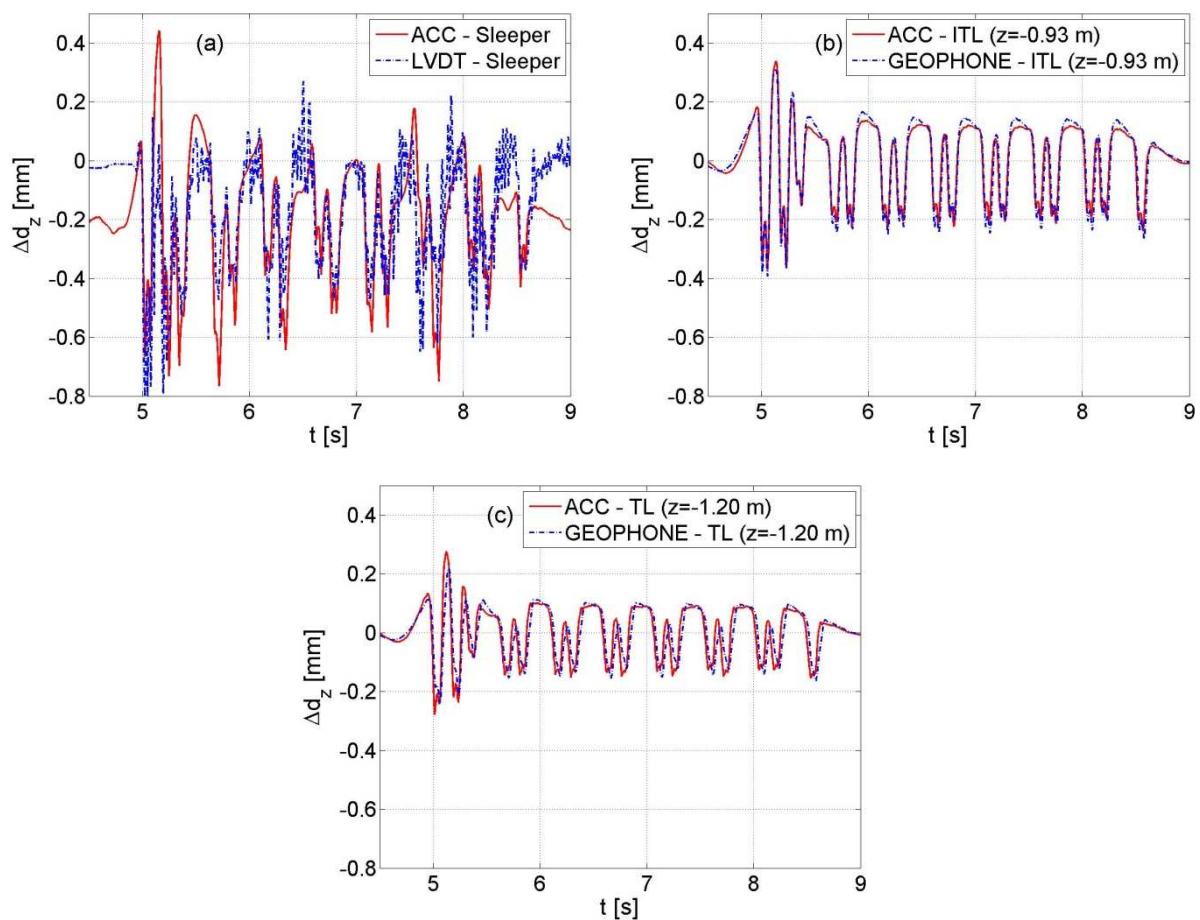
Figure II.42. Comparison between the estimated displacements using the records of different sensors (LVDT, Geophone and Accelerometer) during an Intercity train passage at the three considered depths: (a) Sleeper, (b) Interlayer (ITL, z= -0.93 m) and (c) Transition Layer (TL, z= -1.20 m)

Displacements amplitudes from integrated signals should be defined. Due to the boundary conditions, the deflections at both directions (upwards and downwards, positive and negative respectively) around the mean rest position (Δd_z=0 mm) appear in the integrated signal.

Negative deflections, just under the axle load, develop in the downward direction. Nevertheless, even if the amplitudes agree with the direct displacement measurements by LVDT, it is not possible to determine the amount of real upward displacement from these integrated signals due to the integration boundary conditions. Since the extension stresses are lower than 8% of the total stress amplitude (Figure II.30), most displacements seem to develop in downward direction. The measured value for each axle load is the total displacement amplitude. This amplitude is calculated from peak-to-peak as defined in literature (Bowness et al. 2007; Le Pen et al. 2014; Priest and Powrie 2009; Priest et al. 2010). This peak-to-peak amplitude goes from the axle-peak displacement to the nearest middle coach deflection value (Figure II.43). An average value for each axle type is calculated, indicating a standard deviation lower than 5% around the mean value for one train passage.
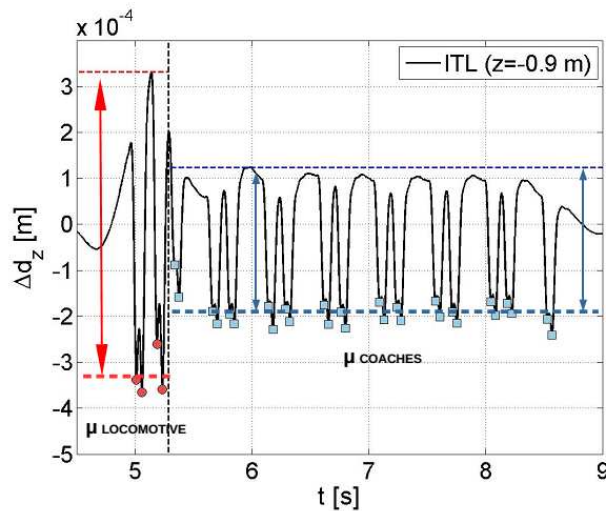
Figure II.43. Displacement amplitudes determination from a displacement signal during the Intercity train passage at 200 km/h

II.4.2.3.2 Displacement vs frequency

Following the method presented in section 2, an additional low-pass Butterworth filter was applied to the signal before being integrated, translating the cut-on frequency from 1.5 Hz to 100 Hz. This implies that it is possible to analyse the influence of each excited frequency on the total displacement. Thereby, it is possible to estimate certain amplitudes from the total displacement signal. Note that each frequency excitation f corresponds to a wavelength λ of the railway system at a given train speed v (Auersch 1994) as shown in Equation (II.12):

$$f = \frac{v_T}{\lambda} \tag{II.12}$$

For instance, if the axles-distance in a locomotive is $\lambda = 2.8$ m, and the locomotive is running at $v_T = 200$ km/h, the excited frequency $f = 19.8$ Hz. Figure II.44a presents the displacement amplitudes on track surface (sleepers) under the axle load exerted by locomotive and coach axles, obtained at each cut-on frequency applying different low-pass filters (adding 0.5 Hz to the cut-on frequency each time) while the cut-on frequency of the high-pass filter is always $f_c=1.5$ Hz. Then, the same analysis is conducted to perform a pass-band filter from 1.5 Hz to the cut-on frequency of the low-pass filter and measure the displacement amplitude. Two accelerometers installed on a sleeper are tested in Figure II.44. The two accelerometers are installed at both sides of the same sleeper. Figure II.44b is a zoom of the first 25 Hz where most displacement amplitudes are developed (and most of the energy is added to the system in the low frequency range (Figure II.37). Three frequency lines corresponding to the main wavelength excitations are also presented in the figure: the half coach distance ($\lambda =13.2$ m), the bogies distance ($\lambda =6.3$ m) and the axles distance ($\lambda =2.8$ m). It appears that the estimated displacement amplitudes for both accelerometers are similar for all the considered frequencies, suggesting that the measurements at similar positions have a good repeatability. For different axle loads (locomotive and coach), it is possible to identify different displacement amplitudes. It appears that about 98 % of the total displacement is caused by the first 25 Hz of excitation, i.e. by wavelengths longer than the axle-distance. Beyond 25 Hz, the displacement amplitude tends to stabilize, as the energy amount in the low frequency range.
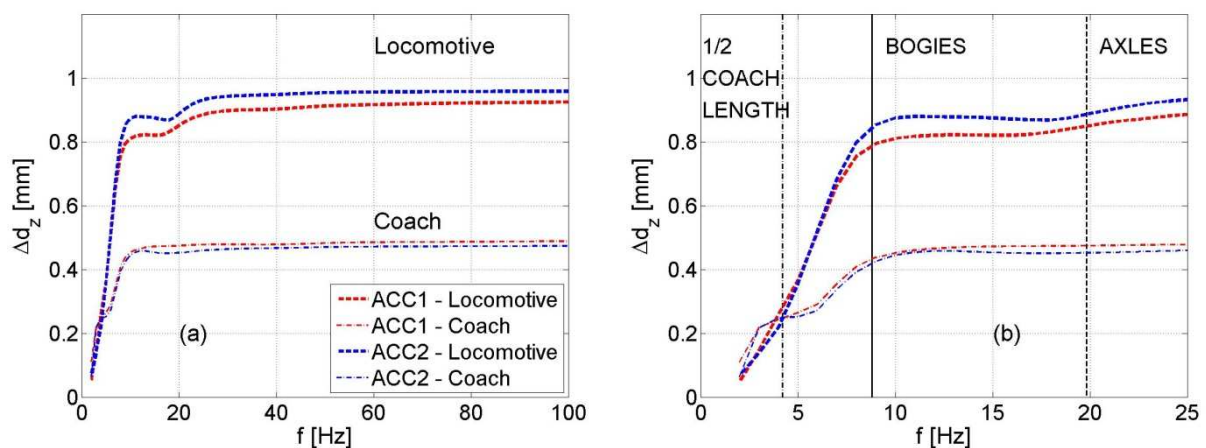
Figure II.44. Comparison between the displacement amplitudes estimated from accelerometers installed at the left side (ACC1) and the right side (ACC2) of a sleeper during the passage of an Intercity train at 200 km/h. (a) 0 to 100 Hz range (b) Zoom on the first 25 Hz

In order to compare the LVDT's displacement response with the double-integrated accelerometer signals, a deflection amplitude analysis is presented in Figure II.45. A reasonable agreement is found between the LVDT measurements and the estimations from the accelerometers records with frequency. The major differences in amplitudes are identified in locomotive axles of track 1 (0.10 mm, being the difference 9%). However, lower differences between LVDT and accelerometers are found for the other cases.
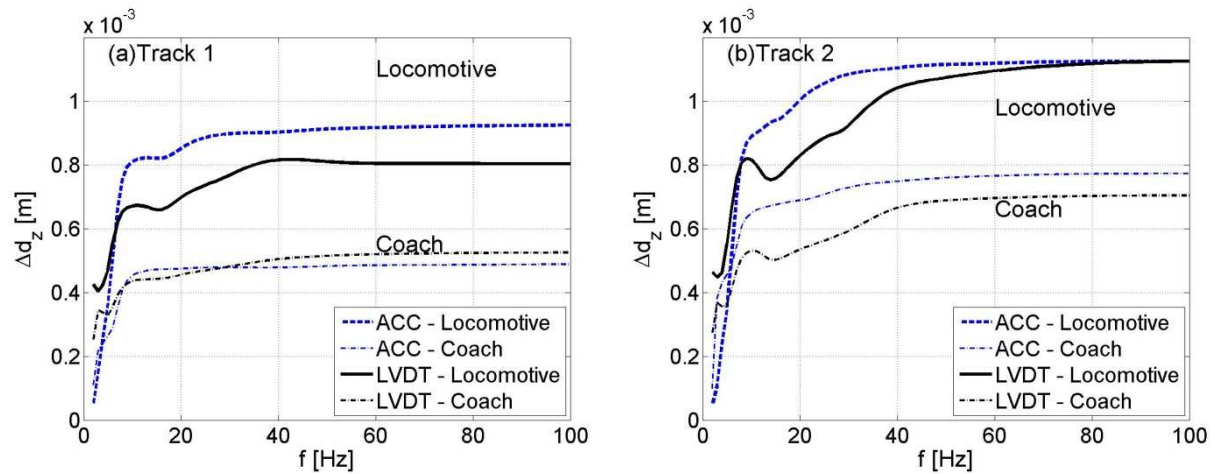
Figure II.45. Comparison of mean displacement amplitude for Locomotive and Coach axle load at each excited frequency measured by LVDT and integrating accelerometers at sleepers of (a) track 1 and (b) track 2 during the passage of Intercity train at 200 km/h

In conclusion, both on-surface sensors (LVDT and accelerometers) allow the displacement amplitude estimation with an accuracy of 0.01 mm.

Figure II.46a and Figure II.46b present the estimated displacement amplitude based on the signals of embedded accelerometers with the cut-on frequencies (low-pass filter) going from 1.5 to 100 Hz every one hertz, at ITL and TL respectively. As for Figure II.44 the high-pass filter cut-on frequency is constant (f_c=1.5 Hz). The corresponding zooms for the first 25 Hz are presented in Figure II.46c and Figure II.46d, respectively. As for Figure II.44b, three frequency lines corresponding to the main wavelength excitations are indicated. Similar displacement amplitudes are obtained from geophone and accelerometer estimations after integrations, for both axle loads (Figure II.46).
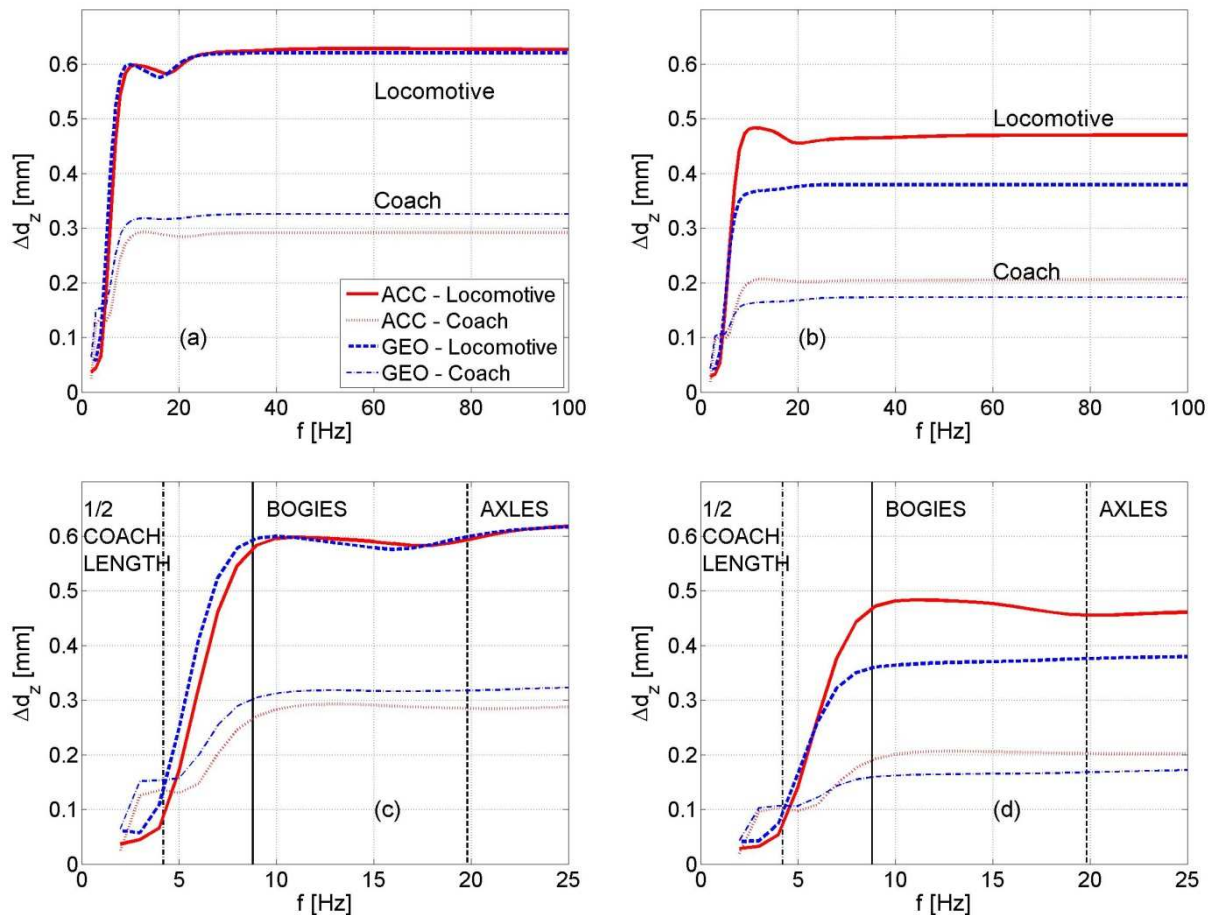
Figure II.46. Comparison between the displacement amplitudes estimated from the records of geophones and accelerometers for an Intercity train running at 200 km/h. Two depths are considered: (a) Interlayer (ITL, -0.93 m) and (b) Transition Layer (Tl, -1.20 m). (c) and (d) Zooms

In ITL, there is an average difference of less than 0.02 mm of total displacement amplitude (6.5% of displacement amplitude) between geophone and accelerometer for the first 25 Hz. For the TL, there is a 0.09 mm difference (18% of displacement amplitude) for the locomotive, and a difference of 0.02 mm is found (10% of displacement amplitude) for the coach. In addition, their amplitude contributions are similar for both sensors and depths. About 98 % of the total displacement amplitude is caused by the first 25 Hz for trains up to 200 km/h. Table II.7 shows the percentage of the total displacement amplitude obtained at each of the four frequencies highlighted. Note that the total displacement amplitude is considered as the amplitude obtained when no low-pass filter is applied to the signals. For the Intercity train considered, running at 200 km/h, more than 85% of the displacement is caused by the frequencies excited by wavelengths longer than the bogie-distance (6.3 m). Moreover, about 10% of the displacement amplitude is caused by the wavelengths included in the range between the axle-distance and the bogie-distance.

130

Table II.7. Percentage of displacement amplitude for different cut-on frequencies when an Intercity train ran at 200 km/h. Each considered cut-on frequency corresponds to a wavelength from the elements of railway loading.

			% of total displacement amplitude			
			½ Coach Length (4.2 Hz)	Bogies (8.8 Hz)	Axles (19.8 Hz)	at 25 Hz
SLEEPER	ACC/ Left	Loco.	30.27 %	85.08 %	91.89 %	96.22 %
		Coach	50.73 %	88.36 %	97.16 %	97.57 %
	ACC/ Right	Loco.	25.68 %	88.02 %	92.29 %	97.40 %
		Coach	52.54 %	88.20 %	95.51 %	97.07 %
EMBEDDED	ACC/ ITL (z=-0.93 m)	Loco.	13.88 %	91.87 %	94.61 %	98.56 %
		Coach	45.89 %	90.75 %	97.95 %	92.29 %
	GEO/ ITL (z=-0.93 m)	Loco.	22.06 %	95.33 %	96.46 %	99.36 %
		Coach	47.24 %	98.16 %	97.85 %	99.08 %
	ACC/ TL (z=-1.20 m)	Loco.	15.09 %	98.19 %	96.92 %	97.77 %
		Coach	49.51 %	92.23 %	98.30 %	106.80 %
	GEO/ TL (z=-1.20 m)	Loco.	24.21 %	94.74 %	98.95 %	99.80 %
		Coach	60.69 %	91.43 %	96.13 %	98.29 %

II.4.2.3.3   Conclusions

Based on the data obtained with accelerometers, geophones and LVDT, the integration method for displacement determination was assessed. It seems that the integration method is suitable for estimating the displacement amplitudes of railway track-bed materials under train loadings. In addition, more than 95% of the displacement amplitude was caused by the excitation of the wavelengths longer than the axle-distance (~2.8 m), indicating that most displacement was due to the first 25 Hz frequency for a train at 200 km/h. Also, the estimated displacements are similar for the three different sensors: accelerometers, geophones and

LVDT, validating the adopted integration method. In addition, there is a good repeatability of the estimated displacements using the records of different sensors installed at equivalent positions (for instance, the different accelerometers installed on the same sleeper). The validity range of the presented integration method using these sensors was tested for trains running up to 200 km/h and loads in the range between 10.5 to 22.5 Mg/axle. Nevertheless, for trains running slower than 80 km/h one of the most energetic frequencies, the half-coach length, could be filtered by the high-pass Butterworth filter. Consequently the displacement amplitudes may be underestimated.

II.4.2.4 Signal translation

To facilitate the comparison of different signals, it is necessary to translate the signals to simulate the scenario where all sensors were installed in the same vertical borehole. For this purpose, the sensor signals were moved horizontally to a reference point indicated in Figure II.15 and Figure II.16. As the distance between sensors was known (Figure II.15 and Figure II.16), to accurately translate the signals the train speed had to be calculated based on the sensor signals. A scheme of how the translation was performed knowing the horizontal distances between the sensors is presented in Figure II.47.
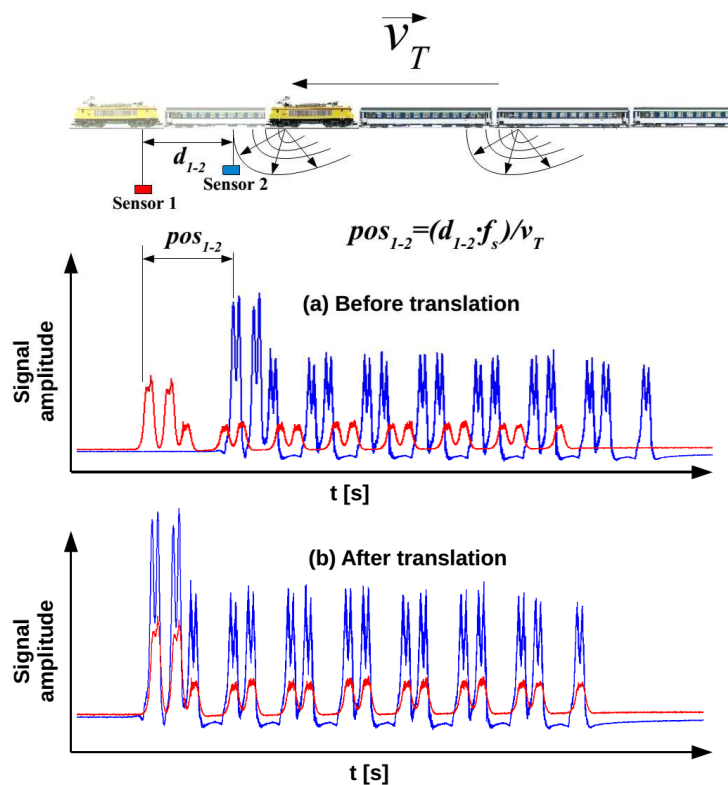
Figure II.47. Scheme of sensor signal translation

The number of signal positions between the two measurements *pos*_{*axles*} to be translated between the two considered axle peaks is calculated using Eq. 9. The main hypothesis for this operation is that when the peak-axle is recorded in a sensor signal, the train axle is supposed to be just over the sensor in that moment. As the primary (compressive) wave velocity (about v_p= 1000 m/s for ITL soil) is much faster than the shear wave velocity, the time for a load (axle) to be transmitted from the surface to a sensor can be calculated using Equation (II.13):

$$t = \frac{z_{inst}}{v_p} \tag{II.13}$$

being z_{inst} the installation depth of the sensor, v_p the average primary wave velocity of the considered track profile and t the time for the excitation to arrive to the sensor. For instance, when the installation depth is 2 m and an average v_p is 1000 m/s, the time for the load to arrive to the sensor is 0.002 s. As the sampling frequency results in $\Delta t=\pm0.0008$ s between signal positions, this hypothesis have an insignificant influence on the results supposing vertically installed sensors after the translation operation (arrival time is about 2 signal positions, shorter if sensor is installed close to the load source). Consequently, for a train running at the maximum speed on the site (200 km/h), 2 signal positions at the chosen sampling frequency represent an error of 90 mm, smaller than the borehole diameter (ϕ=110 mm). Obviously, this error can be much smaller if the two sensors considered in the calculation are vertically closer to each other, for instance, when the vertical strains were calculated based on the displacements estimated from two neighbouring accelerometers.

II.4.2.5 Strain estimation

The strain amplitude estimation is important to define which level of deformation every layer in a track-bed undergoes under different loadings. As the sensor signals are virtually in the same vertical position, using the deflection signals at different levels of the same borehole, the vertical strains can be estimated. The vertical distance between the accelerometer in ITL and the sensor in TL is 0.3 m, and 1.10 m between TL and SBG sensors. The average vertical strain, assuming constant strains between the monitored depths, of a track-bed section can be estimated using Equation (II.14):

$$\Delta\varepsilon_z = \frac{(u_2 - u_1)}{d_{vert}} \cdot 100 \qquad\qquad (II.14)$$

where u_2 is the displacement signal from the shallower accelerometer, u_1 is the displacement signal from the deeper accelerometer and d_{vert} is the vertical distance between both sensors. An example of vertical strain estimation at the ITL (-0.90 / -1.20 m) during the passage of an Intercity train running at 200 km/ is shown in Figure II.48. The different axle-peaks are easily identifiable in the signal, and the strain amplitudes for heavier loads (i.e. locomotive axles) is larger than the vertical strain amplitude developed by lighter loads (i.e. coach loads).

In order to define the strain amplitudes from the signal, the same method used for displacement signals (Figure II.43) is applied to calculate the total strain amplitudes per axle when the strain signals are estimated using displacements at different depths (Figure II.48). Then, average vertical strain amplitude is calculated for each axle type in the signal. Thus, it is not possible to define the amount of compression or extension strains caused by a train axle. Nevertheless, most of the strain amplitudes are compression strains according to the stress signal analysis for the same train type.
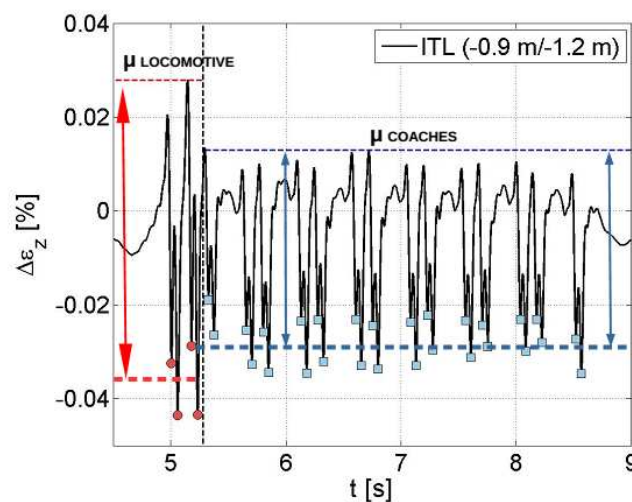
Figure II.48. Vertical strain amplitudes determination from a strain signal estimated at the ITL in the ITL (-0.90 m / -1.20 m) during the Intercity train passage at 200 km/h

II.4.2.6 Hysteresis loops

Using the strain and stress signals, the hysteresis loop of a material between two accelerometers can be estimated. The hysteresis loops give valuable information about the evolution of certain mechanical parameters such as the resilient modulus and damping ratio. Further, the effect of changing the load conditions on the mechanical behaviour of a track-bed material can be evaluated.

Since it is not possible to evaluate the part of strain signal corresponding to the extension stress, all the hysteresis loops are considered as being caused by compression loads. This is performed by a translation of the loop to positive stresses (upwards in Y-axis) and considering all the strain amplitudes as positive. Note that this translation does not affect the size and shape of the hysteresis loop.

II.4.2.6.1 Resilient modulus

The resilient modulus (M_r) is the elastic modulus of a material under a given cyclic axle load. The average resilient modulus can be estimated for every material comprised between two accelerometers or geophones embedded in track. Figure II.49 presents a stress-strain loop in the interlayer (-0.90 m / -1.20 m) caused by the four locomotive axles of an Intercity train running at 200 km/h. The M_r is calculated as the secant modulus of the hysteresis loop, corresponding to the slope of the line connecting the origin point to the peak (Araujo 2010; Suiker et al. 2005; Trinh 2011), as follows Equation (II.15):

$$M_r = \frac{\Delta\sigma_z}{\Delta\varepsilon_z} \qquad\qquad (II.15)$$
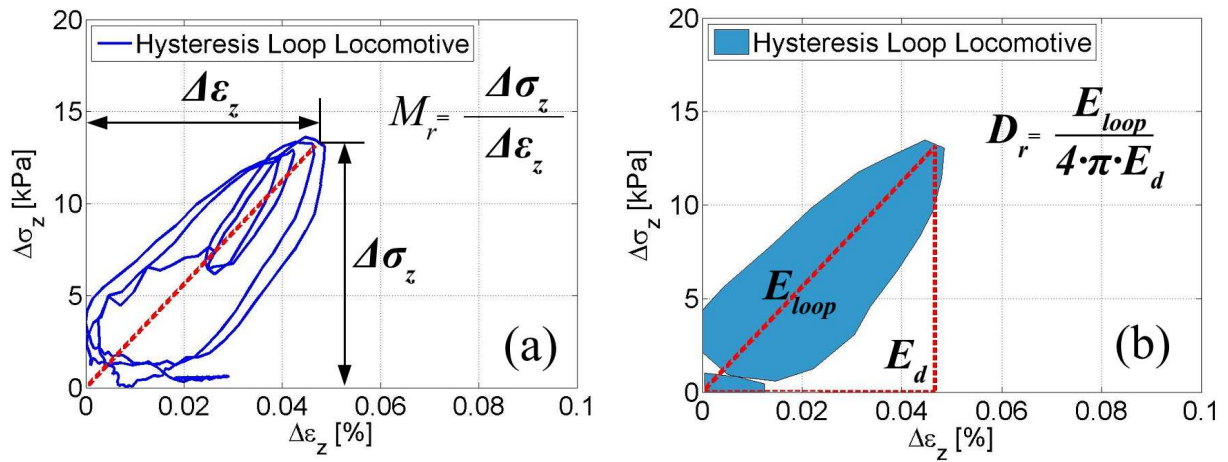
Figure II.49. Scheme of resilient modulus (a) and damping ratio (b) estimations using stress-strain hysteresis loops

II.4.2.6.2 Damping ratio

The damping ratio, D_r, represents the ratio between the energy dissipated by the soil, and the equivalent elastic energy transmitted to the soil. It could be estimated from the hysteresis loops (Al-Shaer et al. 2008; Karl 2005; Meng 2003; Di Prisco and Zambelli 2003), as follows Equation (II.16):

$$D_r = \frac{E_{loop}}{4 \cdot \pi \cdot E_d} \tag{II.16}$$

The dissipated energy (E_{loop}), mainly developed by soil deformation and grain friction, corresponds to the loop inner surface (Figure II.49).

The equivalent elastic energy (E_d), is defined by the surface of the triangle formed by the maximum deviator stress amplitude point of a hysteresis cycle, the value of the maximum strain at the maximum deviator stress and the origin point Equation (II.17):

$$E_d = \left(\frac{\max(\Delta\sigma) \cdot \max(\Delta\varepsilon_z)}{2} \right) \tag{II.17}$$

II.5   TEST CAMPAIGN

After the site selection, the geotechnical prospection, the sensor installation and verification using commercial trains, a test campaign was conducted at the site. The main goal of this campaign was to assess the train speed impact and the axle load effect on the mechanical behaviour of conventional track-bed soils. A test train was employed, running at six different speeds (from 60 km/h to 200 km/h).

II.5.1 Test train characteristics

The selected train for the test campaign was an Intercity train composed of a BB22000 Locomotive and 7 Corail coaches. This train was chosen for several reasons: it is a train able to travel at speeds up to 200 km/h; it is the most frequent train in the site; its geometrical and technical specifications are well known. The intercity train has two different axle types (Locomotive and Coach) with a locomotive axle load that is more or less double of the coach axle load. In addition, the axle loads are relatively homogenous for all trains. The total length of the train is 205 m. The geometrical specifications and axle loads for every axle type of the test train are shown in Figure II.50. The locomotive BB22399 length is 17.48 m with an inter-bogie distance of 9.7 m and an inter-axle distance of 2.8 m. The total mass of the locomotive is 90 tons supported by four axles, a force of about 225 kN/axle. Each 'Corail' coach is 26.4 m long. The distance of a pair of bogies for one coach is 18.4 m, and 8 m between the bogies of the adjacent coaches. As for the locomotive, the inter-axle distance is 2.8 m. The total mass of a coach is 42 tons supported by four axles and consequently the average force per axle is about 105 kN/axle.
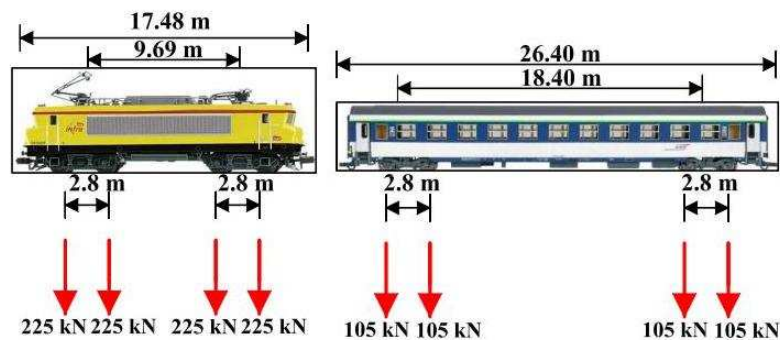
Figure II.50. Geometrical characteristics and axle loads of a BB22000 locomotive and a Corail coach

II.5.2 Test campaign

A total of 12 train passages were performed on the site during 4 days (Table II.8), mostly on track 1 which is more richly instrumented with 33 of the 42 dynamic sensors. Comparison between the measurements in both directions of track 1 showed that similar trend and evolution of the sensors' responses were obtained, but the amplitudes were 50% lower. This could be caused by the different orientation of rail corrugation inducing a large energy of short wavelength excitation.

Table II.8. Train speed, track and direction of every test train passage of the test campaign. (Blue: regular direction, Red: opposite direction)

		Track 1	Track 2
Day 1		200 km/h	
		160 km/h	
		60 km/h	
Day 2		180 km/h	
			100 km/h
		140 km/h	
		20 km/h	
Day 3		100 km/h	
		140 km/h	
		60 km/h	
		160 km/h	
Day 4			180 km/h

In this section, the test train passages travelling in its regular direction on track 1 are analysed, for six speeds: 60, 100, 140, 160, 180 and 200 km/h.

II.5.3 Vertical stresses

The first analysed variable was the vertical stress amplitude. The sensors in positions 12 & 13 (see Figure II.15) are evaluated. The sensor in position 13 was installed in ITL (-0.90 m) while the sensor in position 12 in SBG (-2.3 m). The average vertical stress amplitude for each train passage depends on the axle load, depth of measurement and train speed (Figure II.51). The results show that the axle load and depth are the most determinant parameters to assess the stress amplitude while the train speed effect is only visible in shallower layers as ITL. Figure II.52 presents the average vertical stress amplitude for different axle loads. It is supposed that the vertical stress amplitude developed under a 0 kN

load is 0 kPa, therefore all lines are linked to the origin point. There is a quasi-linear amplification with axle load for the monitored depths. The locomotive axles developed double amplitudes compared to coach axles, due to their axle weight. This linear amplification can be an indicator of the soil elastic behaviour at this site. The stress dynamic amplification is about 15% of the quasi-static amplitude (from 60 to 200 km/h). Indeed, a vertical stress amplitude increase of about 15% was registered with a train speed increase from 60 km/h to 200 km/h: from 12 kPa to 14 kPa under locomotive axles. This amplification seems coherent regarding the deflection amplifications presented in chapter 1 for a ballasted track (Alves Costa et al. 2015), taking into account a critical speed of v_{cr}=650 km/h and a constant dynamic amplification factor over depth. Regarding the extension stresses, they only appear for heavier axles (Locomotive) and the stress amplification with speed is the same for both monitored depths (ITL and SBG), even if their absolute amplitudes (from extension peaks to compression peaks) are taken into account. The extensions could be caused by the shear stress rotation effect of Principal Stresses Rotation (Grabe and Clayton 2009; Ishikawa et al. 2001; Powrie et al. 2007) when heavy loads run over the sensor.
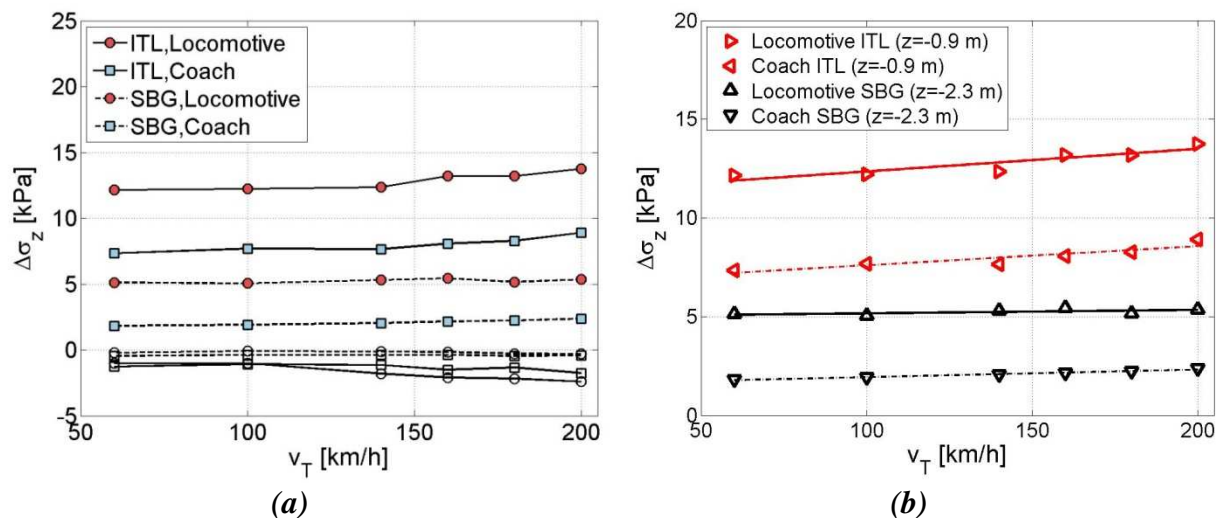
Figure II.51. (a) Average vertical compression (positive values – colour filled symbols) and extension (negative values – no filled symbols) stress amplitudes; (b) positive stress amplitudes trend versus train speed in ITL and SBG

If the vertical stress at 60 km/h is considered as quasi-static, the relative amplification of Locomotive and Coach axles in ITL are 15% and 20%, respectively (Figure II.53a and Figure II.53b). However, if the same analysis is performed on SBG measurements, the Locomotive amplification only reaches 5% (Figure II.53c) while the coach stresses, lower in

absolute amplitude, in SBG (Figure II.53d) are amplified up to 20%. Therefore, the low stress amplitudes are more amplified with train speed at deeper positions.
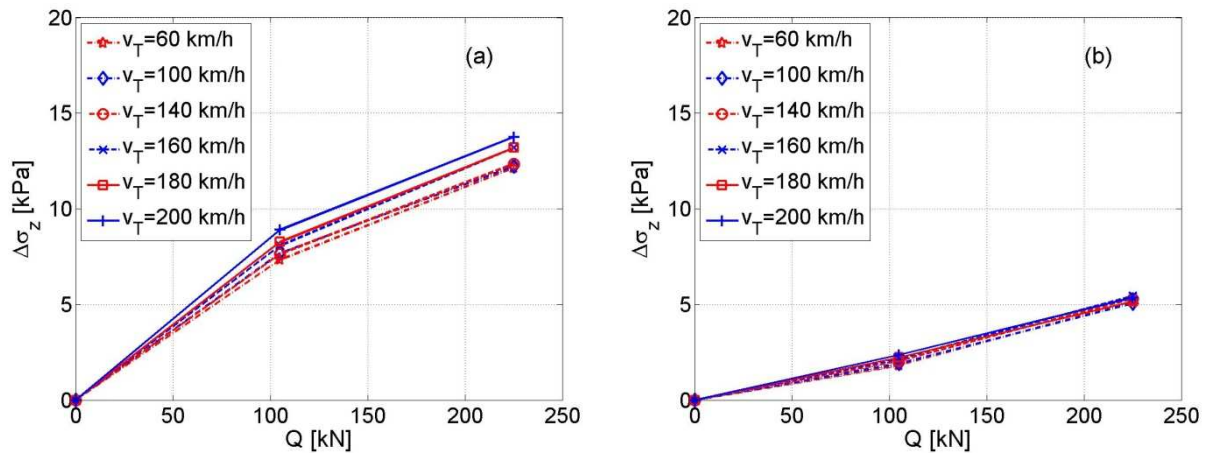
Figure II.52. Average maximum stress amplitude per axle versus axle load for six different train speeds in Vierzon experimentation site. (a) ITL (-0.90 m) and (b) SBG (-2.30 m)
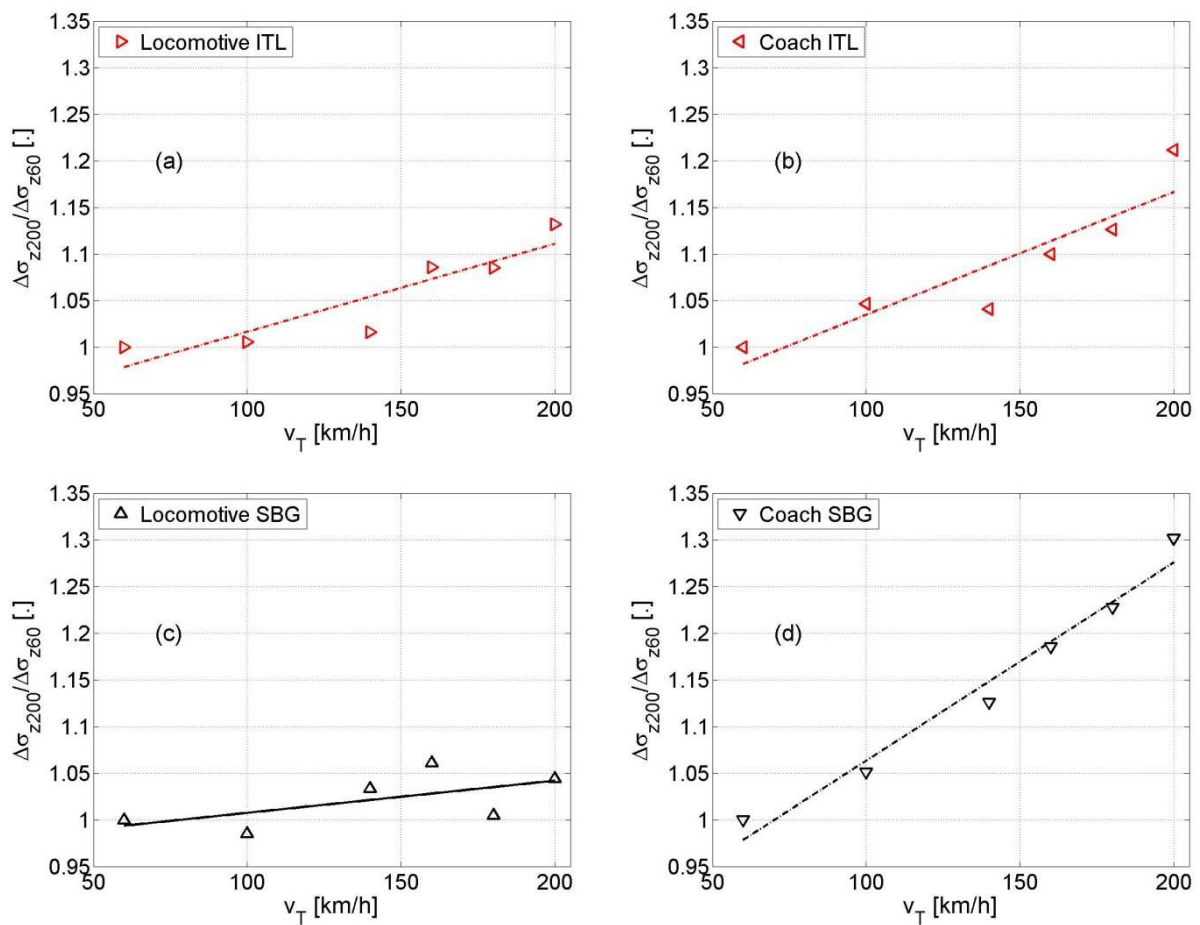
Figure II.53. Dynamic amplification of vertical soil compression stress.

Nevertheless, if a stress of about 100 kPa is considered just below the sleepers for ballasted tracks (Kempfert and Hu 1999), the decrease of stress amplitude in depth does not seem to be linear. This suggests that most energy generated by train axles is dissipated in ballast layer. However, increasing train speed induces an amplification of stresses in all the track-bed materials (mainly in deeper ones as SBG where reached stress amplitudes are smaller).

II.5.4 Particle acceleration

As exposed previously in Figure II.38, the acceleration amplitude is measured considering the signals filtered at f_c=25 Hz. As this study focuses on materials' deformation behaviour under train passages at different speeds, this range of frequency is appropriate.

Figure II.54 assess the train speed impact on the average maximum acceleration amplitude caused by each axle type in the three monitored depths (ITL, TL and SBG). The trend of acceleration amplitude for the considered frequency range (excited by long wavelengths) can be described by Equation (II.18):

$$\Delta a_z = a \cdot \left(1 - e^{b v_T}\right)$$

(II.18)

where Δa_z is the maximum vertical acceleration for a given train speed (v_T), and '*a*' and '*b*' two empirical parameters depending on the axle load and depth, respectively.

It may be appreciated from the results that the generated amplification for a given speed mainly depends on the axle load and monitoring depth. It can be also appreciated that there are a rapid decrease of acceleration amplitudes over depth, mainly through ITL soil. Therefore, the increase of acceleration amplitude is directly proportional to the axle load. The average acceleration amplitude between 60 km/h and 200 km/h is amplified up to 9 times for the locomotives axles in ITL. These acceleration amplitudes in ITL (z=-0.90 m) range from 0.2 m/s² to 1.8 m/s². Moreover, the acceleration amplitudes decrease linearly with lower axle loads (Figure II.55).
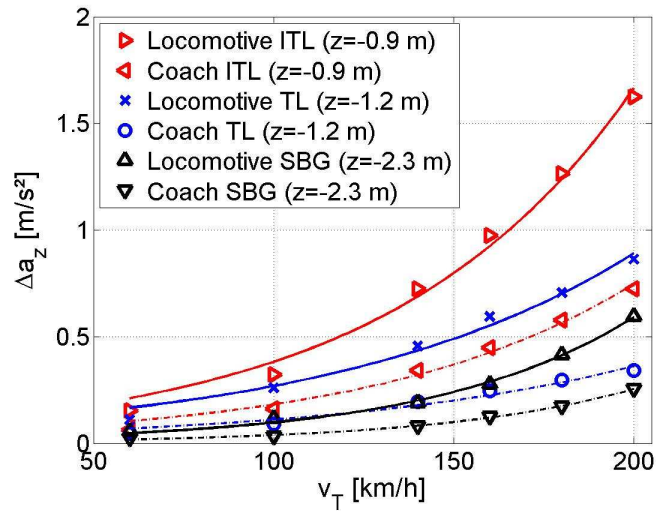
Figure II.54. Evolution of maximum acceleration signals for six different trains' speeds at three different depths

The effect of axle load on acceleration amplitudes is presented in Figure II.55. It is supposed that the vertical acceleration amplitude developed under a 0 kN load is 0 m/s², therefore the origin point is taken into account for lines determination. A linear amplification of acceleration with axle load for all the monitored depths is identified. The acceleration amplitude decrease with depth is notable comparing Figure II.55a and Figure II.55b. The train speed effect appears lower in deeper layers.
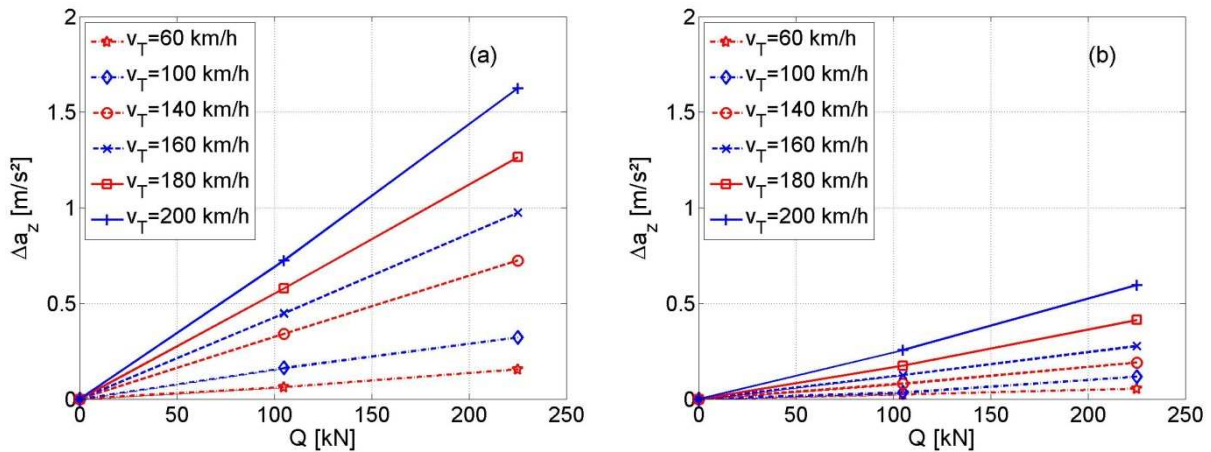
Figure II.55. Average acceleration amplitude per axle versus axle load for six different speeds. (a) ITL (-0.90 m) and (b) SBG (-2.30 m)

II.5.5 Particle velocity

As for the acceleration amplitude analysis, for the particle velocity the signals are also filtered with a low-pass filter f_c=25 Hz. The trend of average particle velocity with train speed is

linear in this case (Figure II.56). The train speed effect is more notorious in shallower layers as ITL. The axle load effect on velocity amplitudes is similar as for acceleration amplitudes. The trend of these amplitudes is also linear with axle load for all the tested speeds and depths (Figure II.57). The magnitude of particle velocity with locomotive axles in ITL (z=-0.90 m) ranges from 0.001 m/s (v_T=60 km/h) to 0.014 m/s (v_T=200 km/h).
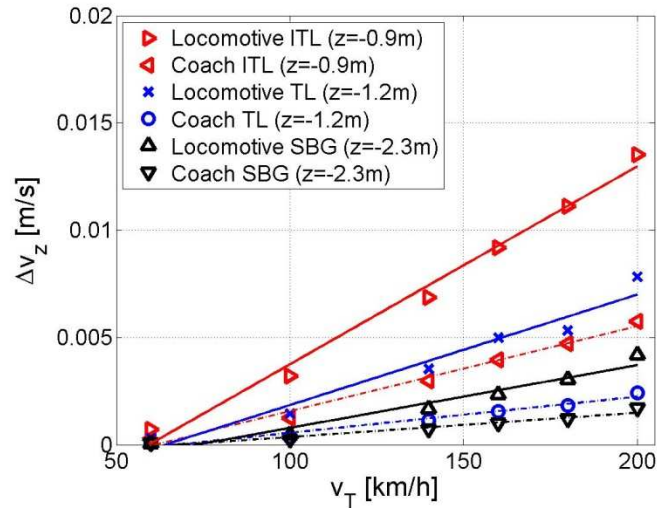
Figure II.56. Evolution of maximum particle velocity signals for six different speeds at three different depths
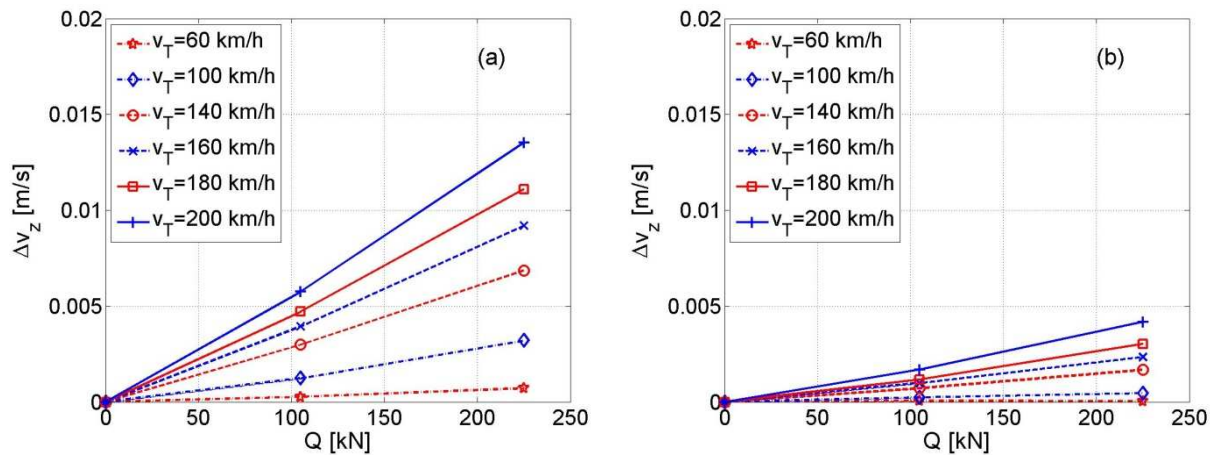
Figure II.57. Average velocity amplitude per axle versus axle load for six different speeds. (a) ITL (-0.90 m) and (b) SBG (-2.30 m)

II.5.6 Vertical displacement

As shown in Figure II.58, the mean displacement amplitudes follow a linear trend with the train speed. The increase in axle loads leads to quasi-static deflection increase even at considered quasi-static low speeds (v_T<100 km/h). Larger deflection amplifications were

found in shallower layers. The amplifications of different loads (locomotive and coaches) at the same depth follow the same trend. In the range of the tested speeds, this trend follows the relation shown in Equation (II.19):

$$\Delta d_z = a + v_T \cdot b \qquad\qquad (II.19)$$

being 'a' (quasi-static amplitude) and 'b' (speed amplification) parameters depending on the axle load and tested depth, respectively.

Note that the very low frequencies for slow trains ($v_T < 80$ km/h) could be erased by applying the high-pass Butterworth filter to avoid base-line effect after integrations. In this case (v_T=60 km/h), the half-length coach excited frequency is 1.8 Hz (one of the most energetic wavelengths, see Figure II.33) and it is partly filtered by the Butterworth high-pass filter. This speed is not taken into account in the estimation of trend lines from Figure II.58. An amplification of about 20% is found if results at v_T=60 km/h are not taken into account.
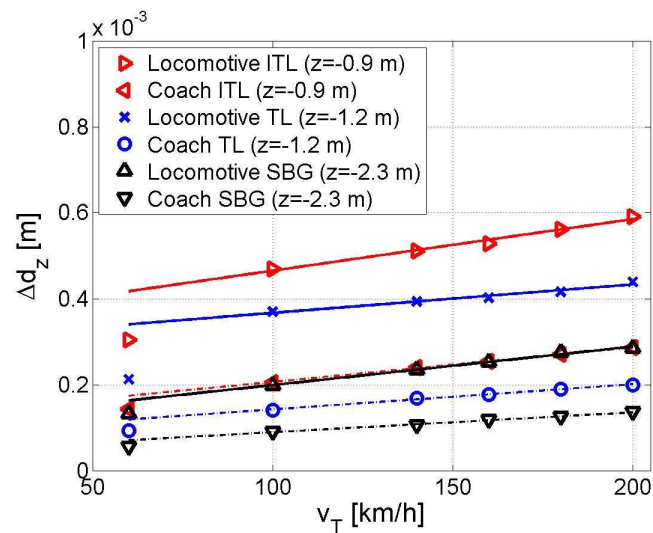
Figure II.58. Evolution of maximum particle displacement signals for six different train speeds at three different depths

The axle load effect can be more easily appreciated in Figure II.59. For 0 kN loads the deflections developed should be 0 m, thereby the origin point is considered to be linked to the different measured points. This figure shows a linear evolution of displacements with axle load for all the tested speed and monitored depths. A maximum deflection of 0.6 mm is found in ITL (z=-0.90 m) under the effect of the Locomotive axles (225 kN/axle). The deflections

caused by Locomotive axles decrease till 0.3 mm at SBG depth (z=-2.3 m). The amplification with speed seems to be of the same order of magnitude at both depths, but the quasi-static amplitudes are largely reduced for deeper layers. Note that the amplifications with speed depend on the mechanical characteristics of track-bed such as the shear wave velocity.
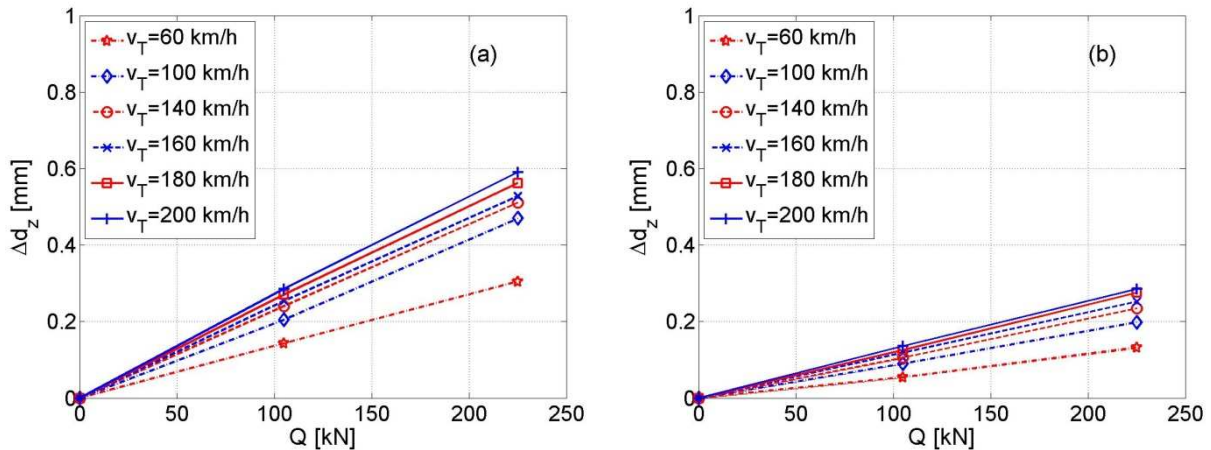

Figure II.59. Average displacement amplitude per axle versus axle load for six different speeds. (a) ITL (-0.90 m) and (b) SBG (-2.30 m)

II.5.7 Vertical strains

Based on the records of accelerometers in ITL, TL and SBG, the vertical strains of ITL and SBG can be estimated (see the procedure in II.4.2.5). The vertical strain amplitudes (Figure II.60) follow a similar trend as the vertical stresses (Figure II.51). The high-pass filter impact on long wavelengths (low frequencies) from low-speed trains (lower than v_T=80 km/h) is compensated when vertical strains from several accelerometers are calculated. Vertical strain amplitudes for low speed trains seem consistent with the other estimated values (Figure II.60). The relationship between the estimated amplitude of vertical strain and axle load is quasi-linear (Figure II.61), as for the measured stress amplitudes per axle (Figure II.52). The absence of load (0 kN) should lead to a strain amplitude under load of 0%, consequently the origin point is taken into account. Moreover, the strain amplification for loads heavier than 105 kN (Corail coaches) is attenuated in the ITL and it is totally linear in deeper layers as SBG (Figure II.61). The same phenomenon was found for the stresses (Figure II.52).

However, the vertical strain evolution with train speed has not the same order of magnitude as stress values amplification with train speed. In addition, it is supposed that stress and strain are not linearly related in the range of tested speeds (till 0.4 times the critical speed of v_{cr}=650

km/h) (Alves Costa et al. 2015). The vertical strain amplitudes in ITL (z=-0.90 m) ranges from 0.035% to 0.07% at 200 km/h. The value for the locomotive axles is reduced to 0.02% in SBG (z=-2.3 m). At the SBG depth, the amplification with train speed is also much lower (about 3 times lower) than in shallower layers.
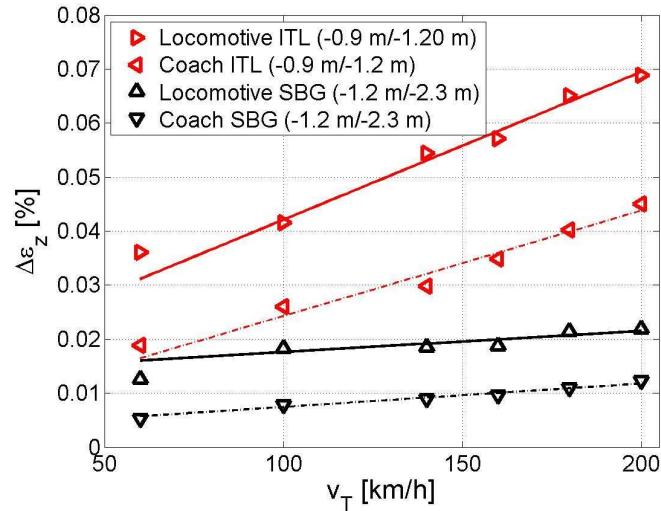
Figure II.60. Maximum strain amplitudes at interlayer (ITL; -0.9 m / -1.2 m) and subgrade (SBG; -1.2 m / -2.3 m) for six train speeds. Axle loads: locomotive: 22.5 Mg/axle and coach : 10.5 Mg/axle
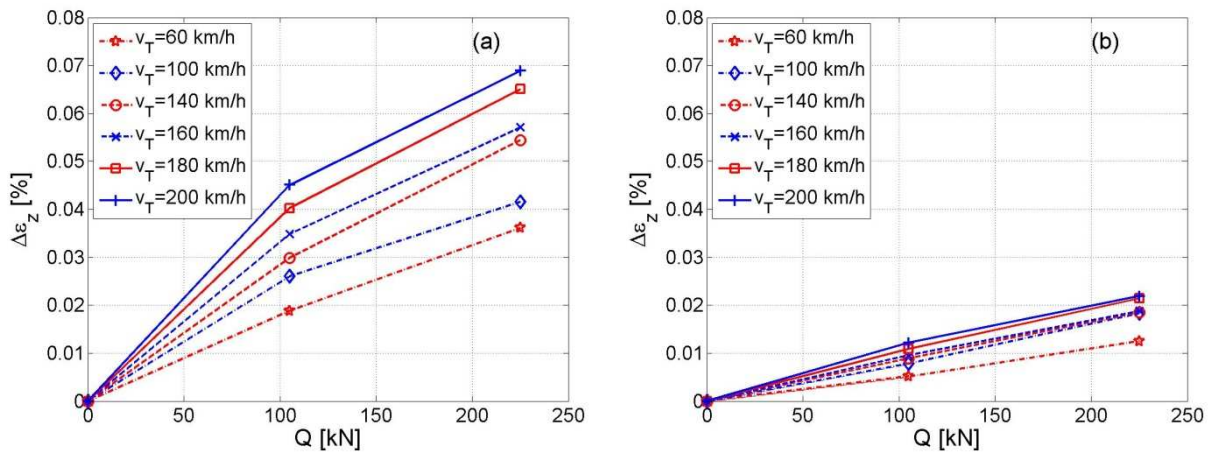
Figure II.61. Average vertical strain amplitude per axle versus axle load for six different speeds. (a) ITL (-0.90 m / -1.20 m) and (b) SBG (-1.20 m / -2.30 m)

II.5.8 Hysteresis loops

The stress-strain hysteresis loops of ITL (-0.90 / -1.20 m) and SBG (-1.20 m / -2.30 m) are analysed in this section to verify the train speed impact on their behaviours. These loops were

built from measurements as previously explained in II.4.2.6. For each site, once the horizontal distance between sensors is defined (allowing the virtual translation to a same virtual borehole, as explained in II.4.2.4), the relationship between strain and stress can be established. Even if some error could be induced in the definition of horizontal distances, the absolute values of modulus and damping ratio are not significantly affected. A variation of less than 1% is expected for the mechanical parameters with an error between -5 cm to +5 cm in the definition of sensors' horizontal distances. Note that the loop shape does not depend on translation.

Even if some extensions (with amplitudes of about 2 kPa) appeared after the passage of locomotive axles (in the Y-axis) and strains were distributed (in the X-axis) between negative and positive values, each loop for each axle type was translated without performing any modification of the shape to the positive part of X and Y axis. This translation was made in order to facilitate the calculation of resilient modulus and damping ratio. The vertical strain amplitude was not divided into negative and positive parts, because it was not possible to quantify the part of the strain signal corresponding to extensions.

Figure II.62 shows the evolution of the hysteresis loop for every speed in ITL (accelerometers installed at -0.90 m and -1.20 m). At a first glance, it seems that the loop surface increases with speed, showing that a higher energy is transferred to the system when speed is increased. The shape is well defined, and it is possible to distinguish the loading and the unloading section in the hysteresis loops, and even the loading and unloading sections between each pair of axles. The loops of SBG were also estimated (Figure II.63). The loops of SBG (accelerometers at z=-1.20 m and z=-2.30 m) are less clearly defined compared to those of ITL because the accelerometers are more spaced between them (1.1 m in SBG instead of 0.30 m in ITL). The smaller strain in deeper layers is also an important factor to be considered in the evaluation of the loop shape. The obtained strains in SBG are the half of those in ITL, which can partly explain the differences in the shape of loop for both layers.
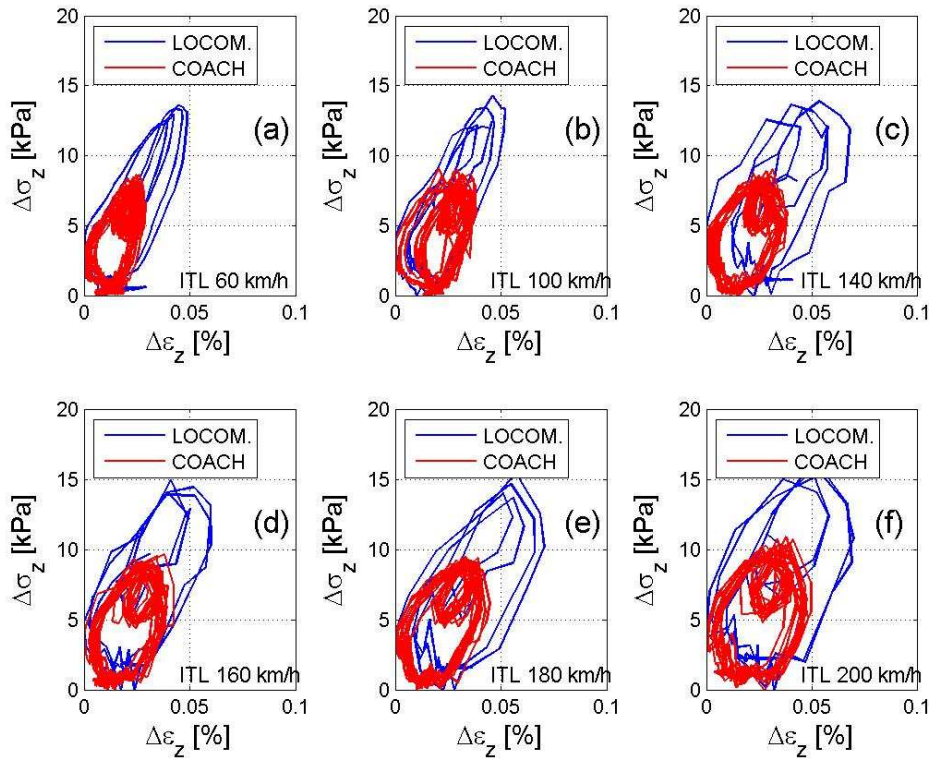
Figure II.62. Estimated stress-strain loops in ITL (-0.9 m / -1.2 m) for six different speeds:
(a) 60 km/h, (b) 100 km/h, (c) 140 km/h, (d) 160 km/h, (e) 180 km/h, (f) 200 km/h
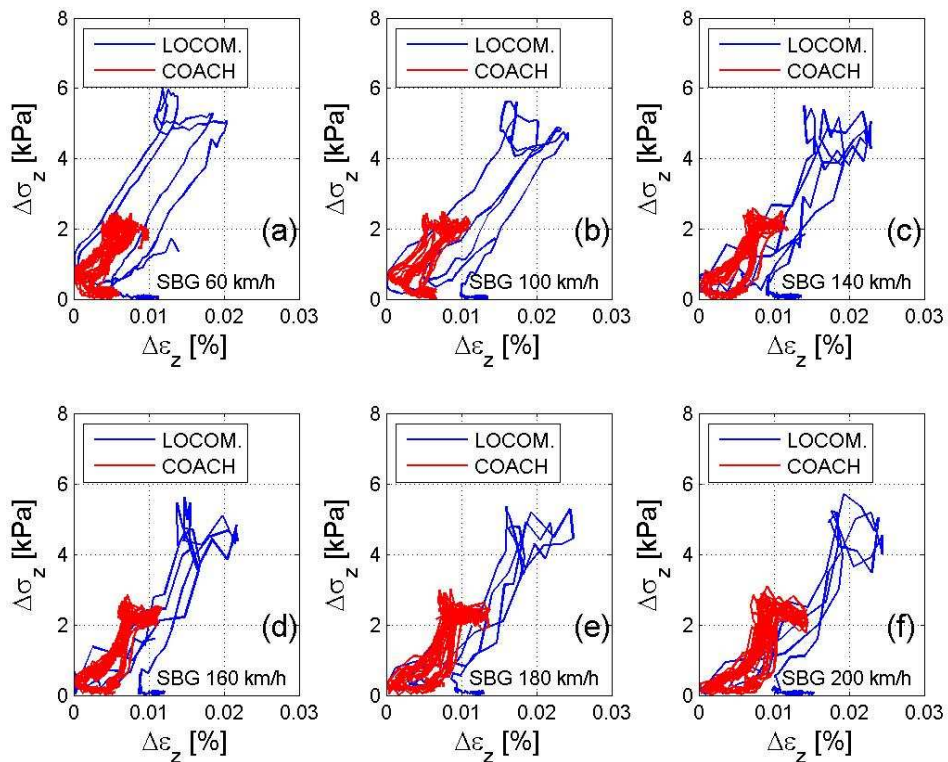
Figure II.63. Estimated stress-strain loops in SBG (-1.2 m/ -2.3 m) for six different speeds:
(a) 60 km/h, (b) 100 km/h, (c) 140 km/h, (d) 160 km/h, (e) 180 km/h, (f) 200 km/h

The analysis of hysteresis loop results are summarized in Figure II.64 for both depths (ITL and SBG) and axle loads (Locomotive and Coach). Figure II.64a and Figure II.64b present the resilient modulus evolution for six different train speeds at ITL and SBG depths while Figure II.64c and Figure II.64d shows the evolution of damping ratio with train speed in ITL and SBG, respectively. Note that analysis methods were explained in sections II.4.2.6.1 and II.4.2.6.2.
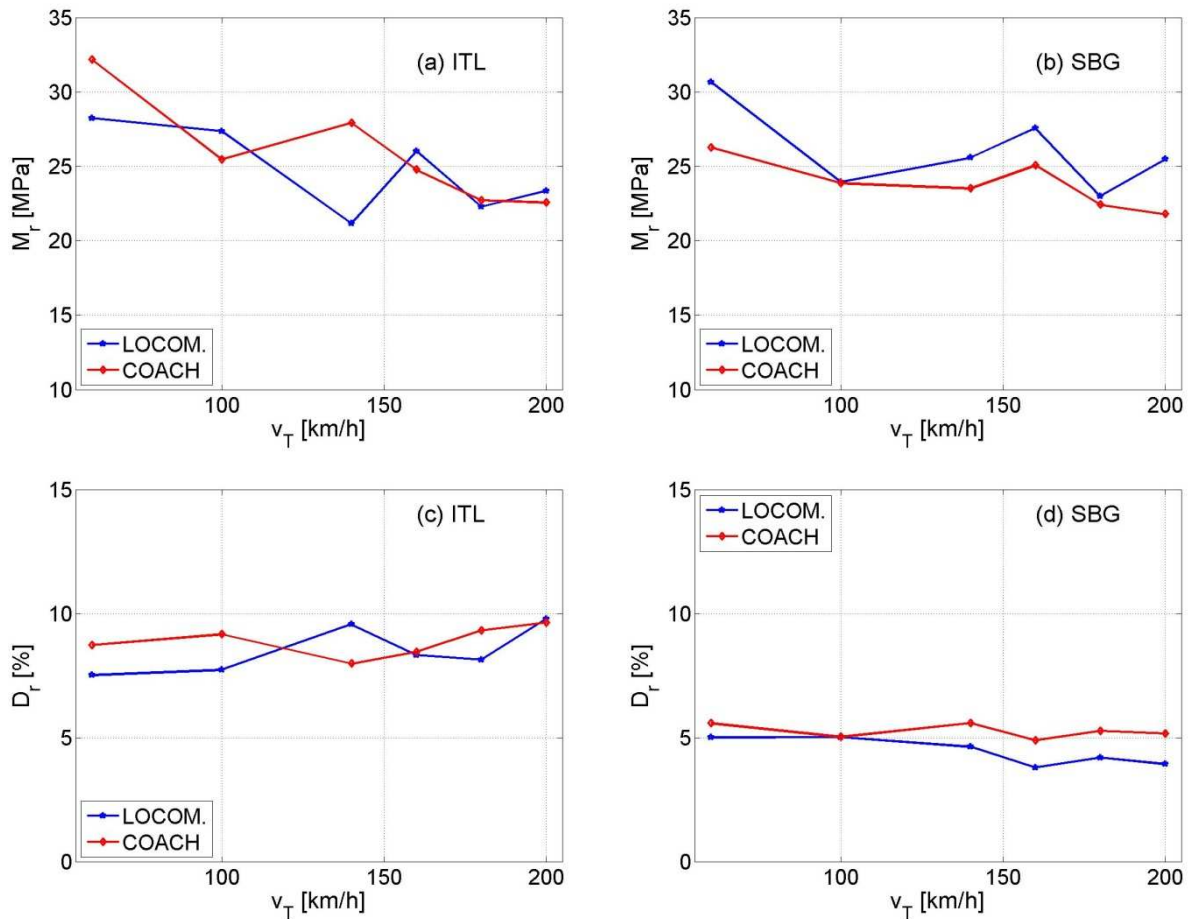
Figure II.64. Variations of resilient modulus (M_r) and damping ratio (D_r) with train speed for ITL soil (a,c) and SBG soil (b,d)

The resilient modulus (M_r) results show that for both axle loads the obtained results are of the same order of magnitude (given that M_r is a soil parameter non-dependant on loading amplitude). This fact justifies the estimation method. A decrease of about 25% of the elastic modulus (from a quasi-static speed of 60 km/h to 200 km/h) is estimated in these measurements, showing a global resilient behaviour but nonlinear with load amplitude. The trend is similar for both soil layers. But in the case of SBG it is a little more stabilized after 100 km/h while in ITL it continues decreasing.

The damping ratio (D_r) is also of the same order of magnitude when it is estimated for two different axle loads, locomotives and coaches. This parameter lightly increases in the case of ITL while it is more stable for SBG. Even if the absolute values of D_r seem very high for a soil of track-bed (10%), this analysis provides relative evolution of D_r with train speed in two depths. The D_r is found much lower in SBG because the equivalent elastic energy to the system in SBG (E_D) is higher compared to the measured stress amplitudes in this layer, that could increase the E_{loop}.

II.6   STATISTICAL ANALYSIS

In order to assess the validity of results obtained during the test campaign, a statistical analysis was performed using the commercial trains running on the Vierzon site. Emphasis was put on the train speed and axle load impact on the material responses.

II.6.1 Train selection

Firstly, a train type selection was performed from the circulations on the site. All the train passages were registered from April 2014 to August 2014. A total of 8165 train circulations were registered on the site in both tracks, corresponding to an average of 70 passages per day and 35 circulations per track. A classification of train type was performed according to their signature (strain gauges glued to the rail) and is presented in Figure II.65a. More than 40% of trains were Intercity trains composed of locomotive BB22000 or BB 26000 model and a variable number of Corail Coaches. 34% traffic involved different types of regional trains (TER). About 21% of trains were mainly freight trains. Only 2% of them were TGV trains. As the Intercity trains are regular in its composition and are the most common train in the zone, it was decided to perform this analysis using the passages of Intercity trains.

Figure II.65b presents a comparison between the train speed and number of axles of Intercity and other trains registered on the site. It is easily appreciable that the Intercity trains ran at a large range of speeds as compared to other trains: the Intercity trains cover a train speed range from 60 km/h to 200 km/h. Note that the speed is also limited for long trains that have large number of axles. This is another reason that justifies the choice of Intercity trains.

(a) (b)
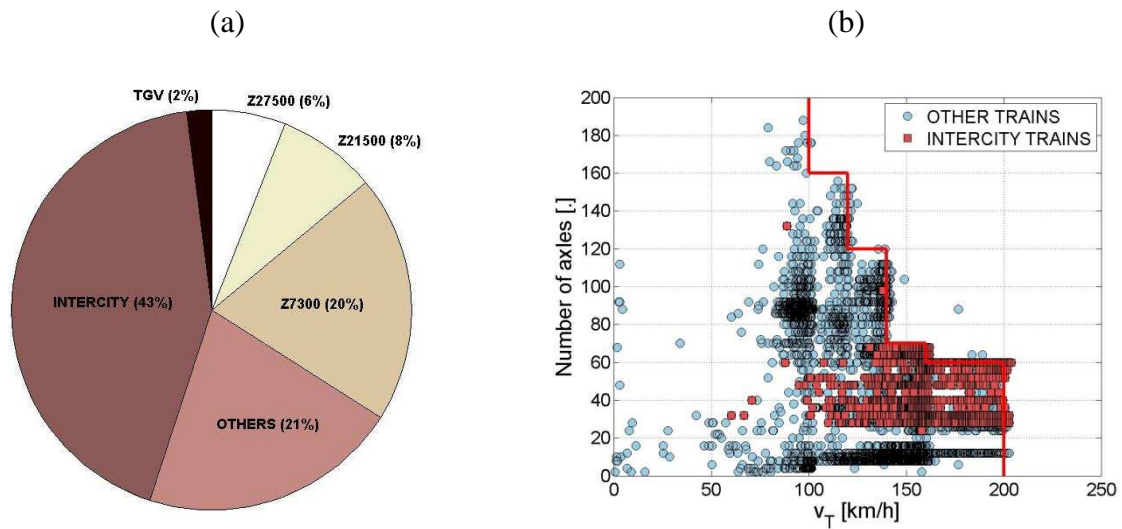
Figure II.65. (a) Type of trains running on the site and (b) Train speed versus number of axles of Intercity trains compared with other trains

II.6.1.1 Speed histogram

Regarding the speed of the registered trains there is one range with high frequency at 160 km/h. More than 40% of the 1790 Intercity trains on track 1 ran at 160 km/h or close to 200 km/h (Figure II.66). Consequently, it can be expected to have more data around these speeds.
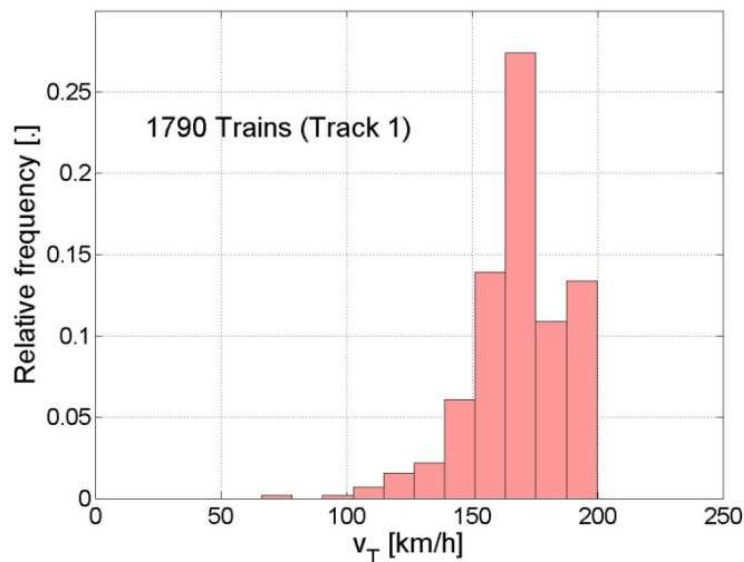
Figure II.66. Histogram of Intercity trains speed on the Vierzon experimentation site

II.6.1.2 Intercity train loading

In order to assess the repeatability of measurements and loadings to the track, a statistical analysis of the locomotive and coach axle loads measured with strain gauges for both left and right rails are shown in Figure II.67. In case of locomotive axles, the difference between the axle load mean values in both rails is only 14 kN, quite small. This could be a result of small differences in elastic conversion factor of each sensor (used to convert rail strains to axial loads). The variation coefficient (standard deviation over mean value) is very low, about 4% (10 kN in average), for both rails of track 1. Similar results were obtained for lighter loads by coaches. The axle load values are well distributed around the mean value for both axle loads and the standard deviation values are very low. It can then be concluded that load is well distributed for both rails (left and right) and all Intercity trains transmit the same load to the track for each axle type (Locomotive and Coach).

II.6.1   *Data analysis*

An analysis of the transmitted loads to track was done for every sensor type. The evolution of vertical compression stress amplitudes obtained by stress sensors for all the Intercity trains are presented in Figure II.68. There is a good correlation between the test campaign results (Figure II.51). The compression stress amplitudes increase by about 20% (from 11 to 14 kPa) with speed from 60 to 200 km/h for locomotives (225 kN/axle) in ITL. This increasing trend is less pronounced at the SBG depth for both axle loads. The standard variations are lower around the trend curve for shallower layers. This is because rolling stock or track defects could amplify the exerted load if the sensor is close to the surface. The energy causing these dynamic amplifications is rapidly attenuated over depth due to soil damping.

Table II.9 and Table II.10 show the normal distribution parameters for the stress amplitudes caused in ITL by Locomotive and Coach axles respectively for five train speed ranges. For Locomotive axles (Table II.9) it can be noted that the average value of stress increases with speed while the standard deviation slightly increases by 1% when the range of faster speeds is reached. This standard deviation around the mean value (coefficient of variation) is low (8%) for all the tested ranges of speeds. However, for lighter axles (Table II.10) the average value also increases with speed (from 8 kPa to 9.6 kPa), but its variation around the average decreases by 3% when trains run faster. The values are of the same order of magnitude than

for Locomotive axles (about 7% of variation coefficient), showing that there is limited dispersion around the average value.
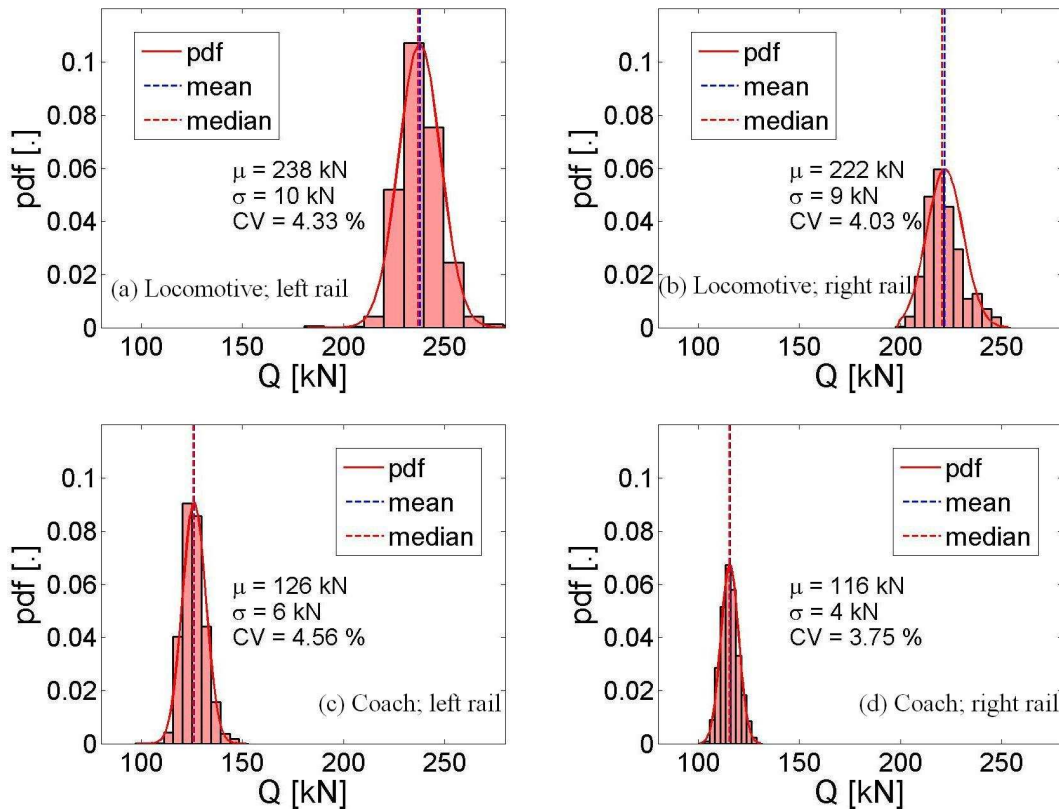
Figure II.67. Statistical analysis of train axle loads on track 1. Locomotive load: (a) left rail; (b) right rail and Coach load: (c) left rail; (d) right rail.
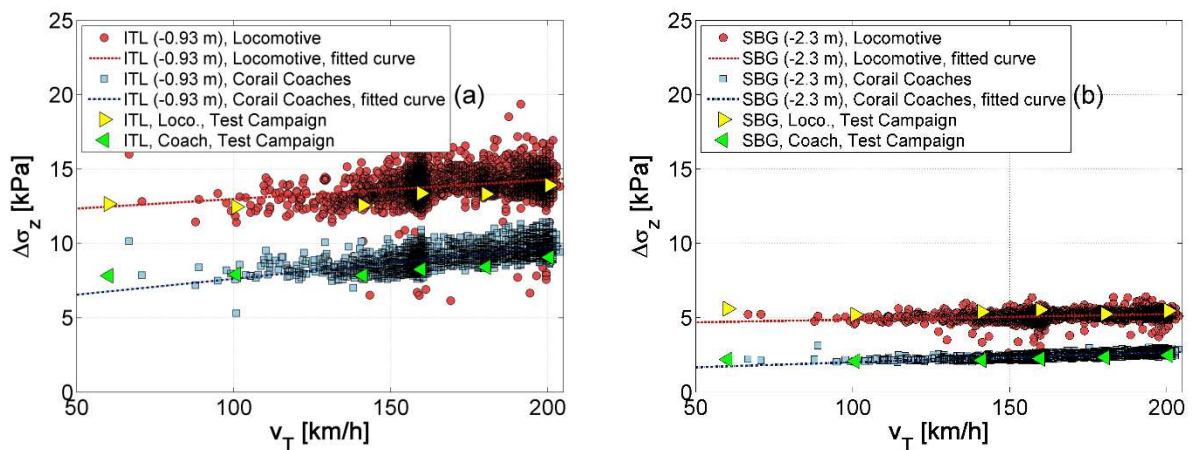
Figure II.68. Vertical stress amplitude caused by Locomotives and Corail Coach axles in (a) ITL and (b) SBG

Table II.9. Normal distribution parameters (mean value μ, standard deviation σ and coefficient of variation CV) for the stress amplitudes caused by Locomotives axles measured in ITL

		Speed Influence / ITL (z=-0.9 m) Locomotive (ΔQ=22.5 Mg/axle)				
		< 120 km/h	120 – 140 km/h	140 – 160 km/h	160 – 180 km/h	> 180 km/h
Δσ$_z$	μ (kPa)	13	13.1	13.7	14.1	14.2
	σ (kPa)	0.903	1.03	1.15	1.05	1.18
	CV (%)	6.97	7.92	8.36	7.45	8.35

Table II.10. Normal distribution parameters (mean value μ, standard deviation σ and variation coefficient CV) for the stress amplitudes caused by Corail Coache axles measured in ITL

		Speed Influence / ITL (z=-0.9 m) Corail coaches (ΔQ=10.5 Mg/axle)				
		< 120 km/h	120 – 140 km/h	140 – 160 km/h	160 – 180 km/h	> 180 km/h
Δσ$_z$	μ (kPa)	8.21	8.29	8.71	9.07	9.65
	σ (kPa)	0.755	0.496	0.608	0.57	0.594
	CV (%)	9.2	5.98	6.98	6.29	6.16

Similar analysis as for stresses was done with the acceleration amplitudes in ITL (Figure II.69a), TL (Figure II.69b) and SBG (Figure II.69c). The acceleration amplitudes are calculated using the method presented in Figure II.38. The increase of acceleration amplitudes in ITL is found to increase rapidly with train speed. The exponential increase of acceleration amplitudes with the train speed upgrade is reduced in the case of TL and SBG. This shows that ITL is able to damp more than 50% of the energy transmitted to the track-bed (because of the higher friction angle and density compared to other materials). The fitting line passes through the origin point because a stopped train does not develop any acceleration amplitude.

The amplitude values are well distributed around the average value for each range of speeds, with variation coefficients lower than 4% for all the speed ranges.

The particle displacements or deflections presented in this section were obtained by integration following the method presented in II.4.2.3. In order to show the good repeatability of this kind of measurements, a comparison between the displacement amplitudes obtained from accelerometers installed on left (acc_1) and on right (acc_2) sides of the same sleeper is presented in Figure II.70. The dispersion between both measurements is found to be lower than 3.5% around the 1:1 value for all the tested speeds.
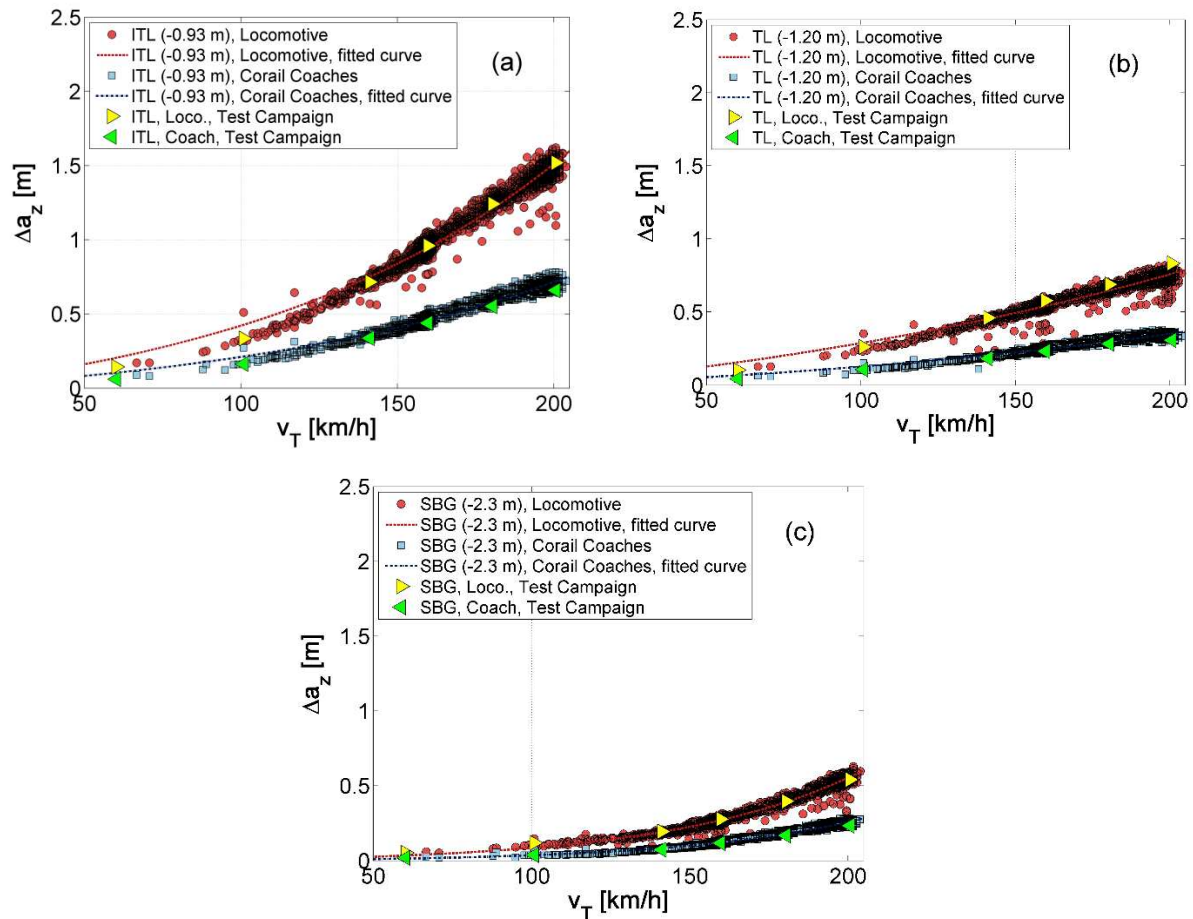
Figure II.69. Vertical acceleration amplitudes (f_c=25 Hz) caused by Locomotives and Corail Coach axles at (a) ITL, (b) TL and (c) SBG
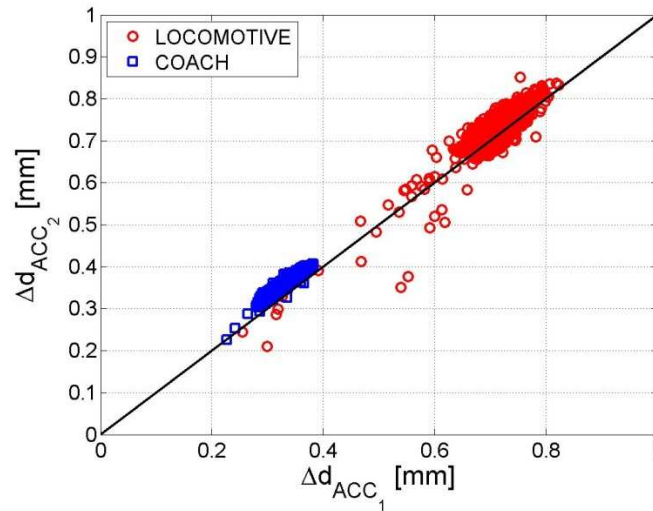
Figure II.70. Comparison of the displacement amplitudes for 1790 Intercity trains, estimated by double-integrating the signals of two different accelerometers installed at both sides of a sleeper

The displacement amplitudes for all the tested trains are assessed in Figure II.71. As expected, the displacement amplification with speed follows a linear trend in the range of registered speeds. This amplification is more notable in ITL (Figure II.71a) than in TL (Figure II.71b) and SBG (Figure II.71c). However, because for the train speeds lower than 80 km/h some energetic frequencies (half coach distance) are filtered by the applied high-pass Butterworth filter during the integration process the estimated displacement amplitudes are lower than the fitted linear trend. This effect is more notable for heavy axles as Locomotives. The point where the linear fitting curve intersects the Y-axis is supposed to be the static ($v_T = 0$ km/h) deflection. This 'static' deflection is decreasing over depth for locomotive and coach axles, from 0.42 mm for Locomotive in ITL (z=-0.9 m) to 0.21 mm in SBG (z=-2.3 m). The increase with train speed is found similar for the three monitored depths. Moreover, the amplitude results are well correlated to the test campaign test (Figure II.58) for the three depths.
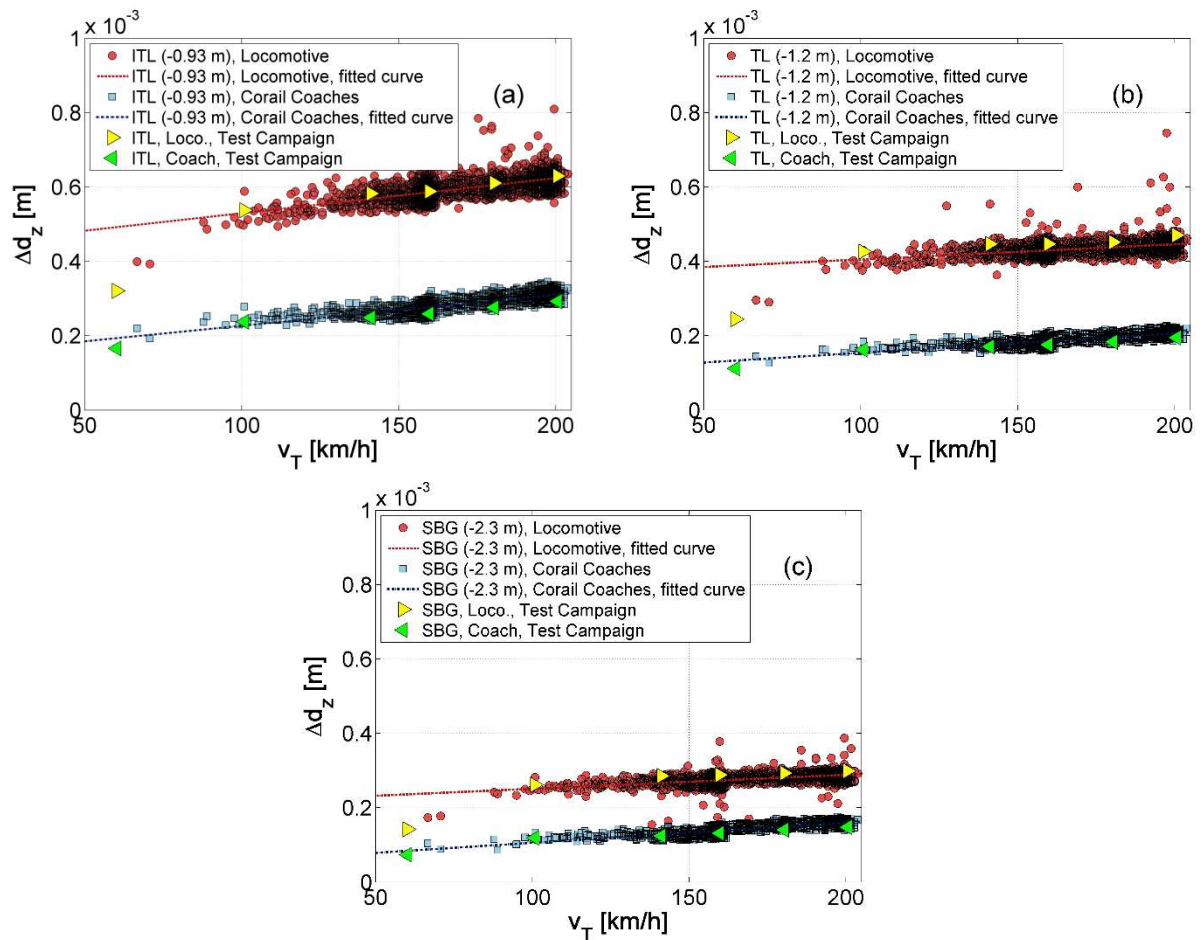
Figure II.71. Vertical displacement amplitudes caused by Locomotives and Corail Coach axles in (a) ITL, (b) TL and (c) SBG

Some standards (SNCF 2007) limit the maximum admissible acceleration amplitudes under train passage on track elements. However, one of the main modes of the track structure to resist the train load is the materials strains (related to their displacements). Then, the main purpose of railway infrastructure administrators to limit the maximum accelerations generated in the structure is to decrease the strains amplitudes developed by the track-bed materials. Nevertheless, the range of considered frequencies of these accelerations limits is not specified. Therefore, given an acceleration amplitude (for instance 1 m/s²) measured using the complete raw signal (Figure II.72a), the corresponding displacement amplitudes obtained (about 0.5 mm in Figure II.72a) are smaller than the displacement amplitudes corresponding to the same acceleration amplitude considering a filtered signal (about 0.6 mm in Figure II.72b) following the filtering method presented in II.4.1.3. Moreover, the accelerations amplitude evolution is more homogenous in filtered signals because the random component of high frequency excitation is not taken into account. Limitations in maximum

157

admissible acceleration amplitudes should be defined for a specific frequency range, trying to take into consideration only long wavelength excitations.
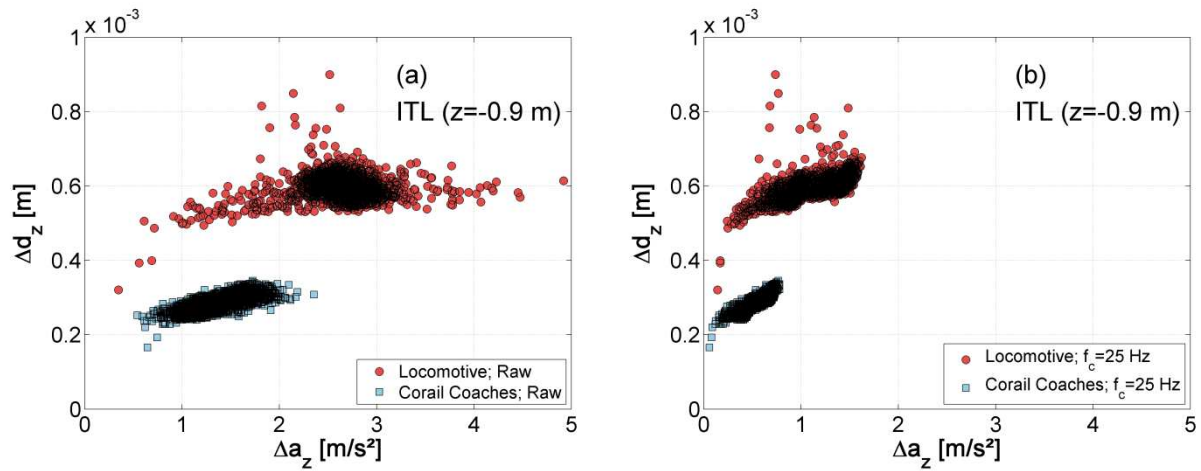
Figure II.72.Vertical displacement amplitudes Δd_z versus vertical acceleration amplitudes Δa_z for locomotive and coach axle loads: (a) raw acceleration signal; (b) filtered (f_c=25 Hz) acceleration signal

Table II.11 shows the normal distribution parameters of displacement amplitudes caused by a locomotive axle in ITL for five train speed ranges. The variation coefficient is about 4% for most of the speed ranges, but is larger for the slowest trains where high-pass filters do not allow performing a proper integration method (speeds lower to 80 km/h), resulting in lower displacement amplitudes that may change the standard deviation. The mean displacement in ITL caused by locomotive axles increases with speed as expected (from 0.5 mm to 0.6 mm). Moreover, the same analysis is performed for the displacement amplitudes caused by coach axles (Table II.12) in ITL, giving variation coefficients of 4% around the average value. The displacement amplification values with speed, from 0.24 mm to 0.3 mm, are half compared to the locomotive axle induced deflections because the locomotive axles are double of the weight of a coach. This suggests a linear increase of deflection amplitudes with axle load.

Finally, the vertical strain signals are calculated for all the passing trains following the method presented in II.5.6. Their amplitudes for all the 1790 Intercity trains registered on track 1 were also statistically analysed. Figure II.73 shows the evolution of strain amplitudes with train speed for ITL (-0.90 m / -1.20 m) and SBG (-1.20 m / -2.30 m) layers. As for the displacement amplitudes, the vertical strain amplitudes follow a linear trend in the range of the tested speeds and the intersection between the linear fitting curve and the Y-axis is

supposed to be the average strain at static loading ($v_T = 0$ km/h) in each layer caused by each axle type. The same order of magnitude of strain amplitudes is obtained for each train speed during the 5 month monitoring. The strain amplitudes developed under axle loading do not evolve with time, suggesting that these two track-bed layers behave as an elastic material in this range of speeds. These results are very similar to the vertical strain amplification obtained during the test campaign (Figure II.60).

Table II.11. Normal distribution parameters (mean value μ, standard deviation σ and variation coefficient CV) for the displacement amplitudes caused by locomotives axles in ITL

		Speed Influence / ITL (z=-0.9 m) Locomotive (ΔQ=22.5 Mg/axle)				
		< 120 km/h	120 – 140 km/h	140 – 160 km/h	160 – 180 km/h	> 180 km/h
Δd_z	μ (mm)	$5.18 \cdot 10^{-1}$	$5.64 \cdot 10^{-1}$	$5.83 \cdot 10^{-1}$	$5.95 \cdot 10^{-1}$	$6.17 \cdot 10^{-1}$
	σ (mm)	$5.02 \cdot 10^{-2}$	$2.3 \cdot 10^{-2}$	$3.11 \cdot 10^{-2}$	$2.94 \cdot 10^{-2}$	$2.48 \cdot 10^{-2}$
	CV (%)	9.71	4.08	5.34	4.94	4.02

Table II.12. Normal distribution parameters (mean value μ, standard deviation σ and variation coefficient CV) for the displacement amplitudes caused by Corail Coach axles in ITL

		Speed Influence / ITL (z=-0.9 m) Corail coaches (ΔQ=10.5 Mg/axle)				
		< 120 km/h	120 – 140 km/h	140 – 160 km/h	160 – 180 km/h	> 180 km/h
Δd_z	μ (mm)	$2.44 \cdot 10^{-1}$	$2.59 \cdot 10^{-1}$	$2.7 \cdot 10^{-1}$	$2.84 \cdot 10^{-1}$	$3.07 \cdot 10^{-1}$
	σ (mm)	$2.04 \cdot 10^{-2}$	$1.12 \cdot 10^{-2}$	$1.39 \cdot 10^{-2}$	$1.54 \cdot 10^{-2}$	$1.37 \cdot 10^{-2}$
	CV (%)	8.36	4.32	5.14	5.43	4.17
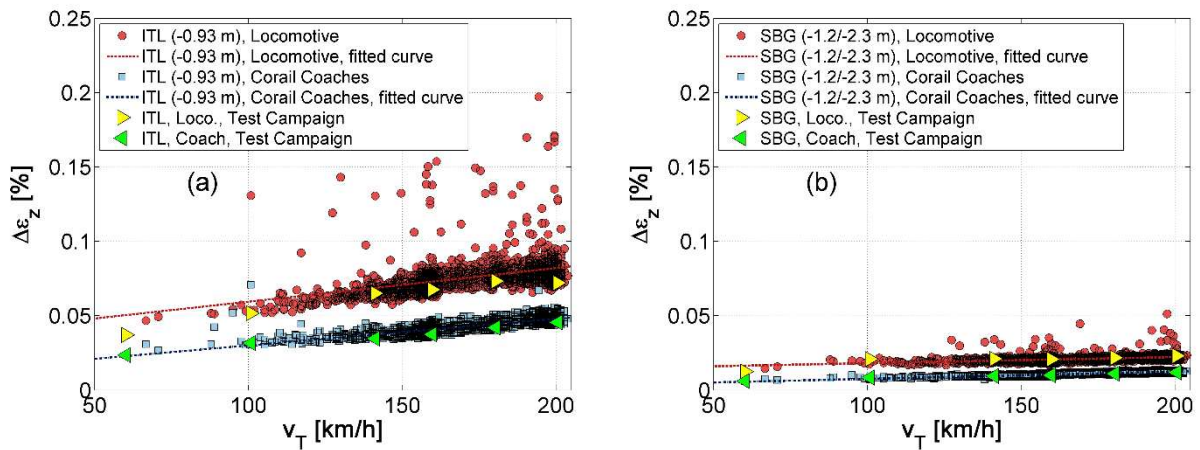
Figure II.73. Vertical strain amplitudes caused by Locomotives and Corail Coach axles in (a) ITL and (b) SBG

Table II.13 presents the normal distribution parameters for the vertical strain amplitudes caused by locomotives axles in ITL and Table II.14 the amplitudes caused by Coach axles in ITL considering five ranges of train speed. The variation coefficient is much larger (15%) for locomotive than for coaches (6%). This difference can be explained by the fact that the first axle impacting the track ('attacking axle' from locomotive) sometimes amplifies the transmitted loading depending on rail/wheel contact effects. A bigger variation was also measured for locomotive axles loads compared to coach axles (Figure II.67). The variation for the lower speed range is higher as for the displacements, owing to the effect of filtered frequencies for the train speeds lower than 80 km/h.

Table II.13. Normal distribution parameters (mean value μ, standard deviation σ and variation coefficient CV) for the vertical strain amplitudes caused by locomotives axles in ITL

| | | Speed Influence / ITL (z=-0.9 m) Locomotive (ΔQ=22.5 Mg/axle) | | | | |
		< 120 km/h	120 – 140 km/h	140 – 160 km/h	160 – 180 km/h	> 180 km/h
Δε$_z$	**μ (%)**	0.0589	0.0659	0.072	0.0758	0.0803
	σ (%)	0.0143	0.0112	0.0131	0.0108	0.0120
	CV (%)	24.3	17.1	18.2	14.2	15

Table II.14. Normal distribution parameters (mean value μ, standard deviation σ and variation coefficient CV) for the vertical strain amplitudes caused by Corail Coach axles in ITL

		Speed Influence / ITL (z=-0.9 m) Corail coaches (ΔQ=10.5 Mg/axle)				
		< 120 km/h	120 – 140 km/h	140 – 160 km/h	160 – 180 km/h	> 180 km/h
$\Delta\varepsilon_z$	μ (%)	0.035	0.0362	0.0393	0.0419	0.0474
	σ (%)	0.00753	0.0024	0.00247	0.00289	0.00278
	CV (%)	21.5	6.64	6.28	6.89	5.87

As the vertical stresses and strains obtained for all the 1790 Intercity trains (Locomotive and Coach axles) are the same as those calculated for the test train passages, a similar resilient modulus (M_r) trend is supposed to be obtained for all the 1790 trains following the method presented in II.4.2.6.1. Figure II.74 present the evolution of M_r with train speed for ITL (Figure II.74a) and for SBG (Figure II.74b) layers. The resilient modulus, the ratio between stress amplitude and strain amplitude, decreases with speed. This decrease with speed is slightly more significant in ITL where strain amplitudes are more sensitive to speed changes. The modulus in SBG is more stabilized with speed due to the lower variations of loads at this depth. Quite low M_r values are obtained due to the 'attacking axles' of locomotives that give larger variability of vertical strains - sometimes the absolute values are much larger than the average value for the monitored depth. A decrease of about 25% is estimated for ITL soil in the range of the tested speeds, suggesting a nonlinear behaviour of material. The same results were obtained during the test-train campaign. A decrease of resilient modulus induces larger deformations of materials during cyclic loadings. The resilient modulus results also show a low dispersion around their mean values. Note that the modulus values estimated for speeds slower than 80 km/h are not considered for the trend for the reason mentioned previously.
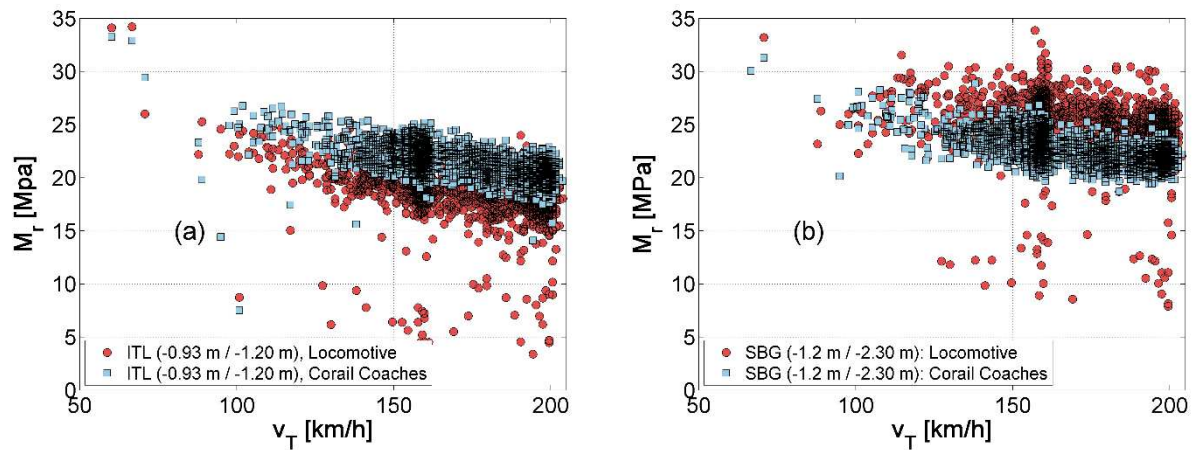
Figure II.74. Estimated resilient modulus of (a) ITL and (b) SBG under Locomotives and Corail Coaches loadings

II.7 SUMMARY

This chapter presented the instrumentation of a conventional track, allowing the assessment of the effect of axle load and train speed on the mechanical behaviour of track-bed materials. A representative conventional site at Vierzon was selected for this purpose. After some prospection tests, the critical speed of the site was defined, around v_{CR}= 650 km/h. Different sensors (such as soil stress gauges, strain gauges, accelerometer or geophones) were installed in each track-bed layer to assess their behaviour under train loadings. Then, a test campaign using an Intercity train was held. In order to evaluate the train speed effect, 6 different speeds were tested. The amplitudes of stress, acceleration, velocity and displacement were evaluated at 3 different depths (ITL, TL and SBG) and for 2 different axle loads (Locomotive and coach axle). It was found that absolute values of dynamic amplifications of stresses, deflections and strains are more notable in shallower layers such as ITL. Moreover, the stress and strain were amplified linearly (for the considered speeds going till 0.4 times the v_{cr} of the considered track) with increasing train speeds and axle loads. However, the profile of the ratio between them (resilient modulus M_r) is non-linear. This resilient modulus seems to decrease when the train speed increases for both ITL and SBG. A statistical analysis of train passages during 5 months confirms the results from the test campaign.

Some particular points are worthy to be highlighted:

     – PANDA dynamic penetrometer is a powerful tool to identify the thicknesses of track-bed layers and its mechanical elastic parameters (elastic modulus E).

- The ITL that is present in most of the French conventional tracks is a very stiff soil with low permeability and composed of a large range of grain sizes: from ballast grains to clay size particles.

- The technical specifications of the sensors to be installed in a track are very important in order to select the most appropriate ones for accurately monitoring different variables under train loadings.

- The stress and strain amplification with train speed depends on soil mechanical characteristics such as shear wave velocity. The critical speed of the site, related to the surface wave velocity (Rayleigh wave speed), controls the amplification of these values. Amplifications of about 30% of stress values, 50% of vertical deflections and strains were measured till speed of 0.4 times the critical speed of the site.

- The quasi-static value of different mechanical variables depends mainly on the axle – weight and distance (depth) from the loading source. There is a rapid attenuation of the amplitude (stress, acceleration or strain) in depth from the loading source. A larger amplitude decrease was found through ITL soil.

- The increase of stress and strain amplitudes is quasi-linear with higher axle-weight, for all the tested depths. This is mainly due to the fact that the soils react mainly in an elastic way.

- The reversible (but non-linear) elastic behaviour of track-bed materials with speed shows that the instrumented track does not present any particular problem and behaves correctly under traffic loadings.

- Admissible acceleration amplitudes in the infrastructure should be defined for a given frequency range, trying to take into consideration only long wavelength excitations (and filtering the random amplitudes generated by small wavelength excitations.

In this study, the amplitudes of stress and strain were obtained for different axle types and different train speeds. Based on these results, specific tests will be performed in the laboratory to investigate the impact of cyclic loading on the long-term and short-term behaviour of ITL soil. Emphasis will be put on the effects of loading shape, loading amplitude as well as the soil moisture content.

III.   LABORATORY EXPERIMENTATION

III.1   INTRODUCTION

In this chapter, the results of laboratory tests performed on ITL soils are presented. It is worth noting that the test loading conditions were defined based on the load and responses measured on track-bed materials during the 'in-situ' experimentation. The main goal is to assess the mechanical behaviour of ITL type soils under different cyclic loads (amplitude, shape and loading frequency) and initial conditions (moisture content, initial soil density and confining pressure).

Two different types of tests, bender element tests (using fine matrix soil of ITL soils) and large-scale triaxial tests (ϕ=300 mm) are described. After that, four tests procedures are defined and some typical tests results are presented. Then, a parametric study is performed in two sub-sections: one refers to parameters affecting the permanent deformations and a second one to the dynamic parameters related to load characteristics.

III.2   MATERIALS

In previous studies (Duong et al., 2013; Trinh et al., 2012), the mechanical behaviour of interlayer soil from 'Sénissiat site' (Trinh 2011) was assessed in the laboratory using a large scale triaxial test (ϕ=300 mm diameter). Because of the difficulties in obtaining intact ITL soil from conventional railway lines, it was decided to reconstitute ITL soil in the laboratory. Furthermore, four different parameters were controlled during and after its reconstitution to be compared to a real ITL soil: grain size distribution, fines plasticity, maximum Proctor density (and optimum moisture content) and mechanical behaviour under monotone loading.

As ITL soil nature and characteristics (fines plasticity and percentage, volume fraction of ballast, etc.) are site dependent (Duong et al. 2014), different ITL soils can be found in the French National railway network. Thus, to specify the characteristics from one of them and study the response under different load characteristics and soil initial conditions, the 'Sénissiat soil' (Trinh 2011) was taken as a reference ITL soil (Figure III.1). This ITL is a

well-distributed grain size soil from 0-63 mm. Moreover, ballast grains (considered as inclusions into the fine matrix soil) constitute a volumetric fraction of 32% (f_v) in ITL. To fabricate a similar ITL soil in the laboratory, 13 different soils were used, from ballast grains to clay particles.
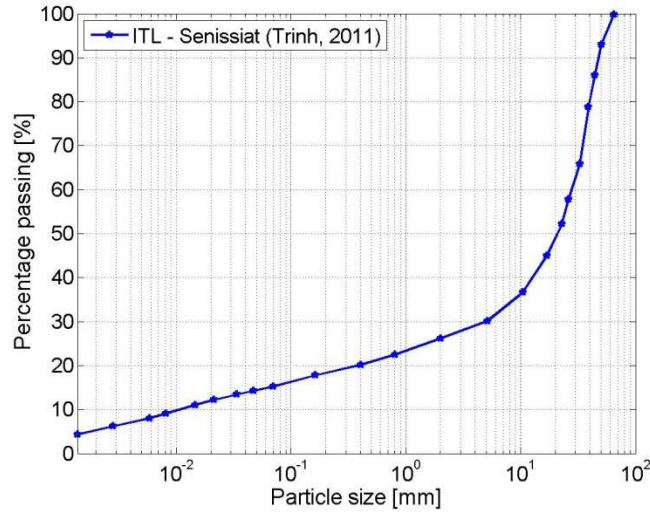
Figure III.1. ITL grain size distribution from 'Sénissiat' experimental site

Figure III.2 shows the grain size distribution curves (GSD) of the 13 different materials constituting the ITL in the laboratory. The quantity of each material is estimated from the intersection between the target ITL GSD (ITL Sénissiat from Figure III.1) and the D_{50} of each grain size distribution curve. Thus, the percentage to be used in the mixture of each constituting material (each one of the 13 considered materials) is defined as follows:

$$M_i = \frac{\left(MD50_{i+1} - MD50_i\right)}{2} + \frac{\left(MD50_i - MD50_{i-1}\right)}{2} \tag{III.1}$$

M_i being the mass percentage of material 'i' to be used in the fabrication of the target material (ITL Sénissiat), $MD50_i$ is the passing percentage at the intersection between the D_{50} of material 'i' and the GSD of the target material. Note that the materials are sorted by size (*i-1, i, i+1, i+2, …*). The estimated quantities in percentage for the 13 materials are given in Table III.1. For 100 kg of ITL material, 65 kg of coarse grain (ballast and gravels) soil and 35 kg of fines (sand and clay) were used.
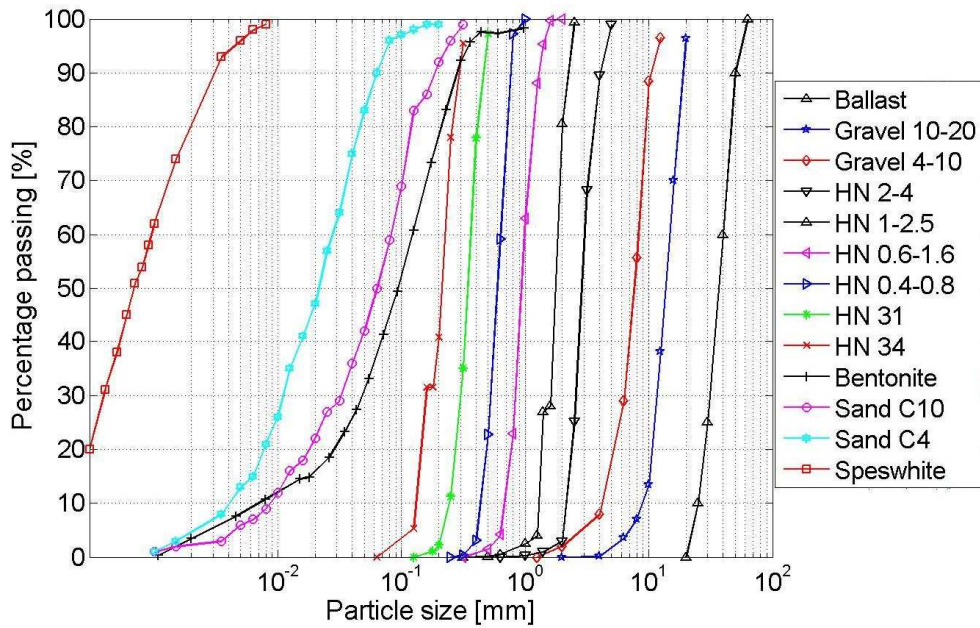
Figure III.2. Different materials used to reconstitute an ITL soil in the laboratory

Table III.1. Weight percentage of each material used in ITL-Lab soil

	Materials	[%]
	1. Ballast	35
Gravels	2. G 10-20	20
	3. G 4-10	10
	4. HN 2-4	5
	5. HN 1-25	4
Sands	6. HN 0,6-1,6	2
	7. HN 0,4-0,8	2
	8. HN 31	1
	9. HN 34	1
Clay	10. Bentonite	2
Finer sands	11. C-4	5
	12. C-10	6
Clay	13. Speswhite	7

The materials were then mixed to obtain a homogenous ITL soil (Figure III.3). The ITL material was fabricated in batches of 50 kg to guarantee the quality of the mix according to the technical requirements. Therefore, the mixing process was divided into four steps.

167
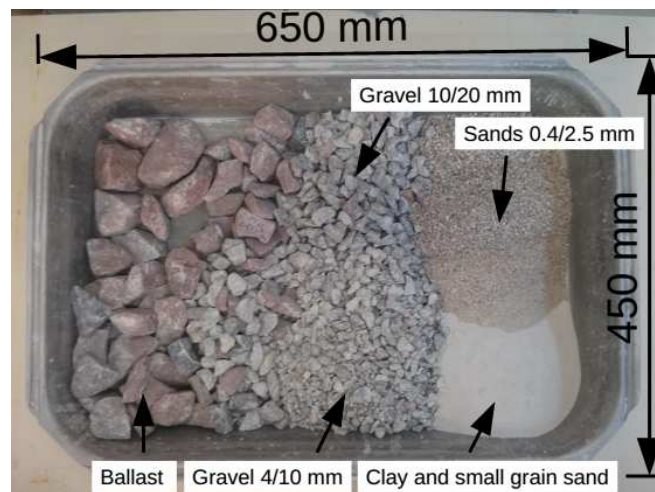
Figure III.3. Example of materials used during ITL fabrication process

First, to mix the 17.5 kg of fines (half of the 35 kg for 100 kg of total ITL-Lab material), the largest sands (from HN 1-2.5 mm to HN34) were dry mixed using a mixer (Figure III.4a) during 2 minutes. Second, 1 litre of water was added to the mix while the mixer blades continued rotating during 3 more minutes (these materials do not react with water as clays). Third, without stopping the rotation of blades, finer soils were added to the mixer (C-4, C-10 and Speswhite kaolinite), leaving bentonite to be the last material added to the mix because it is the most reactive material with water. Finally, in a concrete mixer (Figure III.4b), 32.5 kg (17.5 kg of ballast, 10 kg of gravel '10-20' and 5 kg of gravel '4-10') were mixed with the previous 17.5 kg of fines. During this last mixing, 1.25 litres of water were added while the concrete mixer rotated. The previously cited water quantities were defined in order to obtain a global water content of w=4% after the mixing process.

Figure III.4. (a) ITL soil fines mixing; (b) Ballast + gravel + fines mixer

Four tests were performed for the identification of soil: sieving, sedimentation, Atterberg limits and modified Proctor compaction.

The soil was classified based on the grain size distribution according to the GTR classification (SETRA 1992a; b). This test was performed using the dry soil sieving method after soil washing (AFNOR 1996) for soil particles larger than 80 µm. For the finer soil, the sedimentation method was applied for soil particles smaller than 80µm (AFNOR 1992a). Two GSD verifications performed by sieving and sedimentation were compared with the original ITL from Sénissiat (Figure III.5a). It seems that the ITL-Lab soil follows the same distribution as the target original Sénissiat soil. Sieving-1 and Sieving-2 surround the estimated mix distribution (this calculation was performed using the quantities in weight percentage), showing that the mix estimations were accurate. In Sénissiat soil, about 16% of particles are smaller than 80 µm, to be compared with 11% in ITL-Lab soil. In both cases, this percentage is far from the 4-8% of fine soils in the sub-ballast transition soil (new construction lines) (SNCF 1995) and lower than the 35% boundary to be considered as coarse-grained soil (AFNOR 1992b). Previous studies showed that these fine soils may control the mechanical behaviour of the entire ITL material (Duong et al., 2013; Trinh et al., 2012). The plasticity was determined according to the French standard (AFNOR 1993) using soils particles smaller than 400 µm. Results shows that the Sénissiat ITL has intermediate plasticity (Figure III.5b) as well as the ITL-Lab and the ITL from Vierzon site. The fines from the interlayer soils can be considered as low plastic silts for Sénissiat and low plastic clays for Vierzon and ITL-Lab soils (AFNOR 1992b).
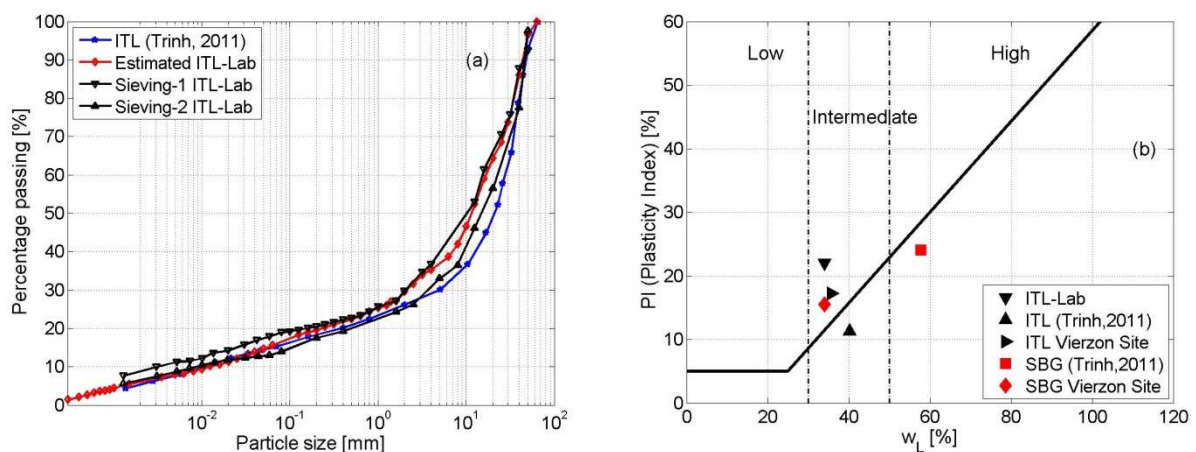
Figure III.5. (a) Grain size distributions of ITL soils reconstituted in the laboratory; (b) plasticity classification diagram of ITL type soils

Proctor compaction tests were carried out on the reconstituted ITL-Lab material (AFNOR 1999). The specific density of ballast and coarse grains (ρ_s) is equal to

ρ_s=2.68 Mg/m^3 (Trinh 2011), that is considered when performing the maximum density corrections. The CBR mould and modified Proctor compactor were chosen because larger grains were above 63 mm in diameter. For Proctor tests only soil lower than 20 mm was used. According to the French standard NF P94-093 (AFNOR 1999), if the percentage of elements larger than 20 mm in weight is lower than 30% of the total, the proctor curve can be determined to perform a correction on the values obtained with the 0-20 mm fraction using Equation (III.2) and Equation (III.3):

Moisture content correction:

$$w' = w - \Delta w \quad \text{and} \quad \Delta w = \frac{m}{100} \cdot w \qquad \text{(III.2)}$$

where w' (%) is the moisture content of the 0/D material, D (mm) is the maximum diameter of the material in mm; w(%) is the moisture content measured on the fraction 0/20 mm; m (%) is the proportion of 20/D grains in the material.

The dry density correction is as follows:

$$\rho'_d = \frac{\rho_d}{1 + \frac{m}{100} \cdot \left(\frac{\rho_d}{\rho_s} - 1 \right)} \qquad \text{(III.3)}$$

where ρ'_d (Mg/m^3) the material dry density of 0/D mm; ρ_d (Mg/m^3) is the material dry density determined on the fraction 0/20 mm and ρ_s (Mg/m^3) is the specific density of soil particles (2.68 Mg/m^3).

Figure III.6 shows the results of modified proctor (fraction 0/20 mm) and their correction allowing estimation of the entire material (0/63 mm). These results are summarized in Table III.2. The estimated maximum dry density and optimum moisture content is similar for both soils. Moreover, the optimum moisture content for ITL-Lab soil is close to the fabrication moisture content (w=4%).
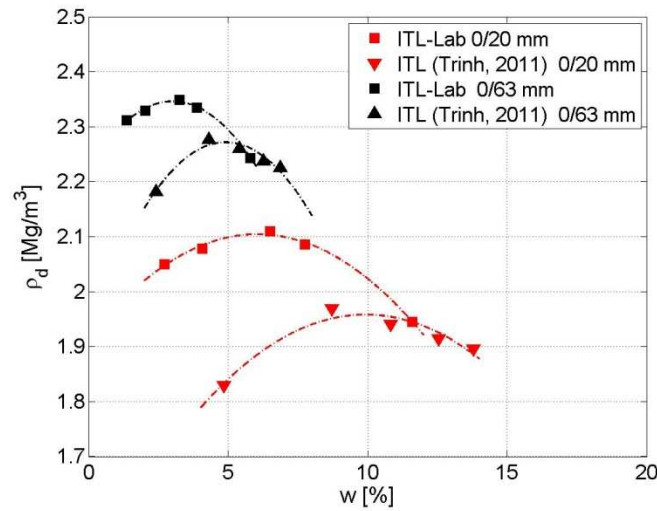
Figure III.6. Modified proctor test results for ITL-Lab and Sénissiat ITL (Trinh, 2011)

Table III.2. Estimated optimum water content and maximum dry densities of the two ITL soils

Soil	ρ_d [Mg/m^3]	w [%]
ITL-Lab	2.34	3.76
Sénissiat ITL (Trinh, 2011)	2.27	4.8

As fine particles control the mechanical behaviour of ITL soil (Duong et al., 2013) when the volumetric fraction of inclusions is low (Pedro 2004; Seif-el-Dine 2007), three fine soils with different bentonite content were fabricated in order to investigate the effect of fine soils. These soils were tested using Bender elements to study the changes in their elastic properties as the maximum shear modulus (G_{max}). The mixing procedure of these soils was the same as for the fines of the complete ITL-Lab soil. Moreover, the same soil characterisation tests were performed as for the ITL-Lab soil: sieving (d>80 µm), sedimentation (d<80 µm), Atterberg limits and Proctor. Table III.3 shows the weight percentages for each fine soil tested with Bender Elements.

The GSDs are similar for the three soils in the range from 0.1 to 2 mm (Figure III.7a). Only a small difference is found for ITL-1 in the finest diameter range (0-0.1 mm). This difference results from a larger amount of Kaolinite in ITL-1 as compared to the two other soils. As the composition of fines in ITL-1 is the same as for ITL-Lab, the plasticity of ITL-1 is the same as that of ITL-Lab (Figure III.5b), while the fines of ITL-2 and ITL-3 have higher plasticity due to the larger amount of bentonite added: for ITL-3, PI = 124 and w_L = 159 %.

Table III.3. Weight percentages for each fine soils tested with Bender Elements

Material	ITL-1 [%]	ITL-2 [%]	ITL-3 [%]
HN 1-2.5	13.33	13.33	13.33
HN 0.6-1.6	6.67	6.67	6.67
HN 0.4-0.8	6.67	6.67	6.67
HN 31	3.33	3.33	3.33
HN 34	3.33	3.33	3.33
Bentonite	6.67	20	33.33
C4	16.67	16.67	10
C10	20	20	13.33
Kaolinite	23.33	10	10
Total	100	100	100
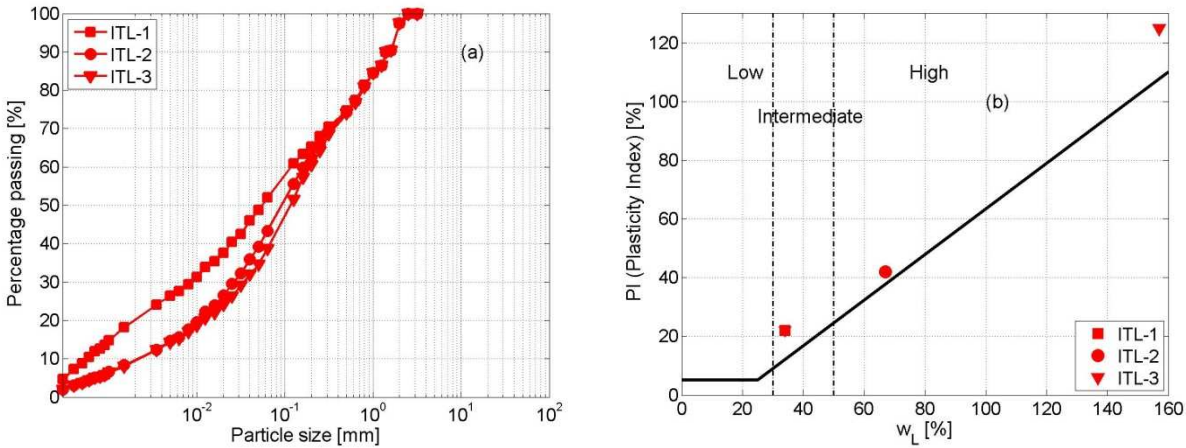
Figure III.7. (a) Grain size distribution of different fine soils; (b) plasticity classification diagram

Note that the visual aspect of each soil (Figure III.8) is also different because of the differences in bentonite (brown colour) quantity and kaolinite quantity (white colour).
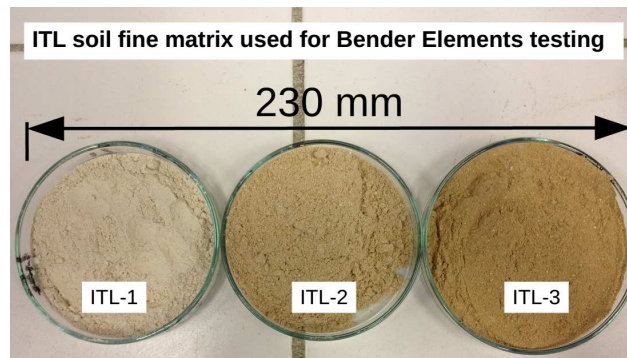
Figure III.8. Example of three different fine soils

Regarding the compaction of these fine soils, the French proctor standard was followed (AFNOR 1999). Here, due to the inexistence of grains larger than 2 mm, the normal proctor compactor and the small mould (as described in the standard) were chosen. Smaller dry densities were reached for very plastic soils (ρ_d=1.61 Mg/m^3) as ITL-3 compared to low plastic soils (ρ_d=1.61 Mg/m^3) as ITL-1. Moreover, the optimum moisture content is higher for ITL-3 (w=14.4%) that that for ITL-1 (w=12.5%). The maximum density values are more easily identifiable for low plastic soils.
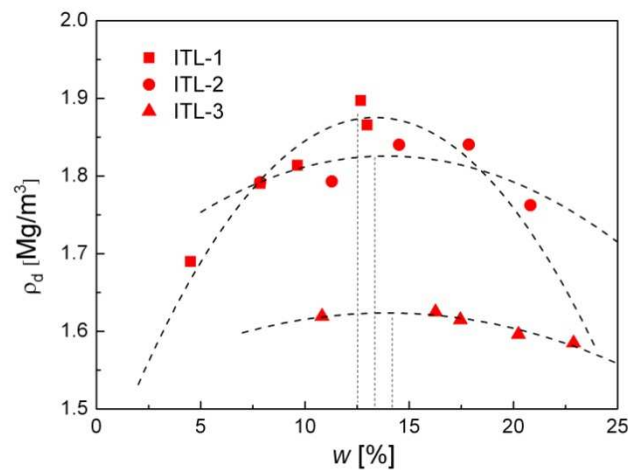
Figure III.9. Normal Proctor test results for the three different fine soils

III.3   DESCRIPTION OF THE EQUIPMENTS

In this section, the equipment and the experimental techniques used are presented. Both the Bender elements and triaxial tests were performed to investigate the low-strain elastic

behaviour of ITL fines and the cyclic mechanical behaviour of ITL-Lab complete soil, respectively.

III.3.1 Bender elements

The bender elements test involves two piezo-electric sensors (benders) that are in contact with a soil sample one face to another (both extremities of a sample). The main purpose of this test is to measure the shear wave velocity for very low strains (Viggiani and Atkinson 1995a; b). The piezo-electric elements are excited with a voltage variation. The variation of voltage induces a movement on one of the sensors (transmitter) and the propagation of this excitation through the soil is measured by the sensor installed at the other sample extremity (receiver). The ratio between the applied forces and the response depends on the bender properties: the shape, the size and the direction of the transmitted sample excitation. The sensors transmit the excitation modifying their width, the piezo-electric elements expand with the voltage variations (Leong et al. 2005). In addition, this expansion can develop longitudinally or in the transverse direction depending on the bender characteristics. The deformation of the elements is of the order of a few nanometers (Leong et al. 2005). The elements constituted by two piezo-electric layers can be designed to dilate, bend or twist according to the polarization and the wiring configuration for the layers.

The shear velocity through the soil is estimated by measuring the time spent by the excitation wave to go from the top to the bottom of the specimen. Different methods are reported in literature (Leong et al. 2005) to estimate this arrival time. Measuring shear waves could be more complicated in some cases than measuring direct loading waves because shear waves could be hidden behind the first wave's arrival or even because of the parasites waves reflected through the sample boundaries (Da Fonseca et al. 2009; Karl 2005). This is called 'near field effect', and is mostly found if the ratio between the height of the sample and the wavelength of the exciting signal is lower than 4 (Brignoli et al. 1996; Lee and Santamarina 2005; Sharifipour 2006).

The soil samples in this study are cylinders of 50 mm height and 50 mm diameter (Figure III.10a). The receiver and transmitter benders are installed at both ends of the sample and connected to an oscilloscope, while the transmitter is also connected to a function generator that induces the excitation signal (Figure III.10b). Signals from the oscilloscope are

recorded through a computer. The samples are compacted using an axial compactor consisting of a jack equipped with a force sensor installed on its top. As the volume of the soil sample is known, the mass of dry material (considering the moisture content during compaction) to be compacted is the same for every sample (ρ_d=1.8 Mg/m^3).
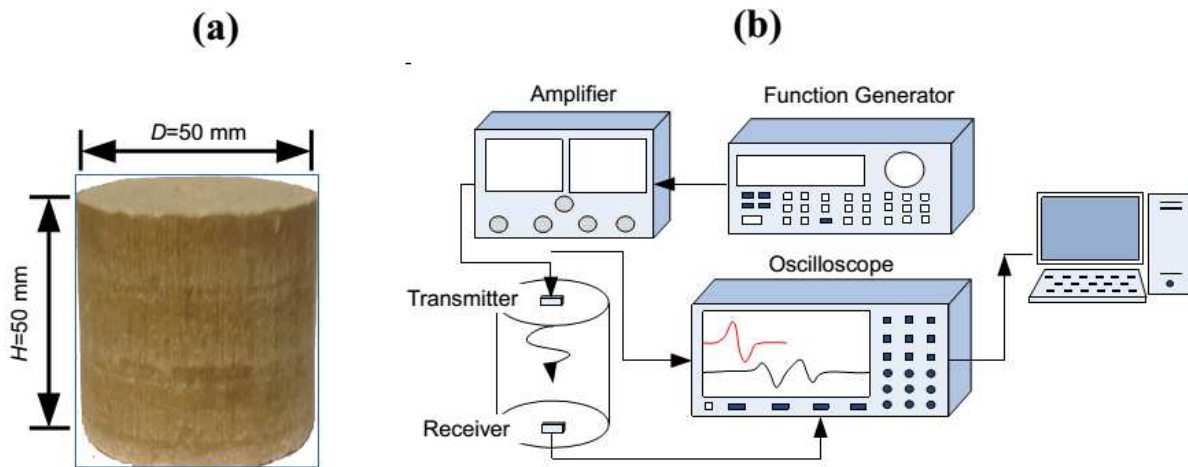
Figure III.10. (a) Bender element sample after compaction; (b) bender element test functional scheme

Figure III.11 presents two photos showing parts of the experimental setup used for bender elements testing. The size of the bender (0.5 mm width) may be noted in Figure III.11b.
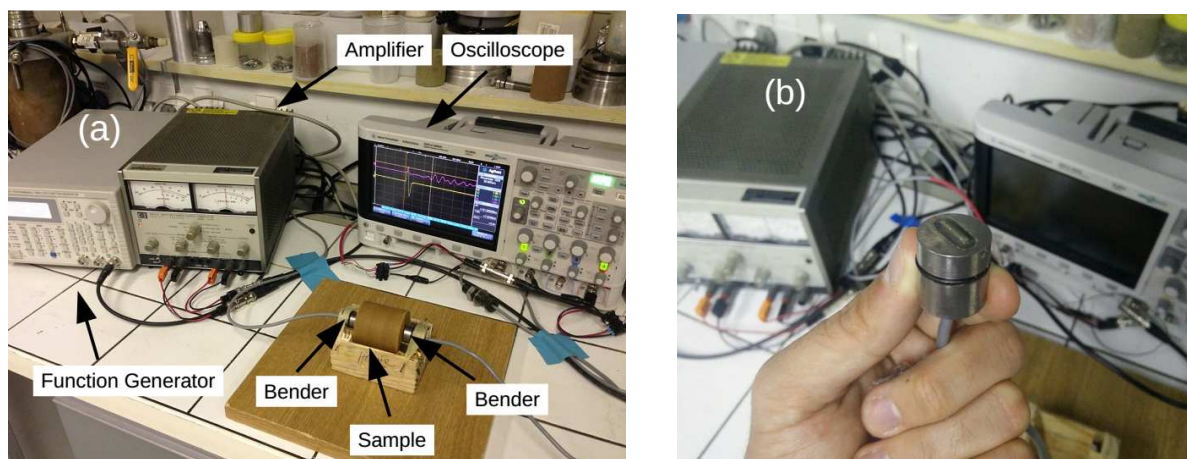
Figure III.11. (a) Bender elements testing equipment; (b) View of a bender

III.3.2 Cyclic triaxial setup

If the ratio between the sample diameter and the largest particle is lower than 5, the effects of triaxial dimensions on the material behaviour of soil could strongly favour a non-

homogeneous strain field (Indraratna et al. 2010). Considering the size of the largest elements in ITL-Lab (up to 60 mm), a large size triaxial cell (Canou et al. 2008; Suiker 2005) was adopted for the test (AFNOR 1994). The soil samples have a diameter of 300 mm and a height of 600 mm. The complete setup, shown in Figure III.12, was designed as a multi-modular system, on which different types of geotechnical tests could be conducted.

This setup was previously used in several studies, some of them concerning the investigation on the behaviour of coarse-grained soils with a fine soil matrix under low-strain cyclic loadings (Canou et al. 2008; Pedro 2004; Seif-el-Dine 2007). Studies concerning the mechanical behaviour of micro-ballast (Karraz 2008) and the influence of the proportion of fine soil on the behaviour of interlayer soils (Duong, 2013; Duong et al., 2013; Trinh, 2011; Trinh et al., 2012) were also performed. The setup consists of a base slab (2.50 m x 2.00 m), with a 4 column loading frame equipped with a servo-hydraulic actuator (MTS system) (Figure III.12). The base can rotate and translate to facilitate the sample preparation.

The triaxial setup (Figure III.13) is mainly composed of the following elements:

- A movable pedestal (triaxial base support) for translation and rotation. This pedestal is mounted on a carriage supported on two rails. The cylindrical base (lower base) is equipped with various holes to ensure the passage of fluids such as water for the confining pressure between the outside and the inside of the cell. This lower base has marks for the confining cells and holes for 12 tie rods.

- An upper sample base with the same diameter as for the sample (300 mm) and with drainage channels to saturate the sample or to apply vacuum.

- Two plexiglas reinforced walls allowing application of the confining pressure to the sample. There is enough space between the inner surface of this cell and the sample to place local measurements sensors around the specimen. A pressure sensor connected to the enclosure allows recording the confining pressure that can go up to 2000 kPa. The confining pressure is regulated using a servo-hydraulic actuator connected to the enclosure. The volume of water could be also measured if the actuator's displacement is known. From this confining pressure liquid exchange (water volume exchange from the cell), the volumetric strain of the soil sample could be assessed.

- A metallic lid having a central passage for the piston and a rigid fastening device till the base of the apparatus (the movable pedestal).

- The axial servo hydraulic actuator has a capacity of 500 kN (axial force sensor is installed at the bottom of the cell where it is measured), and the confining servo-actuator allows a maximum confining pressure of 2 MPa. The cyclic loading frequencies can go up to 40 Hz (depending on the cyclic displacement). This jack must slide through the confining cell head-piece avoiding water leakage from the inside of the confining cell. A LVDT incorporated to the axial actuator allows measuring the vertical displacements of the sample head. The measuring range of this LVDT is ±150 mm from its central position.
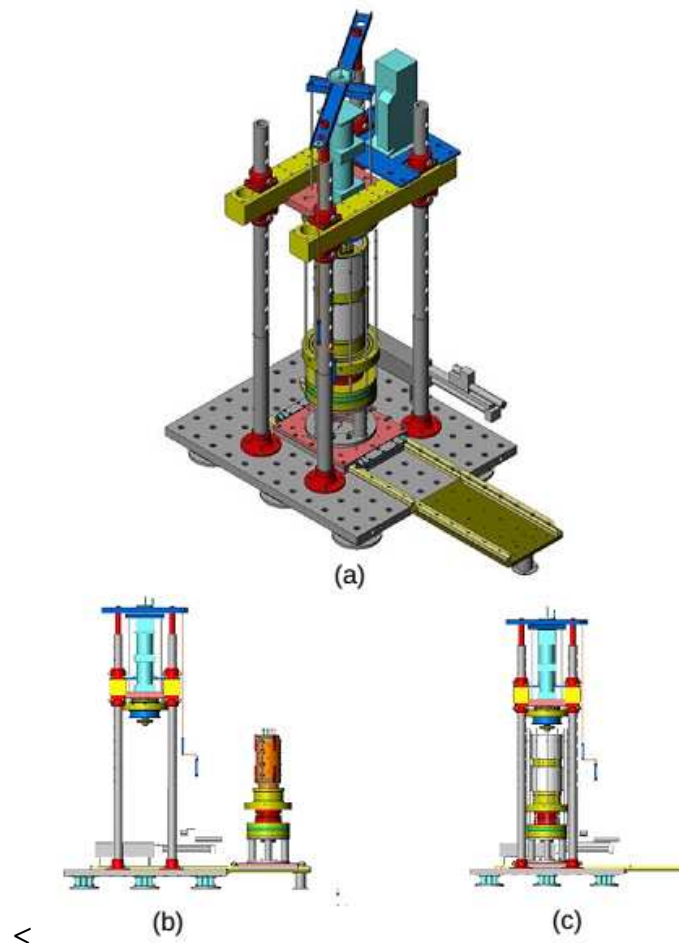
Figure III.12. (a) Scheme of the large size triaxial device; (b) sample preparation before testing; (c) sample placed under the servo-hydraulic actuator (Seif-el-Dine 2007)
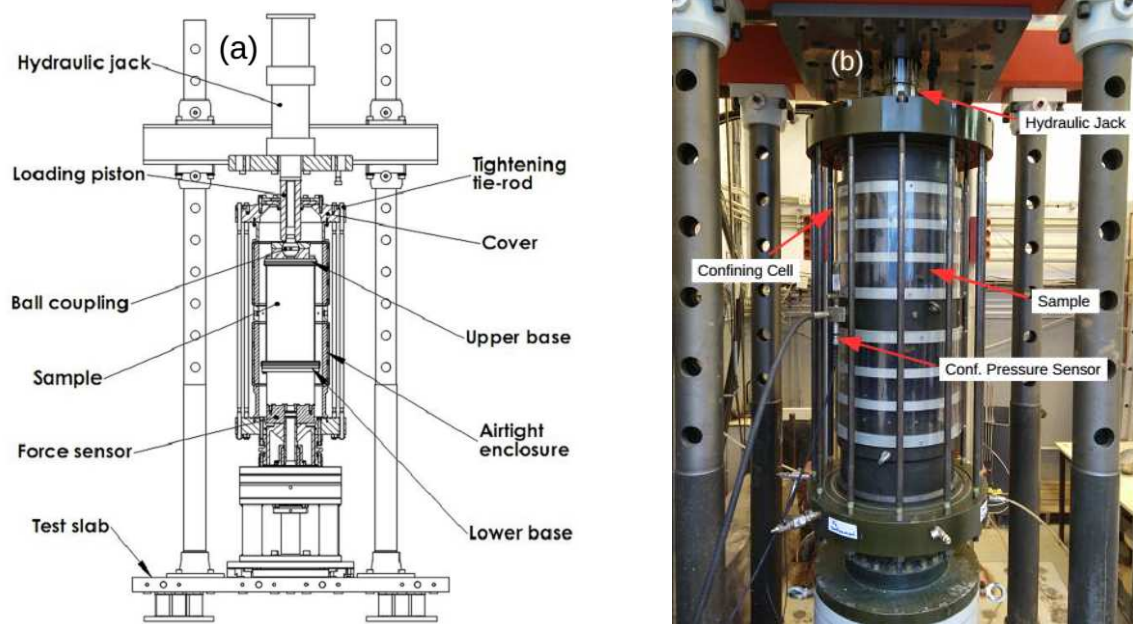
Figure III.13. (a) Simplified representation of the large size triaxial setup; (b) sample being tested on the large scale triaxial setup

The ITL soil has a high density due to its formation process, reaching dry densities as high as 2.4 Mg/m^3 (Trinh 2011). In order to obtain similar ITL conditions, the soil was compacted in a metallic compacting mould using a vibro-hammer (Figure III.14). The sample was compacted in 5 layers of 120 mm height each. Considering a moisture content w=4% during compaction (OPM moisture content), the mass taken for each layer was m_{layer} = 17.75 kg. Thus, with a volume of the specimen V_{spec}=0.04241 m^3, a dry density of ρ_d = 2.01 Mg/m^3 was reached. The final dimensions of the ITL-Lab samples are H=600 mm height and φ=300 mm diameter (Figure III.14).

Concerning the assembly procedure of the sample on the triaxial setup for a regular test with high density compacted soil, it can be divided into 8 stages (Figure III.15):

(a)   Setting of a porous stone and a paper filter on the base support of the triaxial apparatus;

(b)   Unscrewing of the compacting mould base support; the ITL sample was transported to the sample support;

(c)   Remove the four parts of the compacting mould, up and down;

(d)   Setting-up the latex membrane in the membrane mould and application of vacuum for pressing the membrane through the inner surface of the mould; introduction of the membrane around the sample maintaining the vacuum.

(e)   Vacuum was released and membrane mould removed.

(f)   Introduction of a porous stone on the sample (sample's top); installation of two 'O-rings' at the sample boundaries (upper and lower); vacuum was applied to the sample (Δu = -25 kPa).

(g)   Installation of the confining walls and tie rods (12 around the sample); translation of the sample below the servo-hydraulic jack in order to install the head of the confining cell;

(h)   Positioning of the jack (contact with the sample), lowering the confining cell head and closing the cell by clamping the tie rods. When extension efforts (negative deviatoric values) are performed, the axial jack needs to be anchored to the sample. Fastening of tie rods was done. Water filling of the confining cell was performed and air into the confining pressure jack was evacuated by moving the jack while the filling process was performed. Sample vacuum was removed and the average confining pressure was increased to 30 kPa. A verification of the axial jack contact was performed and the position was considered as the initial point. An isotropic stress state was assumed for the sample. The translatable pedestal position was blocked using screws from the pedestal through the slab.

Figure III.14. (a) Scheme of parts constituting the compaction mould; (b) sample being compacted with a vibro- hammer; (c) view of a compacted sample after remoulding
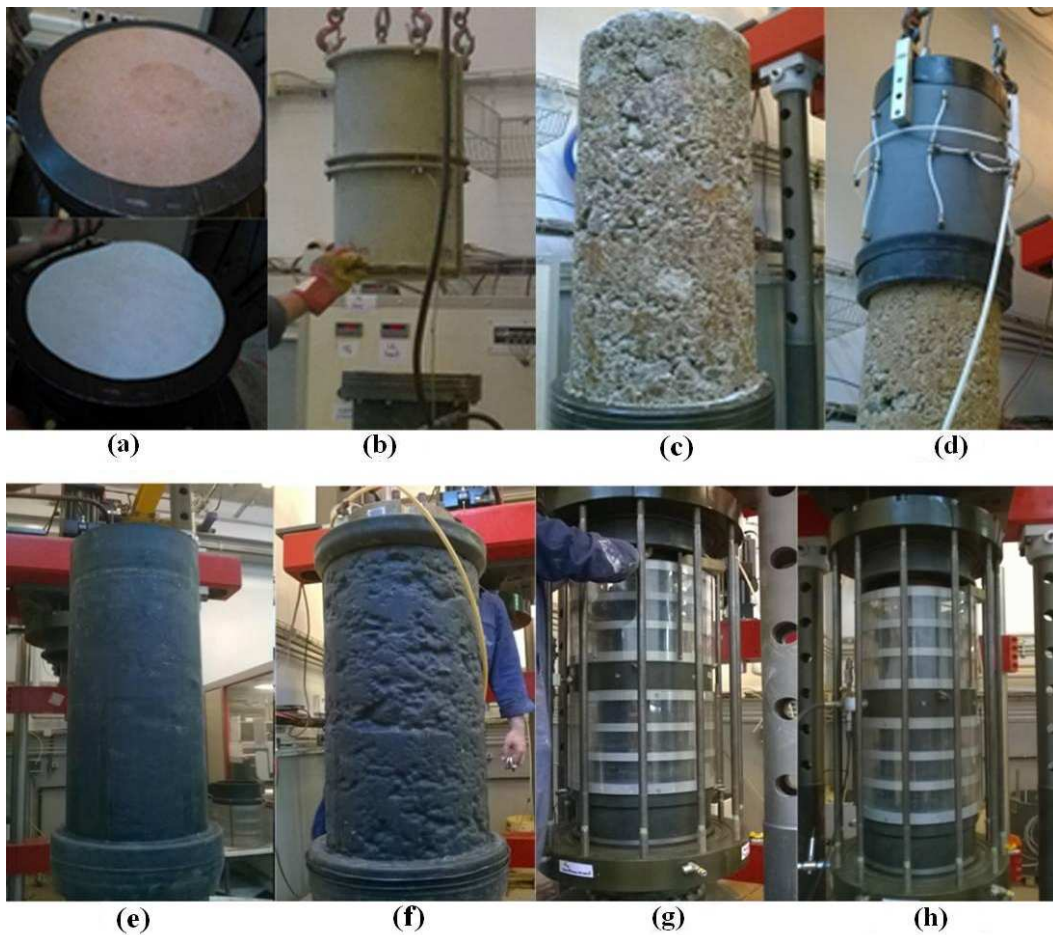
Figure III.15. Experimental procedure used to set up a specimen in the triaxial cell

If the test is under saturated conditions, after the previous (h) point, the saturation process was added by injecting de-aired water from the bottom of the sample till the upper section. This water percolated through the sample (water circuit was open at the bottom and the top during this stage) for 10 h ($\Delta u = 18$ kPa between the bottom and the top considering the height of the water reservoir). The sample saturation was controlled by measuring the Skempton coefficient (Duong 2013; Trinh 2011): while the confining pressure was intentionally increased, measurements of the internal increment of water-pressure were performed to verify the Skempton coefficient. A value of 0.8 was obtained for the ITL-Lab material in the tests. Finally, in order to improve the saturation rate, a back-pressure was applied and it was compensated by the confining pressure. The difference between them corresponds to the effective pressure.

The range of the confining pressure should be predefined because the soil resistance increases with the confining pressure. For a ITL soil in a railway track-bed, the confining pressure is in the range from 10 to 60 kPa (Suiker 2005). In this study, a value of $\sigma_{3=}30$ kPa is adopted. The

four main variables calculated during a test are the deviator stress (q), the mean stress p, the axial strain ε_1 and the volumetric strain ε_v. By measuring the confining pressure σ_3, the axial force over the sample F, the axial displacement of the main jack d_{act} and the displacement of the hydraulic actuator that applies the confining pressure c_{dis} as well, the four variables can be determined, as follows:

$$\varepsilon_1 = \frac{\left(d_{act} - d^0_{act}\right)}{H} \cdot 100 \qquad \text{(III.4)}$$

$$\varepsilon_v = \frac{\left(\left(c_{dis} - c^0_{dis}\right) \cdot r_c^2 \cdot \pi + \left(d_{act} - d^0_{act}\right) \cdot r_d^2 \cdot \pi\right)}{r^2 \cdot H \cdot \pi} \cdot 100 \qquad \text{(III.5)}$$

$$q = \frac{F}{\left(r^2 \cdot \pi \cdot \left(1 + 1.5 \cdot \dfrac{\varepsilon_1}{100}\right)\right)} \qquad \text{(III.6)}$$

$$p = \frac{q}{3} + \sigma_3 \qquad \text{(III.7)}$$

H is the sample height, r is the sample radius, r_d is the radius of the axial jack and r_c is the radius of the confining pressure jack. The axial jack diameter of the used cell is ϕ_d=130 mm and the hydraulic jack for the confining pressure has a diameter of ϕ_c=127 mm. The contact surface used to estimate the deviator stress is corrected taking into account the sample's axial strain. Using these equations, the axial and volumetric strains should be obtained in percentage (%) and the deviator and mean stresses in kPa.

III.4 CHARACTERISATION BY BENDER ELEMENTS

Bender elements tests were performed on fine matrix soils (ITL-1, ITL-2 and ITL-3) to measure the evolution of elastic parameters (shear wave velocity) under different moisture contents but at similar densities. The specimen's length is the same for all the specimens

(L_{spec}=50 mm). The shear wave velocity is calculated using the wave travel time from the transmitter to the receiver (Figure III.16):

$$v_s = \frac{L_{tt}}{t} = \frac{\left(L_{spec} - 2 \cdot L_b\right)}{t} \qquad \text{(III.8)}$$

where L_{tt} is the tip-to-tip distance between the transmitter and the receiver, L_{spec} is the length of specimen, L_b is the length of benders and t is the travel time of the wave between receivers. From the shear wave velocity, the shear stiffness G_{max} can be determined from the elastic wave propagation theory (Leong et al. 2005):

$$G_{max} = \rho \cdot v_s^2 \qquad \text{(III.9)}$$

where ρ is the total density of the soil specimen. As the imposed shear deformations to the samples are very small (about $\varepsilon_1 = \pm 10^{-6}$), the estimated modulus are considered as the maximum shear modulus (G_{max}).
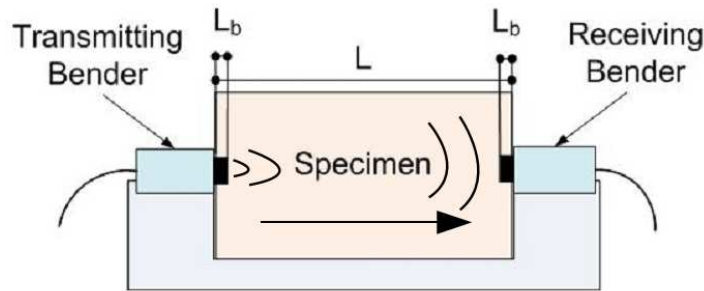
Figure III.16. Functional scheme of shear waves velocity determination using bender elements

Concerning the test conditions, four different excitation frequencies were considered: 15 kHz, 20 kHz, 25 kHz and 30 kHz, and 7 different moistures contents were also considered: 4%, 6%, 8%, 10%, 12%, 14% and 16% for each soil. At least two specimens were tested for each moisture content, making a total of 60 specimens (20 of each fine soil material) tested.

All the four frequencies were applied on each specimen. The test procedure consists of an excitation line (from the transmitter sensor) and a response line (from the receiver sensor) with an identical temporal origin as shown in Figure III.17. Note that in this figure the response voltage is amplified by 10000 to make it visible in the same plot as the transmitted line. The travel time is measured from the beginning of the excitation to the first peak (supposing that it is the first arrival of shear waves) of the response curve. The travel times were found to be very similar for all the excitation frequencies tested (see Table III.4).
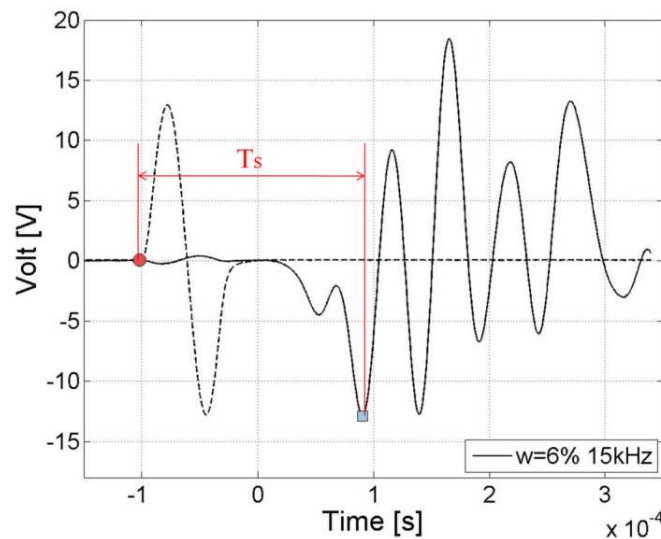
Figure III.17. Bender elements test results (emitted and amplified received signals) for Lab. ITL-1 soil at w=6% and excited at f=15 kHz

As the results are very similar for the four tested excitation frequencies, only the results at f=20 kHz are reported in Figure III.18. It is observed that the shear wave velocity first increases with the increase of moisture content, reaching a maximum and then decreasing. Generally, an increase of shear wave velocity is found for soils with high plasticity. This is mostly the case for moisture contents larger than $w = 6\%$. For instance, the maximum shear wave velocity goes from 250 m/s for soil ITL-1 at w=7% to 350 m/s for soil ITL-3 at w=14.5%. This increase of shear wave velocity with moisture content is mainly due to the increase of the contact area between aggregates/grains. This increase of v_s is more significant in materials with high specific surface like ITL-3. Nevertheless, in materials with low specific surface as ITL-1 (with high quantity of Speswhite kaolinite clay) the maximum shear wave velocity is reached for lower moisture content values. However, when the optimum water content was reached, the suction effect starts to be predominant and the shear wave velocity decreases with further water content increase.

Table III.4. Shear wave velocity results from Bender elements tests

			w=4%		w=6%		w=8%		w=10%		w=12%		w=14%		w=16%	
			Spec.1	Spec.2	Spec.1	Spec.2	Spec.1	Spec.2	Spec.1	Spec.2	Spec.1	Spec.2	Spec.1	Spec.2	Spec.1	Spec.2
ITL-1		Real w (%)	4.71	4.81	6.53	6.35	9.03	8.66	12.50	13.05	14.80	14.70	17.40	17.60	20.90	21.50
		ρ_d (Mg/m³)	1.97	1.97	1.97	1.97	1.93	1.97	1.80	1.82	1.82	1.81	1.80	1.77	1.64	1.65
	V_s	15kHz	234.0	234.0	247.1	244.3	238.0	269.7	213.4	232.0	158.9	167.5	118.9	117.5	96.9	76.5
		20kHz	239.3	241.2	251.7	250.8	243.7	243.9	218.3	238.8	164.7	171.8	122.5	119.4	87.9	78.1
	(m/s)	25kHz	243.7	247.2	259.8	255.8	247.8	250.1	225.8	241.8	167.5	174.3	124.1	120.9	90.9	86.1
		30kHz	247.5	252.5	265.4	260.0	252.4	254.8	229.6	245.6	170.8	177.3	123.0	120.6	84.6	71.2
ITL-2		Real w (%)	4.92	4.97	6.72	6.56	8.02	8.57	11.24	11.24	13.60	13.50	15.03	15.04	16.22	15.53
		ρ_d (Mg/m³)	1.81	1.82	1.82	1.83	1.83	1.83	1.82	1.82	1.81	1.82	1.82	1.84	1.81	1.84
	V_s	15kHz	214.9	197.1	244.6	241.5	256.3	262.6	265.2	261.7	270.7	273.7	271.9	263.3	239.5	254.4
		20kHz	216.8	200.4	246.2	243.0	267.0	269.6	269.3	265.3	274.9	276.9	275.4	265.1	242.8	256.8
	(m/s)	25kHz	219.1	203.8	247.8	244.6	266.2	269.3	272.4	268.3	273.8	277.3	277.8	265.5	241.0	256.8
		30kHz	219.1	207.7	257.3	253.6	278.6	280.7	282.5	280.9	289.8	291.7	290.4	280.8	252.0	269.7
ITL-3		Real w (%)	5.54	5.36	7.88	7.86	10.80	10.99	12.83	12.91	14.67	14.33	16.63	16.78	18.84	18.45
		ρ_d (Mg/m³)	1.80	1.81	1.83	1.81	1.79	1.79	1.78	1.79	1.79	1.81	1.80	1.80	1.77	1.77
	V_s	15kHz	231.0	218.1	248.7	252.3	329.6	338.5	330.7	344.8	322.6	341.1	331.7	323.4	309.0	394.9
		20kHz	234.8	226.6	255.6	251.2	336.6	339.0	333.8	348.4	324.8	339.8	336.1	327.5	314.2	303.4
	(m/s)	25kHz	237.0	227.7	259.7	252.5	335.6	335.2	344.7	356.2	332.1	349.0	343.4	335.0	320.4	308.3
		30kHz	244.6	235.2	268.7	264.0	352.4	356.1	350.6	360.4	336.5	353.8	349.4	340.8	327.3	315.4
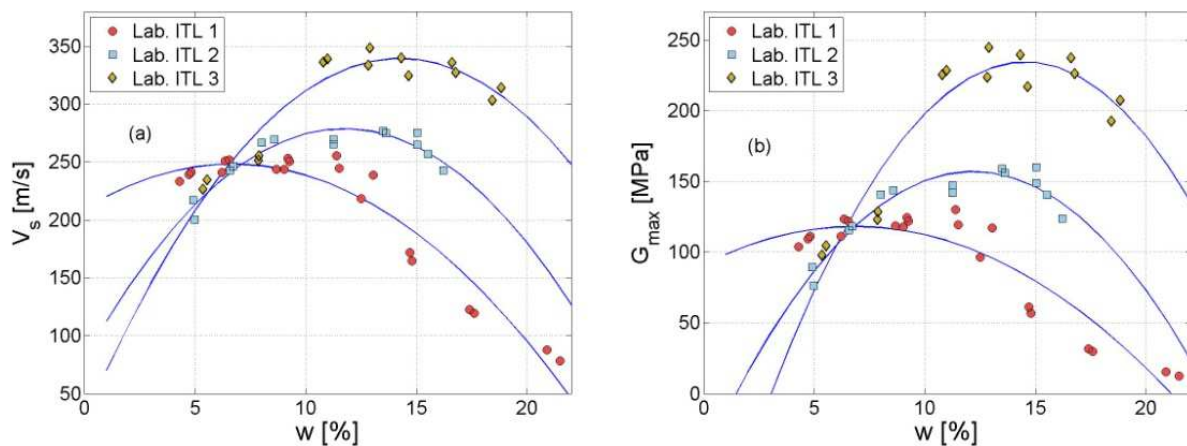
Figure III.18. (a) Shear wave velocity; (b) maximum shear modulus evolution for three different ITL fine matrix soils

III.5 MONOTONIC TRIAXIAL TESTING

Three monotonic drained triaxial tests were performed on the complete ITL soil (ITL-Lab material) including the same fine matrix as ITL-1 soil previously tested with bender elements. The main goal of these experiments was to determine their shear strength parameters and to compare them to those of Sénissiat ITL soil (Trinh 2011). These three triaxial tests were performed at a moisture content w=4%, close to the OPM of both soils. A constant low strain rate of $\dot{\varepsilon}_1 = 0.05\% / min$ was adopted as indicated in the French standard to guarantee that the

test is effectively drained (AFNOR 1994). The characteristics of the three monotonic tests are listed in Table III.5. The three confining pressures chosen (σ_3 of 30, 100 and 200 kPa) were the same as for the Sénissiat ITL (Trinh 2011). Results of both soils are shown in Figure III.19, with three plots: the deviator stress versus effective mean stress, deviator stress versus axial strain and volumetric strain versus axial strain.

The results show that the behaviour observed for σ_3=30 kPa is very similar for both soils. Nevertheless, for higher confining pressures, the maximum deviator stress for the ITL-Lab soil is lower than for the Sénissiat soils at small strains (below ε_1=4%). However, the same deviator stress values and trend are found for larger axial strains (at about ε_1=12%). The maximum deviator stress values obtained for each test increase with the confining pressure. This variation was also observed by Indraratna et al. (1998) on ballast.

Concerning the volumetric behaviour, the soil starts by dilation at about ε_1=1% for low confining pressures, but at about ε_1=4% for higher confining pressures. Both soils behave in a similar way at σ_3=30 kPa and σ_3=200 kPa. The contracting part at σ_3=100 kPa seems to be larger in axial strain for ITL-Lab soil compared to Sénissiat soil.

Table III.5. List of monotonic shear tests performed

Test	σ_3 kPa	ρ_d Mg/m^3	w_{opm} %	ε_{1max} %
EM1	30	2.01		8.5
EM2	100	2.01	4	12
EM3	200	2.01		12
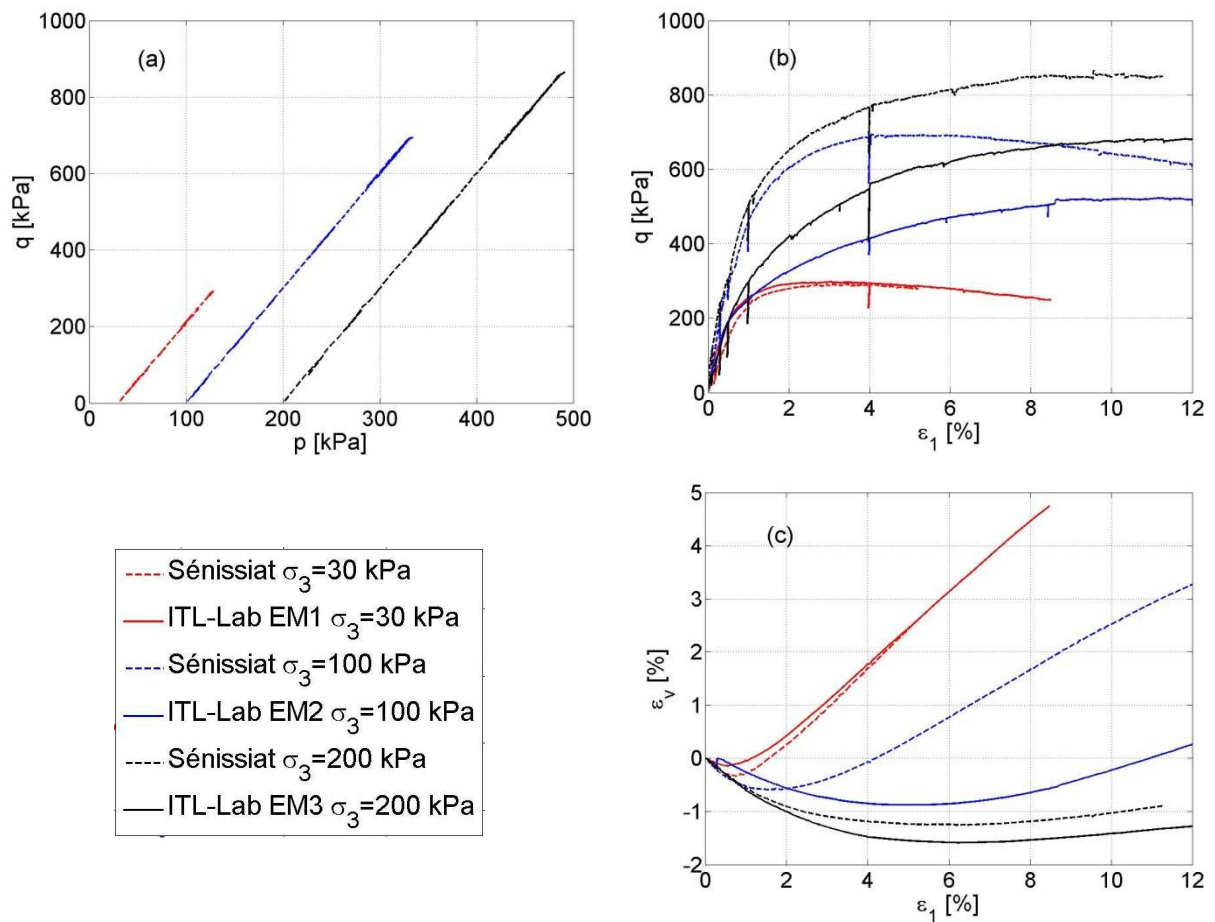
Figure III.19. Monotonic triaxial tests results: comparison between ITL-Lab reconstituted soil and Sénissiat ITL soil tested at three different confining pressures (30, 100 and 200 kPa)

The failure parameters corresponding to Mohr-Coulomb criterion, for the laboratory soil at w=4% were calculated using the results from the three monotonic shear tests. Values were compared to the parameters obtained for Sénissiat soil under similar state conditions (Table III.6). With the maximum q and p values for each monotonic shear test, the critical state line can be expressed as:

$$q = M \cdot p + S$$

(III.10)

being M and S two soil failure parameters. Using these two values it is possible to calculate the apparent cohesion (c) and the internal friction angle (φ) using the following equations (Trinh 2011):

$$\sin(\varphi') = \frac{3 \cdot M}{6 + M} \qquad \text{(III.11)}$$

$$c' = \frac{S \cdot (3 - \sin \varphi')}{6 \cdot \cos \varphi'} \qquad \text{(III.12)}$$

The difference of two degrees between the two soils may be caused by the difference in ballast grains constituted in each soil. An increase of ballast grain amount (volumetric fraction of inclusions) in a coarse-grained soil may increase their shear strength by increasing the friction angle (Pedro 2004). In ITL-Lab, the proportion of ballast grains is indeed slightly smaller than that in Sénissiat ITL soil (Figure III.5a). On the whole, the differences in cohesion and friction angle can be considered as small.

Table III.6. Shear strength parameters of ITL-Lab and Sénissiat ITL

	M	S	c'	φ'
ITL-Lab	1.59	100 kPa	51 kPa	37°
Sénissiat ITL	1.58	116 kPa	60 kPa	39°

The loops of unloading/loading ($\Delta\varepsilon_1$=0.025% of unload) at three different strains (0.3%, 0.5% and 1%) were applied during the tests. All the loops are situated in the contracting zone (Figure III.19). From these loops, the resilient (elastic) modulus can be estimated by calculating their slopes following the French standard (AFNOR 2002). A comparison of resilient modulus between two soils is made in Figure III.20. These results are also plotted in Figure III.21. It is observed that the modulus of ITL-Lab soils increases when the axial deformation is increased, in particular at higher confining pressures. For Sénissiat ITL soils, the modulus decreases at $\Delta\varepsilon_1$=0.5% (Table III.7) as a result of reorganisation of coarse grains (Trinh 2011). This phenomenon is not observed in the ITL-Lab soils. Overall, the values obtained are of the same order of magnitude for both soils.
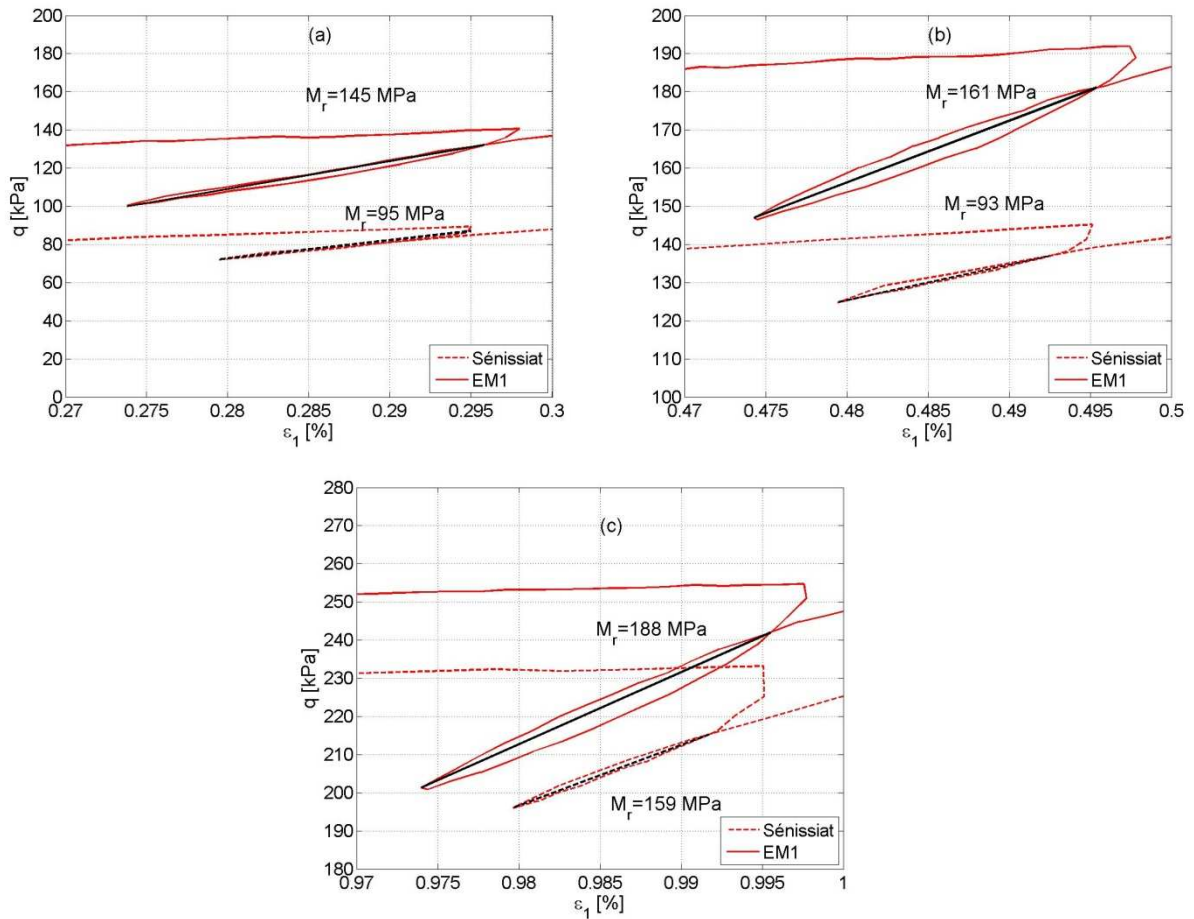
Figure III.20. Unloading/loading loops of ITL-Lab (EM1) and Sénissiat ITL materials (σ_c'=30 kPa) at (a) ε_1=0.3%, (b) ε_1=0.5% and (c) ε_1=1%
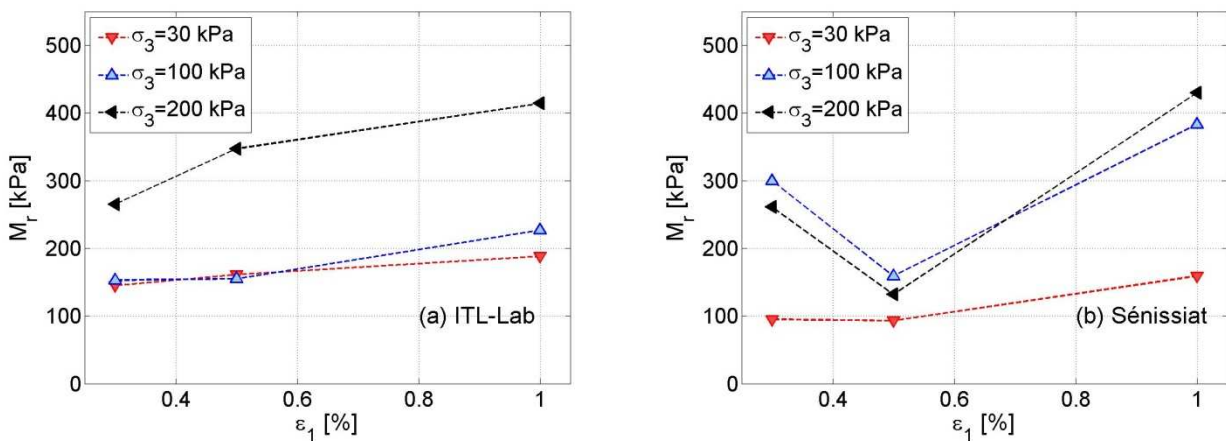
Figure III.21. Resilient modulus from unloading/loading loops: (a) ITL-Lab; (b) Sénissiat ITL

Table III.7. Resilient modulus calculated from unloading/loading loops for ITL-Lab and Sénissiat ITL

		ε_l=0.3%	ε_l=0.5%	ε_l=1%
σ_3=30 kPa	EM1	M_r =145 MPa	M_r =161 MPa	M_r =188 MPa
	Sénissiat	M_r =95 MPa	M_r =93 MPa	M_r =159 MPa
σ_3=100 kPa	EM2	M_r =153 MPa	M_r =155 MPa	M_r =227 MPa
	Sénissiat	M_r =300 MPa	M_r =159 MPa	M_r =383 MPa
σ_3=200 kPa	EM3	M_r =265 MPa	M_r =347 MPa	M_r =414 MPa
	Sénissiat	M_r =261 MPa	M_r =132 MPa	M_r =430 MPa

III.6 CYCLIC TRIAXIAL TESTS

Different cyclic loading tests were performed using the large size triaxial setup, to analyse the cyclic behaviour of ITL soils. The cyclic loading applied simulates the traffic loading according to the measurements presented in chapter II. The effect of different loading parameters (amplitude, frequency, number of cycles and loading history) and soil state parameters (moisture content) are analysed in this section.

First, a description of the four cyclic loading testing procedures adopted is made. Second, the methods of analysis and typical tests for each procedure are presented. Third, an assessment of the parameters impacting the behaviour of ITL soil at large number of cycles is done. Finally, the dynamic parameters of an ITL soil as well as the influence of the loading history are discussed.

III.6.1 Experimental program

The experimental program is described in this sub-section. Some cyclic loadings that are used in several procedures, are firstly presented. The cyclic loadings imposed in three of the four testing procedures simulate the train's bogies. Each cycle represents the loading induced by a bogie. Two different shapes are considered, a 'M-shaped' (Figure III.22a) and a 'sine-shaped' loading (Figure III.22b). The 'M-shaped' loading represents two wheels separated by a distance of d=2.8 m and the load in the middle of both wheels is half the total amplitude caused by them. This type of loading is similar to the measurements conducted at this depth (Lamas-Lopez et al. 2015; SNCF 2009). Sine shape loadings are usually found deeper in track-bed. In this case the load of both wheels of the same bogie cannot be differentiated. In

addition, the distance between two bogies is 6.4 m, the same as the minimum distance between bogies for Intercity trains (between Corail coaches) - the most typical train running on the French conventional lines. As a vertical stress of about $\Delta\sigma_z$=15 kPa (Lamas-Lopez et al. 2015) or $\Delta\sigma_z$=25 kPa (SNCF 2009) were measured during the 'In-situ' experimentations at the ITL equivalent depths (about z=-0.90 m from the ground surface), the loads imposed in this study range from $\Delta\sigma_1$=10 to $\Delta\sigma_1$=30 kPa. For both cyclic loading shapes, the sample was always submitted to compression stresses (no extension was allowed). Moreover, to ensure the continuous contact between the actuator and the sample, a small compression stress of σ_1=2 kPa was left after each cycle (Figure III.22).

Moreover, the simulated speed in the tests that do not seek to evaluate the train speed impact on soil's behaviour is as low as about 50 km/h in order to allow the servo-controlled system to follow properly the predefined loading shape. In the case of 'M-shaped' loading the frequency excited between bogies is f_{bogies}=1.78 Hz, the frequency excited by the wavelength between two consecutive axles is f_{axles}=5.01 Hz and the distance between two vanes (from the middle of each 'M') excites f_{vanes}=3.5 Hz. However, the 'sine-shaped' loading excites the soil only at f_{bogies} frequency.
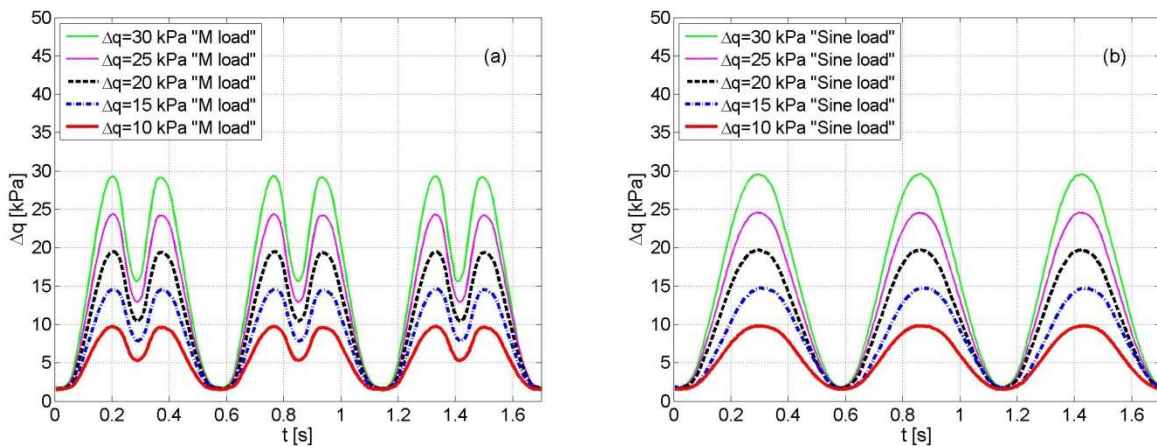
Figure III.22. Typical loading signals applied in the cyclic triaxial tests: (a) M-shaped loading; (b) Sine-shaped loading

Four testing procedures, from A to D, were followed and they are presented in the following sub-sections. Different cyclic loads with 'M' shape loading, 'Sine' loading and 'Cyclic' loading were applied. A third loading shape, the 'Cyclic' loading, was considered only in one testing procedure. This loading shape was based on a sine cyclic loading in which the sample

was submitted to strain-controlled compressions and extensions (explained in detail in the 'Testing Procedure C' section).

Therefore, each test is represented by a specific code as explained in Figure III.23.
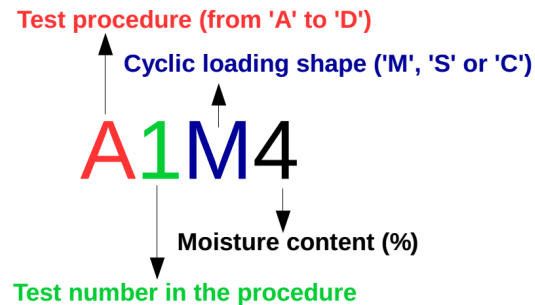
Figure III.23. Test code constituted by 4 parts

III.6.1.1 Testing procedure A: large number of cycles

The testing procedure A corresponds to a cyclic loading test based on the 'M' and Sine loading signals presented in Figure III.24. This procedure aims to assess the evolution of cumulative plastic deformations at large number of cycles for different loading amplitudes, shapes and hydric conditions. Two different hydric state conditions were considered: optimum moisture content ($w = 4\%$) and saturated case ($w = 10\%$). These tests were force-controlled tests and the resulting axial strains were monitored. For each test, five loading amplitudes were tested from 10 to 30 kPa, ranging from the lowest to the highest (because of the loading history influence). Moreover, for each loading amplitude, 90 000 cycles (simulated bogies) were applied (Figure III.24). This number of loading cycles was estimated to be enough to stabilize the permanent deformation evolution taking into account the loading characteristics and the material conditions (Duong et al., 2013; Gunther Gidel, 2001; Trinh, 2011). As the confining pressure was constant during each test (σ_3=30 kPa), the loading path followed a slope 1:3 in the *p-q* diagram (Figure III.24). Samples were isotropically consolidated applying this confining pressure.
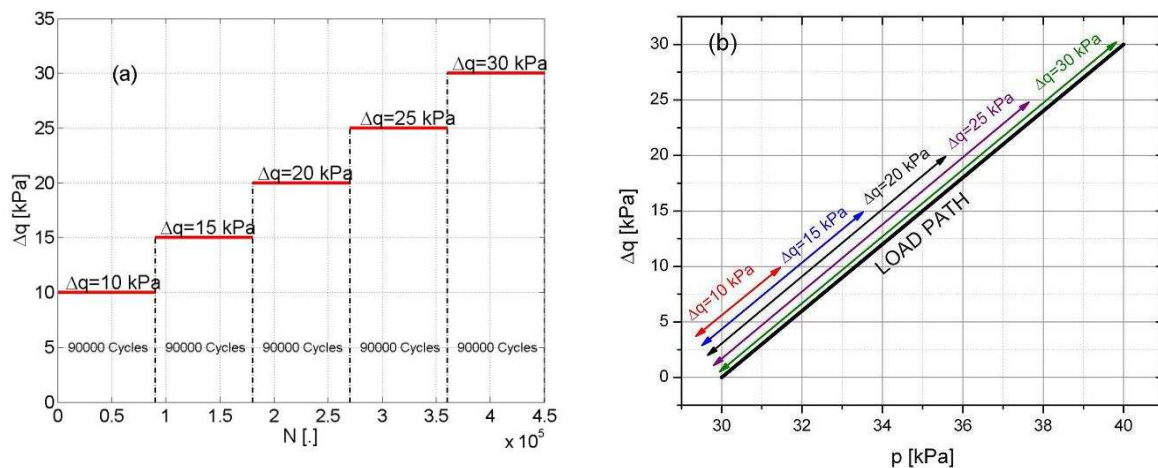
Figure III.24. Typical loading programme with procedure A: (a) deviator amplitude versus number of cycles; (b) corresponding stress paths in the (p, q) plane

A total of 5 tests were performed. The fifth was performed to assess the repeatability of the measurements (A2M10) under saturated conditions and with 'M' loading shape (Table III.8).

Table III.8. List of tests performed following procedure A

Test Code	Material	ρ_d	σ_3	Load shape	Moisture content
A1M4				'M'	4%
A2M10				'M'	10%
A3S4	Lab. ITL	2.01 Mg/m^3	30 kPa	'Sine'	4%
A4S10				'Sine'	10%
A5M10				'M'	10%

III.6.1.2 Testing procedure B: limited number of cycles

The testing procedure B aims to investigate the effect of loading history on the evolution of the dynamic parameters of soil (resilient modulus and damping ratio). The loading amplitude levels increased and decreased and a short number of cycles (100 cycles per loading level) were applied for each loading level (Figure III.25). The same loading shapes, 'M-shaped' and 'sine-shaped' were used but the stress amplitudes reached larger values up to Δq=200 kPa. The samples submitted to this loading procedure B were previously tested with procedure A, thus the test conditions were similar and the sample was conditioned by previous loadings under Δq= 30 kPa following procedure A. Thereby, results in procedure B were influenced by

the previous loadings in procedure A. This influence mostly involves the cyclic loading amplitudes lower than Δq=30 kPa, at which low modulus or damping ratio evolutions are expected.
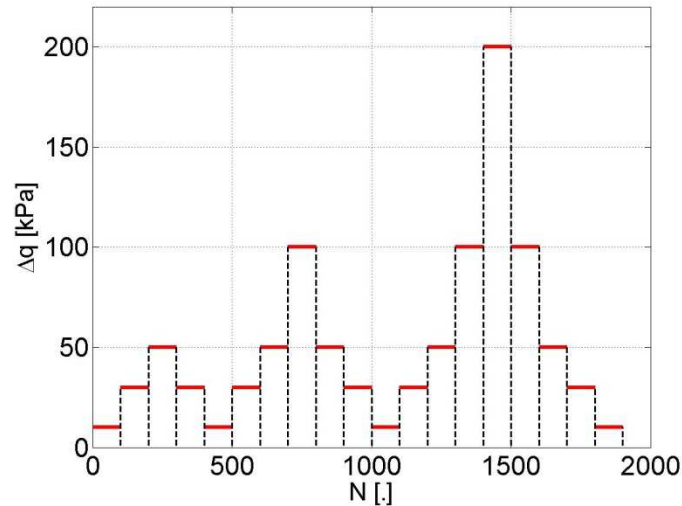
Figure III.25. Loading scheme for procedure B

The five specimens submitted to procedure A loading were subsequently submitted to procedure B testing (Table III.9).

Table III.9. List of tests performed following procedure B

Test Code	Material	ρ_d	σ_3	Load shape	Moisture content
B1M4				'M'	4%
B2M10				'M'	10%
B3S4	Lab. ITL	2.01 Mg/m^3	30 kPa	'Sine'	4%
B4S10				'Sine'	10%
B5M10				'M'	10%

III.6.1.3 Testing procedure C: cyclic deformation controlled test

While procedures A and B correspond to force-controlled tests, procedure C was displacement-controlled test. Moreover, the corresponding cyclic strain amplitudes were very small (even lower than $\Delta\varepsilon_1=\pm10^{-5}$, equivalent to the low strain amplitudes induced by traffic). Local strain sensors were used in this test. Both axial and radial strain sensors were installed

on the sample (Figure III.26). For each test, 2 axial sensors and 2 or 3 radial sensors (average results between them were taken into account in order to estimate sample's strains) were used.
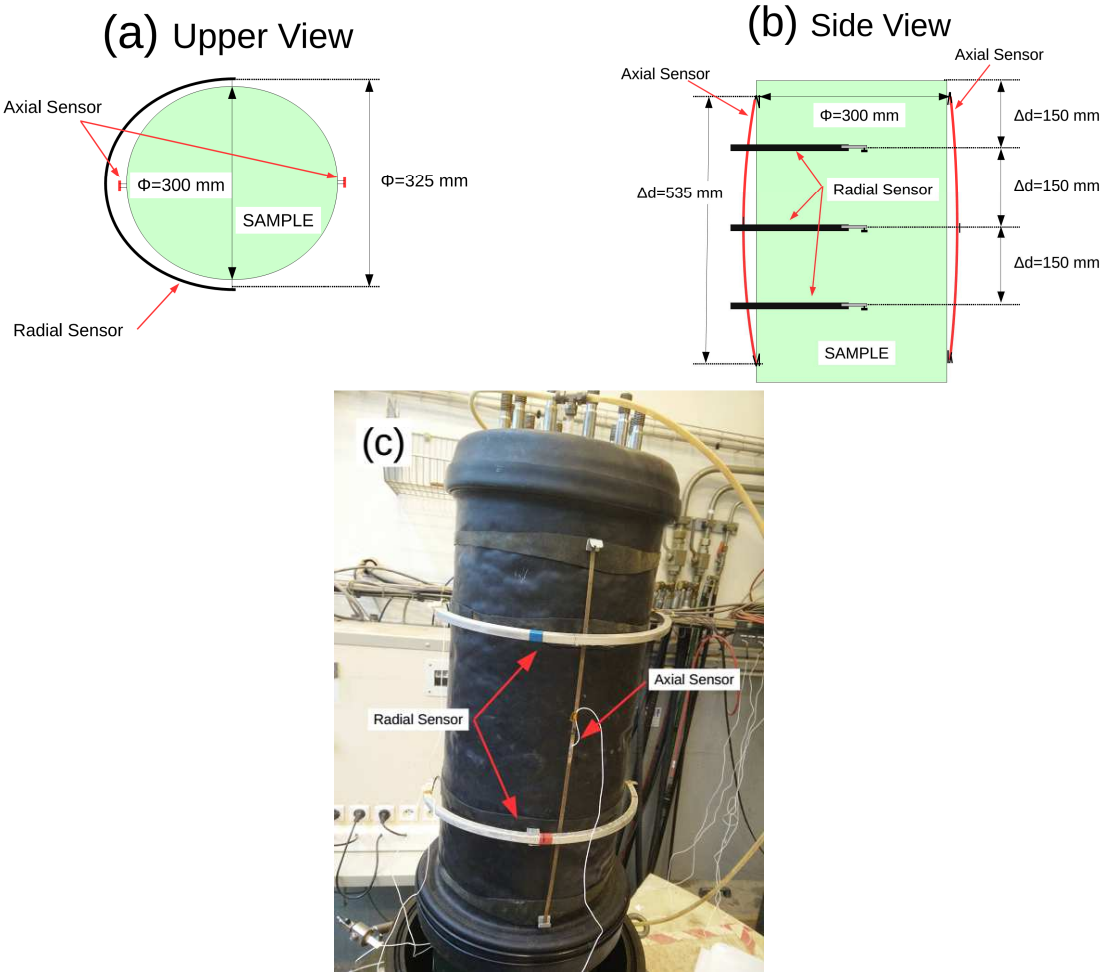
Figure III.26. Local strain sensors: (a) and (b) top and side schemes; (c) view of the specimen equipped with the sensors

The two axial sensors are 540 mm long and 5 mm wide. Strain gauges were installed in the middle of the metallic support. During the installation, a small buckling was induced to the rest position of the axial sensor. The voltage measurements were done during the test, and they are correlated to a displacement between the two boundaries of the metal plate through the sensor calibration curve. The radial sensors follow the same principle, but with the strain gauges glued to a small plate of 30 mm long at the end of a circular aluminium support (of 330 mm of diameter). The voltage differences were correlated to the variations of the diameter of the sensors (distance between two boundaries). These displacement variations (axial and radial) are correlated to the axial and volumetric strains since the initial dimensions of the sample are known:

$$\Delta d_i = f_i(V_i) - f_{i0}(V_{i0}) \tag{III.13}$$

where Δd the displacement between the two ends of sensor i calculated from the function $f(V)$ over parameter V, the voltage from sensor i. Note that each of the 5 installed sensors has different translation functions. In the case of axial strain, only axial sensors were used:

$$\varepsilon_1 = -\frac{\left(\dfrac{\Delta axial_1 + \Delta axial_2}{2}\right)}{L_{axial}} \tag{III.14}$$

where L_{axial} is the initial distance between boundaries of sensors 1 and 2, ε_1 is the axial strain, $\Delta axial_i$ is the axial displacement between boundaries of sensor i. The initial distance between boundaries of sensors 1 and 2 was 535 mm. A minus sign was adopted to convert the data into positive compression strains. The volumetric strains were calculated as follows:

$$\varepsilon_3 = -\frac{\left(\dfrac{\Delta radial_1 + \Delta radial_2 + \Delta radial_3}{3}\right)}{D_{radial}} \cdot 100 \tag{III.15}$$

$$\varepsilon_v = \varepsilon_1 + 2\varepsilon_3 \tag{III.16}$$

Where D_{radial} is the initial distance between the boundaries for radial sensors, $\Delta axial_i$ is the axial displacement between boundaries of sensor i, ε_3 is the strain in the radial direction and ε_v the volumetric strain. The initial distance between the boundaries is 325 mm for the radial sensors.

The loading protocol is shown in Figure III.27 and the test conditions are shown in Table III.10. 50 cycles of compression/extension for 11 cyclic strain amplitudes were considered. The applied strains levels ranged from 0.005% to 0.1 in steps of 0.01% (except for the first step). After application of each strain amplitude level, the residual cumulated

axial stress after 50 cycles was brought back to zero (less than 0.5 kPa of residual cumulated axial stress in average). The applied loading frequency was 0.1 Hz and the sampling frequency was 10 Hz. In addition, three values of the confining pressure σ_3 were applied (25, 50 and 100 kPa).
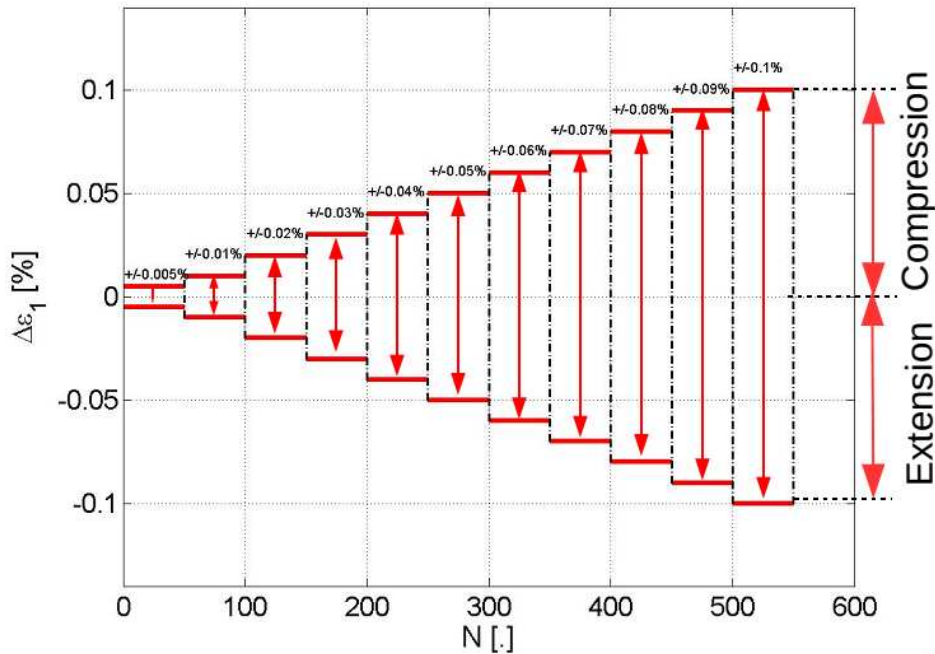
Figure III.27. Loading protocol in procedure C

Table III.10. Test characteristics following procedure C

Test Code	Material	ρ_d	σ_3	Load shape	Moisture content
C1C4	ITL-Lab	2.01 Mg/m^3	30 kPa	'C'	4%
			50 kPa		
			100 kPa		

III.6.1.4 Testing procedure D: simulation of train speed

The procedure D is similar to procedure A. This procedure aims to evaluate how the loading frequency affects the cumulative permanent deformation and how the dynamic parameters evolve. An 'M' shape signal was applied on ITL-Lab soil consolidated at σ_3=30 kPa. Three loading frequencies were considered, simulating train speeds of 100, 160 and 200 km/h, respectively (Figure III.28). Note that the inter-axles wavelength excites a frequency of f_{axles}= 10 Hz for v_T=100 km/h while the same wavelength excites f_{axles}=19 Hz for v_T=200 km/h. When higher frequencies were attempted (v_T=200 km/h), the servo-hydraulic

system did not properly follow the imposed 'M' signal and the middle part (between two simulated axles) was shorter than for the lower simulated speeds. This could impact the cyclic energy imposed to the sample. Therefore, following procedure A, in procedure D 90 000 cycles were applied for each stress amplitude level (from $\Delta q=10$ kPa to $\Delta q=30$ kPa). However, for each loading amplitude level, 30 000 cycles of the three considered simulated speeds were applied to complete a total of 90 000 cycles per level (Figure III.29). The corresponding test conditions are presented in Table III.11.
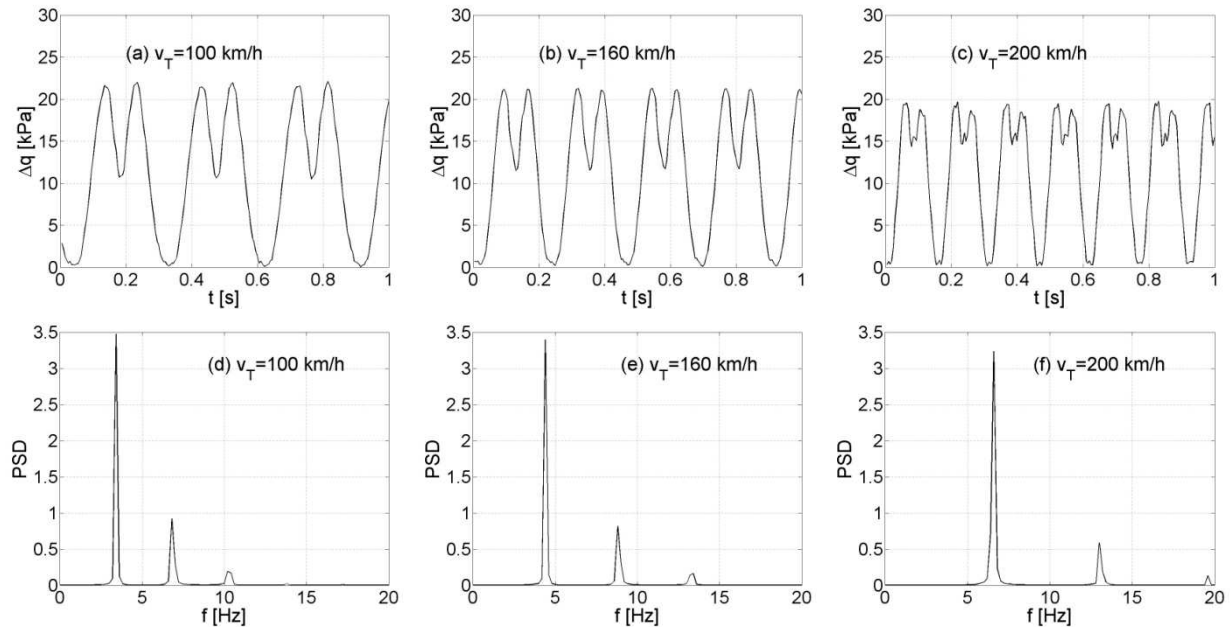
Figure III.28. One second duration of M-shape cyclic loading considering the speeds of (a) 100 km/h, (b) 160 km/h and (c) 200 km/h. Their PSD energy values are presented in (d), (e) and (f), respectively.
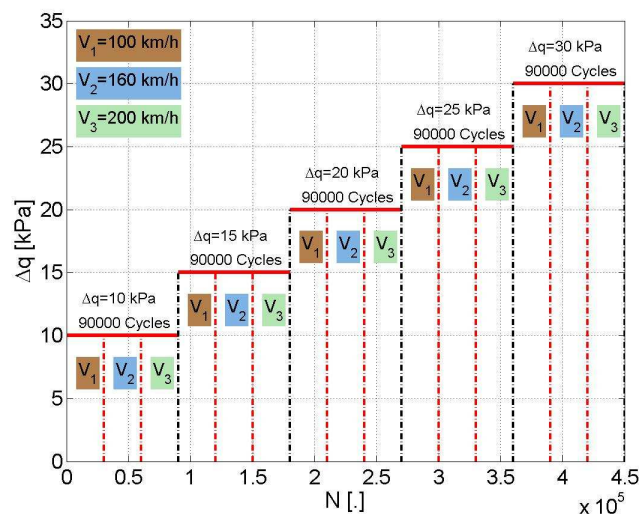
Figure III.29. Loading protocol in procedure D

Table III.11. List of tests following procedure D

Test Code	Material	ρ_d	σ_3	Load shape	Moisture content
D1M4	Lab. ITL	2.01 Mg/m^3	30 kPa	'M'	4%
D2M10				'M'	10%

III.6.2 Analysis methods and typical test results

III.6.2.1 Testing procedure A: large number of cycles

Following the literature review presented in chapter I (Duong et al., 2013; Gidel, 2001; Trinh, 2011), the permanent (plastic) and maximum resilient + permanent (elastic + plastic at the end of each cycle) axial strain are defined based on the axial strain signal response measured during the test (see Figure III.30).
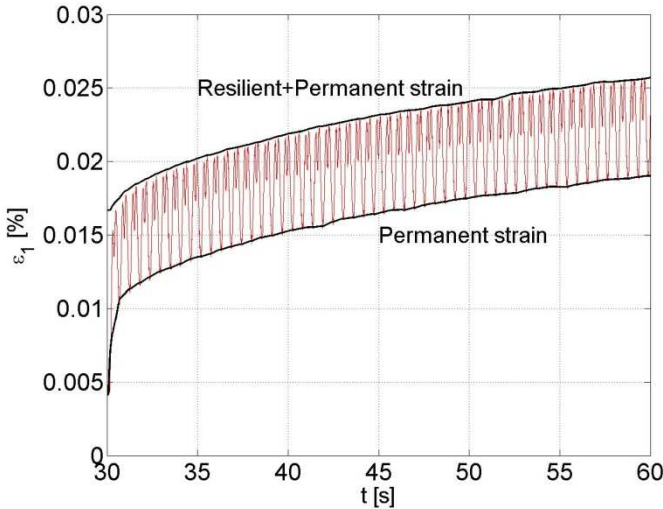
Figure III.30. Permanent and 'Permanent + Resilient' strain calculated from M-Shaped loading cycles - Zoom on the first 60 s in A2M10 test.

For each loading amplitude level, most of the cumulated permanent strain was produced during the first cycles (Figure III.31). In addition, this permanent strain became stable after about 20.000 cycles for each loading level. The permanent strain increased with the increase of loading amplitude when compared to the cyclic loading amplitude considered previously. Therefore, the elastic strain amplitude was more or less stable for the entire cyclic loading

amplitude levels. This elastic strain amplitude is thus related to the cyclic load amplitude (Figure III.31).
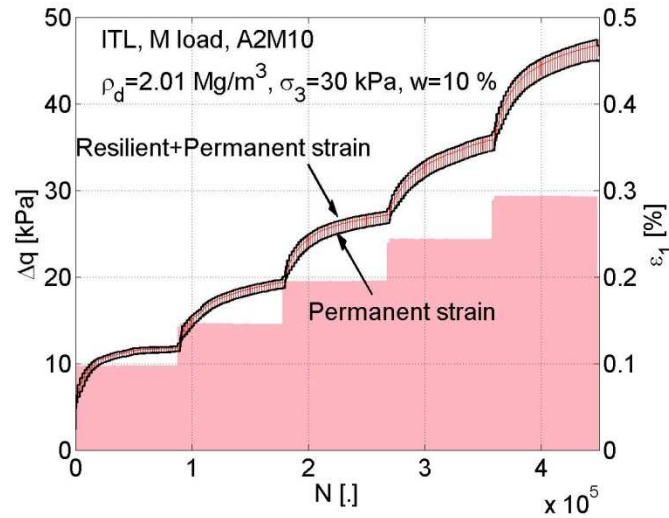
Figure III.31. Axial deformation from test A2M10 (the loading levels are also presented)

Supposing an ITL soil at OPM (*w*=4%), the maximum deviator stress value reached in the monotonic tests is $q = 298$ kPa (Figure III.19) under similar conditions as in 'procedure A' tests ($\rho_d = 2.01$ Mg/m³ and $\sigma_3 = 30$ kPa). If it is supposed that ITL-Lab and Sénissiat ITL behave in the same way for saturated conditions, the maximum deviator stress under monotonic loading should be about 183 kPa (Trinh 2011). Note that the ITL soil shear strength parameters were taken from Trinh (2011) in this estimation for σ_3=30 kPa.

A typical parameter that controls the cyclic behaviour of soils is the cyclic stress ratio n_{cyclic} that normalizes the cyclic loading amplitude by the shear resistance obtained under monotonic loading, q_{max}:

$$n_{cyclic} = \frac{\Delta q_{cycle}}{q_{max}} \tag{III.17}$$

The corresponding values of n_{cyclic} applied in the tests are presented in Table III.12.

Table III.12. Estimated cyclic stress ratio values for cyclic loading amplitudes considered in the tests following procedure A under saturated and OPM conditions

Δq_{cycle}	n_{cyclic} (OPM)	n_{cyclic} (Saturated)
10 kPa	0.03	0.05
15 kPa	0.05	0.08
20 kPa	0.06	0.11
25 kPa	0.08	0.14
30 kPa	0.10	0.16

As cyclic loading amplitudes are small compared to the static soil shear strength (Table III.12), the permanent deformations, after each level, are quite small (up to $\varepsilon_1^p \sim 0.5\%$ in the saturated case). Therefore a low level of repeatability is obtained using this type of material (Gidel, 2001), especially when there is variability in soil initial state. The permanent deformation (ε_1^p) for each loading level depends on the previous loading history. Nevertheless, it is possible to estimate the "real" soil behaviour by eliminating the effect of previous loading history (as if only one loading level had been applied to the soil) following the method presented by Gidel (2001) for unbound granular materials (presented in Chapter I). As 90 000 cycles were applied for each cyclic sequence, the total permanent deformation estimated for each of the first 90 000 cycles under each stress amplitude is calculated as:

$$\left(\varepsilon_1^p\right)_{\Delta q_i}^N = \left(\varepsilon_1^p\right)_{\Delta q_{(i-1)}}^N + \left(\partial\varepsilon_1^p\right)_{\Delta q_i}^N \tag{III.18}$$

being $\left(\varepsilon_1^p\right)_{\Delta q_i}^N$ the total estimated permanent deformation for cycle number N at loading level Δq_i, $\left(\varepsilon_1^p\right)_{\Delta q_{(i-1)}}^N$ the total estimated permanent deformation at cycle number N estimated for the previous loading level (if any), $\left(\partial\varepsilon_1^p\right)_{\Delta q_i}^N$ the relative permanent axial deformation at cycle number N and at loading level Δq_i (assuming that it starts at zero for its first cycle). An example of this permanent deformation estimation for two successive cyclic loading amplitudes levels is given in Figure III.32.
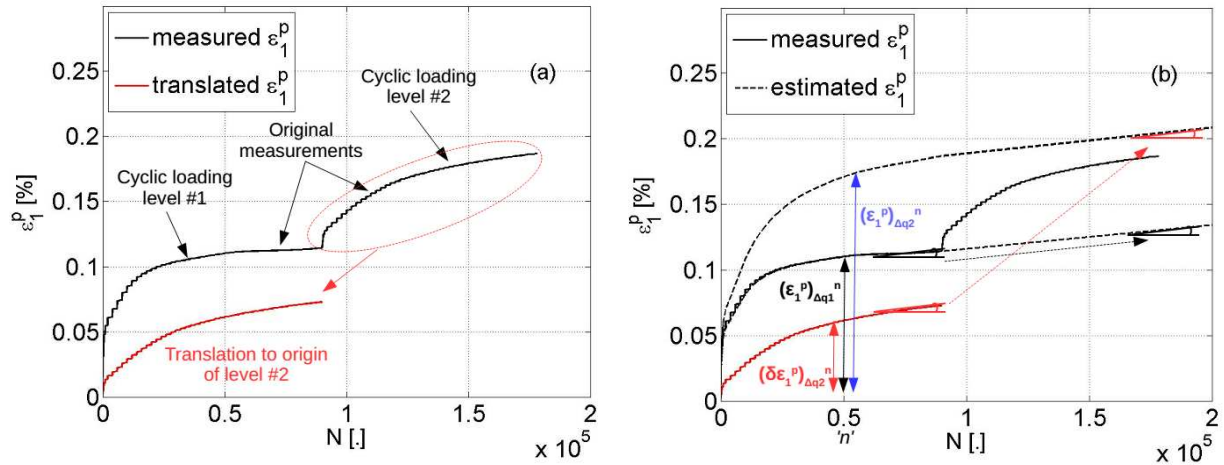
Figure III.32. (a) Translation of permanent deformation of level 2 through the origin of previous loading level; (b) identification of permanent deformation parameters used for the deformation estimation

This estimation is accurate for the first 90 000 cycles (number of cycles applied for each cyclic loading level with procedure A). Beyond, the estimation could be inferred by extrapolating the slope defined by the permanent deformation evolution of the last 100 cycles at each stress loading level. This extrapolation leads to larger estimated permanent deformations at 450 000 cycles than that measured at 450 000 cycles when the cyclic loadings are performed level by level.
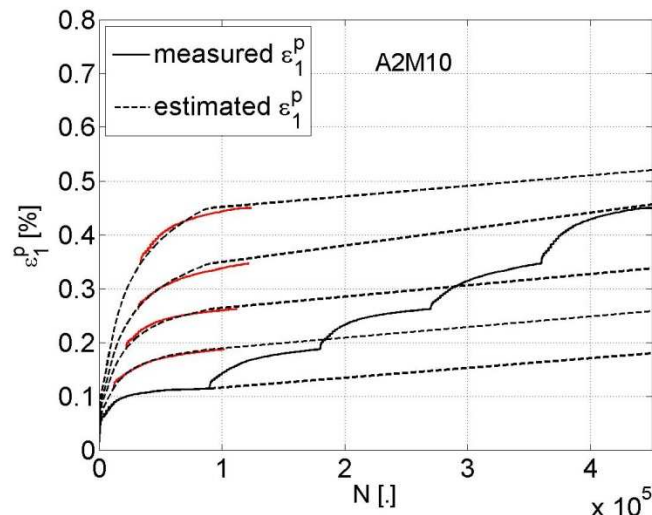
Figure III.33. Extrapolation of the shape of permanent deformations evolution considering loading history for test A2M10

Figure III.33 shows that the relative (partial) deformation of a stress loading level (in red) fits with a part of the estimated total permanent deformation. Figure III.34 is a zoom the first

90 000 cycles from Figure III.33, where the permanent cumulative deformations begin to stabilize in case of low cyclic loading amplitudes.
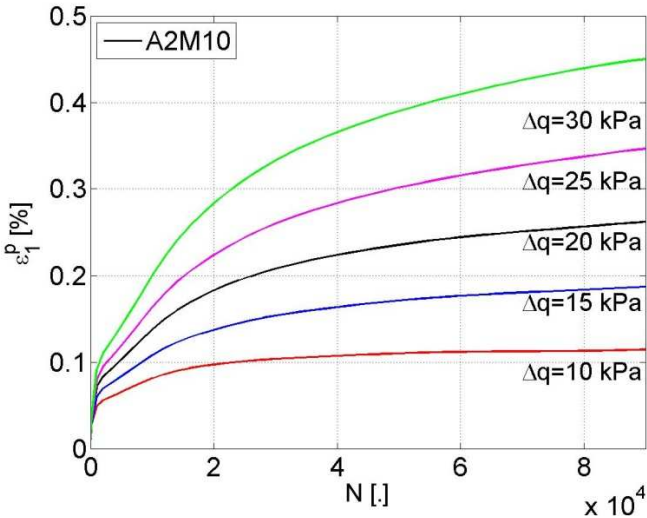
Figure III.34. Corrected shape of permanent deformation evolution for the tested loading amplitudes

Even though the repeatability of this type of tests is poor (Gidel, 2001), the shape and the relative permanent deformation registered for each loading level in the two equivalent tests (A2M10 and A5M10) are very similar (Figure III.35). An average difference of 10 % in relative permanent deformation for each loading level was found.
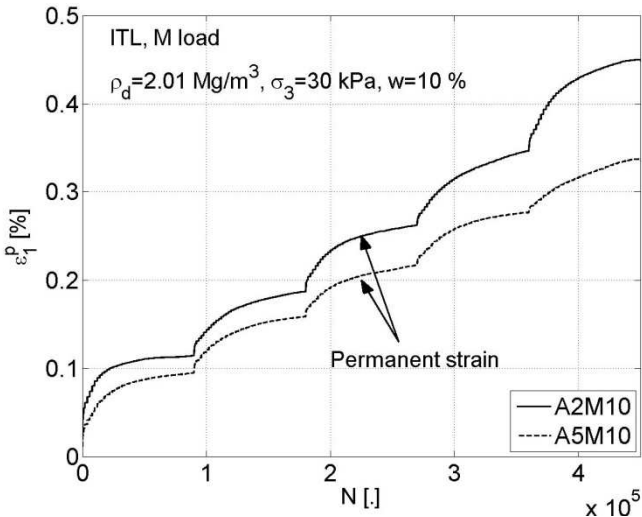
Figure III.35. Comparison between the permanent deformations obtained from tests A2M10 and A5M10

Taking into account the estimated permanent deformation at 90 000 cycles for each loading stress level, it may be seen in Figure III.36 that for the equivalent tests and loading shapes, the evolution of this deformation is similar, following a quasi-linear trend with the cyclic stress level.
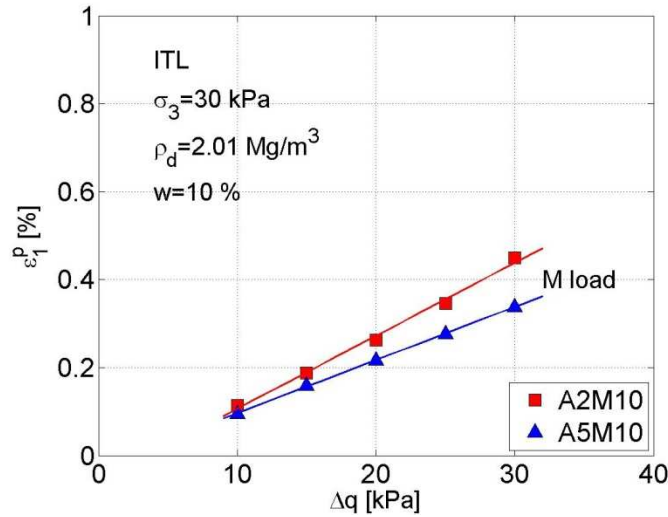
Figure III.36. Comparison between the maximum permanent deformations reached after each cyclic sequence in A2M10 and A5M10 tests

Once the total permanent deformation evolution for each stress loading level was assessed, the procedure A tests are also used to analyse the frequency-domain behaviour of the load (deviator stress) and the response (axial deformation) signals. Figure III.37 shows the Power Spectrum Density (PSD) of the deviator stress (left) and axial strain (right) signals of the last 10 cycles applied at Δq=10 kPa loading level. These PSD signals are determined by:

$$PSD = \frac{2 \cdot |FFT(X)|^2}{L_{vec}}$$
(III.19)

where *FFT(X)* the Fast Fourier Transform of signal *X*, constituted of a vector of L_{vec} positions. The resulting *PSD* vector is calculated for half the sampling frequency f_s and has (L_{vec}/2+1) positions. The test signals were registered at 200 Hz; however, only the first 15 Hz are shown in Figure III.37 because no more excited frequencies were found beyond this frequency using the signal shown in Figure III.22a.

Each loading frequency (Figure III.37a) caused a proportional response in the same frequency of its strain signal (Figure III.37b). In this case, three frequencies are excited because the test corresponds to a 'M shape' load.
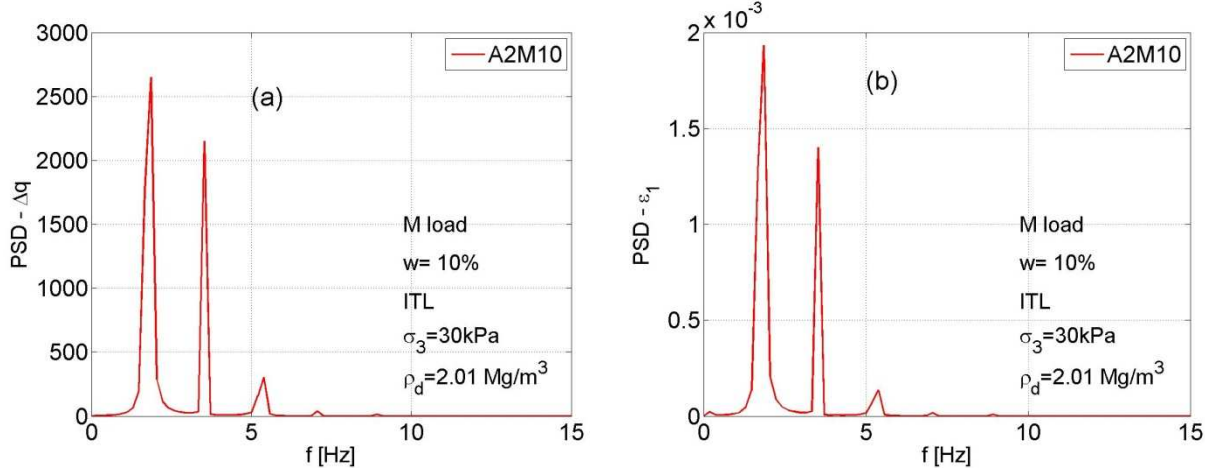
Figure III.37. (a) Power Spectrum Density (PSD) of deviator loading signal; (b) PSD of the corresponding axial deformation response (Δq=10 kPa / 10 cycles)

The evaluation of the energy contribution of each frequency is shown in Figure III.38. A low-pass Butterworth filter was applied for every 0.1 Hz. The resulting signals (from 0 Hz up to the filtered frequency) were subjected to a trapezoidal integration. All values (every 0.1 Hz) were collected in a vector (Figure III.38) that represents the amount of incremental energy provided by each frequency, starting from 0 Hz. Both signals, the loading and its response, are similar in shape evolution. Most of the energy is provided by the larger wavelengths (lower excited frequency, f_{bogies}=1.78 Hz). The frequencies beyond 6 Hz do not provide additional energy, neither in the loading signal nor in the response signal.
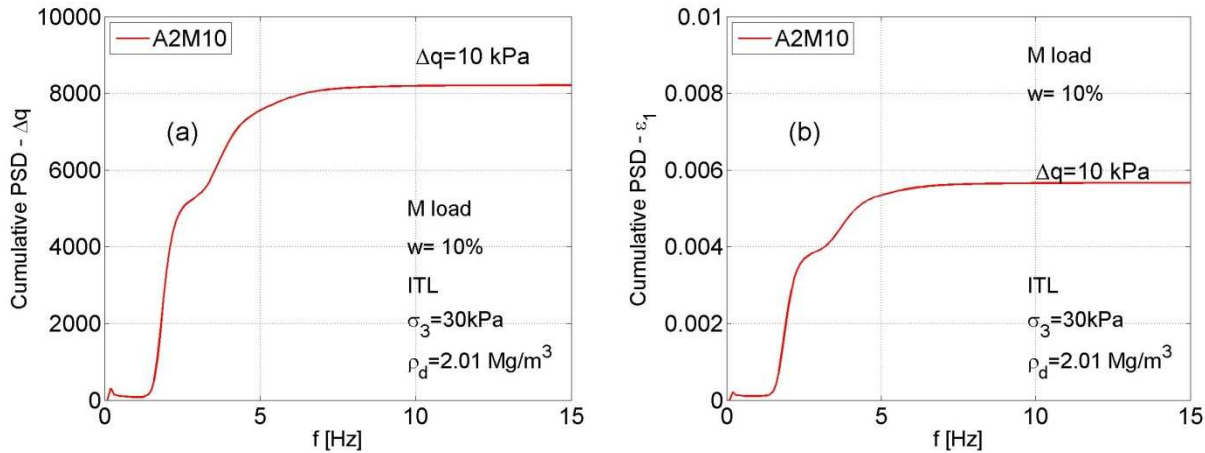
Figure III.38. Cumulative energy per frequency calculated from the PSD of (a) deviator loading signal and (b) the axial strain response (Δq=10 kPa / 10 cycles)

III.6.2.2 Testing procedure B: limited number of cycles

All tests with procedure B ended when the total axial deformation reached ε_1=6%, limit value for the triaxial cell. As the samples were loaded previously at Δq=30 kPa with large number of cycles (procedure A), only larger amplitudes (Δq=50, 100 and 200 kPa) increased the deformation. The cyclic stress ratios estimated for the different hydric conditions are given in Table III.13. These values show that for a cyclic loading amplitude $\varDelta q$=200 kPa the n_{cyclic} value is about 67 % of the ITL monotonic resistance if the sample is at OPM moisture content, while the value reached 110% if the sample is saturated.

Table III.13. Estimated cyclic stress ratios for cyclic loading amplitudes applied with procedure B under saturated and OPM conditions

$\varDelta q_{cycle}$	n_{cyclic} (OPM)	n_{cyclic} (Saturated)
10 kPa	0.0336	0.0546
30 kPa	0.1007	0.1639
50 kPa	0.1678	0.2732
100 kPa	0.3356	0.5464
200 kPa	0.6711	1.0929

As the cyclic stress ratios are greater than those in the tests with large number of cycles (Procedure A), the permanent deformations are also much larger. When the cyclic shear amplitude is $\varDelta q$=100 or 200 kPa, the maximum axial deformation (ε_1=6%) is reached after a small number of cycles when the sample is saturated (Figure III.39). Only the ITL samples at OPM (w=4%) can sustain the entire test with procedure B.
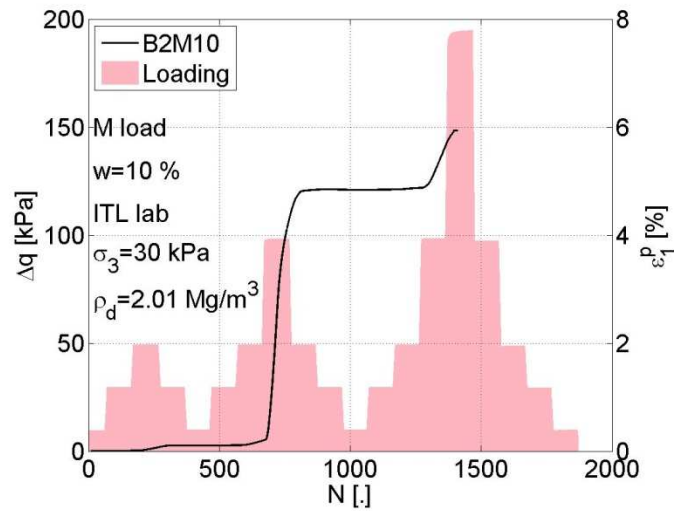
Figure III.39. Cyclic loading amplitude (magenta) and sample's permanent deformation evolution in B2M10 test

The hysteresis loops are estimated using the deviator stress signal applied to the sample and the axial strain response. Examples of these loops (4 different cyclic load amplitudes) are shown in Figure III.40. The 'curved' shape obtained is typical for coarse grained materials, even ballast (Suiker et al. 2005).
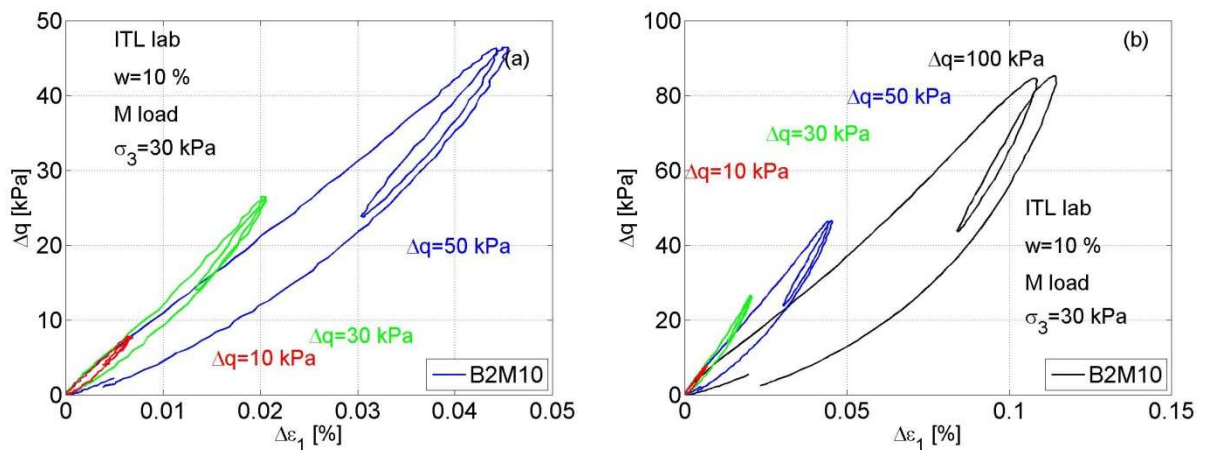
Figure III.40. Hysteresis loops in 'stress-strain' diagram for different cyclic loading amplitudes: (a) zoom on 10, 30 and 50 kPa cyclic amplitudes; (b) 100 kPa cyclic amplitude

In the stress-strain diagram, the intermediate unloading/reloading (middle part between two simulated train axles) for each 'M shaped' hysteresis loop presents a higher slope than the entire loop (unloading till $\Delta q = 0$ kPa).
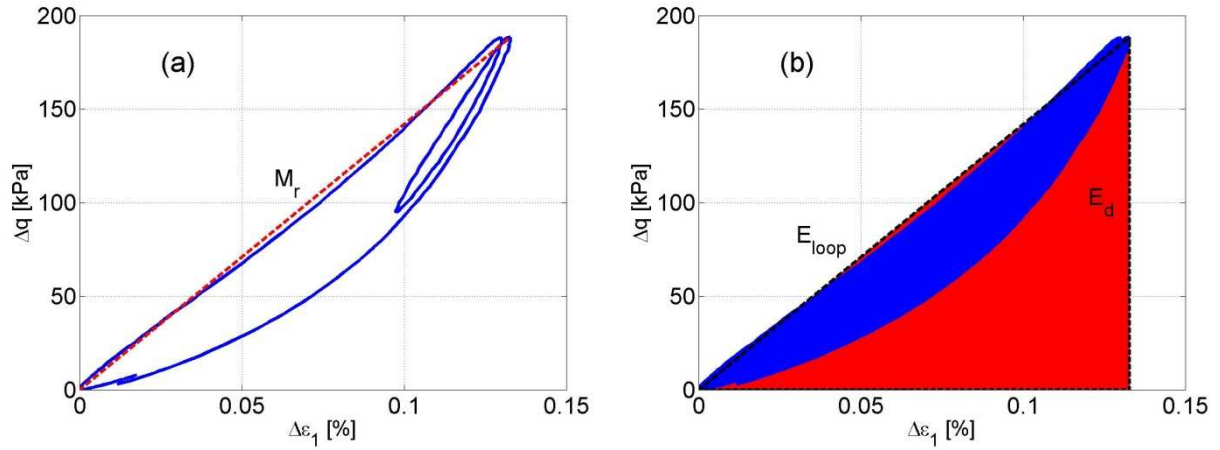
Figure III.41. (a) Resilient modulus (M_r); (b) damping ratio (D_r) estimation from the hysteresis loop obtained with procedure B

Figure III.41 shows how the resilient modulus and damping ratio D_r are calculated from the hysteresis loops with procedure B. The resilient modulus is calculated as the secant modulus from the origin point using the expression:

$$M_r = \frac{\Delta q}{\Delta \varepsilon_1}$$

(III.20)

The damping ratio is calculated for each cycle by:

$$D_r = \frac{E_{loop}}{4 \cdot \pi \cdot E_d}$$

(III.21)

where E_{loop} is the energy dissipated defined by the surface of the hysteresis loop in the 'stress – strain' diagram and E_d is the equivalent elastic energy defined by the surface of the triangle formed by the value of the maximum deviator stress, the value of the maximum strain and the origin.

The resilient modulus and the damping ratio are calculated for all loops and the results from two equivalent tests (B2M10 and B5M10) are shown in Figure III.42 allowing the assessment of the test repeatability. The resilient modulus is stable for the first two stress levels (Δq=10 and 30 kPa, already reached during procedure A). However, when higher amplitudes (Δq=50, 100 and 200 kPa) are applied, the resilient modulus decreases strongly during the

207

first cycles and then becomes stable again. The higher the amplitude, the higher the modulus decrease: for the ITL saturated material, in the beginning $M_r = 60$ MPa, and at the last cycle $M_r = 20$ MPa under $\Delta q=200$ kPa). A good repeatability is observed in terms of resilient modulus for all the cycles in both tests.

Concerning the damping ratio, higher loading amplitudes cause a rapid increase of this parameter. Nevertheless, the damping ratio rapidly attenuates after the first cycles and tends to stabilize. When the changes of deviator cyclic loading amplitudes are higher, the damping ratio increase is also higher during the first cycles but the final stabilization is longer. The damping ratio for both tests differs mainly during the first cycles, after that the order of magnitude being the same (about 2-3%).
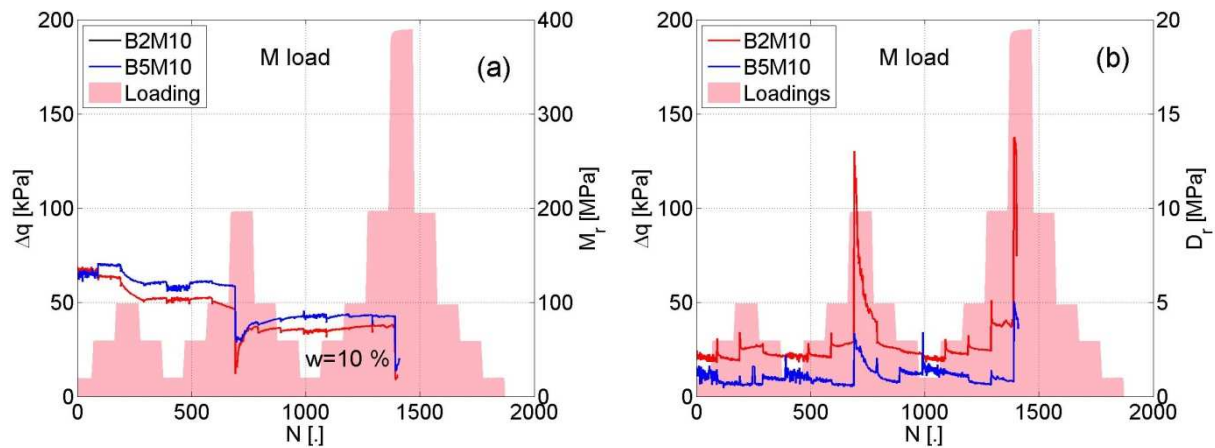
Figure III.42. (a) Resilient modulus; (b) damping ratio evolution from B2M10 and B5M10 tests

III.6.2.3 Testing procedure C: deformation controlled cyclic test

The hysteresis loops obtained for tests with procedure C are different from the previous ones because loading was controlled in deformation instead of stress. As a result, negative values of deviator q were induced. An example of the corresponding loading/unloading loop in the stress-strain diagram is presented in Figure III.43.
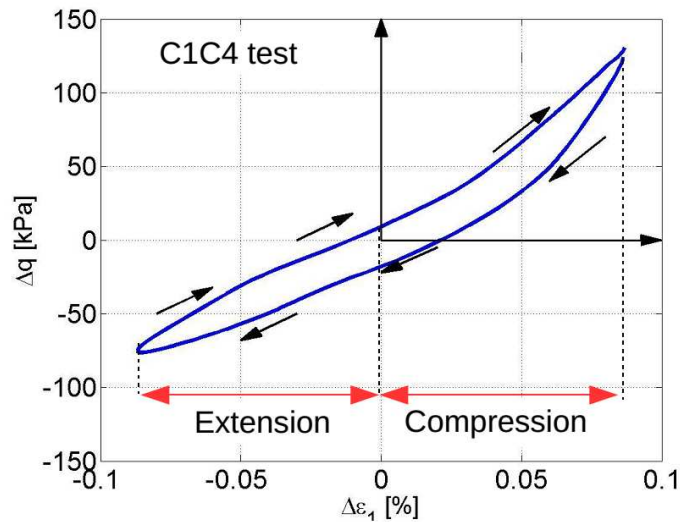
Figure III.43. Example of hysteresis loop corresponding to test with procedure C ($\Delta\varepsilon_1$=+/- 0.1%, σ_3=100 kPa)

The last cycles of each loading level (eleven for each of the three confining pressures) were further analysed (Figure III.44). It is observed that the loop surface increases with the strain amplitude while the secant slope (related to elastic behaviour) of each loop decreases at higher strains amplitudes. Moreover, the absolute value of maximum and minimum deviator stresses (compression and extension) increase for all the strain amplitudes. Concerning the extension part (negative values of q), a stress asymptote is found corresponding to each confining pressure. Lower negative values of deviator stress asymptote are observed for higher confining pressures. Furthermore, the loop surface (related to the dissipated energy) also increases with the confining pressure. The curve-shaped hysteresis loops, typical for coarse-grained soils, are similar to the previously obtained compression loading loops from tests with procedure B.
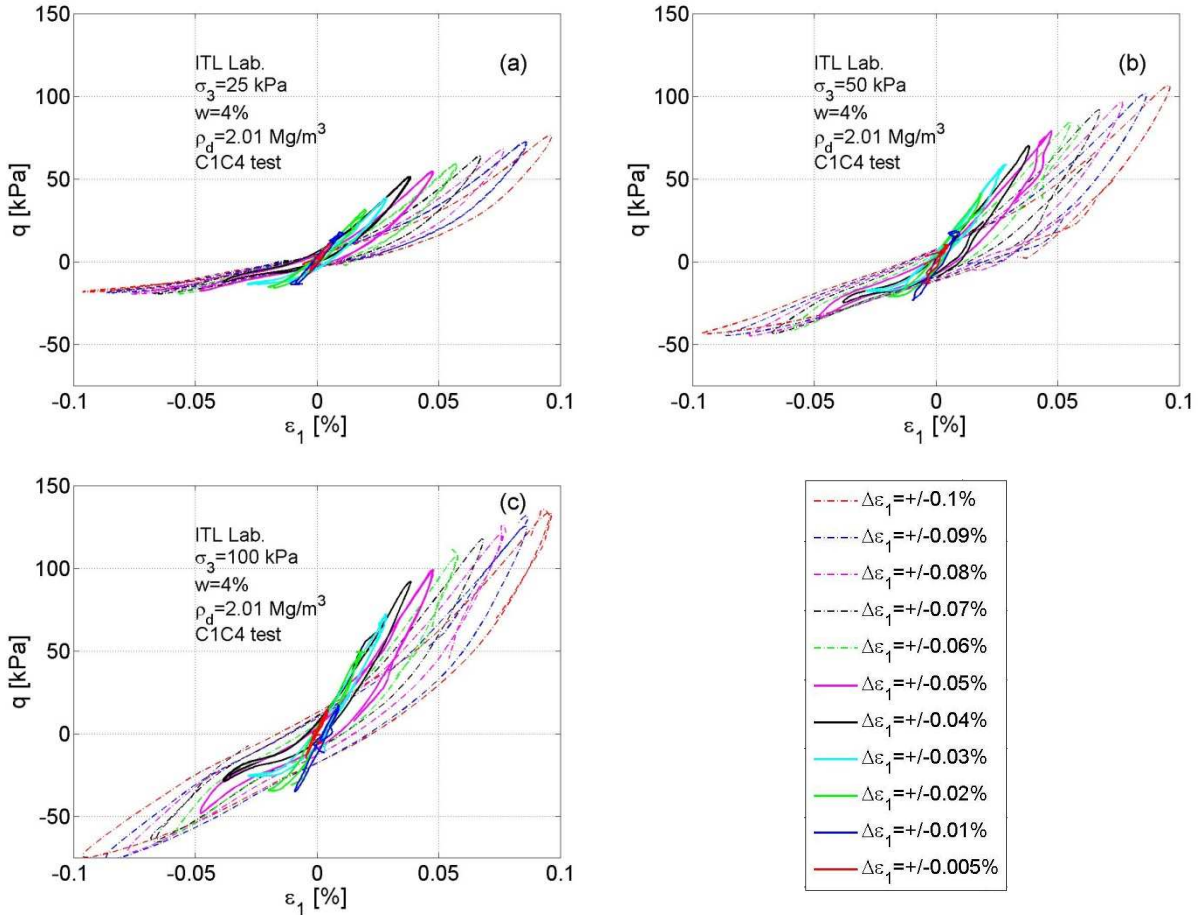
***Figure III.44. Last hysteresis loops for different deformation levels: (a) σ₃=25 kPa case;
(b) σ₃=50 kPa case; (c) σ₃=100 kPa case***

The calculations of the resilient modulus and the damping ratio for these loops are slightly different from the compression-only cyclic loading cases (testing procedures A, B and D). The resilient modulus is also calculated as the secant modulus. But instead of measuring the slope from the origin till the maximum deviator stress amplitude, it is measured from the lowest point (extension) to the highest point (compression), as shown in Figure III.45a. For the damping ratio calculation, the equivalent elastic energy considered is the triangle between the origin point, the maximum positive strain value and the corresponding deviator stress value (Figure III.45b).
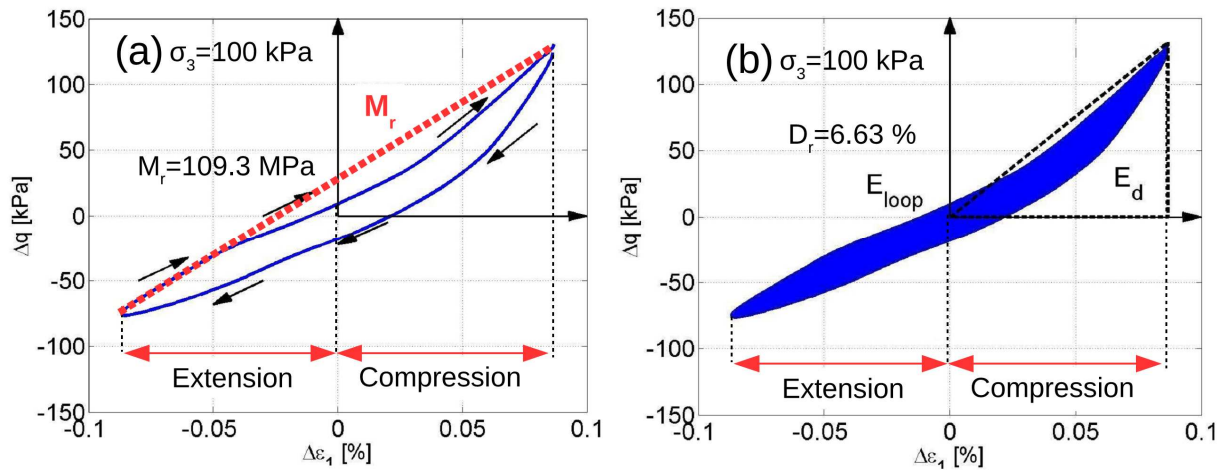
Figure III.45. (a) Resilient modulus (M_r); (b) damping ratio (D_r) estimation from hysteresis loop obtained with testing procedure C (C1C4 test, σ_3=100 kPa)

III.6.2.4 Testing procedure D: simulation of train speed

Procedure D is similar to procedure A. However, different loading frequencies were applied at each cyclic stress loading level. An estimation of permanent axial deformations considering the loading history can be assessed with these tests. Even if the results cannot be compared to those obtained with 'procedure A' because of the different loading frequencies used in both tests, the shape of each cyclic amplitude level fits with the estimated axial strain deformation evolution (Figure III.46), justifying the previously presented method for unbound materials.
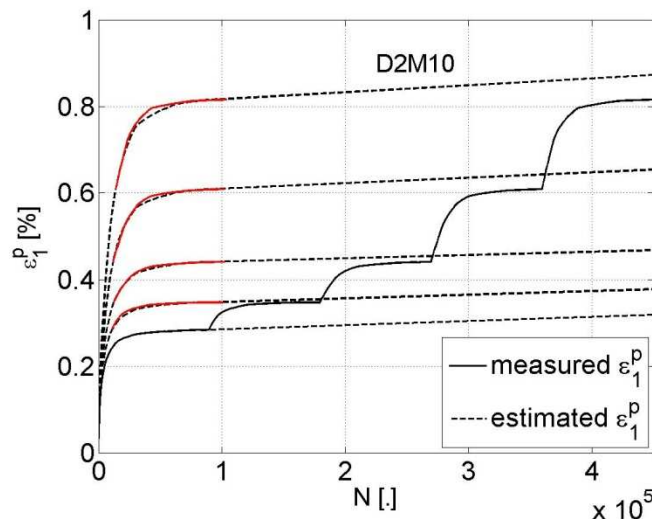
Figure III.46. Estimation of permanent deformation shape definition considering loading history

According to the results presented in Figure III.46, the estimated axial strain deformation in the first 90 000 cycles for the 'procedure D' cycles are shown in Figure III.47.
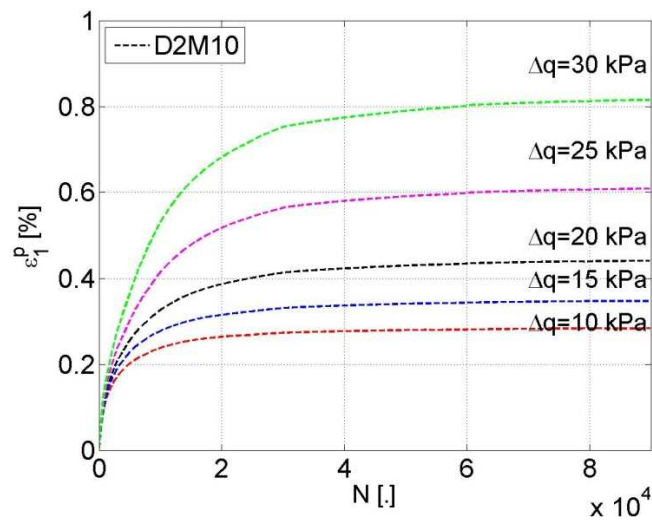
Figure III.47. Permanent deformation evolution shape's correction for the tested loading amplitudes

The hysteresis loop taken into account in further analysis is the last one of every simulated train speed (cycle number 30 000 per each simulated train speed, when the loop's shape was stabilized). Unlike in 'procedure A' (low frequency loading), the servo-controlled system was not able to properly follow the designed signal for the load (and their cyclic stress amplitudes) for high speeds (v_T=200 km/h) when the sample was saturated (w=10 %). Moreover, when the simulated speeds increased, there was an increase of difference between the designed load and the actuator performance (Figure III.48). Larger differences were found in the actuator performance for saturated ITL-Lab soil. This was due to the softer ITL material compared to the ITL at OPM moisture content on one hand and the high frequency loading on the other hand. A degradation of loop's shape in the middle of M-bogie load (between two axles' load) is observed when higher train speeds were simulated. The resilient modulus and the damping ratio are calculated in the same way as for 'procedure B' (Figure III.41).
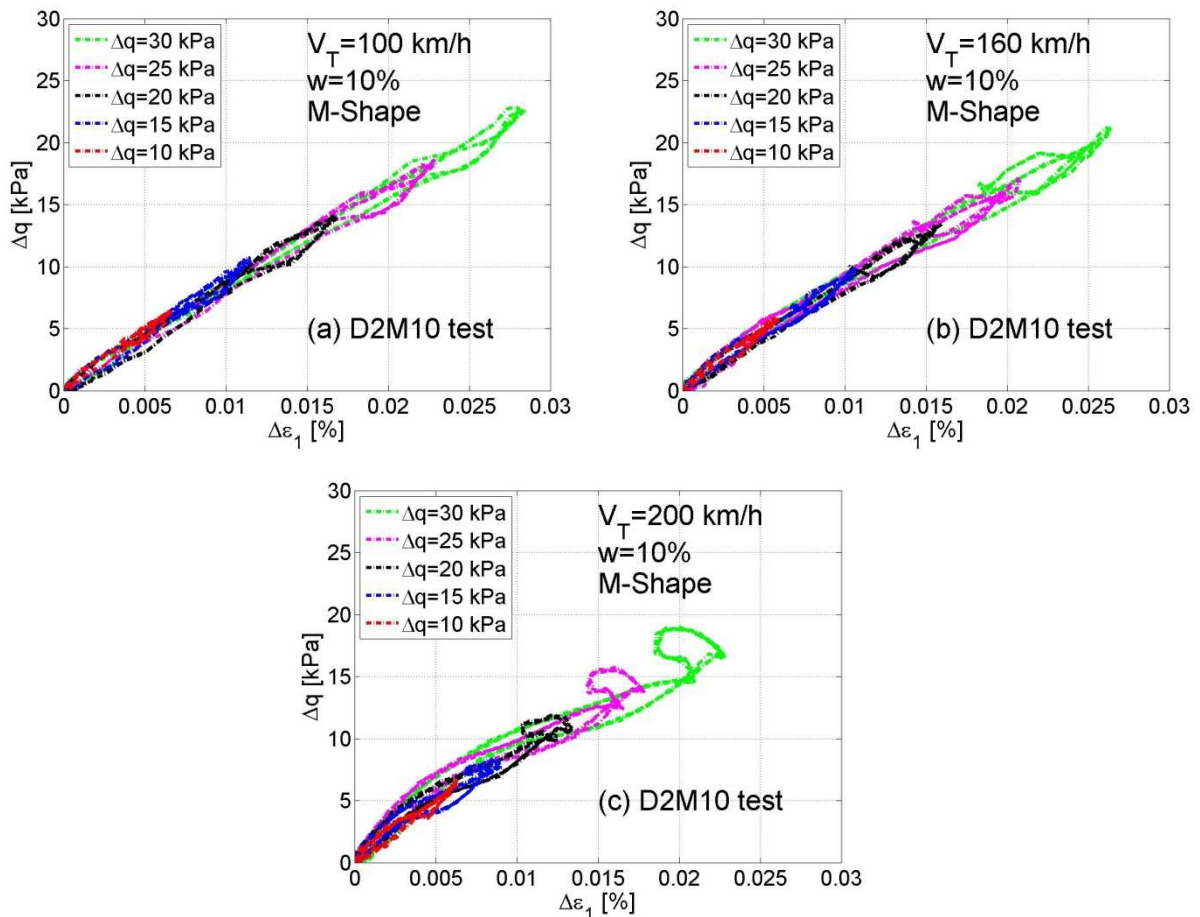
Figure III.48. Last hysteresis loops for different loading amplitudes: (a) 100 km/h speed; (b) 160 km/h speed; (c) 200 km/h speed

III.6.3 Parameters influencing the permanent deformation

In this section, the different parameters influencing the permanent deformation are described.

III.6.3.1 Moisture content effect

One of the parameters that influence most the accumulation of permanent deformations is the soil moisture content or water content *w*. A comparison between the accumulation of axial deformation for a saturated soil and another at OPM moisture content (Figure III.49) shows that for the saturated case the total cumulated axial strain can be 100 times larger, whatever the cyclic loading shapes ('M' or 'Sine'). Further examination shows that the total permanent strains (ε_I^p) seem to be higher in the case of 'Sine' cyclic loading. When ITL-Lab soil is

saturated (w=10%) a total permanent deformation of $\varepsilon_1{}^p$=0.9% is obtained at N=450 000 for 'sine-shaped' cyclic loading while $\varepsilon_1{}^p$=0.45% when loaded with 'M-shaped' cycles.
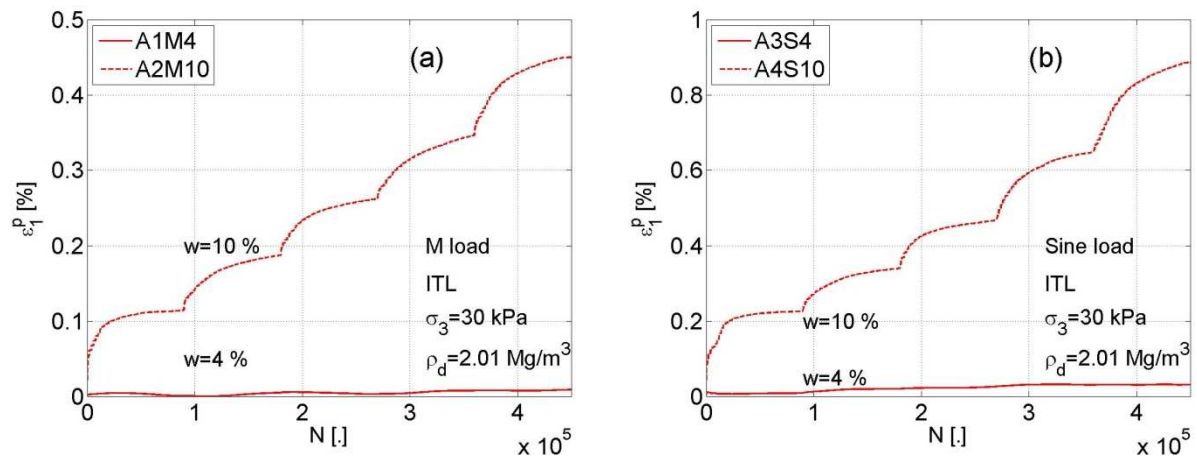
Figure III.49. Difference between permanent deformation results obtained at w=4% and w=10% performing (a) 'M-Shape' and (b) 'Sine-shaped' cyclic loading using testing procedure A

Regarding the tests with procedure D, the results are similar. The accumulation of permanent strains is about 100 times higher for the saturated ITL samples as compared to the OPM ITL samples (Figure III.50).
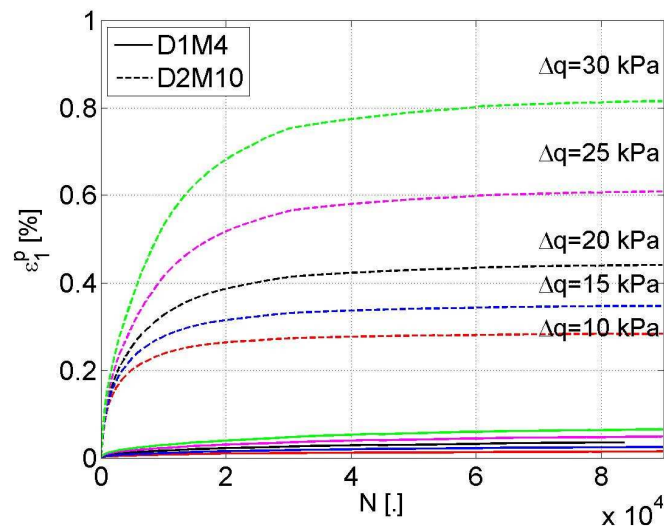
Figure III.50. Comparison of the accumulation of axial permanent deformation for the different cyclic stress levels between tests D1M4 (OPM) and D2M10 (saturated)

Moreover, the shape of the strain accumulation curves depends mainly on the hydric state of soil (Figure III.51). If the cumulative permanent strains for each cyclic loading level are

214

normalized with respect to the maximum permanent strain reached for a given loading level, in the saturated samples more than 80% of their total strain is produced during the first 20 000 cycles (Figure III.51). However, the accumulation of permanent deformation is slower in the case of OPM, with only about 50% of the total axial strain developed for the same cycles (Figure III.51). Also, regarding the deformation accumulation rate, the saturated soils accumulate axial strains about twice faster than the unsaturated soils.
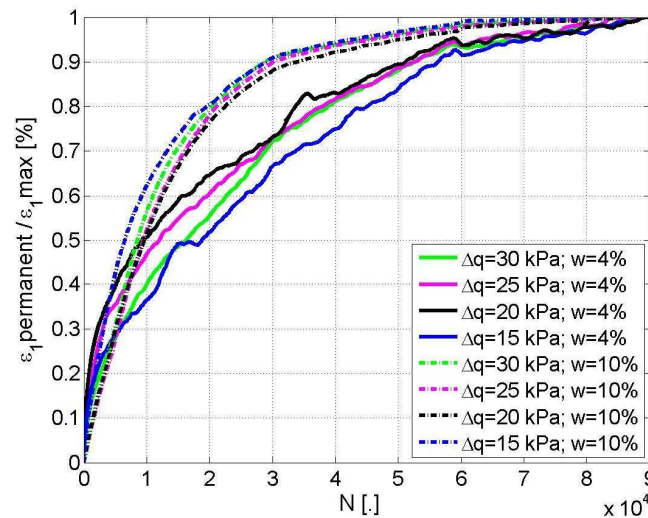
Figure III.51. Normalized permanent deformation for different cyclic loading amplitudes for two moisture contents (w=4% and w=10 %). Tests D1M4 and D2M10

III.6.3.2 Amplitude of deviator stress amplitude and shape of loading signal

Once the test repeatability in terms of cumulative permanent strain was demonstrated under the same loading conditions (shape and cyclic loading amplitudes), the influence of the loading amplitude and shape can be assessed. Figure III.52 shows that both 'M' and 'Sine' cyclic loading shapes follow a quasi-linear trend with cyclic loading amplitude in the range of loading amplitudes considered. Note that the total permanent deformation (ε_I^p) in Figure III.52 is the axial permanent strain value at 90 000 loading cycles as shown in Figure III.34. In addition, it is observed that the total permanent deformations increase more rapidly (larger slope) in the case of 'Sine' cyclic loadings as compared to the 'M' shape cyclic loadings. Note that only the results from the saturated tests are shown because the axial cumulated permanent strains in case of OPM samples are close to zero ($\varepsilon_I^p \sim 0\%$) for all the cyclic loading amplitudes.
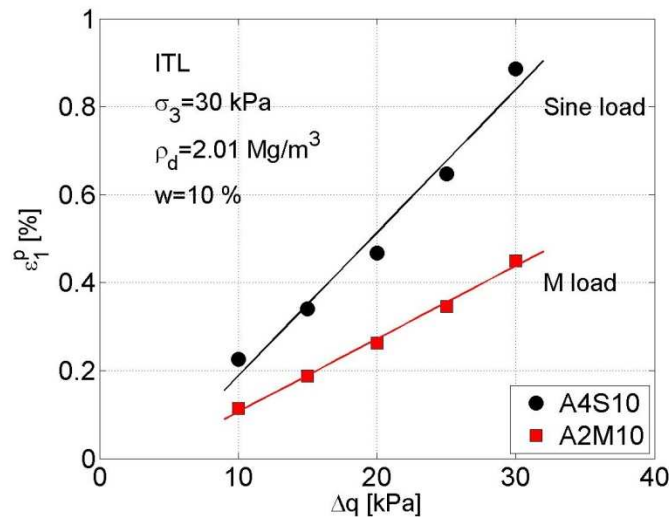
Figure III.52. Influence of the cyclic loading shape on permanent deformations accumulation for different cyclic loading amplitudes with procedure A

III.6.3.3 Influence of loading frequency

In this sub-section, the reason why the 'Sine' shape cyclic loading caused larger deformations than the 'M' shape loadings is addressed. Firstly, the PSD of 10 cycle loading signal (Δq) is calculated (Figure III.53). These 10 cycles were the last ones of each cyclic sequence. For higher loading amplitudes, the same frequencies are excited, but more energy is transferred to the system. In the case of 'Sine' shape loading, only one frequency appears to be excited while three main frequencies are excited in the 'M' shape loading. Moreover, the amount of energy provided by each frequency seems to be directly related to the cyclic loading stress amplitude. Therefore, more energy seems to be provided in the low frequency range for 'Sine' shape loadings.
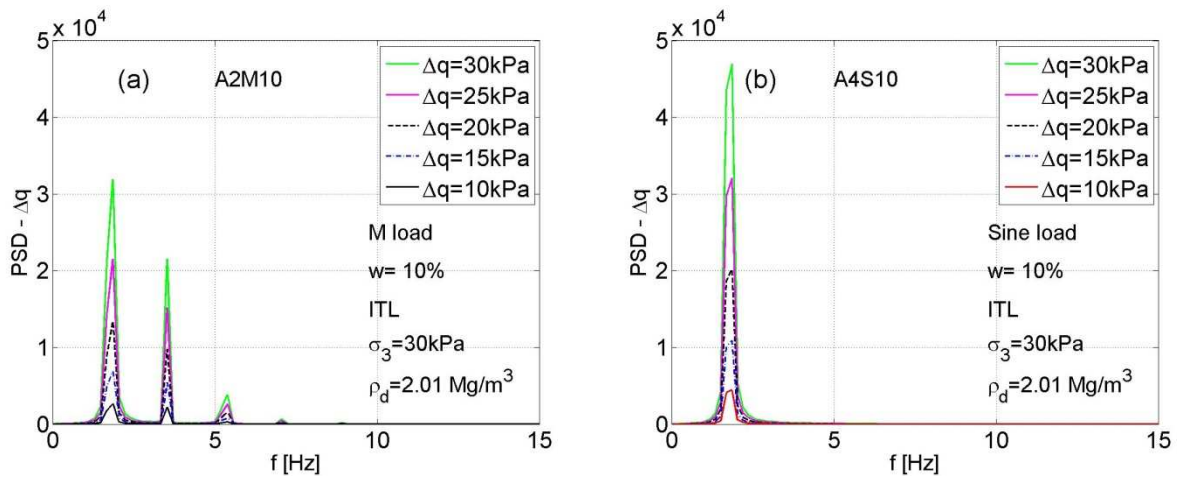
Figure III.53. PSD of deviator loading signal: (a) M-Shaped cyclic loading; (b) Sine-shaped loading (different cyclic loading amplitudes / 10 cycles)

Secondly, the PSD is determined for the response signal ($\Delta\varepsilon_1$) during the same 10 cycles (Figure III.54). Similar results are obtained: more energy is developed by the sample in the low frequency range under the 'Sine' shaped cyclic load. However, the energy amount is dispersed in the 5 first Hz for the 'M' shaped signal (depending on the excited wavelengths). The same energy amplification ratio with the cyclic loading stress amplitude is found as for the deviator stress signal case (Figure III.53). The cumulated energy per frequency is assessed for each curve by integrating the surface (trapezoidal integration) included in the PSD. This curves are calculated by integrating only the part below a given cut-off frequency (as explained in III.6.2.1) and repeating the operation every 0.1 Hz.
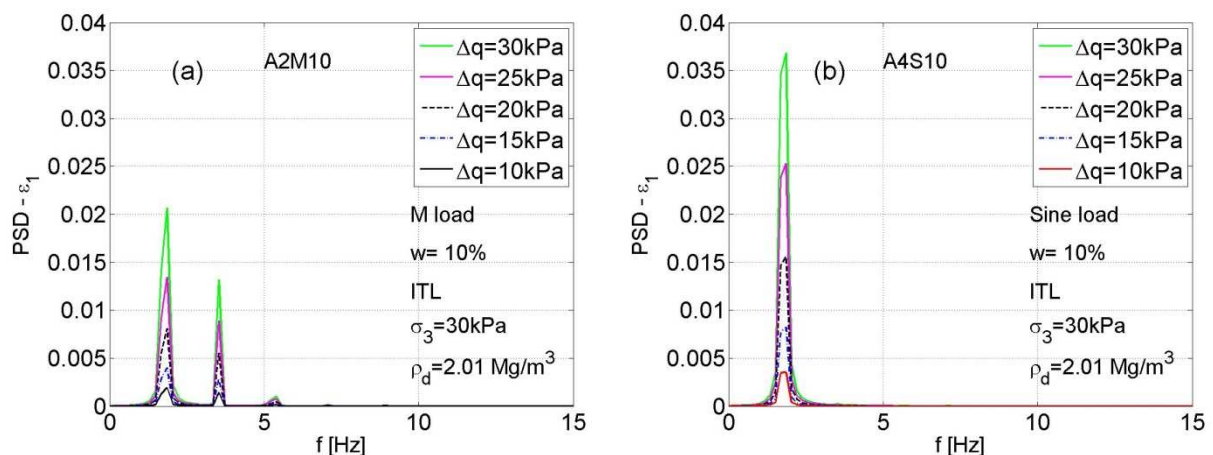
Figure III.54. PSD of axial deformation response: (a) 'M' Shaped cyclic loading; (b) Sine-shaped loading (different cyclic loading amplitudes / 10 cycles)

The results for a cyclic deviator stress amplitude Δq=10 kPa (all loading shapes and soil hydric states) are shown in Figure III.55. It is observed that the maximum load cumulative energy (Figure III.55a) is similar for the identical cyclic loading shapes ('M' or 'Sine') for lower moisture contents. Lower saturation rates induce slightly higher cumulative energy amounts in the loading signal. The 'Sine' loading signal develops its entire energy at only one frequency (about f = 1.78 Hz), and the 'M' cyclic load develops about 50% of the total energy at the inter-bogie frequency (f = 1.78 Hz), the rest of energy under loading frequencies being comprised between 2 and 5 Hz. Furthermore, the 'Sine' loading signal provides more energy for the 15 first Hz (frequency at which cumulative energy is stabilized) than the 'M' shape cyclic loading. However, the moisture content plays a significant role in the energy developed by the response signal, the axial strain signal (Figure III.55b). For instance, the saturated samples develop more energy in their response than the samples at the OPM moisture content. But the 'Sine' shape loading always induces more energy in the sample's response. This difference with the 'M' shaped loadings is larger if the sample is saturated. This is due to the larger energy content in the low-frequency range for the 'Sine' shape loadings. Moreover, similar tests (A2M10 and A5M10) give similar total cumulative PSD results at 15 Hz, justifying the coherence of results as well as the test repeatability.
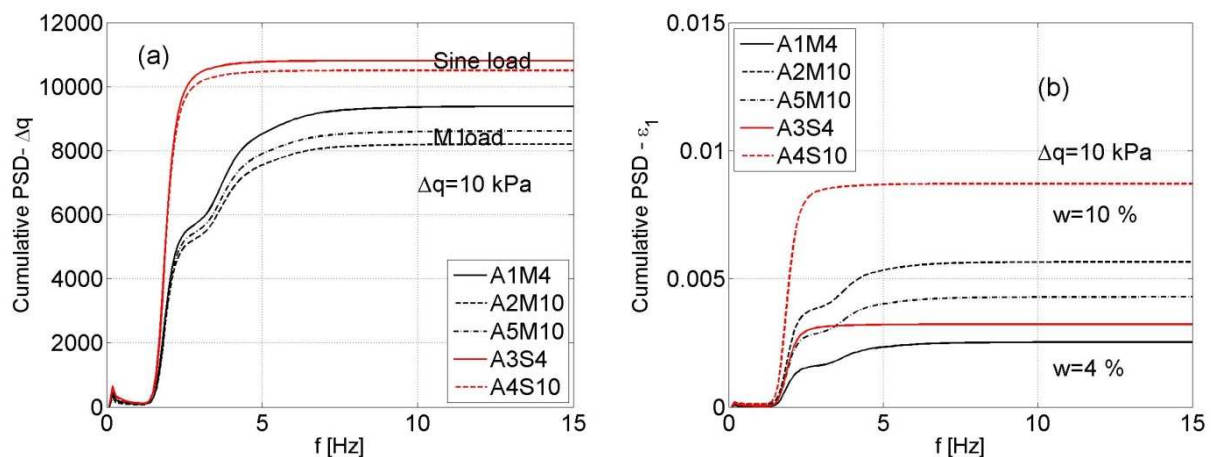
Figure III.55. (a) PSD of deviator loading signal and (b) axial deformation response (Δq = 10 kPa / 10 cycles). 'M' Shape and Sine cyclic loadings are considered under two different moisture contents (w = 4% and w = 10%)

The cumulated energy contained in the PSD stabilizes at 15 Hz for both the cyclic load (Δq) and deformation ($\Delta \varepsilon_1$) responses (Figure III.55). The influence of the small wavelengths (frequencies larger than f=2 Hz) is more significant in the 'M' shape loading signals at larger deviator stress amplitudes (for Δq=30 kPa these frequencies provide about 40% of the total

energy). Therefore, the parameter chosen to measure the amount of energy provided or developed by the system is the cumulative PSD energy at 15 Hz. The amount of cumulative PSD increases with the cyclic amplitude, for loading and response (Figure III.56).
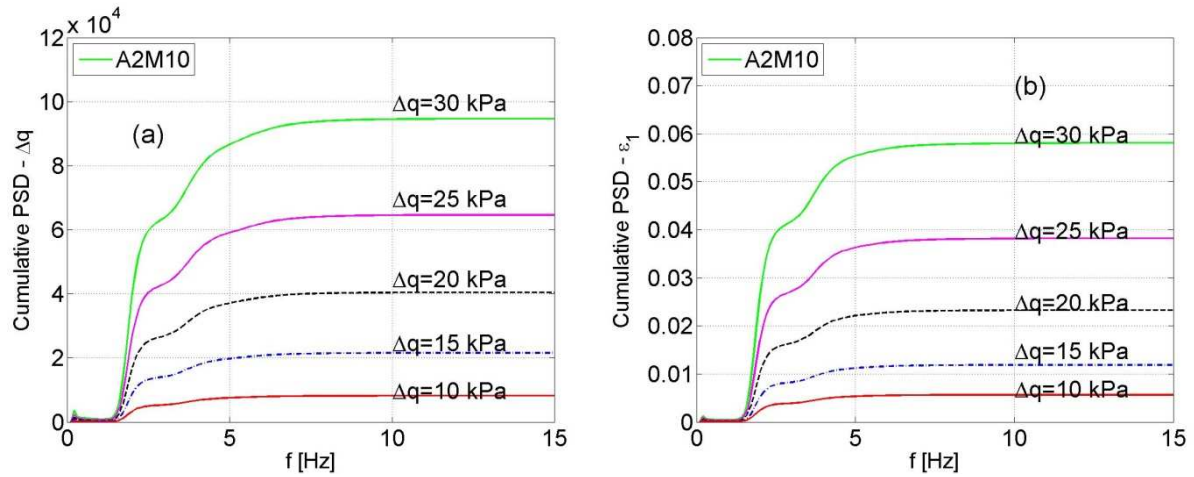
Figure III.56. Cumulative energy per frequency calculated from the PSD of (a) deviator loading signal and (b) the axial deformation responses (different cyclic loading amplitudes / 10 cycles)

The trend of total cumulative energy measured in the soil's response for different stress cyclic loading amplitudes is equivalent, showing the repeatability of tests (Figure III.57).
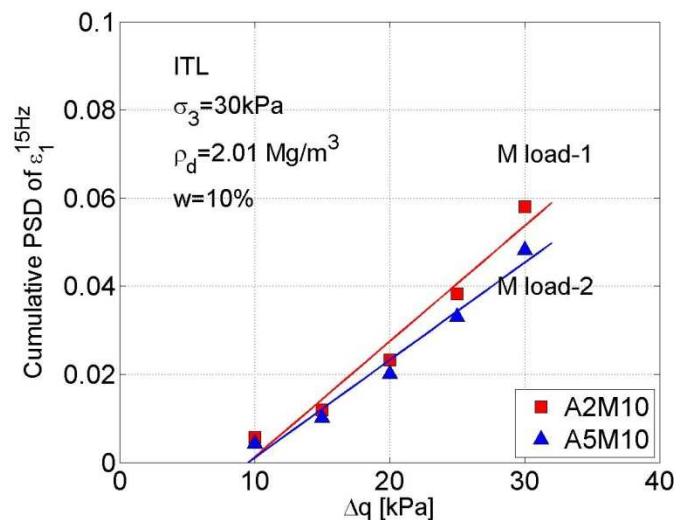
Figure III.57. Comparison between the maximum cumulative PSD energy developed by the soil's response (in 10 cycles) for each loading amplitude in A2M10 and A5M10 tests

219

III.6.3.4 Influence of energy content

The amount of energy in PSD diagrams measured on the response for 10 cycles increase with the considered loading amplitude. This energy content is calculated as the PSD surface included in the frequency domain for the first 15 Hz. Moreover, it could be calculated for the cyclic loading (Δq) and response ($\Delta \varepsilon_1$). Therefore, the shape of a load (and its response) determines the energy applied to the sample. Different shapes and sample states (moisture content) may lead to different energy content in sample responses (Figure III.58). Thus, the relationship between load (deviatoric stress) and response (axial strain) also depend on loading frequency (depending on the loading shape). Saturated samples always develop more energy in their responses than samples at OPM moisture content, and the loading shape differences are more notorious in the saturated case. Furthermore, the 'Sine' shape loads developed more energy in their response signal on saturated samples than 'M' shape loads (Figure III.58). While for the OPM samples, a similar amount of energy developed for both loading shapes in the range of cyclic amplitudes considered.
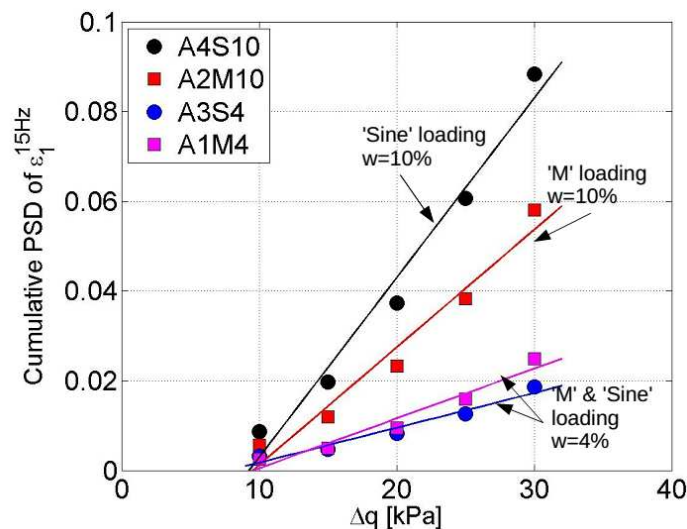
Figure III.58. Influence of the cyclic loading signal shape on the maximum cumulative PSD developed by the material's response (in 10 cycles) for the cyclic deviator amplitudes considered

While the cumulative axial strains of OPM samples are almost zero, the value is about 0.5-0.8% for the saturated samples with procedure A ($N = 450\ 000$ cycles). It is appreciated that the total permanent deformation for each cyclic loading level is related to the developed energy under a cyclic loading (10 cycles of response in the stabilized section, last cycles of each loading level). Then, for each given soil state parameter (moisture content,

density, confining pressure, etc.), the permanent strain values at 90 000 cycles are related to the energy developed by the soil's response. These values show a quasi-linear relationship with the energy content at 15 Hz (Figure III.59) for saturated soil. However, for the soil at OPM moisture content, this straight line will be shorter in the energy content axis (because of the lower developed cumulative PSD energy for saturated soils), and the permanent strains are close to zero, that may result in a low slope line close to the x-axis (Figure III.59). Consequently, the ITL material's total permanent deformation at large number of cycles can be determined by the developed response signal energy (related to the loading cyclic shape) and the soil state conditions.
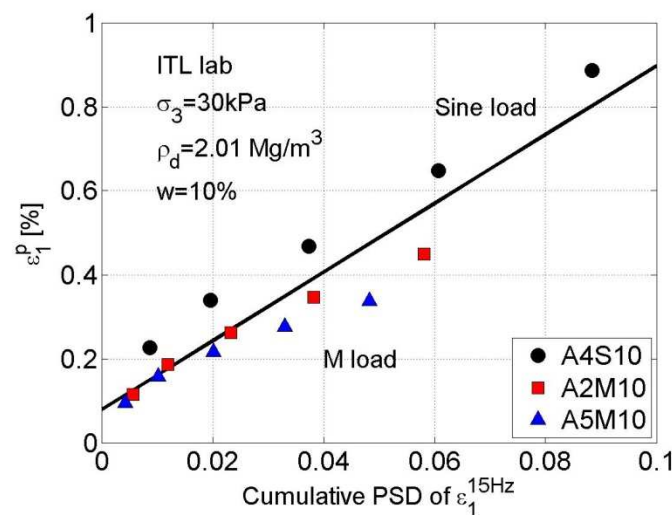
Figure III.59. Relationship between the maximum cumulative PSD energy developed by the material's response (during 10 cycles) and the maximum permanent deformation for each cyclic loading amplitude considered (w=10%)

III.6.4 Assessment of dynamic parameters

This sub-section focuses on the assessment of the evolution of the dynamic parameters under different loading conditions. The results with procedures B, C and D are used. Two dynamic parameters are investigated - the resilient modulus and the damping ratio. Several parameters like the cyclic strain amplitude, the loading frequency, the loading history and the soil state conditions can affect the two dynamic parameters.

III.6.4.1 Small strain behaviour

The evolution of the dynamic parameters, under different soil state conditions, is assessed based on the results from the tests following procedure C. Small strain amplitudes were induced to the samples to simulate the train-induced axial strains to the ITL, ranging from 0.005% to 0.1%. Regarding the evolution of resilient modulus M_r, there is a decrease (mainly for strains lower than $\Delta\varepsilon_1=10^{-5}$) when the cyclic amplitude of the strain increases (Figure III.60a). Moreover, M_r increases with the confining pressure, and the decrease with cyclic strain amplitude is parallel for the three confining pressures considered ($\sigma_3=25$, 50 and 100 kPa).

The damping ratio has similar values of about 5% for the cyclic strain amplitudes larger than $\Delta\varepsilon_1=0.04\%$ (Figure III.60b). For lower cyclic strain amplitudes, the hysteresis loop surface is too small to use for accurately estimating the damping ratio. A larger sampling frequency is needed in order to better define the hysteresis loops. Moreover, it seems that for the cyclic strain amplitudes ranging from $\Delta\varepsilon_1=0.04\%$ to $\Delta\varepsilon_1=0.1\%$, the confining pressure does not affect the damping ratio. The energy dissipated by the material with increasing cyclic strain amplitudes is proportionally the same as the induced energy for the considered strain amplitudes (constant ratio between induced equivalent elastic energy and dissipated energy by the sample).
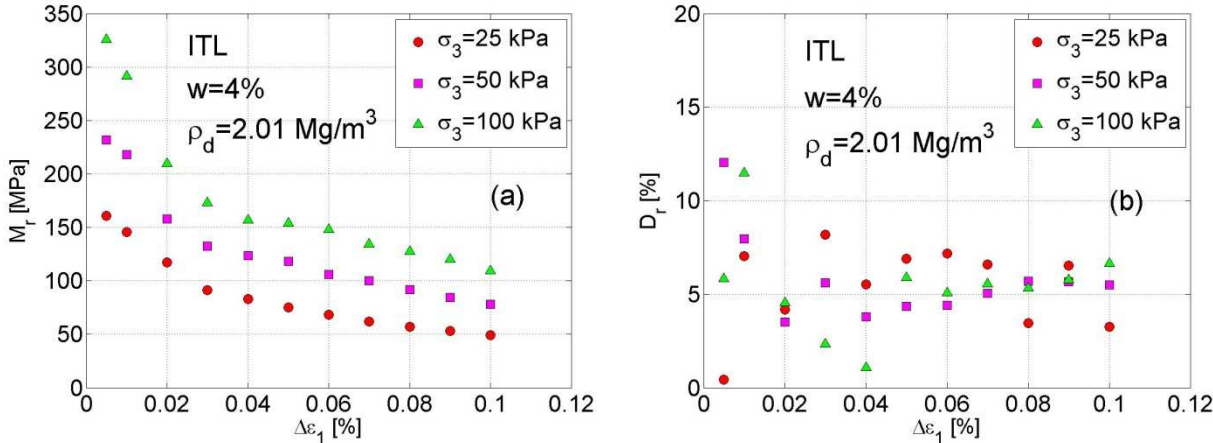
Figure III.60. (a) Resilient modulus; (b) damping ratio evolution under different strain amplitudes and confining pressures (procedure C)

III.6.4.2 Elastic modulus M_r evolution versus cyclic loading amplitude

The loading history affects the soil behaviour and the evolution of dynamic parameters. The resilient modulus is influenced by the cyclic loading history. In this sub-section, the tests with procedure B are used to assess this behaviour.

At the beginning of the test (Figure III.61a) when a low stress cyclic amplitude was applied (Δq=10 kPa), the maximum resilient modulus of the entire test was observed. However, a little noise around the average value can be appreciated due to the small size loops and the variability of the slope. Moreover, this noise around the mean value is found in different loading stages where these low cyclic stress amplitudes Δq=10 kPa were applied.

When the cyclic stress amplitude is increased, there is a sudden decrease of resilient modulus, mainly for the first cycles. Then, the resilient modulus starts to stabilize and recovers a part of the previous decrease till a new asymptotic value is reached. This recovery is about half the lost modulus value during the first cycles after a cyclic stress amplitude increase (Figure III.61b). Therefore, this modulus decrease happens when new higher cyclic stress amplitudes which have not been reached before are applied. The higher the cyclic stress amplitude, the higher the moduli decrease during the first cycles.

This modulus decreasing is mainly due to the large plastic deformations induced during these first cycles when a new stress level is applied. There is a link between the modulus decrease and the rate of permanent deformation. Nevertheless, if cyclic stress amplitude is lower than the maximum one applied previously, the resilient modulus remains more or less constant at the previous level. In addition, for lower stress cyclic amplitudes, a slight increasing trend appears (for instance from cycle N = 1500).
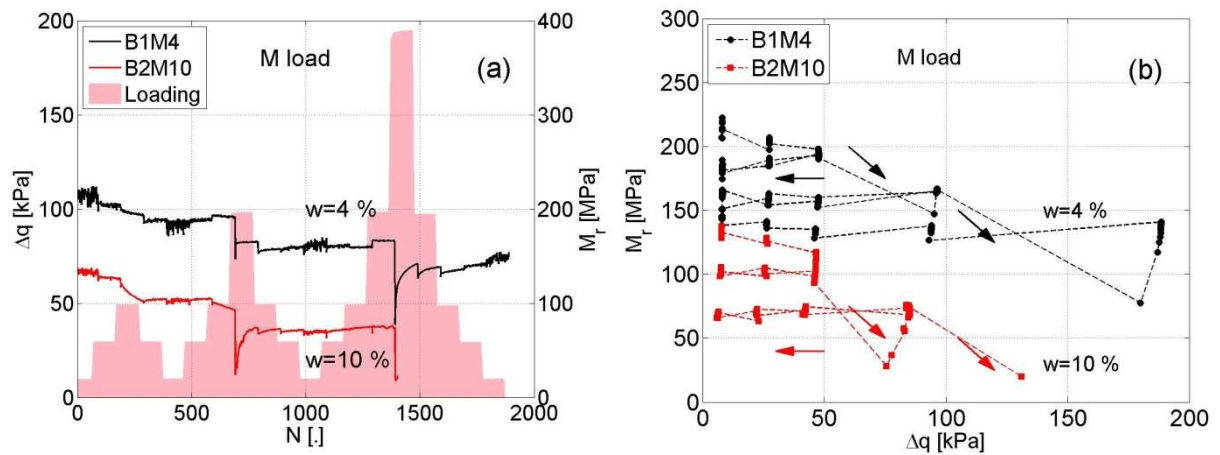
Figure III.61. Testing procedure B for two different moisture contents considering a 'M-shaped' cyclic loading: (a) resilient modulus versus number of cycles; (b) resilient modulus versus cyclic loading amplitude

Regarding the influence of soil hydric state, the difference seems to be the same between the saturated soil and the soil at OPM moisture content - the resilient modulus evolution is parallel for both soils. The saturated ITL soils present 30% lower resilient modulus compared to the OPM ITL soils. Nevertheless, the permanent deformations are much higher for saturated soils, for which soil the permanent axial strain reach ε_I=6% during after N=5 cycles when cyclic stress loading amplitude is Δq=200 kPa. After analysing the 'M shape' cyclic loading tests (Figure III.61), 'Sine' shape cyclic loading tests are analysed (Figure III.62). Similar resilient modulus values and evolution with loading history are found for the two hydric states considered.
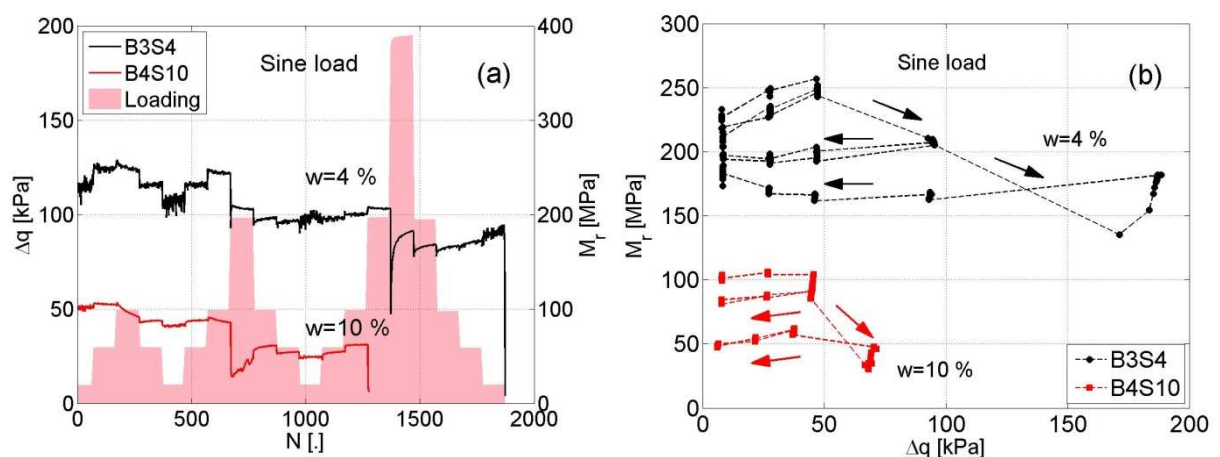
Figure III.62. Testing procedure B for two different moisture contents considering a 'sine-shaped' cyclic loading: (a) resilient modulus versus number of cycles; (b) resilient modulus versus cyclic loading amplitude

224

III.6.4.3 Damping ratio D_r evolution with loading amplitude

As observed in tests with small loading amplitude (Chapter III.6.4.1), the damping ratio does not depend on the confining pressure. Nevertheless, from the results with procedure B it seems that the damping ratio does not depend on moisture content (Figure III.63a). The values obtained are about 3% for both soil hydric states. A damping ratio increase is observed after each amplitude increase during the first cycles. Moreover, this increase is about 5 times higher for saturated samples (Figure III.63a) as compared to OPM ITL samples. Nevertheless, it is rapidly attenuated until a stabilized value (Figure III.63b) after the first cycles. For very low cyclic stress amplitudes (Δq=10 kPa), the damping ratio estimation accuracy is lower compared to the resilient modulus calculation, some noise appearing around the mean value (dispersion around the average is lower than 5%).
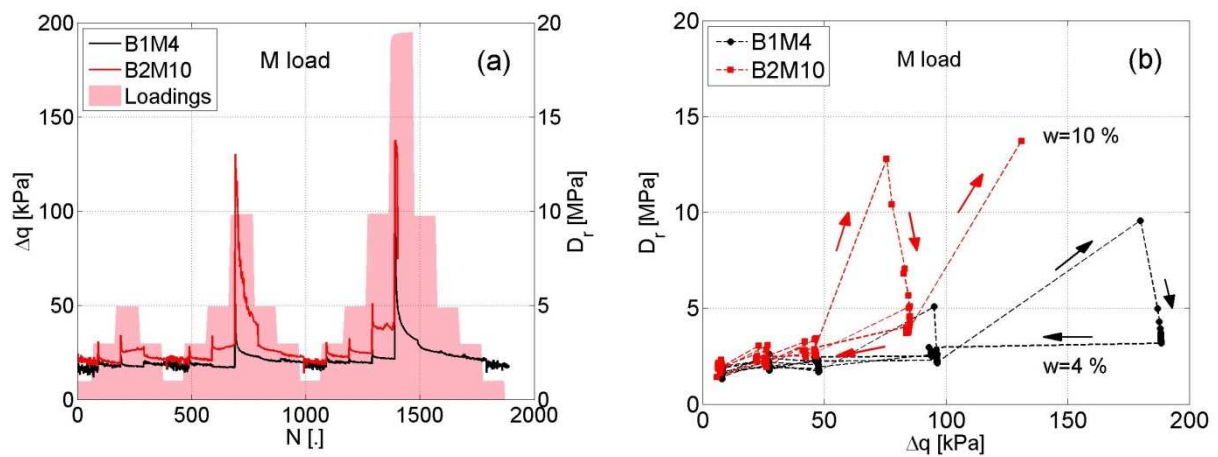
Figure III.63. Testing procedure B for two different moisture contents considering a 'M-shaped' cyclic loading: (a) damping ratio versus number of cycles; (b) damping ratio versus cyclic loading amplitude

The same evolution of damping ratio is found for the 'Sine-shaped' cyclic loadings following 'procedure B' tests (Figure III.64a). The saturated soils increase rapidly their damping ratio during the first cycles after the increase of cyclic stress (Figure III.64b), but it attenuates rapidly.
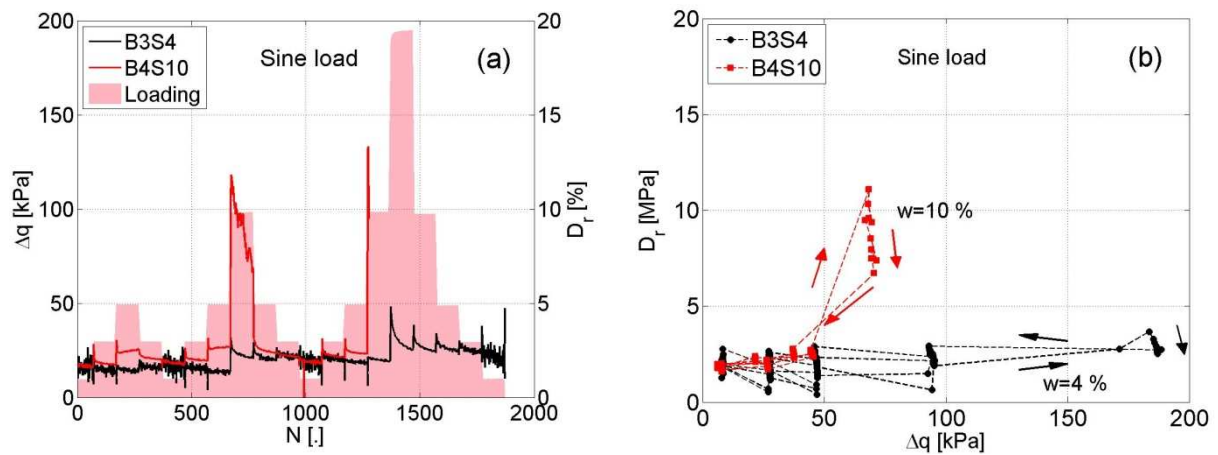
Figure III.64. Testing procedure B for two different moisture contents considering a 'sine-shaped' cyclic loading: (a) damping ratio versus number of cycles; (b) damping ratio versus cyclic loading amplitude

III.6.4.4 Influence of the simulated train speed

From the tests with procedure D, the influence of simulated train speed on the dynamic parameters is assessed. Regarding the resilient modulus (Figure III.65a), the values are of the same order of magnitude as those for a soil under equivalent conditions (Figure III.61). Moreover, there is a constant difference of 33% between the soil at OPM and the saturated soil (Figure III.65a) as observed in the tests with procedure B (Figure III.61). The increase of simulated train speed (different excited frequencies) does not seem to have a significant effect on soil modulus. However, a slightly higher decrease of modulus is found when the simulated train speed is higher (v_T=200 km/h) in both hydric cases.

The damping ratio values appear to be similar (stabilisation at about 2% for cyclic stress amplitudes higher than Δq=20 kPa) for both the hydric soil states and for all the five cyclic stress amplitudes (Figure III.65b). Nevertheless, a decreasing trend with cyclic stress amplitude is identified in the range of the tested amplitudes. As the damping ratio is estimated based on the last cycles of each loading level, where the value may be more or less stable, the decrease could be caused by the soil densification process (void index diminution after large number of cycles). The saturated soils present higher damping ratio than those at OPM. Furthermore, more dissipated energy is expected when in the case of saturated soils. This can be explained by the effect of suction in unsaturated soils. In addition, this damping ratio increase is larger for higher excited frequencies or higher simulated train speeds.
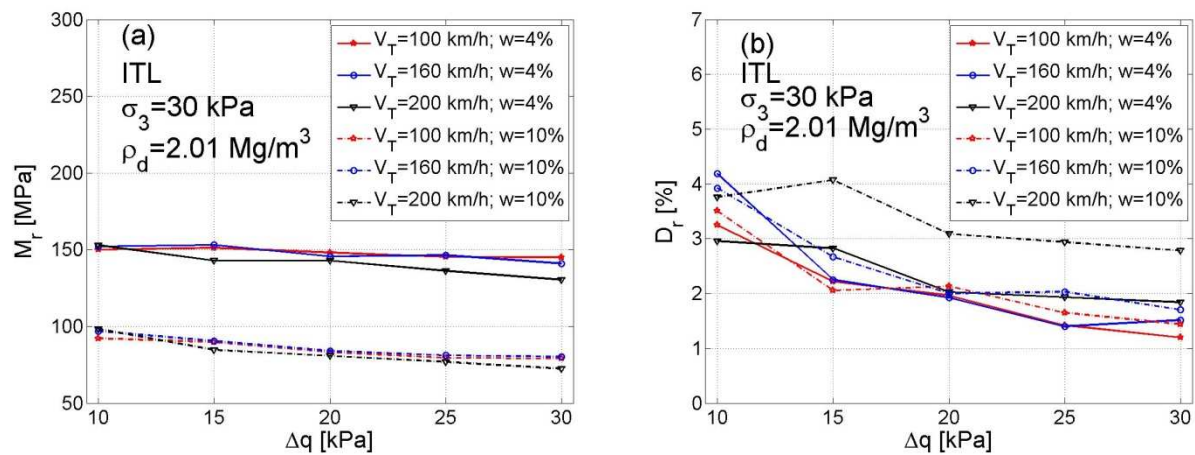
Figure III.65. Simulated speed vs cyclic loading amplitude for two different moisture contents (w=4% and w=10%): (a) resilient modulus; (b) damping ratio

III.7 SUMMARY

It is difficult to obtain intact Interlayer soil (ITL) samples from conventional railway lines. Therefore, the ITL soil from Sénissiat was taken as reference (Trinh 2011) and a ITL-Lab soil was reconstituted using 13 different materials from clay to ballast. This unbound coarse-grained soil was tested under various types of monotonic and cyclic loadings, to investigate the effect of railway traffic loadings on ITL soil.

Consequently, a characterisation was conducted on the ITL-Lab soil. It was found that the grain size distribution, the plasticity index and the OPM moisture content were similar to those for the real ITL from Sénissiat. About 15% of fines (in mass) were present in the ITL-Lab soil; an intermediate value of plasticity index *PI* was found in Casagrande chart; an optimum moisture content of *w*=4% was determined taking into account the entire ITL soil grain distribution. Moreover, as the fine matrix soils in unbound coarse-grained materials could play an important role (Duong et al., 2013; Trinh et al., 2012), different fine plastic soils were reconstituted in order to analyse their elastic properties under different initial states. Three fines soils were reconstituted (grains smaller than 2 mm) with identical grain size distribution but different plasticity indexes (the first one corresponds to the fine soil in the ITL-Lab).

The ITL-Lab soil was tested using a large scale triaxial setup (Φ=300 mm diameter specimens, 6 times larger than the largest grain in the ITL soil). In addition, the elastic behaviour of fine matrix soils under different moisture contents was tested on 50 mm cylindrical samples using bender elements (fine soils were sieved at 1 mm).

Regarding the behaviour of fine matrix soils that control the behaviour of the whole ITL soils if the volumetric fraction of inclusions (as ballast) is low, it was observed that the elastic modulus depends on soil's plasticity. Taking into consideration the samples at the same dry density and different moisture contents, the elastic modulus evolves differently for the three soils. The modulus increased toward a maximum value where the moisture content was close to their optimum Proctor value. Afterwards, the modulus decreased with the increase of moisture content. This can be explained by the increase of aggregate/grain contact surface with moisture content increase on the dry side of Optimum, and by the suction decrease with the increase of moisture content on the wet side of Optimum. The higher the plasticity, the higher the optimum moisture content value and the higher the elastic modulus.

A comparison with the results of Sénissiat ITL soil at w=4% and under three confining pressures (σ_3=30, 100 and 200 kPa) showed that the friction angle (φ =37° ITL-Lab and φ =39° Sénissiat ITL) and the cohesion (c=50.7 kPa ITL-Lab and c'=60 kPa Sénissiat ITL) were similar for both soils. More similarities were found for tests at σ_3=30 and 200 kPa in terms of maximum shear strength and volume change behaviour. The small difference observed in the estimated parameters was attributed to the small differences of ballast volumetric fractions (lower ballast content was adopted in ITL-Lab to obtain a more homogeneous material).

Concerning the cyclic testing on ITL-Lab, two loading shapes ('M' and 'Sine') were considered with four procedures. The effect of loading history, the small strain cyclic behaviour and the effect of simulated train speeds on dynamic parameters were investigated.

The tests with large number of loading cycles showed that the permanent deformations should be corrected taking into account the loading history. The total permanent deformation increases with the number of cycles in a linear way for cyclic stress ratios up to n_{cyclic}=0.16 and its evolution depends on the cyclic loading shape. Thus, the energy in load signal Δq_{cycle} and that in strain response signal $\Delta\varepsilon_1$ of equivalent number of cycles (taken from

the part in which the permanent strain evolution stabilized) were related differently for each loading shape. Thereby, the relationship between stress (load) and strain (response) is conditioned by the loading shape (excited frequencies), even though the soil behaviour is mainly elastic. Furthermore, this relationship is also related to the soil's hydric conditions. Though the energy content in load was the same for different moisture contents, the developed energy in response was higher when the soil was saturated. Moreover, it depended also on loading shape - 'Sine' cycles developed more energy in saturated ITL. A good repeatability was obtained in the tests, showing the quality of sample preparation. Moreover, the energy developed by the soil's response, regardless of the loading shape, was related to the damage of the sample through the permanent strain.

The impacts of some parameters like the cyclic strain amplitude, the loading frequency (simulated train speed) and the loading history on the dynamic parameters (elastic modulus and damping ratio) were assessed. An increase of cyclic strain amplitude induced a resilient modulus decrease. Moreover, this decrease was higher for the cyclic strain amplitudes around $\Delta\varepsilon_I = 10^{-5}$. Furthermore, An increase of confining pressure increased the resilient modulus. The damping ratio was stable for all the confining pressures, especially for $\Delta\varepsilon_I > 0.04\%$ where the hysteresis loop's surface estimation was expected to be more accurate. Regarding the loading history impact, only the cyclic stress amplitudes higher than those applied previously on the sample led to a significant decrease of resilient modulus during the first cycles. Then, the modulus started to recover until a new stable and lower value than the previous one. In addition, higher moisture contents led to lower modulus. Constant modulus differences were found for soils at different moisture contents under similar loading paths. Besides, the damping ratio was found similar (about 3%) for different moisture contents. But in the case of saturated soils there is a strong increase during the first cycles of loading amplitudes because the dissipated energy was higher with larger strains. Finally, the increase of loading frequency or simulated train speed results in a slight decrease of resilient modulus, in particular when the soil is saturated. Moreover, the damping ratio evolution with cyclic stress amplitude is similar for all the hydric conditions and all cyclic stress amplitudes considered. However, higher damping ratios were found in the case of saturated soils at higher simulated train speeds.

IV. SYNTHESIS AND APPLICATIONS

IV.1 INTRODUCTION

In this chapter, possible applications of the developed results previously presented are proposed, in the form of analytical models and experimental protocol. The proposed methods can help the dynamic track behaviour assessment, considering the mechanical parameters of track materials as well as loading parameters such as axle load and train speed.

The chapter consists of two main sections. The first section describes two analytical models for track's dynamic behaviour modelling. The first model deals with the stress distribution under train loads. This model takes into account the train speed impact and the elastic mechanical properties of each layer constituting the track. The second analytical model deals with the longitudinal propagation of vibration and deflections. The dynamic amplification with train speed is taken into account in the model. In the second section, a comparison is made between 'Laboratory' results and '*In-situ*' measurements. Firstly, the track-bed materials' behaviour is analysed. The cumulative PSD of the response under equivalent loads by different trains on the ITL and subgrade materials are analysed, and qualitatively compared with the 'Laboratory' results. Secondly, the measurements by the on-surface sensors are correlated with those by the sensors embedded in the track-bed. The main goal of this comparison is to define a relatively simple experimental protocol for quantifying the aggressiveness of different traffic loads on conventional tracks.

IV.2 ANALYTICAL MODELLING OF TRACK'S DYNAMIC BEHAVIOUR

Two analytical models for track dynamic behaviour are presented in this section, one for the stress distribution through the track bed and another for the longitudinal deflection propagation. The same train model was considered in the analysis with the two models. As the Intercity train was used during the test campaign and the statistical analysis of the 'In-situ' measurements, this type of trains was also used to develop the models. Moreover, a typical train configuration (Locomotive + 7 Coaches) was considered (Figure IV.1).
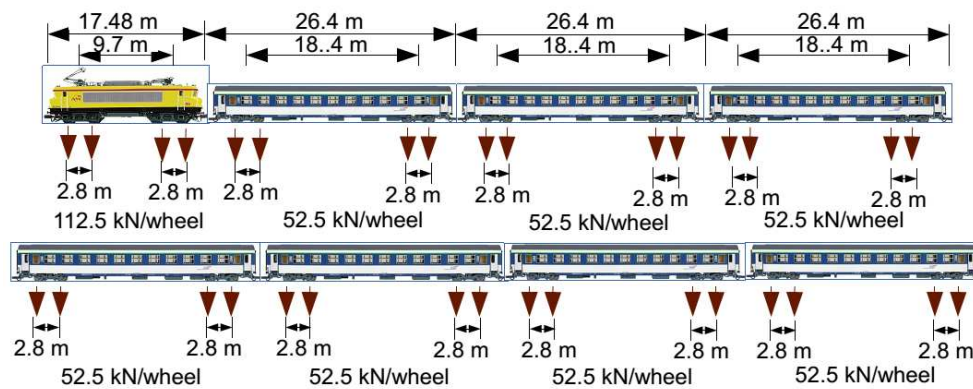
Figure IV.1. Scheme of a typical Intercity train and static wheel load

IV.2.1 Stress transmission model

As shown in Chapter II, in Vierzon experimentation site, the vertical stress during a train passage was measured at two different depths, ITL (z=-0.90 m) and SBG (z=-2.3 m), for speeds ranging from 60 km/h to 200 km/h. In this section, based on the recorded data, the dynamic factor was analysed, and the Boussinesq elastic model and load spread model were evaluated. Then, based on the theory of stochastic stress diffusion in particular media (Bourdeau and Harr 1989), a modified load spread model using cumulative Gaussian stress distribution was developed. The influence of internal friction angle and the ratio of soil elastic modulus from different track-bed layers were evaluated.

From the vertical stress signals measured in Vierzon and by multiplying time by train speed, the time-domain signals were converted to distance-domain signals obtaining the longitudinal vertical stress signals for ITL and SBG at 60 km/h, and 200 km/h (Figure IV.2). This is possible because the materials (thickness, composition) and the stresses developed at ITL and beyond are considered as homogenous for this experimentation site. Note that the initial point (distance = 0 m) in X-axis corresponds to the start of recording time (a data buffer of 5 seconds before the arrival of the first axle was considered). The signals in shallower layers (ITL) present a 'M-shaped' signal, each 'M' cycle represents a bogie load constituted by 2 axles. It is observed that the distances of two adjacent peaks are keeping constant when the train speed increases from 60 km/h to 200 km/h. In this part of signals negative stress values were recorded. This could be attributed to the reaction of uplift force (Le Pen et al. 2014; Selig and Waters 1994), and these values are taken into consideration in calculating the stress amplitude by considering the whole amplitude from the lowest value to the highest one. The

maximum stress developed under coaches' bogies in ITL is about 8 kPa (Figure IV.2a). This stress value decreased until about 2 kPa at the SBG (Figure IV.2b). This clearly shows the decrease of stress amplitude over depth - the deeper the level, the lower the stress amplitude. Furthermore, it is easy to identify each axle for ITL depth ('M-shaped' bogie), but the axle identification becomes difficult for SBG depth. Also, when the speed increases from 60 km/h to 200 km/h, the increase of $\Delta\sigma_z$ peak values is more appreciable in ITL than in SBG.
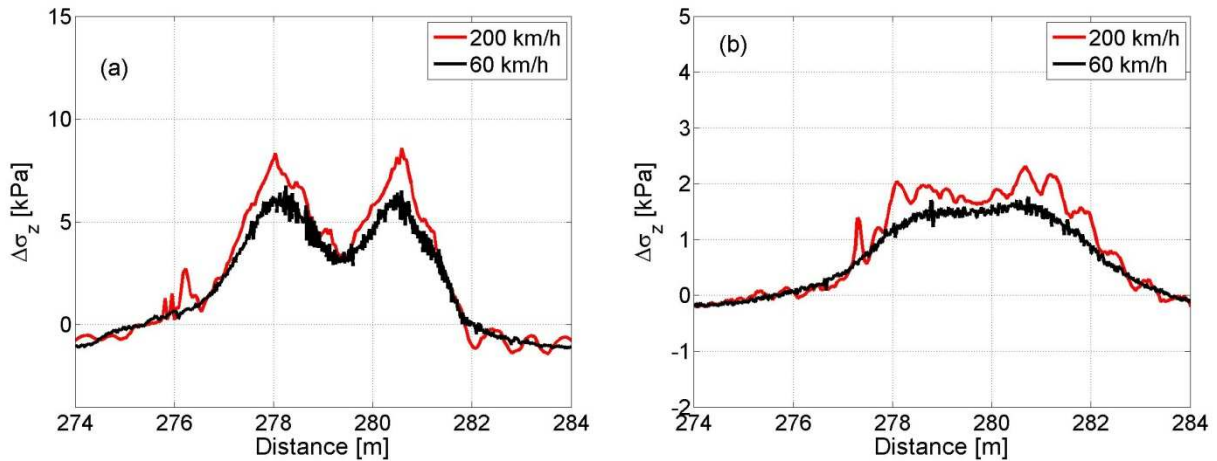
Figure IV.2. Measured vertical stress of Corail coach bogie at two depths: (a) ITL (-0.96m); (b) SBG (-2.3m)

The measured stress amplitudes at six speeds for ITL and SBG are depicted in Figure IV.3. These stress amplitudes were defined as the average value of four axles in locomotive and 28 axles in coaches, respectively. The method used for determining the vertical wheel load is presented as follows (AREA 1994; Bian et al. 2014; Doyle 1980; Li and Selig 1998; Priest and Powrie 2009):

$$P = \phi_{sp} \cdot P_s \qquad (IV.1)$$

where P is the dynamic wheel load (kN), P_s is the static wheel load (kN) and ϕ_{sp} is the impact factor which is expressed as function of train speed. An empirical method which is applicable for evaluating dynamic amplification of wheel load on rail was proposed by the Office of Research and Experiments of International Union of Railways (ORE), French National Railways (SNCF) and German Railways (DB), based on the measurements of rail stress (Birmann 1965; Doyle 1980; Health et al. 1972):

$$\phi_{sp} = 1 + k \cdot (\frac{v_T}{100})^3 \qquad\qquad (\text{IV.2})$$

where k a constant parameter that depends on track's geometry and the state of track elements and rolling stock. A value of k = 0.031 was recommended in Doyle (1980). In Figure IV.3, the dynamic stresses can be estimated using the impact factor of Equation (IV.2) and the results are compared with the measured values. A good general agreement is obtained, showing that Equation (IV.2) that was developed based on the measurement of forces at rail level can be used to well evaluate the speed impact factor for track substructures.
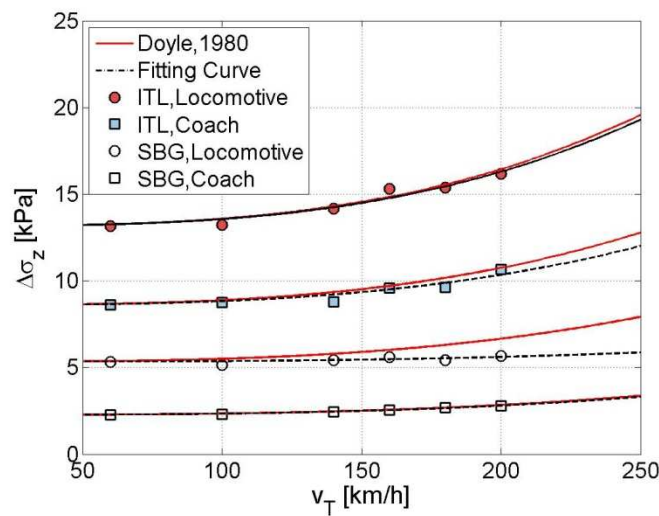
Figure IV.3. Relationship of stress amplitudes and train speeds

Boussinesq model can be used to determine the surface load-induced stress distribution within a semi-infinite elastic medium. It is the most popular method that has been used to calculate the vertical stress distribution in substructures, assuming that the ballast and subgrade layers form an elastic, homogeneous and isotropic material (Doyle 1980; Powrie et al. 2007; Priest et al. 2010; Selig and Waters 1994). This implies that soil behaves mostly in an elastic way because most of the permanent deformations under actual train loads are developed during the first loading cycles. This is particularly the case for the ITL material that was created long time ago. Two typical forms of load are usually considered for Boussinesq model: a point load or an uniform load acting over a surface (in railways it could be considered under sleeper stress).

If point loads are considered, the vertical stress $\Delta\sigma_z$ under a series of punctual loads Q_i can be calculated as follows:

$$\Delta\sigma_z = \sum \frac{3Q_i}{2\pi} \cdot \left(\frac{z_i^{\,3}}{(x_i^{\,2} + y_i^{\,2} + z_i^{\,2})^{2.5}} \right) \tag{IV.3}$$

where i is the number of wheel loads, x_i, y_i and z_i are the distances in three axes from the wheel load i to the considered measuring point. Using a train of punctual loads (separated as in Figure IV.1) and after superimposing all wheel loads of a whole train, a large difference between peak values is found. This can be due to the considered elastic behaviour hypothesis. For example, performing this calculation, a peak stress of 58 kPa in ITL is obtained by calculation in case of locomotive, while a value of 13 kPa was recorded in the field. This suggests that the method using a point load is not appropriate for calculating the stresses in railway substructures.

In case of uniform load, $\Delta\sigma_z$ (kPa) is obtained by double integrating Equation (IV.3):

$$\Delta\sigma_z = \sum \frac{3P_i}{2\pi} \int_{\varepsilon=-L/2}^{\varepsilon=+L/2} \int_{\eta=-B/2}^{\eta=+B/2} \frac{z^3}{((x-\varepsilon)^2 + (y-\eta)^2 + z^2)^{2.5}} \, d\varepsilon d\eta \tag{IV.4}$$

where L and B represent the effective length and width of sleeper, respectively, P_i is the uniform contact pressure between sleeper and ballast, $d\varepsilon$ and $d\eta$ are the differential length and width of a sleeper, x, y, z are the distances from the measuring point to the punctual load position. In practice, the P_i between the sleeper and ballast can be determined using Equation (IV.5) (Salim 2004):

$$P_i = \left(\frac{q_r}{B \cdot L} \right) \cdot F_2 \tag{IV.5}$$

where q_r is the maximum rail seat load (kN) and F_2 is a parameter depending on the sleeper type and track typology. Many researchers focused on the determination of rail seat load, and in most cases the rail is assimilated to a beam on a continuous linear elastic foundation (Clarke 1957; Doyle 1980; Priest and Powrie 2009; Selig and Waters 1994). After transforming the continuous deflection to discrete deflection as illustrated in Figure IV.4, the

maximum rail seat load q_r can be determined with three parameters: track global modulus, sleeper spacing and maximum rail deflection (AREA 1994; Clarke 1957). Profillidis (1983) and Salim (2004) proposed to take q_r equal to $0.5Q$ for a sleeper spacing of 0.6 m. Note that this value can depend also on USP if there is any on the considered track.
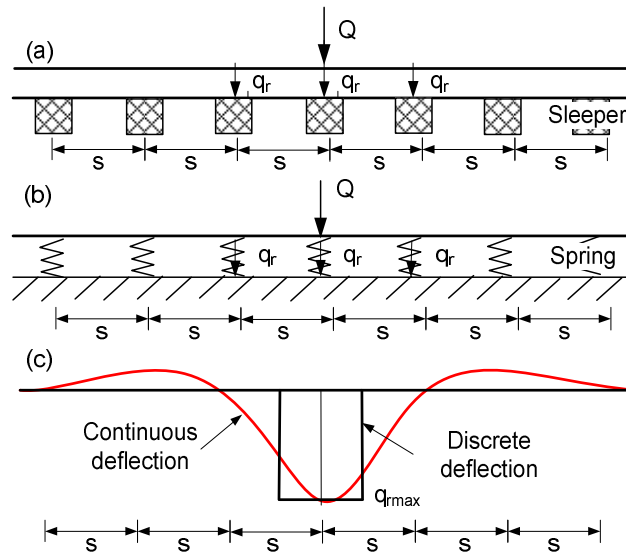
Figure IV.4. General modelling of rail track deflection for determining rail seat load

The results of stress calculation using Equation (IV.4) and Equation (IV.5) show also large differences with the measurements: for locomotive, 50 kPa and 10 kPa peak stresses are calculated for ITL and SBG respectively, while only 10 kPa and 5 kPa were measured for ITL and SBG respectively. Therefore, the Boussinesq elastic model with uniform pressure is not appropriate for evaluating the stress distribution in multi-layered substructures, either. This can be also due to the elastic behaviour hypothesis in the model.

The load spread model modifies the previous Boussinesq model (punctual load), and it is another widely used approach for estimating the vertical stress distribution in substructures (AASHTO 2002; Alves Costa et al. 2015; Burd and Frydman 1997; Murthy 2002; Zhai et al. 2004). This approach assumes that the vertical stress distributes uniformly over an area below a sleeper, delimited by a dispersion cone with spread an angle θ. The vertical stress is calculated as follows:

$$\sigma_z = P \cdot \left[\frac{B \cdot L}{(B + 2z \tan \theta)(L + 2z \tan \theta)} \right] \qquad (IV.6)$$

Giroud and Han (2004) concluded that the load spread angle $\theta = \pi/4 - \varphi/2$, where φ is the internal friction angle of each layer. It is worth noting that in this method only the load spread angle of the first layer (Ballast) is taken into consideration. In fact, ballast thickness in ballasted tracks is calculated in order to obtain a homogeneus load from traffic for deeper materials. As demonstrated by Burmister (1958) through an elasticity-based analysis, on the axis of a circular load, the vertical stress at the interface of a two-layer medium decreases with the increase of the modulus ratio between the upper and lower layers. In road applications, Giroud and Han (2004) proposed an empirical expression to calculate the stress distribution angle variation based on the modulus ratio between the upper layer layer and the subgrade layer:

$$\tan\theta_1 = \tan\theta_0 \left[1 + 0.204 \cdot \left(\frac{E_{up}}{E_{sg}} - 1 \right) \right] \qquad (IV.7)$$

where E_{up} and E_{sg} are the moduli of the base course (upper layer) and the subgrade soil in the interfaces between every two layers or materials. Respectively, θ_0 represents the stress distribution angle through the first layer from the load track contact where it could be considered that $E_{up}=E_{sg}$, and $\theta_0=38.5°$ in the case of unpaved roads (Giroud and Han 2004). The empirical mean moduli estimated from the dynamic penetrometer tests (PANDA) at Vierzon site are 133 MPa, 103 MPa, 95 MPa, 77.5 MPa for the Ballast, ITL, TL and SBG materials, respectively (Escobar et al. 2014; Lamas-Lopez, Cui, Costa D'Aguiar, et al. 2015). According to previous researches (Burd and Frydman 1997; Clarke 1957; Trinh 2011), an initial load spread distribution angle $\theta_0=45°$ for ballast can be adopted (load is transmitted through ballast from the sleeper-ballast interface). The spread angles for other deeper layers are estimated using Equation (IV.7). Figure IV.5 shows the parameters involved in the estimation of distributed vertical stresses for every track-bed material interface from the track-bed surface.
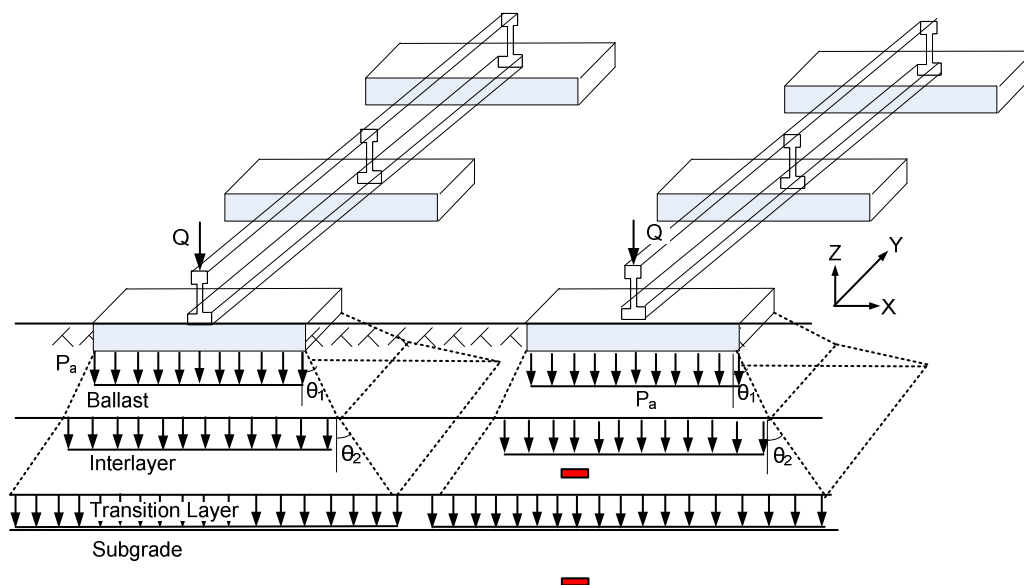
Figure IV.5. Scheme of 'Load Spread Model'

If the vertical stress calculation by the load spread method and the measurements at 60 km/h, for ITL and SBG are compared, the calculation shows bell-shaped curves, in the middle of every two axles, against the 'M-shaped' measured curves. In addition, the maximum values of calculations are located in the middle of 'M' shapes. This is due to the superimposition over depth adopted in the calculations between the load of two axles. Nevertheless, the difference between the calculated peak values and the measured peak values is smaller than in the case of two previous Boussinesq approaches (Figure IV.6). This load spread method is more accurate for lower axle loads and deeper measuring positions. The recorded stress amplitudes for a coach and a locomotive and the calculated stresses right beneath the axle load based on the above-mentioned methods are presented in Figure IV.6. It can be noted that the estimated results from the load spread method agree the best with the measurements. Considering the drawbacks of the load spread method as mentioned previously, an improved model is developed here to describe the longitudinal and perpendicular stress distributions in substructure.
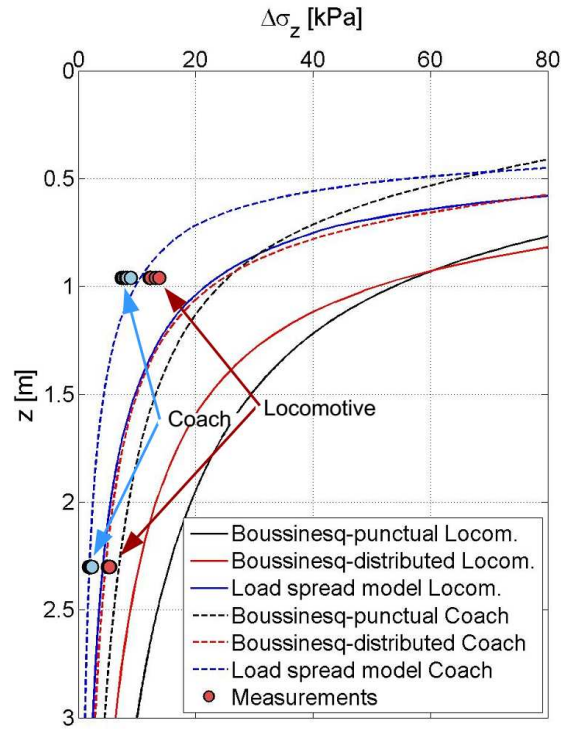
Figure IV.6. Vertical stress amplitude under traffic load over depth. Theoretical calculations and measurements

Bourdeau and Harr (1989) described the transmission of applied load through gravel material based on the theory of stochastic stress diffusion in particular media developed by Sergeev (1969). Instead of assuming continuity and homogeneity of the granular material constituting the substructure, the heterogeneity and variability of particles in each soil layer are accounted for (Bourdeau 1989). The load transmission results from the propagation of contact forces between particles. Thus, random fluctuations occur in the horizontal direction when a vertical force propagates from a particle to its neighbour. A diffusion-type equation was developed to express such propagation (Bourdeau and Harr 1989; Bourdeau 1989, 2009):

$$\frac{\partial \overline{\sigma_z}}{\partial z} = D \frac{\partial^2 \overline{\sigma_z}}{\partial x^2} \qquad (IV.8)$$

where $\overline{\sigma_z}(x,z)$ represents the vertical stress in the granular material, and D is the coefficient of diffusion which governs the lateral load spread rate. Harr (1977) and Bourdeau (1989) pointed out that D can be expressed as a function of internal friction angle φ and depth z:

$$D = v_{dif} \cdot z = K_0 \cdot z = (1 - \sin\phi) \cdot z \qquad (IV.9)$$

where the coefficient of diffusivity v_{dif}, that accounts for the soil compaction state, is related to the coefficient of earth pressure K_0. In the case of an applied pressure, P, uniformly distributed over a strip of width *2a*, Harr (1977) obtained the solution of Equation (IV.10):

$$\frac{\sigma_z(x,z)}{P} = \psi(\frac{x+a}{z\sqrt{v_{dif}}}) - \psi(\frac{x-a}{z\sqrt{v_{dif}}}) \qquad \text{(IV.10)}$$

being ψ the normal cumulative Gaussian distribution function:

$$\psi(x) = \int_0^x \frac{1}{\sqrt{2\pi}} e^{-\frac{t^2}{2}} dt \qquad \text{(IV.11)}$$

In this study, the uniformly distributed pressure *P* is determined by developing the load spread method. The width *2a* over depth is considered as a function of spreading angle θ shown in Figure IV.7. The coefficient of diffusivity v_{dif} is calculated through Equation (IV.9) considering the loading spread angles (θ_i) calculated using Equation (IV.7) at each interface. Consequently, this spreading width *2a* depends also on the elastic modulus ratio between every two track-bed materials.
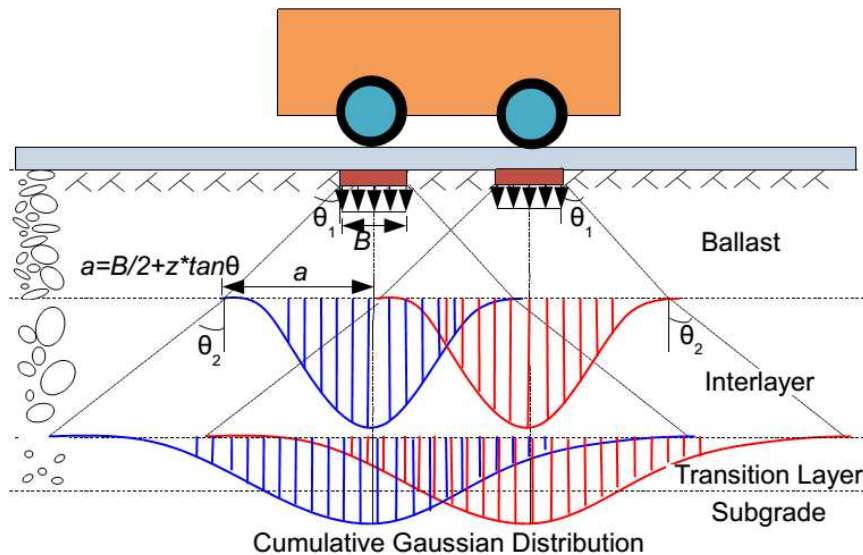
Figure IV.7. Scheme of modified spread model

Based on Equation (IV.7) to Equation (IV.11), a new estimation of stress distribution can be made. Figure IV.8 shows the comparison between the new calculation and the field

240

measurements, for both ITL (Figure IV.8a) and SBG (Figure IV.8b). A good agreement is obtained, and the difference between the calculated and measured peak values becomes much smaller than the previous estimations. Bigger differences are found for shallower layers (ITL), where load difussion is more affected by the load support conditions (as sleeper positioning), load dissipation in depth and longitudinal distribution hypothesis.
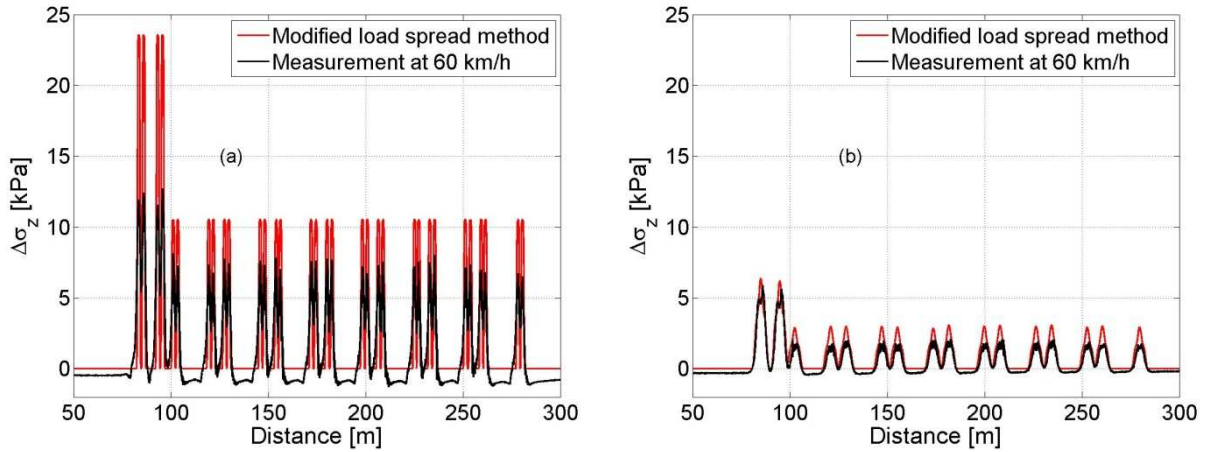
Figure IV.8. Comparison of calculation (modified spread model) and measurements: (a) ITL (-0.96m); (b) SBG (-2.3m)

Combining the dynamic amplification equation (depending on train speed) and the proposed 2D stress distribution model, a new analytical expression is obtained, that allows the prediction of stress distribution in multi-layered substructures such as the French conventional ones with the presence of ITL, taking into account the train speed and the variability of material properties:

$$\sigma_z(x,z) = \phi_{sp} \cdot P_s \cdot \left[\psi(\frac{x+a}{z\sqrt{v_{dif}}}) - \psi(\frac{x-a}{z\sqrt{v_{dif}}}) \right] = P \cdot \left[1 + k(\frac{v_T}{100})^3 \right] \cdot \left[\psi(\frac{x+a}{z\sqrt{v_{dif}}}) - \psi(\frac{x-a}{z\sqrt{v_{dif}}}) \right] \text{(IV.12)}$$

The key parameter of this model is the modulus ratio E_{lower}/E_{upper}. Figure IV.9 depicts the influences of $E_{ITL}/E_{Ballast}$ (Figure IV.9a) and E_{SBG}/E_{TL} (Figure IV.9b) on the stress predictions in ITL and SBG layers, respectively. It appears that the vertical stress on the axis of wheel load clearly decreases with the decrease of E_{lower}/E_{upper}. Moreover, the diffused range slightly expands with the decrease of E_{lower}/E_{upper}. It should be noted that in Figure IV.9 only the first modelled locomotive bogie is showed, the following locomotive bogie loading the modelled track at 30 m distance.
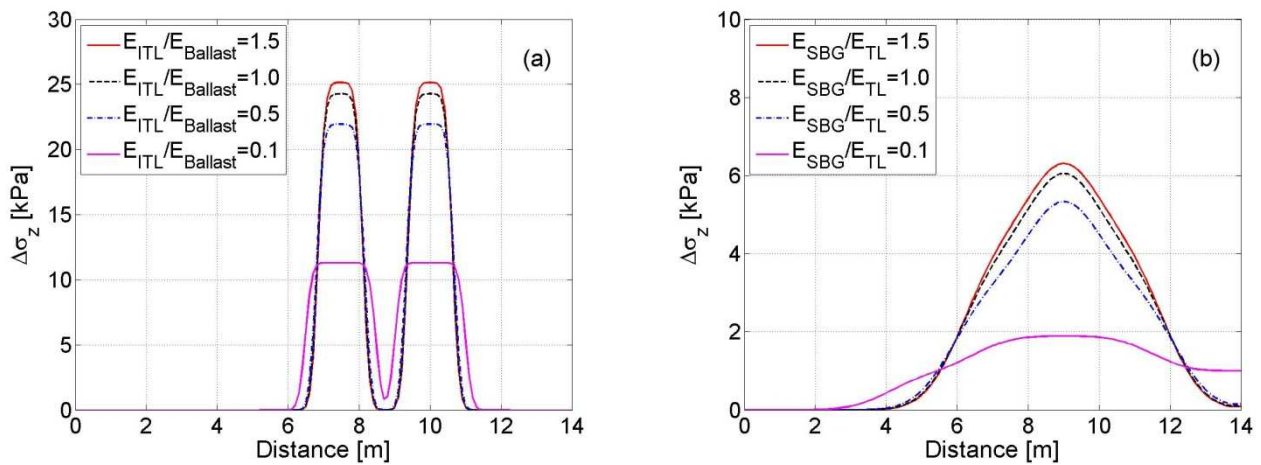
Figure IV.9. Stress distribution under a Locomotive bogie:
(a) in ITL with different $E_{Ballast}/E_{ITL}$ and (b) in SBG with different E_{SBG}/E_{TL}

Figure IV.10 presents a summary of the input parameters, the variables and the output result when using this stress repartition analytical model.

Figure IV.10. Summary of the analytical stress repartition model

IV.2.1   *Vibration analytical model*

The model consists of three parts: vibration amplification with train speed, deflection amplitude decrease over depth and longitudinal vibration propagation. The proposed model uses track parameters with clear physical meanings. Moreover, it is quite simple and can thus be easily applied in practical railway engineering.

From the prospection results (see Chapter II), a profile with 4 layers was defined: Ballast, Interlayer (*ITL*), Transition layer (*TL*) and Subgrade (*SBG*). The thickness of the ballast layer was 50 cm in average with 41 cm fresh ballast and 9 cm fouled ballast. A track static modulus of E_{v2}=100 MPa on the top of ballast was considered in this study. It was obtained through LWD (light weight deflectometer) tests (Escobar et al. 2014; Vennapusa and White 2009). The average shear wave velocity of the first 5 m of track-bed determined by MASW (Multiple Analysis of Surface Waves) is about v_s = 200 m/s. A damping ratio D_r=0.05 (5%) for ITL soil was estimated from large-scale triaxial tests under similar loading as traffic loading conditions (Cui et al., 2014; Lamas-Lopez et al., 2015; Trinh, 2011; Trinh et al., 2012).

In order to monitor the acceleration amplitudes developed by long wavelengths, the data recorded by accelerometers mainly in low-frequency range (Cui et al. 2014) were used (see Chapter II). These accelerometers were installed at sleeper, z=-0.9 m (ITL), z=-1.2 m (TL) and z=-2.3 m (SBG) depths under the rail. Figure IV.11a shows the comparison of time domain displacements at v_T=60 km/h (ITL) and v_T=200 km/h (TL). In order to analyse the amplitude attenuation along the track, signals in distance domain are considered. After multiplying time by train speed, the vibrations in distance domain are obtained (Figure IV.11b). Note that the axle or bogie location (peaks) at v_T=60 km/h and v_T=200 km/h keep consistent. As a deflection amplitude validation was performed at different depths, the integration method could be applied. The front and rear parts of the signals, representing the longitudinal vibrations while train approached or left away from the sensor position, are highlighted in spotted frames.
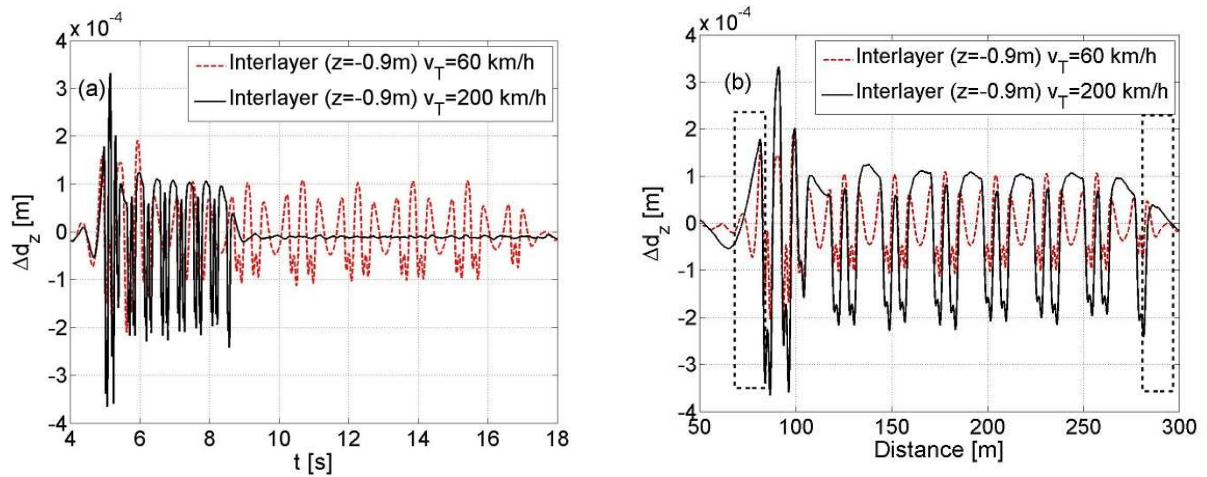
Figure IV.11. Transformation of (a) time-related curve to (b) distance-related curve

Typical acceleration measurements, in ITL and TL, and their corresponding displacement estimations extracted from the front (locomotive axle loading) and rear (Corail coach loading) parts of the signals (Figure IV.11b) are presented in Figure IV.12. There are two main reasons for extracting these parts of signals: they correspond to the dynamic responses of track-bed when trains are approaching and leaving; obtaining the information of about 3 to 5 adjacent sleepers (Profillidis 1983, 2000; Selig and Waters 1994) and testing two different axle loads (Locomotive and Corail coaches). As shown in Figure IV.12a and Figure IV.12b, the acceleration amplitudes are amplified with the train speed mainly in the vertical axis compared to the longitudinal axis. The track deflections in Figure IV.12c and Figure IV.12d also indicate that the train-induced displacements are amplified with the train speed, not only at surface but also in track-bed structure. There is some longitudinal uplift on the measured points after the loading axle passage (see Figure IV.12c and Figure IV.12d). Similar phenomenon was identified by other researchers (Le Pen et al. 2014; Raymond 1985; Timoshenko 1926).
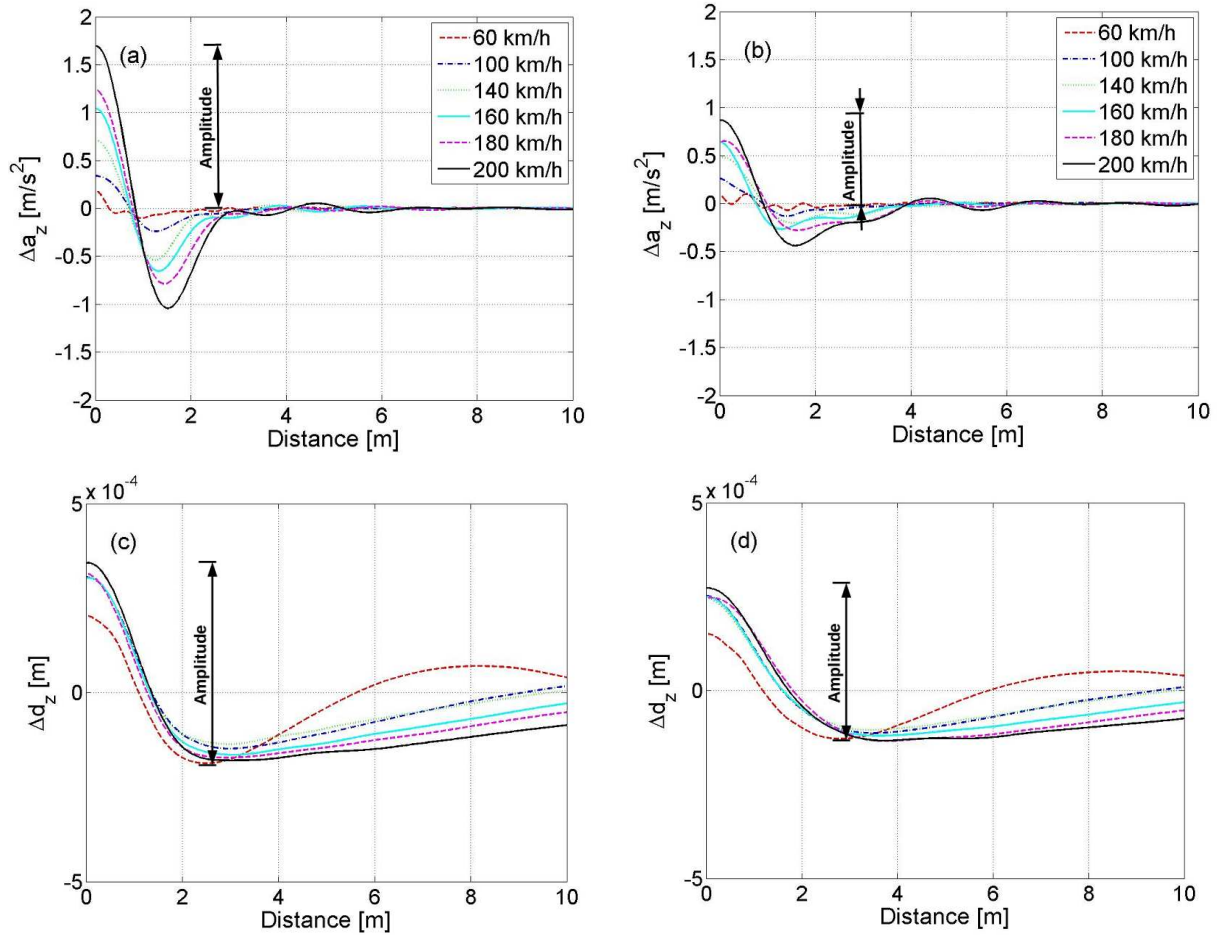
Figure IV.12. Comparisons of acceleration and displacement for different speeds: (a) Δa_z in ITL (Locomotive); (b) Δa_z in TL (Locomotive); (c) Δd_z in ITL (Locomotive); (d) Δd_z in TL (Locomotive)

Moreover, the deflection amplitudes attenuated over depth and the amplifications due to the impact of train speed appeared in all the track-bed layers. The train speed-induced amplification continues to grow up until reaching the site critical speed. Note that the issue of critical speed has drawn much attention in the previous researches. Krylov (1996) conducted a theoretical analysis of the large increase in vibration when superfast trains run at speeds approaching the Rayleigh wave velocity on the ground (Alves Costa et al. 2015; Madshus and Kaynia 2000; Semblat et al. 2000). The surface movement observation and numerical analyses allowed concluding that the critical speed is controlled by the minimum phase velocity of the first Rayleigh mode of soil and embankment profile (Connolly et al. 2014; Degrande and Lombaert 2000; Madshus and Kaynia 2000; Sheng et al. 2004). Costa et al. (2015) numerically simulated the speed effect using a dimensionless parameter, $M = v_T/v_s$, where v_T is the train speed and v_s is the average shear wave velocity of track subgrade material. In a homogeneous half-space, the dynamic amplification factor (DAF), defined by

245

$\Delta d/\Delta d_s$, where Δd_s is the static displacement, can be normalized by $M=v_t/v_s$ (Alves Costa et al. 2015; Sheng et al. 2004). To develop an empirical and simple method, a function called $f_{DAF}(M)$ representing the M-DAF relationship is adopted to justify the hypothesis that the conventional track-bed is homogeneous in a half-space.

The average shear wave velocity v_s=200 m/s obtained by MASW was used to determine the normalized parameter, $M=v_t/v_s$. Some authors (Bian et al. 2014; Madshus and Kaynia 2000; Sheng et al. 2004) showed that for the speeds lower than 70 km/h, the dynamic axle load can be considered as a quasi-static load. In this study, the displacement amplitude at 60 km/h was considered as a quasi-static deflection and the DAF was obtained by $\Delta d_i/\Delta d_{60}$. A curve relating M to DAF for different layers is presented in Figure IV.13.
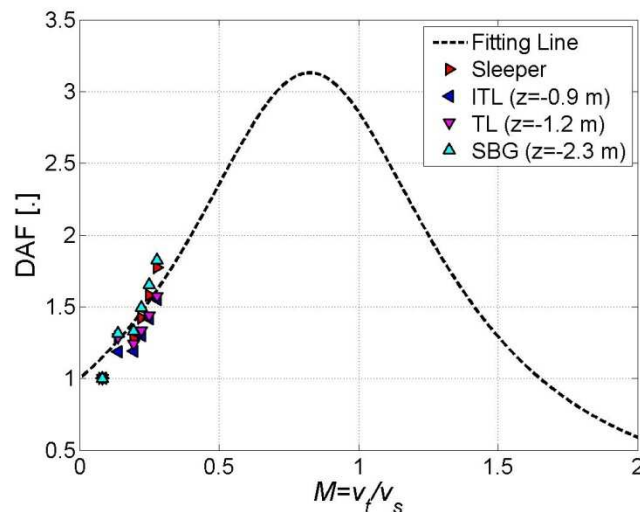
Figure IV.13. Fitting curve of Dynamic Amplification Factor of deflections versus $M=v_T/v_s$ for sleeper, ITL, TL and SBG

Based on the numerical simulation results published in literature (Alves Costa et al. 2015), an empirical expression is proposed, Equation (IV.13), by fitting the field data:

$$f_{DAF}(M) = \frac{M + 0.0001}{(M)^3 - 1.65(M)^2 + 0.0001} \tag{IV.13}$$

With this equation and the average shear wave velocity, the dynamic amplification of conventional track-bed can be assessed. Note that the issues of predicting the vibration transmission in track-bed is complex because of the heterogeneity and discontinuity of track-

bed materials and the difficulty of determining the damping properties of these materials. This can be done only with rational assessments on the amplitude attenuation in layered soil using empirical and theoretical methods.

The vertical displacement amplitudes in different layers of the investigated site are shown in Figure IV.14. It appears that a significant attenuation occurs in ITL, as compared with the situations in TL and SBG. This strong attenuation can be appreciated for all speeds.
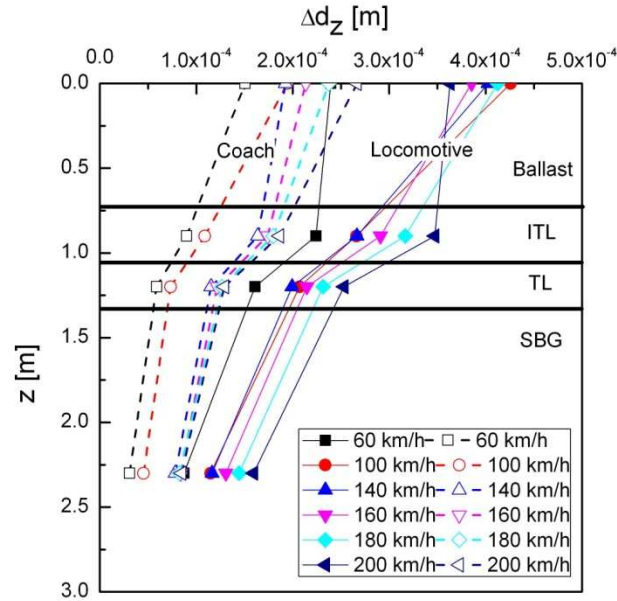
Figure IV.14. Measured displacement amplitude attenuation over depth, from sleeper to SBG

The amplitude attenuation over depth was discussed by several authors, and can be expressed by an exponential function. Some studies (Auersch 1994) pointed out the strong influence of material damping for high frequencies, and proposed the following expression for assessing this influence Equation (IV.14):

$$A(z) = A_0 \prod_{j=1}^{m} \prod_{i=1}^{n} e^{-aD_i f_j z_i} = A_0 e^{-a\sum (D_i \cdot z_i) \cdot \sum f_j} = A_0 e^{-a\overline{D}\cdot z \cdot \sum f_j} \qquad \text{(IV.14)}$$

where a is a constant depending on track-bed properties, D_i is the damping ratio of layer i, $\overline{D}$ is the weighted arithmetic mean, f_j is one of the train-induced frequencies and $A(z)$ is the vertical amplitudes at depth z. This study (Auersch 1994) also analysed the increase of damping ratio D_r due to the vibration transmission from stiffer top layers to relatively soft

247

layers. However, others authors (Kim and Lee 2000) indicated that a similar exponential decrease shape is found for most of the soil, because of the soil damping properties. Therefore, if the hypothesis of a homogenous track-bed is taken into account (no multi-layered track-bed), Equation (IV.15) can be used to estimate the attenuation factor of track deflections over depth:

$$f_{AC}(z) = e^{-a \cdot \overline{D} \cdot z} \tag{IV.15}$$

Three different attenuation curves are shown in Figure IV.15. Curve (a) closely fits the measurements at sleeper, in TL and SBG, while curve (b) follows the displacements of sleeper and ITL. The area between the two curves can be considered as the vibration energy loss related to the presence of ITL. To develop a continuous equation to describe the variations of attenuation coefficient over depth by considering the track-bed as a homogenous material, an attenuation curve (c) between (a) and (b) in Figure IV.15 is taken into account. This curve considers parameter a as an empirical constant for all the track-bed layers. Meanwhile, the average damping ratio is kept equal to 0.05. A value of 9 is then obtained for the constant by fitting the measurements at all depths using Equation (IV.15). It is important to underline that the degree of saturation and fine content are key factors for the resilient modulus, damping ratio and other mechanical properties of ITL (Duong et al., 2013; Lamas-Lopez, Cui, et al., 2014; Trinh et al., 2012). Therefore, this simplified parameter is only suitable for empirically estimating the amplitude attenuation.
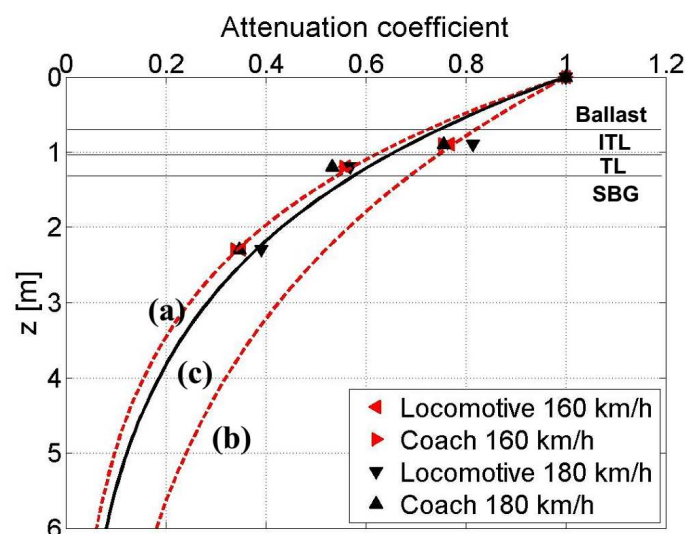
Figure IV.15. Attenuation coefficient variation over depth

In addition, a longitudinal deflection expression $u(x)$ is proposed based on the previous achievements and the field data obtained. Combining the dynamic amplification factor f_{DAF} (M), the attenuation coefficient $f_{AC}(z)$ and $u(x)$, the vibrations of track-bed can be predicted in a 2D space.

For the purpose of modelling the mechanical behaviour of railway support structures, the partial differential equation of Winkler beam model was developed by several authors (Hendry 2007; Kenny 1954; Timoshenko 1926):

$$EI\frac{\partial^4 u_y}{\partial x^4} + \rho A \frac{\partial^2 u_y}{\partial t^2} + c\frac{\partial u_y}{\partial t} + k u_y = P\delta(x,t) \tag{IV.16}$$

where EI (MN·m^2) is the flexural rigidity of rails, k (MPa) is the stiffness coefficient of the foundation, ρA_{rail} (kg/m) is the mass per unit length of rail, c (N·s/m) is the damping coefficient and $P\delta(x,t)$ represents the applied point load with the Dirac delta function. A solution of Equation (IV.16) is presented in Equation (IV.17) (Fryba 1999; Hendry 2007; Hung and Yang 2001; Krylov 1995):

$$u(x) = Ae^{-b'\lambda x}\left[D_1\cos(a_1\lambda x) + D_2\sin\cdot(a_2\lambda x)\right] \quad \text{with} \quad \lambda = \left(\frac{k}{2EI}\right)^{\frac{1}{4}} \tag{IV.17}$$

where λ a variable depending on the foundation stiffness k and flexural rigidity of rail EI, x is the horizontal distance from the axle load, A is the amplitude of deflection when x=0, b' is a parameter depending on the damping properties of material, a_1 and a_2 are variables defined by the train speed while D_1, D_2 are constant.

It is worth noting that Equation (IV.17) only allows calculating the surface displacements. To calculate the inner vibration of track-bed, this equation should be modified. In Figure IV.16, the longitudinal vibrations in SBG at 60 km/h and 100 km/h and the fitting lines following the form of Equation (IV.17) are presented. Equation (IV.18) describes the general expression of these fitting lines:

$$u(x) = Ae^{-bx}\left[\cos(\omega_{v_t} x) - \sin(\omega_{v_t} x)\right] \tag{IV.18}$$
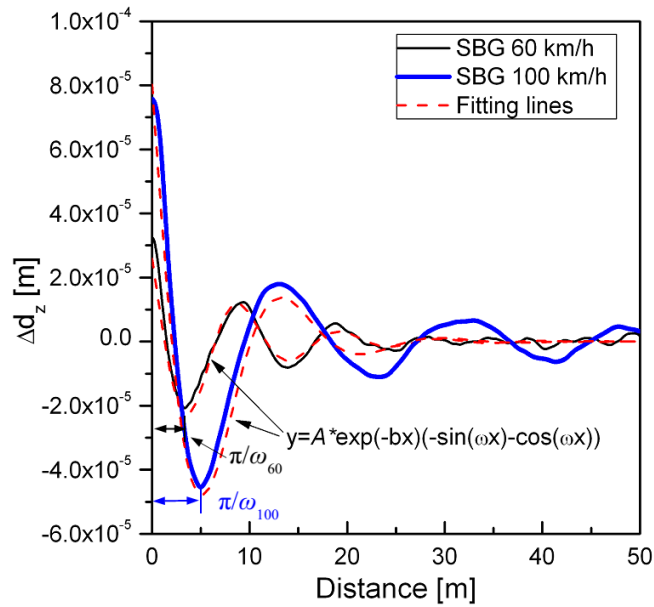
Figure IV.16. Relationship between displacement and distance

where b is an empirical parameter representing the longitudinal decay factor, variable ω is the circular frequency of a sinusoidal function as illustrated in Figure IV.16. Consequently, $2\pi/\omega$ is the period.

The period of vibration amplitudes gradually decreases with distance as shown in Figure IV.16. This attenuation depends on b and can be described by the negative exponential part of the equation. It should be mentioned that parameters from Equation (IV.18) are obtained by Nonlinear Least Squares Fitting (NLSF), a conventional fitting method. Moreover, it can be observed that the data from SBG agree well with this modified equation. Parameter b ranges from 0.2 to 0.3 and depends on train speed: it increases for speed up to 140 km/h and then decreases when the train speed reaches 200 km/h). As mentioned above, b depends on track-bed stiffness, rail flexural rigidity and damping properties of material. It can then be concluded that b is a constant for each track-bed material. Therefore, the average values are used in this study: 0.16 for sleeper, 0.29 for ITL, 0.25 for TL and 0.21 for SBG.

The relationships between parameters ω and v_T are illustrated in Figure IV.17. Note that ω is also obtained by nonlinear fitting of field data. It appears that ω decreases with speed until 140 km/h and becomes constant after this speed. In other words, the wavelength in Equation (IV.17) becomes larger when the speed is increased, and tends to be constant after a certain speed. This can be explained by the power spectrum density (PSD) analysis: more

cumulative energy can be obtained if higher frequencies are loaded or train speed increases (Lamas-Lopez, Alves Fernandes, et al. 2014). In the longitudinal profile shown in Figure IV.16, a higher envelope area and wavelength are indeed observed when train speed increases. Hereafter, an empirical relationship between ω and v_T based on the field data is proposed Equation (IV.19) and Equation (IV.20) and presented in Figure IV.17:

$$\omega_{vT} = -0.0042 \cdot v_T + 0.97 \quad \text{for} \quad v_T \leq 140 km/h \tag{IV.19}$$

$$\omega_{vT} = 0.38 \quad \text{for} \quad v_T \leq 140 km/h \tag{IV.20}$$
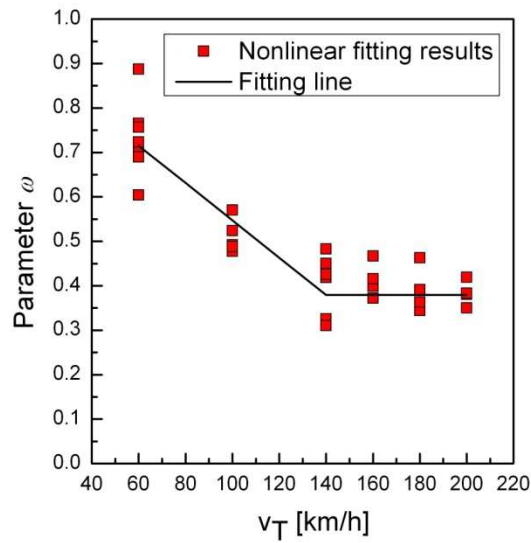
Figure IV.17. Train speed versus parameter ω

To transform the normalized amplitudes to absolute amplitudes, it is necessary to establish a relationship between deflection amplitudes and material properties. According to the full elastic-interaction theory (Paul and Hashemi 1981; Timoshenko and Goodier 1951), the static displacement u at distance r caused by a punctual load P on a homogenous half-space is given by Equation (IV.21):

$$u = \frac{P(1-v^2)}{\pi E r} \tag{IV.21}$$

where υ is the Poisson's ratio and E the global track elastic modulus (track stiffness). To solve a dynamic problem, the displacement can be approximated using the normalized amplitude $u^*(f,r)$ multiplied by the soil parameters (Auersch, 2005, 2006, 2014):

$$u(f,r) = \frac{P(1-\upsilon)}{2\pi G} \cdot u^*(f,r) = \frac{P(1-\upsilon)}{2\pi G} \frac{e^{-D \cdot \frac{\omega r}{v_s}}}{r} \cdot \begin{cases} 1 & for \ \dfrac{\omega r}{v_s} \leq 2.5 \\[2ex] \sqrt{(\dfrac{\omega r}{v_s})/2.5} & for \ \dfrac{\omega r}{v_s} > 2.5 \end{cases} \qquad \text{(IV.22)}$$

The normalized amplitude $u^*(f,r)$ depends on distance r, circular frequency $\omega = 2\pi f$, damping ratio D and shear wave velocity v_s. The soil elastic parameter part, $\dfrac{P(1-\upsilon)}{2\pi G}$, is composed of Poisson's ratio υ, axle load P and shear modulus G. In this equation, the soil Young's modulus, $E=2G(1+\upsilon)$, is used to transform the normalized amplitudes to absolute amplitudes. Finally, a general form of all the three mechanisms is developed Equation (IV.23):

$$u(x,z,v_t) = \frac{P(1-\upsilon^2)}{\pi E} \cdot f_{DAF}(\frac{v_t}{v_s}) \cdot f_{AC}(z) \cdot e^{-bx} \cdot \left[\cos(\omega_{v_t} x) - \sin(\omega_{v_t} x)\right] \qquad \text{(IV.23)}$$

where Young's modulus $E = 100$ MPa, Poisson's ratio $\upsilon=0.33$ (Alves Costa et al. 2015; Auersch 2015), the wheel load of locomotive $P = 112.5$ kN and the wheel load of coach $P = 50.25$ kN.

Figure IV.18 presents the comparison between the model predictions and the field measurements at ITL depth for the locomotive and coach loadings. Train speed impact can be appreciated in subfigures (a) to (c) corresponding to the following train speeds: 60 km/h, 100 km/h and 200 km/h. A good agreement between the analytical model and the measurements is obtained for different speeds and wheel loads. In particular, the displacement propagation in these layers presents a sinusoidal shape and exponentially attenuates in distance. The period of the sinusoids, defined by the term $2\pi/\omega$, increases with train speed. The deflection amplitudes in SBG are lower than in ITL, due to the factor of attenuation over depth represented by e^{-bx}. After the first complete period, the amplitudes decline rapidly in all layers and tend to zero. Figure IV.18 also shows that the initial amplitude varies with the axle load, speed and depth, through $f_{DAF}(M)$ and $f_{AC}(z)$.
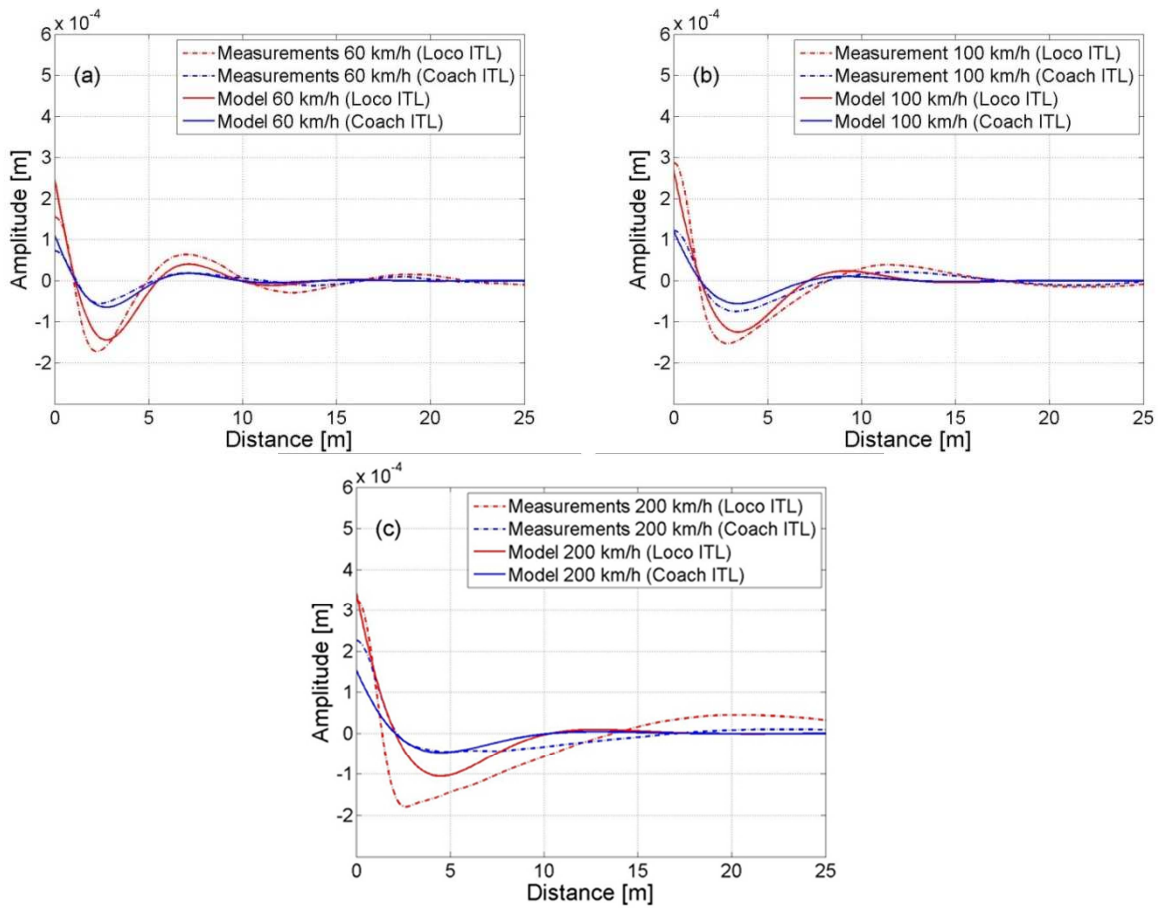
Figure IV.18. Comparisons between model and measurements in ITL: (a) 60 km/h; (b) 100 km/h; (c) 200 km/h

Figure IV.19 presents a summary of the input parameters, the variables and the output result using this vibration analytical model.
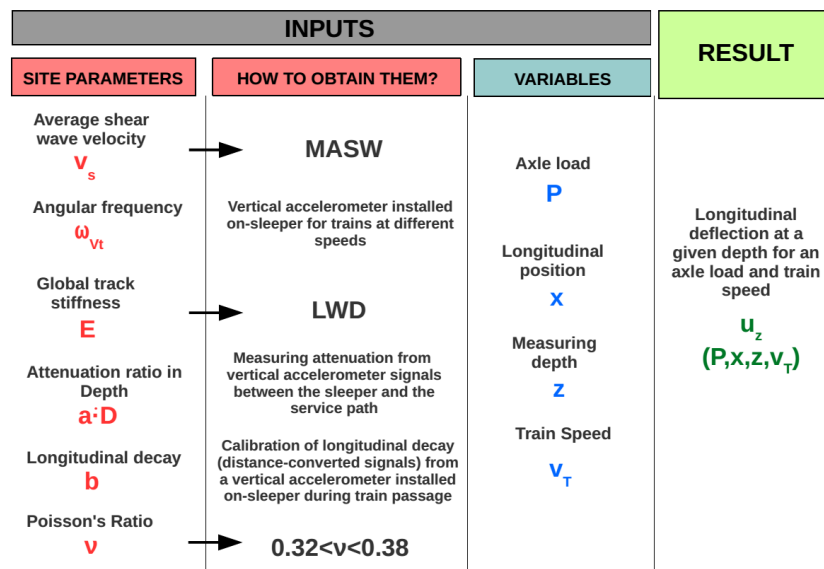
Figure IV.19. Summary of the analytical vibration model

IV.3   COMPARISON BETWEEN 'IN-SITU' & LABORATORY INVESTIGATIONS

The 'in-situ' monitoring allowed recording the responses of track materials for a short time period during a train passage: data recording lasted 45 s, and normally a train took less than 5 s to pass through the instrumented zone. In addition, in the monitoring zone, tracks were stable even under the heaviest loads exerted by the locomotives of Intercity trains running at 200 km/h. The rate of deterioration evolution over time (track settlement rate) was normal in the French conventional network. The recorded data was analysed in depth in Chapter II, identifying the main parameters influencing the behaviour of tracks.

In the laboratory, a conventional railway track material like the ITL was tested under different kinds of cyclic loadings at large number of cycles. The results obtained were used to assess the evolution of the elastic parameters and the permanent deformation of soil. Moreover, in Chapter III, for given soil state conditions (consolidation stress, moisture content, dry density, etc.), the soil permanent deformations were related to the cyclic deviatoric amplitude and the loading shape. It was concluded that, in the range of the cyclic loading amplitudes considered (lower than 16% of the soil's maximum shear strength identified by monotonic tests), the relationship of cyclic loading amplitude with the maximum permanent deformation after a large number of cycles is linear. Moreover, higher permanent deformations were identified under 'Sine-shaped' cycles than under 'M-shaped' cycles. This is because 'sine-shape' loading induced higher energy in both the loading signal and the response signal. Furthermore, the cyclic loading amplitude was also related to the energy developed by the materials' response (axial deformation) in the stabilized zone (last cycles of each cyclic loading level). Thereby, different loading shape or different cyclic loading amplitude may induce different developed energy contents in the material, and the soil's dynamic parameters (as modulus and damping ratio) are affected by these loading conditions, as seen in Chapter III. As a result, the higher levels of energy in the material's response correspond to larger permanent deformations.

In this section, the energy developed in the track response at different depths is correlated with the loading energy for different loading shapes. These different loading shapes resulted from different types of trains with different geometrical configuration of loads. Only qualitative comparisons can be made between 'in-situ' and laboratory results, because even under the same loading conditions, a low soil state conditions variation is expected.

Moreover, the inertia term in the equation of motion, the mass effect (supporting structure and loading mass) can be taken into account only in the 'in-situ' conditions. It is worth noting that the resilient modulus of ITL material estimated using 'in-situ' data was found lower than that determined in the laboratory because of this inertia term. However, a quantitative comparison of elastic modulus variations for both field and laboratory conditions showed a similar decreasing trend with the increase of cyclic loading amplitude (or train speed).

Firstly, in order to evaluate the amount of energy induced to a material or system, the amounts of energy developed for different cyclic loading amplitude levels in the laboratory (see Chapter III) are presented in Figure IV.20. It seems that the amount of cumulative PSD energy in loading signal is proportional to the cyclic loading amplitude (see method presented in Chapter III). Thus, the amount of energy included in a loading signal is an indicator of the induced load into a system. Following this reasoning, the stress signals obtained from the 'Vierzon experimental site' can be used to evaluate the induced loading to a track-bed material.
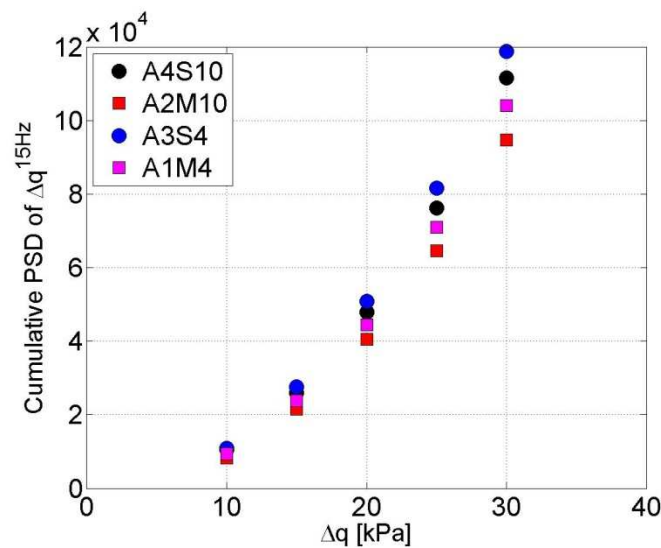
Figure IV.20. Relationship between energy in loading signal and cyclic load amplitude for different loading shapes and hydric states

Moreover, for a given hydric state, the amount of response energy is also proportional to the axial deformation per cycle (Figure IV.21).
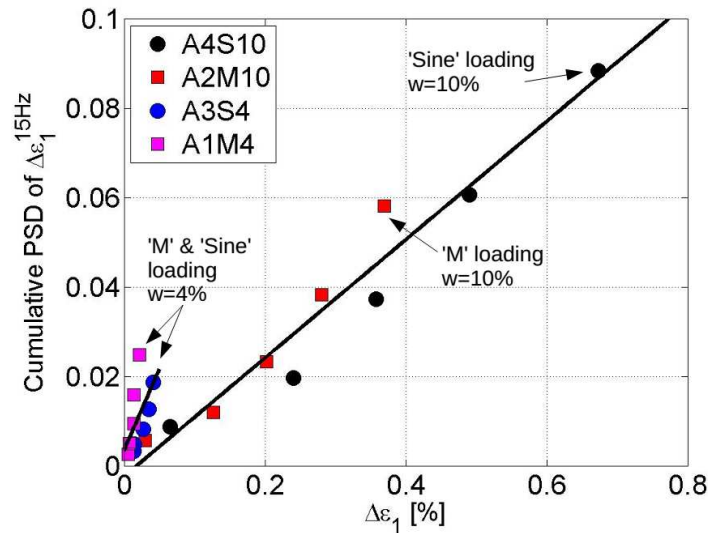
Figure IV.21. Relationship between the maximum developed energy measured in axial strain signal and the axial strain amplitude for different loading shapes and hydric states

Secondly, following the laboratory data analysis, the relationship between the amount of energy induced by loading (deviatoric load signal) and the response (axial strain signal) depends on the loading shape and material's hydric state (Figure IV.22). This means that the cyclic stress-strain behaviour of the material (elastic response under a given load) depends on the cumulated energy and its response. Therefore, it can be concluded that the relationships between the maximum cumulated energy in stress and strain signals (Figure IV.22) are related to the soil's resilient behaviour.
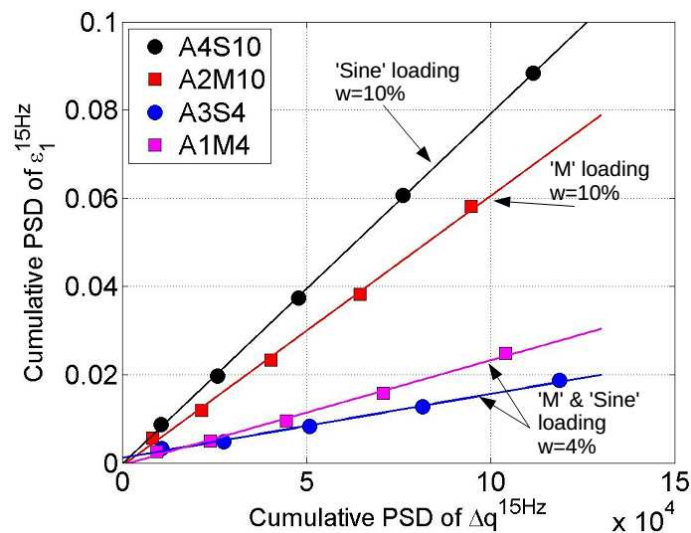
Figure IV.22. Relationship between the energy in the induced load signal and the energy in the response signal for different loading shapes and hydric states

For equivalent loading levels, the higher the energy developed by the response, the lower the resilient modulus of the material. Consequently, lower moduli are found in saturated ITL soils (more developed response energy) as compared to ITL soils at OPM (where lower response energy values were obtained).

The 'in-situ' data recorded under the passage of different types of trains were used to perform the comparison with the results from laboratory tests. Normally, with different axle geometrical configuration in different train models, the excited frequencies are expected to be different. In this study, two different train models, a 'TER Z21500' and a 'TGV Réseau', were selected. This is for several reasons: the axle load value of their coaches is very similar (around 150 kN/axle), the service speeds are similar (v_T=180~200 km/h) and their geometrical axle configurations are different (Figure IV.23).
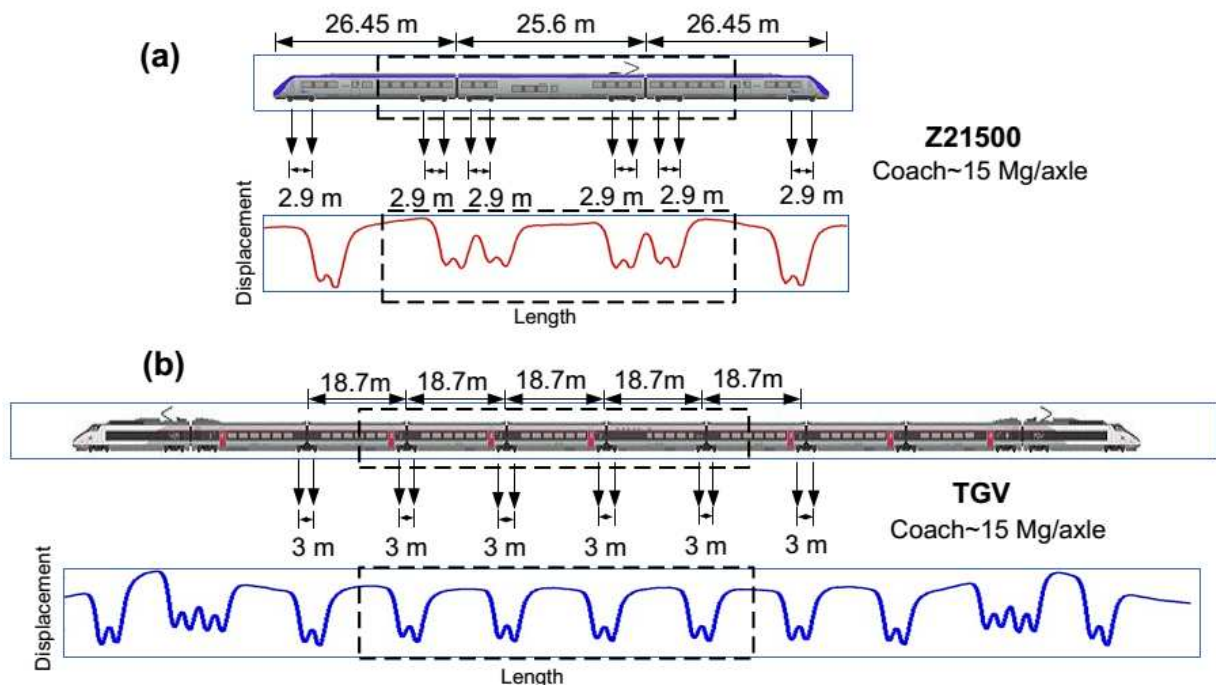
Figure IV.23. Outline and displacement signature of (a) TER Z21500 and (b) TGV trains. Extracted signal is also shown for each train.

In order to compare the track's response under equivalent loadings, only the signal corresponding to 8 coach's axles (4 bogies) in the middle of each train is considered in each case.

IV.3.1 Train types impact on ITL behaviour

The ITL behaviour is analysed under the loading by both types of trains. First, a comparison of the induced load at ITL by each type of train is made based on the records of a stress sensor installed at ITL (z=-0.90 m). Figure IV.24 presents the vertical stress ($\Delta\sigma_z$) signals induced by TER (Figure IV.24a) and TGV (Figure IV.24b) trains.
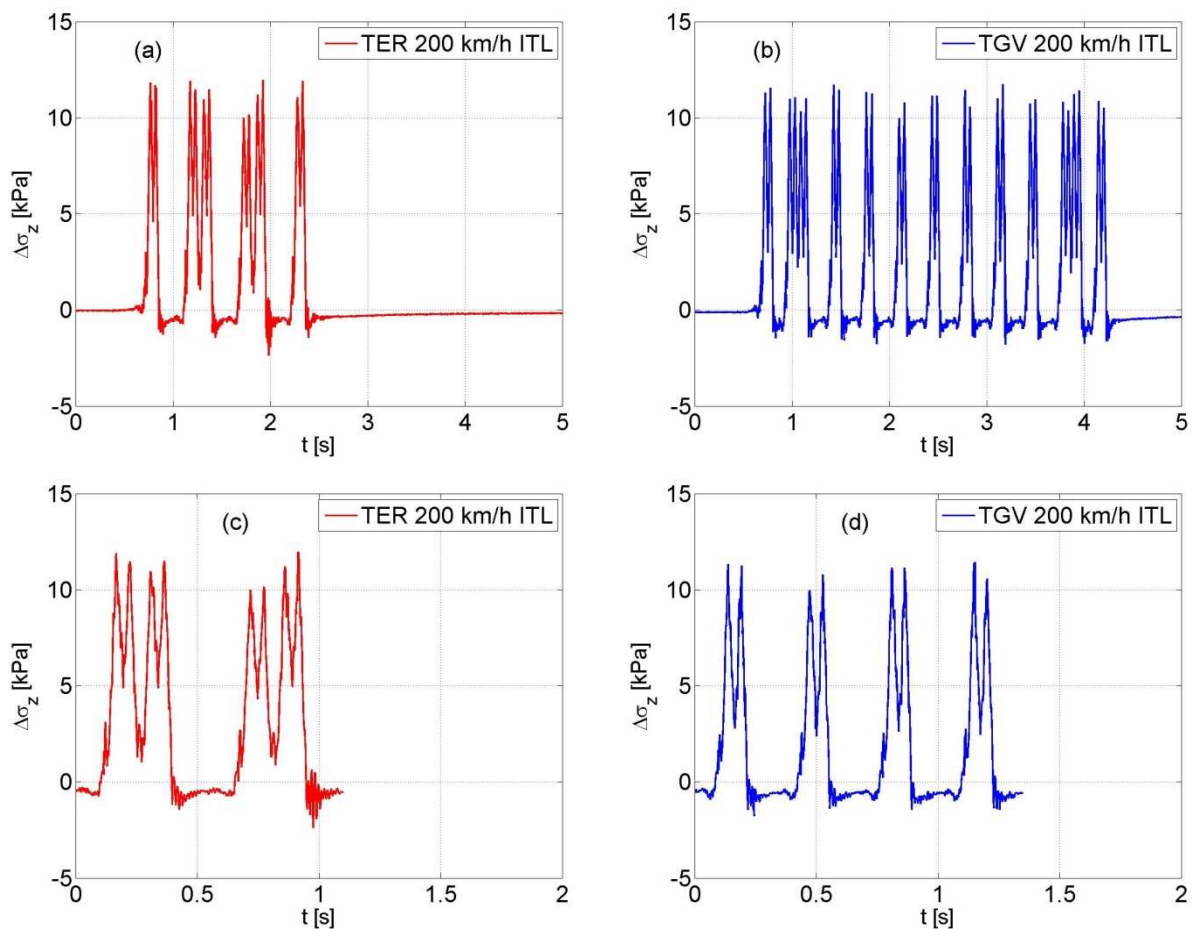
Figure IV.24. Vertical stress measurement in ITL under (a) TER Z21500 and (b) TGV loadings. Signal extractions of 4 bogies of the same axle load from (c) TER and (d) TGV trains.

The beginning of these signals (point zero) corresponds to 5 s before the passage of the first train axle (buffer of data logger). As shown in Figure IV.11, the time-related curves are transformed to distance–related curves. Once the time-domain is converted to distance-domain and the train's geometry is well known, the signal section corresponding to the 8 coach axles presented in Figure IV.23 is extracted. The signal section spans from the middle

point of the adjacent coach to the first axle to the coach middle point after the 8th axle. In the TGV case, the first considered bogie is the middle one between the second and the third coaches. These signal sections considered in further calculations are presented in Figure IV.24c for TER and in Figure IV.24d for TGV. The amplitudes of the vertical stress for each axle are found very similar for both trains, about $\Delta\sigma_z$=11.5 kPa in average. Moreover, low vertical stress variability is observed for all the 8 considered axles.

Moreover, as the bogies-distance wavelengths are smaller for adjacent coaches of TER than for the case of a TGV, this excited frequency is a little higher for TER: 7 Hz for TER against 6.5 Hz for TGV at 200 km/h. Beyond these frequencies, no more important energy peaks are observed. As the frequency-domain is not suitable for discerning which signal has more energy, the parameter of total cumulative energy at a given frequency is chosen for this purpose. Figure IV.25b presents the cumulative energy included in the vertical stress PSD signals by every 0.1 Hz frequency. This vertical stress cumulative PSD is more or less stabilized from 15 Hz, beyond which no significant energy is generated to the system. More than 80% of the energy (considering that the 100% is the total at 25 Hz) is caused by the frequencies lower than 8 Hz. In addition, the energy difference between both trains at 25 Hz is lower than 10% of the total energy in TGV or TER case. Consequently, we can reasonably consider that the load of 8 axles (same speed and same axle weight) is equivalent for both trains.
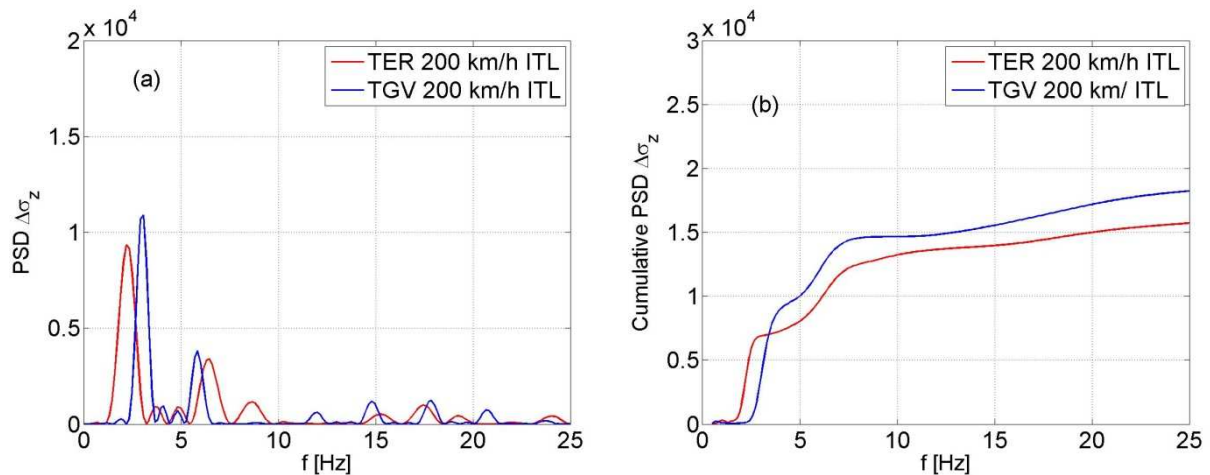
Figure IV.25. (a) Power Spectrum Density (PSD) of vertical stress signal in ITL for 4 bogies; (b) Cumulative PSD energy versus frequency

Once the induced energy is assessed for both trains, the developed energy by the track-bed mechanical response in ITL can be analysed. The variable that will be considered as indicator for the material's response is the vertical displacement. The vertical displacement signals in ITL are presented in Figure IV.26a for TER and in Figure IV.26b for TGV. The same 8 axles response are extracted from the whole signal, and the results are presented in Figure IV.26c for TER and in Figure IV.26d for TGV. Note the considered signal was extracted in the same manner as for the vertical stress signal. It appears that the vertical displacement amplitudes are similar for both trains (around 0.4 mm per axle). However, their spatial configurations are different.
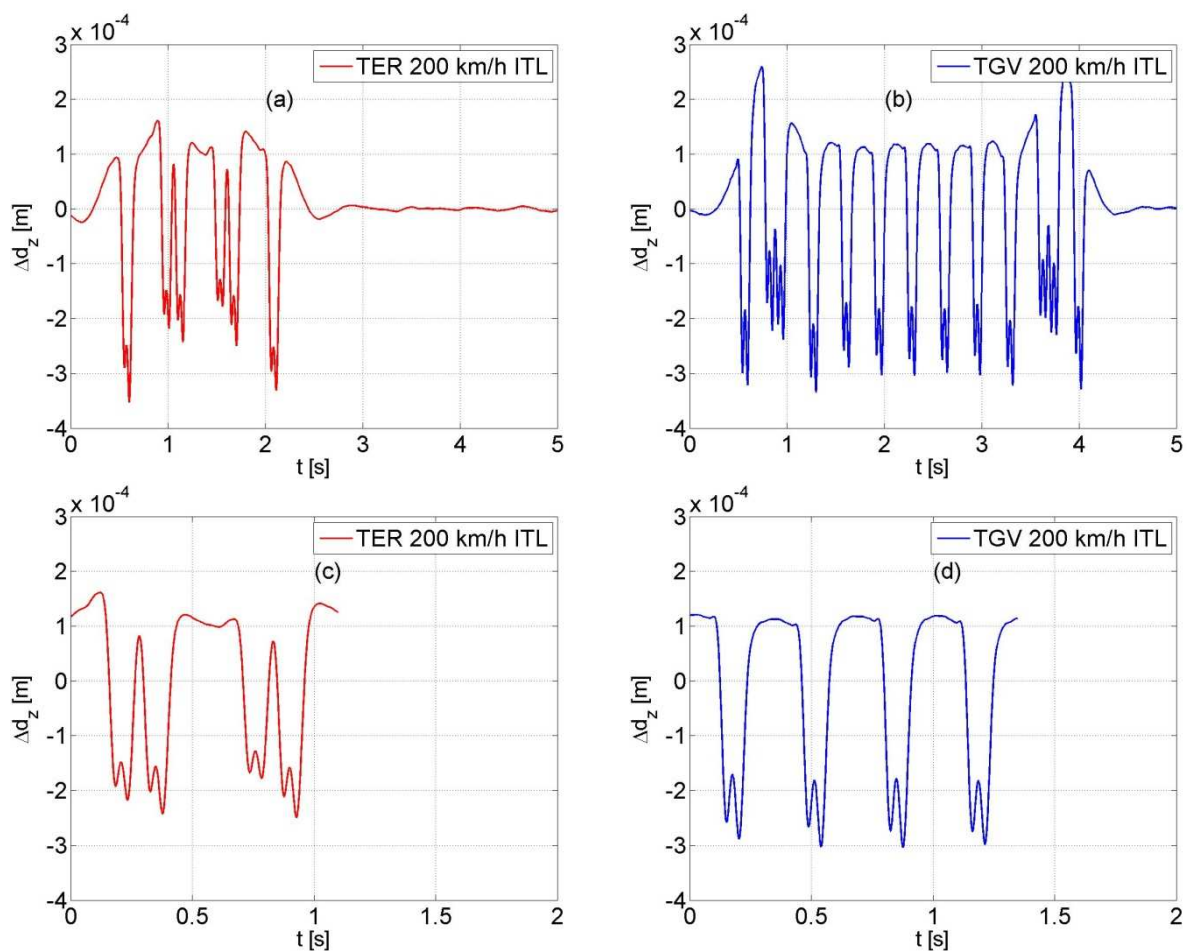
Figure IV.26. Vertical displacements in ITL under (a) TER Z21500 and (b) TGV train loadings. Signal extractions of 4 bogies of the same axle load from (c) TER and (d) TGV trains.

In order to assess the response energy development, the same procedure as for the vertical stress signals is used for the vertical displacement ones. Figure IV.27a presents the frequency-domain response of the vertical displacement for both trains. The same excited frequency

differences are found as for the vertical stress signal. Nevertheless, the cumulative PSD diagram (Figure IV.27b) shows a difference between both trains, of about 20% of the total energy developed by a TGV in ITL. Therefore, it can be concluded that under similar loadings, the TGV configuration develops more energy in ITL than the TER Z21500 one.
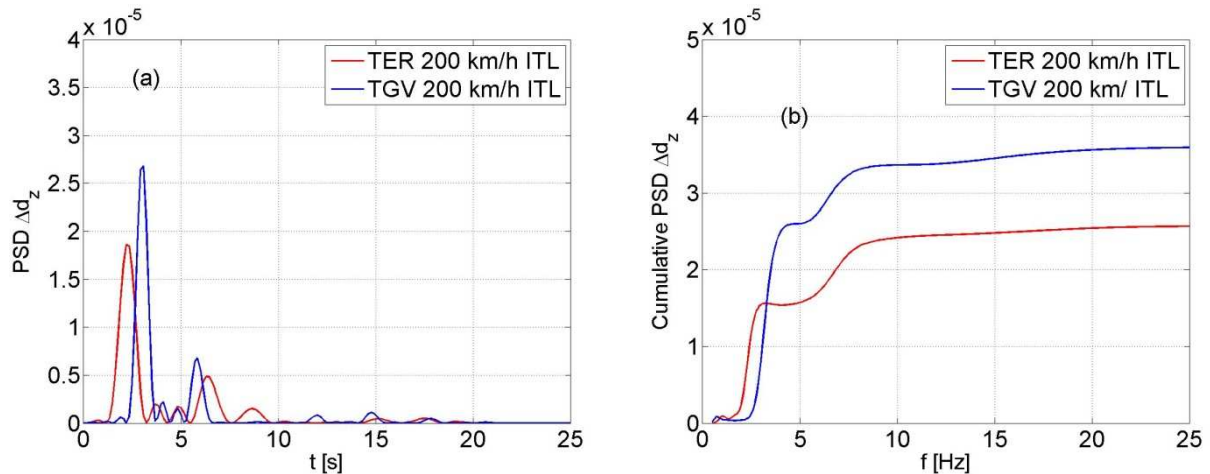
Figure IV.27. (a) Power Spectrum Density (PSD) of vertical displacement signal in ITL for 4 bogies; (b) Cumulative PSD energy versus frequency

As described in Chapter II, only about 2% of the traffic on Vierzon site involved TGV trains (usually running at about 200 km/h), and 8% TER Z21500. Most of the TER Z21500 trains (90%) run at about 150 km/h, but some of them running faster, at speeds between 180 and 200 km/h. In order to perform a comparison, only the trains running at a similar speed are compared because the train speed can influence the energy transferred to the track-bed and the energy developed by the track's response. The trains running at 180-200 km/h are selected for this purpose.

The data of May 2014 was used to calculate the total cumulated transferred energy to each layer and the developed energy by each layer (ITL and SBG depths are considered) in the first 25 Hz. Figure IV.28 presents the comparative results for different trains. It is observed that for both layers, ITL and SBG, the relationship between the inferred energy and the developed response energy depends on the train type and train configuration. Larger variability of energetic response developed in shallower layers (ITL) compared to deeper layers where load attenuated significantly. Furthermore, the range of developed energetic response by TGV is always higher than that by TER in both layers.

Based on the observation that the order of magnitude of resilient modulus is the same for both depths under train axle loadings (see Chapter II), a trend line is attempted linking the points that correspond to the same type of train at different depths. This line represents the track-bed trend in developing an energetic response when a given amount of energy is induced by traffic loading.
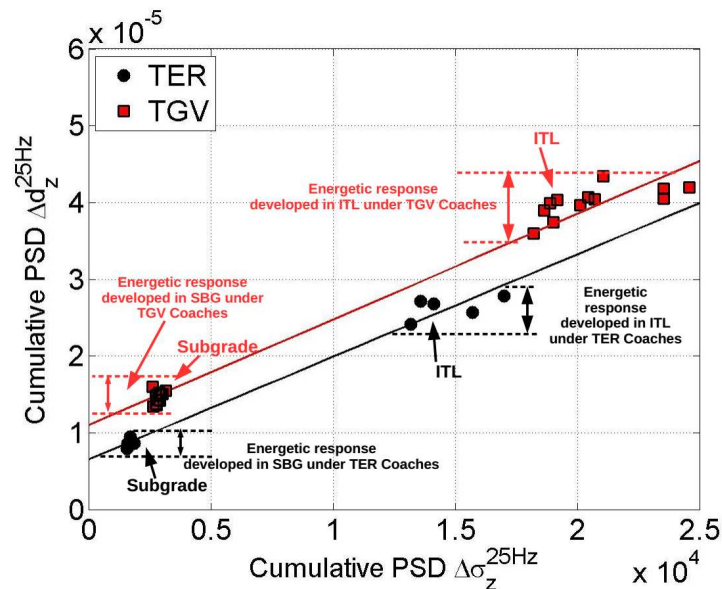
Figure IV.28. Relationship between induced energy (vertical stress) and developed energy (vertical displacement) of TER and TGV trains at ITL (-0.90 m) and SBG (-2.3 m)

Even though the relationship between the induced energy and the response energy depends on the elastic behaviour of soil, it was identified in Chapter III that the cumulative response energy is related to the permanent deformations reached under each cyclic loading (Figure IV.29). Moreover, the cumulative response energy was measured using cycles taken from the stabilized zone (where low permanent deformations per cycle were produced) after a large number of cycles. Nevertheless, Vierzon site being a stable track, and only higher traffic loadings (increasing train speed or axle load) may cause larger track permanent deformations during the first loading cycles. Therefore, based on the relationship in Figure IV.28, it can be inferred which train configuration can cause larger deformation of track-bed materials when higher levels of loading energy are induced.
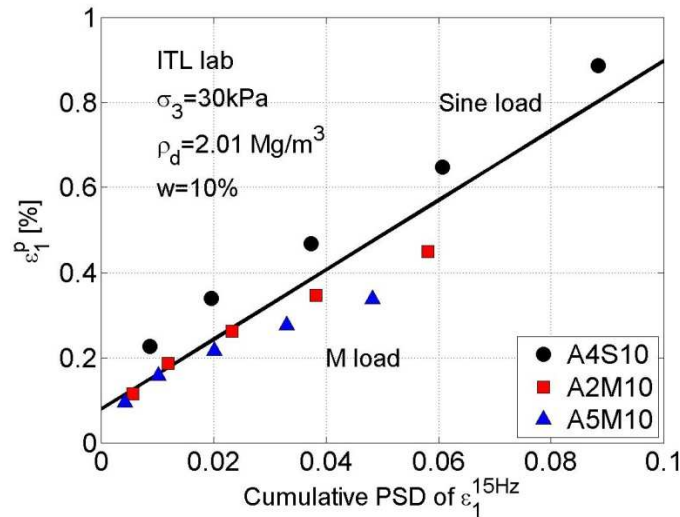
Figure IV.29. Relationship between the maximum cumulative PSD energy developed by the material's response (during 10 cycles) and the maximum permanent deformation for each considered cyclic loading amplitude (w=10%)

IV.3.2 Industrial application – On-surface measurements

Once the ITL response under different train loadings is assessed using embedded accelerometers, a similar analysis is conducted using the on-surface accelerometers installed in 'Vierzon Experimental Zone'. This analysis aims at comparing the results of loading and response based on the on-surface accelerometers with those previously obtained based on the embedded accelerometers. The advantage is obvious: the accelerometers installed on sleepers would allow the railway infrastructure operators to obtain more easily the global track's response under traffic loading thanks to their rapid and easy installation.

The same trains are taken into account (TER Z21500 and TGV) and the same 8 axles (4 bogies) are extracted from the analysed signals. As the imposed loads in layers of ITL and SBG were measured using stress sensors, they are unable to be installed on-surface. Consequently, this load is estimated based on the records of strain gauges glued to the rail (see Chapter II). These gauges measured the deformation of the rail during the passage of a train, and this deformation is proportional to the imposed load from each train axle using a conversion factor (from µm/m to kN). Figure IV.30 shows the full strain gauge signal (translated from µm/m of rail to load using the same coefficients as described in Chapter II) during the passage of a TER and a TGV. The extracted signals for the 8 considered axles (same as previous section) are also presented in Figure IV.30.
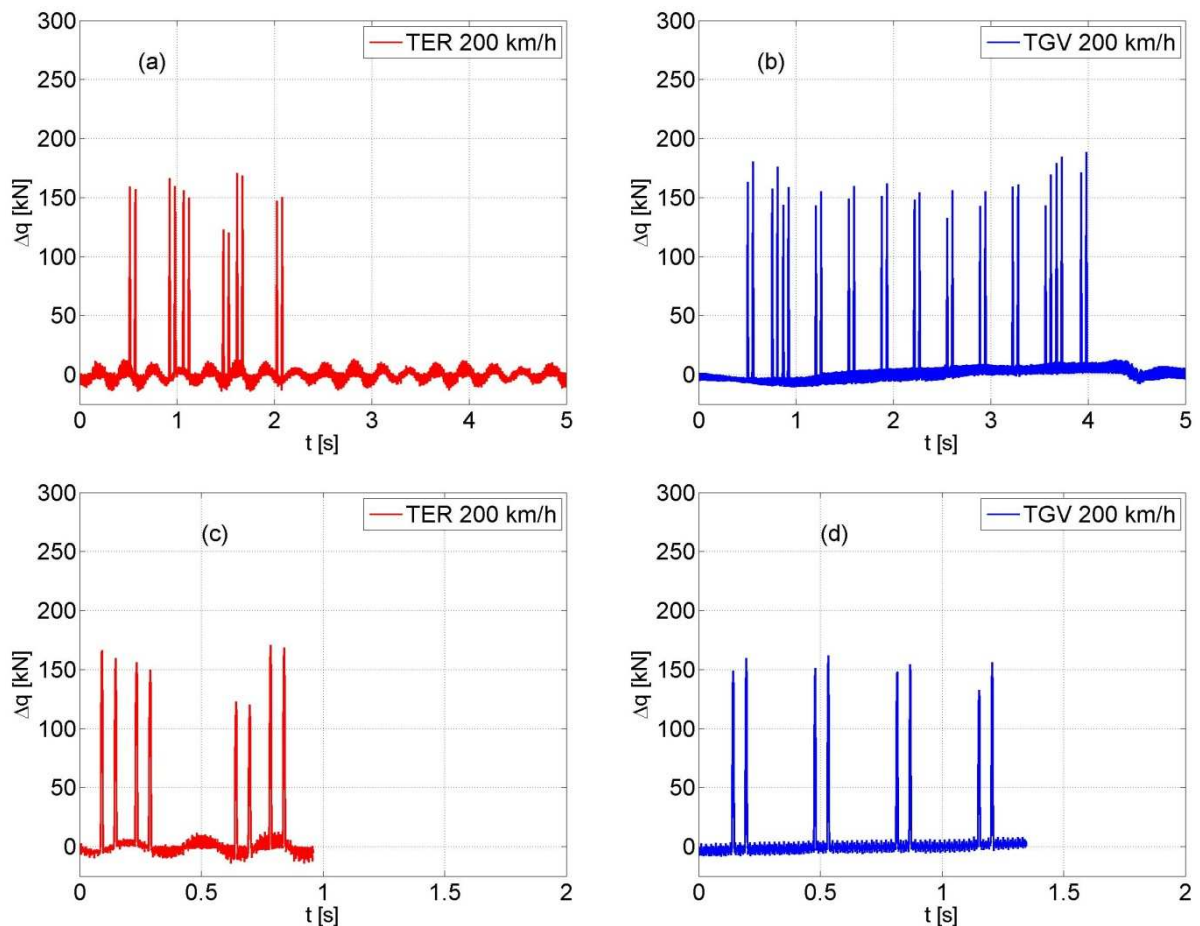
Figure IV.30. Axle load estimated from rail strain (strain gauge glued to the rail) under (a) TER Z21500 and (b) TGV trains loading. Signal of 4 bogies of the same axle load for (c) TER and (d) TGV trains.

Following the method presented in the previous sections, the cumulative induced energy for each frequency is determined for the extracted signals shown in Figure IV.30c and Figure IV.30d. Basically, the excited frequencies for this strain gauge are different from those recorded by the stress sensors because these gauges are glued to a different material (rail). The rail excites a larger range of frequencies for both trains (0-150 Hz) due to the influence of small wavelength defects in the high frequency range (Figure IV.31a). Most of the energy is developed by the low frequencies (excited by long wavelengths) and is stabilized from 150 Hz for both trains (Figure IV.31b). Even higher frequencies are excited (as 200 Hz in the TGV case of Figure IV.31a), limited amount of energy was developed by the signal for these high frequencies. The cumulative energy in PSD stabilizes at a given frequency (as stress signals embedded in track-bed). After analysing the maximum energy developed (at the stabilized zone after 150 Hz) (Figure IV.31b), it reveals that the loading levels for both trains

are the same. The difference in this cumulated PSD energy is lower than 1% of the total developed by each train.
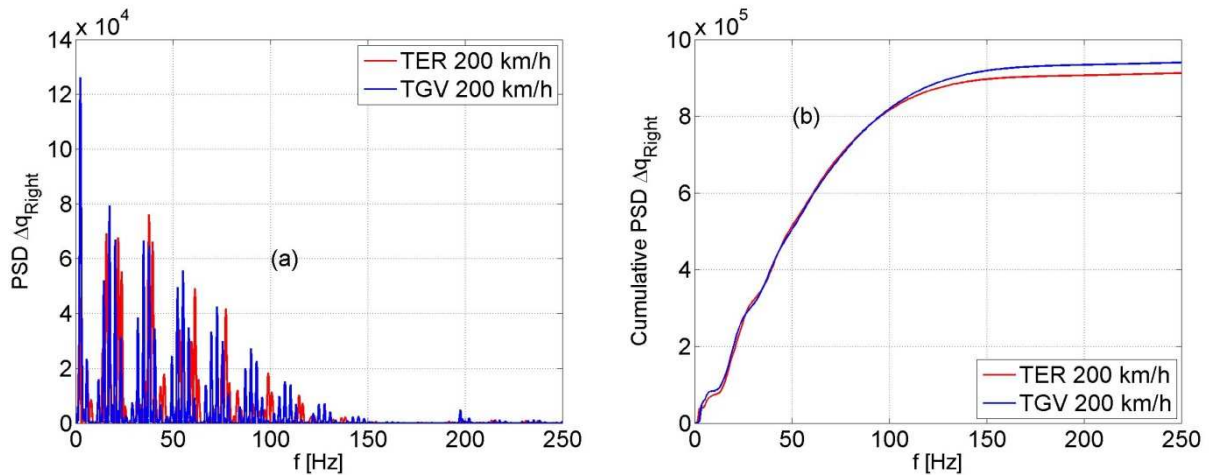
Figure IV.31. (a) Power Spectrum Density (PSD) of rail strain extracted signal in ITL for 4 bogies and (b) Cumulated PSD energy of vertical displacement signal for frequency from 0 to 250 Hz

The identified loading level equivalence allows the track's response to be analysed using the on-surface accelerometers. The same method as for the embedded accelerometers in ITL (Figure IV.26) is used in the analysis. The sleeper's deflections are calculated from the accelerations and used as track's response. It appears that the cumulative energy from the vertical deflection's PSD from accelerometers installed on sleeper also stabilized at 15 Hz as for the embedded accelerometers (Figure IV.27). Thus, the maximum cumulative energy at 250 Hz (where energy stabilized) can be determined for both TER and TGV trains.

Consequently, the track's load and response under each train passage are determined using the on-surface measurements (Figure IV.32). As for the embedded measurements (Figure IV.28), the on-surface results (Figure IV.32) for TER and TGV trains (at speeds ranging from 180 to 200 km/h) show a higher energy response under 8 passenger's coach axles of TGV trains that that under equivalent load by TER trains. The accumulative energy borders (min and max) measured in vertical deflection's PSD are well defined for both train types (Figure IV.32). The range of developed energy is much larger for TGV trains than for TER trains. Therefore, for equivalent loadings, the axle's configuration (different excited frequencies) greatly influences the track energy response. In addition, it also appears that by measuring the track's response on-surface (sleeper's vertical deflection for instance), it is possible to identify which type of trains results in higher energetic response.
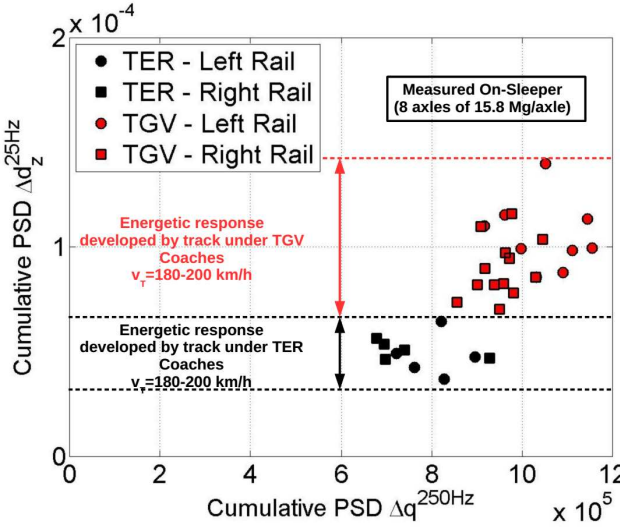
Figure IV.32. Relationship between the induced energy (vertical axle load) and the developed energy (vertical displacement) at sleeper (z=0.0 m) for TER and TGV trains

From these results, it can be concluded that if a train service speed upgrade is performed on this track, a lower impact is expected for TER trains than for TGV trains. If higher traffic loads that have not been encountered by the track yet are applied on the infrastructure, larger permanent deformations are expected. Interestingly, the impact of train loadings on the infrastructure can be assessed based on on-surface monitoring.

The ballast layer plays a capital role in the track-developed energy. Changes in mechanical properties of ballast will greatly affect the developed energy of the entire track-bed. Performing this kind of analysis would help more easily identify where the track-bed mechanical response under similar train loadings is evolving faster. An increase or decrease of the developed energy under similar railway loads is an indicator of the degradation of track-bed mechanical performance.

IV.4 SUMMARY AND PERSPECTIVES

In this chapter, two analytical models were proposed. The first one allows the determination of the propagation of vertical stresses and the second one allows the determination of the propagation of longitudinal deflections under a train axle passage. An analysis method was also developed allowing a quantitative comparison between laboratory results and field measurements.

The first analytical model required 5 input parameters and 3 variables to assess the vertical stresses during a train passage at a given depth in the track-bed. To develop this model, three stress distribution models based on Boussinesq elastic theory were first assessed under different stress spreading conditions. The hybrid model considering a load normal longitudinal distribution depending on the soil's elastic parameters showed a good correlation with measurements. The key parameters for this model are the track-bed layers moduli and their thicknesses. At a given depth, the stiffer the soil compared with the subjacent layer, the higher the stress reached. The track-bed soils' internal friction angles seem to have limited effect on the results.

The second model have 6 input parameters that are easily identifiable based on the results from on-surface monitoring and geotechnical/geophysical track prospections, and 4 variables to assess the propagation of vertical deflections at a given position of a track-bed. A good correspondence between measurements and model was found with an error lower than 10%. Moreover, using the proposed soil's elastic parameters as the global track stiffness and Poisson's ratio, the deflection amplitude just under the loading (origin point) was also well determined, with an error lower than 2%. However, as track-bed soil is assumed to be layered, larger deflection attenuation in depth was found for the ITL soil compared to the other track-bed materials. Thereby, the track-bed was homogenized using at least two measurements for the materials at different depths (on-sleeper and service path for instance). A deflection attenuation factor was determined by exponentially fitting data. It was observed that the main parameter controlling the deflection amplification with train speed is the average shear wave velocity for the first 5 m of track-bed.

For the comparison between the in-situ and laboratory results, a method was developed based on the analysis of the induced energy and the response energy. For the in-situ conditions, the load and response energies were determined from the records of different sensors installed at different in-situ track positions. For the laboratory conditions, the cyclic deviatoric stress amplitude was linearly related to the accumulated energy developed in the low frequencies of deviatoric loading signals. It should be noted that these laboratory tests were controlled by deviatoric amplitude. The same relationship was found in the material's response, between the axial strain amplitude and the energy accumulated in these signals. Moreover, it appears that the amount of energy developed by a given axial strain amplitude depends on the moisture content. Therefore, it is concluded that the stress-strain relationship of a material is related to

the energy developed by a loading and response signals during a cyclic loading. Note however that this is only valid when limited permanent deformations develop after each cyclic loading or the material behaviour is mostly elastic. The laboratory tests also brought to light the linear relationship between the response energy and the maximum accumulative permanent deformations. This relationship depends mainly on the soil's moisture content and the loading's shape and amplitude have limited effects.

Based on the consideration of energy, the impact of a given train loading on track's behaviour can be analysed. Firstly, the effect of axle configuration that defines the excited frequency on soil's energetic response was investigated. In order to make the comparison under similar loads, two equivalent loads from TER and TGV trains running at similar speeds were taken into account. TGV has the different axle configuration than TER, thus, different frequencies are excited depending on train typology, however higher cumulative PSD energy in the responses was measured in ITL and SBG for the former. Secondly, the same analysis was performed using on-surface measurements. The measurements were done by on-surface sensors as accelerometers on sleepers and strain gauges glued to the rail. These sensors can be installed easily and do not need boreholes. This analysis aims at evaluating the global track's response. The load analysis showed that the energetic contents of both TGV and TER applied equivalent loads. However, there was a clear difference between the energetic responses developed under the effects of TGV and TER trains. For both trains running between 180-200 km/h during May 2014, the energetic response was larger in the case of TGV trains. This is in agreement with the observation on the behaviour of ITL or SBG soils. It is worth noting that an increase of train speed or weight per axle will also increase the track's energetic response.

In conclusion, the parameter controlling the track behaviour is the track energetic response developed under traffic loading. This parameter can be determined simply based on the measurements by an accelerometer on sleeper. Thus, by installing vertical accelerometers on sleepers, the evolution of the track mechanical behaviour can be monitored. The spacing between the monitoring points depends on several factors such as the expected accuracy, the changes of track elements, the geological formations etc. With an accelerometer installed every 3 sleepers (~1.8 m), a good resolution of a complete railway line behaviour can be obtained. In order to measure the energetic response developed by the track, a low energetic consumption sensor installed on sleepers (or to their fastening system), with a large autonomy and able to recharge itself using train vibrations, should be developed. This kind of sensors

should also be wireless and transfer information between them using peer to peer technology (linking them to a data logger).

The energetic response could be calculated for every passing train and compared to other measurements under equivalent loadings (same train type, different moments). This method can be applied to all track sections and consequently a digitalization and continuous monitoring of infrastructure can be achieved. Other analyses that could be performed is to follow a single train journey (same train type all over the route) and estimate the energetic response of every point in which an accelerometer is installed. As a result, the points along a railway line where large response energetic develops can be identified. A higher energetic response could be due to softer subgrade soils, higher soil degree of saturation or significant degradation.

The geophysical survey can be also applied for a continuous control. As one of the main elastic parameters is the global track modulus, its monitoring would make possible the analysis of the track evolution. This can be done through measuring the average shear wave velocity in track-bed materials. This average shear wave velocity could be determined for the subgrade between two measuring points using the passive MASW method. This method does not use railway traffic loading to estimate the shear wave velocity through a material between two monitored sleepers, but uses the ambient noise. For this purpose, capacitive accelerometers allowing recording very low frequencies are required. The measuring depth depends on the distance between the monitored sleepers.

More applications can be developed with monitored sleepers, some of them concerning the increase the preventive maintenance or the railway operation security on the infrastructure. This method also allows the detection of foreign elements as falling rocks over railway tracks. In the future, these sensors that control the mechanical behaviour of the track could interact with the operation signalling system. Therefore, this interaction between the infrastructure mechanical state and the signalling system could optimize the use of the infrastructure according to the track mechanical performance at every moment (modifying the maximum service speed or allowable axle weight).

CONCLUSION AND FURTHER RESEARCH

CONCLUSIONS

A study on the dynamic behaviour of conventional railway track-bed materials has been presented. Emphasis was put on the assessment of the impact of traffic upgrade. Both field monitoring at a representative site selected (Vierzon) based on well-defined criteria and laboratory testing were conducted. The analysis of '*in-situ*' data brought a general overview on the dynamic amplification of mechanical variables such as stress and strain under different axle loads and speeds at different track-depths. The amplitude of track material response in stress or deflection was found proportional to the axle load. The dynamic amplification factor reached a value of 3 when the train speed was closer to the surface wave velocity. The resilient modulus measured in the shallower layers decreased by about 15% in a non-linear but reversible fashion when the train speed increased from 60 km/h to 200 km/h. In the laboratory testing, a representative ITL track-bed material was prepared and tested under different conditions defined based on the field monitoring results. The cyclic loadings were defined to assess the effects of cyclic amplitude, loading shape (Sine-shaped and M-shaped), loading frequency and moisture content. The dynamic response of the ITL material was evaluated after small and large numbers of cycles. It was observed that the resilient modulus decreased and the damping ratio increased (in particular during the first loading cycles) when the cyclic loading amplitude increased. The shape of the cyclic loading influenced the induced energy to the system and the soil response. The permanent deformation at large number of cycles follows a linear relationship with the amount of energy induced at each loading level.

Based on the results from field monitoring and laboratory testing, 2-D analytical models were established allowing describing the vertical stress and deflection transmission. Some mechanical parameters such as the moduli of track-bed layers, their damping ratios, thicknesses, the ratio between the moduli of adjacent layers and the average track surface wave velocity were found to be the key parameters governing the track dynamic behaviour. Besides, a comparison between field and laboratory results was made in terms of track energetic response under equivalent loads. For this purpose, different train models, TGV and TER, were taken into account. It was found that the energy developed by TGV trains is higher

at all track layers and at surface as well, suggesting their higher aggressiveness to the track-bed.

In the following, the main findings are summarised in more details.

- The ITL has an important role in the mechanical behaviour of a conventional track. This naturally formed layer greatly contributes to the mechanical stability of track. This layer could evolve under the effect of higher load amplitudes generated by traffic upgrade: the layer thickness or density can increase due to the development of permanent deformations. Furthermore, if a track renewal or maintenance operation is required for a conventional track and its ITL needs to be removed, due to mud pumping issues caused by subgrade fines for instance, the role of the ITL should be replaced by a transition soil (like sub-ballast) from ballast to subgrade, with low permeability, high stiffness (and consequently density) and thick enough to properly distribute the loads through the subgrade soil.

- The moduli and thicknesses of conventional track-bed layers, key parameters in the dynamic behaviour of a conventional track, can be effectively assessed by analysing the tip resistance results from a dynamic cone penetrometer test (as the PANDA). At the monitoring site, larger moduli were found in ITL and TL soils compared to the SBG due to the higher soil density and the presence of coarse inclusions. Analysis methods were provided in this thesis in other to better delimitate and mechanically assess the different layers from conventional layers by combining the obtained data in geo-endoscopic and DCP tests.

- More than 98% of track deflections were developed in the low frequency range, caused by long wavelength elements of the train load. In addition, 95% of the total deflection amplitudes under a train axle are generated by the wavelengths longer than the inter-axle distance of a train (about $\lambda = 2.8$ m for an Intercity train; f=21 Hz at 200 km/h).

- The maximum stress, acceleration, deflection and strain amplitudes were developed in the soil just under the train axle loads. These amplitudes depend mainly on the track elastic parameters such as the shear wave velocity or the track-bed layer modulus. The ratio between the moduli of adjacent layers is a key parameter for the stress distribution over depth. Moreover, these maximum peak values were amplified by the train speed increase. The surface wave velocity of vibrations is considered as the critical velocity v_{cr} of a track section, at which the track response reaches a local

maximum when the train speed is close to this value. This surface wave velocity v_R depends mainly on the elastic parameters of track subgrade such as the average track-bed shear wave velocity v_s.

- The train speeds till 0.4 times the v_{cr} of the monitoring Vierzon site were considered in the study. The amplifications were found to reach about 30% in stress, and 50% in vertical deflection and strain. Furthermore, the relationship between the stress, deflection/strain amplification and the train speed was found quasi linear, while the relationship between the acceleration and speed is rather exponential (in the range 0-25 Hz) for the tested speeds. The changes of deflection and strain with train speed are supposed to become also exponential for speeds closer to the critical speed of the site. The deflection amplification rate was found similar for all the monitored depths.

- The change of peak value amplification is also quasi linear with increasing train axle load at all the monitored depths. The stress decrease, acceleration, deflection and strain peak values is exponential over depth. In addition, all these amplitudes exponentially attenuate over depth. However, it is worth noting that the attenuation in ITL layer is more pronounced due to its higher stiffness, higher density and larger damping ratio as compared to other soils. When measuring the peak amplifications with speed during 5 months (using commercial train passage) it has been measured a low variability around the average value for vertical stress, deflection and strain amplitudes in the range of speeds tested.

- The ratio between the stress and strain amplitudes is defined as the soil resilient modulus M_r. This modulus was found to be non-linear with train speed. It decreases when the train speed increases for both ITL and SBG, but mostly for shallower layers as ITL where larger strain amplifications are developed. Note however that this change is reversible in the very stable Vierzon site with no special maintenance operations required in the last years and low permanent deformations rates (longitudinal levelling evolution is normal compared to the rest of conventional lines). Modulus decreases and damping ratio increases (mainly in shallower layers) can be expected under traffic upgrade.

- The loading history impact on the resilient modulus M_r was investigated through laboratory testing. The results revealed that only the application of a cyclic stress amplitude higher than that underwent by the soil in its history decreases the modulus strongly during the first cycles, with significant permanent strains produced. After

that, the modulus starts to recover to a new stable and lower value than the previous one. This modulus attenuation is non-linear with the loading amplitude and occurs mainly in the cyclic strain amplitude range comprised between $\varDelta\varepsilon_I=10^{-5}\%$ and $\varDelta\varepsilon_I=10^{-3}\%$. The damping ratio was found similar for different moisture contents. However, in the case of saturated soils there is a strong increase during the first loading cycles of a loading amplitude – the dissipated energies are larger because of the larger cyclic strains.

- For the saturated ITL soils, the total permanent deformation after a large number of cycles increases with the cyclic loading deviator amplitude in a linear way for the tested cyclic stress ratios up to $n_{cyclic}=0.16$. By contrast, this permanent deformation is close to 'zero' for higher density soils as the ITL at OPM. The total permanent deformation rate depends not only on the cyclic stress ratio but mainly on the moisture content. The deformation can be 100 times larger for saturated soils compared to the same soil at OPM under the same number of loading cycles.

- The relationship between the permanent deformation and the cyclic loading amplitudes depends also on the cyclic loading shape because the amount of energy provided to the system and the energy developed are different in each case - higher energies were observed for Sine-shaped loadings as compared to M-shaped loadings. Moreover, the induced energetic content of the loading signal was found to be directly related to the cyclic deviator amplitude. The different loading shapes considered induced similar energy amounts to the system. Nevertheless, the energetic content of the soil's response depends on the cyclic strain amplitude and the moisture content. The energy amount was estimated by considering the cycles after stabilisation of the permanent strain evolution, where the soil behaviour is mainly elastic and low permanent deformations per cycle are developed. Saturated soils developed always higher energy response than OPM soils. In addition, the energetic response of Sine-shaped loads was found larger than the M-shaped loads, especially for saturated soils. At similar load amplitude, a higher energetic response results in lower resilient modulus values. Constant modulus differences were found for soils at different moisture contents.

- The energy developed by the soil's response, regardless of the loading shape or strain rate, was found to be linearly related to the permanent strain developed. This observation was used to compare the energetic responses of two different train types, TER and TGV, at similar speeds and with equivalent total axle loads but different axle

spatial configurations. The different axle configurations resulted in different loading frequencies but similar total energy in the low frequency range. For the three considered positions (surface, ITL and SBG), it was found that the TGV train developed larger amount of energy, suggesting a higher aggressiveness to the track-bed; this is in agreement with the observation in the laboratory when comparing the effects between the Sine-shaped and M-shaped loadings.

FURTHER RESEARCH TOPICS

The present study allows better understanding the dynamic behaviour of materials constituting the railway conventional track-beds in the context of traffic upgrade. In light of the findings obtained, various research axes can be proposed.

- Considering the evolution of the volumetric fraction f_v of ballast grains in ITL over depth, it seems important to investigate the effect of f_v of inclusions on the cyclic behaviour of coarse grain soils with a fine matrix soil. This will allow to complete the study by analysing the material with fine soils as predominant components. This study can be based on the works of Pedro (2004) and Seif el Dine (2007), dealing with monotonic behaviour of fine matrix soils with inclusions.
- Using the vibration data from field monitoring, the evolution of transfer function between different track-bed layers can be analysed in order to appreciate the frequencies that transmit more energy to the track subgrade. The S-transform (or Stockwell transform) could be used to investigate how the main excited frequencies evolve during a train passage (before, during and after). This kind of analyses could illustrate the mechanical response evolution of a track-bed structure before and after an external loading.
- Further investigations are needed on the determination methods of the critical speed of a track to better define the deflection amplification with speed. As the elastic parameters of each track-bed layer can be obtained from different geotechnical tests (as DCP), the amplification curves obtained for a given track (depending on their typology and components) could help further analyse the response amplification. This analysis could be performed by modelling the track behaviour using track FEM models. An integrated track 'prospection & modelling' protocol could be useful for

railway administrators in order to improve and optimize the geotechnical solutions in maintenance, renewal or traffic upgrade operations.

- The use of geophysical methods as MASW in prospecting the elastic behaviour of track-bed layers is to be enhanced, however it is already used in track service paths to assess the track's subgrade. The MASW method could be used in an active or passive way. The mostly used nowadays in railway industry is the active way that requires an external excitation, from a hammer for instance. However, it could be also interesting to use as excitation the train moving load and identify how waves propagate through the track-bed to the sensors by identifying propagation patterns in them. Moreover, to perform passive measurements, only ambient noise is recorded, but the sensors used should be able to measure very low frequencies. In this case, the elastic parameters of track-bed could be obtained without external excitation in a continuous way. Modifications of the mechanical behaviour of the infrastructure could be instantly checked.

- The effect of soil moisture content on the energetic response of each type of load should be further explored. Given the importance of moisture content in permanent deformation production, it is interesting to determine the relationship between the moisture content and the permanent strain. This relationship would help in the determination of the track degradation rate.

- The digitalization of railway infrastructure is also one of the main points to be improved in the near future. Nowadays, the railway network (conventional and high speed) is controlled in a discrete way. The track monitoring frequency is higher for highly used lines, with discrete in time track levelling measurements every two weeks (Mauzin) which seems to be a very low rate. In order to enrich the recorded information about the global track mechanical state at every monitored point and to reinforce the railway network preventive maintenance, a new monitoring system using vibration records on surface (sleepers for instance) should be developed to assess mechanical parameters able to reveal the 'track element failures' or a 'variation of the response trend'. These mechanical parameters are complementary data to the longitudinal levelling and other track surveillance data (drones for example). All the data obtained from different types of measurement can be correlated between them in order to better determine the possible causes of track deterioration or define which track elements works better for each situation. The selection of the measuring points will depend mainly on the longitudinal variation of the global stiffness and the track

elements variation (change in sleeper types, transition zone, bridge, tunnel …). Moreover, as each sensor is also related to the characteristics of the monitored position (sleeper typology and year of installation, rail typology and year of installation, subgrade soil, fastening system, rail pads, …), correlations of the track mechanical performance due to different track elements or mechanical state situations can be detected (big data analysis). Therefore, the installation of this monitoring system into an entire network could be considered as a data mining operation. Consequently, a better knowledge of the track behaviour, due to the mechanical performance of each element (performing mechanical behaviour correlations), can be analysed in the scale of an entire network. This kind of measurements will also greatly increase the control frequency of the track status, providing quasi-continuous information of the infrastructure mechanical behaviour.

- A monitoring network system should be developed to automatically identify the zones where larger energetic responses are developed for equivalent traffic loads and the most susceptible sites to be damaged by the traffic loadings. A quantitative estimation of the aggressiveness of each train could be used by the railway administrators to adjust the toll fares to be applied to the operation companies. In addition, it can also depend on the track or rolling stock mechanical state. Changes of energetic response under equivalent loadings can be related for example to changes in track stiffness or to the wheel/rail contact.

REFERENCES

AASHTO. (2002). *American Association of State Highway and Transportation Officials. Guide for design of new and rehabilitated pavement structures*. Washington DC.

Adam, D., Kopf, F., and Adam, C. (2003). *Der dynamische Lastplattenversuch mit dem Leichten Fallgewichtsgerät – Theoretische und experimentelle Untersuchungen. Bauingenieur, Band 79*. Springer, Düsseldorf.

ADIF. (2005). *Supertrack. Final Report. Adif & Cedex Final Report – Instrumentation, Monitoring And Physical Modeling Of High-Speed Line*. Madrid.

AFNOR. (1992a). *NF P94-057 - Sols: Reconnaissance et essais - Analyse granulométrique des sols - Méthode par sédimentation.*

AFNOR. (1992b). *NF P11-300 - Classification des matériaux utilisables dans la construction des remblais et des couches de forme d'infrastructures routières.*

AFNOR. (1993). *NF P94-051 - Sols: Reconnaissance et essais - Détermination des limites d'Atterberg - Limite de liquidité de la coupelle et limite de plasticité au rouleau.*

AFNOR. (1994). *NF P94-074 - Sols: Reconnaisance et essais - Essais à l'appareil triaxial de révolution.*

AFNOR. (1996). *NF P94-056 - Sols: Reconnaissance et essais - Analyse granulométrique des sols - Méthode par tamisage à sec après lavage.*

AFNOR. (1999). *NF P94-093 - Sols: Reconnaissance et essais - Détermination des références de compactage d'un matériau.*

AFNOR. (2002). *NF P94-425 - Roches: Détermination du module de Young et du coefficient de Poisson.*

AFNOR. (2003). *NF EN 13450. Granulats pour ballast de voies ferrées*. France.

AFNOR. (2004). *Mélanges avec ou sans liant hydraulique - Partie 7: Essai triaxial sous charge cyclique pour mélanges sans liant hydraulique*. Paris (France).

AFNOR. (2010). *NF EN 1097-2. Essais pour déterminer les caractéristiques mécaniques et physiques des granulats - partie 2: méthodes pour la détermination de la résistance à la fragmentation*. France.

AFNOR. (2011). *NF EN 1097-1. Essais pour déterminer les caractéristiques mécaniques et physiques des granulats - partie 1: détermination de la résistance à l'usure (micro-deval)*. France.

Alias, J. (1984). *La voie ferrée – Techniques de construction et d'entretien*. Eyrolles, Paris

(France).

Alias, J. (1986). "Characteristics of wave formation in rails." *Rail International*, 17(11), 17–23.

Allaart, A. P. (1992). "Design principles for flexible pavements." TU Delft.

Al-Shaer, A. (2006). "Analyse des déformations permanentes des voies ferrées ballastées - Approche dynamique." Ecole Nationale des Ponts et Chaussées.

Al-Shaer, A., Duhamel, D., Sab, K., Foret, G., and Schmitt, L. (2008). "Experimental settlement and dynamic behavior of a portion of ballasted railway track under high speed trains." *Journal of Sound and Vibration*, 316(1-5), 211–233.

Alves Costa, P., Calçada, R., Silva Cardoso, A., and Bodare, A. (2010). "Influence of soil non-linearity on the dynamic response of high-speed railway tracks." *Soil Dynamics and Earthquake Engineering*, 30(4), 221–235.

Alves Costa, P., Colaço, A., Calçada, R., and Cardoso, A. S. (2015). "Critical speed of railway tracks. Detailed and simplified approaches." *Transportation Geotechnics*, Elsevier Ltd, 2, 30–46.

Alves Fernandes, V. (2014). "Numerical Analysis of Nonlinear Soil Behavior and Heterogeneity Effects on Railway Track Response." Ecole Centrale Paris.

Amini, F. (2003). *Potential applications of dynamic and static cone penetrometers in MDOT pavement design and construction. Final report*.

Anbazhagan, P., Indraratna, B., Rujikiatkamjorn, C., and Su, L. (2010). "Using a seismic survey to measure the shear modulus of clean and fouled ballast." *Geomechanics and Geoengineering*, 5(2), 117–126.

Andersen, L. (2002). *Wave propagation in infinite structures and media*. Aalborg University.

Andersen, L., and Nielsen, S. R. K. (2003). "Vibrations of a track caused by variation of the foundation stiffness." *Probabilistic Engineering Mechanics*, 18(2), 171–184.

Araujo, N. (2010). "High-Speed trains on ballasted railway tracks. Dynamic stress field analysis." University of Minho.

AREA. (1994). *American Railway Engineering Association. Manual For Railway Engineering*. Washington DC.

Arias, A. (1970). "A measure of earthquake intensity." *Seismic design for nuclear plants*, R. J. Hansen, ed., MIT Press, Cambridge, (MA) USA, 438–483.

ASTM. (2007). *D1883-07 Standard Test Method for CBR (California Bearing Ratio) of Laboratory-Compacted Soils*.

Auersch, L. (1994). "Wave Propagation in Layered Soil: Theoretical Solution in Wavenumber

Domain and Experimental Results of Hammer and Railway Traffic Excitation." *Journal of Sound and Vibration*, (173), 233–264.

Auersch, L. (2005). "The excitation of ground vibration by rail traffic: theory of vehicle–track–soil interaction and measurements on high-speed lines." *Journal of Sound and Vibration*, 284(1-2), 103–132.

Auersch, L. (2006). "Ground vibration due to railway traffic-The calculation of the effects of moving static loads and their experimental verification." *Journal of Sound and Vibration*, 293, 599–610.

Auersch, L. (2014). "The use and validation of measured, theoretical, and approximate point-load solutions for the prediction of train-induced vibration in homogeneous and inhomogeneous soils." *International Journal of Acoustics and Vibration*, 19(1), 52–64.

Auersch, L. (2015). "No Title." *Noise and Vibration Mitigation for Rail Transportation Systems*, Springer, Berlin, Germany, 401–408.

Aursudkij, B. (2007). "A Laboratory Study of Railway Ballast Behaviour under Traffic Loading and Tamping Maintenance." The University of Nottingham.

Aw, E. S. (2007). "Low Cost Monitoring System to Diagnose Problematic Rail Bed : Case Study at a Mud Pumping Site." Massachusetts Institute of Technology.

Banimahd, M., Woodwar, P. K., Kennedy, J., and Medero, G. M. (2012). "Behaviour of train-track interaction in stiffness transitions." *Proceedings of the ICETransport*, 165.

Barksdale, R. D. (1972). "Laboratory evaluation of rutting in base course materials." *Proceedings of the Third International Conference on Structural Design of Asphalt Pavements*, London (UK), 161–174.

De Barros, F. C. P., and Luco, J. E. (1995). "Stresses and displacements in a layered half-space for a moving line load." *Applied Mathematics and Computation*, 67(1-3), 103–134.

Bastin, R. (2005). *Development of German non-ballasted track forms*. ICE, UK.

Bayerischen Staatsministerium. (2012). *Dynamic Plate-Load Testing with the Aid of the Light Drop-Weight Tester. TP BF-StB Part B 8.3*.

Benz, M. A. (2009). "Mesures dynamiques lors du battage du pénétromètre Panda 2." Université Blaise Pascal (Clermont-Ferrand).

Bergman, L. A. (1948). *Ultrasonics and their scientific and technical applications*. Wiley, New York, USA.

Bezin, Y., Farrington, D., Penny, C., Temple, B., and Iwnicki, S. (2010). *The dynamic response of slab-track constructions and their benefit with respect to conventional*

ballasted track. Taylor & Francis, Manchester (UK).

Bian, X., Jiang, H., Cheng, C., Chen, Y., Chen, R., and Jiang, J. (2014). "Full-scale model testing on a ballastless high-speed railway under simulated train moving loads." *Soil Dynamics and Earthquake Engineering*, Elsevier, 66, 368–384.

Birmann, F. (1965). "Track Parameters, Static and Dynamic." *Proceedings of the Institution of Mechanical Engineers*, 180(6), 73–85.

Bodet, L. (2005). "Limites theoriques et experimentales de l'interpretation de la dispersion des ondes de rayleigh: Apport de la modelisation numerique et physique." Ecole Centrale de Nantes - LCPC.

Bolton, M. D., and Wilson, J. M. R. (1990). "Soil stiffness and damping." Cambridge.

Boore, D. M. (2001). "Effect of Baseline Corrections on Displacements and Response Spectra for Several Recordings of the 1999 Chi-Chi , Taiwan , Earthquake." *Bulletin of the Seismological Society of America*, 91(October), 1199–1211.

Boore, D. M. (2003). "Analog-to-Digital Conversion as a Source of Drifts in Displacements Derived from Digital Recordings of Ground Acceleration." *Bulletin of the Seismological Society of America* , 93 (5), 2017–2024.

Boore, D. M., and Bommer, J. J. (2005). "Processing of strong-motion accelerograms: needs, options and consequences." *Soil Dynamics and Earthquake Engineering*, 25(2), 93–115.

Boore, D. M., Stephens, C. D., and Joyner, W. B. (2002). "Comments on Baseline Correction of Digital Strong-Motion Data: Examples from the 1999 Hector Mine, California, Earthquake." *Bulletin of the Seismological Society of America* , 92 (4), 1543–1560.

Bourdeau, P. L. (1989). "Modeling of membrane action in a two-layer reinforced soil system." *Computers and Geotechnics*, 7(1), 19–36.

Bourdeau, P. L. (2009). "Stochastic modeling of load-induced settlement in loose granular materials." *Journal of Aerospace Engineering*, 22(1), 33–42.

Bourdeau, P. L., and Harr, M. E. (1989). "Stochastic theory of settlement of loose cohesionless soils." *Geotechnique*, 39(4), 641–654.

Bowness, D., Lock, a. C., Powrie, W., Priest, J. a., and Richards, D. J. (2007). "Monitoring the dynamic displacements of railway track." *Proceedings of the Institution of Mechanical Engineers Part F: Journal of Rail and Rapid Transit,* 221(December 2005), 13–23.

Brandl, H. (2004). "Geotechnical aspects for high-speed railways." *International Seminar on Geotechnics in Pavement and Railway Design and Construction*, Athens.

Breul, P. (1995). *Caractérisation des matériaux de remblai à l'aide de l'endoscopie et de la*

pénétration dynamique. Clermont Ferrand.

Brignoli, E. G. M., Gotti, M., and Stokoe, K. H. (1996). "Measurement of shear waves in laboratory specimens by means of piezoelectric transducers." *Geotechnical Testing Journal*, 19(4), 384–397.

Brough, M., Ghataora, G., Stirling, A., Madelin, K., Rogers, C., and Chapman, D. (2006). "Investigation of railway track subgrade. Part 2: case study." *Proceedings of the Institute of Civil Engineering Transportation*, 159(2), 83–92.

Brough, M., Stirling, A., Ghataora, G., and Madelin, K. (2003). "Evaluation of railway trackbed and formation: a case study." *NDT & E International*, 36(4), 145–156.

Brown, S. F. (1996). "Soil mechanics in pavement engineering." *Géotechnique*, 46(3), 383–426.

Burd, H. J., and Frydman, S. (1997). "Bearing capacity of plane-strain footings on layered soils." *Canadian Geotechnical Journal*, 34(2), 241–253.

Burmister, D. M. (1958). "Evaluation of pavement systems of the WASHO road test by layered system methods." *Highway Research Board*, (177), 26–54.

Cai, Y., Sun, H., and Xu, C. (2008). "Response of railway track system on poroelastic half-space soil medium subjected to a moving train load." *International Journal of Solids and Structures*, 45(18-19), 5015–5034.

Calon, N. (2011). *Influence des caractéristiques hydromécaniques des plates-formes ferroviaires sur la tenue géométrique de la voie*. Paris (France).

Calvo-Poyo, F. J. (2005). *Diseño y características de la vía ferroviaria*. Grupo Editorial Universitario, Granada.

Canou, J., Dupla, J.-C., Seif-el-Dine, B., Dinh, A.-Q., Karraz, K., and Bonnet, G. (2008). "Dispositif triaxial dynamique de grande taille pour sols et matériaux grossiers." *Journées Nationales de Géotechnique et de Géologie de l'Ingénieur JNGG'08 - Nantes*, Nantes, 8.

Cassan, M. (1988). *Les essais in-situ en mécanique de sols. Tome 1 réalisation et interpretation*. (E. Eyrolles, ed.), Paris.

Chai, G., and Roslie, N. (1998). "The Structural Response and Behavior Prediction of Subgrade Soils using Falling Weight Deflectometer in Pavement Construction." *3rd International conference on road and airfield pavement technology*.

Chaigneau, L. (2001). "Caractérisation des millieux granulaires de surface à l'aide d'un pénétromètre." Université Blaise Pascal.

Chen, R. P., Zhao, X., Bian, X. C., and Chen, Y. M. (2013). "Dynamic soil pressure and

velocity of slab track subgrade in High-Speed railway." *Advances in Environmental Vibration; Sixth International Symposium on Environmental Vibration: Prediction, Monitoring, Mitigation and Evaluation*, Shanghai.

Chen, R., Zhao, X., Wang, Z., Jiang, H., and Bian, X. (2013). "Experimental study on dynamic load magnification factor for ballastless track-subgrade of high-speed railway." *Journal of Rock Mechanics and Geotechnical Engineering*, Taibah University, 5(4), 306–311.

Cheng, C., Bian, X., Jiang, H., and Jiang, J. (2014). "Model testing on dynamic behaviors of the slab track of high-speed railway." *Proceedings of the 9th International Conference on Structural Dynamics, EURODYN 2014*, A. Cunha, E. Caetano, P. Ribeiro, and G. Müller, eds., Porto, 813–818.

Chua, K. M. (1988). "Determination of CBR and elastic modulus of soils using a portable pavement dynamic cone penetrometer." *Proceedings of the first symposium on penetration testing ISOPT-1*, Orlando, 407.

Clarke, C. W. (1957). "Track loading fundamentals." *Railway Gazette*, 106, 45–48.

Connolly, D., Giannopoulos, a., Fan, W., Woodward, P. K., and Forde, M. C. (2013). "Optimising low acoustic impedance back-fill material wave barrier dimensions to shield structures from ground borne high speed rail vibrations." *Construction and Building Materials*, Elsevier Ltd, 44, 557–564.

Connolly, D., Giannopoulos, a., and Forde, M. C. (2013). "Numerical modelling of ground borne vibrations from high speed rail lines on embankments." *Soil Dynamics and Earthquake Engineering*, Elsevier, 46, 13–19.

Connolly, D., Kouroussis, G., Woodward, P., Verlinden, O., Giannopoulos, A., and Forde, M. (2014). "Field testing and analysis of high speed rail vibrations." *Soil Dynamics and Earthquake Engineering*, Elsevier, 67, 102–118.

Connolly, D. P., Alves Costa, P., Kouroussis, G., Galvin, P., Woodward, P. K., and Laghrouche, O. (2015). "Large scale international testing of railway ground vibrations across Europe." *Soil Dynamics and Earthquake Engineering*, Elsevier, 71, 1–12.

Connolly, D. P., Kouroussis, G., Giannopoulos, a., Verlinden, O., Woodward, P. K., and Forde, M. C. (2014). "Assessment of railway vibrations using an efficient scoping model." *Soil Dynamics and Earthquake Engineering*, Elsevier, 58, 37–47.

Connolly, D. P., Kouroussis, G., Laghrouche, O., Hoc, C. L., and Forde, M. C. (2014). "Benchmarking railway vibrations - Track, vehicle, ground and building effects." *Construction and Building Materials*.

Coronado Garcia, O. (2005). "Etude du comportement mecanique de materiaux granulaires compactes non satures sous chargements cycliques."

Couvert, J. (2007). "Very high speed as a response to an objective commercial demand." *Workshop on Sustainability and Technological Development for the Railway., BCN RAIL*, Barcelona.

Cui, X., Zhang, N., Zhang, J., and Gao, Z. (2014). "In situ tests simulating traffic-load-induced settlement of alluvial silt subsoil." *Soil Dynamics and Earthquake Engineering*, Elsevier, 58, 10–20.

Cui, Y. J., Lamas-Lopez, F., Trinh, V. N., Calon, N., D'Aguiar, S. C., Dupla, J. C., Tang, A. M., Canou, J., and Robinet, A. (2014). "Investigation of interlayer soil behaviour by field monitoring." *Transportation Geotechnics*, Elsevier Ltd, 1(3), 91–105.

d'Onofrio, A., Silvestri, F., and Vinale, F. (1999). "Strain rate dependent behavior of a natural stiff clay." *Soils and Foundations*, 39(3), 69–82.

Dahlberg, T. (2003). "Railway track dynamics - a survey." Linköping University, Linköping.

Dahlberg, T. (2010). "Railway Track Stiffness Variations – Consequences and Countermeasures." *International journal of civil engineering*, 8(1), 1–12.

Degrande, G., and Lombaert, G. (2000). "High-speed train induced free field vibrations: in situ measurements and numerical modelling." *Proceedings of Wave 2000 International Workshop, wave propagation, moving load, vibration reduction*, (December), 29–41.

Degrande, G., and Schillemans, L. (2001). "Free Field Vibrations During the Passage of a Thalys High-Speed Train At Variable Speed." *Journal of Sound and Vibration*, 247(1), 131–144.

Dobry, R., and Vucetic, M. (1987). "Dynamic properties and seismic response of soft clay deposits." *International Symposium on Geotechnical Engineering of Soft Soils*, Mexico City, 51–87.

Doyle, N. F. (1980). *Railway track design: a review of current practice. Australian Government Publishing Services*, Sydney.

Duong, T. V. (2013). "Etude du comportement hydromécanique des plateformes ferroviaires anciennes en vue du renforcement par «soil-mixing»." Université Paris-Est (Marne la Vallée).

Duong, T. V., Cui, Y. J., Tang, A. M., Calon, N., and Robinet, A. (2014). "Assessment of conventional French railway sub-structure: a case study." *Bulletin of Engineering Geology and the Environment*, 1–12.

Duong, T. V., Cui, Y. J., Tang, A. M., Dupla, J. C., Canou, J., Calon, N., and Robinet, A.

(2014). "Investigating the mud pumping and interlayer creation phenomena in railway sub-structure." *Engineering Geology*, Elsevier B.V., 171, 45–58.

Duong, T. V., Tang, A. M., Cui, Y. J., Trinh, V. N., Dupla, J. C., Calon, N., Canou, J., and Robinet, A. (2013). "Effects of fines and water contents on the mechanical behavior of interlayer soil in ancient railway sub-structure." *Soils and Foundations*, 53(6), 868–878.

Duong, T. V., Trinh, V. N., Cui, Y. J., Tang, A. M., and Calon, N. (2013). "Development of a Large-Scale Infiltration Column for Studying the Hydraulic Conductivity of Unsaturated Fouled Ballast." *Geotechnical Testing Journal*, 36(1), 20120099.

Elaskar, A. (2006). *Développement d'une méthode de diagnostic et d'evaluation du potentiel des plates-formes ferroviaires. Mémoire d'ingénieur CUST*. Clermont Ferrand.

Escobar, E., Benz, M. A., Haddani, Y., Lamas-Lopez, F., Calon, N., and Costa D'Aguiar, S. (2014). "Reconnaissance dynamique des sites ferroviaires à l'aide du pénétromètre PANDA-3." *Journées Nationales de Géotechnique et de Géologie de l'Ingénieur JNGG2014*, Beauvais, 11.

Esveld, C. (2001). *Modern Railway Track, 2nd Ed. MRT Productions*. Duisburg, Germany.

Fairhurst, C. (1961). "Wave mechanics of percussive drilling." *Mine and Quarry Engineering*, (April), 169–178.

Ferreira, P. A. (2010). "Modelling and Prediction of the Dynamic Behaviour of Railway Infrastructures At Very High Speeds."

Ferreira, P. A., and López-Pita, A. (2015). "Numerical modelling of high speed train/track system for the reduction of vibration levels and maintenance needs of railway tracks." *Construction and Building Materials*, Elsevier Ltd, 79, 14–21.

Da Fonseca, A. V., Ferreira, C., and Fahey, M. (2009). "A framework interpreting bender element tests, combining time-domain and frequency-domain methods." *Geotechnical Testing Journal*, 32(2), 91–107.

Fortunato, E., Pinelo, A., and Matos Fernandes, M. (2010). "Characterization of the fouled ballast layer in the substructure of a 19th century railway track under renewal." *Soils and Foundations*, 50(1), 55–62.

Franz, O., and Nigel, Q. (2001). *Innovative Track Systems Criteria for their Selection*. Köln.

Freitas da Cunha, J. P. (2013). "Modelling of Ballasted Railway Tracks for High-Speed Trains." Universidade do Minho.

Fröhling, R. D. (1997). "Deterioration of railway track due to dynamic vehicle loading and spatially varying track stiffness." University of Pretoria.

Fryba, L. (1999). *Vibration of solids and structures under moving loads*. Thomas Telford,

London.

Galvín, P., and Domínguez, J. (2007). "Analysis of ground motion due to moving surface loads induced by high-speed trains." *Engineering Analysis with Boundary Elements*, 31(11), 931–941.

Galvín, P., and Domínguez, J. (2009). "Experimental and numerical analyses of vibrations induced by high-speed trains on the Córdoba–Málaga line." *Soil Dynamics and Earthquake Engineering*, 29(4), 641–657.

Galvín, P., Romero, a., and Domínguez, J. (2010). "Vibrations induced by HST passage on ballast and non-ballast tracks." *Soil Dynamics and Earthquake Engineering*, 30(9), 862–873.

Ganji, V., Gukunski, N., and Maher, A. (1997). "Detection of underground obstacles by SASW method – Numerical aspects." *Journal of Geotechnical and Geoenvironmental Engineering*, 123(3), 212–219.

Giannakos, K. (2004). *Actions on the railway track*. Papazissis Publ., Athens (Greece).

Giannakos, K. (2010). "Loads on Track , Ballast Fouling , and Life Cycle under Dynamic Loading in Railways." *Journal of transportation engineering - ASCE*, 136(December), 1075–1084.

Gidel, G. (2001a). "Comportement et valorisation des graves non traitées calcaires utilisées pour les assises de chaussées souples." Université de Bordeaux.

Gidel, G. (2001b). "Nouvelle approche pour l'étude des déformations permanentes des graves non traitées à l'appareil triaxial à charge.pdf." *Bulletin des Laboratoires des Ponts et Chaussées*, 233, 5–21.

Giroud, J. P., and Han, J. (2004). "Design Method for Geogrid-Reinforced Unpaved Roads. I. Development of Design Method." *Journal of Geotechnical and Geoenvironmental Engineering*, 130(8), 775–786.

Grabe, P. J., and Clayton, C. R. I. (2009). "Effects of Principal Stress Rotation on Permanent Deformation in Rail Track Foundations." *Journal of Geotechnical and Geoenvironmental Engineering*, (April), 555–566.

Haddani, Y. (2005). "Caractérisation et classification des milieux granulaires par geondoscopie." Université Blaise Pascal.

Haddani, Y., Saussine, G., Breul, P., Navarrete, M. B., and Gourves, R. (2011). "Estimation de la portance et de la raideur des plateformes ferroviaires par couplage d'essai Panda et geondoscope." *GEORAIL, Symposium international Geotechnique ferroviaire, Paris, 19-20 mai 2011*, Paris (France).

Hall, L. (2000). "Simulations and analyses of train-induced ground vibrations." Royal Institute of Technology, Stockholm, Sweden.

Hall, L. (2003). "Simulations and analyses of train-induced ground vibrations in finite element models." *Soil Dynamics and Earthquake Engineering*, 23(5), 403–413.

Hardin, B. O., and Black, W. L. (1966). "Sand stiffness under various triaxial stresses." *Journal of the Soil Mechanics and Foundations Division*, 92(2), 27–42.

Harr, M. E. (1977). *Mechanics of particulate media*. McGraw Hill, New York, USA.

Health, D. L., Waters, J. M., Shenton, M. J., and Sparrow, R. (1972). "Design of conventional rail track foundations." *ICE Proceedings*, 51(2), 251–267.

Hendry, M., Barbour, L., and Hughes, D. a. (2010). "Track displacement and energy loss in a railway embankment." *Proceedings of the ICE - Geotechnical Engineering*, 163(1), 3–12.

Hendry, M. T. (2007). "Train-induced Dynamic Response of Railway Track and Embankments on Soft Peaty." University of Saskatchewan.

Hendry, M. T. (2011). "The geomechanical behaviour of peat foundations below rail-track structures." University of Saskatchewan.

Hendry, M. T., Martin, C. D., and Barbour, S. L. (2013). "Measurement of cyclic response of railway embankments." *Canadian Geotechnical Journal*, 50(January), 1–14.

Hornych, P., Corté, J. F., and Paute, J. L. (1993). "Etude des déformations permanents sous chargements répétés de trois graves non traitées." *Bulletin des Laboratoires des Ponts et Chaussees*, 184, 77–84.

Hung, H. H., and Yang, Y. B. (2001). "Elastic waves in visco-elastic half-space generated by various vehicle loads." *Soil Dynamics and Earthquake Engineering*, 21(1), 1–17.

Indraratna, B., Ionescu, D., and Christie, D. (1998). "Shear Behaviour of Railway Ballast based on Large Scale Triaxial Testing." *Journal of Geotechnical and Geoenvironmental Engineering*, 124(May), 439–449.

Indraratna, B., Tennakoon, N., Nimbalkar, S., and Rujikiatkamjorn, C. (2013). "Behaviour of clay-fouled ballast under drained triaxial testing." *Géotechnique*, 63(5), 410–419.

Indraratna, B., Thakur, P. K., and Vinod, J. S. (2010). "Experimental and Numerical Study of Railway Ballast Behavior under Cyclic Loading." *International journal of geomechanics*, 10(August), 136–144.

Ishibashi, I., and Zhang, X. (1993). "Unified dynamic shear moduli and damping ratios of sand and clay." *Soils and Foundations*, 33(1), 182–191.

Ishihara, K. (1996). "Soil Behaviour in Earthquake Geotechnics." *Oxford Engineering*

Science Series, 46.

Ishihara, K., Yasuda, S., and Yoshida, Y. (1990). "Liquefaction-induced flow failure of embankments and residual strength of silty sands." *Soils and Foundations1*, 30(3), 69–80.

Ishikawa, T., Sekine, E., and Miura, S. (2001). "Cyclic deformation of granular material subjected to moving-wheel loads." *Canadian Geotechnical Journal*, 48, 691–703.

Ishikawa, T., Sekine, E., and Miura, S. (2011). "Cyclic deformation of granular material subjected to moving-wheel loads." *Canadian Geotechnical Journal*, 48(5), 691–703.

Iwasaki, T., Tatsuoka, F., and Takagi, Y. (1978). "Shear Moduli of Sands under Cyclic Torsional Shear Loading." *Soils and Foundations*, 18(1), 39–50.

Jacqueline, D. (2014). "Caractériser l'état de serrage du ballast par la propagation d'ondes." *Journnées Techniques Acoustique et Vibrations, Bordeaux, 5 juin 2014*, Bordeaux (France).

Jamiolkowski, M., Lanellotia, R., Marchetti, S., Nova, R., and Pasqualini, E. (1979). "Design parameters for soft clays." *Proc 7th Eur Conf Soil Mech Found Eng*, 27–57.

Kaewunruen, S., and Remennikov, a M. (2006). "Non-destructive evaluation for dynamic integrity of railway track structure." *International Conference on Structural Integrity and Failure*, (September), 294–299.

Kaewunruen, S., Remennikov, A. M., and Ave, N. (2015). "Under sleeper pads: field investigation of their role in detrimental impact mitigation." *Railway Engineering 2015*, 17.

Karl, L. (2005). "Dynamic Soil Properties out of SCPT and Bender Element Tests with Emphasis on Material Damping." Universiteit Gent (Belgium).

Karraz, K. (2008). "Comportement cyclique à long terme d un matériau granulaire modèle pour application aux infrastructures ferroviaires."

Karrech, A. (2007). "Comportement des materiaux granulaires sous vibration: Application au cas du ballast." Ecole Nationale des Ponts et Chaussees (ENPC) - Paris.

Kempfert, H. G., and Hu, Y. (1999). "Measured dynamic loading of railway underground." *Proceedings of the XI Panamerican Conference on Soil Mechanics and Geotechnicall Engineering*, Foz do Iguazu, Brazil, 5.

Kennedy, J., Woodward, P. K., Medero, G., and Banimahd, M. (2013). "Reducing railway track settlement using three-dimensional polyurethane polymer reinforcement of the ballast." *Construction and Building Materials*, Elsevier Ltd, 44, 615–625.

Kenny, J. T. (1954). "Steady-state vibrations of beam on elastic foundation for moving load."

Journal of Applied Mechanics, 76, 359–364.

Khan, Z., Cascante, G., El-Naggar, H., and Lai, C. (2009). "Evaluation of first mode of vibration, base fixity, and frequency effects in resonant- column testing." *GEOHALIFAX 2009*.

Khan, Z., El Naggar, M. H., and Cascante, G. (2011). "Frequency dependent dynamic properties from resonant column and cyclic triaxial tests." *Journal of the Franklin Institute*, Elsevier, 348(7), 1363–1376.

Kim, D. S., and Drabkin, S. (1995). "Investigation of vibration induced settlement using multifactorial experimental design." *Geotechnical Testing Journal*, 18(4), 463–471.

Kim, D.-S., and Lee, J.-S. (2000). "Propagation and attenuation characteristics of various ground vibrations." *Soil Dynamics and Earthquake Engineering*, 19(2), 115–126.

Knothe, K., and Grassie, S. L. (1993). "Knothe, Grassie - 1993 - Modelling of Railway Track and Vehicletrack Interaction at High Frequencies.pdf." *Vehicle System Dynamics*, 22, 209–262.

Knowles, R. D. (2006). "Transport shaping space: differential collapse in time–space." *Journal of Transport Geography*, 14, 407–425.

Konrad, J. M., Grenier, S., and Garnier, P. (2007). "Influence of Repeated Heavy Axle Loading on Peat Bearing Capacity." *Canadian Geotechnical Conference*, Ottawa, 1551–1558.

Kornylo, J., and Jain, V. (1974). "Two-pass recursive filter with zero phase shift." *IEEE transactions on acoustics speech and signal processing*, 22(5), 384–387.

Kouroussis, G. (2009). "Modélisation des effets vibratoires du trafic ferroviaire sur l'environnement." Polytech Mons (Belgium).

Kouroussis, G., Gazetas, G., Anastasopoulos, I., Conti, C., and Verlinden, O. (2011). "Discrete modelling of vertical track-soil coupling for vehicle-track dynamics." *Soil Dynamics and Earthquake Engineering*, Elsevier, 31(12), 1711–1723.

Kouroussis, G., Van Parys, L., Conti, C., and Verlinden, O. (2014). "Using three-dimensional finite element analysis in time domain to model railway-induced ground vibrations." *Advances in Engineering Software*, Elsevier Ltd, 70, 63–76.

Kouroussis, G., and Verlinden, O. (2015). "Prediction of railway ground vibrations: Accuracy of a coupled lumped mass model for representing the track/soil interaction." *Soil Dynamics and Earthquake Engineering*, Elsevier, 69, 220–226.

Kouroussis, G., Verlinden, O., Connolly, D. P., Fan, W., Forde, M. C., Percival, M., and Woodward, P. K. (2015). "An experimental analysis of embankment vibrations due to

high speed rail." *Railway Engineering 2015*.

Krylov, V. V. (1995). "Generation of ground vibrations by superfast trains." *Applied Acoustics*, 44(2), 149–164.

Krylov, V. V. (1996). "Vibrational impact of high-speed trains. I. Effect of track dynamics." *The Journal of the Acoustical Society of America*, 100(5), 3121–3134.

Krylov, V. V., Dawson, a. R., Heelis, M. E., and Collop, A. (2000). "Rail movement and ground waves caused by high-speed trains approaching track-soil critical velocities."

Kurzweil, L. (1972). *Dynamic Track Compliance. U.S. Department of Transportation, Transport Systems Centre, CambridMgae. , Report No. GSP-067*. Cambridge, (MA) USA.

Lam, H. F., and Wong, M. T. (2011). "Railway ballast diagnose through impact hammer test." *Procedia Engineering*, 14, 185–194.

Lamas-Lopez, F., Alves Fernandes, V., Cui, Y. J., Costa D'Aguiar, S., Calon, N., Canou, J., Dupla, J. C., Tang, A. M., and Robinet, A. (2014). "Assessment of the double integration method using accelerometers data for conventional railway platforms." *Proceedings of the Second International Conference on Railway Technology: Research, Development and Maintenance*, Ajaccio, Corsica, 19.

Lamas-Lopez, F., Cui, Y. J., Costa D'Aguiar, S., Calon, N., Robinet, A., Tang, A. M., Dupla, J. C., and Canou, J. (2015). "In-situ investigation of the behaviour of a French conventional railway platform." *Proceedings of the Transportation Research Board TRB 2015*, Washington DC.

Lamas-Lopez, F., Cui, Y. J., Dupla, J. C., Canou, J., Tang, A. M., Costa D'Aguiar, S., Calon, N., and Robinet, A. (2014). "Increasing loading frequency : effects on railways platforms materials." *Proceedings of the Second International Conference on Railway Technology: Research, Development and Maintenance*, Ajaccio, Corsica, 18.

Lamas-Lopez, F., Cui, Y. J., Dupla, J. C., Tang, A. M., Canou, J., Calon, N., and Costa D'Aguiar, S. (2015). "Effect of water content on long-term cyclic behaviour of railways platforms materials." *Proceedings of the Asia-Pacific Unsaturated Soils conference: Research & Applications*, Guilin Institute of Technology, Guilin (China), 1488–1494.

Lashine, A. K., Brown, S. F., and Pell, P. S. (1971). *Dynamic properties of soils. Rep. No. 2, Submitted to Koninklijke/Shell Laboratorium*. Nottingham (UK).

Lee, J. S., and Santamarina, J. C. (2005). "Bender Elements: Performance and Signal Interpretation." *Journal of Geotechnical and Geoenvironmental Engineering*, 131(9), 1063–1070.

Lekarp, F., and Dawson, A. (1998). "Modelling permanent deformation behaviour of unbound granular materials." *Construction and Building Materials*, 12(1), 9–18.

Lekarp, F., Isacsson, U., and Dawson, A. (2000). "State of the art.I: Resilient response of unbound aggregates." *Journal of transportation engineering - ASCE*, 3(February), 66–75.

Leong, E. C., Yeo, S. H., and Rahardjo, H. (2005). "Measuring shear wave velocity using bender elements." *Geotechnical Testing Journal*, 28(5), 488–498.

Li, D., and Selig, E. T. (1998). "Method for railroad track foundation design. II: Applications." *Journal of Geotechnical and Geoenvironmental Engineering*, 124(4), 323–329.

Li, X. S., Yang, W. L., Shen, C. K., and Wang, W. C. (1998). "Energy injecting virtual mass resonant column system." *Journal of Geotechnical and Geoenvironmental Engineering*, 124(5), 428–438.

Lichtberger, B. (2005). *Track Compendium*. Eurail Press, Hamburg.

Lim, W. L. (2004). "Mechanics of Railway Ballast Behaviour." The University of Nottingham.

Lombaert, G. (2014). *SNCF Workshop Rivas : Transmission path mitigation measures*.

Lopez-Pita, A. (2010). *Alta velocidad en el ferrocarril*. Universitat Politecnica de Catalunya. Iniciativa Digital Politecnica, Barcelona.

Lu, M., and McDowell, G. R. (2007). "The importance of modelling ballast particle shape in the discrete element method." *Granular Matter*, 9(1-2), 69–80.

Lunne, T., Robertson, P. K., and Powell, J. J. M. (1997). *Cone penetration testing in geotechnical practice*. (B. A.-H. Publishers, ed.), UK.

Madshus, C., and Kaynia, a. M. (2000). "High-Speed Railway Lines on Soft Ground: Dynamic Behaviour At Critical Train Speed." *Journal of Sound and Vibration*, 231(3), 689–701.

Martí-Henneberg, J. (2013). "European integration and national models for railway networks (1840-2010)." *Journal of Transport Geography*, 26, 126–138.

Meng, J. (2003). "The influence of loading frequency on dynamic soil properties." Georgia Institute of Technology.

Menq, F. Y. (2003). "Dynamic Properties of Sandy and Gravelly Soils." The University of Texas at Austin.

Merger, M., and Polino, M. N. (2004). *Towards a European Intermodal Transport Network: Lessons from History. A Critical Bibliography*. AHICF, Paris (France).

Mishra, D., Tutumluer, E., Boler, H., Hyslip, J. P., and Sussman, T. (2014). "Instrumentation and Performance Monitoring of Railroad Track Transitions using Multidepth Deflectometers and Strain Gauges." *93rd Annual Meeting of the Transportation Research Board*, Washington, DC.

Miura, S., Takai, H., Uchida, M., and Fukada, Y. (1998). "The mechanism of railway tracks." *Japan Railway & Transport Review*, 3, 38–45.

Moayerian, S. (2012). "Effect of Loading Frequency on Dynamic Properties of Soils Using Resonant Column." University of Waterloo.

Mok, Y. J., Sanchez-Salinero, I., Stokoe, K. H. I., and Roesset, J. M. (1988). "In situ damping measurements by crosshole seismic method. In Earthquake Engineering and Soil Dynamics II." *ASCE Special Conference*, ASCE, Park City, Utah, 305–320.

Müller-Boruttau, F. H., and Breitsamer, N. (2004). *Elastic Elements Reduce the Loads Exerted on the Permanent Way*.

Murthy, V. N. S. (2002). *Geotechnical engineering: principles and practices of soil mechanics and foundation engineering*. Marcel Dekker Press, New York, USA.

Nasreddine, K. (2004). "Effet de la rotation des contraintes sur le comportement des sols argileux." Ecole Nationale des Ponts et Chaussées.

Nielsen, J. C. O., and Igeland, a. (1995). "Vertical dynamic interaction between train and track - influence of wheel and track imperfections." *Journal of Sound and Vibration*, 187(5), 825–839.

Paderno, C. (2010). "Comportement du ballast sous l'action du bourrage et du trafic ferroviaire." Ecole Polytechnique de Lausanne.

Pappin, J. W. (1979). "Characteristics of a grnular material for pavement analysis." University of Nottingham.

Paul, B., and Hashemi, J. (1981). "Contact pressures on closely conforming elastic bodies." *Journal of Applied Mechanics*, 48(3), 543–548.

Pedro, L. S. (2004). "De l'étude du comportement mécanique de sols hétérogènes modèles à son application au cas des sols naturels." Ecole Nationale des Ponts et Chaussées (Marne la Vallée).

Pedro, L. S., Dupla, J. C., and Canou, J. (2005). "Comportement mecanique d'un sol grossier." *Revue française de geotechnique*, 112, 35–42.

Le Pen, L., Watson, G., Powrie, W., Yeo, G., Weston, P., and Roberts, C. (2014). "The behaviour of railway level crossings: Insights through field monitoring." *Transportation Geotechnics*, Elsevier Ltd, 1(4), 201–213.

293

Picoux, B., and Le Houédec, D. (2005). "Diagnosis and prediction of vibration from railway trains." *Soil Dynamics and Earthquake Engineering*, 25(12), 905–921.

Powrie, W., Yang, L. a, and Clayton, C. R. I. (2007). "Stress changes in the ground below ballasted railway track during train passage." *Proceedings of the Institution of Mechanical Engineers, Part F: Journal of Rail and Rapid Transit*, 221(2), 247–262.

Priest, J. A., and Powrie, W. (2009). "Determination of Dynamic Track Modulus from Measurement of Track Velocity during Train Passage." *Journal of Geotechnical and Geoenvironmental Engineering*, 135(November), 1732–1740.

Priest, J. A., Powrie, W., Grabe, P. J., Clayton, C. R. I., and Yang, L. (2010). "Measurements of transient ground movements below a ballasted railway line." *Géotechnique*, 60(9), 667–677.

Di Prisco, C., and Zambelli, C. (2003). "Cyclic and dynamic mechanical behaviour of granular soils: experimental evidence and constitutive modelling." *Revue française de génie civil*, 7(7), 881–910.

Profillidis, V. (1983). "La voie ferree et sa modelisation mathematique." Ecole Nationale des Ponts et Chaussées.

Profillidis, V. (2000). *Railway Engineering*. Cambridge Press.

Puffert, D. (2009). *Tracks Across Continents, Paths through History: the Economic Dynamics of Standardization in Railway Gauge*. University of Chicago Press, Chicago, IL (USA).

Quezada, J. C. (2012). "Mécanismes de tassement du ballast et sa variabilité." Université de Montpellier 2.

Raymond, G. P. (1985). "Analysis of track support and determination of track modulus." *Transportation research record*, 1022, 80–90.

Raymond, G. P. (2000). "Track and support rehabilitation for a mine company railroad." *Canadian Geotechnical Journal*, 37, 318–332.

Révol, G. (2005). *Mise au point d'une méthode de diagnostic des plates-formes SNCF, mémoire d'ingénieur CUST*. Clermont Ferrand.

Richart, F. E., Wood, R. D., and Hall, J. R. (1970). *Vibration of soils and foundations*. Prentice-Hall, New-Jersey.

Rix, G., and Meng, J. (2005). "A Non-Resonance Method for Measuring Dynamic Soil Properties." *Geotechnical Testing Journal*, 28(1), 12125.

Roth, R., and Dinhobl, G. (2008). *Across the Borders: Financing the World's Railways in the Nineteenth and Twentieth Centuries*. Ashgate, Aldershot (UK).

Rujikiatkamjorn, C., Indraratna, B., Nimbalkar, S., and Tennakoon, N. (2012). "Behaviour of

clay-fouled ballast under drained triaxial testing." *Géotechnique*, (July 2011), 1–10.

Salim, M. (2004). *Deformation and degradation aspects of ballast and constitutive modelling under cyclic loading*.

Saussine, G. (2004). "Contribution à la modelisation de granulats tridimensionnels: application au ballast." Université de Montpellier.

Sawangsuriya, A. (2012). "Wave Propagation Methods for Determining Stiffness of Geomaterials." *"Wave Processes in Classical and New Solids,"* 44.

Sawangsuriya, A., Bosscher, P. J., and Edil, T. B. (2005). "Alternative testing techniques for modulus of pavement bases and subgrades." *Proceedings of the 13th Annual Great Lakes Geotechnical and Geoenvironmental Engineering Conference, Geotechnical Applications for Transportation Infrastructure, ASCE, Geotechnical Practice Publication, No.3*, Milwaukee (WI), 108–121.

Seif-el-Dine, B. (2007). "Etude du comportement mécanique de sols grossiers à matrice." Ecole Nationale des Ponts et Chaussées (Marne la Vallée).

Selig, E. T., and Waters, J. M. (1994). *Track Geotechnology and Substructure Management*. Thomas Telford, Derby, England.

Semblat, J., Duval, A., and Dangla, P. (2000). "Numerical analysis of seismic wave amplification in Nice (France) and comparisons with experiments." *Soil Dynamics and Earthquake Engineering*, 19, 347–362.

Sergeev, I. J. (1969). "The application of probability - process equations to the theory of stress distibution in non-cohesive soil foundation beds (discussion)." *Soil Mechanics and Foundation Engineering*, 6(2), 84–88.

SETRA. (1992a). *Guide technique GTR : Réalisation des remblais et des couches de forme. Fascicule 1 – Principes généraux. LCPC*.

SETRA. (1992b). *Guide technique GTR : Réalisation des remblais et des couches de forme. Fascicule 2 – Annexes techniques. LCPC*.

Sharifipour, M. (2006). "Caractérisation des sols par propagation d'ondes: analyse critique de la technique des bender extender elements." Ecole Centrale de Nantes.

Sheng, X. (1999). "Ground vibration generated by a load moving along a railway track." *Journal of Sound and Vibration*, 228(1), 129–156.

Sheng, X., Jones, C. J. C., and Thompson, D. J. (2004). "A theoretical model for ground vibration from trains generated by vertical track irregularities." 272, 937–965.

Shenton, M. J. (1985). "Ballast deformation and track deterioration." *Proceedings of the conference on track technology*, Nottingham (UK), 253–265.

Sitharam, T. G., and Anbazhagan, P. (2006). "Measurements of Dynamic Properties and Soil Profiling Using Multichannel Analysis of Surface Waves." *Invited Keynote in 4th Karl Terzaghi Memorial Workshops*, Madgaon, Goa, 6.

SNCF. (1995). *ST N° 590B : Spécification technique pour la fourniture des granulats utilisés pour la réalisation et l'entretien des voies ferrées*. Paris (France).

SNCF. (1996a). *IN0259 : Conception, réalisation et entretien: des ouvrages de drainage et l'écoulement, des structure d'assise et des plates-formes. Référentiel Infrastructure SNCF*. Paris (France).

SNCF. (1996b). *IN0260 : Dimensionnement des structures d'assise pour la construction et la réfection des voies ferrées. Référentiel Infrastructure SNCF*.

SNCF. (2005). *Track measurements in Beugnâtre*.

SNCF. (2007). *IN2542 Référentiel Infrastructure. Relèvement de la vitesse limite des circulations et cas assimilés. Dispositions techniques à respecter*.

SNCF. (2009). *Mesures de pression sous ballast*.

SNCF-INFRA. (2009). *R-2520-2009-1. Mesures d'acceleration verticales dans la plate-forme*.

SNCF-INFRA. (2011). *Référentiel Infrastructure -Procédure IN4103 (in French)*. Paris (France).

Sol-Sánchez, M., Moreno-Navarro, F., and Rubio-Gámez, M. C. (2015). "The use of elastic elements in railway tracks: A state of the art review." *Construction and Building Materials*, 75, 293–305.

Stewart, H. E. (1986). "Permanent strains from cyclic Variable-Amplitude loadings." *Journal of Geotechnical Engineering*, 112(6), 646–660.

Stokoe II, K. H., Wright, G. W., James, A. B., and Jose, M. R. (1994). *Characterization of geotechnical sites by SASW method. In: R.D. Woods, ed. Geophysical characterization of sites: ISSMFE Technical Committee #10*. Oxford Publishers, New Delhi (India).

Studer, J. A., and Koller, M. G. (1997). *Bodendynamik; Grundlagen, Kennziffern, Probleme*. Springer, Berlin, Germany.

Su, L., Indraratna, B., and Rujikiatkamjorn, C. (2011). "Non-destructive assessment of rail track condition using ground penetrating radar." *13th International Conference of the IACMAG*, 478 – 482.

Su, L., Indraratna, B., Rujikiatkamjorn, C., and Christie, D. (2011). "Laboratory and field testing study on non-destructive assessment of ballast conditions using ground penetrating radar." *9th World Congress on Railway Reserach - May 22-26*.

Suiker, A. S. J. (2005). *Static and cyclic triaxial testing of coarse-grained and fine-grained granular materials*. Delft.

Suiker, A. S. J., Selig, E. T., and Frenkel, R. (2005). "Static and Cyclic Triaxial Testing of Ballast and Subballast." *Journal of Geotechnical and Geoenvironmental Engineering*, (June), 771–783.

Sussmann, T. R., Selig, E. T., and Hyslip, J. P. (2003). "Railway track condition indicators from ground penetrating radar." *NDT and E International*, 157–167.

Sweere, G. T. H. (1990). "Unbound Granular Bases for Roads." TU Delft.

Sy, A., and Campanella, R. G. (1991). "An alternative method of measurement SPT Energy." *Proceedings of the 2nd International conference on recent advances in Geotechnical Engineering and soils dynamics*, 499–505.

Takemiya, H. (2003). "Simulation of track–ground vibrations due to a high-speed train: the case of X-2000 at Ledsgard." *Journal of Sound and Vibration*, 261(3), 503–526.

Takemiya, H., and Bian, X. (2005). "Substructure Simulation of Inhomogeneous Track and Layered Ground Dynamic Interaction under Train Passage." *Journal of Engineering Mechanics*, 131(7), 699–711.

Thompson, D. J., and Jones, C. J. C. (2006). *Noise and vibration from railway vehicles. In: Iwnicki S, editor. Handbook of railway vehicle dynamics*. CRC Press, Taylor & Francis.

Timoshenko, S. P. (1926). "Method of Analysis of Statical and Dynamical Stresses in Rail." *2nd International Conference of Applied Mechanics*, Zurich (Switzerland), 407–418.

Timoshenko, S. P., and Goodier, J. N. (1951). *Theory of Elasticity*. McGraw Hill, New York, USA.

Tokimatsu, K. (1995). "Geotechnical site characterization using surface waves." *Proceedings of the 1st International Conference on Earthquake Geotechnical Engineering*, Tokyo (Japan), 36.

Trinh, V. N. (2011). "Comportement hydromécanique des matériaux constitutifs de plateformes ferroviaires anciennes." Université Paris-Est (Marne la Vallée).

Trinh, V. N., Tang, A. M., Cui, Y.-J., Dupla, J.-C., Canou, J., Calon, N., Lambert, L., Robinet, A., and Schoen, O. (2012). "Mechanical characterisation of the fouled ballast in ancient railway track substructure by large-scale triaxial tests." *Soils and Foundations*, Elsevier, 52(3), 511–523.

UIC. (2009). *UIC Code 714 R. Classification of lines for the purpose of track maintenance*. Paris.

Ulaby, F. T. (1997). *Fundamentals of applied electromagnetics*. Prentice-Hall, Upper Saddle

River, NJ.

Varandas, J. N. (2013). "Long-Term Behaviour of Railway Transitions Under Dynamic Loading."

Vega, J., Fraile, a., Alarcon, E., and Hermanns, L. (2012). "Dynamic response of underpasses for high-speed train lines." *Journal of Sound and Vibration*, Elsevier, 331(23), 5125–5140.

Vennapusa, P. K. R., and White, D. J. (2009). "Comparison of light weight deflectometer measurements for pavement foundation materials." *ASTM Geotechnical Testing Journal*, 32(3), 239–251.

Viggiani, G., and Atkinson, J. H. (1995a). "Stiffness of Fine-Grained Soil at Very Small Strains." *Géotechnique*, 45(2), 249–265.

Viggiani, G., and Atkinson, J. H. (1995b). "Interpretation of Bender Element Tests." *Géotechnique*, 45(1), 149–154.

Vorster, D., and Gräbe, P. (2013). "The use of ground-penetrating radar to develop a track substructure characterisation model." *Journal of the South African Institution of Civil …*, 55(3), 69–78.

Wilson, J. M. R., and Bolton, M. D. (1989). "An experimental and theoretical comparison between static and dynamic torsional soil tests." *Géotechnique*, 39(4), 585–599.

Wolf, J. (1985). *Dynamic soil–structure interaction*. Prentice-Hall, Englewood Cliffs, New Jersey.

Wolff, H., and Visser, A. T. (1994). "Incorporating elasto-plasticity in granular layer pavement design." *Proceedings of the Institution of Civil Engineers: Transport*, 105(4), 259–272.

Wong, R. C. K., Thomson, P. R., and Choi, E. S. C. (2006). "In Situ Pore Pressure Responses of Native Peat and Soil under Train Load: A Case Study." *Journal of Geotechnical and Geoenvironmental Engineering*, 132(10), 1360–1369.

Woodward, P. K., Kennedy, J., Laghrouche, O., Connolly, D. P., and Medero, G. (2014). "Study of railway track stiffness modification by polyurethane reinforcement of the ballast." *Transportation Geotechnics*, Elsevier Ltd.

Xu, X., Jiang, H. G., Bian, X. C., and Chen, Y. M. (2013). "Accumulative settlement of saturated silt subgrade under cyclic traffic-loading." *Advances in Environmental Vibration; Sixth International Symposium on Environmental Vibration: Prediction, Monitoring, Mitigation and Evaluation*, Shanghai, 493–501.

Yang, J., Li, J. B., and Lin, G. (2006). "A simple approach to integration of acceleration data

for dynamic soil–structure interaction analysis." *Soil Dynamics and Earthquake Engineering*, 26(8), 725–734.

Zeng, C., Xia, J., Miller, R. D., Tsoflias, G. P., and Wang, Z. (2012). "Numerical investigation of MASW applications in presence of surface topography." *Journal of Applied Geophysics*, Elsevier B.V., 84, 52–60.

Zhai, W. M., Wang, K. Y., and Lin, J. H. (2004). "Modelling and experiment of railway ballast vibrations." *Journal of Sound and Vibration*, 270(4-5), 673–683.

Zhan, Y. X., and Jiang, G. L. (2010). "Study of dynamic characteristics of soil subgrade bed for ballastless track." *Journal of Rock and Soil Mechanics*, 31(Feb.), 392–396.

Zhou, S. (1997). "Caractérisation des sols de surface à l'aide du pénétromètre dynamique léger à energie variable type PANDA." Université Blaise Pascal - Clermont -Ferrand.

Zuada-Coelho, B. E. (2011). "Dynamics of railway transition zones in soft soils." TU Delft.